The Influence of Bed Roughness on the Dynamics of Gravity Currents

Rachel Louise Batt

Submitted in accordance with the requirements for the degree of
Doctor of Philosophy

The University of Leeds

Centre for Computational Fluid Dynamics, School of Applied Mathematics and School of Earth and Environment

September 2008

PAGE NUMBERING AS ORIGINAL

BEST COPY AVAILABLE.

VARIABLE PRINT QUALITY

Acknowledgements

Derek Ingham and Lionel Elliott have supported and encouraged me throughout these years and I owe many many thanks to them for their wisdom and guidance (and patience!). I would also like to thank Jeff Peakall for interesting discussions and his unerring enthusiasm and Gareth Keevil for help in the lab.

It is impossible to acknowledge on one page the support, advice and above all friendship that I have been lucky enough to find in the last four years. It has been a privilege to work and play amongst such outstandingly clever and generous people. In acknowledgement that I have a tendency towards 'verbal diarrhoea' I'll try and be concise! I would like to thank...

Domi Tobler and Ellie John for being part of 'the girls' and for red wine, mojitos, erdinger, stella, coffee, tea, the Clock, Madrid and other trips to come, but above all for good times and Wensleydale and fruit cake; Vu and Heather for your company in the office and putting up with my addiction to tea! And Phil Kellman, our honorary office mate, for sharing tea times, garibaldi and climbing. Ransome Corney, Mat Roberts, Anika Austen and Jo Walker for looking after me at the beginning, great food and good hiking! Franzi Schrodt and Susanna Lutman for hugs and support and girly nights in; Matt Box and Al Young for company round the camp fire and for saving me from climbing with Dave; Andrea Lewis for her continued warmth, support and generosity. For putting up with me chattering away and above all for her company on the crag and hill, now we can start ticking that wish list!

Rach Spraggs should be given a medal for what she's put up with! Without her support, shoulder(!), loyalty and selflessness this would have been a lot harder. Instead she, and the unconditional support (licking) of hug on four legs Dex, have got me through it smiling. Thanks Rach.

James, thank you with all my heart. The future looks exciting.

None of this would have been possible without the nurture, support and love of my family. I cannot even begin to write the thanks I owe to my Mum, so I will simply say 'Thank You'.

Finally I must acknowledge that ever-perplexing question, that I will continue to research exhaustively: How do people survive without tea?

Abstract

To date the influence of bed roughness on the propagation and dynamics of gravity currents has been largely neglected. A new physical modelling dataset has been compiled, which details the fundamental affects of several bed roughnesses on lock-release gravity currents. Five bed configurations were chosen encompassing 'grain' and 'form' type elements at a range of spacings. 1%, 5% and 10% initial density excesses were studied and the effect of removing the buoyant ambient fluid between the elements examined. Observations due to changing the current depth relative to the element height were also made. Ultrasonic Doppler velocimetry profiling (UDVP) and video capture techniques were used to analyse streamwise and vertical velocity structures and the affects on the front speed and distance travelled by the current. A 1D depth-averaged model solves modified 2-layer shallow water equations using the method of characteristics to obtain temporal velocity and depth evolution for a current under the influence of a general roughness quantity. 2D and 3D depth-resolved CFD simulations use the commercial software FLUENT to solve the RANS equations and transport of a scalar for the dense current with the RNG $k-\varepsilon$ turbulence model. The CFD predictions were well validated by the new experimental dataset and provide supplementary predictions of concentration, lateral motion and activity in the vicinity of the roughness elements. Comparison of 2D and 3D models resulted in the conclusion that the 3D model is vital for accurate simulation of internal dynamics of gravity current propagation over beam type bed roughness. In general, the distance that the front travels decreases with any bed roughness present. This reduction increases with element spacing. The streamwise mean velocity profiles show a reduced velocity maximum further from the bed. Decreased entrainment results from breakdown of larger billows. Also observed is a thicker current, a rounder profile and a shorter, diluted head. Areas of increased vertical motion within the current, associated with decreased horizontal motion are observed, indicative of ejections of ambient fluid from between the elements. The presence of this fluid is found to contribute to $\approx 50\%$ of the current retardation. There are also similarities with the effects of bed roughness in open channel and pipe flows, most notably there is a critical element spacing ($w/k_r \approx 7$) where the effects of roughness are greatest (where w is element spacing and k_r is element height). The experimental and numerical results demonstrate that the application of existing models that rely on experimental validation with smooth beds to situations where a rough boundary is present may lead to significant errors.

Contents

List of Figures

List of Tables

Nomenclature

Greek

α	resistance coefficient at the bed
α_b	buoyancy flux reduction factor
α_k, α_ε	inverse effective Prandtl numbers for k and ε
β	empirical constant used in the front condition
β_0	turbulence model constant
γ	resistance coefficient at the fluid interface
Γ	curve in the method of characteristics where values are known
$\delta_{i,j}$	Kroneker delta
δx	cell length
δy	cell width
δz	cell height
δt	timestep
Δ	bedform height
$\Delta\rho$	density ratio $(\rho_1 - \rho_2)/\rho_1$
ΔB	velocity shift due to bed roughness
ε	turbulence eddy diffusivity
η	positive characteristic
η_0	turbulence model constant
κ	von Karman constant, 0.4
$\bar{\kappa}$	a form of the resistance coefficient
κ_s	laminar coefficient of diffusivity of salt in water
κ_t	turbulent coefficient of diffusivity of salt in water
λ	wavelength
λ_+	gradient of positive characteristic curve
λ_-	gradient of negative characteristic curve
λ_b	bedform length
μ	molecular or dynamic viscosity
μ_{eff}	effective molecular viscosity
μ_t	turbulence viscosity
ν	kinematic viscosity
$\hat{\nu}$	ratio of effective molecular viscosity to molecular viscosity
ν_{eff}	effective kinematic viscosity
ν_t	eddy viscosity
ξ	negative characteristic
ϖ	order of the numerical method
ϖ_0	finite differencing method (forward/backward/central)
ρ	density
ρ_1	density of the gravity current
ρ_2	density of the ambient fluid

ρ_g	as for ρ_1
ρ_w	as for ρ_2
ϱ	grid refinement ratio
σ	resistance coefficient at the fixed lid
τ_w	wall shear stress
$\bar{\bar{\tau}}$	stress tensor
ϕ	numerical solution for a general variable
ϕ_*	exact solution for a general variable
ϕ_1, ϕ_2	numerical solution for a fine and course mesh
φ	scalar or fluid concentration
Ψ	ratio of bedform height to bedform length, Δ/λ_b
ω	turbulence eddy frequency

Roman(Upper Case)

A, B, C	coefficient terms used in simultaneous PDE analysis
A',B'...F'	functions used in the method of characteristics
A_1	actual fractional fine mesh error
$\bar{A}$	matrix of coefficients in the method of characteristics
C	concentration
C''	resistance coefficient
C_μ, C_ν, C_τ	turbulence model constants
C_1, C_2, C_3	constants with values zero or unity
$C_{1\varepsilon}$, $C_{1\varepsilon}$	turbulence model constants
C_H	Chezy resistance coefficient
C'_H	modified Chezy resistance coefficient
D_*	dimensionless constant
D_{90}	diameter of at least 90% of the grains in a grain sample
D_{in}	inside diameter of a pipe
E''	function used in the method of characteristics
$E_{\eta,\xi}$, $F_{\eta,\xi}$, $G_{\eta,\xi}$	coefficients on positive or negative characteristic curves
E_1	estimated fractional fine mesh error, or ordered error estimator
F	location of the free surface
F_1, F_2	flow forces upstream and downstream
F_i	additional sources in the Navier-Stokes equations
Fr	Froude number
Fr_{da}	depth-averaged Froude number
G_k	production of mean TKE
G_b	production of turbulence due to buoyancy
H	constant total height of ambient and gravity current fluids
H'	laboratory tank height
H_{rad}	hydraulic radius
I, J	locations where variable values are known
I_t	turbulence intensity
K, K_1	locations where variable values are unknown
L	tank length or characteristic length
M_t	turbulent Mach number
O	stagnation point
P, Q,...,T	coefficient terms of partial differential equations
P', Q',...,T'	coefficient terms of partial differential equations
Pr_t	turbulent Prandtl number

R	reattachment length (figure 1.8)
R^{con}	unscaled continuity residual
R_n^{con}	continuity residual of the n^{th} time step
R_{1-5}^{con}	largest continuity residual of the first five time steps
R^u, R^v, R^w, R^C	unscaled residuals of u, v, w and C
$R_1 ... R_6$	flow regions in diagrams of the characteristic curves
R_ε	additional function in RNG $k-\varepsilon$ turbulence model
Re	Reynolds number
Re_{da}	depth-averaged Reynolds number
Ri	Richardson number
S_0	channel longitudinal slope
S_k, S_ε	user-defined source terms for k and ε
S_f	channel friction slope
$S_{i,j}$	mean rate of strain tensor
Sc	Schmidt number
U	Characteristic velocity
V1, V2, V3	location of vortices (figure 1.8)
W	tank width
X	spread rate
Y_m	representative of dilation dissipation

Roman(Lower Case)

a, b	simplifying functions used in the method of characteristics
a_s	speed of sound
a_{nb}	influence coefficients of neighbouring cells
a_p	influence coefficient of cell p
c	column vector
c_s	roughness constant
d	rib or beam width
e	difference in fine and coarse solutions relative to fine mesh
f	friction factor
$\bar{f}$	rough terms in PDE's
f_*	function of x and t
f_0	dimensionless Darcy-Weisbach friction factor
f_1, f_2, f_3	friction factors
f_i	i^{th} derivative the Fortran NAG routine D02AGF
f_{int}	friction factor at the fluid interface
g	acceleration due to gravity
g'	acceleration due to reduced gravity
g_1, $g_2 ...$	general terms used in Richardson extrapolation
g_s'	acceleration due to reduced gravity (Peters, 1999)
g_s''	acceleration due to reduced gravity (Peters, 1999)
h	characteristic height
h_0	initial height of current fluid
h_1	height of theoretical gravity current
h_2	height of theoretical ambient fluid
h_{da}	depth-averaged gravity current height
h_d	dune height
h_f	height of the gravity current front
h_h	head height

h_n	nose height
h_R	rib or beam height
k	turbulence kinetic energy
k'	viscous dissipation factor
$\tilde{k}$	constant of proportionality
k_r	bed roughness height
k_s	equivalent roughness height
k_s^+	dimensionless roughness height
$k_{s,grain}$, $k_{s,form}$	equivalent roughness height of grain and form components
m	mass
n	no. of observations or ordinary differential equations
n_1	no. of unknown parameters in Fortran NAG routine D02AGF
n_M	Manning n, resistance coefficient
p	pressure
p_0	pressure at the fluid interface
p_1	gravity current pressure
p_2	ambient fluid pressure
p_f	pressure force
q_1, q_2,...,q_{n_1}	unknown parameters in Fortran NAG routine D02AGF
r	ratio of ambient fluid to gravity current densities, ρ_2/ρ_1
r_m	match point in Fortran NAG routine D02AGF
s	pitch
t	time
t_0	initial time or characteristic time, $x_0/\sqrt{g'h_0}$
t_{int}	t intercept
u	velocity component in x-direction
$\bar{u}$	average velocity in x-direction
$\bar{u}_{max}$	maximum average velocity in x-direction
u'	fluctuating velocity in x-direction
u_1	theoretical streamwise velocity of the gravity current
u_1'	theoretical velocity below a cavity downstream
u_2	theoretical streamwise velocity of the ambient fluid
u_1c	constant upstream velocity in bottom layer
$u_1'c$	constant downstream velocity in bottom layer
u_*, u_τ	shear velocity
u_{da}	depth-averaged streamwise velocity in the gravity current head
u_f	streamwise velocity at the gravity current front
u_i	velocity component in i^{th} coordinate direction
u_{max}, u_{min}	maximum or minimum streamwise velocity
u_{nb}	horizontal velocity component in neighbouring cells
u_p	horizontal velocity component in cell p
u_rms	root mean square value of the horizontal velocity component
v	velocity component in y-direction
v_{max}, v_{min}	maximum or minimum vertical velocity
w	velocity component in z-direction *or* spacing between roughness elements
x, y, z	coordinate variables
x_0	initial front position (lock length)
x_*	current length when buoyancy-viscous phase begins
x_f	location of the gravity current front or current length
x_i	i^{th} coordinate variable
x_s	current length when slowing begins
y^+	dimensionless wall unit

Superscripts

A, B	coefficients of uniform flow
C	denoting concentration
u, v, w	denoting velocity components in x, y, z directions
con	denoting the continuity equation

Subscripts

0	initial value
η, ξ	of the positive and negative characteristics, respectively
da	depth-averaged
f	front
nb	neighbouring cells
p	cell number
$grain$, $form$	components of bed roughness
i, j	coordinate direction 1, 2 or 3
max, min	maximum or minimum of variable
rms	root mean square value of the variable
I, J	location with known variable value
K	location with unknown variable value

Acronyms

CFD	Computational fluid dynamics
CFL	Courant-Friedrichs-Lewis (numerical stability condition)
DNS	Direct numerical simulation
GCI	Grid convergence index
HTAG	Heavier than air gas
LDA	Laser Doppler anemometry
LES	Large-eddy simulation
LIF	Lasar induced fluorescence
ODE	Ordinary differential equation
PDE	Partial differential equation
PIV	Particle image velocimetry
PTV	Particle tracking velocimetry
RANS	Reynolds-Averaged Navier-Stokes
RNG	Renormalisation group ($k - \varepsilon$ turbulence model)
UDF	User-defined function
UDS	User-defined scalar
UDVP	Ultrasonic Doppler velocimetry profiling
VOF	Volume of fluid

Chapter 1

Introduction

1.1 The significance of gravity currents and bed roughness

Gravity currents, or density currents, occur due to the effect of the gravitational force on two bodies of fluid where differences in the fluid density resulting, for example, from concentration or temperature discontinuities, cause flow propagation to occur in a direction normal to that of gravity. The phenomena can occur with liquids or gases moving into less dense liquids or gases that are in motion or quiescent. The density difference need only be a few percent but can be much greater. Gravity currents can be invisible, propagating as a cold front in an exchange with warm air. Often they occur in particulate form as 'turbidity' currents. For example in landslides, the flow is not made up of one uniform fluid, instead it carries thousands of small and large particles in suspension. The implications can be substantial, for example, submarine landslides on ocean floors can gouge large channels in the seabed and impact on the human environment by damaging submarine infrastructure. Avalanches, where the density difference is generated by thousands of tiny particles of powder-snow suspended in the air, are another example of a gravity current. Again they can present a serious hazard to the human environment. Man-made gravity currents are observed in industrial situations, such as, the accidental release of dense gas which might be poisonous or explosive; and oil spills on the sea (Hoult, 1972; Fannelop and Waldman, 1972) both of which result in severe and potentially wide-spread environmental impact. The modelling and subsequent increased understanding of these phenomena clearly has significant benefits, be it for human or environmental safety reasons or the efficient management of various scenarios natural and man-made.

We need only consider the foregoing examples to understand the relevance of investigating the influence of bed roughness on gravity currents. The sea floor is not smooth, an avalanche path is rarely so, more typically encompassing mountainsides, forests and, in a worst case scenario, residential areas. A cold front can occur over a variety of terrain. If a heavier than air gas is released from an industrial setting, there is a high possibility that this will be in or near an urban environment so the surface that it interacts with will not be smooth. A number of questions arise: What is the effect of this surface? Does it have an effect at all? Will it slow the current or speed it up? Will particulate currents behave differently? What if the roughness is sparse or what if it is dense? And so on. To investigate and increase understanding of the various and complex fundamental flow dynamics of gravity currents the general approach has been to simplify the situation by assuming that the bed is essentially smooth. The present investigation does not intend to prove that these studies are in error, but to extend them by asking: What influence does bed roughness have on the dynamics of gravity currents?

1.2 Definition of bed roughness

Bed roughness is classified in the present study by arrays of elements that occur at intervals such that an adjacent element influences the gravity current before the flow dynamics have fully adjusted to the effects of the previous element and complete flow blocking does not occur, i.e. the elements are not considered stand alone obstacles. For example, a cityscape including tall and low buildings over which a sea breeze is propagating may be described as bed roughness while one single building should not.

1.3 Literature review

This section is intended to provide a general overview of the physical attributes of gravity currents and a discussion of known effects of different types of roughness and investigations that have been performed to date. Reviews of specific methods, theoretical and experimental, can be found at the start of the corresponding chapters.

An excellent general compilation of fundamental knowledge on gravity currents can be found in Simpson (1997) or summarised in Huppert (2006). Moodie (2002) gives a summary of some different methods of theoretical models and highlights restrictions on the theory. The most detailed study of bed roughness effects on gravity currents

to date is Peters and Venart (2000), and Jimenez (2004) gives a review of turbulent flows over rough walls for open channels. It must be highlighted that the fundamental characterisation of bed roughness and its effects is still a highly active area of research in pipe and channel flows, despite several decades of work. The complexities of natural roughness have proven to be extremely difficult to characterise (Rouse, 1965; Yen, 2002).

A substantial amount of literature concerns the development of models for particle-driven or turbidity currents. Since the methodology of the present study involves non-particulate, saline currents, this review does not specifically cover previous studies in this area. However, an overview of the dynamics and structure of particle-driven and turbidity currents can be found in Kneller and Buckee (2000).

1.3.1 The anatomy of gravity currents

Characteristic gravity current shape

The anatomy of a gravity current is particularly complex. The primary component of motion is away from the point of release and parallel to the bed. At the leading edge, a frontal zone forms which, creates a sharp dividing interface between the two fluids. The basic shape of the current has been discussed and developed through observations in many studies. Von Karman (1940) proposed a model, as shown in figure 1.1, with theory based on Bernoulli's equation applied to steady, irrotational flows. However, this theory was rejected by Benjamin (1968) due to the assumption of conservation of energy required for such derivations being unjustifiable, thus the wholly irrotational flow required for a profile, such as shown in figure 1.1, is not possible. Von Karman (1940) did note the existence of a distortion in the interface of the real flow profile. He also correctly established the existence of a 'head' at the front of the gravity current that had a crest higher than the main body of the flow although, as proven again by Benjamin, a head wave of this shape cannot actually occur under the assumption of energy conserving flow. Keulegan (1957) carried out extensive experimental studies on gravity currents and directly observed the existence of a breaking wave region behind the 'head' of the current. From the observations of Keulegan (1958), Benjamin (1968) constructed a modified form of a gravity current shown in figure 1.2. Keulegan (1957, 1958) observed that when the front is at great depths or moving at high speed, the deflected waters at the head will form eddies, waves will be generated on the interface and intense mixing occurs. Benjamin (1968) also proved the inevitability of wave-breaking on the backward side of the head and therefore the energy losses that would ensue. He details many of the main features

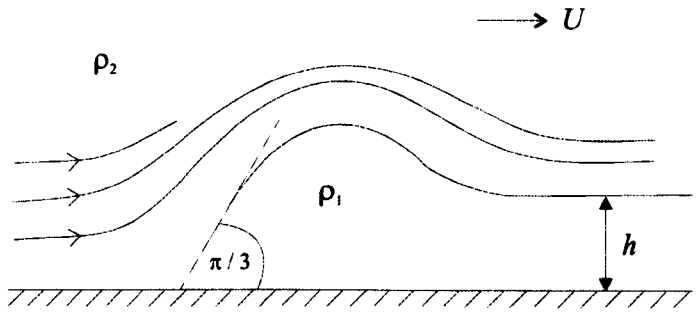

Figure 1.1: The form of the head of a gravity current propagating over a horizontal surface as suggested by Von Karman (1940).

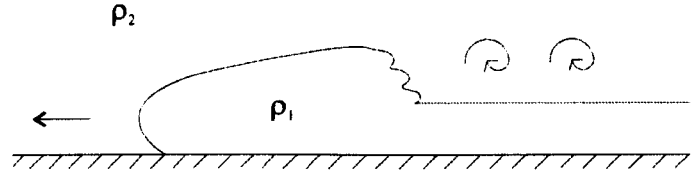

Figure 1.2: The form of the head of a gravity current propagating over a horizontal surface as suggested by Benjamin (1968).

of gravity currents through the application of the theory of flow force balance to an air-filled cavity and the liquid into which it is advancing. Through analogy with these results, he draws conclusions for the interaction of two fluids of different densities. The one considerable difference between the cavity flow and that of the gravity current is the wave-breaking process. This turbulent motion generates significant mixing between the two fluids of a gravity current and thus causes loss of definition of the density interface. However, for the propagation of a 'bubble', the interface will remain a smooth surface.

Investigations in lock release cases with varying initial lock length to initial height ratios (x_0/h_0) have shown that the head shape changes as the ratio increases or decreases about 1 (Hacker *et al.*, 1996). More recently it has been established that the head shape also changes with the ratio of initial current height to ambient height ratios (h_0/H) in fixed volume (lock-release and lock-exchange) flows. Shin *et al.* (2004) carried out a range of experiments for h_0/H between 0.11 and 1 and found for full height releases the current is practically uniform in depth like a constant flux case. Smaller release heights have a more noticeable depression behind the head, therefore a more pronounced raised head with a clearer slope on the density interface of the main body of the current.

The Reynolds number (Re) of a gravity current can also affect the current shape and is an important consideration if analogies are to be made with 'real' currents. Schmidt (1911) found that for Re $\lesssim$ 1000, the current morphology is dependent on Re but for Re $\gtrsim$ 1000 similar characteristics can be observed regardless of changes in Re. Keulegan

(1957, 1958), Simpson and Britter (1979) and Parsons and García (1998) agree with this observation although they notice that slight increases in Froude number (Fr) have been observed for Re greater than 1000. Discussion of Fr and the relevance to scaling can also be found in Kneller and Buckee (2000). For very small Re $\lesssim$ 10 Simpson and Britter (1979), found that the head is not distinct.

Mixing and entrainment

The mixing between the current and ambient fluids is a result of gravitational and shear instabilities at the gravity current head (Simpson and Britter, 1979). Simpson (1972) analysed the effects of the bottom boundary on the head of a gravity current studying the forms of these instabilities. The two main types are billows (resembling Kelvin-Helmholtz instabilities) and a complex shifting pattern of lobes and clefts, see figure 1.3. Billows are vortices caused by the breaking waves as established by Benjamin (1968) and theorised by Prandtl (1952). They appear, in basic form, as rolls of fluid along the density interface in the region of velocity shear above the front. Slightly different structured billows have been observed to form dependent on low or high Re (Parsons and García, 1998). Benjamin (1968), through the flow force balancing theory has shown that the breaking waves behind the head will remain when the theory is reduced to a two-dimensional case thus implying the retention of billows. This is confirmed by Britter and Simpson (1978) and Patterson *et al.* (2005) using a slip boundary to create a '2D' current. However, it has been shown that in the three-dimensional case, there is a mechanism for the dissipation of billows (Hacker *et al.*, 1996; Cantero *et al.*, 2003) not present in 2D.

The lobe and cleft formation occurs due to the effects of instabilities at the bottom boundary on the front. Their existence proves the three-dimensional nature of the flow. Simpson (1972) concluded that they are generated by less dense fluid over-ridden by the denser fluid, see figure 1.4. The buoyancy force induced by the lighter fluid has the effect of disrupting the billows and thus affects the mixing of the head at the top. It also raises the foremost point of the gravity current above the surface, thus moving the stagnation point beneath the head. Hartel *et al.* (2000b) found that the stagnation point is behind and slightly below the nose and does not coincide with it as previously thought (figure 1.4). They calculated the volume flux of the overrun fluid and found it to be very small and to decrease as Re increases. Since the energy available for a buoyancy-driven instability downstream of the head, such as that suggested by Simpson

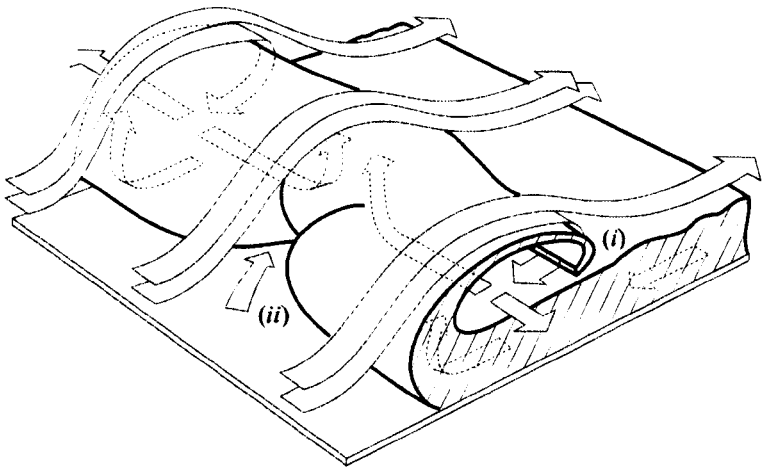

Figure 1.3: Sketch of the instabilities and three-dimensional motion in a gravity current head, after Simpson *et al.* (1977). (*i*) Billows forming behind the head, and (*ii*) cleft with lobes forming either side.

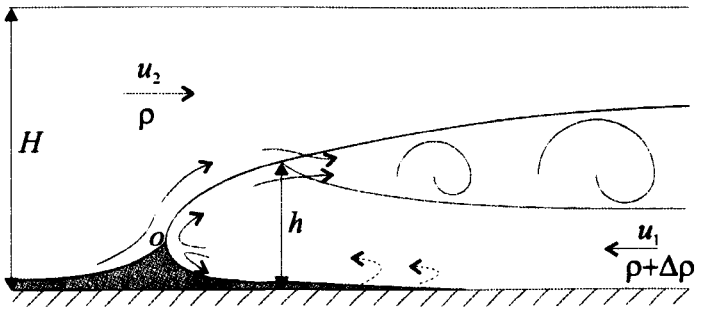

Figure 1.4: Schematic of a gravity current head, after Simpson (1972) where H is total fluid depth, O the stagnation point, h the current head height, ρ the ambient fluid density and u_1 and u_2 are the streamwise velocity of the current and ambient fluids, respectively.

(1972), depends on the amount of fluid entrained, Hartel *et al.* (2000b) conclude that this cannot be the primary mechanism for the generation of lobes and clefts. Instead, they suggest that they form due to a local instability generated at the leading edge of the current. This is illustrated in more detail using stability analysis and direct numerical simulations in Hartel *et al.* (2000a), although there exists insufficient experimental data to confirm these analyses.

Simpson and Britter (1979) found that for a constantly fed flow, whether surface stress is present or not, the fluid in the gravity current is mixed outside the current head behind it forming a mixed layer above the current body. Hence a thick velocity and density interface between the gravity current and the ambient fluid is formed. In both constant flux and fixed volume cases, the fluid in the head is initially unmixed even during the initial slumping stages of the lock release (Hallworth *et al.*, 1996). However, for fixed volume releases, the mixing and internal structure of the flow is different and has been

shown to be dependent on the aspect ratio of the fluid in its initial state. Hacker *et al.* (1996) use a ratio defined by the lock height to lock length h_0/x_0, whereas Hallworth *et al.* (1996) use lock length to lock height x_0/h_0. For ease of comparison, it is taken as x_0/h_0 here. Hacker *et al.* (1996) found that for larger aspect ratios (> 1), mixed fluid is detrained from the head and replaced by denser fluid from the body of the current until no more unmixed fluid is available and the head is eroded. With an aspect ratio of unity, Kelvin-Helmholtz billows mix deeply into the current and produce a region of stratification between a main vortex and the head. Eventually the vortex loses its energy and the current becomes analogous to that generated by the larger aspect ratio. A small aspect ratio (< 1) current has a head height comparable to its body depth. There is little supply of dense fluid behind the head and so the billows break directly into a region of mixed fluid. Gradually all the fluid in the current becomes mixed but denser fluid in the head maintains a leading front until eventually the stratification extends into the head. Hallworth *et al.* (1996) found that gravity currents with identical initial cross-sectional areas but different aspect ratios are diluted at different times and so propagate at different speeds. Also, the entrainment of ambient fluid into the current is spatially non-uniform, it occurs mostly at the head and decreases monotonically with increasing initial volume behind the gate. Hallworth *et al.* (1996) noticed the occurrence of 'abrupt transitions' in the flow, i.e. when the current head changes abruptly from dense to dilute. This mechanism is explained by Amy *et al.* (2005) and is dependent on the concentration and Re of the current. However, it is peculiar to laboratory generated currents and has not been observed in natural currents.

In a more quantitative study, Ellison and Turner (1959) found that for flow down inclines, entrainment decreases as the Richardson number (Ri) increases and is negligible for $\mathrm{Ri} > 0.8$.

The height of the current

Difficulties in choosing the location within the current to measure the height have been encountered in many experimental studies (e.g. Marino *et al.*, 2005) and can have substantial repercussions on subsequent analysis. For example, the Froude number (Fr) requires the height of the current to be known. A value of h just behind the head where flow can be shallower will give a larger Fr than deeper h measurements taken elsewhere. Shin *et al.* (2004) suggests that Fr in the current body should be calculated using a height taken from a region away from non-hydrostatic influences. Re also varies with

height. One Re value can be calculated in the head and a different one in the body of the current (Peters, 1999). It can be calculated using the total height of the fluids but since it is the Re of the current that is of interest it is more commonly calculated using $h_0/2$, the maximum height of an energy conserving current (e.g. Shin *et al.*, 2004).

In the laboratory, the height of the current depends on the experimental method and if a fixed volume lock exchange is used it will depend on the aspect ratio of the flow. In this case, differences are observed in the current height, for example, between dense body height, total dense and mixed layer height, head height and nose height (Simpson, 1972). Benjamin (1968) noted that for energy conserving flow, in his cavity model theory, the liquid must occupy half the space between the top and bottom planes of the channel for the steady flow without energy losses, i.e. $h = \frac{1}{2}H$. Flows with $h < \frac{1}{2}H$ are possible with energy losses but flows with $h > \frac{1}{2}H$ are not possible without some external source of energy. Analysis of energy conserving gravity current flow performed by Shin *et al.* (2004) found that the only non-trivial case is $h = h_0/2$, i.e. for an energy conserving partial depth release, the height of the current after release is half its initial lock depth before release.

Benjamin (1968) found a theoretical maximum current to ambient height ratio (h/H) of 0.347 for fixed volume releases including energy losses. An identical result was found by Klemp *et al.* (1994) and the experiments of Simpson and Britter (1979) obtained a maximum value of 0.33. However, Shin *et al.* (2004) proved that ratios of $h/H > 0.347$ are possible with lock exchange flows. The previous theoretical values are derived through shallow water theory and consideration of the speed of the characteristics analogous to a piston problem. However, shallow water theory is not valid at the front where non-hydrostatic forces are present so a constant depth and front velocity faster than the maximum characteristic speed is a possibility (Shin *et al.*, 2004).

The correlation of the nose to head height ratio (d_n/h_h) with Re for a current in the range $300 \leq \mathrm{Re} \leq 10000$ can be given by

$$\frac{d_n}{h_h} = 0.61\mathrm{Re}^{-0.23\pm0.1} \tag{1.1}$$

(Simpson, 1972). Subsequent studies agree with this relationship and it is important for understanding the instabilities generated at the front that depend on the nose height and stagnation point (Simpson and Britter, 1979; Hartel *et al.*, 2000b; Cantero *et al.*, 2007a).

The bore

The formation of a bore is another feature of lock release currents. Rottman and Simpson (1983) observed an expansion wave propagating back from the disturbance generated by removal of the partition which upon collision with the upstream end wall reflects back towards the current front. The nature of this reflection has been the subject of much discussion. Rottman and Simpson (1983) found that it is dependent on the initial dense fluid to ambient height ratio (h_0/H) and specified that there was a difference for $h_0/H > 0.5$. Klemp *et al.* (1994) showed that it takes the form of a rarefaction wave for $h_0/H \leq 0.5$ but becomes a bore for $h_0/H > 0.5$ as reversed flow and subsequent interaction with the end wall increase. D'Alessio *et al.* (1996) gives $h_0/H = 0.5$ for the condition on formation of the bore but this is a theoretical value and subject to simplifications used in the derivation (Moodie, 2002). Shin *et al.* (2004), through different theoretical analysis, found that a bore will form for releases greater than $h_0/H = 2/3$. This value agrees with observations in the region of 0.7 from experiments (Rottman and Simpson, 1983).

Typical gravity current profiles over a smooth bed

Gravity current flow over a smooth bed has been examined intensively. The internal structure of the current is discussed, for example, in Kneller *et al.* (1999) and Zhu *et al.* (2006). Typical results for the internal downstream horizontal and vertical velocities can be seen in figure 1.5 (*a*), with sketches of characteristic profiles of downstream horizontal velocity, density and turbulence kinetic energy throughout the depth of the current head (1.5 (*b*) and (*c*)). The arrival of the head is defined in the velocity time series by a sharp increase in both the vertical and horizontal velocity components. The billows behind the current head can be identified as large structures within the downstream horizontal velocity data. The vertical velocities are significantly smaller than the horizontal component with the majority of vertical motion at the front where the current forces itself into the ambient fluid. The concentration profile shows high concentration fluid lower in the profile, identifying the high density of the gravity current and low concentration above in the ambient fluid. Over a smooth bed, the velocity maximum is typically low down in the flow profile, which can be modelled from this point down to the bed using a log-law profile (Kneller *et al.*, 1999). The location of the turbulence kinetic energy minimum is typically observed to coincide with the velocity maximum and the turbulence kinetic energy typically attains maximum values at the density interface and near the

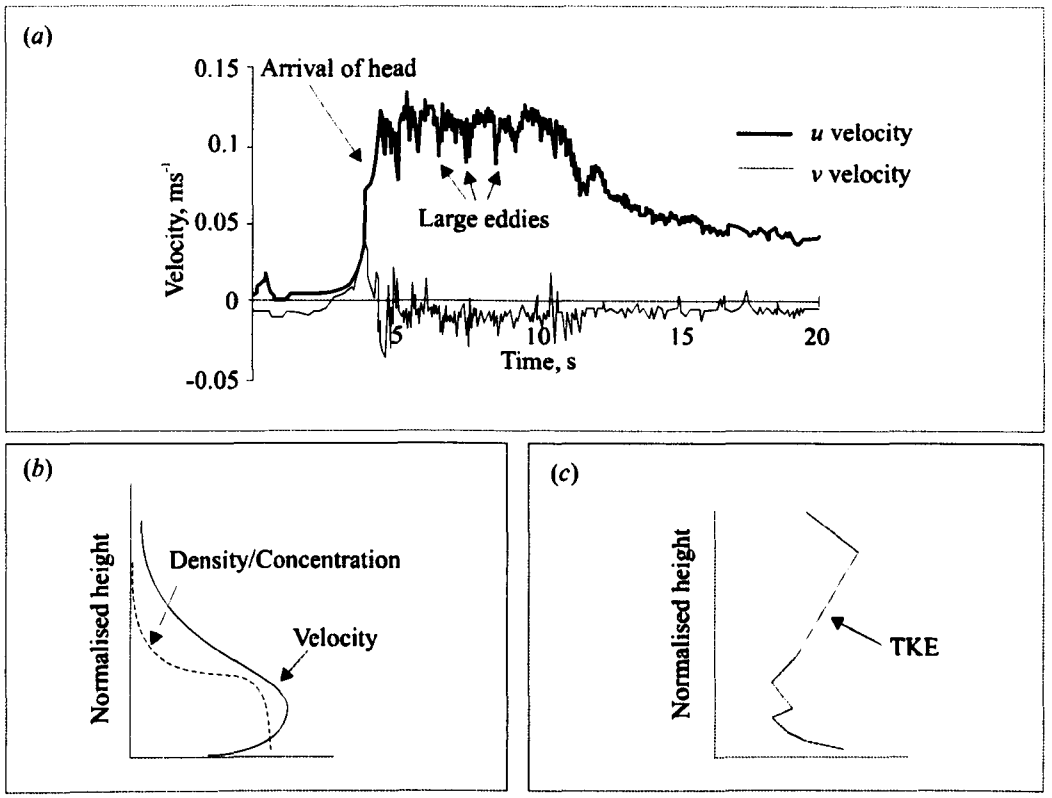

Figure 1.5: Typical results for saline lock-release laboratory gravity currents propagating over smooth surfaces after Kneller *et al.* (1999). (*a*) Time series of downstream horizontal and vertical velocity, (*b*) sketch of horizontal velocity and density profiles through the current depth, (*c*) sketch of turbulence kinetic energy profile through the current depth.

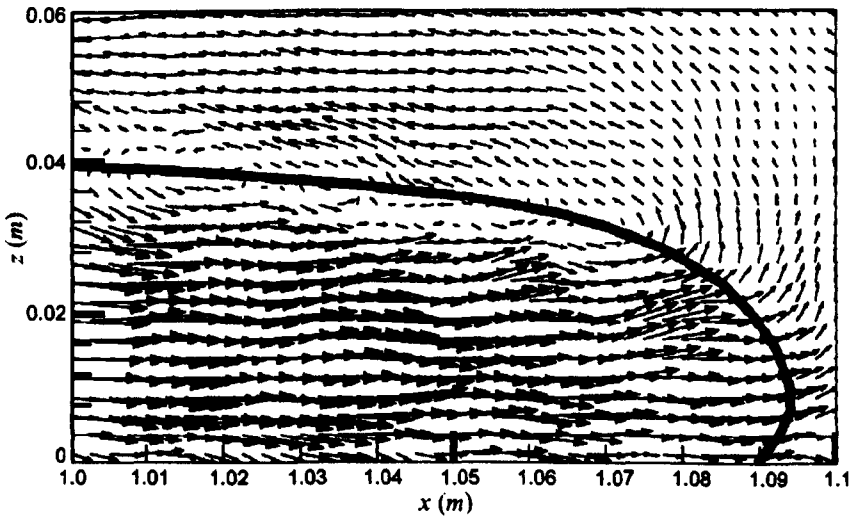

Figure 1.6: Velocity vector field, generated by PIV data within a gravity current head, adapted from Zhu *et al.* (2006). Solid black line represents the approximate outline of the gravity current head.

bed (Kneller *et al.*, 1999; Best *et al.*, 2001).

Zhu *et al.* (2006) produced vectors of velocity at points within a gravity current head (figure 1.6) from experimental particle image velocimetry (PIV) data. The strong downstream horizontal component of velocity is evident within the current fluid, with weaker negative velocities at higher depths in the overlying ambient fluid. The front is clearly identified by the strong upward motion to the right of the image. The billows can also be observed behind the head, created by the shear at the density interface between the current and ambient fluid. Chapter 2 provides further discussion of methods for gathering experimental datasets.

1.3.2 The front position and speed

Establishing the speed of the front is one of the primary objectives in many gravity current analyses. Despite being a long-standing component of gravity current research, the complexity of the instability in the flow dynamics at the front mean that the position and hence the speed of the current front is still a priority topic to date. An up-to-date and detailed discussion can be found in Cantero *et al.* (2007b).

Clearly the speed of the front will change from the instigation of the motion to the eventual quiescence. Since the flow in this problem is transient, the motion moves in phases dependent on the balance of the forces in the flow at that time (Huppert and Simpson, 1980; Didden and Maxworthy, 1982; Rottman and Simpson, 1983; Marino *et al.*, 2005; Cantero *et al.*, 2007b). For a full height ratio current (i.e. $h_0/H = 1$), when a lock partition is suddenly removed the fluid at the front collapses in an initial slumping phase (Huppert and Simpson, 1980) of constant front velocity before a balance of buoyancy and inertial forces dominates the flow (Rottman and Simpson, 1983). From the results of Rottman and Simpson (1983), Hallworth *et al.* (1996) specify the empirical expression for the length travelled before slowing begins (x_s) as

$$\frac{x_s}{x_0} = 3 + 7.4\frac{h_0}{H}. \tag{1.2}$$

The current advances along the horizontal surface in this inviscid self-similar phase with a decreasing speed proportional to $t^{-1/3}$ (Hoult, 1972). The buoyancy-inertia balance is maintained so long as the inertia forces are large in comparison to the viscous forces that result from the shear generated at the interface between the fluids and by contact with the lower boundary. When this balance no longer holds, it has been found that a

current moving along a rigid boundary will have length of order

$$x_* = \left(\frac{{x_0}^5 {h_0}^5 g'}{\nu^2}\right)^{\frac{1}{7}} \tag{1.3}$$

and the flow is said to enter the buoyancy-viscous regime (Didden and Maxworthy, 1982; Huppert, 1982). The speed of the front has been found to further decrease in the viscous self-similar phase with $t^{-4/5}$ (Huppert, 1982).

For low Re currents, the inertia-buoyancy regime is shorter or can appear absent (Huppert and Simpson, 1980; Amy *et al.*, 2005; Marino *et al.*, 2005; Cantero *et al.*, 2007b). Cantero *et al.* (2007b) found that whether the flow undergoes the transition from slumping phase to viscous phase via the inertial phase or not depends on the initial Re of the flow and the size of the release. For larger releases, with high Re, the slumping phase is maintained for longer and the inertial phase is apparent. When the current is generated from a continuous flux source (e.g. Simpson and Britter, 1979, Peters *et al.*, 1997), the initial slumping phase does not occur and the first flow regime is the inviscid self-similar phase.

Systems of governing equations that describe the flow can be derived and solved either analytically or numerically for the velocity and other quantities required for different models relating to gravity currents. These have been investigated extensively by previous authors and the subject is covered in more depth in section 3.2.1.

1.3.3 Bed roughness

In many 'real' studies of gravity currents, the macroscale characteristics of the bed are given, such as the slope or substantial ridges or steps, but a truer physical characterisation of the bed is omitted. In some cases this is justified since the bed can be classified as hydraulically smooth but whether this has been formally established in any one investigation or is simply an assumption is often not presented in the data or perhaps has not been considered. With this in mind, it would be of significant benefit to compile a detailed database of known natural occurrences of gravity currents with details such as the speed, spread, depth and concentration of the current and finer details of the bed such as the presence of, for example, bed forms, and the height and distribution of these 'roughness elements'. This task was not performed in the present study due to the time constraints involved in compiling such information, particularly since the details of an event are not always provided by one source and therefore rigorous searches and cross-referencing are required. Moreover, the spontaneity of natural gravity currents means

that collection of field data is difficult.

In the case of turbidity currents, it is common practise to analyse deposits and infer flow processes that might result in the formations observed. The stratification of deposits in rock outcrops and the orientation of larger particles can be used retrospectively to deduce finer details such as the nature of turbulence in the flow. Data from recent events or laboratory studies can then be used to support any hypotheses. Similar inverse hypotheses could therefore be used the generate more detailed datasets of the flow dynamics in the presence of bed roughness. An example of the above is the pyroclastic currents that resulted from the eruption of Mt.Vesuvius in AD 79 and destroyed the Roman town of Herculaneum (e.g. Sigurdsson *et al.*, 1982; Gurioli *et al.*, 2002). This context represents an urban roughness condition at the bed. Results indicate that some of the buildings would be classified as obstacles rather than a roughness since they cause substantial flow deflection. However, the effects of several 'small' steps between 0.1-0.5 m high have been observed and the resulting turbulence and particle deposition from the current in relation to these steps has been suggested by analysing the facies in the lee of the steps. A step of height 0.5 m that was not high enough to affect the entire flow was found to induce an abrupt flow transition inducing the settling of heavier particles and partial removal of fine material. A series of smaller steps up to 0.4 m high were purported to result in an increase in flow turbulence, in this case instigating a transition from non-turbulent to turbulent transport. The inclusion of the effects of the urban roughness caused a change in the interpretation of some of the deposits to be described as the results of flow transformations in response to irregularities at the bed (Gurioli *et al.*, 2002).

Until recently most model investigations into gravity currents have considered the flow over a smooth rigid boundary. Flow down slopes (e.g. Middleton 1966a, 1966b, Britter and Linden, 1980), flow over or through obstacles (e.g. Rottman *et al.*, 1985, Hatcher *et al.*, 2000), flow over permeable surfaces (e.g. Marino and Thomas, 2002) and various other aspects affecting these important phenomena have been studied but there has been little attention applied to characterising the flow over a homogeneously rough surface. The most notable studies to date are those of Peters (1999), Kubo (2003), Özgökmen *et al.* (2004a) and Özgökmen and Fischer (2008). Peters (1999) performed experiments of constant flux gravity currents of different densities flowing over square roughness elements, Kubo (2003) carried out experiments and a numerical study of particle-driven gravity currents flowing over 'humps' as a bedform analogy, and Özgökmen *et al.* (2004a) and Özgökmen and Fischer (2008) simulated oceanic overflows (stratified saline gravity

currents) over a sinusoidal bed topography. These studies are discussed further subsequently.

It should be noted that the presence of elements on the bed does not immediately imply that the bed is rough, even if they meet the general description of bed roughness given, for the present study, in section 1.2. In typical boundary layer flows, if the elements are small and within the boundary layer or the flow is laminar then the flow dynamics will not feel the effects of the roughness. As the flow increases in turbulence, i.e. the Reynolds number increases, the effect of the roughness can still remain within the hydraulically smooth regime until a critical level is reached and the roughness begins to take effect. As the Reynolds number continues increasing, the roughness effects increase proportionately in a transitional regime where the dynamics are dependent on the Reynolds number and the geometry of the roughness elements. Within the boundary layer, the viscous sublayer thickness reduces due to the diminishing damping effect of the wall on the flow until the sublayer can no longer be maintained and the flow is considered fully rough. The roughness effects are approximately constant, independent of further increases in Re and proportional to a roughness Reynolds number. This theory was first established by Nikuradse (1933) who classified the different regimes of the flow as hydraulically smooth, transitional and fully rough based on a roughness Reynolds number for sand grain roughness. Note that for a given surface, as the boundary layer thickness and Reynolds number change, the classification of that surface can change, even from effectively rough to hydraulically smooth. Further details of the effects of roughness on the boundary layer can be found in textbooks, for example Chow (1959), Schlichting (1960) and Cebeci and Bradshaw (1977).

Different types of roughness

Naturally occurring roughness, depending on the scale, can constitute almost any array of objects over which a fluid flows. Therefore, it is not possible to explicitly identify every different type. In order to understand the effects of roughness on fluids, a variety of artificial elements have been used experimentally and theoretically, resulting in the categorisation of different roughness 'types' the varying effects of which can be related back to the natural environment. This use of artificial elements is justified by the complexity of natural roughness (Rouse, 1965).

The investigation of the effects of bed roughness on flows in pipes, ducts and in open channels spans several decades and continues to date (Jimenez, 2004). In all of these

contexts, the roughness elements can take a variety of forms, for example natural coarse sand or man-made steel rivets. There is an obvious divide between 'grain' type roughness and 'form' type roughness whereby the roughness could be characterised by either of these or both. A flat bed of coarse sand would be categorised as a grain type roughness, a series of triangular shaped ridges in an otherwise smooth bed would be a form type roughness, combine these as a dune field and the result is a composite grain and form type bed roughness (Van Rijn, 1984).

In most roughness studies, reference is given to the fundamental work of Nikuradse (1933) which was based on the effects of coarse sand in pipes. In the pursuit of characterising all roughnesses, the results of Nikuradse (1933) have been used for decades to generate a theoretical roughness type, the so-called 'equivalent sand roughness height', k_s*. Essentially this involves relating the roughness effects of a study back to the results of Nikuradse (1933). Thus the effects of that roughness on the flow are known based on the effects of an equivalent sand roughness. Grain type roughnesses correlate well to this representation, as might be expected. However, there is substantial debate as to the effective representation of form type roughnesses by a single k_s value. Rouse (1965) and Yen (2002) query how one value can describe the effects of the size, shape and spatial distribution of larger roughness elements such as bedforms. In particular, if flow separation occurs around an element, changes to the flow dynamics could be significantly more than k_s can prescribe (Yen, 2002). In turbulent boundary layer studies, it has been contested that the equivalent roughness, k_s, is a bad parameterisation of roughness resulting in very different roughness geometries having very different effects on the turbulent stresses but with nominally identical roughness functions (e.g. Krogstad and Antonia, 1999, Orlandi and Leonardi, 2008). Hence risking misrepresentation of the required roughness with potentially serious inaccuracies in the flow field. With this is mind, Orlandi and Leonardi (2008) recently suggested that bed roughness would be better parametrised in terms of its affects on turbulence characteristics of the flow.

For single-phase flow conditions it is known that rod roughness perpendicular to the flow which involve a gap between one element and the adjacent one can be categorised into 'd-type' and 'k-type' roughnesses depending on the length scales presumed to represent the flow over them. This idea was established by Perry *et al.* (1969) who characterised k-type roughness by a roughness function dependent on the Reynolds number based on

*Note that this does not always have to be an equivalent *sand* roughness height, it can be related to other known results but since Nikuradse (1933) was a very thorough study it appears to be the most commonly used.

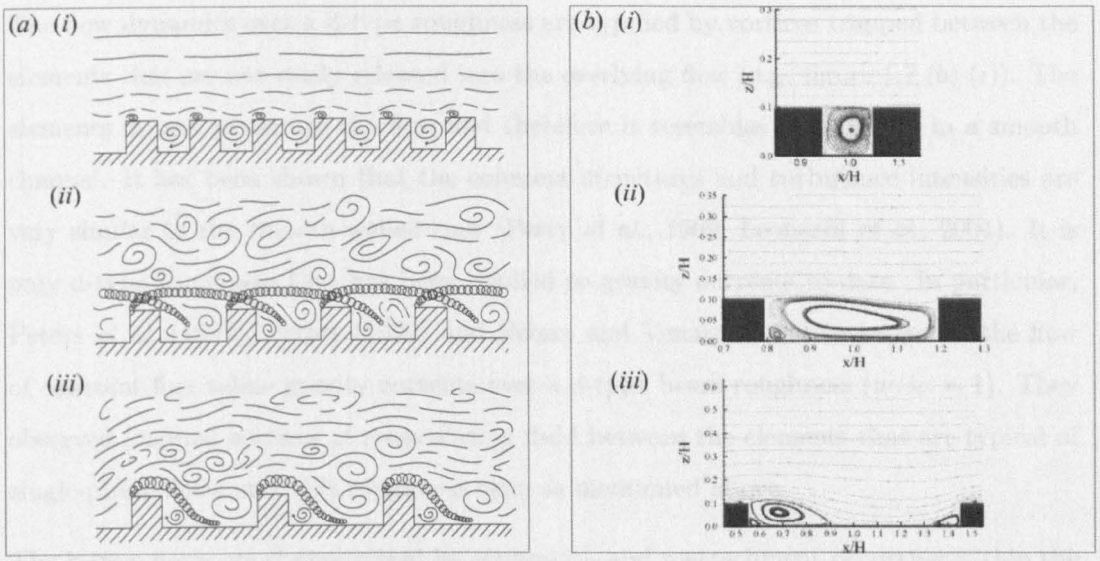

Figure 1.7: Sketches of the reaction of the flow to different bed spacings for single-phase pipe or open channel flows over square beams. (*a*) After Chow (1959) and (*b*) numerical data of Cui *et al.* (2003). Both show d-type (*i*) and k-type (*iii*) element spacings and the possible intermediate spacing (*ii*).

shear velocity and on a length associated with the size of the roughness. The function describing the d-type roughness was found to depend on the diameter of the pipe and not on the roughness scale and gives rise to different flow dynamics[†]. Physical descriptions of flow dynamics corresponding very well with these three categories were observed previous to Perry *et al.* (1969). Chow (1959) suggested three categories for the description of flow over a beam-type roughness: isolated-roughness flow, wake-interference flow and quasi-smooth, shown in figures 1.7 (*a*) (*i*), (*ii*) and (*iii*), respectively. Of these, figures 1.7 (*a*) (*i*) and (*iii*) represent d and k-type roughness effected flows, respectively, but Chow (1959) identifies wake-interference flow independently of the others. More recently, the element spacing to height ratio, w/k_r, has been used in research to categorise roughness into d or k-type, although this appears to be under discussion. For example, Leonardi *et al.* (2003b), Leonardi *et al.* (2004) and Ikeda and Durbin (2007) suggest a value of $w/k_r \gtrsim 3$ for a roughness to be described as k-type after the work of Bandyopadhyay (1987), while Cui *et al.* (2003b) suggest a value of $w/k_r \gtrsim 4$ based on the work of Tani (1987) and Okamoto *et al.* (1993). However, they also consider an intermediate type roughness classification of $w/k_r = 4$, which suggests agreement with the observations of Chow (1959), see figures 1.7 (*a*) and (*b*) (*ii*).

[†]These results have still not been proven explicitly and hence are still not fully understood, particularly for the d-type case but they are still very commonly used to describe roughness element spacings (Jimenez, 2004).

The flow dynamics over a d-type roughness are typified by vortices trapped between the elements that are not easily released into the overlying flow (e.g. figure 1.7 (*b*) (*i*)). The elements do not penetrate the flow and therefore it resembles that of flow in a smooth channel. It has been shown that the coherent structures and turbulence intensities are very similar to the smooth-walled case (Perry *et al.*, 1969; Leonardi *et al.*, 2004). It is only d-type roughness that has been applied to gravity currents to date. In particular, Peters *et al.* (1997), Peters (1999) and Peters and Venart (2000) investigated the flow of constant flux saline gravity currents over a d-type beam roughness ($w/k_r = 1$). They observed trapped vortices of recirculating fluid between the elements that are typical of single-phase flows over this roughness type as mentioned above.

The k-type flows are characterised by separation and reattachment occurring within the distance between two adjacent elements (e.g. figure 1.7 (*b*) (*iii*)) and the ejection of larger and more frequent eddies into the overflow (Perry *et al.*, 1969). There is strong interaction between the roughness elements and the main body of flow and therefore both the height of the roughness elements and the space between them are crucial parameters (Ashrafian *et al.*, 2004). Leonardi *et al.* (2003b) find that when w/k_r is large enough the reattachment length is not influenced by the presence of other elements. This critical spacing is generally agreed to be $w/k_r \approx 7$ (Cui *et al.*, 2003b; Leonardi *et al.*, 2003b; Ashrafian *et al.*, 2004; Ikeda and Durbin, 2007). There is some variation in results of research into the value of the corresponding reattachment length: Cui *et al.* (2003b) suggest a value of about $4k_r$ while Ikeda and Durbin (2007) find a value of $4.5k_r$ and Leonardi *et al.* (2003b) report a value of $4.8k_r$. For roughness spacings below the critical w/k_r value, the upstream face of the next element acts as a vertical blocking wall causing an adverse pressure gradient resulting in a shortened reattachment length. A larger reattachment length implies larger eddy development at the downstream wall of an element and therefore increased strength of the outward ejection of these eddies into the main body of the flow. Hence $w/k_r \approx 7$ can also be interpreted as representative of the spacing for which the maximum strength of ejection occurs (Leonardi *et al.*, 2004). Similar results would have significant implications for gravity current propagation, particularly with respect to entrainment. Leonardi *et al.* (2004) find that in the vicinity of the elements, flow structures are less elongated than for flow over a smooth wall and as w/k_r increases, the coherence is further reduced in the streamwise direction and attains a minimum when $w/k_r \approx 7$. Finally, for larger values of w/k_r, the normal wall motion induced by the roughness is confined to smaller regions and the overlying fluid dynamics are once again similar to those encountered above a smooth wall (Leonardi *et al.*, 2004).

The so-called intermediate flows are characterised by separation with a recirculating eddy about the same size as the cavity between the elements with reattachment on the upstream face of the adjacent element and the overflow affected by the ejected eddies, refer to figure 1.7 (*b*) (*ii*). This flow description agrees with that of Chow (1959) for wake-interference flow shown in figure 1.7 (*a*) (*ii*), and also agrees with the results of Leonardi *et al.* (2004) where for $3 < w/k_r < 7$ the effects of the wall on coherent structures and turbulence intensities extends approximately $2k_r - 5k_r$ above the top of the elements.

In an attempt to further characterise the bed roughness for single-phase open-channel flows, Schlichting (1936) derived a 'solidity' function. This is defined by the total projected frontal roughness area per unit wall-parallel projected area. It was found that the effects of the roughness increased until there was a solidity of about 0.15 and then decreased since the elements start to shelter each other so the roughness effects of individual elements lessen. d-type flows have a solidity of about 0.5 in the extreme limit of mutual sheltering (Schlichting, 1936). Rouse (1965) found optimum 'concentration' between 15-20% produced the greatest resistance, in good agreement with the solidity values of Schlichting (1936). Values below approximately 15% caused the resistance to vary in direct proportion to the concentration of the roughness elements with the constant of proportionality varying with the relative drag of individual roughness elements. This line of research caused Rouse (1965) to query the reliability of estimating roughness parameters based on the results of Nikuradse (1933) since the exact concentration of the elements used in that study is unknown and even using a reasonable approximation, does not agree with the results of Rouse (1965).

It must be noted that very recently, Orlandi and Leonardi (2008) have suggested, perhaps controversially, that the characterisation of roughnesses to date should be discarded and a new approach adopted. They suggest, through the results of an extensive range of direct numerical simulations that roughness is better parametrised through its impact on turbulence in the near wall region. In particular, through the root mean square of the wall normal velocity fluctuation at the element crests. In their work, Orlandi and Leonardi (2008) have created a database of 'numerical experimental' data for different roughness types for reference. Clearly, categorisation of a roughness type is not a simple task and is subject to considerable ongoing research.

More 'natural' elements, like the macroscale bedforms suggested by Yen (2002), have been used by Kubo (2003) to study the effects of three adjacent 'humps' on a lock-release particle-driven gravity current. The hump geometries were 1.2 or 3.6 cm high

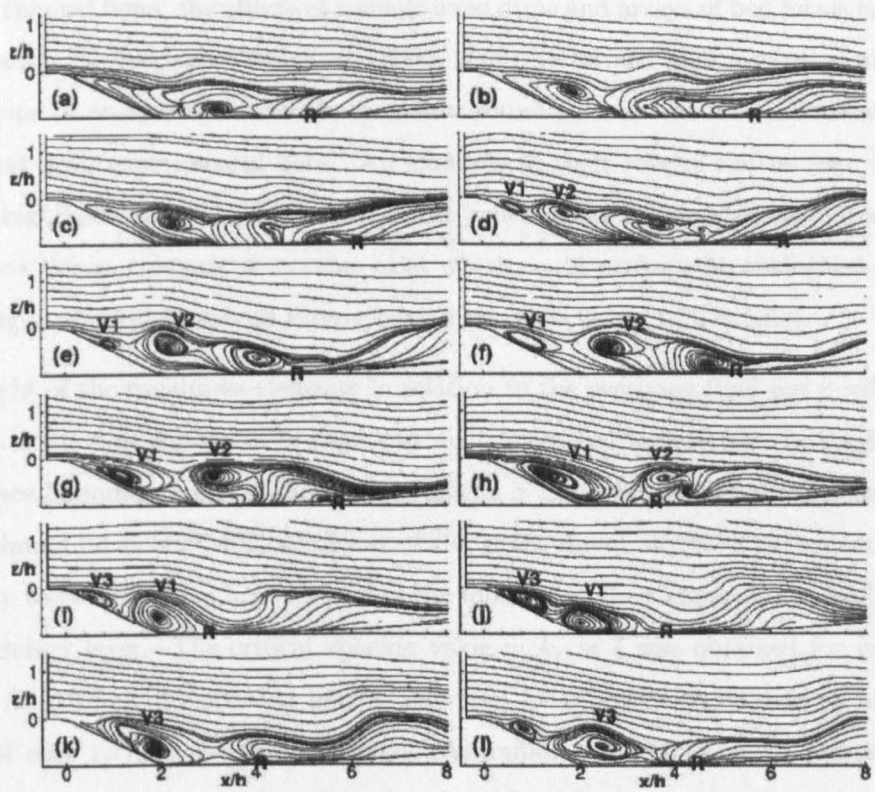

Figure 1.8: Results of numerical study by Yue *et al.* (2006) of open channel flow over a fixed dune using LES. (*a*) - (*l*) shows consecutive timesteps highlighting the development and life-time of vortices (V) and the approximate location of the reattachment point (R).

with symmetrical slopes either side of a peak of horizontal length 50 cm or 100 cm[‡]. The aspect ratios (height to wavelength) were between 0.006 and 0.036. In the terms of duct flow, w/k_r values approximated using the wavelength, since the humps are symmetric, and the height, were found to be $\approx 27 < w/k_r < 167$. Therefore, the humps could potentially be categorised as k-type. However, this should only be applied loosely as their proximity is augmented by the effects of the up and downward slopes which could result in another classification being more appropriate. The topography applied by Özgökmen *et al.* (2004a) and Özgökmen and Fischer (2008), using a bumpy bed described numerically using sinusoidal perturbations also represents more natural elements. However, in Özgökmen and Fischer (2008) in particular, the close proximity of the bumps results in recirculating vortices observed in the flow field similar to those seen between d-type elements.

[‡]Note that in Kubo (2003) there is some ambiguity in the slope dimensions. The text implies that it is the slope itself that is 50 or 100 cm. However, the diagram in figure 2 (*b*) and the values of 'hump length' in table 1 (*c*) therein suggest that it is in fact the horizontal distance from the peak to the bottom of the slope.

In open channel flows, the effects of a single fixed dune and arrays of bed forms have been investigated. For example, Yue *et al.* (2005, 2006) performed high resolution numerical simulations to analyse the streamlines of flow round such an element and showed good agreement with experimental data. An example of their results can be seen in figure 1.8 and highlight that for non-adjacent dunes, where there is a gap between upward and downward slopes, coherent structures exist which could perhaps be analogised to those occurring in the widely spaced k-type beam cases (see figure 1.7 (*b*) (*iii*)).

The height of the roughness elements in relation to the overlying fluid has a substantial impact on the flow dynamics in pipe and duct flows, particularly on the modelling of turbulence boundary layers. The relative height is important because the channel half height should be at least $40k_r$ (Jimenez, 2004) if the direct effects of the roughness elements on the overflow are not required in the model, i.e. the roughness lies solely within the boundary layer. The critical spacing value $w/k_r \approx 7$ was obtained for roughness heights 5 - 10% of the channel height and have been shown to hold for a roughness height of only 1.7% of the channel height (Ashrafian *et al.*, 2004; and Krogstad *et al.*, 2005). In gravity current studies, the principle body of fluid in motion over the roughness elements is the current and therefore, as an approximation, the conservative assumption that $h_f = h_0/2$ can potentially be used to calculate the roughness height as a percentage of the current height for experimental currents[§]. For Kubo (2003), the height of their humps corresponds to 6-18% of the channel depth, or 12-36% of the conservative current depth. However, they note that this causes at least 10-30% blocking effects on the current which, in the present study, is more indicative of a series of obstacles rather than roughness elements.

The anatomy of gravity currents propagating over rough surfaces

The significance of the lower boundary on gravity currents has been implied in section 1.3.1 (Britter and Simpson, 1978; Simpson and Britter, 1979). The earliest record of roughness effects on gravity currents, to the author's knowledge, is in experiments undertaken by O'Brien and Cherno (1934), as cited by Keulegan (1957). No difference was found in the velocity of the salt water between tests run in a channel with a hard wood bottom painted with red lead and a channel with a bottom covered with coarse sand. However, the small velocities in the saline laboratory gravity currents mean that viscous layers within the flow adjacent to the walls will be sizeable (Keulegan, 1957). Clearly,

[§]In the present study, k_r of the beam-type bed-roughness corresponds to $\approx 2.5\%$ of the tank height and $\approx 5\%$ of the gravity current height.

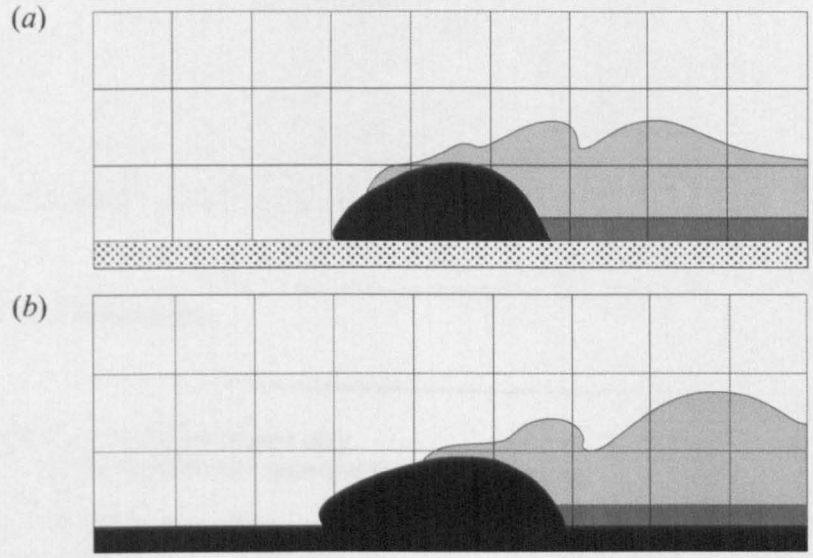

Figure 1.9: Reproduction of the representative tracings from video frame analyses from Hallworth *et al.* (1996). Saline lock-release gravity current flow over (*a*) a bed of coarse granules of ≈2 mm diameter (dots) and (*b*) over a smooth bed (black). Designed to show the relative cross-sectional shape of the head (black). Dark grey layer behind the head represents fluid in the current body that has been somewhat diluted. Light grey represents highly mixed fluid.

for roughness to take effect, the size of the rough elements in relation to the size of the tank and the possible velocity scales must be considered.

The profile of the head is expected to change with the introduction of roughness on the bed. Hallworth *et al.* (1996) performed experiments with saline lock-release gravity currents with a thin layer of granules of diameter ≈2 mm on the bed (although they do not state if they were fixed or moveable). They found that the shape of the head is dependent on the roughness, see figure 1.9 and, that entrainment is much higher, more than double that of the smooth case at approximately 20 dimensionless units downstream of the point where entrainment commenced. The thickness of the current behind the head increased relative to the head in the rough case which, they comment, is physically reasonable in terms of turbulence generated at the bed.

The results of Peters (1999) show that head and layer heights increase with increasing surface roughness and develop in a similar way to smooth surface flows, i.e. after an initial growth they stabilise. The difference between the head heights with smooth and rough beds in that study is considered to be the result of the increased entrainment at the front which induces additional mixing as the nose interacts with each roughness element. Thompson *et al.* (2007) found that a gravity current induced by a sea breeze flowing over an urban roughness (New York City, maximum height 200 m over Manhattan)

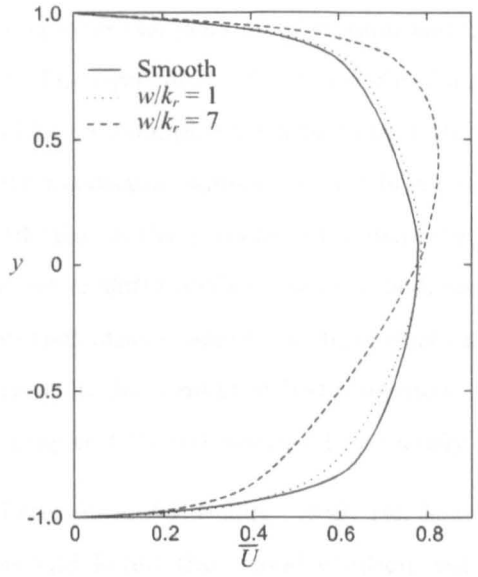

Figure 1.10: Downstream horizontal velocity profiles through the flow depth in a duct for a smooth bed and beds of transverse square beams with spacings (w) of one and seven times the height (k_r) of the beams. Reproduced from Orlandi et *al.* (2006).

has a head height that ranges from about 2.5 to over 7 times the body height over the urban landscape while over their 'smooth' grassland conditions, it's consistently only 2-3 times the body depth, i.e. the ratio of head height to body height has approximately doubled. This result contrasts with the observations of Hallworth *et al.* (1996) who suggested that this ratio should decrease in the presence of roughness. This could be a result of several physical differences. The sea breeze model is a temperature induced current at a large scale and based on many specific parameters, including ambient cross winds, irregular topographical features, temperature fluxes from the urban grid model and other variables. Hallworth *et al.* (1996) investigate a saline, laboratory scale model flowing into a quiescent ambient and over a regular, granular surface.

In a recent numerical study, Özgökmen and Fischer (2008) concluded that the distribution of entrainment in the case of rough bottomed gravity currents is totally different to those with smooth beds. They suggest that entrainment initiates earlier due to vertical motion induced by the roughness, but also finishes earlier, due to the increasing effects of form drag. The overall result of this process is that the mass of current remains similar to that of the smooth case but with different entrainment characteristics. They observe that the interfacial instabilities become less pronounced and tend towards the spatial scales of the roughness elements beneath the current. However, it should be noted that the magnitude of their roughness is of the same order as the current depth in most of their cases and their flow initiates with a pre-stratified saline current.

In the presence of bed roughness the velocity maximum should move further from the bed (Kneller *et al.*, 1999). The equivalent velocity profile of a single-phase flow through a pipe or a duct has a profile, for example shown in figure 1.10, with a logarithmic profile holding below the velocity maximum, similar to that below a gravity current nose. It can be seen in figure 1.10 that in the presence of a beam type bed roughness on one wall of the duct, the maximum shifts further from the bed, as predicted for the gravity current case. It is possible that other observations from duct and open channel flows will also hold for gravity currents in the context of bed roughness, for example the effects of element spacing shown in figure 1.10 and discussed previously.

In a larger scale study, Petersen and Ratcliffe (1989) ran heavier than air gas (HTAG) tests over rough surfaces and found that cloud dilution can be greatly enhanced by increasing the size of the surface roughness. Concentrations were 2 to 6 times less over an urban area, and 8 to 25 times less downwind of a processing facility in an urban area. When studying the effects of the rough elements on the concentration in the head, Peters *et al.* (1997) observed that when the dilution is such that the density difference reduces to only 10% of the maximum for that current, the head still remains intact. Their normalised front position data collapses well indicating that the position of the current as a function of time, scales with the density difference for all bed types. They found that near the end of the channel, the normalised mean head concentration in the flows over the rough surfaces were at least 20 times less than the equivalent smooth surface flow. They also noticed that with increasing roughness size, the normalised mean fluid density difference in the head decreased almost asymptotically. Their results show that, the contribution of trapped packets of lighter fluid in the rough cases, is much more significant to the head dilution and thus deceleration of the current than Simpson (1972) and Simpson and Britter (1979) allow for.

Sea breeze frontal passages have been retarded by up to 50% (≈ 5 ms^{-1}) as they approach New York City due to the urban boundary conditions (Thompson *et al.*, 2007). As discussed in section 1.3.2, the velocity of the gravity current depends on which are the dominating forces acting on it at the time and therefore which flow regime it is within. Özgökmen and Fischer (2008) observed a constant phase where the initial propagation speed is constant for all cases, followed by a decrease in speed with the increase in the amplitude of their roughness configuration. They suggest that the reduction in speed due to roughness is a result of the increased form drag from the elements. Peters (1999) found that even for the smallest roughness elements (6 mm), there was a 50% decrease in the distance to viscous transition compared to the smooth case. However,

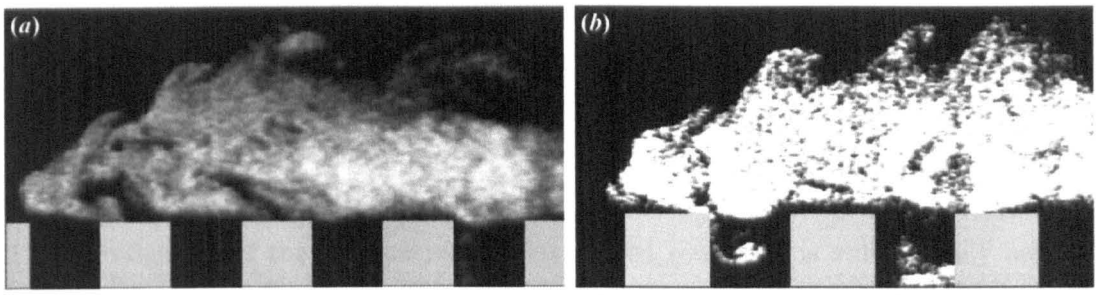

Figure 1.11: Visualisation of experiments with a gravity current propagating over a d-type rough surface, Peters and Venart (2000). (*a*) 'Light' current propagating over a rough bed, (*b*) 'Heavy' current propagating over a rough bed.

this distance only decreased slightly between the smallest (6 mm high) and largest (25 mm high) roughness scales used. In the buoyancy-inertia regime, the initial front velocity decreased linearly with roughness scale (Peters, 1999) and deceleration rates increased in the buoyancy-viscous regime. This is confirmed by Peters and Venart (2000), although previously, Peters *et al.* (1997) found that there is no inertia dominated regime, i.e. the viscous dominated decelerating regime takes over straight away. This contrasting view is apparently an inconsistency in these works since the experimental setup and all other conditions appear identical.

Peters *et al.* (1997) and Peters and Venart (2000) attributed the deceleration to the less dense fluid trapped beneath the current in the cavities between the beams. This fluid became entrained and mixed into the denser fluid, thus reducing the density excess and weakening the buoyancy flux, i.e. the driving force of the flow. When the density difference between the current and the ambient fluid is small, the current is able to lift above the roughness elements so that this mixing effect and the consequent current dilution does not occur to such an extent, see figure 1.11 (*a*). Thus the light current maintains its density and its speed for longer and the flow dynamics are more analogous to that over a smooth surface but still slightly slower due to energy loss to the trapped vortices (Chow, 1959). For a 'heavy' current (figure 1.11 (*b*)), the interaction with the trapped lighter ambient fluid is much more vigorous so that the dilution is increased over the length of the channel and the current will decelerate more rapidly.

Kubo (2003) found that under the influence of the hump topography the current did not travel as far as smooth cases in the same time period and deposition from the current occurred much sooner and more so on the stoss (upstream) slope of the humps. The study did not measure internal experimental velocity fields or concentration so effects on internal dynamics that might shed light on this issue are not available and further

investigation is necessary. Unfortunately, this is beyond the scope of the present study but would be an interesting extension.

1.3.4 Summary

The investigation of the fundamental effects of bed roughness is still a highly active research topic in pipe and open channel flows, despite several decades of dedicated research. The complexity involved in modelling bed roughness effects on any flow should not be underestimated. With such a quantity of work incorporating or focussing entirely on the effects of roughness, it should be apparent that significant effects will also be important in the gravity current arena. The added complication of density differences and the consequent intricate frontal dynamics result in a highly complex phenomena for experimental or numerical modelling. However, with these differences in mind, it is possible that several of the observations for single-phase flows through roughened pipes might also hold for gravity current flows, qualitatively if not quantitatively.

From the sparse studies that have been performed on the effects of bed roughness on gravity currents and potential effects from relevant pipe and open channel studies, the following might be expected and will be considered in the present study:

- A velocity maximum occurring further from the bed, higher in the current depth.
- Reduced current speed.
- Reduced concentration within the current head.
- Increased entrainment, particularly from ambient fluid beneath the head.
- Increase (or decrease) in the current depth, dependent on the roughness and other parameters.
- Effects due to the height of the roughness relative to the fluid height.
- Effects due to different types of roughness elements, for example grain and form roughnesses.
- Varying effects due to the roughness element configuration and spacing.

1.4 Aims of this thesis

The global aim of this thesis is to use experimental and numerical methods to create a knowledge database of the fundamental dynamics and flow structure of lock-release gravity currents flowing over rough surfaces and to discuss the implications for this case.

To the author's knowledge, as demonstrated in the previous section, there is little existing work dedicated to understanding the effects of bed roughness on lock release gravity currents. With this objective in mind, this thesis has three primary investigatory aims:

1. To carry out a reproducible and easily modified set of experiments in order to compile a new, accurate data set to extend and compliment the existing smooth bed studies. This data will be analysed in an experimental context and used for rigorous theoretical comparison.

2. To study existing depth-averaged gravity current models and mathematical forms of including bed roughness in order to create a model for the rough surface and to fully validate this model using available data.

3. To use the CFD commercial software FLUENT to study the fully depth-resolved forms of the governing equations, including modifications for bed roughness, in order to create 2D and 3D numerical models and to fully validate this model using experimental data.

1.5 Thesis outline

This thesis is split into seven chapters, including the current chapter one. Essentially, it is designed so that chapter two addresses aim one, chapter three covers aim two, and chapters four, five and six fulfill aim three. Chapter seven concludes the present study.

Chapter 2 Chapter 2 contains a review of some of the existing experimental literature on methods and techniques for studying gravity currents, including roughness. The experimental methodology used in this study is outlined and measurement techniques explained. Results and observations for the fundamental flow structures and dynamics of gravity currents flowing over bed roughness are presented. The chapter concludes with a discussion of the effectiveness of the techniques used, the effects of bed roughness, and the subsequent implications of these results.

Chapter 3 This chapter introduces the depth-averaged (1D) model used in the present study. Existing models and theories are discussed and terms for the inclusion of bed roughness are outlined. This is followed by a derivation of the governing equations and the assumptions and boundary conditions applied. The method of characteristics solution procedure is explained and applied to the smooth and the rough bed cases. 1D results are presented and validated with existing experimental data in the smooth case. A concluding discussion analyses the effectiveness of the solution method, the value of 1D models and the theoretical effects of bed roughness.

Chapter 4 Existing literature implementing fully depth-resolved numerical models is reviewed along with some work to date on the inclusion of bed roughness in such studies. The essential geometry of the simulations is outlined and models for the multiphase, turbulent nature of the flow are discussed. Two methods for the inclusion of bed roughness are explained and the solution method and model verification and validation procedures are covered.

Chapters 5 & 6 The results of the depth-resolved numerical models are split between these two chapters into 2D model results and 3D model results. Both include an outline of the simulations performed herein and the models undergo rigorous verification and validation with experimental data where available. Chapter six concludes with a discussion of the data and numerical techniques and the implications with regards to the effect of bed roughness on gravity currents.

Chapter 7 This concludes the present study with a summary of the fundamental effects of bed roughness on gravity currents that have been established through the use of experimental and numerical modelling herein. Implications derived from these conclusions are presented. Satisfaction of the aims of the thesis is demonstrated and conclusions are drawn on the techniques used in the investigation. Finally, suggestions for future work are proposed.

Chapter 2

Experimental investigation: Smooth and rough surfaces

2.1 Introduction

In this chapter the experimental methodology used in this study is outlined and the measurement techniques are explained. A brief review of relevant methods and techniques is included. Results and observations for the fundamental flow structures and dynamics of gravity currents flowing over bed roughness are presented. The chapter concludes with a discussion of the general effects of bed roughness with attention given to the effects of varying different parameters, namely, the initial density of the current, the removal of ambient fluid from between the roughness elements and the height of the fluid relative to the element height. Comments are also included on the effectiveness of the techniques used herein.

2.2 Literature Review

Laboratory experiments on gravity currents and analogous phenomena have been carried out for more than half a century. The results of many of these studies have been discussed in section 1.3. This review aims to cover some common methods and measurement techniques used for research on homogeneous currents as in the present study. Further description of experiments, techniques and applications can be found in Simpson (1997) and in Kneller and Buckee (2000).

2.2.1 Experimental configuration

The flume

The simplest flume for gravity current experiments is a lock-release or lock-exchange tank* whereby the dense fluid that will form the current is separated from the less dense ambient by a removable partition at a certain distance along the tank which creates a lock box. If the experiments require no end-wall effects then the partition is positioned in the centre of the tank (lock-exchange, Grobelbauer *et al.*, 1993; Shin *et al.*, 2004; Lowe *et al.*, 2005; Tanino *et al.*, 2005). If the end-wall effects are of interest, for example if the dynamics and effects of the bore are also under study then the lock length is shorter so that the backward propagating flow reflects off the end wall (creating the bore) and the current propagates towards the opposite 'far end wall' (lock-release, Keulegan, 1957,1958; Simpson, 1972; Rottman and Simpson, 1983; Hacker *et al.*, 1996; Kneller *et al.*, 1999; Zhu *et al.*, 2006). For experiments on axisymmetric gravity currents a cylindrical lock containing the denser fluid is placed in the centre of the tank, surrounded by the ambient fluid and then removed to release the current (Huppert, 1982). Alahyari and Longmire (1996) used a novel lock 'sector', i.e. a wedge shaped volume, which allowed them to set up their measuring equipment efficiently and with better flow coverage.

Other methods of simulating gravity currents experimentally involve releasing dense fluid from a reservoir suspended above the tank (Ellison and Turner, 1959; Hallworth *et al.*, 1998; Best *et al.*, 2001). The fluid is released as a jet and evolves into a typical current once it hits the bottom of the tank. This method is useful for gathering experimental data of the current in the constant phase but the initial conditions simulated by the lock-release or lock-exchange methods are absent.

A continual flux current can be generated by pumping the dense fluid into the ambient fluid from one end of the tank, with an outflow weir at the opposite end enabling the displaced water to overspill (Britter and Simpson, 1978; Simpson and Britter, 1979; Peters, 1999; Peters and Venart, 2000; Buckee *et al.*, 2001). This method also removes the initial adjustment of the current as it leaves the lock and no bore forms. This configuration is used when the inviscid self-similar or viscous phases are of interest, where a fully formed current, independent of any slumping or bore effects, is required. Huppert (1982) carried out continual flux axisymetric experiments by pouring dense fluid (silicone oils) into the centre of a perspex sheet to record the spreading rates.

*Note that in Kneller and Buckee (2000) they do not differentiate between a lock-release and lock-exchange tank. This is however an important consideration for modelling boundary effects on the flow.

Natural and laboratory gravity currents are typically subject to 'no-slip' on boundaries. To understand some of the features of the current it is useful to be able to control this condition. Thus, experiments have been designed in order to simulate inviscid flow, or 'free-slip' on the walls of the tank. The use of a moving floor ahead of the advancing current has the desired effect (Britter and Simpson, 1978; Simpson and Britter, 1979; Parsons and García, 1998). Less dense fluid is pumped into the tank from the same end as the moving floor, i.e. in the opposing direction to the oncoming denser current which is pumped into the tank from below. The floor moves at the same speed as the ambient fluid so that it maintains the denser fluid at rest (an 'arrested wedge') on the fixed floor downstream of the moving conveyor. Another means of creating free-slip is to generate an overflow whereby the current is released into a denser ambient and thus the current propagates along the surface (Ellison and Turner, 1959; Didden and Maxworthy, 1982; Hallworth *et al.*, 1996). However, unless this is required to model a natural process, this method can incur additional errors due to free surface effects.

Sets of experiments have also been undertaken on slopes (Ellison and Turner, 1959; Middleton, 1966a; Buckee *et al.*, 2001) and porous beds (Marino and Thomas, 2002) to study the effects of more natural topographies on gravity currents. Slopes are commonly generated using a 'tilting' tank where the slope angle can be varied for comparative analyses. Marino and Thomas (2002) used a flume with a false mesh floor raised from the tank floor to create a porous bed over (and through) which their lock-release current flowed.

The fluids

A saline solution with a fresh water ambient is the simplest means of creating a density difference for the study of the typical gravity current structure. The solution density can be changed with ease and experimental measurement remains uncomplicated by the presence of particles. Best *et al.* (2001) showed that sediment-free studies are in many ways a good analogy for low density sediment bearing currents so this simple method can potentially be used to study the effects of a broad range of conditions. The addition of alcohol (propan2ol) or sodium iodide can be used to reduce the ambient fluid density or increase the current density, respectively (Kneller *et al.* 1997, 1999; Lowe *et al.*, 2005). Gaseous gravity currents can be generated, for example, for heavier-than-air-gas (HTAG, Petersen, 1987, 1989) and smoke propagation studies. However, it is common for these studies to use saline or liquid because it is easier and often less dangerous to handle (e.g.

Fleischmann and McGrattan, 1999; Weng *et al.*, 2002). Fluid temperature also creates a density difference and is particularly relevant to atmospheric studies, for example, cold fronts. However, like gases, laboratory experiments are harder to set up using this method and often analogised to saline work.

In addition to changing the fluid density, the viscosity of the current solution can be simply increased by adding sugar to the current fluid (Keulegan, 1957; Simpson, 1972). For studies of much higher viscosities Huppert (1982) used silicone oils and Amy *et al.* (2005) used glycerol.

Bed roughness

In nature, bed roughness might be a grain type roughness such as sand or gravel or a form type such as ripples or dunes, as discussed in section 1.3.3. In the laboratory, simplified versions of these roughnesses have been studied extensively for their effects on pipe and open channel flow including different grades of sand, grooves, different shaped riblets and wire grids (see Jimenez, 2004 for an overview of pipes). Flow over dunes and ripples have been studied extensively, for example Maddux *et al.* (2003a, 2003b) studied the dynamics of a turbulent continual flux flow in a flume over a bed of 3D fixed dunes with 1 mm mean diameter coarse sand but little has been done specifically on gravity currents.

In the gravity current literature, Hallworth *et al.* (1996) used a thin layer of granules with a mean grain diameter of about 2 mm for an entrainment study but did not go into detail on how these granules were included in the tank setup. Peters (1999) and Peters and Venart (2000) studied the effects of 'd-type' beams perpendicular to the flow using beams of sizes 6, 13, 19 and 25 mm square pinned to the bed of the tank and a continual flux current pumped over them. In a lock-release particle-driven gravity current study, Kubo (2003) looked at the effects of a ramp followed by a series of 'humps' on sediment deposition. However, the material and method by which the topography is included is not stated. Moreover, the height of the topography relative to the fluid means blocking occurs which is characteristic of arrays of obstacles, rather than bed roughness. See chapter 1 for further background on bed roughness studies.

2.2.2 Data capture and measurement techniques

Typical physical characteristics and current height

Photography and video capture techniques provide a relatively simple 'dataset' to physically observe any qualitative changes to the flow dynamics resulting from the laboratory configuration in use. They can be used as pointers to potential changes or factors of interest in a quantitative study and aid in the interpretation of quantitative results.

A higher resolution method for visualising the typical current shape, including the interfacial mixing and billows, is laser induced fluorescence (LIF, Parsons and García, 1998; Peters, 1999; Peters and Venart, 2000). The fluid is illuminated using a dye that fluoresces at the wavelength of the laser light and features of the flow are captured with a high speed video camera. It can be effectively combined with particle image velocimetry (PIV) to give a fully qualitative and quantitative dataset. The billows and current outline can also be visualised using shadowgraphs and bromide paper (Simpson, 1997; Lowe *et al.*, 2005) which can give good interfacial definition for observing the billows. This method has also been used for the study of lobes and clefts (Simpson, 1972) and to obtain height readings, as described below.

Accurate measurement of the height is important in laboratory work for the calculation of Froude numbers and Reynolds numbers, which give an indication of the effects of scale on the results when comparing to natural currents. However, since the density interface is typically a poorly defined region of high mixing, establishing the upper boundary of the current to measure the height is a difficult task. There are also notorious problems with choosing where along the length of the current to take measurements (Shin *et al.*, 2004). Due to these discrepancies, care must be taken to be consistent when using these techniques and to be clear where the measurements have been taken. One simple method is to mark the height of whichever part of the current is required on the side of the tank as accurately as possible, at required times (Keulegan, 1958; Middleton, 1966a). Clearly this method is subject to human error and difficulties with interfacial definition but it gives a simple indication of the height. Video capture or photography and shadowgraphs can be used to record the current and then measure the height from the video frames, thus reducing human error and the need for time coordination (Simpson and Britter, 1979; Simpson, 1997). Simpson (1972) performed experiments using slit lighting with a fluorescing dye to measure the nose height.

A more theoretically defined method is to use the data from velocity measurements and

integrate them over the depth to obtain a depth-averaged velocity and height, using the equations:

$$uh = \int \overline{u} dy \tag{2.1}$$

$$u^2 h = \int \overline{u}^2 dy \tag{2.2}$$

following the method of Ellison and Turner (1959).

Density, concentration and entrainment

Measuring the changing concentration levels of the current during experiments enables the study of mixing and entrainment which are essential to the distribution of energy in the flow and ultimately the transport of sediment. For homogeneous currents, Didden and Maxworthy (1982) and Parsons and García (1998) used conductivity probes and Keulegan (1957, 1958) used parallel wire electrodes with success. With the advance of laser technology, LIF has become an accurate non-intrusive method for visualising the flow and measuring concentration (Peters, 1999; Peters and Venart, 2000).

Hallworth *et al.* (1996) used a novel neutralisation technique with an alkaline current and an acidic ambient. Universal pH indicator solution turns the acid red (pH $<$ 4) and the alkaline purple (pH $>$ 10) and regions of mixing are shades in between depending on the ratio of acid to alkaline in the mixed fluid. Thus the volume fraction of one fluid to the other can be calculated by measuring the pH in these mixed regions to give a quantitative value for concentration and mixing.

Another relatively simple method is to record light attenuation in a dyed current (Hacker *et al.*, 1996). A light is placed on one side of the tank directed perpendicular to the current through the flume side walls. A video camera captures the current and the light from the other side of the tank. The film is processed and in regions of the current where the dye is darker, light has been attenuated and current fluid is thus more concentrated. The amount of light that is emitted can be calculated and is proportional to the concentration and hence the amount of mixing occurring.

Front position and speed

The position of the front as a function of time for lock-release (or lock-exchange) experiments is a simple and useful dataset to compile for indication of any immediate effects of the tank configuration on the current. The front position and speed are frequently used to validate theoretical methods (e.g. Rottman and Simpson, 1983) so their accuracy is

essential. Plotting the front position as a function of time establishes which phase of the flow the current is governed by in the time period of interest, where the phase transitions occur and hence any differences in these transitions for different flow conditions. The front speed is calculated for the constant speed phase from the front position data.

A common method for capturing the front position is to record the experiments with a video camera from flow initiation over the required time period or distance and to measure the distance that the front has travelled along the tank at regular intervals in time or space (Middleton, 1966a; Didden and Maxworthy, 1982; Rottman and Simpson, 1983; Lowe *et al.*, 2005). Since many experimental techniques involve the use of video cameras for the study of other flow characteristics or as an experimental record this data is often readily available. A similar method involves marking the position of the front on the tank or noting the time at regular time or space intervals, respectively.

Velocity

There are intrusive and non-intrusive techniques for measuring the internal velocities in gravity currents. PIV is a laser based non-intrusive method that has been successfully used to study all three components of velocity in gravity currents to a high level of accuracy (Zhu *et al.*, 2006). Kneller *et al.* (1997, 1999) and Buckee *et al.* (2001) used laser Doppler anamometry (LDA), another non-intrusive technique, to obtain downstream and vertical velocities with a velocity resolution of ± 2 mms^{-1}. However, laser based equipment is expensive, requires the refractive indices of the fluids to be matched, cannot be used with particles and can be complex to setup depending on the facilities available. Consequently, if a study is not primarily interested in gaining high resolution internal velocity data then other techniques are more commonly used. Acoustic methods such as ultrasonic Doppler velocity profiling (UDVP, Best *et al.*, 2001) are simpler to implement but this is an intrusive method so has to be setup so as to minimise the interference with the flow dynamics. The UDVP method also only captures the component of velocity along which the transducers are aligned (see section 2.3) so in order to obtain a 3D dataset, i.e. three components for one point, three probes are required, one directed along each axis. However, since the largest component of velocity in gravity currents is along the downstream horizontal (assuming the component is aligned parallel with the bed), after the initial slumping phase, data from probes on this axis can give a good indication of the effects of the condition under investigation on the current before a more complex method is applied. Particle tracking velocimetry (PTV) is another

simpler method than PIV or LDA but gives similar accuracy (Thomas *et al.*, 2003). It's simplicity is due to the use of halogen lamp light rather than lasers. The light illuminates particles carried by the flow and images for particle tracking are obtained using a video camera and recorded as a luminescence signal.

Turbulence

The term 'turbulence' covers several variables, e.g. root mean-squared velocities (u_{rms}), turbulent kinetic energy, etc. and can be measured in different ways depending on which or how many of these datasets are required. The question of whether a flow is turbulent or not is typically determined by calculation of a flow Reynolds number using a characteristic velocity and length scale of the flow and the fluid's dynamic viscosity:

$$Re = UL/\nu \tag{2.3}$$

Note that this value can vary substantially depending on which values of U and L are taken. Flows with Re $\gtrsim$ 2000 are considered turbulent. The calculation simply requires the use of measurement techniques previously outlined to obtain the necessary parameters in equation (2.3). However, for a more detailed study of the turbulence structure, for example calculation of Reynolds stresses, high resolution velocity data in more than one dimension is required to determine more accurately the scale of the turbulent fluctuations within the flow. More sensitive equipment, such as anemometers (e.g. LDA Kneller *et al.*, 1997; Kneller *et al.*, 1999; Buckee *et al.*, 2001) are used for resolution down to small length scales and velocity capture methods such as PIV can obtain three-dimensional data and UDVP has high enough resolution to calculate the root mean square velocity in one dimension and for the study of the fundamental turbulence structures within the flow (e.g. the presence of turbulent interfacial instabilities can be readily observed from this data (Best *et al.*, 2001)).

2.2.3 Summary

Gravity currents are highly complex flow processes. Hence experimental studies of them advance as the ability of new technology to capture higher resolution data and thus finer details increases. Since bed roughness effects are a relatively unstudied topic in this subject, the present experiments aim to create an accurate preliminary dataset using the simpler flow measurement techniques outlined in the foregoing review. Additional techniques have been applied when considered essential in understanding the fundamental effects of roughness.

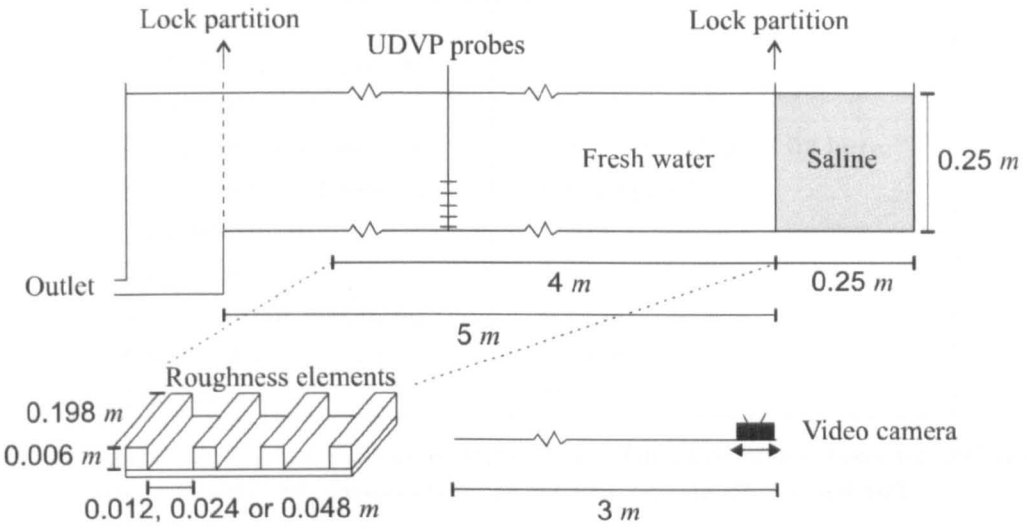

Figure 2.1: Sketch of the tank configuration and dimensions used in the present study. The sand, spheres and beams roughness elements are mounted on perspex sheets 2 mm thick and placed in the bottom of the tank covering a 4 m long region from the lock partition. Dimensions of the beams roughness are shown.

In light of the present literature, simple bed roughnesses have been used to study a variety of roughness types in order to create initial datasets for several 'bedforms' that can be expanded on in future work.

2.3 Experimental methodology

All experiments herein were carried out in the Sorby Environmental Fluid Dynamics Laboratory at the University of Leeds. The flume tank used was designed specifically for the study of lock-release density currents, see figures 2.1 and 2.2 (a) and (b). It is fixed to the wall of the laboratory on adjustable brackets and is constructed as one unit with a plunge tank at one end with an outlet pipe. There are two lock partitions, one at either end, so that studies of reflected currents (bores) can also be undertaken. There is a fresh water source with a hose immediately above the tank for filling.

Tank configuration and dimensions

The flume is used with just one lock partition in place at the right hand end. It is 5 m long from lock partition to lock partition, 0.2 m wide and 0.3 m high, filled with fresh water to a maximum depth of 0.25 m in the present experiments. The lock box is 0.25 m long, 0.3 m high and 0.2 m wide so that when filled to 0.25 m it creates a 2D lock box

Tank height, H'	0.3 m
Ambient fluid height, H	0.25 m
Flow temperature	$\approx 18°$c
Initial current density, ρ_1	999.2/1048.11/1098.02 kg/m^3
Initial ambient density, ρ_2	998.2 kg/m^3
Tank width, W	0.2 m
Tank length, L	5 m
Initial current height, h_0	0.25 m
Lock length, x_0	0.25 m
Current volume	12.5 l

Table 2.1: Initial conditions typical of all experiments. The three values shown for the initial current density represent three excesses over the ambient, namely 1%, 5% and 10%.

length to initial fluid height aspect ratio (x_0/h_0) of 1 and an initial current to ambient height ratio (h_0/H) of 1. These specifications are summarised as initial conditions in table 2.1.

Five vertically aligned UDVP probes are set up 3 m from the lock partition at the half-width of the tank ($W/2 = 0.1$ m) and directed along the centre plane of the current. The probes were mounted in a rig with 3 different configurations depending on the run (see figure 2.3 (b) and (c)). For a standard run, they were at 6, 27, 48, 68 and 89 mm above the bed. To obtain more data points below the nose of the front, in order to calculate k_s values, the probes were mounted at 6, 17, 27, 37 and 48 mm and then shifted up 5 mm to 11, 22, 32, 42 and 53 mm in a second repeat experiment. One vertical probe is positioned at 2.89 m from the lock partition, at the tank half-width with the probe tip 190 mm above the bed. The setup parameters of the UDVP (see table 2.2) were selected so that each probe measured a distance of 30.9 mm (bin 35) from a starting position 5 mm upstream of the probes.

The video camera is attached to a carriage setup on a track parallel to the tank in order to retain the head of the current in the view finder as it propagates (see figure 2.3). The camera view is initialised at the lock box just before the current is released and can follow the current head the full length of the tank.

The tank is modified for the presence of roughness by using perspex inserts with the required roughness elements, see figure 2.2 (f). There are four inserts for each roughness type, each 1 m long and 0.198 m wide so that they fit into the first 4 m of the tank from the lock partition. There are five roughness element shapes used in the present study, namely, coarse sand ($\approx$2 mm diameter but true grain distribution unknown), 6

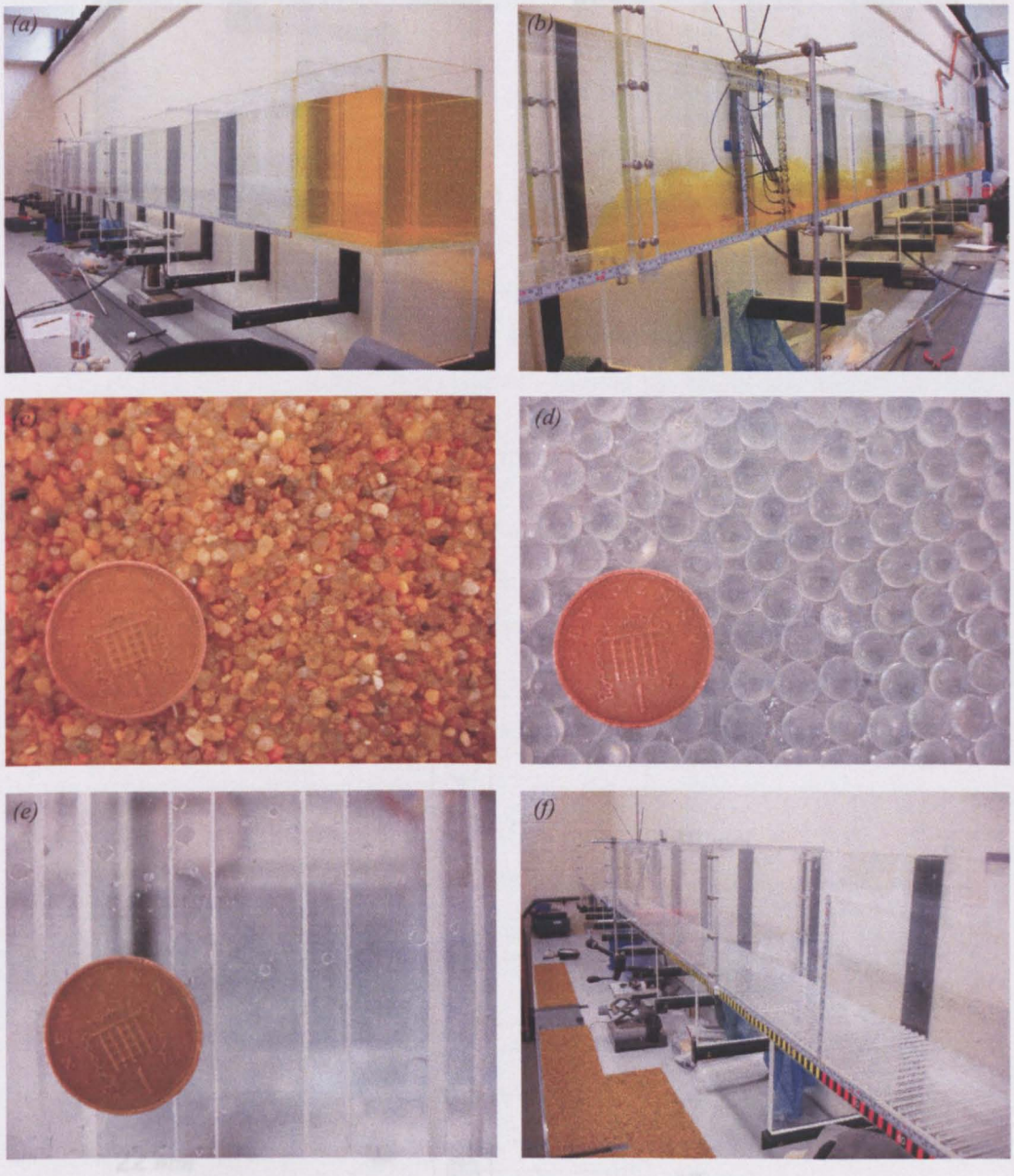

Figure 2.2: Photographs of different aspects of the flume setup. (*a*) The flume setup before release (without the camera rigged), (*b*) Gravity current after release showing position of probes with respect to the current, (*c*) ≈2 mm coarse sand roughness, (*d*) 6 mm diameter glass spheres roughness, (*e*) 6 mm high, 12 mm apart perspex beams roughness, (*e*) The flume with the beams in place and sand inserts on the work surface.

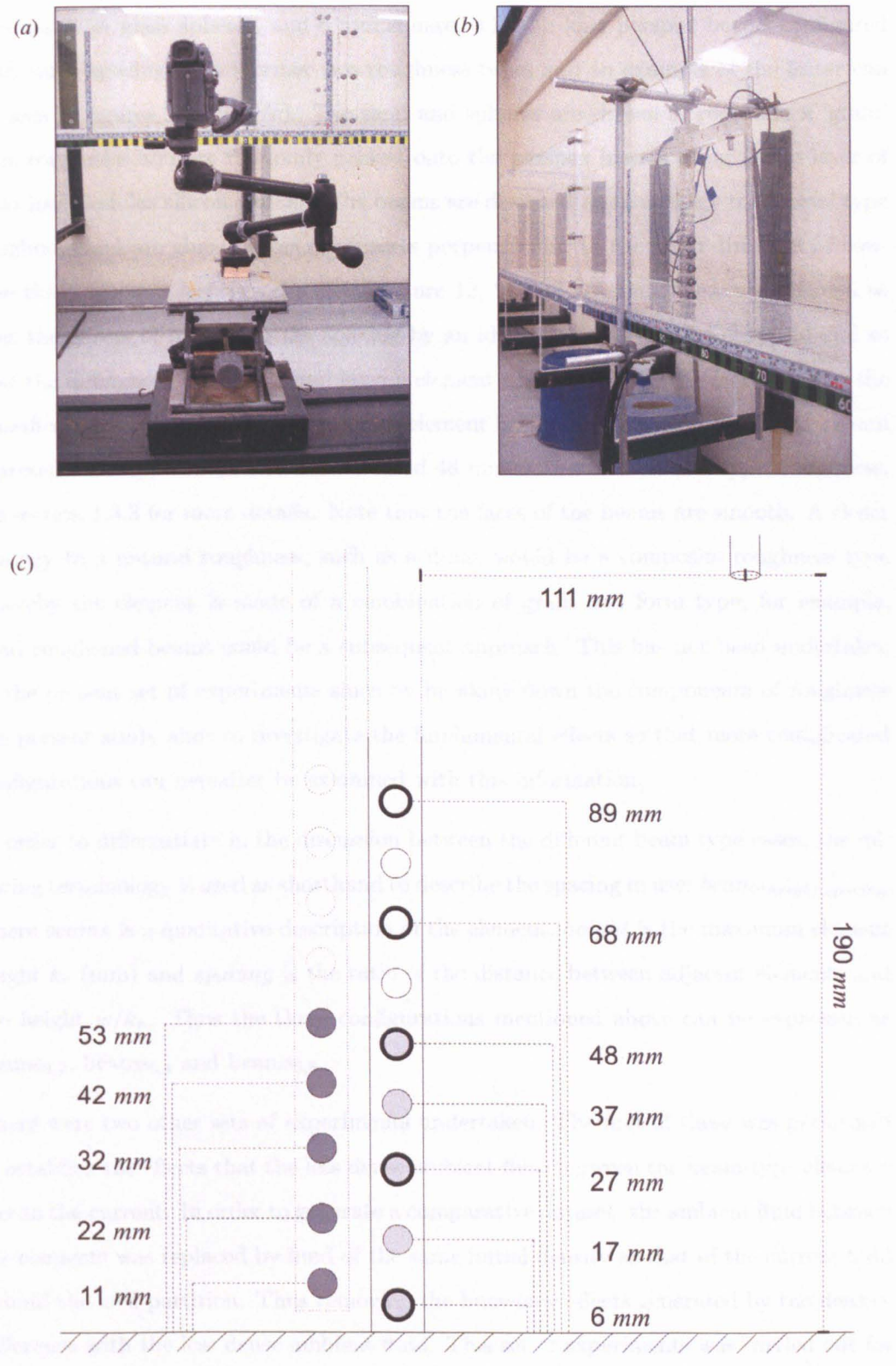

Figure 2.3: Camera and UDVP rig setup in the laboratory. (a) Camera rig and positioning facing the tank, (b) UDVP rig in the tank, (c) Diagram of the different probe positions within the UDVP rig (not to scale). The measurements relate to heights from the tank bed. The right hand side with bold circles represent the standard probe setup, the light grey shows the configuration with the probes close-packed and at the lowest setting near the bed. The left hand side dark grey circles show the close-packed probe setting shifted up 5 mm.

mm diameter glass spheres, and 6 mm square, 0.198 m long perspex beams configured with three spacings. The former two roughness types and an example of the latter can be seen in figures 2.2 $(c) - (e)$. The sand and spheres are chosen to represent a 'grain' type roughness and are randomly packed onto the perspex inserts using a thin layer of clear low modulas silicon sealant. The beams are designed as an analogy to a 'form' type roughness and are glued across the inserts perpendicular to the main direction of flow. The three spacings between the elements are 12, 24 and 48 mm. These were chosen so that the effects of increasing the spacing by an identical factor can be observed and so that the differences between d and k-type element spacings can be discussed. Under the classification of Perry *et al.* (1969), for an element height $k_r = 6$ mm, a spacing of 12 mm represents a d-type roughness while 24 and 48 mm are considered a 'k-type' roughness, see section 1.3.3 for more details. Note that the faces of the beams are smooth. A closer analogy to a natural roughness, such as a dune, would be a composite roughness type whereby the element is made of a combination of grain and form type, for example, sand roughened beams could be a subsequent approach. This has not been undertaken in the present set of experiments since by breaking down the components of roughness the present study aims to investigate the fundamental effects so that more complicated configurations can hereafter be examined with this information.

In order to differentiate in the discussion between the different beam type cases, the following terminology is used as shorthand to describe the spacing in use: $beams_{height,spacing}$, where *beams* is a qualitative description of the element, *height* is the maximum element height k_r (mm) and *spacing* is the ratio of the distance between adjacent elements and the height w/k_r. Thus the three configurations mentioned above can be expressed as $\text{beams}_{6,2}$, $\text{beams}_{6,4}$ and $\text{beams}_{6,8}$.

There were two other sets of experiments undertaken. The first of these was performed to establish the effects that the less dense ambient fluid between the beam-type elements has on the current. In order to generate a comparative dataset, the ambient fluid between the elements was replaced by fluid of the same initial density as that of the current fluid behind the lock partition. Thus removing the buoyancy effects generated by the density difference with the less dense ambient fluid. This set of experiments was carried out for the 5% density excess only and therefore fluid of this density was inserted between the elements. These experiments with dense fluid within the gaps were performed for the d-type $\text{beams}_{6,2}$ case and the k-type $\text{beams}_{6,8}$ case.

The final set of experiments involved reducing the total height to which the tank and

lock-box were filled by half in order to observe the effect of increasing the bed roughness height relative to the current height. Again these experiments were performed using only the 5% density excess. However, all five bed roughness configurations were investigated. Since the gravity current height in these cases is significantly reduced, the probes were setup so that they could obtain the required data, i.e. the lowest probe configuration shown in figure 2.3 (c) was used whereby the probes were mounted at 6, 17, 27, 37 and 48 mm.

Front position and internal velocity measurement

The front position of the current in time was measured using a Sony PAL DV video camera, recording 720 × 576 pixels at 25 Hz. By analysing the video frame by frame, the location of the gravity current front can be measured at the required time intervals. The speed of the front in the constant phase is calculated by plotting the front position in time and fitting a linear best fit line through the data using the greatest amount of data points to gain the highest R^2 value. The gradient $\frac{dx_f}{dt}$ of this line gives the speed. If all of the data points are used in the fit then the R^2 value decreases and it is assumed that values that are not consistent with data within the constant speed phase are being included. Hence, the speeds displayed herein for the smooth case are for the time period from 0 within which R^2 is high and thus the current can be said to be within the constant phase. Beyond this, the remaining data lies within a different phase. For consistency, the same amount of data is used in the rough cases as in the smooth case.

Ultrasonic Doppler velocity profiling (UDVP) was used to measure the velocity field within the gravity currents. The use of UDVP has been proven in its use in investigations of gravity currents (Best *et al.*, 2001). It can be used to measure negative and positive components of velocity to which the probes are aligned in the flow, i.e. a horizontally aligned probe will give readings for the downstream horizontal velocity component.

The UDVP transmits an ultrasound pulse in a straight line from the probe at a certain frequency which in these experiments is 4 MHz. The transducers then switch almost instantaneously from transmitting to receiving and the transducer receives the echo reflected from the surface of small particles suspended in the flow. By detecting the Doppler shift frequency as particles pass through the measurement volume, the flow velocity can be calculated at one point. This is carried out simultaneously to obtain velocity measurements along a profile. The return signal or echo detecting the shift frequency is 'gated' at certain return times and enables the velocity to be measured at 128 points (in this study, but this value can be changed) along the beam of the

ultrasound. This effectively splits the length of flow through which the beam penetrates into 128 measurement volumes or bins. The length of the measuring volume in the experiments presented here was 0.74 mm. The height of the bin varies with the distance from the transducer since it is a function of the beam divergence which in turn is a function of the transducer size and ultrasound frequency. For the 4 MHz probes used, beam divergence is 2.5° about the beam axis, i.e. 5° in total. The result of this is that the beam measurement volume increases with increasing distance from the probe. The finite amount of time required in switching between transmitting and receiving means that the first measurement point is a minimum of 5 mm from the tip of the probe. This is the location of the first bin in these experiments. Thus the measurement window covered by the ultrasound beam was 5 - 98.98 mm. For the streamwise horizontal velocity data, an array of five 4 MHz ultrasonic probes was used which were multiplexed using the UDVP logger. The time taken for each profile measurement is a function of the maximum measurement distance and the finite time required for data processing and switching between channels. With the current setup, the sampling time for each profile was 39, 21 and 17 ms for 1, 5 and 10% currents, respectively, and the switching time between the probes was 15 ms so that each of the profiles sampled at approximately 3.09 Hz for the 1% runs, 4.63 Hz for the 5% runs and 5.21 Hz for the 10% runs. The parameters used by the UDVP for the streamwise horizontal velocity measurements in the present experiments can be seen in table 2.2. For the vertical velocity data, one 4 MHz ultrasonic probe was used.

Bed roughness measurement

The bed roughness is measured using the velocity profile data. Below the velocity maximum of a current profile the current velocity diminishes to zero at the bed. Within this inner region, below u_{max}, drag at the lower boundary creates a logarithmic velocity profile where the von Karman-Prandtl log law of the wall applies (Kneller *et al.*, 1999). This can be written in terms of the equivalent roughness, k_s, as

$$\frac{\overline{u}}{u_*} = 2.5ln\frac{y}{k_s} + 8.5 \tag{2.4}$$

where u_* is the shear velocity, y is the height from the bed, the value 2.5 comes from the von Karman constant and 8.5 is based on the sand grain pipe experiments of Nikuradse (1933), and hence the k_s value found using this method is an equivalent *sand* roughness (Southard, 2006). By finding the zero velocity intercept of a least squares regression of $\overline{u}$ vs lny for the velocity data below the maximum, and using equation (2.4) the value

Frequency (MHz)	4		
Transducer & probe diameter (mm)	5 & 8		
Measurement window (mm)	5 - 98.98		
Maximum velocity (mms^{-1})	99.2	248	348
Measurement bin length (mm)	0.74		
Number of channels	128		
Velocity resolution (mms^{-1})	0.781	1.953	2.740
Ultrasound velocity (ms^{-1})	1480		
Sampling time for each profile (ms)	39	21	17
Delay time between profiles (ms)	15		
Sampling frequency/probe (Hz)	3.09	4.63	5.21
Pulse repetition frequency (Hz)	1072	2681	3762
Number of profiles	3000		
Channel width (mm)	5.92		

Table 2.2: Parameters of the ultrasonic Doppler velocity profiler used in the present experiments. Where three values are given, from left to right these correspond to 1%, 5% and 10% parameters.

of k_s can be estimated.

Accuracy and errors

One source of error was in the accurate positioning of the probes. This was minimised by rigging the probe mount so that it was held by fixed rails which kept it in place (see figure 2.3 (*b*)). The positioning of the mount was checked before each run was carried out. It is estimated that the error in the horizontal and vertical positioning of the probes was not more than ± 1 mm.

Another source of error comes from parallax effects when capturing the video footage. This is the distance related error when the measurement undertaken relies on the 'field of view' as with video capturing systems (Tian *et al.*, 2002). The error is reduced by placing the device facing side on, perpendicular to the object of interest, i.e. the front in the present study, and moving the camera steadily with the object.

The accuracy of the calculation of the k_s values is dependent on the data that can be captured below the nose; hence it is dependent on the number of UDVP probes below the nose. For the experiments with the different bed roughnesses, there is some variability in the number of probes that can obtain measurements below the velocity maximum, even with the probe shift, because the current height is quite small relative to the probe size and the position of u_{max} is still relatively close to the bed. In the smooth case it proved

impossible to obtain UDVP probe data below the maximum since it was so close to the bed, a technique with higher resolution like PIV or LDA is required for more accurate measurement in this zone for this case.

Preparation and experimental procedure

The tank was prepared for each run by first being thoroughly rinsed to remove any salt residue from previous runs that might alter the fluid density. The roughness elements, if used, were then slotted into the bottom of the tank and the lock partition positioned and sealed with grease to prevent leakages of dense fluid before it was released from the lock. The main body of the tank was filled with fresh water as the ambient fluid, and the saline solution prepared using table salt and fresh water to create density excesses of 1, 5 and 10% (checked with hydrometers) and dyed for visibility. Several of the 1% runs were seeded with a negligible amount of kaolin clay to aid in velocity measurement accuracy but not enough to significantly alter the density excess. The temperature of both fluids was checked to be equivalent so that the governing density difference was generated only by the difference in density due to concentration. The UDVP was checked for probe rig positioning and correct measurement parameters in the logging computer. The camera position was also checked and the name of the run recorded for ease of processing.

For the set of experiments to be used for analyses of the effects of the buoyant ambient fluid between the elements, the dense fluid was inserted between the elements by first filling the main body of the tank with fresh water as for the regular setup and then using a syringe and pipe to carefully and slowly pump by hand the dense fluid into place to minimise mixing with the displaced ambient. This dense fluid was dyed with purple dye in order to visualise its movement once the current was released.

Once the above preparation and checks had been carried out, the lock box was filled with the dense fluid. The UDVP and camera were started and the lock partition removed manually as smoothly as possible to minimise disturbance to the free surface and thus external flow effects on the current. For this reason the experiments required at least 2 people, one to remove the lock while another operated the camera.

On completion of each experiment, the data was downloaded to a PC and processed through a filtering code (Keevil *et al.*, 2006) to remove background noise and anomalous spikes in the results for subsequent post-processing analysis.

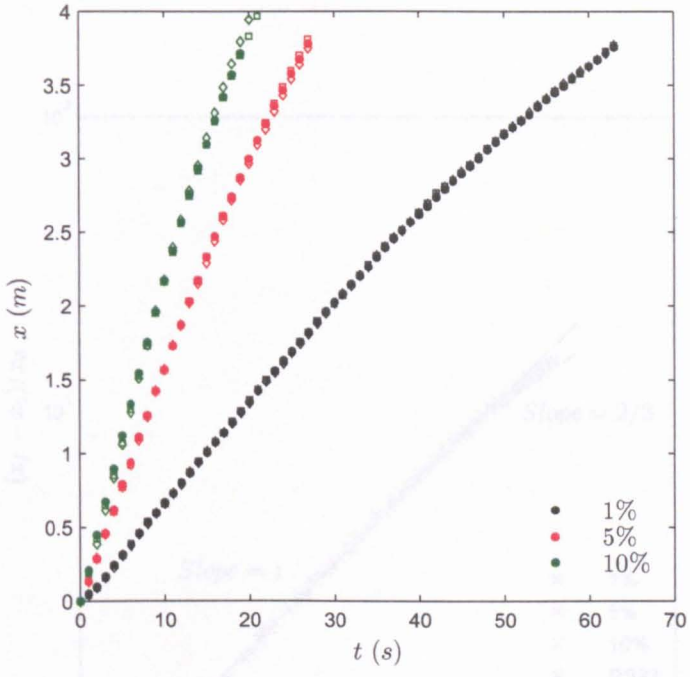

Figure 2.4: The position of the front as a function of time after release. Three runs for 1%, 5% and 10% density excesses under identical smooth bed conditions.

2.4 Verification and validation

Quantitative verification was accomplished by repeating three runs with identical smooth bed conditions and comparing them for each density excess. Figure 2.4 shows the position of the front as a function of time under these conditions. It is clear from this figure that the results are almost indistinguishable between runs for all densities. This illustrates that the experiments are reproducible and subject only to the initial and boundary conditions of the experiments and not to large errors.

In order to validate the experiments, the smooth cases are compared to existing experimental results. Rottman and Simpson (1983) showed that by normalising the front position data with the lock length in space and in time[†] and plotting it on a log scale, in the initial phase, the current front position collapses onto a line of slope 1 regardless of the initial lock conditions. Evidence of this for the present experiments can be seen in figure 2.5; the results presented are clearly consistent with the experimental data of Rottman and Simpson (1983). For simple qualitative validation, figure 2.6 shows that a gravity current with a smooth bed generated in the present experiments has typical head features consistent with previous full height release experiments (compared here

[†]Note that t_0 is defined as $x_0/\sqrt{g'h_0}$ and is verified in section 3.3.2.

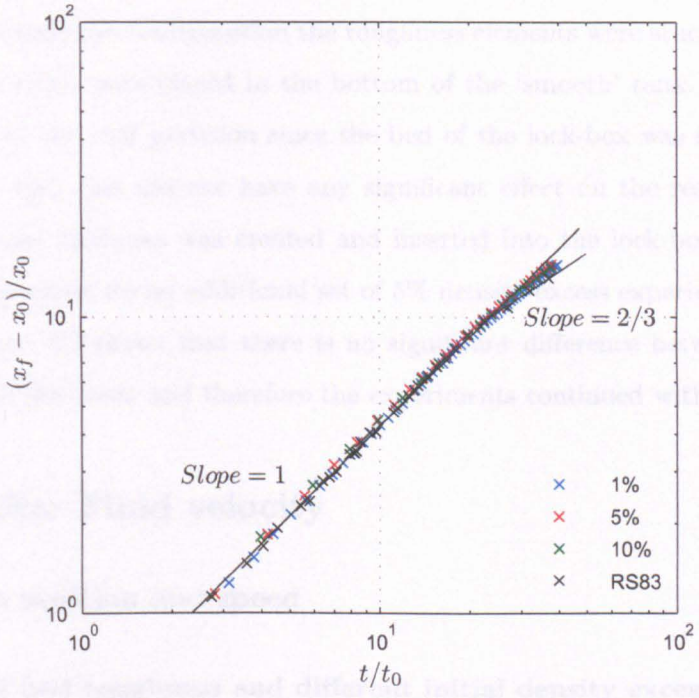

Figure 2.5: The normalised front position as a function of time for 1%, 5% and 10% experiments under smooth bed conditions with the experimental data of Rottman and Simpson (1983). Time was normalised using the expression $t_0 = x_0/\sqrt{g'h_0}$. The initial phase is represented by the line of slope 1, the inviscid self-similar phase by the line with slope 2/3.

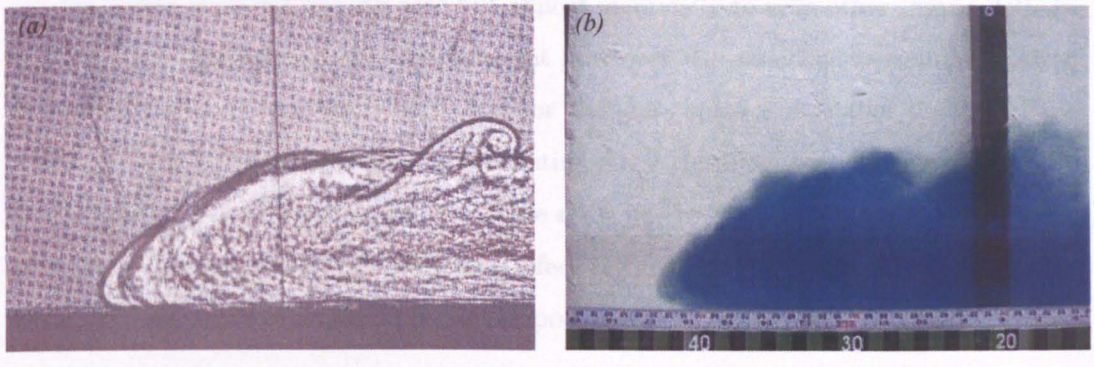

Figure 2.6: Visual verification of the present experiments. Laboratory gravity current propagating along a smooth horizontal surface. (*a*) Shadowgraph visualisation, from Simpson (1997) p. 148 and (*b*) video frame from present experiments (5% density difference).

to Simpson (1997) but there are many images of 'typical' gravity current heads in the literature).

In the experimental tank configuration the roughness elements were stuck to 2 mm thick perspex sheets which were placed in the bottom of the 'smooth' tank. This created a 2 mm step up at the lock partition since the bed of the lock-box was still smooth. In order to verify that this did not have any significant effect on the results, a perspex insert of the same thickness was created and inserted into the lock-box and the front position was measured for an additional set of 5% density excess experiments with each bed type. Figure 2.7 shows that there is no significant difference between the results with or without the insert and therefore the experiments continued without the insert.

2.5 Results: Fluid velocity

2.5.1 Front position and speed

The effects of bed roughness and different initial density excess on the front position and speed.

Figures 2.8 - 2.10 show that, for the most part, in the presence of any bed roughness gravity currents do not propagate as far as in the smooth case, regardless of the initial density excess of the fluid. The two anomalies to this general rule are the 1% density excess currents propagating over coarse sand and spheres, shown in figure 2.8, where the current position is almost identical to the smooth case at any given time. In the 5% case, the fronts have travelled less distance over the grain-type beds and are therefore moving slower than the smooth case but almost identically to each other (figure 2.9). In the 10% case, the front position for current flow over the sand bed is again similar to the smooth case but the equivalent data for the glass spheres is similar to that of the $\text{beams}_{6,2}$ case (figure 2.10). This is interesting since the $\text{beams}_{6,2}$ configuration is the closest packed case and the beams are of the same height as the diameter of the spheres, perhaps suggesting a common roughness effect regardless of the shape of the roughness itself. However, this observation is not supported by the results for the other densities.

The time at which the currents begin to slow down under the affects of roughness is independent of the bed roughness type but the rate at which it propagates thereafter is dependent, with the beam type roughnesses incurring a greater slowing effect. For this type of roughness, the retarding effect on the flow increases with spacing in the 1% case (figure 2.8) while for the two higher density currents (figures 2.9 and 2.10), a difference

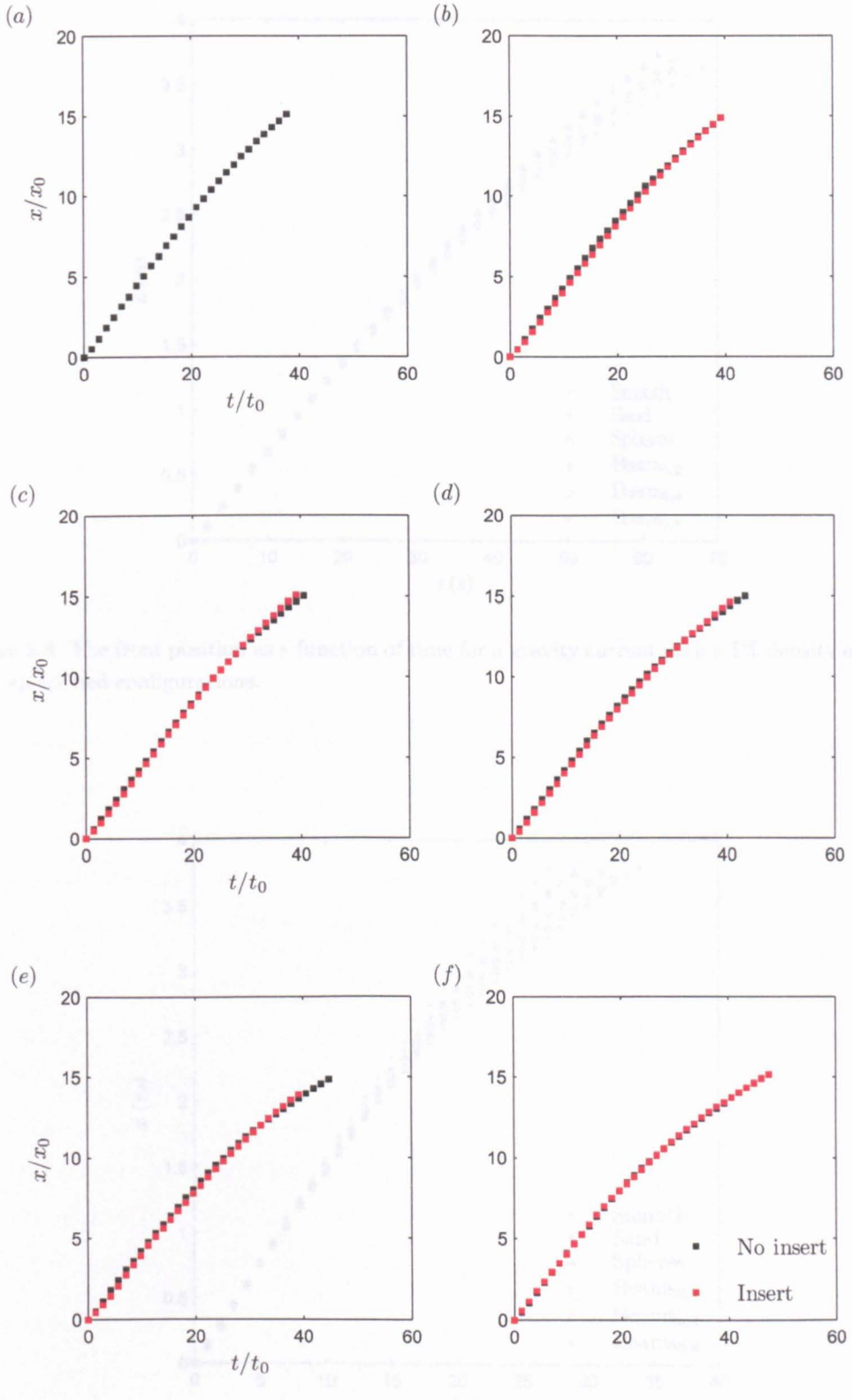

Figure 2.7: The front position as a function of time, normalised using x_0 and $t_0 = x_0/\sqrt{g'h_0}$, for a 5% density excess with and without an inserted perspex sheet in the lock box for (a) smooth, (b) sand, (c) spheres, (d) beams$_{6,2}$, (e) beams$_{6,4}$ and (f) beams$_{6,8}$ bed configurations. Note that the insert is not present in the smooth case, it is included for completion.

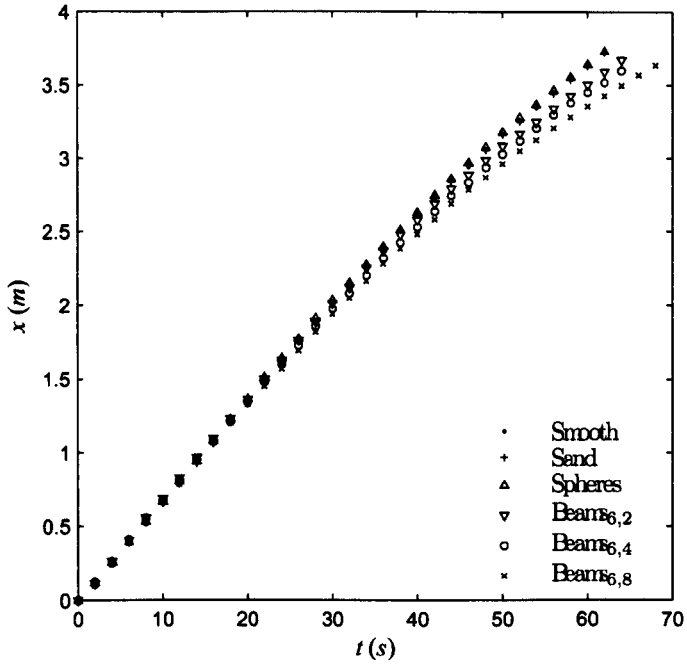

Figure 2.8: The front position as a function of time for a gravity current with a 1% density excess with all six bed configurations.

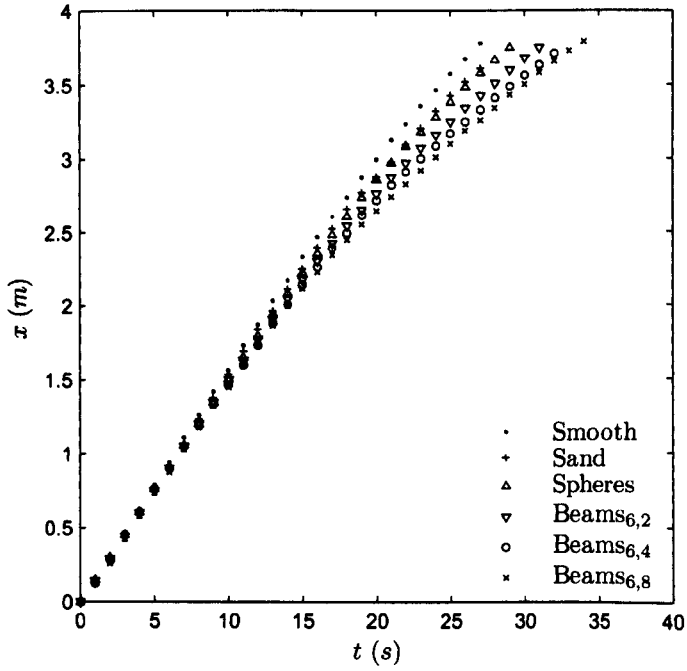

Figure 2.9: The front position as a function of time for a gravity current with a 5% density excess with all six bed configurations.

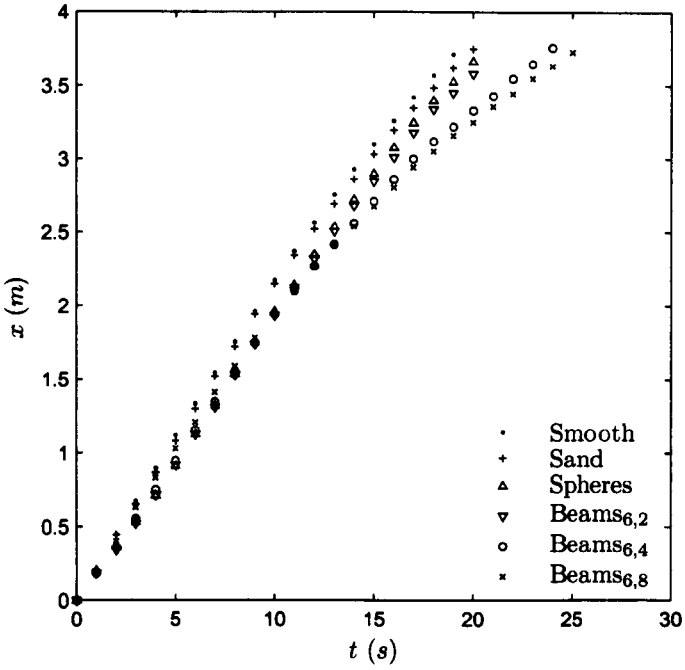

Figure 2.10: The front position as a function of time for a gravity current with a 10% density excess with all six bed configurations.

can be observed between the propagation of the front over the d-type and k-type beds at later times. This is particularly exaggerated in the 10% case (figure 2.10) where the data from the two k-type spacings diverges from the rest and this suggests a relationship between the distance the current propagates with time and the type of spacing, d- or k-type, at least for square beam roughnesses.

There is a significant difference observed in figures 2.8 - 2.10 in the time at which the current begins to slow down for each of the three initial densities. However, if the time is normalised with respect to the initial density excess using $t_0 = x_0/\sqrt{g'h_0}$ and displayed on a log-log scale (figure 2.11), it can be observed that the data collapses particularly well for the smooth and sand beds and also quite well for the other beds. This implies that the relative position of the current at a given time is essentially independent of the initial density of the current.

Front speeds calculated using the gradient, $\frac{dx_f}{dt}$, of the linear best fit of the front position data in figures 2.8 - 2.10 are shown in tables 2.3 $(a) - (c)$. The values in these tables were calculated based on a linear regression over the time period within which the data from the smooth runs are estimated to be in the constant speed phase, as described in section 2.3. It can be seen that the R^2 values for the rough cases are not consistently as high over this time period. This consistent variation suggests that this is not the result

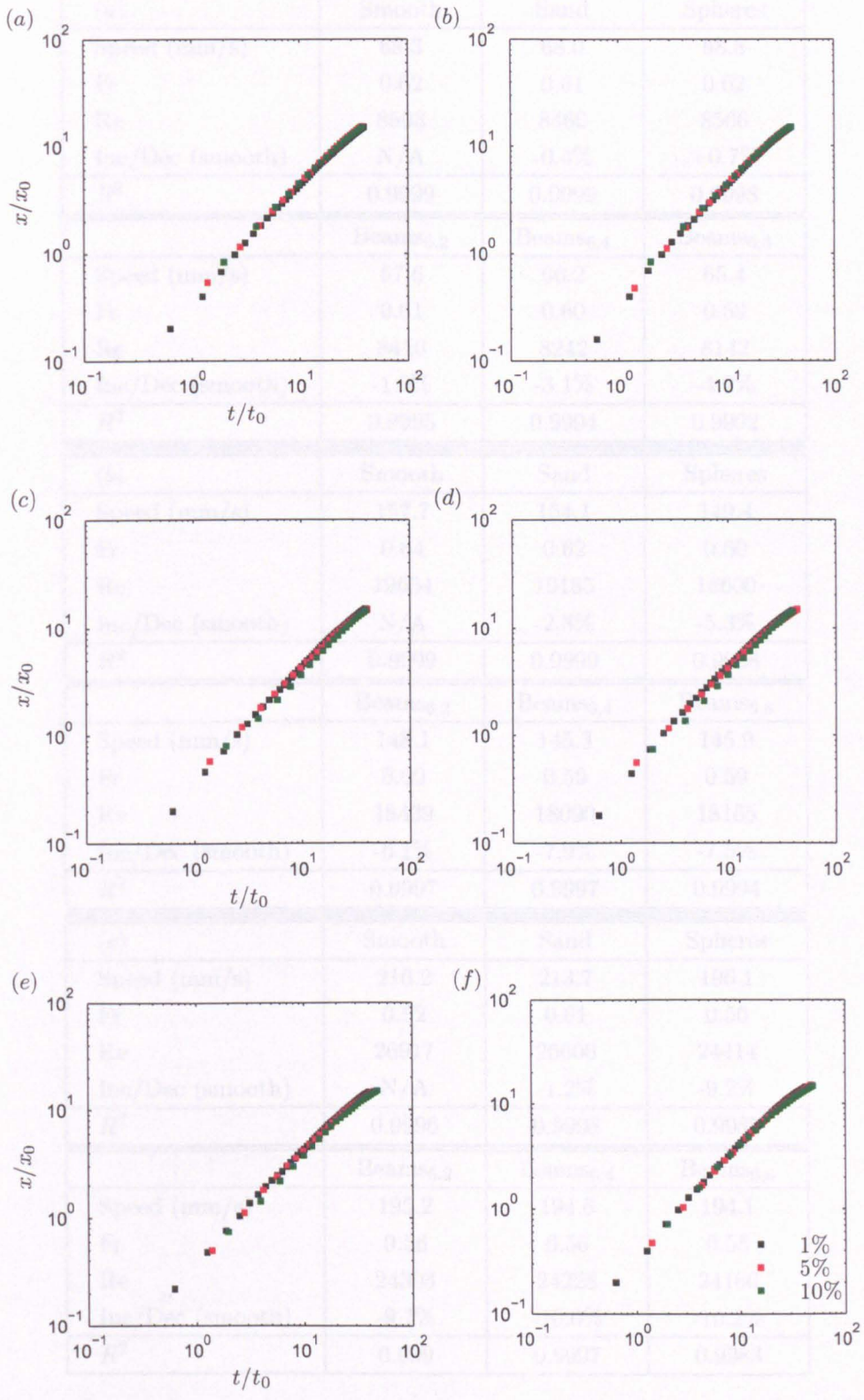

Figure 2.11: The front position as a function of time, normalised using x_0 and $t_0 = x_0/\sqrt{g'h_0}$ for gravity currents of 1%, 5% and 10% initial density excesses with (*a*) smooth, (*b*) sand, (*c*) spheres, (*d*) beams$_{6,2}$, (*e*) beams$_{6,4}$ and (*f*) beams$_{6,8}$ bed configurations.

(*a*)	Smooth	Sand	Spheres
Speed (mm/s)	68.3	68.0	68.8
Fr	0.62	0.61	0.62
Re	8503	8466	8566
Inc/Dec (smooth)	N/A	-0.4%	+0.7%
R^2	0.9999	0.9999	0.9998
	$Beams_{6,2}$	$Beams_{6,4}$	$Beams_{6,8}$
Speed (mm/s)	67.6	66.2	65.4
Fr	0.61	0.60	0.59
Re	8416	8242	8142
Inc/Dec (smooth)	-1.0%	-3.1%	-4.2%
R^2	0.9995	0.9994	0.9992

(*b*)	Smooth	Sand	Spheres
Speed (mm/s)	157.7	154.1	149.4
Fr	0.64	0.62	0.60
Re	19634	19185	18600
Inc/Dec (smooth)	N/A	-2.3%	-5.3%
R^2	0.9999	0.9999	0.9998
	$Beams_{6,2}$	$Beams_{6,4}$	$Beams_{6,8}$
Speed (mm/s)	148.1	145.3	145.9
Fr	0.60	0.59	0.59
Re	18439	18090	18165
Inc/Dec (smooth)	-6.1%	-7.9%	-7.5%
R^2	0.9997	0.9997	0.9994

(*c*)	Smooth	Sand	Spheres
Speed (mm/s)	216.2	213.7	196.1
Fr	0.62	0.61	0.56
Re	26917	26606	24414
Inc/Dec (smooth)	N/A	-1.2%	-9.2%
R^2	0.9996	0.9998	0.9985
	$Beams_{6,2}$	$Beams_{6,4}$	$Beams_{6,8}$
Speed (mm/s)	195.2	194.6	194.1
Fr	0.56	0.56	0.55
Re	24303	24228	24166
Inc/Dec (smooth)	-9.7%	-10.0%	-10.2%
R^2	0.999	0.9997	0.9983

Table 2.3: Front speeds for all six bed roughnesses for (*a*) 1%, (*b*) 5%, and (*c*) 10% density excess calculated using the first 60% of the front speed data where the smooth case is within the constant speed phase. Also shown is the percentage increase or decrease in front speed with respect to the smooth experiment.

of measurement error but rather that the rough cases behave in a different manner to the smooth case and are therefore not governed by the same flow regimes.

As expected, the speed of the current increases with the increase in the initial density excess of the current. The 1% current propagates at a speed of only approximately 43% of the 5% current front speed in the smooth case, and similar differences apply in the rough cases. The 10% case shows an increase of approximately a third relative to the 5% case. Other than the effect of the spheres on the front speed of the 1% density current, tables 2.3 $(a)-(c)$ confirm that the presence of bed roughness has a slowing effect on the current. The anomalous result is probably due to experimental error. Other than this discrepancy, if the percentage decrease compared to the smooth case is considered, for all densities it can be seen that the sand bed has the least retarding effect. The widest spaced $\text{beams}_{6,8}$ case has the most significant slowing effect in all except the 5% currents but in this case the difference between this result and the slightly closer packed, $\text{beams}_{6,4}$ case, is only 0.4%. Furthermore this suggests that there might be a maximum spacing beyond which the effects of this type of bed roughness on the front speed do not change substantially. Clearly, the grain type roughnesses have less effect than the beam-types, even in the spheres case where the diameter is identical to that of the beams.

The Froude and Reynolds number at the front, calculated using $Fr = \frac{u_f}{\sqrt{g'h_0/2}}$ and $Re = \frac{u_f h_0/2}{\nu}$, where $\nu = 1 \times 10^{-6}$ m^2s^{-1} is the kinematic viscosity of fresh water at 20°C, can also be seen in tables 2.3 $(a)-(c)$. Clearly, when the Froude and Reynolds numbers are calculated with these parameters, the currents can be classified as turbulent and subcritical in all cases. The lower values for the 1% current are to be expected since the density difference, and hence the buoyant driving force of the flow, is smaller. In the 5% and 10% cases it can be seen that there is a decrease in Fr and Re under the influence of any bed roughness. The coarse sand shows the smallest magnitude change in these values, the spheres are the next most effective and the effect of the beams appears to increase with increasing spacing. The data in tables 2.3 (b) and (c) also suggest a possible connection between the spheres and the d-type beams, $\text{beams}_{6,2}$ and similarities between the two k-type beam cases. Fr and Re are also calculated subsequently in section 2.5.4, using the depth averaged values h_{da} and u_{da}. The values presented here give an indication of the effect of the retardation at the front on these parameters using a conservative value for h.

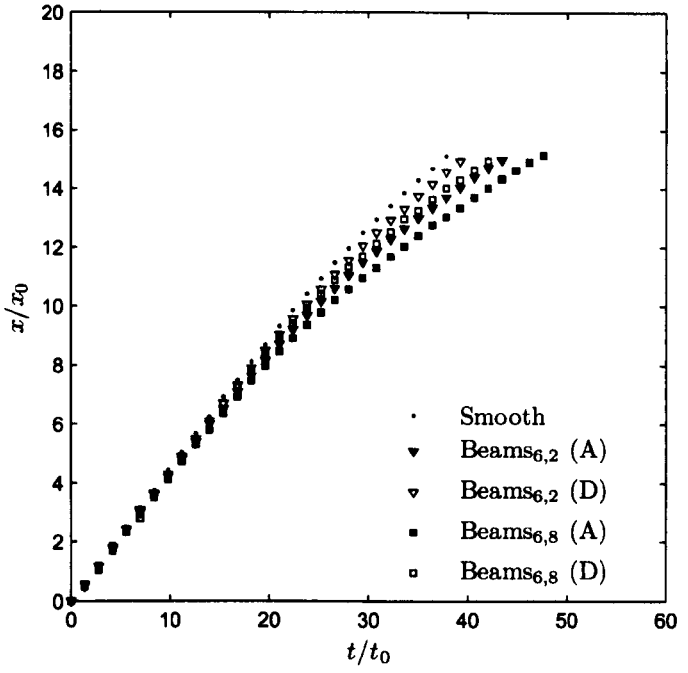

Figure 2.12: The front position as a function of time for the 5% density excess with (D) and without (A) dense fluid initialised between the roughness elements. Also displayed is the smooth bed result for comparison.

	Beams$_{6,2}$	Beams$_{6,8}$
Speed (mm/s)	153.2	151.9
Fr	0.62	0.61
Re	19074	18912
Inc/Dec (smooth)	-2.9%	-3.7%
Inc/Dec (ambient)	+3.4%	+4.1%
R^2	0.9999	0.9999

Table 2.4: Front speeds generated with a 5% density excess for a bottom boundary with beams$_{6,2}$ and beams$_{6,8}$ both with dense fluid initialised between the elements. Calculated using the first 50% of the front speed data. Also shown is the percentage increase or decrease in front speed with respect to the smooth experiment and the percentage increase or decrease with respect to the equivalent results for the regular cases with ambient fluid between the elements.

The effects on the front position and speed by the removal of the ambient fluid from between the roughness elements

Figure 2.12 demonstrates the significant effect that replacing the ambient fluid between the roughness elements with dense fluid (5% excess) in the beams$_{6,2}$ and beams$_{6,8}$ cases has on the distance travelled by the current. The gravity current still slows down but it is able to maintain a higher speed than when buoyant ambient fluid was present. This

implies that this less dense fluid is one of the principle retarding effects resulting from the presence of bed roughness. However, the fact that the current does not revert to a propagation speed similar to that of the smooth case implies that this is not the only cause of the change in speed and there are other roughness effects present. Moreover, it can be observed that the difference between the distance travelled by the current over the two roughness element spacings is maintained and appears very similar regardless of the density of the fluid between the elements.

For both element spacings, confirmation that the removal of the ambient fluid causes the current speed to increase relative to the equivalent original experiments but decrease relative to the smooth bed case can be seen in table 2.4. The presence of bed roughness causes the current speed to reduce by 3-4% regardless of the buoyancy effects. The equivalent experiments with ambient fluid in the cavities (table 2.3 (*b*)) showed that the roughness has a 6.1% and 7.5% reduction in front speed compared to the smooth case for the beams$_{6,2}$ and beams$_{6,8}$ beds, respectively. This combined information implies that the effects of buoyancy potentially contribute to about 50% of the reduction in front speed while the remaining retardation results from other effects of the elements on the current.

The effects on the front position and speed by decreasing the total fluid height by half

A reduction in the height of the fluid in the tank effectively doubles the relative height of the roughness elements. This provides insight into the affects of increasing the roughness height on the propagation of the gravity currents. Due to time constraints, these experiments were performed for the 5% density excess currents only.

Figure 2.13 shows the comparison of the front position as a function of time for all bed roughnesses for a gravity current generated in half the original fluid depth. The sand and spheres have similar slowing effects on the current, as observed in the full height case, although the increased size of the spheres results in a slightly increased retardation. The significantly increased slowing effects of the beam-type roughnesses are again highlighted and it can also be observed that there is little difference in the front position of the current for the two wider k-type spacings, as suggested by the 5% and 10% full height results.

The difference between the front positions of the full height and half height cases can be seen in figure 2.14 for each of the bed roughness types. The data has been normalised using x_0 and $t_0 = x_0/\sqrt{g'h_0}$ which is dependent on the variable parameter h_0. In

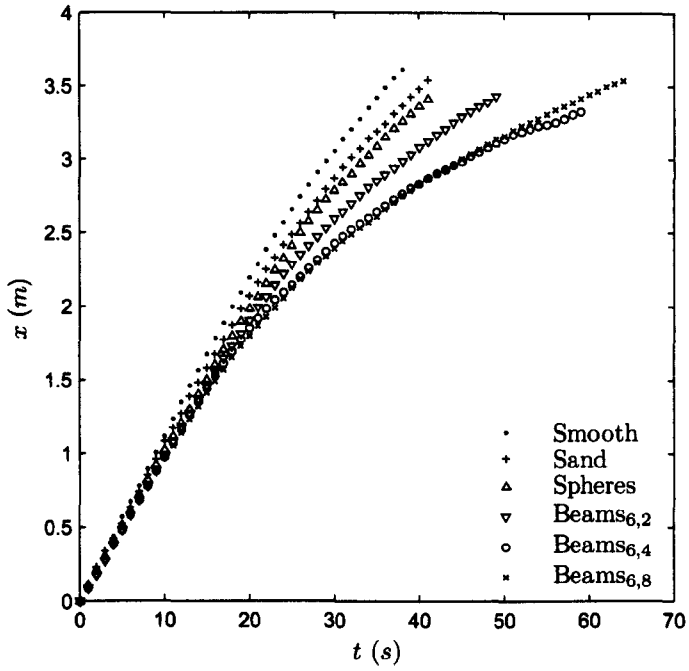

Figure 2.13: The front position as a function of time for half fluid height release of a 5% density excess gravity current and all of the six bed configurations.

	Smooth	Sand	Spheres
Speed (mm/s)	111.4	104.3	99.5
Fr	0.64	0.60	0.57
Re	6935	6493	6194
Inc/Dec (smooth)	N/A	-6.4%	-10.7%
Inc/Dec (full)	-29.4	-32.3%	-33.4%
R^2	0.9999	0.9996	0.9998
	$\text{Beams}_{6,2}$	$\text{Beams}_{6,4}$	$\text{Beams}_{6,8}$
Speed (mm/s)	97.6	95.5	92.2
Fr	0.56	0.55	0.53
Re	6076	5945	5740
Inc/Dec (smooth)	-12.4%	-14.3%	-17.2%
Inc/Dec (full)	-34.1	-34.3%	-37.9%
R^2	0.9996	0.9994	0.9999

Table 2.5: Front speeds for all six bed roughnesses for half fluid height release of a 5% density excess gravity current. Calculated using the first 49% of the front speed data where the smooth case is within the constant speed phase. Also shown is the percentage increase or decrease in front speed with respect to the smooth experiment and the percentage increase or decrease with respect to the full tank height equivalent.

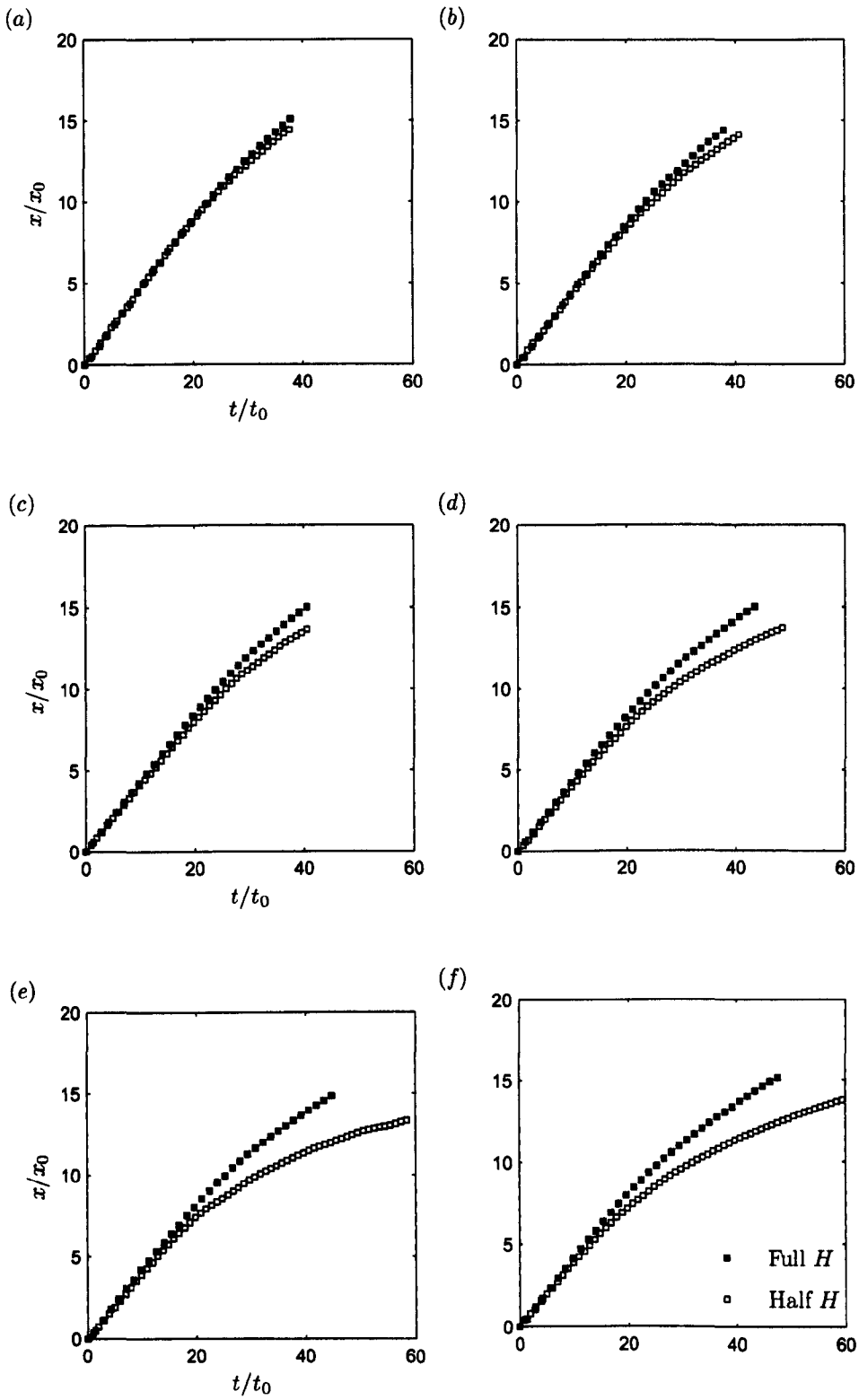

Figure 2.14: The front position as a function of time for full and half fluid height releases of a 5% density excess gravity current. Data is normalised using x_0 and t_0 since t_0 is given by $x_0/\sqrt{g'h_0}$, i.e. dependent on the changed parameter, h_0. (*a*) Smooth, (*b*) sand, (*c*) spheres, (*d*) beams$_{6,2}$, (*e*) beams$_{6,4}$ and (*f*) beams$_{6,8}$.

the smooth case, it can be observed in figure 2.14 (a), for the time period of these experiments, the front position is approximately independent of the initial release height, although this may change for later times. However, in the rough cases, figures 2.14 (b) to (f), the two datasets do not collapse and hence additional effects can be attributed to the increase in roughness height relative to the fluid depth. The beam-type roughnesses had greater slowing effects on the full height currents compared to the grain roughness types and this appears to be exaggerated when their relative height is increased, see figures 2.14 (d) to (f). This is confirmed by the calculations of the percentage decrease in front speed relative to the smooth data shown in table 2.5 compared to the equivalent calculations shown in table 2.3 (b).

It should be noted that for roughness elements of this relative height and spacing, certainly for the beams and spheres beds, the height of the roughness elements (up to 6 mm) is at most an order of magnitude smaller than the conservative approximation of the height of the current ($h_0/2 = 0.0625$) and can be expected to be less. Therefore, the effects observed thus far for this case could be categorised as the result of an array of successive small obstacles in the path of the flow rather than that of a bed roughness. Therefore, the effects of the elements on the flow dynamics may be significantly different to those expected from a smaller more typical bed roughness and an investigation and characterisation of these affects are not sought further in the present study.

2.5.2 Horizontal velocity profiles

The effects of bed roughness and different initial density excess on the horizontal velocity profiles

Time series contours of the streamwise downstream horizontal velocity results, generated by the five horizontal probes, for all three initial density excesses can be seen in figures 2.15 - 2.17. Complementary downstream horizontal velocity profiles from this data are shown in figures 2.18 - 2.20.

For a smooth run with a 5% density difference (figure 2.16 (a)) the results reiterate that the present study is consistent with what has been observed in previous experiments: A head region is present with relatively constant velocities and a mean velocity maximum near the bed. Large fluctuations in velocity are observed at the density interface behind the head indicating the presence of billows, followed by a lower velocity 'tail' region and a negative reverse flow above the gravity current where the ambient fluid is forced upstream as it is displaced by the current. The mean velocity maximum in the head

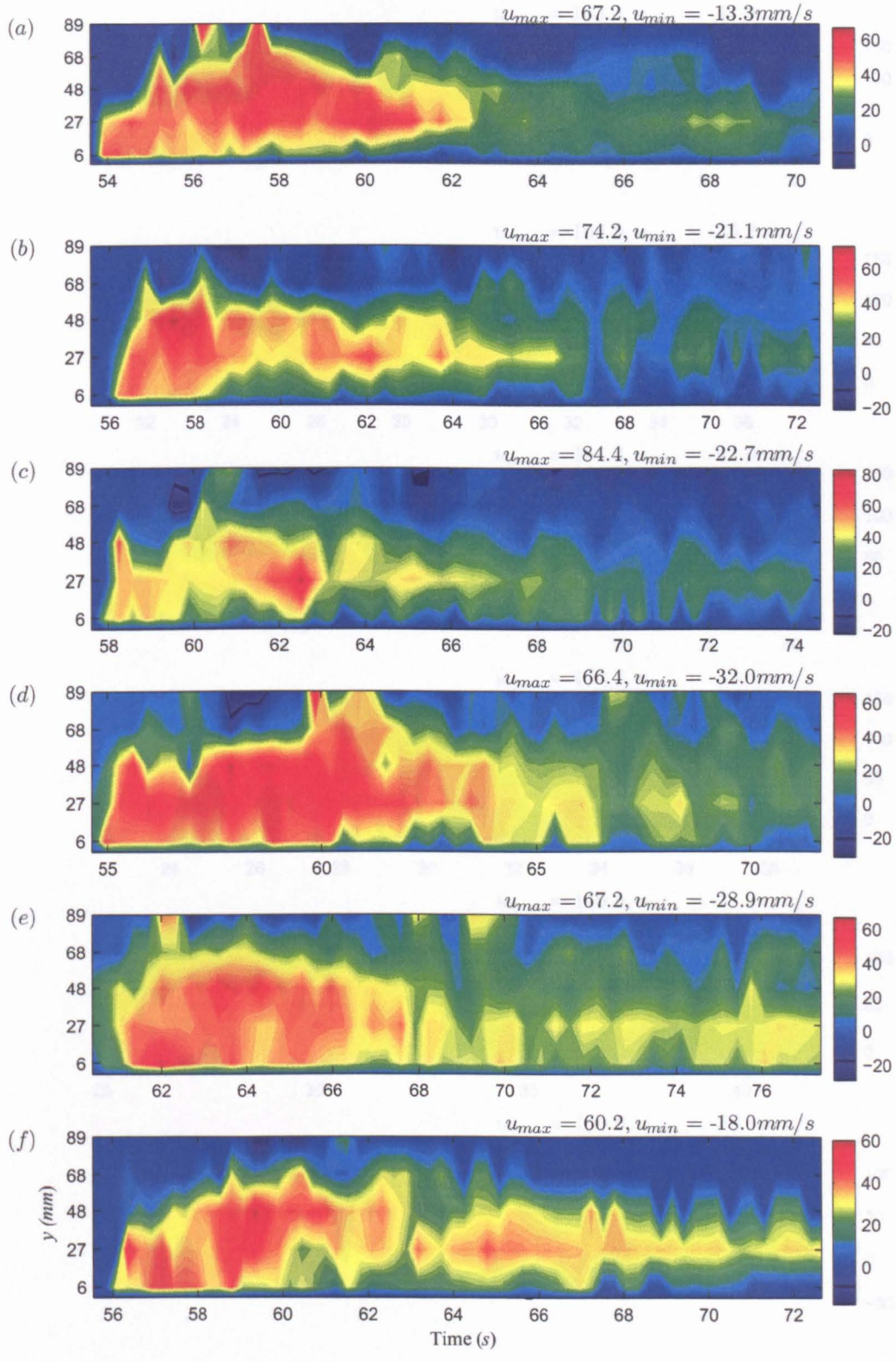

Figure 2.15: Time series contours of downstream horizontal velocity, u (mm/s) up to the maximum probe depth for a 1% gravity current with a standard probe configuration. (a) Smooth, (b) sand, (c) spheres, (d) beams$_{6,2}$, (e) beams$_{6,4}$ and (f) beams$_{6,8}$.

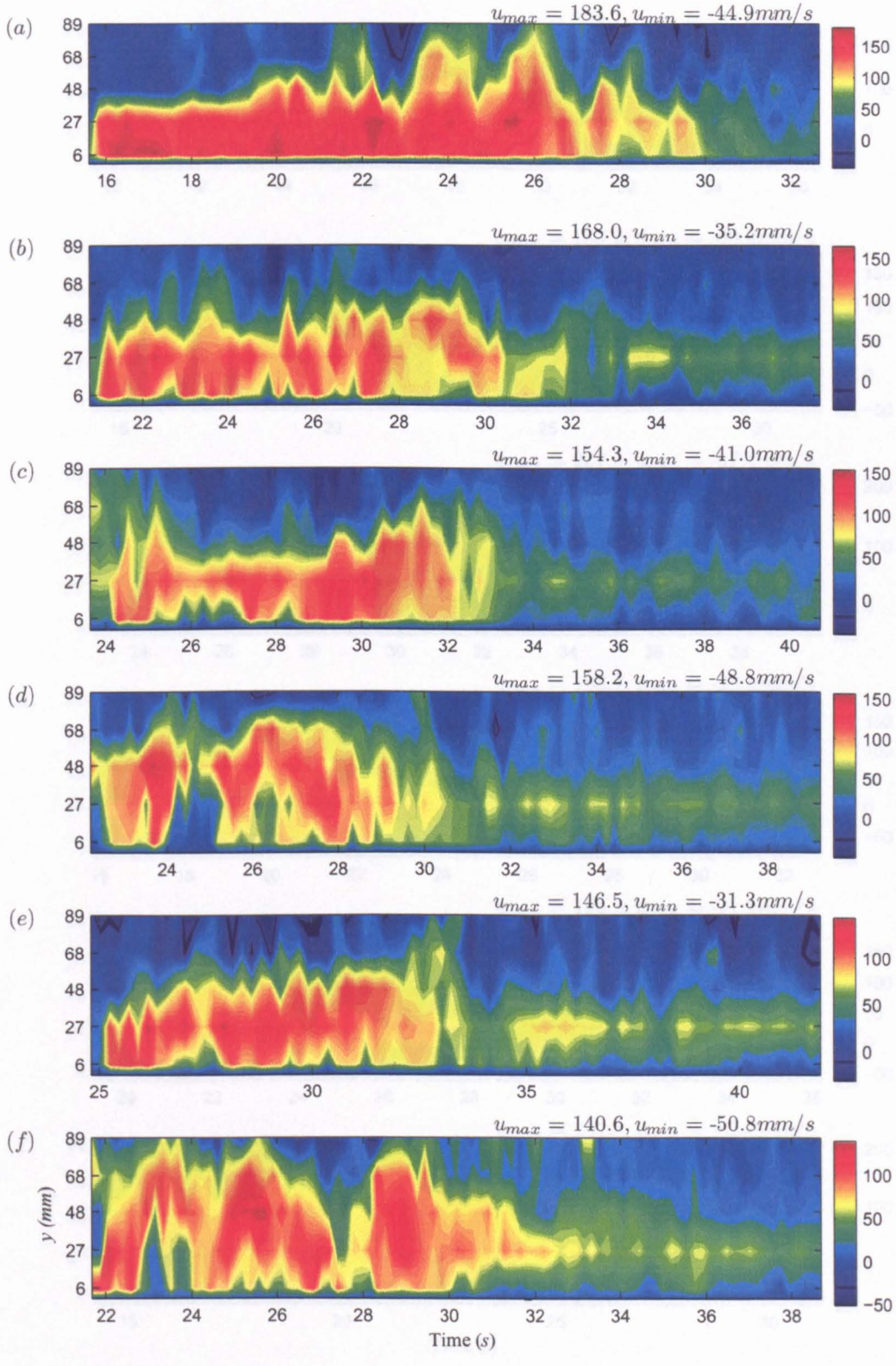

Figure 2.16: Time series contours of downstream horizontal velocity, u (mm/s) up to the maximum probe depth for a 5% gravity current with a standard probe configuration. (a) Smooth, (b) sand, (c) spheres, (d) beams$_{6,2}$, (e) beams$_{6,4}$ and (f) beams$_{6,8}$.

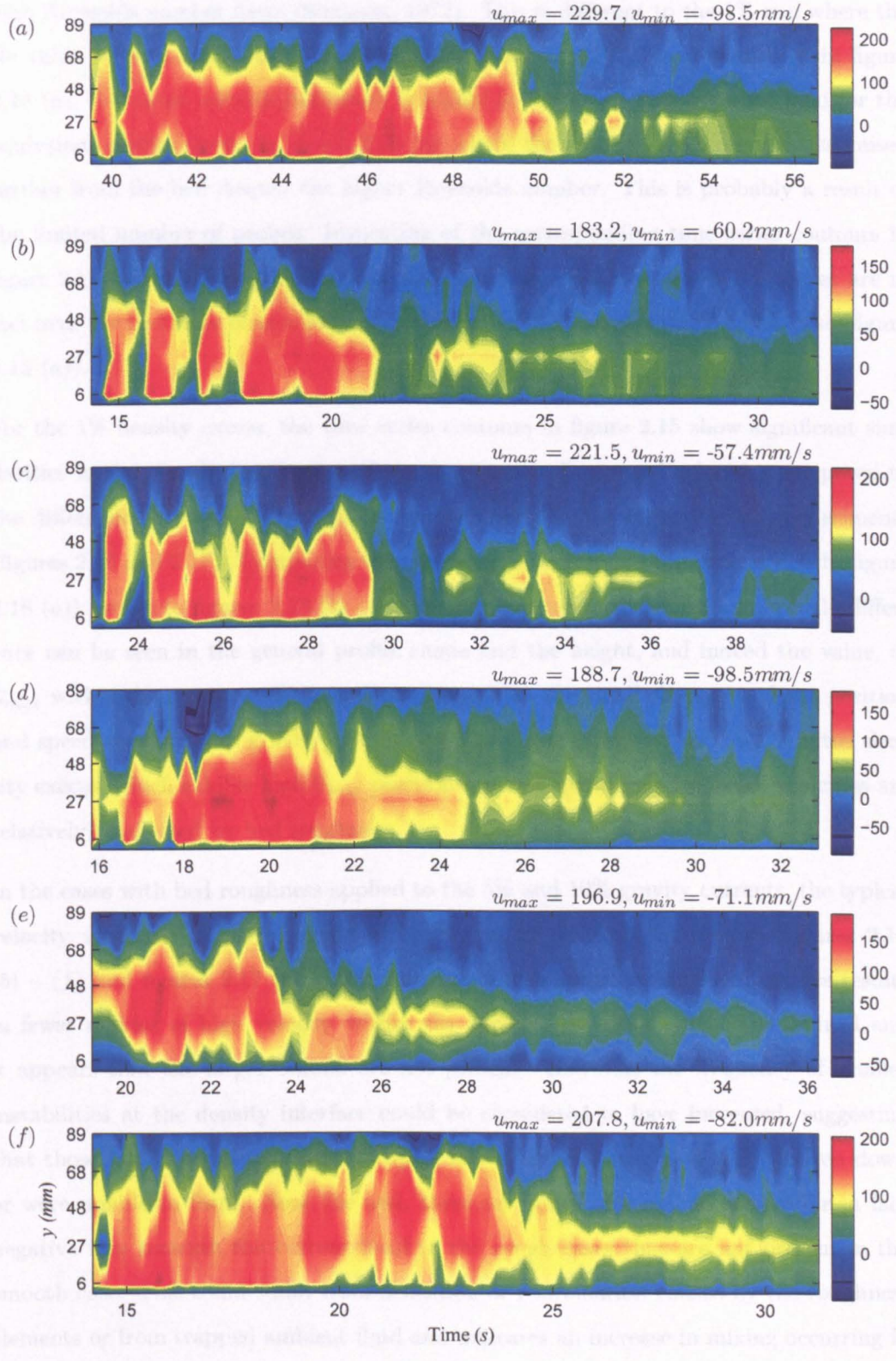

Figure 2.17: Time series contours of downstream horizontal velocity, u (mm/s) up to the maximum probe depth for a 10% gravity current with a standard probe configuration. (a) Smooth, (b) sand, (c) spheres, (d) beams$_{6,2}$, (e) beams$_{6,4}$ and (f) beams$_{6,8}$.

in the 5% case is confirmed in figure 2.19 (a) to be very near the bed, as expected in high Reynolds number flows (Simpson, 1972). This is different to the 1% run where the Re value is lower and hence, as suggested by Simpson (1972) and confirmed in figure 2.18 (a), the mean velocity maximum is higher in the flow. This does not hold for the equivalent results shown in figure 2.20 (a) where the velocity maximum is also raised further from the bed despite the higher Reynolds number. This is probably a result of the limited number of probes. Inspection of the corresponding time series contours in figure 2.17 indicates that in general the higher downstream horizontal velocities are in fact near the bed more consistently with this high density excess than the 1% case (figure 2.15 (a)).

For the 1% density excess, the time series contours in figure 2.15 show significant similarities in the overall distribution of the downstream horizontal velocities compared to the differences between the rough and smooth cases in the higher density experiments (figures 2.16 and 2.17). Comparing the velocity profile through the current depth (figure 2.18 (a)) profile to figures 2.18 (b) – (d) for the bed roughened cases, again little difference can be seen in the general profile shape and the height, and indeed the value, of $\overline{u}_{max}$ within the currents. This evidence along with the small changes in front position and speed suggests that gravity currents such as those generated by the 1% initial density excess, which exhibit high $\overline{u}_{max}$ positions and comparatively low basal velocities are relatively unaffected by bed roughness.

In the cases with bed roughness applied to the 5% and 10% gravity currents, the typical velocity structure is not observed as clearly as in the smooth case, see figures 2.16 (b) – (f) and figures 2.17 (b) – (f). In general, the presence of bed roughness results in fewer regions of high velocity within the current, the head is less well defined and it appears that the larger billows are not present. However, the frequency of smaller instabilities at the density interface could be considered to have increased, suggesting that those larger structures in that region in the smooth case have been broken down or were unable to form. Near the bed, there are zones of very low positive or in fact negative flow beneath the current head in the rough cases that are not present in the smooth case. This could result from deflection or recirculation caused by the roughness elements or from trapped ambient fluid and indicates an increase in mixing occurring in this region.

The velocity profiles throughout the current depth shown in figures 2.19 and 2.20 indicate that the presence of any type of roughness on the bed of a 5% or 10% current decreases

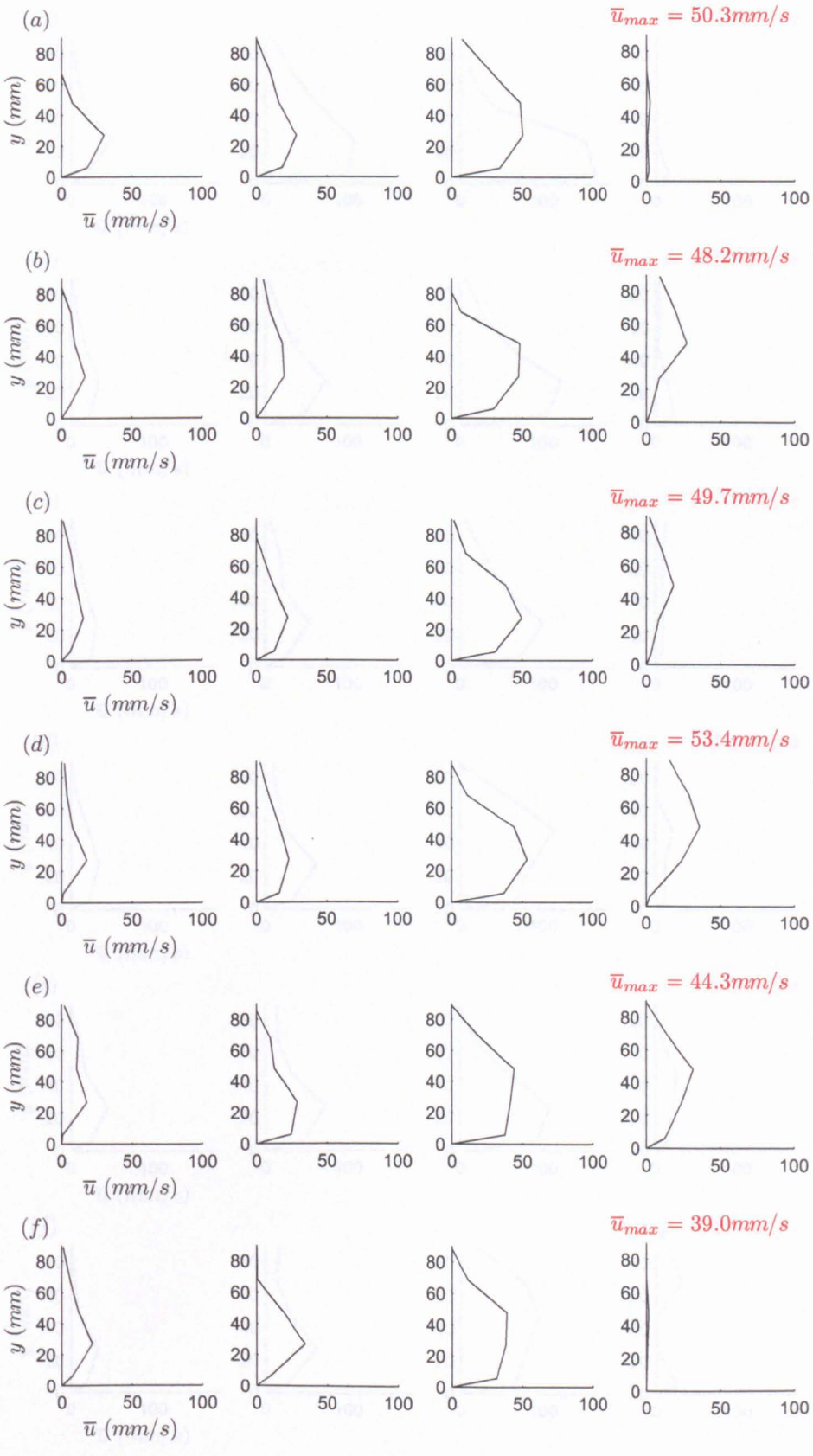

Figure 2.18: Downstream horizontal velocity profiles at $x = 2.97$ m as a function of depth for a 1% density difference, averaged temporally over 5 s and spatially over 3 bins. Profiles from right to left of flow before the current head, in the head, in the body and in the tail for (a) smooth, (b) sand, (c) spheres, (d) beams$_{6,2}$, (e) beams$_{6,4}$ and (f) beams$_{6,8}$.

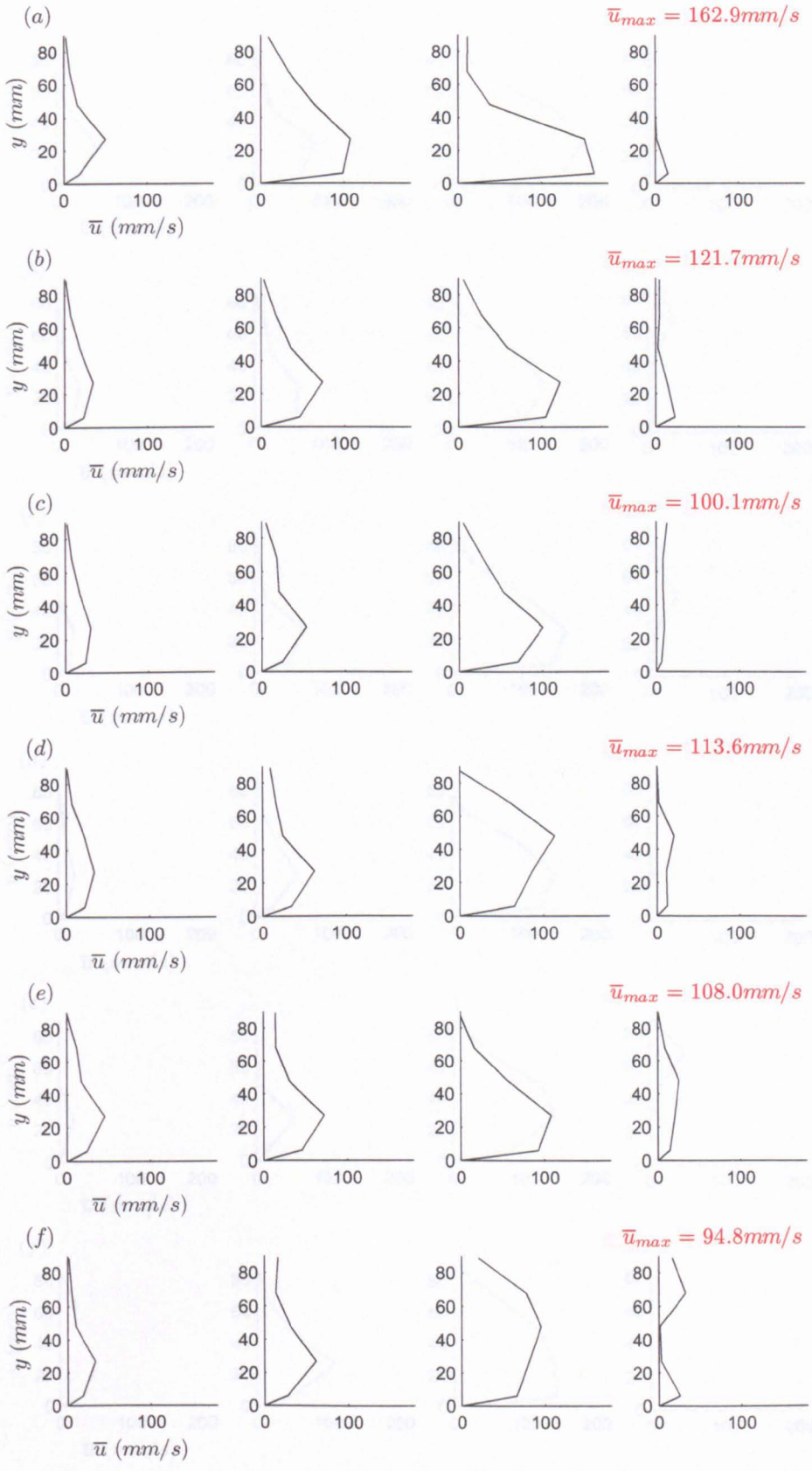

Figure 2.19: Downstream horizontal velocity profiles at $x = 2.97$ m as a function of depth for a 5% density difference, averaged temporally over 5 s and spatially over 3 bins. Profiles from right to left of flow before the current head, in the head, in the body and in the tail for (a) smooth, (b) sand, (c) spheres, (d) beams$_{6,2}$, (e) beams$_{6,4}$ and (f) beams$_{6,8}$.

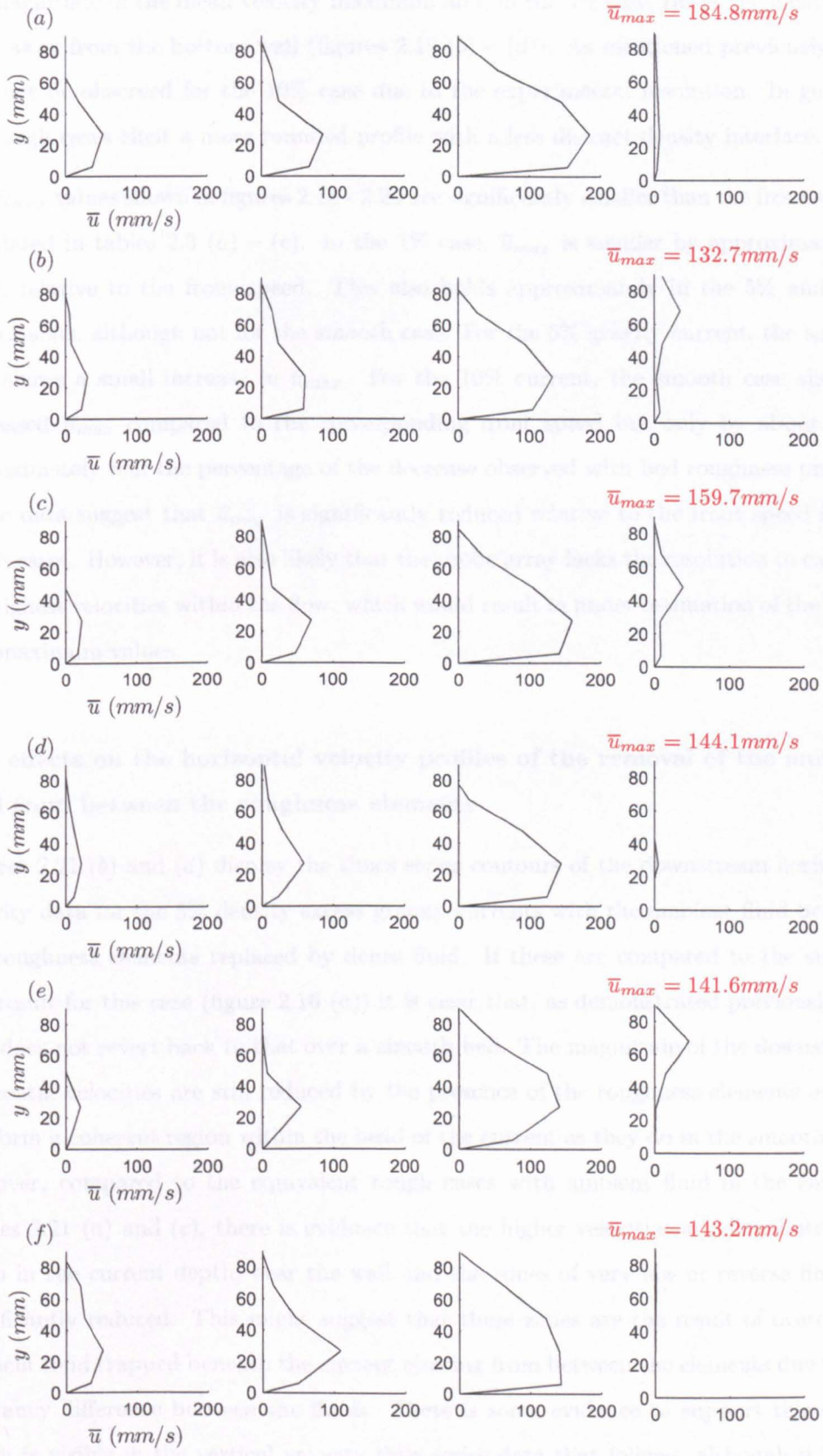

Figure 2.20: Downstream horizontal velocity profiles at $x = 2.97$ m as a function of depth for a 10% density difference, averaged temporally over 5 s and spatially over 3 bins. Profiles from right to left of flow before the current head, in the head, in the body and in the tail for (a) smooth, (b) sand, (c) spheres, (d) beams$_{6,2}$, (e) beams$_{6,4}$ and (f) beams$_{6,8}$.

the magnitude of the mean velocity maximum and, in the 5% case, raises the location of $\overline{u}_{max}$ away from the bottom wall (figures 2.19 (b) – (d)). As mentioned previously, this may not be observed for the 10% case due to the experimental resolution. In general, the rough cases elicit a more rounded profile with a less distinct density interface.

The $\overline{u}_{max}$ values shown in figures 2.18 - 2.20 are significantly smaller than the front speeds calculated in tables 2.3 (a) – (c). In the 1% case, $\overline{u}_{max}$ is smaller by approximately a third, relative to the front speed. This also holds approximately in the 5% and 10% experiments, although not for the smooth case. For the 5% gravity current, the smooth case shows a small increase in $\overline{u}_{max}$. For the 10% current, the smooth case shows a decreased $\overline{u}_{max}$ compared to the corresponding front speed but only by about 14%, approximately half the percentage of the decrease observed with bed roughness present. These data suggest that $\overline{u}_{max}$ is significantly reduced relative to the front speed in the rough cases. However, it is also likely that the probe array lacks the resolution to capture the highest velocities within the flow, which would result in under-estimation of the mean and maximum values.

The effects on the horizontal velocity profiles of the removal of the ambient fluid from between the roughness elements

Figures 2.21 (b) and (d) display the times series contours of the downstream horizontal velocity data for the 5% density excess gravity currents with the ambient fluid between the roughness elements replaced by dense fluid. If these are compared to the smooth bed result for this case (figure 2.16 (a)) it is clear that, as demonstrated previously, the flow does not revert back to that over a smooth bed. The magnitude of the downstream horizontal velocities are still reduced by the presence of the roughness elements and do not form a coherent region within the head of the current as they do in the smooth case. However, compared to the equivalent rough cases with ambient fluid in the cavities, figures 2.21 (a) and (c), there is evidence that the higher velocities are distributed low down in the current depth, near the wall and the zones of very low or reverse flow are significantly reduced. This might suggest that these zones are the result of overridden ambient fluid trapped beneath the current ejecting from between the elements due to the buoyancy difference between the fluids. There is some evidence to support this effect, which is visible in the vertical velocity time series data that follows, although it is not possible to determine if the relevant horizontal and vertical zones exactly coincide.

From figure 2.21 it can also be postulated that the removal of the ambient fluid from

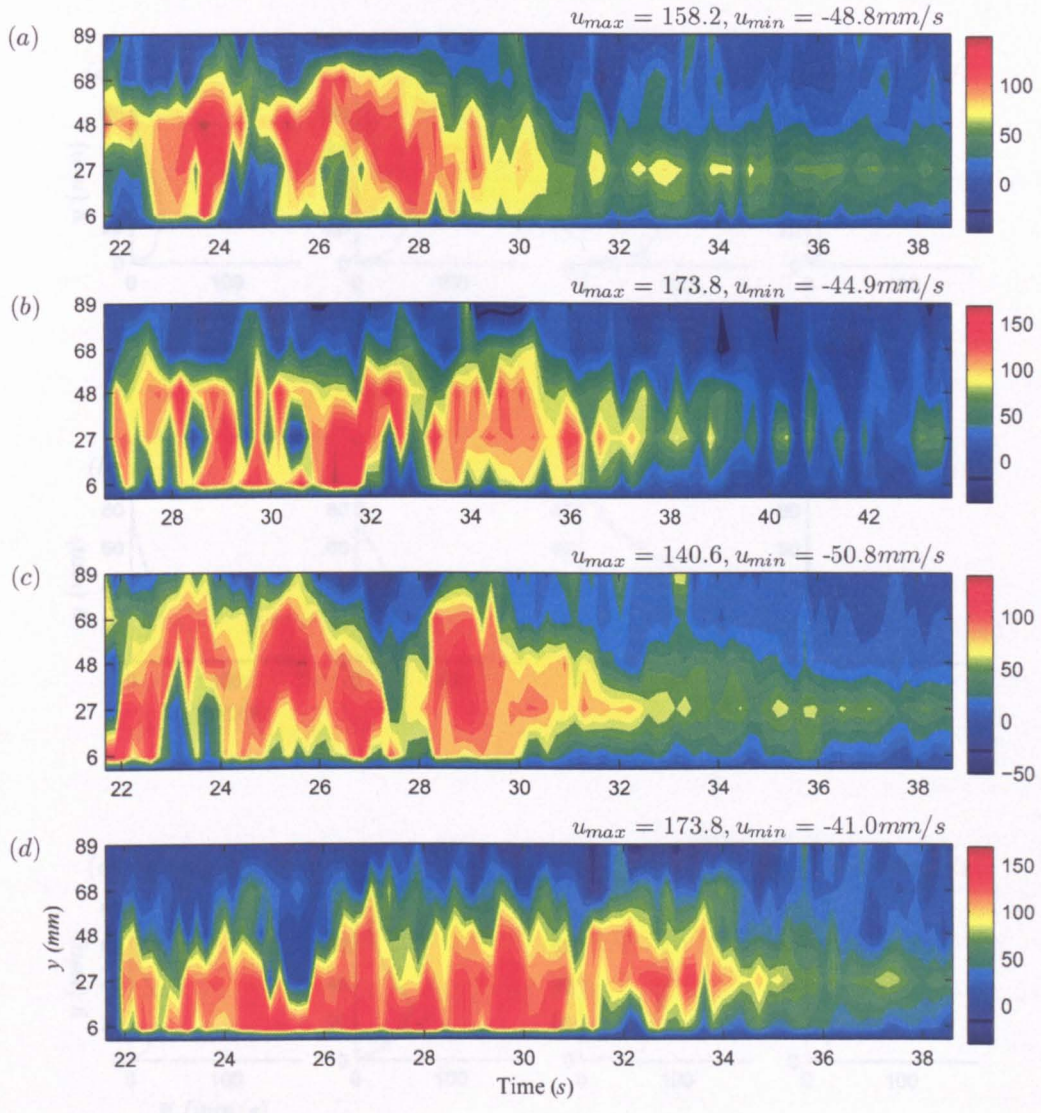

Figure 2.21: Time series contours of downstream horizontal velocity, u (mm/s) up to the maximum probe depth for a 5% gravity current with a standard probe configuration. (a) beams$_{6,2}$ with ambient fluid between the elements, (b) with dense fluid between the elements, (c) beams$_{6,8}$ with ambient fluid between the elements, (d) with dense fluid between the elements.

between the roughness elements has a more noticeable affect on the k-type bed roughness (figure 2.21 (c) and (d)) than the equivalent d-type case. Observe that the beams$_{6,8}$ case shown in figure 2.21 (d) shows velocity values distributed much more like the smooth case, although reduced in magnitude, than the beams$_{6,2}$ case in figure 2.21 (b). The corresponding downstream horizontal velocity profiles for the data, shown in figure 2.22 (d), confirm this. It appears that with this wider element spacing the increased amount of buoyant ambient fluid between the elements is able to significantly redistribute the velocity field within the current, more so than for the d-type spacing where there are more elements and thus smaller cavities.

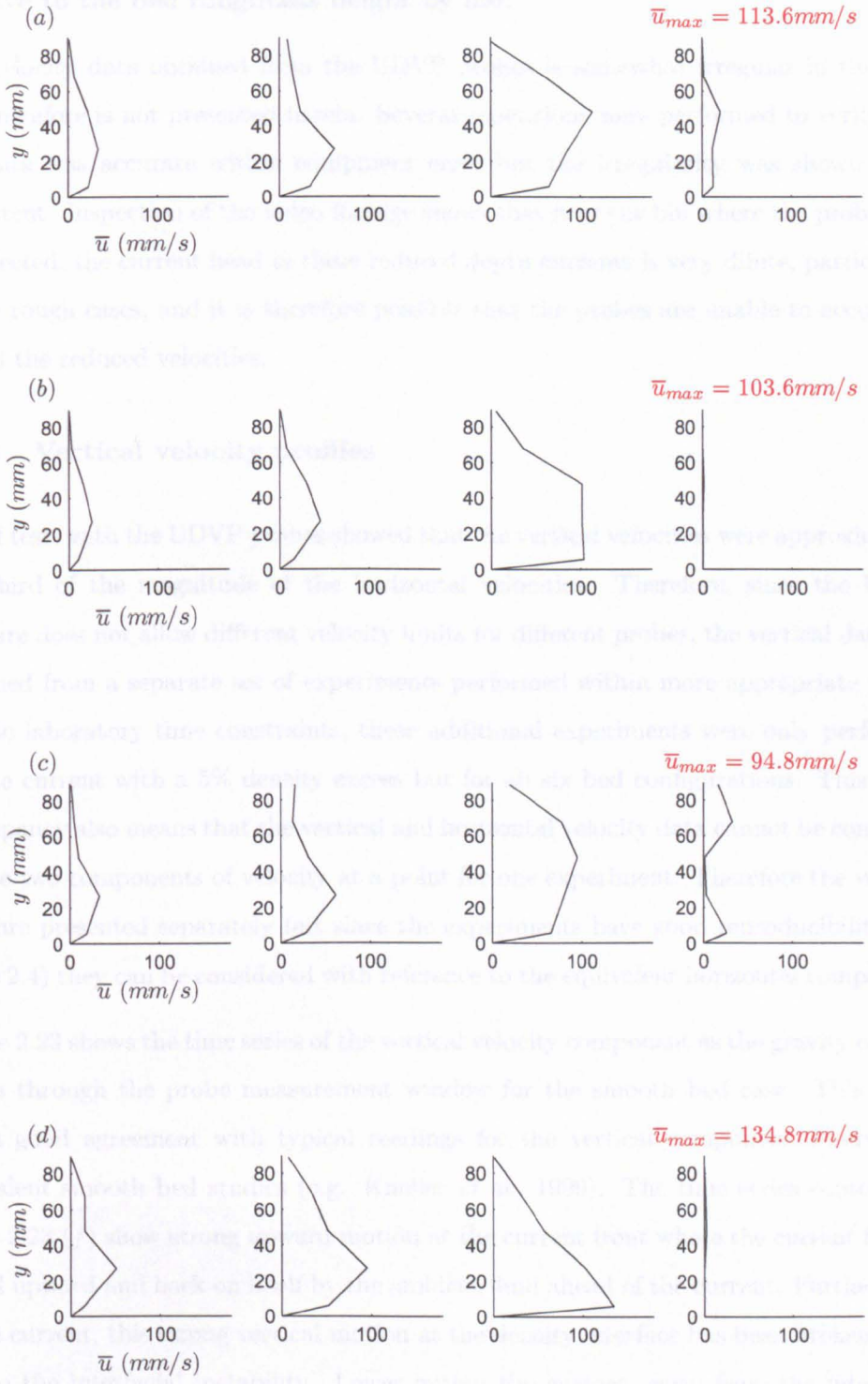

Figure 2.22: Downstream horizontal velocity profiles at $x = 2.97$ m as a function of depth for a 5% density difference, averaged temporally over 5 s and spatially over 3 bins. Profiles from right to left of flow before the current head, in the head, in the body and in the tail for (a) beams$_{6,2}$ with ambient fluid between the elements, (b) with dense fluid between the elements,(c) beams$_{6,8}$ with ambient fluid between the elements, (d) with dense fluid between the elements.

The effects on the horizontal velocity profiles of decreasing the fluid height relative to the bed roughness height by half

The velocity data obtained from the UDVP probes is somewhat irregular in this case and therefore is not presented herein. Several repetitions were performed to verify that the data was accurate within equipment error but the irregularity was shown to be consistent. Inspection of the video footage shows that near the bin where the probe data is collected, the current head in these reduced depth currents is very dilute, particularly in the rough cases, and it is therefore possible that the probes are unable to accurately record the reduced velocities.

2.5.3 Vertical velocity profiles

Initial tests with the UDVP probes showed that the vertical velocities were approximately one third of the magnitude of the horizontal velocities. Therefore, since the UDVP software does not allow different velocity limits for different probes, the vertical data was obtained from a separate set of experiments performed within more appropriate limits. Due to laboratory time constraints, these additional experiments were only performed for the current with a 5% density excess but for all six bed configurations. This slight discrepancy also means that the vertical and horizontal velocity data cannot be combined to give two components of velocity at a point for one experiment. Therefore the vertical data are presented separately but since the experiments have good reproducibility (see figure 2.4) they can be considered with reference to the equivalent horizontal component.

Figure 2.23 shows the time series of the vertical velocity component as the gravity current passes through the probe measurement window for the smooth bed case. This result shows good agreement with typical readings for the vertical component observed in equivalent smooth bed studies (e.g. Kneller *et al.*, 1999). The time series contours in figure 2.23 (f) show strong upward motion at the current front where the current fluid is forced upward and back on itself by the ambient fluid ahead of the current. Further back in the current, this strong vertical motion at the density interface has been broken down due to the interfacial instability. Lower within the current, away from the interfacial region there is little vertical motion where the current propagation is dominated almost entirely by the streamwise horizontal component of velocity as seen in figure 2.16 (a).

Time series contours for the data obtained for all of the bed roughnesses for a 5% density excess current can be seen in figure 2.24. It can be observed that there is an overall reduction in the magnitude of the positive vertical velocities due to the presence of

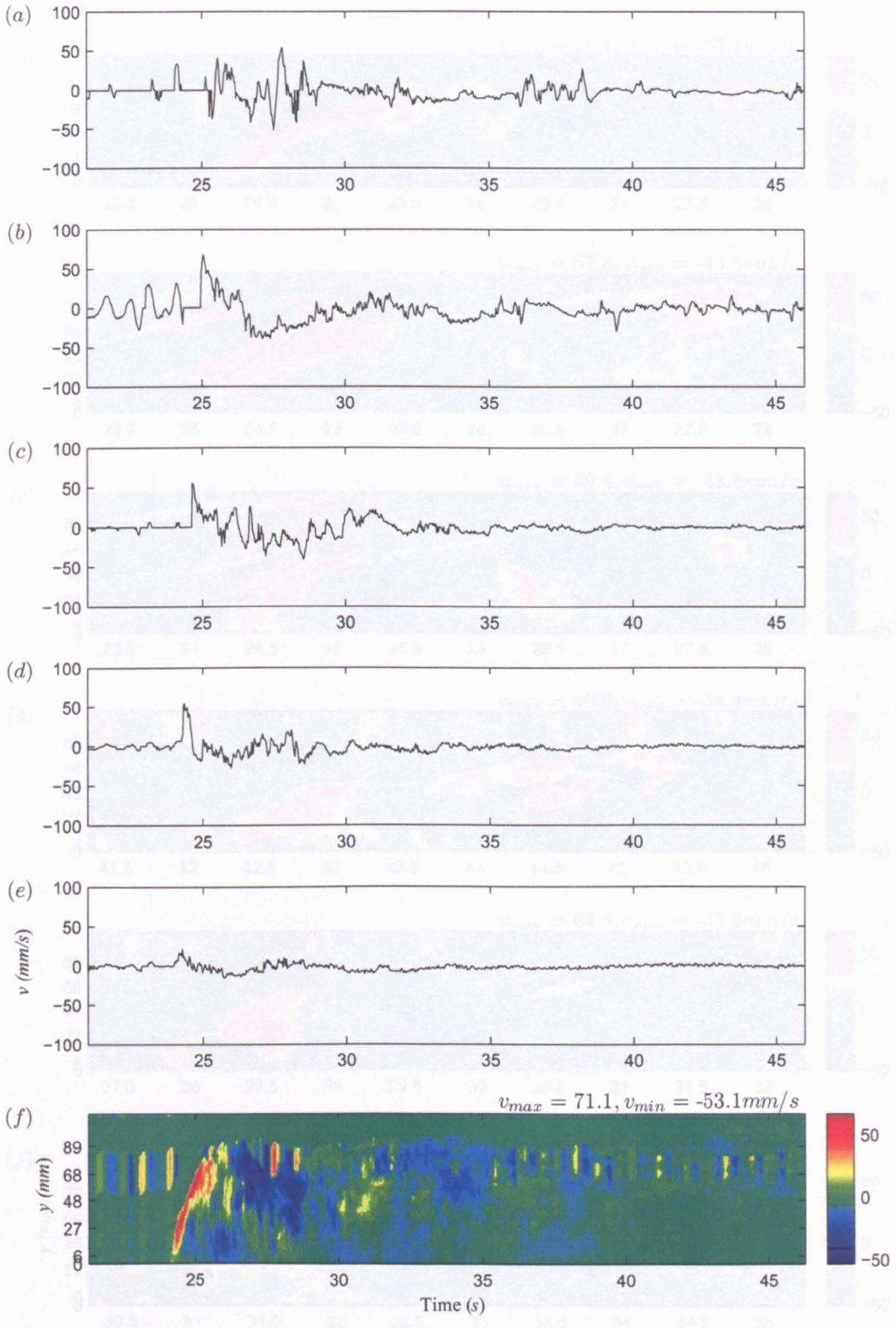

Figure 2.23: Time series of downstream vertical velocity, v (mm/s) for a 5% gravity current with a smooth bed at the horizontal probe locations in the standard probe configuration. (a) Bottom probe to (e) top and (f) vertical velocity component time series contours throughout the current depth.

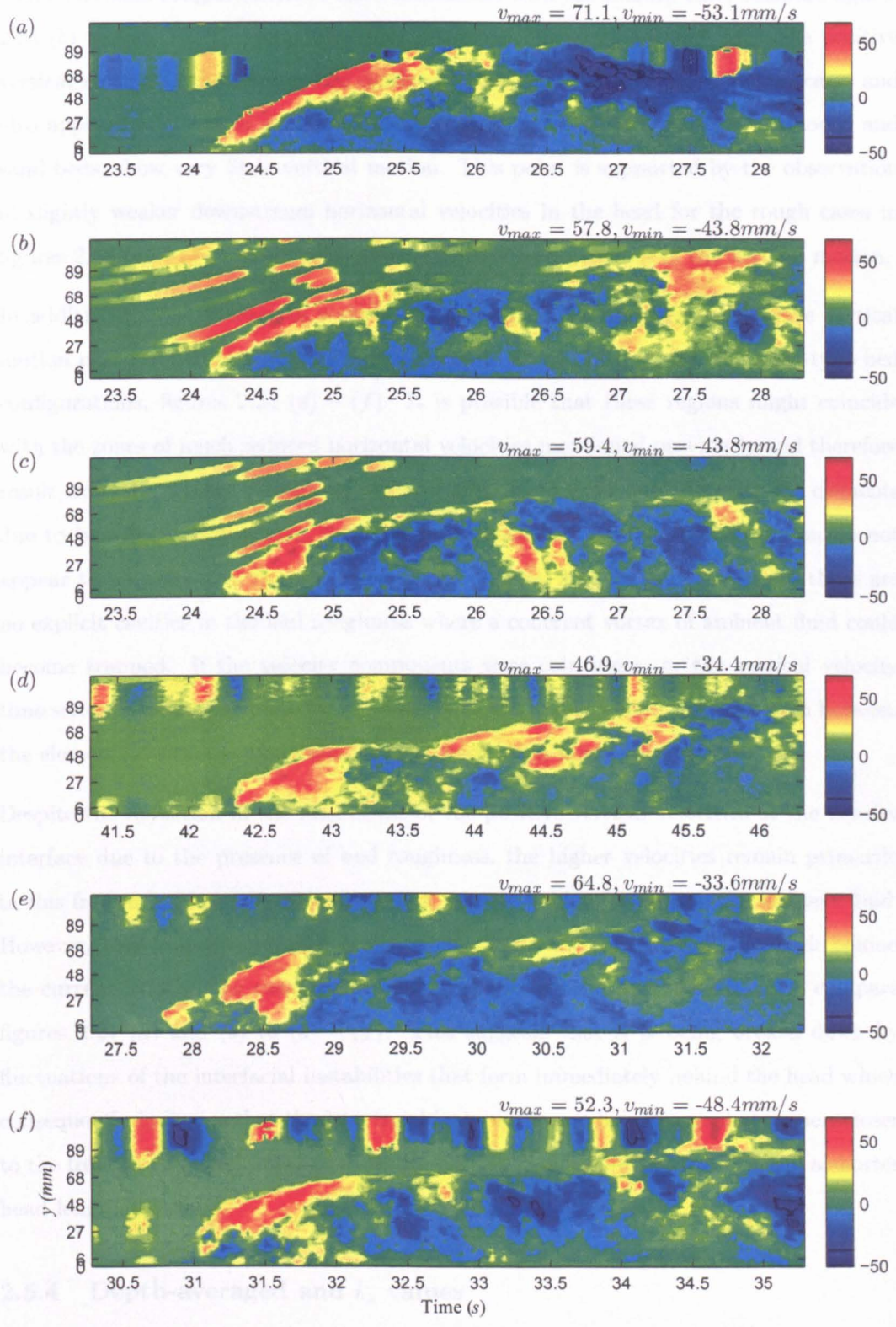

Figure 2.24: Time series contours of downstream vertical velocity, v (mm/s) for a 5% gravity current with a (a) smooth, (b) sand, (c) spheres, (d) beams$_{6,2}$, (e) beams$_{6,4}$ and (f) beams$_{6,8}$.

any bed roughness. However, as was observed for the equivalent downstream horizontal series, the sand roughness shows close similarities with the smooth case, compare figures 2.24 (b) to (a). For the remaining four bed types (figures 2.24 $(c) - (f)$), the positive vertical motion at the front is less confined to the interface than in those two cases and also appears in the nose and head of the current, in regions that, for the smooth and sand beds, show very little vertical motion. This point is supported by the observation of slightly weaker downstream horizontal velocities in the head for the rough cases in figures 2.16 $(c) - (f)$ which could enable the increased presence of the vertical motion.

In addition to the increase in vertical motion within the nose region, positive vertical motion near the bed further back in the current can be observed for the beam-type bed configurations, figures 2.24 $(d) - (f)$. It is possible that these regions might coincide with the zones of much reduced horizontal velocities mentioned previously and therefore result from the upward ejection of vortices of ambient fluid from between the elements due to buoyancy. Notice that these near-wall zones of positive vertical motion do not appear to be present in the grain type cases (figures 2.24 (b) and (c)) where there are no explicit cavities in the bed roughness where a coherent vortex of ambient fluid could become trapped. If the velocity components were coincident, or the vertical velocity time series data was available for the cases with the ambient fluid removed from between the elements, further confirmation of this observation might be compiled.

Despite the reduction in the magnitude of the positive vertical velocities at the density interface due to the presence of bed roughness, the higher velocities remain primarily in this frontal locality where the intruding current fluid is forced into the ambient fluid. However, this frontal interfacial region does not persist coherently as far back behind the current front in the rough cases compared to the sand and smooth cases, compare figures 2.24 (a) and (b) to $(d) - (f)$. This suggests that it is being broken down by fluctuations of the interfacial instabilities that form immediately behind the head which consequently indicates that the interfacial instabilities are being generated sooner, closer to the front in the rough cases than in the smooth case, potentially resulting in a shorter head length.

2.5.4 Depth-averaged and k_s values

The effects of bed roughness and different initial density excess on the depth-averaged and k_s values

The depth-averaged downstream horizontal velocity and height have been calculated

(*a*)	Smooth	Sand	Spheres
u_{da} (mm/s)	47.7	47.8	46.6
h_{da} (mm)	62.9	45.7	50.9
Fr_{da}	0.83	0.72	0.69
Re_{da}	2050	2299	2306
	$\mathrm{Beams}_{6,2}$	$\mathrm{Beams}_{6,4}$	$\mathrm{Beams}_{6,8}$
u_{da} (mm/s)	50.7	42.9	40.0
h_{da} (mm)	44.8	47.4	45.2
Fr_{da}	0.77	0.63	0.60
Re_{da}	2212	3028	1832
(*b*)	Smooth	Sand	Spheres
u_{da} (mm/s)	136.6	98.7	87.6
h_{da} (mm)	40.3	53.2	53.2
Fr_{da}	1.02	0.64	0.61
Re_{da}	5706	5356	4534
	$\mathrm{Beams}_{6,2}$	$\mathrm{Beams}_{6,4}$	$\mathrm{Beams}_{6,8}$
u_{da} (mm/s)	103.3	94.7	91.7
h_{da} (mm)	43.8	42.2	60.7
Fr_{da}	0.7	0.66	0.53
Re_{da}	4814	4198	5883
(*c*)	Smooth	Sand	Spheres
u_{da} (mm/s)	170.7	121.2	143.5
h_{da} (mm)	45.9	44.3	44.5
Fr_{da}	0.81	0.53	0.69
Re_{da}	8613	5924	7035
	$\mathrm{Beams}_{6,2}$	$\mathrm{Beams}_{6,4}$	$\mathrm{Beams}_{6,8}$
u_{da} (mm/s)	127.7	128.2	124.2
h_{da} (mm)	44.0	56.4	61.7
Fr_{da}	0.62	0.56	0.51
Re_{da}	6210	7806	8424

Table 2.6: Depth-averaged values for (*a*) 1%, (*b*) 5%, and (*c*) 10% density difference. Fr and Re calculated using u_{da} and h_{da}.

using 5 probes in the current head over 5 s and 3 bins using equations (2.1) and (2.2), respectively. Mean values for the flow Reynolds numbers (Re_{da}) and Froude numbers (Fr_{da}) were calculated using these values. Tables 2.6 (*a*) – (*c*) show these results for the 1%, 5% and 10% gravity currents, respectively. The depth-averaged velocities are in general approximately 35% smaller than the corresponding front speeds and slightly smaller than the velocity maxima $\overline{u}_{max}$ displayed with the velocity profiles. However, it must be noted again that the velocity profiles are likely to be missing the highest

velocity zones and therefore significantly underestimating the flow speeds. The u_{da} of the 1% currents show varying responses to the bed roughness, relative to the smooth case, but the magnitude of the effects are for the most part significantly smaller than for the higher density currents. In the 5% and 10% cases, the depth-averaged velocity of the gravity currents flowing over rough surfaces is significantly decreased relative to the smooth case. In fact, the magnitude of the decrease is over 25% under most rough bed conditions. There does not appear to be any clear trend in the exact magnitude of the decrease in u_{da} relative to the smooth case for a particular bed type or spacing. Therefore, it would appear that for an improved indication of those effects, the front speed results should be observed since the depth-averaged data at present only indicates that there is a general decrease in velocity.

The depth-averaged height data, h_{da}, shown in tables 2.6 (a) – (c) also proves inconclusive. In the 1% case, it appears that there is a significant overall decrease in the height relative to the smooth current height. However, the 5% data suggests an overall increase in height, varying from about 5% to 50%, with no apparent trend in the data with respect to the roughness type or spacing. The 10% case suggests that under the influence of coarse sand, spheres and the d-type beams the height decreases a small amount while for the k-type beds, the height is more significantly increased. Again, these results highlight the sensitivity of this method of calculating the depth-averaged values on the number of data points available.

The k_s values calculated using equation (2.4) can be seen in figure 2.25 with the velocity data below the velocity maximum used to calculate them. At the present resolution, the k_s data is inconclusive. It does not show any specific indication of correlations between the increase and decrease in value with the density or the bed type. It is encouraging that the order of magnitude of the values agree in some cases, for example the 1% and 5% cases for the spheres roughness (figures 2.25 (c) right and middle) and the 5% and 10% cases of the beams$_{6,2}$ roughness (figures 2.25 (d) middle and left) but this does not hold for all of the data. Note that there is no data available for the 5% smooth case since there was no probe data available below the velocity maximum of the current. It should also be noted that these are 'best fit' values that have been calculated with at least four probe values where possible, including the velocity maximum. The data is subject to some error due to its method of calculation, i.e. by combining the data from two experiments with a probe shift and as a result some 'clustering' of the values is apparent undermining the fit of the line. For this reason, the data from these probe 'shifted' experiments were not used in the velocity profiles previously. Data right down to the bed is not available

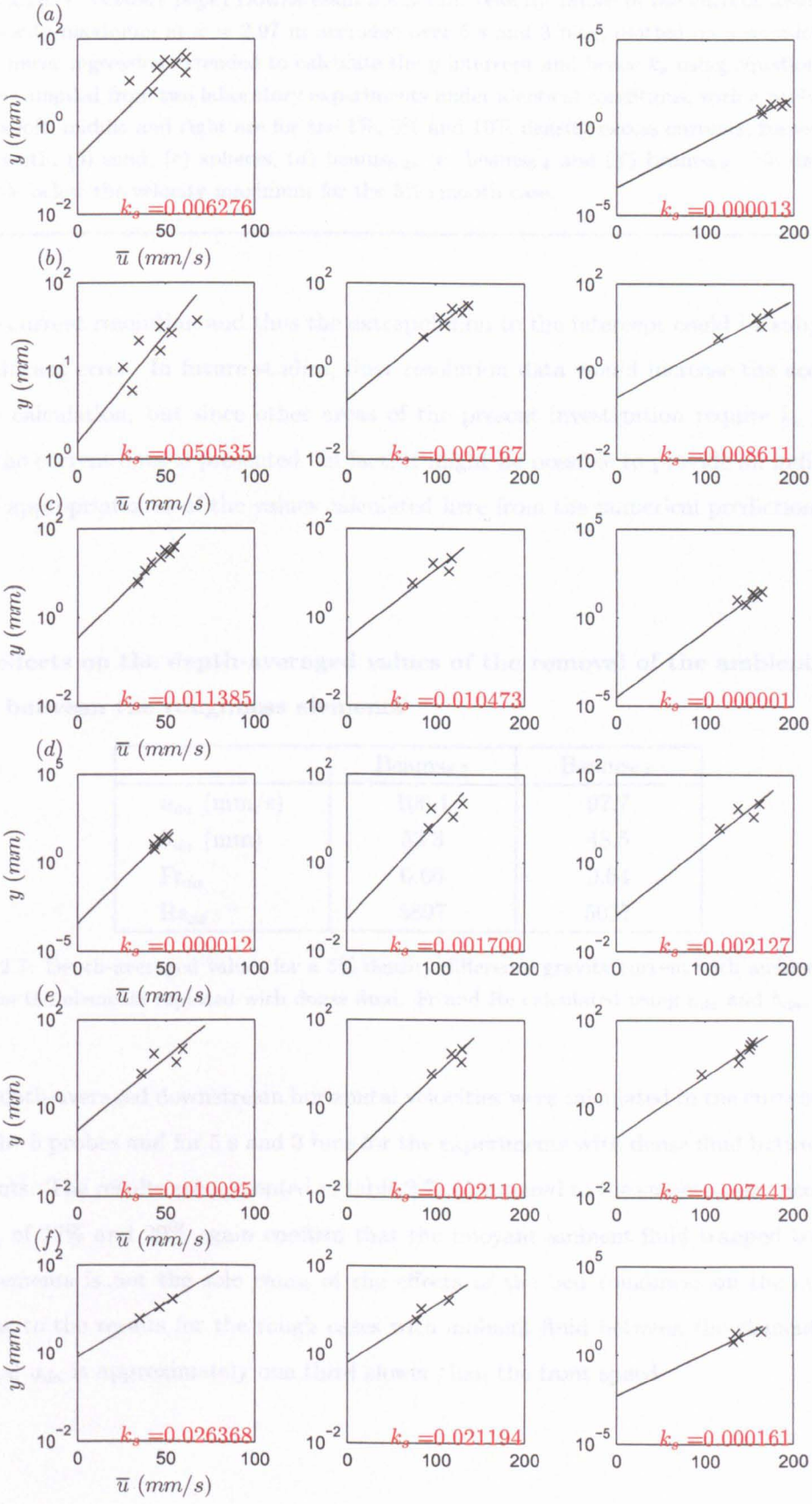
(a)
(b)
(c)
(d)
(e)
(f)
y (mm)
$\overline{u}$ (mm/s)
k_s =0.006276
k_s =0.000013
k_s =0.050535
k_s =0.007167
k_s =0.008611
k_s =0.011385
k_s =0.010473
k_s =0.000001
k_s =0.000012
k_s =0.001700
k_s =0.002127
k_s =0.010095
k_s =0.002110
k_s =0.007441
k_s =0.026368
k_s =0.021194
k_s =0.000161

Figure 2.25: (*Previous page*) Downstream horizontal velocity values in the current head below the velocity maximum at $x = 2.97$ m averaged over 5 s and 3 bins, plotted on a semi-log scale with a linear regression extended to calculate the y intercept and hence k_s using equation (2.4). Data is compiled from two laboratory experiments under identical conditions, with a probe shift. Results left, middle and right are for the 1%, 5% and 10% density excess currents, respectively. (*a*) Smooth, (*b*) sand, (*c*) spheres, (*d*) beams$_{6,2}$, (*e*) beams$_{6,4}$ and (*f*) beams$_{6,8}$. No data was available below the velocity maximum for the 5% smooth case.

---

at the current resolution and thus the extrapolation to the intercept could be subject to a significant error. In future studies, finer resolution data would increase the accuracy of the calculation, but since other areas of the present investigation require k_s values then the current data is presented. In fact, it might be possible to provide an indication of the appropriateness of the values calculated here from the numerical predictions that follow.

The effects on the depth-averaged values of the removal of the ambient fluid from between the roughness elements

	Beams$_{6,2}$	Beams$_{6,8}$
u_{da} (mm/s)	106.1	97.7
h_{da} (mm)	53.3	48.5
Fr_{da}	0.66	0.64
Re_{da}	5897	5037

Table 2.7: Depth-averaged values for a 5% density difference gravity current with ambient fluid between the elements replaced with dense fluid. Fr and Re calculated using u_{da} and h_{da}.

The depth-averaged downstream horizontal velocities were calculated in the current head over the 5 probes and for 5 s and 3 bins for the experiments with dense fluid between the elements. The results are presented in table 2.7. Compared to the smooth case, decreases in u_{da} of 22% and 29% again confirm that the buoyant ambient fluid trapped between the elements is not the sole cause of the effects of the bed roughness on the current. Similar to the results for the rough cases with ambient fluid between the elements, the internal u_{da} is approximately one third slower than the front speed.

2.6 Results: Turbulence

The downstream horizontal root mean squared velocities, u_{rms}, have been calculated using the following equation:

$$u_{rms} = \left[\frac{1}{n}\sum_{i=1}^{n}(u_i - \overline{u})^2\right]^{\frac{1}{2}} \tag{2.5}$$

where n is the number of observations, u_i is the downstream horizontal velocity at a point and $\overline{u}$ is the time averaged at a point downstream horizontal velocity. The results shown in figures 2.26 (a), 2.27 (a) and 2.28 (a) within the current head have a typical smooth bed gravity current u_{rms} profile (Buckee *et al.*, 2001) with reduced values at the mean velocity maximum and an increase at the interface where more mixing occurs due to interfacial instabilities. At the head, the 1% current shows little change from the smooth profile and magnitude of u_{rms} under the sand and beams$_{6,2}$ bed conditions, figures 2.26 (b) and (d). However, for the spheres and the k-type beam roughnesses, figures 2.26 (c), (e) and (f) the profile appears 'straightened' to give an almost constant u_{rms} value throughout the current depth.

For the 5% current, the effects are more substantial. It appears that in the smooth case the change in u_{rms} with depth is much more variable than in the rough bed cases with distinct maxima and minima. Although more significant than in the 1% case the profiles in the rough cases (figures 2.27 (b) – (f)) do not vary with height as dramatically as the smooth case. This observation also holds for the 10% density excess (figure 2.28). These results suggest that the turbulence is being redistributed throughout the current depth in all rough bed cases, regardless of the initial density excess of the current. The reduced u_{rms} at the density interface at the top of the current compared to the smooth case, suggests reduced turbulence fluctuations in this locality which could be indicative of the damping of the billows instabilities that are typically present in this region and has previously been implied in the velocity data.

The most significant difference between the different density excesses is that the 5% case appears to show an increase in u_{rms} near the bed under rough bed conditions while the 1% and 10% cases show very little change from the smooth case. It is possible that this is indicative of an effect due to the density excess. Where the 1% case is significantly slower, due to the reduced buoyant driving force, it does not appear to feel the effects of the bed roughness as significantly as the 5% case. Conversely, the 10% case has such an increased driving force that again those currents may be affected differently by the bed roughness. This observation perhaps suggests that there is a 'transitional' density

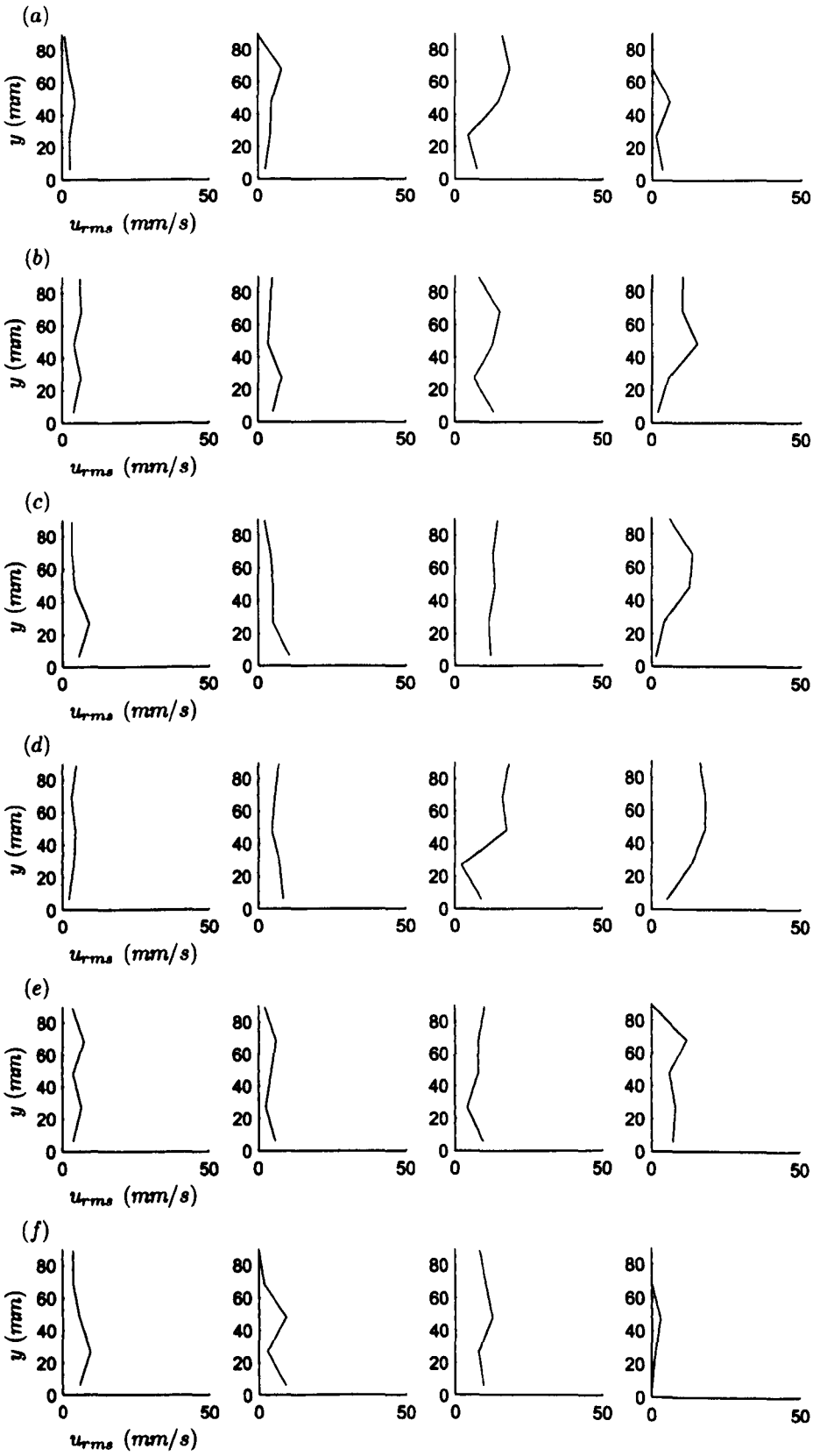

Figure 2.26: Downstream horizontal root mean squared (rms) velocity profiles as a function of depth for a 1% density difference, averaged temporally over 5s and spatially over 3 bins. Profiles from right to left of flow before the current head, in the head, in the body and in the tail for (*a*) smooth, (*b*) sand, (*c*) spheres, (*d*) beams$_{6,2}$, (*e*) beams$_{6,4}$ and (*f*) beams$_{6,8}$.

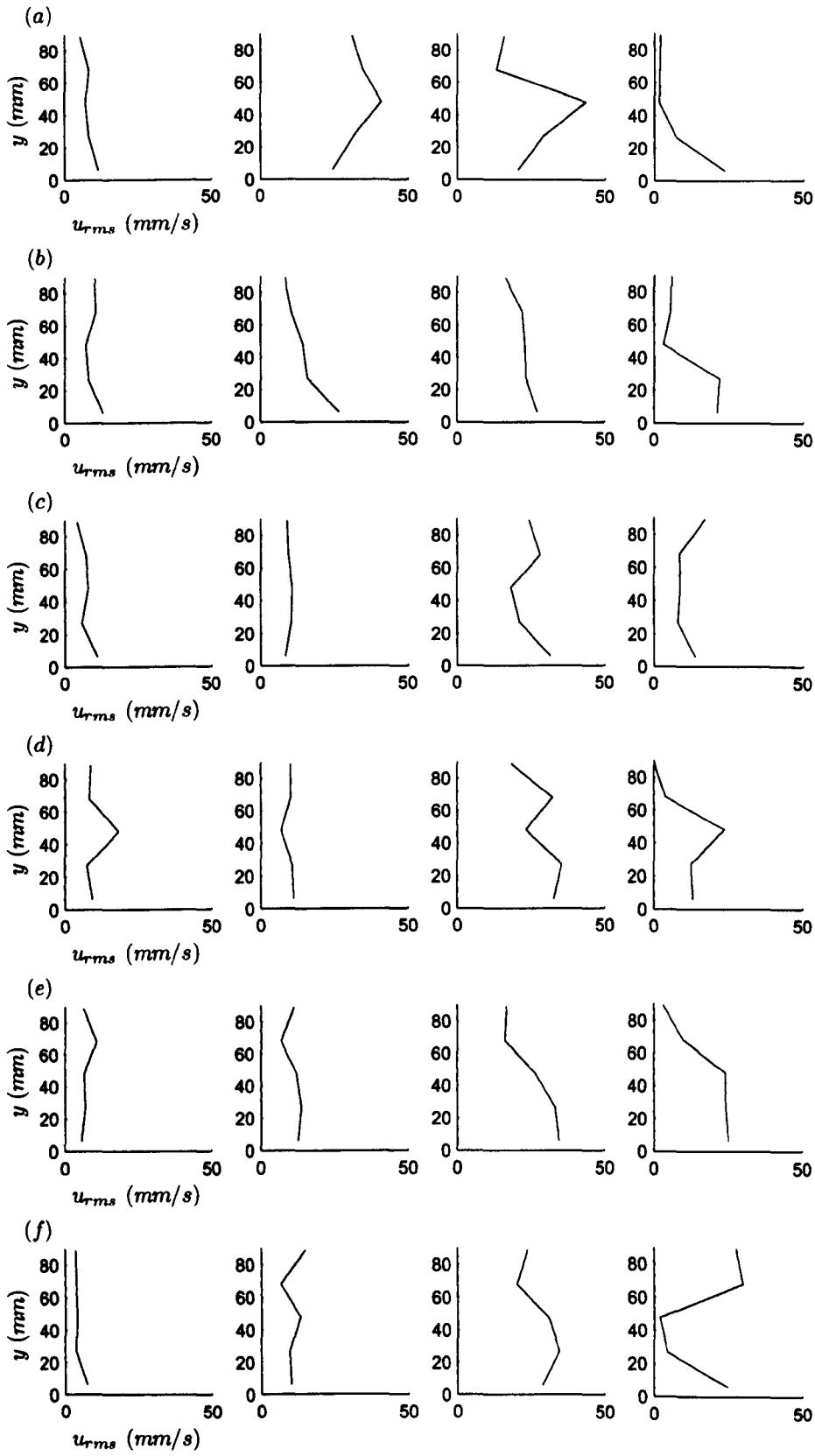

Figure 2.27: Downstream horizontal root mean squared (rms) velocity profiles as a function of depth for a 5% density difference, averaged temporally over 5s and spatially over 3 bins. Profiles from right to left of flow before the current head, in the head, in the body and in the tail for (a) smooth, (b) sand, (c) spheres, (d) beams$_{6,2}$, (e) beams$_{6,4}$ and (f) beams$_{6,8}$.

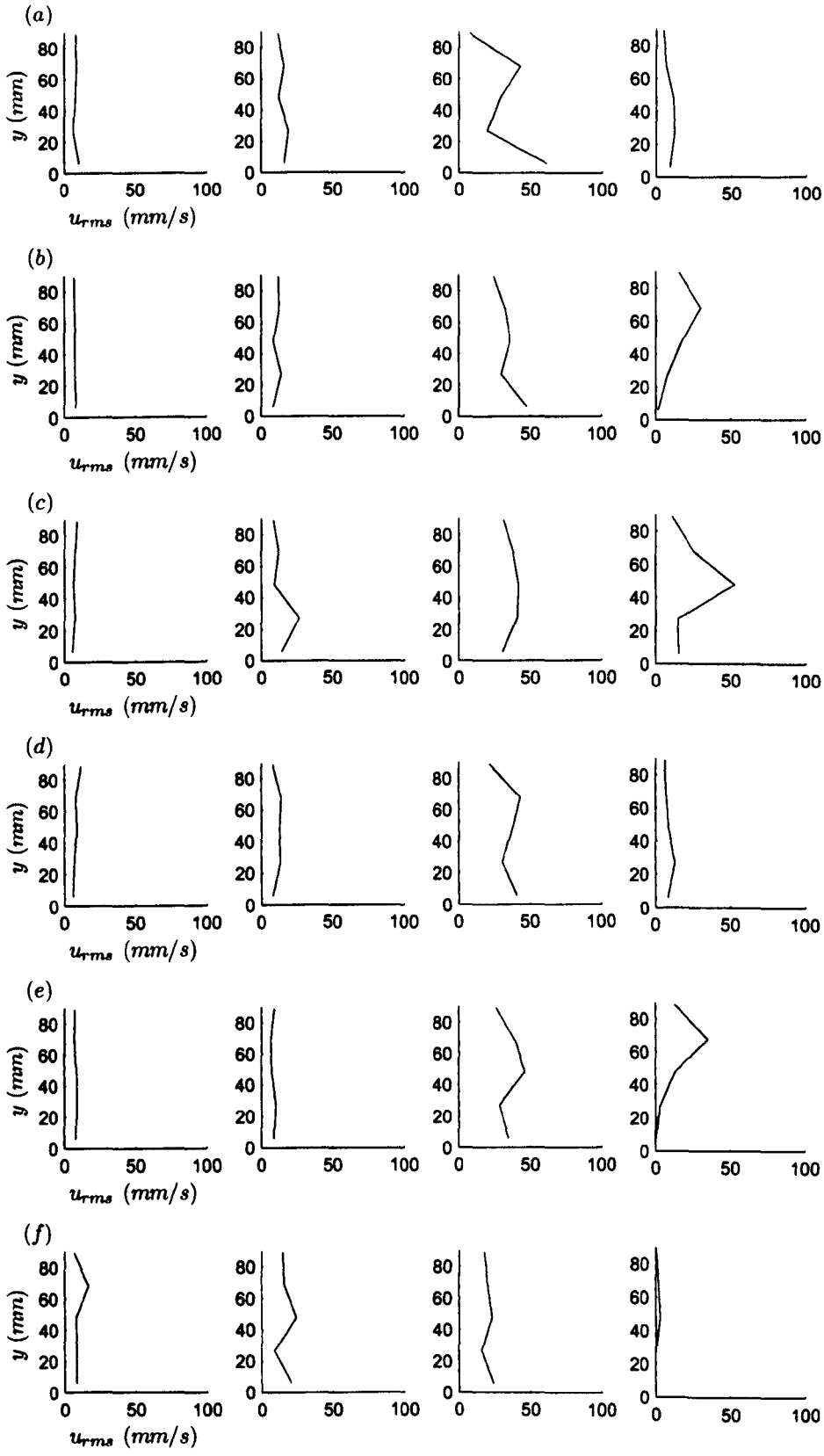

Figure 2.28: Downstream horizontal root mean squared (rms) velocity profiles as a function of depth for a 10% density difference, averaged temporally over 5 s and spatially over 3 bins. Profiles from right to left of flow before the current head, in the head, in the body and in the tail for (*a*) smooth, (*b*) sand, (*c*) spheres, (*d*) $\text{beams}_{6,2}$, (*e*) $\text{beams}_{6,4}$ and (*f*) $\text{beams}_{6,8}$.

excess at which the near-wall region of the current will be affected more than higher or lower excesses.

2.7 Discussion

Some discussion of the experimental results has been undertaken simultaneously with the presentation of the data in the present chapter to enable interpretation of the different measurements independently. This section combines the results of the present set of experiments and discusses them with reference to variables considered to be of key influence in the effects of bed roughness: initial density excess, roughness type, the spacing of the beam-type roughness, the effect of the removal of ambient fluid at the bed and change in roughness element height relative to fluid height. Finally a brief discussion of the measurement techniques is included.

The effects of bed roughness on gravity currents of initial density excesses of 1%, 5% and 10%

The results for the 1%, 5% and 10% density excesses show that the primary effect of bed roughness is to reduce the speed at which the gravity currents propagate. The nature and magnitude of this effect is critically dependent on the type of roughness and its configuration on the bed, as discussed subsequently. Currents flowing over bed roughness still propagate at a constant speed in the same manner as the smooth case for an initial period before undergoing a slowing transition which varies depending on the roughness type. The front position data collapses well for the constant speed phase for each bed type regardless of the initial density (figure 2.11) even though the roughness effects on the internal flow dynamics for the 1% case are relatively small. Therefore, it can be said that the distance that a current will travel over a given roughness type during this constant speed phase scales with the density difference, as commonly observed in existing smooth bed investigations and as observed by Peters *et al.* (1997) in their constant flux study on roughness effects.

In general, the presence of bed roughness results in fewer regions of high velocity distributed within the current, the head is less well-defined and it appears that the larger billows are not present. The results suggest that this is due to the increased presence of smaller instabilities at the density interface that may either break down or prevent the formation of larger billows. There does not appear to be a significant increase or

decrease in the magnitude of the vertical velocities relative to the horizontal velocities in the presence of bed roughness, rather there is an overall reduction in both velocity components and the roughness affects the distribution of the velocities[‡]. In the case of the horizontal component this results in a redistribution of horizontal velocities about the velocity maxima such that the profile appears more rounded, less skewed towards the maximum. The mean velocity maxima, $\bar{u}_{max}$, are smaller and further from the bed compared to the smooth case. Therefore it can be confirmed that the location of the velocity maximum is a function of the bed roughness, as predicted by both Kneller *et al.* (1999) and Buckee *et al.* (2001). In the vertical direction, an overall reduction in the magnitude of the positive vertical velocities is observed in the presence of any bed roughness. In fact, the present experiments indicate that when a rough bed is present there is significant positive vertical motion present within the nose and the head of the currents, not solely at the front and density interface as typically observed in the smooth case. Moreover, these new internal regions of vertical motion can be correlated with regions of reduced downstream horizontal velocities and may result from deflection or recirculation caused by the roughness elements or the upward ejection of vortices of ambient fluid from between the elements due to buoyancy. These mechanisms will all result in increased mixing within the head. Conversely, despite the increased vertical activity within the head, the frontal interfacial region is reduced and does not extend coherently as far back behind the current as observed in the smooth case. One likely result of this process is that the current head length is shorter when travelling over a rough surface.

These characteristics of a rough bed are not as clearly observed for the 1% density excess. This does not mean that the bed roughness is not affecting the current flow, rather it may be attributed to the already elevated location of $\bar{u}_{max}$ in the smooth case for this low density and the subtlety of the changes not being captured with the current probe resolution. Moreover, the 'lightness' of the fluid in this case will limit the interaction of the current with the elements, as discussed below. For the 1% density excess currents, whilst the front position at a given time, and thus the speed of the current, is affected by the presence of bed roughness, the downstream horizontal velocity field distribution does not appear to have changed considerably. This indicates that the roughness is having only a limited affect and is not interacting with higher regions of the flow. However, this could be predicted since the current is 'lighter' and therefore the ambient fluid will not be as influential in this case. To take affect, the ambient fluid at the bed relies on buoyancy induced by the density difference with the current when it is overridden. In the 1% case,

[‡]Based solely on the 5% current studied, which is assumed here to be representative.

this buoyancy force is weaker because the density difference between the ambient and the current is smaller and since the current dilutes during propagation due to other means of entrainment, for example at the density interface, the density difference also reduces, possibly to the extent that the ambient fluid between the elements does not incur enough buoyancy to eject. Hence, reduced effects on the internal flow structure at this density excess and exaggerated effects on the flow structure in the 10% case. This mechanism is similar to that observed by Peters *et al.* (1997) with reference to roughness effects on heavier and lighter currents. They found that lighter currents tended to float over the roughness elements with little interaction, while as the density increased the heavier fluid interacted more strongly with the roughness. It is not possible to determine at this stage if there is a scaling that can describe the increase in the magnitude of the effects on the flow structure as the initial density excess of the current increases but since the front position data collapses it is possible that there is an appropriate scaling that would enable a similar operation to be performed on the internal velocity structures.

The root-mean-squared velocities suggest that the turbulence has also been redistributed more uniformly throughout the current head depth and is less localised at the velocity maxima and the interface in the rough cases. The sphere and beam type roughnesses potentially cause the large structures at the interface to be broken down or remain small. These smaller structures that replace the large billows in these cases form more quickly behind the head of the current and this implies that the head is smaller in length than for the smooth case. Most of the effects on the internal flow structure can be attributed to the presence of the ambient fluid beneath the current and are discussed further subsequently. However, it is also possible that the reduction in the vertical and downstream horizontal velocity components due to the presence of roughness might coincide with an increase in the magnitude of the lateral velocity component that is not resolved in the present dataset. The cause of the shortening of the length of the current head in the presence of roughness is difficult to establish without vertical velocity data for the cases with the effects of the ambient fluid removed.

The effects of bed roughness types

The distance that the gravity current travels is affected by the type of roughness and its configuration on the bed. The grain roughnesses had a limited effect on the current speed ($\approx$ 5% at most), while the form roughnesses were much more influential (up to $\approx$ 10%) with the k-type roughness having a more pronounced effect than the d-type

roughness. In fact the sand case has been shown to have very little effect overall and maintains velocity distributions very similar to the smooth case. This could be expected since the coarse sand represents the smallest roughness 'height' at $\approx$ 2 mm. In this case the reduced amount of overridden ambient fluid is likely to have less effect and the roughness effects are probably solely generated by the increase in surface friction due to the close packing and irregularity of the sand. The spheres case has a greater effect at retarding the current and changing the internal structure, more like the most densely packed beams$_{6,2}$ case. This is to be predicted since the spheres have the same diameter as the beams height, i.e. 6 mm, and the spherical shape means that close packing, such as with the coarse sand, can only be achieved to a certain extent and this implies that although the surface friction may still be high there is an increase in the amount of ambient fluid in the cavities. These cavities will not be as large or regular as in the beam type cases but the similarity between this case and the beams$_{6,2}$ bed results could indicate a similarity in the effective roughness of these two bed types, regardless of their very different shapes.

The principal difference in the grain and form roughness types appears to be the magnitude of the disruptions to the velocity flow structure in the near wall regions. These variations may be predominantly attributed to the volume of ambient fluid that is overridden by the current and either trapped between the roughness elements or more immediately entrained into the head. However, these variations could also be attributed to the interactions between the flow and the roughness elements themselves, or the packing of the elements. The effects of packing on the grain type bed roughnesses are beyond the scope of the present study. However, this would be an interesting extension to the current dataset. The experiments performed herein that replaced the ambient fluid between the beam type elements with dense fluid have proven the significance of the effects of the presence of the trapped ambient fluid on the beam roughness types. It would be interesting to perform a set of equivalent experiments with a thin film of dense fluid over the grain type elements to determine the existence and magnitude of similar effects.

The effects of bed roughness spacing and the presence of the trapped ambient fluid between the elements

The changes to the front speed as a result of bed roughness are clearly important. However, the significance of the changes to the internal velocity structure that have been proven to result from the trapped ambient fluid could also have huge implications for

sediment transport in gravity currents. The interaction of the overridden ambient fluid and the roughness elements with the current is particularly important for understanding and characterising the effects of bed roughness on gravity currents in comparison to single phase rough flows, since the buoyancy forces induced by this ambient fluid are not present in the latter but are of fundamental importance to any gravity current study. The removal of the ambient fluid at the bed proved that this is the predominant cause of disruptions to and redistribution of the velocity field within the current head and an increase in mixing and entrainment in this region, and hence forms a significant contribution to the retardation of the flow. In fact, the front speed data suggests that the trapped ambient fluid contributes to approximately 50% of the reduction in front speed. However, it is not the only cause and there are other roughness effects, although these appear primarily to be slowing effects at the front with less impact on the internal flow structure. These other effects could be attributed to a loss of energy to maintain the vortical motion in the fluid trapped between the elements regardless of its density. However, it is necessary to perform very high resolution experiments with details of the flow dynamics between the roughness elements to confirm this. Hence, the subsequent use of CFD to enable predictions of the finer flow structures in these regions.

Overall, the retardation of the gravity current increases with the increase in the beam roughness element spacing. However, the gravity current propagation over d-type and k-type beam roughnesses show different characteristics. The front position at a given time for the two k-type cases used in the present study ($beams_{6,4}$ and $beams_{6,8}$) appear to be quite similar, suggesting that there is a critical spacing above which increasing the distance between the elements has little effect[§]. The effects of the k-type element spacing penetrate higher into the current depth, possibly since the volume of buoyant ambient fluid that is released from between the elements in these cases is more significant and is therefore potentially not entrained as quickly into the overflowing current. In the d-type case the volume of ejected fluid packet will be small by comparison and therefore can be expected to be broken up and entrained more quickly lower in the head causing less disruption.

The front position data suggests that the difference in retardation of the current under the influence of the d-type and k-type roughness is not due to the trapped ambient fluid. As mentioned above, without this fluid the currents are faster but the difference between

[§]This general rule will hold up to a point. When the elements become too far apart the flow dynamics will revert to that over a smooth bed with the highly dispersed elements representing very small individual obstacles in the path of the current.

the d-type and k-type front positions at a given time remains approximately the same. The ≈50% contribution to the reduction in speed due to the trapped ambient fluid holds for both element spacings. Since it cannot be attributed to the presence of the trapped ambient fluid, the difference in the spacing types could be a result of the loss of energy to maintain the vortical motion between the elements. As the gap between the elements is larger in the k-type case, it stands to reason that it requires more energy to maintain a vortex in motion in that locality. In fact, due to the separation that can occur at an element in the k-type case, it is possible that two primary vortices develop, one at the downstream face of an element and the other at the upstream face of the adjacent one. In the d-type case, the gap is so reduced that there is only one principal vortex and less energy is required to maintain the rotation. Therefore the current does not lose as much energy in this process and a greater speed can be maintained.

Conversely, the removal of the ambient fluid from between the elements does show significant differences in the resulting internal velocity structure for the currents with the d-type and k-type element spacings. Both show a lower velocity maximum, probably as a result of the reduced surface friction. However, the d-type case shows little change in the internal velocities. This is likely to be caused by the close packing of the elements such that the surface friction still has significant effect. On the other hand, the k-type shows a dramatic change, partly as a result of the exaggerated reduction in surface friction for this case. Moreover, because the larger volume of ambient fluid trapped between the elements in the equivalent regular case caused such disruption to the flow structure in the overflowing current that its removal is much more apparent than the removal of the small volumes of ambient trapped in the d-type case.

Note that after some time or distance, as the current dilutes through mixing and entrainment, the density difference between the current and the trapped ambient fluid will reduce. Thus the strength of the buoyancy force at the bed will diminish and so will the effects of the overridden ambient fluid on the current. At this point, the flow structure may change and eventually stabilise, perhaps similar to the 1% density case where the density difference is much smaller from the start. For longer-lived gravity currents, such as those in submarine channels that may last for days, the buoyancy effects should primarily manifest in the head and the initial parts of the current body. Once dense fluid replaces the lighter fluid between the elements, the more distal parts of the gravity current will exhibit very limited buoyancy effects. As a consequence of this, the influence of bed roughness on gravity currents will potentially change both spatially and temporally. Therefore, an interesting extension to this investigation would be to study the effects of

changing the density of the fluid that is initialised between the bed roughness elements.

The effects of decreasing the fluid height relative to the bed roughness height by half

The results showed clearly that the effects of the bed roughness on the front position and speed are dependent on the current height. However, by reducing the total fluid height by half, it is probable that the relative height of the beam roughness elements meant that they interacted with the current more like a series of obstacles. As such, the current was subject to significant blocking effects from the beam-type elements that are not present when the roughness is small relative to the current height. Therefore, the flow dynamics could be expected to be significantly altered and not representative of the effects of roughness. An investigation of the effect of the height of the roughness elements on the propagation of gravity currents with increased resolution would enable further definition as to what height constitutes roughness effects and what results in the effects of an array of obstacles.

Measurement techniques

The use of the video capture technique was proven to be relatively simple but very successful for establishing the front location and hence the front speed of the currents. It also supplies useful visual aids for interpretation and records.

The results confirm that the UDVP velocity measurement technique enables relatively easy 1D measurement of the downstream horizontal velocity component of lock-release gravity currents as has been shown previously (Best *et al.*, 2001). Even with only five probes, the typical gravity current profile can be generated for the smooth cases for 1%, 5% and 10% density excess currents. For clarification of the change in the downstream horizontal velocities with depth and higher resolution of flow structures within the time series contours measurements with several more probes, or a higher resolution technique like PIV or LDA would be beneficial. Despite initial problems with constraining the vertical velocity probes, the data from the single probe was satisfactory. However, it would again be beneficial to implement another measurement technique that would enable coincident velocity component readings at a point with sufficient accuracy. This would also provide data for the calculation of more accurate fluctuating velocities and hence Reynolds stresses and turbulent kinetic energy which would allow, for example, better determination of the fate of the billows at the interface.

For calculation of k_s values, particularly in the 5% case where the current mean velocity maximum is typically closer to the bed, and as should also be observed for the 10% case with greater resolution, a technique like PIV would again be useful. This would enable greater resolution to obtain more data points below the maximum for indication of the present measurement accuracy.

Summary

This chapter has presented the results of a set of experiments designed to establish the fundamental influence of form and grain roughness on saline lock-release gravity currents with different concentrations of 1-10%. The experiments have demonstrated that the presence of any bed roughness reduces the distance covered by the current before it deviates from the initial constant speed phase and enters subsequent slower phases. This transition occurs earlier with increasing bed roughness effects. The influence of the bed roughness also manifests in the internal flow dynamics. For the heavier currents (5% and 10%) the height of u_{max} is clearly increased, as previously theoretically predicted, while its magnitude is smaller. The magnitude and patterns of the vertical velocity distribution within the current head also change dramatically as a consequence of bed roughness. The interfacial instability generated at the front does not persist coherently as far back into the following flow in the rough cases, which suggests that the length of the head of the current is typically shorter. Within the head itself, regions of high positive vertical motion are present associated with regions of reduced downstream horizontal activity. In particular, in the beam roughness cases these regions of high vertical velocity near the bed may represent the ejection of vortices of buoyant ambient fluid into the overlying head. These modifications to the velocity fields correspond to variations in turbulence. In the presence of bed roughness more uniform redistribution of turbulence is observed within the head, relative to the smooth cases.

The type of bed roughness, grain or form, plays a fundamental role in defining the magnitude and nature of the changes to the gravity current dynamics. The small-scale grain roughness shows little influence on the internal flow dynamics but does increase the basal friction. The larger-scale grain roughness shows similarities in its affects to the closest spaced d-type form roughness, having increased influence on the internal flow structure. However, it is the k-type form roughnesses that have the most significant impact on the current since with increasing length of the cavities between the elements, the impact of the trapped ambient fluid increases.

In order to assess the relative impact of the increased roughness (and the resulting frictional increase) and the influence of the buoyancy forces produced by the trapped ambient fluid, the cavities between the beams were filled with fluid of the same initial density as the current. The results of this exercise demonstrate that each of these effects contributes to $\approx$ 50% of the retardation of the flow, relative to the smooth currents. Finally, an attempt was made to estimate the k_s values for each of the bed roughness types in order to characterise them in such a way that similar values may be implemented in the subsequent CFD work (see chapter 4).

These manifold effects on flow speed, flow structure and turbulence distribution, demonstrated with saline currents, can be expected to have significant analogous consequences for sediment transport in particle-laden gravity currents. Furthermore, long duration currents will be susceptible to the spatial and temporal changes in the influence of the bed roughness, in particular the reduced impact from buoyant trapped ambient fluid with time.

The present results are expanded in chapters 5 and 6 where 2D and 3D CFD techniques are applied to examine the effects of such bed roughnesses on the finer details of gravity current dynamics. The CFD simulations in those chapters are partially validated by the dataset provided by these experiments.

Chapter 3

Depth-averaged theoretical model

3.1 Introduction

This chapter introduces a depth-averaged (1D) model. Existing models and theories are discussed and terms for the inclusion of bed roughness are outlined. This is followed by a derivation of the governing equations and the assumptions and boundary conditions applied. The method of characteristics solution procedure implemented in the present study is explained and applied to smooth and rough bed cases.

The results of these models for the smooth and rough cases are then presented and validation with experimental data has been performed for the smooth case. Also included are the results of implementing different conditions at the front in the smooth case. Complete flow profiles of the characteristics are displayed for currents generated with $h_0/H \leq 0.5$. The depth and velocity profiles throughout the domain extracted from these results show the evolution of these parameters after release for flow over rough and smooth surfaces.

3.2 Literature review

Earlier mathematical models, such as those of Von Karman (1940) and Benjamin (1968) have already been mentioned in section 1.3. However, these represent only the earliest of extensive theoretical studies over several decades, continuing to the present day. The governing equations are essentially the same but it is the treatment of them and the parameters included that differ.

Simplified theoretical models have been developed with extensive use of shallow water theory and the shallow water equations. The governing equations and their solutions.

along with some terms that may be applied or considered for the effects of bed roughness are covered in the present review. A good review of the application of the shallow water equations to gravity currents can be found in Moodie (2002). There is much discussion in the existing literature with reference to the use of suitable front conditions required by some methods, including that of the present study. Alternative reviews of this contentious topic can be found, for example, in Marino *et al.* (2005). A review of fully depth-resolved models can be found in chapter 4.

In hydraulics, terms accounting for bed roughness are included in the resistance coefficient. A detailed review of resistance in open channels, with substantial discussion of bed roughness, can be found in Yen (2002).

3.2.1 Governing equations and solution methods

The principal governing equations for incompressible, laminar fluid flow are the Navier-Stokes equations:

$$\frac{\partial u_i}{\partial t} + u_i \frac{\partial u_i}{\partial x_j} = -\frac{1}{\rho}\frac{\partial p}{\partial x_i} + \nu \nabla^2 u_i + F_i \tag{3.1}$$

$$\frac{\partial u_i}{\partial x_i} = 0 \tag{3.2}$$

for $i, j = 1, 2, 3$. The assumption that the flow is incompressible is valid since the fluids involved are water and saline, neither of which are highly compressible under the conditions in the present study.

Depending on the problem to be solved, this set of equations can be reduced to involve only the terms necessary for a specific situation. They are commonly reduced to the Euler equations in two or three dimensions. Through the assumption of shallow water theory* most investigators reduce the equations further to give the shallow water equations in one or two layers (e.g. Hoult, 1972 or Rottman and Simpson, 1983, respectively, among many others). Although the hydrostatic assumption involved in the derivation of the equations is violated at the front and cannot hold until a short while after release when modelling lock exchanges, Shin *et al.* (2004) note that it allows analytical theory to be developed and it has been proven numerous times to be valid in most cases. They suggest that it appears that various approximations are not that important to the description of the bulk propagation of the current if that is the requirement of the study. Cases

*Essentially that $h << L$ for h a typical current height and L a typical length scale (Acheson, 1990).

and methodology when non-hydrostatic forces cannot be circumvented are discussed in section 3.2.4.

The shallow water equations can be solved using long-time similarity solutions when enough time has passed so that the effects of the initial release no longer govern the flow dynamics. Fannelop and Waldman (1972) and Hoult (1972) solved the depth-averaged version of the equations in one and two layers, respectively. Their results have been discussed by Grundy and Rottman (1985) with attention to how rapidly the similarity solutions become relevant as a solution method after the initial phase of collapse, i.e. the value of the earliest 'long-time'. Gratton and Vigo (1994) also solve the one layer system, developing the work of Grundy and Rottman (1985) further and reassessing certain aspects of it. They find that there are four types of self-similar solution that depend on the criticality of the flow.

Rottman and Simpson (1983) studied the initial phases of flow generated by the changing balance of forces for gravity currents created in a lock-exchange tank with a 'fixed lid'. A fixed lid condition can be applied to the top boundary so that the combined height of the current fluid and the lighter fluid above it is constant. This essentially implies that the ambient fluid is deep in comparison to the current so that the effect of the current on the free surface will be negligible and vice versa. This is a common assumption and has been used often in previous studies (e.g. Bonnecaze *et al.*, 1993; Klemp *et al.*, 1994; Montgomery, 1999; Shin *et al.*, 2004). An alternative method is to include the free surface in the governing equations with the introduction of a variable to describe it and the assumption that pressure is zero on this fluid interface (e.g D'Alessio *et al.*, 1996; Montgomery, 1999; Moodie *et al.*, 1998; Moodie, 2002).

Rottman and Simpson (1983) use the one-dimensional, two-layer shallow water equations and initial conditions associated with an instantaneous release from a lock with an initial dense fluid height (h_0) and length (x_0) specified and the velocity set to zero throughout the domain. The boundary conditions imply that the current is symmetrical about the end wall and the velocity is zero at the walls. They use the method of characteristics (see for example, Ames (1965) or Abbott (1975), also described in section 3.5) with a front condition modified from Benjamin (1968), to derive and solve an ordinary differential equation that relates the velocity of the current to its height. The validity of their results is limited to $h_0/H < 0.5$, where H is the constant height of the ambient fluid. Within this limit, however, the characteristic results show good agreement with their experimental results. The initial method in the present study follows this theory and is

detailed more expansively in section 3.3. Klemp *et al.* (1994) furthered their work with an additional condition for the criticality of the flow for $h_0/H > 0.5$. Shin *et al.* (2004) also derived an additional condition and a slightly different front condition to account for partial depth releases and those with $h_0/H > 0.5$.

D'Alessio *et al.* (1996) include a free surface in their shallow water equations and derive them in two and three dimensions but reduce them to the one dimensional case for solving. They solve them in 'full' one dimensional form along with a non-dimensionalised, weak-stratification model (where $\rho_2/\rho_1 << 1$) using a finite difference method with the MacCormack scheme (LeVeque, 1997). This is an explicit, conservative, second-order accurate method involving a forward difference followed by a backward difference. Artificial viscosity is included to dampen oscillations. They also solve their weak stratification model using a similarity solution method, the method of characteristics and a Godunov method (LeVeque, 1997) to compare it against the full set of equations and show the spectrum of solution methods applicable for solving such a model. This method does not use a front condition, instead the front is analogised with a discontinuity in the flow. Although the observed dynamics at the front show that this is clearly not the case (e.g. Simpson, 1972) and that without a front condition entrainment, turbulence and other non-shallow-water effects at the front cannot be accounted for, it is another means of capturing the front. Also, discontinuous solutions for conservation laws have been well studied and the method enables a completely theoretical model to be developed without the need for empirical results. The same authors also solved the shallow water equations in three layers using the finite difference method and the MacCormack scheme for the modelling of intrusive gravity currents (D'Alessio *et al.*, 1997).

Bonnecaze *et al.* (1993), among others, solve the shallow water equations in one and two layers with a similar one dimensional system to Rottman and Simpson (1983) but with alterations for a particle driven gravity current. They include another equation for the volume fraction occupied by the particles which includes a settling velocity and modification to the reduced gravity, making it a function of this fraction. This set of equations can be reduced to the homogeneous case when required by setting the volume fraction appropriately. The one layer case is studied since in nature it is usually a small denser current intruding into a relatively deep ambient fluid. Hence, the effect of the ambient fluid is considered negligible and is not included in the solution process. However, there is little data available for real life comparisons and when the size of the advancing current is more comparable to the height of the ambient fluid, as is the case in most experimental setups, the effects of the ambient fluid cannot be neglected. Thus

the two layer equations are necessary. Bonnecaze *et al.* (1993), Bonnecaze *et al.* (1996) and Bonnecaze and Lister (1999) use a front condition derived from the work of Huppert and Simpson (1980), based on an empirical Froude number, with a finite difference method. In their method, they nondimensionalise their governing equations and apply a two-step Lax-Wendroff scheme, second-order in time and space. Several investigators have included other additional terms for different channel geometries or different current specifications. For example source terms to include a slope in the tank can be included accounting for the increase in friction that occurs in this case (Bonnecaze and Lister, 1999; Moodie *et al.*, 1998; Montgomery, 1999; Montgomery and Moodie, 1999).

Similar to Bonnecaze *et al.* (1993), Moodie *et al.* (1998) also include additional terms and an additional equation for the motion of particles in the flow. However, the work conducted by Bonnecaze *et al.* (1993) on particle driven gravity currents and subsequent work using similar methods (Bonnecaze and Lister, 1999, Engblom *et al.*, 2001) has been repudiated by Moodie *et al.*, 1998. They find, through dimensional analysis, that due to non-hydrostatic forces generated by the presence of terms describing the particles, the shallow water equations are not valid for the solution of the problem when the density difference between the fluids is solely generated by particles suspended within the current and not supported by an additional uniform difference in the interstitial fluid density as well. Further discussion follows in section 3.2.4.

Montgomery (1999) showed that the shallow water equations can be written as a system of hyperbolic conservation laws including forcing or source terms when necessary. A numerical method of solution is guaranteed not to converge to non-solutions if it can be written in conservation form (LeVeque, 1997). A simple way of assuring this is to start with the partial differential equation (PDE) in conservative form and then use finite difference discretisations as usual. If the scheme converges to a solution then it is a 'weak solution' of the conservation laws (LeVeque, 1997). Montgomery (1999) derives a two-dimensional system for two-layer, thin top or bottom layer, weakly-stratified fluids, free surface and fixed lid cases. The hyperbolicity of the system of equations is proven and jump conditions are created to couple the lower and upper layer equations on either side of the discontinuity using methods for Rankine-Hugoniot jump condition derivation (Montgomery and Moodie, 2001). A second-order accurate and total variation diminishing (TVD) relaxation scheme for solving a system of hyperbolic conservation laws including forcing or source terms is derived by modifying a method developed by Jin and Xin (1995). A generalisation of this method can be found in Montgomery and Moodie (2003) where the scheme is proven for an initial value problem (IVP), using Burgers'

equation as an example, and for an initial boundary value problem (IBVP) using the two-layer shallow water equations in one dimension with forcing terms for slope and frictional drag. Several other theoretical studies, using the shallow water equations for compositional and particulate currents with and without source or forcing terms, have been carried out using this method (Moodie *et al.*, 1998; Montgomery and Moodie 1998, 1999; Moodie, 2002; Antar and Moodie 2003, 2005). However, a rigorous comparison of most of this work with experimental or even other validated theoretical results has yet to be undertaken.

A different theoretical model for fixed volume releases, is derived through the use of 'box models' where the current is considered to take the shape of a series of non-entraining rectangles or 'boxes' with constant cross-sectional area (Huppert and Simpson, 1980; Hallworth *et al.*, 1996; Hogg *et al.*, 2000). The shallow water equations are not used explicitly but shallow water theory is applied. This method is useful for simpler analyses of the currents and is usually used in conjunction with experimental studies where a more detailed profile of the current is not necessary for comparison. It does not require a numerical method of solution.

3.2.2 The front condition

The theoretical determination of the speed of the gravity current has been attempted in many ways and is often the focus of a theoretical or experimental study. A simple approximation of the horizontal velocity, u, can be made from the basic balance of energy of a dam break (Simpson, 1997). In this situation, the gravitational potential energy lost must equal the kinetic energy gain thus implying:

$$\frac{mu^2}{2} = mg\frac{h}{2} \tag{3.3}$$

i.e.

$$u = \sqrt{gh} \tag{3.4}$$

where m is the mass, $h/2$ the mean height of the centre of gravity and g the magnitude of the gravitational acceleration. Clearly, this can be extended to the flow of two fluids with a density difference between them. This difference, no matter how small, will reduce the driving force on the fluid to below normal by $\Delta\rho/\rho$ where $\Delta\rho$ is the density difference. Since the gravitational presence is one of the main driving forces, this will modify equation (3.4) as follows:

$$u = \sqrt{g'h} \tag{3.5}$$

where $g' = g\Delta\rho/\rho$. There appears to be some discrepancy in the exact form of this density difference. If ρ_1 is the density of the current and ρ_2 the density of the ambient fluid, some authors use a reduced gravity given by

$$g' = g\left(\frac{\rho_1 - \rho_2}{\rho_2}\right) \tag{3.6}$$

(Von Karman, 1940; Benjamin, 1968; Simpson and Britter, 1979; Bonnecaze *et al.*, 1993; Klemp *et al.*, 1994; Peters, 1999). While others use one of the form

$$g' = g\left(\frac{\rho_1 - \rho_2}{\rho_1}\right) \tag{3.7}$$

(D'Alessio *et al.*, 1996; Moodie *et al.*, 1998; Montgomery, 1999; Shin *et al.*, 2004; Marino *et al.*, 2005). However, for small densities, this difference is marginal. Moodie and Pascal (2001) point out that equation (3.7) is particularly useful for the special case of an air/water interface where $\rho_2 \to 0$, as in dam break problems.

Von Karman (1940), through the assumption of conservation of energy and the application of Bernoulli's equation to steady, irrotational flow, determined an equation for the velocity of the progression of the front of the form:

$$u = \sqrt{2g'h} \tag{3.8}$$

Benjamin (1968) defined a dimensionless constant for the flow of an air-filled cavity into a liquid, in terms of the depth of the cavity as follows:

$$D_* = \frac{u}{\sqrt{g'h}} = \sqrt{\left[\frac{(H-h)(2H-h)}{H(H+h)}\right]} \tag{3.9}$$

where H is the total depth of the cavity and liquid. For application to gravity currents, Benjamin (1968) found $D_* = \sqrt{2}$. Thus, although rejecting the theory behind the calculation of Von Karman (1940), the same conclusion for u (equation (3.8)) has been reached. Equation (3.9) has been proven by Klemp *et al.* (1994) to be a reliable description of the front propagation for an inviscid problem. They found, however, that it lacks the capacity of a full set of equations to account for surface drag and mixing on the interface and hence overestimates the speed when compared to laboratory data.

Rottman and Simpson (1983) among others use the front condition of Benjamin (1968) which is derived later in this chapter. Other theoretical and experimental front conditions have been derived and imposed. For example, Huppert and Simpson (1980) postulated the expression

$$u = \begin{cases} 1.19\sqrt{g'h_f} & \text{for } h/H < 0.075 \\ \left(\frac{h}{H}\right)^{-\frac{1}{3}}\sqrt{g'h} & \text{for } h/H < 0.075 \end{cases} \tag{3.10}$$

based on experimental results, while Shin *et al.* (2004) derived the expression

$$u = \left[\left(1 - \frac{h}{H}\right) g'h\right]^{\frac{1}{2}} \tag{3.11}$$

using a similar method to Benjamin (1968) but taking into account a control volume including both sides of the current interface, the theoretical solution $h = h_0/2$ and the Boussinesq assumption. This condition has the advantage that it contains no free parameters.

3.2.3 Rough boundary terms

Although there is little other existing literature specifically on the application and effects of bed roughness on gravity currents, these effects are considered frequently in hydraulic engineerng studies of open channel and pipe flow (e.g. Chow, 1959, Liggett, 1975, Streeter and Wylie, 1983, French, 1994). In particular, the use of the Chezy or Manning equations, developed in 1769 and 1889, respectively, for computation of the average velocity of the flow, includes a resistance coefficient that can be specified to describe the type of roughness present. These equations were first derived for uniform, steady flow but they have become widely used in non-uniform and unsteady flow (French, 1994). Using open channel flow theory the velocity of a uniform flow can be computed approximately using a semi-empirical uniform flow equation of the form

$$\bar{u} = C_H H_{rad}^A S_0^B \tag{3.12}$$

where $\bar{u}$ = average velocity, H_{rad} = hydraulic radius of the channel, S_0 = channel longitudinal slope, which can be considered as the *friction* slope, S_f, C = resistance coefficient and A and B = coefficients.

The Chezy form of equation (3.12) has been found to have parameters $A = B = \frac{1}{2}$ and $C_H = Chezy\ C$ to be determined by measurement or estimate. In the Manning equation, $A = \frac{2}{3}$, $B = \frac{1}{2}$ and $C_H = \frac{1}{n_M}$ where $n_M = Manning\ resistance\ coefficient$ and the equation is entirely empirical. Note that the coefficients n_M and C_H are related by the equation

$$C_H = \frac{1}{n_M} H_{rad}^{\frac{1}{6}} \tag{3.13}$$

Also, these coefficients are not dimensionless. The $Chezy\ C_H$ has dimensions of acceleration, i.e. m/s^2 and the $Manning\ n$ (n_M) has dimensions $s/m^{1/3}$. Clearly, equation

(3.12), in both of the forms defined above, can be rearranged to determine the friction slope when the other parameters are known or estimated. Hence enabling one method of developing a simple means of including a form of roughness on the bed.

The estimation of the coefficients is the primary difficulty in the prediction of resistance (Yen, 2002). Theoretically, one would expect that coefficients of resistance would depend on the Reynolds number of the flow, the boundary roughness and the shape of the channel. More details of the definition of the resistance coefficient can be found in Rouse (1965). One of the first pioneers of the effects of wall roughness on the flow was Nikuradse (1933), who investigated the flow through sand-roughened pipes. Further effects on pipes were explored by Moody (1944) among others. In pipe flow, the dimensionless Darcy-Weisbach friction factor (see Streeter and Wylie, 1983 pp. 227-229), f_0, is used to determine the resistance. This is obtained by using the Darcy-Weisbach equation for pipes:

$$h_f = f_0 \frac{L}{D_{in}} \frac{\bar{u}^2}{2g} \tag{3.14}$$

where D_{in}=inside diameter of the pipe, L=length of the channel under consideration and $\bar{u}$=the average velocity of the flow. This can be written as

$$\bar{u} = \sqrt{\frac{8g}{f_0}} \sqrt{H_{rad} S} \tag{3.15}$$

for flow in open channels (Streeter and Wylie, 1983). On comparison with the Chezy form of equation (3.12), we obtain

$$C_H = \sqrt{\frac{8g}{f_0}} \tag{3.16}$$

where the friction factor, f_0, is determined through the same method as for flow in pipes, i.e. using diagrams correlating relevant flow variables (e.g. Nikuradse, 1933, Moody, 1944, Streeter and Wylie, 1983). For idealised straight rough channels at high Re numbers f_0 is mainly a function of bed roughness. For smooth channels it is a function of Re (Rouse, 1965; Yen, 2002).

There is no general equation to determine the value of the resistance coefficient for any given flow characteristics. Discussion of the use of the Chezy, Manning and Darcy-Weisbach expressions can be found in Moody (1944) and Yen (2002), for example. Yen (2002) suggests that there is no real advantage in using one of them over another. The advantage of f_0 is that it is directly related to the development of fluid dynamics. Chezy

C_H is the simplest and has the longest historical usage and the Manning n has the advantage that it is almost constant, almost independent of flow depth, Re or roughness height for fully developed turbulent flow over a rigid rough surface.

In defining f_0, the equivalent roughness height, k_s, conceived by Nikuradse (1933) is frequently used since it can be calculated from the velocity profile of the flow, independent of any contextual variations. k_s has been discussed previously in section 1.3.3. In the context of bedforms the definition of k_s is slightly more complex. Yen (2002) suggests that large bedforms behave similar to large roughness elements and can be described as a 'macroroughness'. If these are considered as large-scale densely distributed fixed elements, then technically they can be characterised by k_s, however, it is unlikely that this single value will be able to accurately represent the effects of size, shape and spatial distribution. Added to this is the possibility of flow separation.

One solution is to perform a 'linear separation' (Yen, 2002) where the resistance coefficient is split into 'grain' roughness and bedform or 'form' roughness. This concept is presented and methodology is discussed by Van Rijn (1984). k_s is split into the components $k_{s,grain}$ and $k_{s,form}$, defined respectively by the following:

$$k_{s,grain} = 3D_{90} \tag{3.17}$$

and

$$k_{s,form} = 1.1\Delta\left(1 - e^{-25\Psi}\right) \tag{3.18}$$

where D_{90} is the grain particle diameter, Δ = bedform height, $\Psi = \frac{\Delta}{\lambda}$ and λ is the bedform length. The final k_s value is then simply the sum of these two grain and form components, i.e. $k_s = k_{s,grain} + k_{s,form}$. This can be substituted into the relevant equation to calculate the resistance coefficient.

For density currents, Middleton (1966b) adapts expression (3.16) to give

$$C'_H = \sqrt{\frac{8g'}{f}} \tag{3.19}$$

where g' is now the reduced gravity as defined previously and f is made up of the resistance from the bottom and sides of the channel (f_0) and from the fluid interface (f_{int}) and is given by:

$$f = f_0 + \frac{W}{W + 2h} f_{int} \tag{3.20}$$

where W is the width of the channel. f_0 is determined as above by analogising the current to a river flowing over a chosen type of roughness element. f_{int} is more difficult to predict since it depends on the physical state of the interface (French, 1994 p. 544; Middleton, 1966b). Middleton (1966b) only predicts it in a 'semi-quantitative' manner and suggests, from his experimental evidence, that it decreases with decreasing Fr and increasing Re.

Peters (1999) generated a spread rate model using similar a methodology to Didden and Maxworthy (1982):

$$X = \tilde{k}\left(\frac{g_s'' Q^3}{\nu_{eff}}\right)^{\frac{1}{5}} t^{\frac{4}{5}} \tag{3.21}$$

where $\tilde{k}$ is a constant of proportionality, $Q = UH$, the product of the mean velocity and height scale for the layer. Further, g_s'' is a rough-surface-reduced gravity term for the bottom layer that accounts for the decrease in mean layer density due to the mixing of the current with the ambient fluid trapped in the spaces between the elements, defined by

$$g_s'' = \alpha_b g_s' \tag{3.22}$$

where g_s' is the gravity, reduced by the difference between the densities of the fluid in the current and the spaces between the beams and α_b is a buoyancy flux reduction factor that accounts for the decrease in mean layer density due to the mixing of these two fluids, given by

$$\alpha_b = \frac{2}{2 + \left(\frac{h_R}{H - h_R}\right)} \tag{3.23}$$

where h_R is the height of the rib. The term ν_{eff} is an effective viscosity that allows for the effect of roughness, defined by

$$\nu_{eff} = \frac{C''}{4} Q \tag{3.24}$$

where the friction coefficient C'' is defined using an empirical expression that relates it to the roughness scale for flows over a fully rough plate (Mills and Huang, 1983):

$$C'' = \left(2.635 + 0.618 ln \frac{L}{k_s}\right)^{-2.57} \tag{3.25}$$

Here L is a length scale and k_s is the equivalent grain roughness of sand, correlated to transverse ribs with the formula

$$k_s = h_R^{\left[3.4 - 3.7\left(\frac{s}{h_R}\right)^{0.73}\right]} \tag{3.26}$$

for roughness arrays with $s/d = 2$ where s is the 'pitch', the sum of the rib width and the space between the ribs, and d is the rib width.

In analytical studies, the shallow water equations have been solved for gravity currents with frictional drag terms but not specifically for flow over a homogeneous bed roughness (e.g. Hatcher *et al.*, 2000; Hogg and Woods, 2001). A significant amount of work has also been undertaken in theoretically modelling one- to multi-layer flows over obstacles using shallow water theory. In these investigations, in contrast to the above models, the bed topography is described more explicitly using a variable that accounts for the height of the bed. The inclusion of such an influence is relatively simple, however, the solutions become more complicated and the possible violation of the hydrostatic assumption must be addressed, see section 3.2.4. For steady one- and multi-layer flows, details can be found in, for example, Baines (1984), Lawrence (1993) and Zhu and Lawrence (1998). Additionally, Baines and Guest (1988) consider blocking effects on similar flows. For gravity currents there is the added complexity of modelling transience and the frontal phenomena. Examples can be found in Lane-Serff *et al.* (1995) for flow over obstacles and Montgomery and Moodie (2003) for flow over a sinusoidal bed, although the latter is not validated.

3.2.4 The hydrostatic assumption

As mentioned previously in this review, and discussed in more detail in subsequent sections, the one or two layer shallow water equations are used to describe gravity currents theoretically. Shallow water theory implies that vertical length scales are small in comparison to horizontal length scales and therefore vertical accelerations are small in comparison to horizontal ones. Thus, we can assume that the pressure at any point is effectively equal to the static pressure due to its depth below the free surface. Along with the dynamic boundary condition of a continuous pressure field across the interface the pressure fields in each layer are derived and these imply that the horizontal pressure gradients driving the flow are independent of depth and thus so are the horizontal velocities. Hence the flow is described as hydrostatic. This assumption cannot hold at the front of the current and hence front conditions are required to complement the theory.

It is particularly relevant to consider this assumption in light of the present topic since topography could introduce effects that would make predictions based on shallow-water theory in error (Moodie, 2002). It has been indicated in single and multi-layer flows that if the topography in question is sufficiently long and smooth so that horizontal

scales are much larger than vertical scales, the flow can still be assumed hydrostatic (Baines, 1984). However, if the bed topography causes significant excitation of vertical components so that the streamline curvature deflects by a magnitude of order one, the hydrostatic assumption is no longer valid (Zhu and Lawrence, 1998). This can be interpreted, with reference to gravity currents, to hold when a current encounters a topography with magnitude of order one (O(1))† (Moodie, 2002) or a slope much greater than 1/10 (Montgomery, 1999).

Moodie *et al.* (1998), Moodie (2000) and Moodie (2002) also discuss the implications of including particles in the equations on the hydrostatic assumption. They suggest that particulate forms of the shallow water equations are valid for the case when the interstitial fluid is equal or less dense than the ambient, only if the particle equation is 'decoupled' from the main governing equations. The justification for this is that if the particles and their settling velocities are driving the flow then vertical structures in the horizontal velocity field are unavoidable and this can be proven by scaling analysis. However, it must be noted that the results of Bonnecaze *et al.* (1993) and Bonnecaze and Lister (1999) show good agreement with experimental data, despite violating this rule.

A non-hydrostatic 'correction' has been developed (Antar and Moodie, 2003; Antar and Moodie, 2005). However the added complexity means that the equations including this addition were not solved without other assumptions, limiting the applicability of the model. The results do not appear to have been validated with experimental data and the correction does not appear to have been adopted in subsequent studies.

3.2.5 Summary

The shallow water equations have clearly been successfully used to model gravity currents. There are several methods of solution available and the choice of method partly depends on whether a front condition is to be applied or avoided. The study into appropriate front conditions has been extensive and is still an active research topic. The ideal model would be two-layer with a free surface and not subject to hydrostatic constraints requiring a front condition. However, this is not realistic in a depth-averaged model, particularly when this is not the sole purpose of the study, rather the purpose is to get a good depth averaged prediction for the current height, front speed and location at a

†Where the magnitude of the topography is calculated from the ratio of the maximum height of the bed to the upstream ambient fluid depth.

time. Since the present investigation seeks to model the resultant effects of bed roughness through the resistance coefficient method, rather than modelling the bed topography as an explicit variable, the hydrostatic assumption should not be in significant danger of violation. However, the characterisation of the roughness coefficient is also subject to significant ongoing research and is not easily defined. In the present study, the method of characteristics was used to solve the 2-layer shallow water equations, after Rottman and Simpson (1983) with the front condition of Benjamin (1968). The bed roughness was characterised using a roughness coefficient with arbitrarily chosen values in order to test the method.

3.3 Smooth boundary theory

In order to understand and interpret any work including boundary roughness it is necessary to generate a smooth boundary control model. The Navier-Stokes equations accurately describe fluid flow. Hence, with some assumptions and the application of known theory, the shallow water equations for flow in two layers can be derived as a model with the attributes required for a specific problem. This section covers the necessary assumptions and theory and leads to the derivation of the equations relating to the smooth bed case.

3.3.1 Shallow water theory and assumptions

For the mathematical formulation, the model is simplified by considering a two-dimensional gravity current propagating along a rigid horizontal surface assuming no mixing occurs and that the flow is inviscid. Inviscid fluid theory completely neglects the effect of friction generated by the surface over which the front is advancing. In this way, the lobe and cleft instability, as mentioned in section 1.3.1, will be absent but the formation of billows will still occur. Thus neglecting more complicated three-dimensional mechanisms, but retaining the basic two-dimensional profile of the gravity current. Clearly, in modelling real fluids, frictional forces will always be present and have to be accounted for but useful approximations to various aspects of a gravity current, for example the front speed, may be determined from applying inviscid theory.

The assumption of no mixing, imposed on the fluids, implies that the interface between them can be analogised with a free surface. Thus the fluid particles on the interface must remain on the interface. Using Acheson (2003) the kinematic condition at a free

surface is derived to describe this phenomenon:

Let $F(x,y,t) = y - h(x,t)$ where y is the vertical height of a fluid element from the bottom boundary and $h(x,t)$ is the height of the free surface. Postulate that $F(x,y,t)$ remains constant for any particular element on the free surface. Thus, it follows that

$$\frac{DF}{Dt} = \frac{\partial F}{\partial t} + (\underline{u} \cdot \nabla)F = 0 \quad \text{on} \quad y = h(x,t) \tag{3.27}$$

Substituting $F(x,y,t)$ into equation (3.27) gives

$$\frac{\partial F}{\partial t} = -\frac{\partial h}{\partial t}, \quad u\frac{\partial F}{\partial x} = -u\frac{\partial h}{\partial x}, \quad v\frac{\partial F}{\partial y} = v \tag{3.28}$$

Hence equation (3.27) is equivalent to the condition

$$\frac{\partial h}{\partial t} + u\frac{\partial h}{\partial x} = v \quad \text{on} \quad y = h(x,t) \tag{3.29}$$

After the dense fluid is released from the lock box, the height of this denser fluid decreases substantially and the length the fluid covers horizontally increases with time. Thus, the characteristic horizontal length scale of the flow, L, is much larger in magnitude than the vertical scale, h, i.e. $h << L$, and the flow can be defined as 'shallow'.

Shallow water theory assumes that: The fluid is well mixed vertically with a hydrostatic pressure gradient; the density of the flow is constant and therefore the problem is considered incompressible; viscosity is negligible; and the depth of the fluid is very small in comparison to the characteristic length of the body of water (Acheson, 1990).

3.3.2 The governing equations

The equations necessary for the solution of this problem, with mixing between the dense and ambient fluids at the interface neglected, are derived from the Navier-Stokes equations for incompressible, laminar fluid flow. In a general three-dimensional tensor form these are given by:

$$\frac{\partial u_i}{\partial t} + u_i\frac{\partial u_i}{\partial x_j} = -\frac{1}{\rho}\frac{\partial p}{\partial x_i} + \nu\nabla^2 u_i + F_i \tag{3.30}$$

$$\frac{\partial u_i}{\partial x_i} = 0 \tag{3.31}$$

for $i,j = 1,2,3$.

For two-dimensional, inviscid flow, equations (3.30) and (3.31) reduce to the Euler equations:

$$\frac{\partial u_i}{\partial t} + u_i \frac{\partial u_i}{\partial x_j} = -\frac{1}{\rho}\frac{\partial p}{\partial x_i} + F_i \tag{3.32}$$

$$\frac{\partial u_i}{\partial x_i} = 0 \tag{3.33}$$

for $i, j = 1, 2$ and where $F_i = (0, -g)$ is the buoyancy force.

In component form, equations (3.32) and (3.33) can be re-written as:

$$\frac{\partial u}{\partial t} + u\frac{\partial u}{\partial x} - v\frac{\partial u}{\partial y} = -\frac{1}{\rho}\frac{\partial p}{\partial x} \tag{3.34}$$

$$\frac{\partial v}{\partial t} + u\frac{\partial v}{\partial x} - v\frac{\partial v}{\partial y} = -\frac{1}{\rho}\frac{\partial p}{\partial y} - g \tag{3.35}$$

$$\frac{\partial u}{\partial x} + \frac{\partial v}{\partial y} = 0 \tag{3.36}$$

Now, rearranging the continuity equation (3.36) and integrating with respect to y gives:

$$v = -y\frac{\partial u}{\partial x} + f(x, t) \tag{3.37}$$

Since there is no velocity in the vertical direction on the bottom horizontal boundary, the condition $v = 0$ at $y = 0$ can be imposed implying that $f(x, t) = 0$. Thus

$$v = -y\frac{\partial u}{\partial x} \tag{3.38}$$

At $y = h(x, t)$ the kinematic boundary condition applies. Hence, on equating (3.38) with (3.29) at $y = h(x, t)$ one obtains:

$$\frac{\partial h}{\partial t} + u\frac{\partial h}{\partial x} + h\frac{\partial u}{\partial x} = 0 \tag{3.39}$$

For conservation of mass, equation (3.39) must hold in both of the layers.

The interface between the two fluids can be analogised to a free surface varying gradually with small curvature so that, by the assumption of shallow water, compared with gravitational acceleration, g, the acceleration in the vertical direction can be ignored. This hypothesis is verified at the end of this section through a non-dimensional analysis of the equations.

By neglecting the acceleration in the vertical direction, equation (3.35) becomes

$$0 = -\frac{1}{\rho}\frac{\partial p}{\partial y} - g \tag{3.40}$$

Thus the vertical pressure distribution is rendered essentially hydrostatic. On integration with respect to y, this yields:

$$p = -\rho g y + f_*(x,t) \tag{3.41}$$

If the pressure is given by $p = p_0(x,t)$ on the interface of the two fluids at $y = h_1(x,t)$, then

$$p = \rho g(h_1 - y) + p_0 \tag{3.42}$$

an hydrostatic relation between the pressure in the layer and its thickness. Thus, in the upper layer, where $y > h_1$ and the density of the fluid is ρ_2, equation (3.42) becomes:

$$p = \rho_2 g(h_1 - y) + p_0 \tag{3.43}$$

and likewise for $y < h_1$ and density ρ_1, in the bottom layer,

$$p = \rho_1 g(h_1 - y) + p_0 \tag{3.44}$$

Equation (3.34) can now be written in the form:

$$\frac{Du}{Dt} = -\frac{1}{\rho}\frac{\partial p_0}{\partial x} - g\frac{\partial h_1}{\partial x} \tag{3.45}$$

From equation (3.45), it can be seen that the rate of change of u for any element in the fluid is independent of y. Thus, if u is initially independent of y then it will remain so, implying that u and h are dependent on x and t only.

Hence equation (3.34) can be written:

$$\frac{\partial u}{\partial t} + u\frac{\partial u}{\partial x} = -\frac{1}{\rho}\frac{\partial p_0}{\partial x} - g\frac{\partial h_1}{\partial x} \tag{3.46}$$

Thus the set of equations (3.34)-(3.36), for the two layers, becomes:

$$\frac{\partial u_1}{\partial t} + u_1\frac{\partial u_1}{\partial x} = -\frac{1}{\rho_1}\frac{\partial p_0}{\partial x} - g\frac{\partial h_1}{\partial x} \tag{3.47}$$

$$\frac{\partial u_2}{\partial t} + u_2\frac{\partial u_2}{\partial x} = -\frac{1}{\rho_2}\frac{\partial p_0}{\partial x} - g\frac{\partial h_1}{\partial x} \tag{3.48}$$

$$\frac{\partial h_1}{\partial t} + u_1 \frac{\partial h_1}{\partial x} + h_1 \frac{\partial u_1}{\partial x} = 0 \tag{3.49}$$

$$\frac{\partial h_2}{\partial t} + u_2 \frac{\partial h_2}{\partial x} + h_2 \frac{\partial u_2}{\partial x} = 0 \tag{3.50}$$

where the subscripts 1 and 2 indicate the bottom and top layers, respectively. Equations (3.47)-(3.50) are the 'Shallow Water' equations for one-dimensional flow in two layers.

For this problem, equations (3.47)-(3.50) are subject to the following initial conditions:

$$h_1(x,t) = \begin{cases} h_0 & (0 \leq x \leq x_0) \\ 0 & (x_0 < x) \end{cases} \qquad \text{at} \quad t = 0 \tag{3.51}$$

and the boundary conditions:

$$u_1(x = 0, t) = 0 \tag{3.52}$$

$$\left.\frac{\partial h_1}{\partial x}\right|_{x=0} = 0 \tag{3.53}$$

Verification of the neglect of vertical acceleration through a non-dimensional analysis

Let L be a characteristic length scale and h_0 a typical value for $h_1(x,t)$. Considering the second and fourth terms of equation (3.46), the non-dimensional value for u can be derived as $u \sim (gh_0)^{1/2}$. On comparison with the first term of the same equation, a typical time scale, $t \sim L/(gh_0)^{1/2}$, is obtained. Applying these known non-dimensional variables to the continuity equation (3.36), gives a non-dimensional value for v, namely $(gh_0)^{1/2}h_0/L$. For shallow water theory to be applicable, $h_0 << L$ and hence $v << u$, thus v is negligible in comparison to u. If the non-dimensionalised terms are then applied to equation (3.35), it can be seen that all terms on the right hand side of this equation, those of the vertical acceleration, are of order gh_0^2/L^2 and are therefore very small in comparison with the gravitational acceleration, g, on the left hand side. Hence, the vertical acceleration of the elements in the fluid is neglected.

3.3.3 Simplification of the governing equations using the Boussinesq approximation

Let H be the total height of the ambient fluid where

$$H = h_1(x,t) + h_2(x,t) \tag{3.54}$$

and H is constant due to the assumption of a fixed lid, see section 3.2.1. Equating equations (3.49) and (3.50) and using the commutative nature of derivatives, we obtain:

$$\frac{\partial H}{\partial t} + \frac{\partial}{\partial x}(u_1 h_1 + u_2 h_2) = 0 \tag{3.55}$$

Since H is constant, integrating with respect to x and imposing the condition that both velocities vanish at $x = 0$, implies the condition:

$$u_1 h_1 + u_2 h_2 = 0 \tag{3.56}$$

The pressure at the interface, $p_0(x,t)$, is eliminated by multiplying equations (3.47) and (3.48) by ρ_1 and ρ_2, respectively, and subtracting the equation resulting from the first multiplication from that resulting from the second to obtain:

$$\rho_1 \frac{\partial u_1}{\partial t} - \rho_2 \frac{\partial u_2}{\partial t} + \rho_1 u_1 \frac{\partial u_1}{\partial x} - \rho_2 u_2 \frac{\partial u_2}{\partial x} = g(\rho_2 - \rho_1)\frac{\partial h_1}{\partial x} \tag{3.57}$$

Equations (3.54) and (3.56) can be rearranged to yield h_2 and u_2 in terms of H, h_1 and u_1. Thus equation (3.57) becomes:

$$(1+ra)\frac{\partial u_1}{\partial t} + \left[1 - ra\left(\frac{H+h_1}{H-h_1}\right)\right] u_1 \frac{\partial u_1}{\partial x} - \left[g' - (1+a)^3 \frac{r u_1^2}{H}\right] \frac{\partial h_1}{\partial x} = 0 \tag{3.58}$$

with the introduction of non-dimensional parameters $a = h_1/(H - h_1)$ and $r = \rho_2/\rho_1$, where $g' = (|\rho_1 - \rho_2|)/\rho_1$ is the reduced gravity.

Assuming that the relative density variations are not too large, i.e. $\Delta\rho/\rho << 1$, the Boussinesq approximation can be invoked, which in simple terms means that density variations are retained in the gravitational forces but neglected in the advection terms. For this reason, r is set as 1 except where it multiplies g. On division by $(1+a)$, equation (3.58) can be written:

$$\frac{\partial u_1}{\partial t} + (1-2a)u_1 \frac{\partial u_1}{\partial x} + g' \left\{1 - \left[\frac{h_1}{H} + \left(1 - \frac{h_1}{H}\right)^{-2} \frac{u_1^2}{g'H}\right]\right\} \frac{\partial h_1}{\partial x} = 0 \tag{3.59}$$

Thus two simultaneous equations for the dependent variables h_1 and u_1 have been derived:

$$\frac{\partial u_1}{\partial t} + (1-2a)u_1 \frac{\partial u_1}{\partial x} + g'(1-b)\frac{\partial h_1}{\partial x} = 0 \tag{3.60}$$

$$\frac{\partial h_1}{\partial t} + u_1 \frac{\partial h_1}{\partial x} + h_1 \frac{\partial u_1}{\partial x} = 0 \tag{3.61}$$

where

$$b = \frac{h_1}{H} + \frac{u_1^2}{g'H}\left(1 - \frac{h_1}{H}\right)^{-2} \tag{3.62}$$

The equations must be solved subject to the initial and boundary conditions (3.51) - (3.53) given at the end of section 3.3.2.

3.3.4 The front condition: smooth boundary

The height and velocity at the front of the gravity current cannot be determined by the governing equations. At the front, the vertical acceleration and viscous dissipation will be important since it is here that the heavier fluid is forcing its way into the lighter fluid. Thus the shallow water equations, as derived in section 3.3.2 using the hydrostatic assumption and neglecting vertical acceleration and viscous effects, are invalid.

To overcome this problem, an independently derived front condition is imposed. Various front conditions have been derived and implemented, as discussed in section 3.2.2. Some are constructed theoretically while others rely on empirical values. In the present work, the front condition is derived through the theory of flow force balance as used by Benjamin (1968), thus continuing the methodology of Rottman and Simpson (1983). Benjamin (1968) noticed that after the initial slump, the flow propagates along the horizontal boundary in a similar way to an air-filled cavity advancing into a liquid. Without loss of generality through this analogy, the flow force balance can be determined:

Consider figure 3.1. If the cavity is considered stationary to the oncoming liquid, at 0 a stagnation point occurs where the flow encounters it. Upstream, where the liquid fills the height of the channel and is unaware of the displacement, it has depth H and the velocity is constant u_1. Far downstream, under the free surface created by the cavity, the flow is also constant with height h_2 and velocity u_1'. If the density of the liquid is ρ and that of the cavity is negligible, ignoring viscosity and surface tension as for shallow water theory and assuming conservation of energy, Bernoulli's equation for a steady flow can be applied:

$$p + \frac{1}{2}\rho \underline{u}^2 + \rho g y = \text{constant on a streamline} \tag{3.63}$$

where p is the pressure and $\underline{u}$ is the fluid velocity. Applying the theorem along the upper boundary, with the velocity and pressure zero at 0, the pressure far upstream can

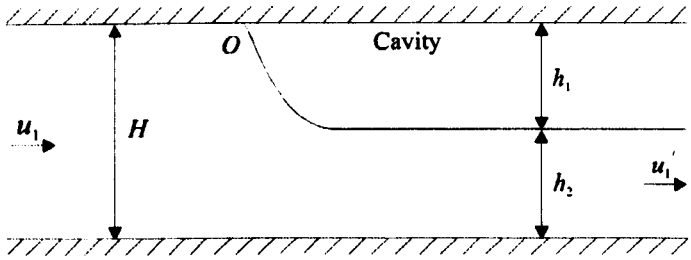

Figure 3.1: Model proposed by Benjamin (1968) for steady flow past a cavity analogised to the gravity current phenomenon. O is the stagnation point.

be determined as $p_0 = -\frac{1}{2}\rho \underline{u}^2$. The pressure in the liquid below this boundary has a hydrostatic variation with depth and so the total pressure can be written

$$p = p_0 + \frac{1}{2}\rho g H \tag{3.64}$$

Hence, the total pressure force across the channel far upstream can be written

$$p_f = p_0 H + \frac{1}{2}\rho g H^2 = \frac{1}{2}\rho(-u_1^2 H + g H^2) \tag{3.65}$$

The total flow force is given by the momentum flux plus the pressure force. Thus, the flow force in the upstream region is given by equation (3.65) + $\rho u_1^2 H$, i.e.

$$F_1 = \frac{1}{2}\rho(u_1^2 H + g H^2) \tag{3.66}$$

The same theory must also hold far downstream but with zero pressure on the upper surface. Thus the flow force in this region is given by

$$F_2 = \rho\left(u_1'^2 h_2 + \frac{1}{2} g h_2^2\right) \tag{3.67}$$

Now, these two forces must equate since the flow force does not vary in a steady flow when there are no external horizontal forces present. Thus, setting equation (3.66) equal to equation (3.67), we obtain

$$\frac{1}{2}u_1^2 H - u_1'^2 h_2 = \frac{1}{2} g h_2^2 - \frac{1}{2} g H^2 \tag{3.68}$$

By conservation of mass: $u_1 H = u_1' h_2$. Therefore, from equation (3.68), it follows that

$$u_1^2 = g h_2 \frac{h_2^2 - H^2}{H(h_2 - 2H)} \tag{3.69}$$

This can easily be written in terms of the height of the cavity, using $h_2 = H - h_1$, namely

$$u_1 = \sqrt{\frac{2 - h_1/H}{1 - h_1/H}(1 - h_1/H)gh_1} \tag{3.70}$$

This result is generated for a smooth free surface due to the nature of the cavity being filled with air. In the actual problem, for two liquids, the free surface is broken up at the front and turbulence is generated and hence viscous dissipation occurs as mentioned above. To account for this event, u_1 is modified by a factor k', say, where $k'^2 = \frac{\beta^2}{2}$ and β is an empirical constant.

Applying this modification to equation (3.70), at the front of the gravity current in this investigation, gives the front condition

$$u_f = \left[\frac{\beta^2}{2}\frac{2 - h_f/H}{1 + h_f/H}(1 - h_f/H)g'h_f\right]^{\frac{1}{2}} \tag{3.71}$$

where $h_f(t)$ is the front depth, $u_f(t)$ is the front speed and the reduced gravity term g' is introduced due to the density difference between the two liquids. Note that when $\beta^2 = 2$, the result for a cavity flow is obtained.

3.4 Rough boundary theory

In deriving the shallow water equations for smooth boundaries, assumptions were made that neglected any effect that the frictional forces might have on the problem. It is now necessary to reintroduce the appropriate factors for the model incorporating the surface roughness. The frictional resistance manifests itself in the form of shear along the walls of the channel and, as required in this study, the bottom. This section discusses the inclusion of a bed roughness by implementing a Chezy type equation.

3.4.1 Chezy type equations

Chezy's equation for the average velocity of a uniform flow can be written as

$$u = C_H\sqrt{H_{rad}S_0} \tag{3.72}$$

where H_{rad} is the hydraulic radius, S_0 is the channel longitudinal slope, to be taken as the frictional slope S_f. C_H is the resistance coefficient given by the Chezy constant, $C_H = \sqrt{\frac{8g}{f}}$. where f is a friction factor to be specified, with reference to pipe flow theory, depending on the roughness of the bed (French, 1994).

3.4.2 Chezy's equation applied to the shallow water equations

The inclusion of terms for the shear in shallow water theory results in the equation of general form

$$\frac{\partial u}{\partial t} + u\frac{\partial u}{\partial x} = -\frac{1}{\rho}\frac{\partial p_0}{\partial x} - g\frac{\partial h}{\partial x} - gS_f \tag{3.73}$$

where S_f is the frictional slope. Application of the Chezy equation (3.72) with $S_0 = S_f$ implies that the frictional slope can be written as

$$S_f = \overline{\kappa}\frac{u^2}{H_{rad}} \tag{3.74}$$

where

$$\overline{\kappa} = \frac{1}{C_H^2} = \frac{f}{8g} \tag{3.75}$$

The error in assuming that the hydraulic radius H_{rad} can be taken as the depth h is small (Liggett, 1975) therefore we obtain the following expression

$$S_f = \overline{\kappa}\frac{u^2}{h} \tag{3.76}$$

Substituting equation (3.76) into equation (3.73), the general form for the conservation of momentum in a hydrostatic pressure field becomes

$$\frac{\partial u}{\partial t} + u\frac{\partial u}{\partial x} = -\frac{1}{\rho}\frac{\partial p_0}{\partial x} - g\frac{\partial h}{\partial x} - g\overline{\kappa}\frac{u^2}{h} \tag{3.77}$$

In order to extend this theory to two layers, the physics of the situation must be considered. Clearly, the gravity current of the denser fluid will be affected by the introduction of bed roughness, thus the shear term must figure in the equation for this layer. However, as the less dense fluid over-rides the denser current, it will also be affected. Since the interface is the region where the effects will be transmitted from the one fluid to the other, similar shear terms, in each of the fluids, are included to account for this. However, when the fluids are travelling at the same speed, the shear interaction at the interface must vanish so that the terms applied here must be modified to be of the form

$$\rho_1 g\overline{\kappa}\frac{1}{(u_1 - u_2)^2}h \tag{3.78}$$

where ρ_1 is the density of the denser fluid and u_1 and u_2 are the speeds of the different fluids. Applied to each layer at the interface, the terms must be equal and opposite. On the bottom boundary, if the fluid is moving in the positive direction, then the shear will

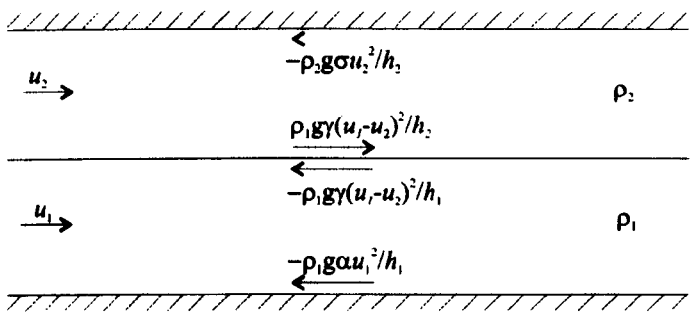

Figure 3.2: Sketch of the resistant forces of Chezy type acting on two liquids of different densities where $\rho_1 > \rho_2$ and $u_1 > u_2$.

be in the negative direction, counteracting the motion near the wall. If the denser fluid is travelling faster than the less dense fluid above it then, in the reference frame of the less dense fluid, i.e. bringing the less dense fluid motion to rest, the flow will still be moving in the positive direction. Thus, the shear on the more dense fluid side of the interface will operate in the negative direction. Therefore, the shear in the less dense fluid side of the interface will be equal but in the opposite direction, i.e. positive. A sketch to this effect is shown in figure 3.2, where and α, γ and σ are the values of $\overline{\kappa}$ for the bottom boundary, the fluid interface and the top boundary, respectively.

Note that if the velocity of the less dense fluid is faster than that of the more dense fluid, i.e. if $u_2 > u_1$, then the shear terms at the interface will be in the opposite directions to those shown, in each layer. If the channel is open there will be no effects felt on the free surface of the less dense fluid. However, if the channel is enclosed, as for example, flow in a rectangular pipe, then the roughness can also be applied at the top boundary with effect on the less dense fluid. Also, if u_2 is flowing towards the left i.e. in the negative direction, as we are modelling in the present problem, then the rough term on the top boundary must be in the opposing direction to the flow and so will be positive. The terms for the top boundary will be included here but can be neglected if required.

Incorporating these terms into equations (3.47) and (3.48), the equations governing the fluids in the two layers can be written

$$\rho_1\frac{\partial u_1}{\partial t}+\rho_1 u_1\frac{\partial u_1}{\partial x}=-\frac{\partial p_0}{\partial x}-\rho_1 g\frac{\partial h_1}{\partial x}-C_1\alpha\rho_1 g\frac{u_1^2}{h_1}-C_2\gamma\rho_1 g\frac{(u_1-u_2)^2}{h_1} \tag{3.79}$$

$$\rho_2\frac{\partial u_2}{\partial t}+\rho_2 u_2\frac{\partial u_2}{\partial x}=-\frac{\partial p_0}{\partial x}-\rho_2 g\frac{\partial h_1}{\partial x}+C_3\sigma\rho_2 g\frac{u_2^2}{h_2}+C_2\gamma\rho_1 g\frac{(u_1-u_2)^2}{h_2} \tag{3.80}$$

$$\frac{\partial h_1}{\partial t}+u_1\frac{\partial h_1}{\partial x}+h_1\frac{\partial u_1}{\partial x}=0 \tag{3.81}$$

$$\frac{\partial h_2}{\partial t} + u_2\frac{\partial h_2}{\partial x} + h_2\frac{\partial u_2}{\partial x} = 0 \tag{3.82}$$

where the constants C_1, C_2 and C_3 take values of either unity or zero. When C_1, C_2 and C_3 are zero, these equations revert to the smooth boundary form, and when they are all unity roughness will be applied at the bed, the interface between the dense and ambient fluid and the top wall, as shown in figure 3.2. In the solution of equations (3.79)-(3.82), the majority of the terms will simplify in the same way as for the smooth boundary theory. Beginning with the subtraction of equation (3.80) from equation (3.79), to obtain

$$\rho_1\frac{\partial u_1}{\partial t} - \rho_2\frac{\partial u_2}{\partial t} + \rho_1 u_1\frac{\partial u_1}{\partial x} - \rho_2 u_2\frac{\partial u_2}{\partial x} \tag{3.83}$$

$$= g(\rho_2 - \rho_1)\frac{\partial h_1}{\partial x} - C_1\alpha\rho_1 g\frac{u_1^2}{h_1} - C_2\gamma\rho_1 g(u_1 - u_2)^2\left[\frac{1}{h_1} + \frac{1}{h_2}\right] - C_3\sigma\rho_2 g\frac{u_2^2}{h_2}$$

Using the Chezy form for the roughness coefficients, equation (3.75), we have,

$$\alpha = \frac{f_1}{8g}, \quad \gamma = \frac{f_2}{8g} \quad \text{and} \quad \sigma = \frac{f_3}{8g} \tag{3.84}$$

where, f_1, f_2 and f_3 are friction factors specified using generally excepted values from pipe flow analysis. Applying the same transforms for h_2 and u_2 as used in the smooth bed theory:

$$h_2 = H - h_1, \qquad u_2 = -\frac{u_1 h_1}{H - h_1} \tag{3.85}$$

we obtain

$$(1 + ra)\frac{\partial u_1}{\partial t} + \left[1 - ra\left(\frac{H + h_1}{H - h_1}\right)\right]u_1\frac{\partial u_1}{\partial x} - \left[g' - (1 + a)^3\frac{ru_1^2}{H}\right]\frac{\partial h_1}{\partial x} \tag{3.86}$$

$$= -\frac{u_1^2}{8h_1}\left[C_3 f_3 r a^3 + C_1 f_1 + C_2 f_2(1 + a)^3\right]$$

where $r = \rho_2/\rho_1$ and $a = h_1/(H - h_1)$. Applying the Boussinesq approximation (i.e. $r = 1$ where it does not directly multiply g), and dividing by $(1 + a)$ gives the following result

$$\frac{\partial u_1}{\partial t} + (1 - 2a)u_1\frac{\partial u_1}{\partial x} + g'\left\{1 - \left[\frac{h_1}{H} + \left(1 - \frac{h_1}{H}\right)^{-2}\frac{u_1^2}{g'H}\right]\right\}\frac{\partial h_1}{\partial x} \tag{3.87}$$

$$= -\frac{u_1^2}{8Ha}\left[C_3 f_3 a^3 + C_1 f_1 + C_2 f_2(1 + a)^3\right]$$

Hence, the two equations for the calculation of h_1 and u_1 for flow over a rough surface are as follows

$$\frac{\partial u_1}{\partial t} + (1-2a)u_1\frac{\partial u_1}{\partial x} + g'(1-b)\frac{\partial h_1}{\partial x} = -\frac{u_1^2}{8Ha}\left[C_3 f_3 a^3 + C_1 f_1 + C_2 f_2 (1+a)^3\right] \quad (3.88)$$

$$\frac{\partial h_1}{\partial t} + u_1\frac{\partial h_1}{\partial x} + h_1\frac{\partial u_1}{\partial x} = 0 \quad (3.89)$$

where

$$b = \frac{h_1}{H} + \frac{u_1^2}{g'H}\left(1 - \frac{h_1}{H}\right)^{-2} \quad (3.90)$$

Equations (3.88) and (3.89) must be solved subject to the same initial and boundary conditions (3.51) - (3.53) as for the smooth boundary theory given in section 3.3.2.

3.4.3 The front Condition: rough boundary

Since similar theory and assumptions have been applied in the rough boundary case as for the smooth boundary, a front condition will also be required in this case. An identical condition will not necessarily apply since the β term does not take into account the effect of any rough elements on the front. However, it is dependent on h_f which is calculated from values within the main body of the flow which will be subject to the effects of the rough terms and thus in the present study, the problem will be solved implementing the 'smooth' front condition, expression (3.71).

Shin *et al.* (2004) derived a front condition using a similar method to Benjamin (1968) but taking into account a control volume including both sides of the current interface, the theoretical solution $h = h_0/2$ and the Boussinesq assumption. This condition is given by

$$u_f = \left[\left(1 - \frac{h_f}{H}\right) g' h_f\right]^{\frac{1}{2}} \quad (3.91)$$

Unlike condition (3.71), it contains no free parameters and is found explicitly using values calculated during the solution procedure. Thus the effects of the rough terms on the front should be transmitted through these values without the need for specification of β. It is possible that the theory of Shin *et al.* (2004) could be used to derive a rough front condition with no free parameters and this remains for future study.

3.5 Method of characteristics: smooth case

The flow in this problem is transient so the motion will move in phases dependent on the balance of the forces in the flow at that time, as discussed in section 1.3.1. In each phase different flow phenomena occur in different regions of the fluid. The method of characteristics essentially supposes that the domain under investigation can be filled with curves that describe the natural flow phenomena for these regions so that the dependent variables, often the fluid velocity or concentration, can be determined throughout. The following theory is derived with reference to Ames (1965).

General form for two simultaneous partial differential equations

Consider the velocity components u and v of the flow, given by the solutions of the two simultaneous first-order equations of the form

$$P\frac{\partial u}{\partial x} + Q\frac{\partial u}{\partial y} + R\frac{\partial v}{\partial x} + S\frac{\partial v}{\partial y} = T \tag{3.92}$$

$$P'\frac{\partial u}{\partial x} + Q'\frac{\partial u}{\partial y} + R'\frac{\partial v}{\partial x} + S'\frac{\partial v}{\partial y} = T' \tag{3.93}$$

Given sufficient initial and boundary conditions, it is supposed that the solution is known in some region bounded by a curve Γ along which the values of u and v are known. In order to to continue the solution throughout the rest of the domain adjacent to this curve, we look for partial derivatives of u and v.

Since it is assumed that u and v are known on Γ, along Γ one can state:

$$\delta u = \frac{\partial u}{\partial x}\delta x + \frac{\partial u}{\partial y}\delta y \tag{3.94}$$

$$\delta v = \frac{\partial v}{\partial x}\delta x + \frac{\partial v}{\partial y}\delta y \tag{3.95}$$

Thus a system of four equations relating to the unknowns $\frac{\partial u}{\partial x}$, $\frac{\partial u}{\partial y}$, $\frac{\partial v}{\partial x}$ and $\frac{\partial v}{\partial y}$ has been obtained and in matrix form, can be written:

$$\begin{pmatrix} dx & dy & 0 & 0 \\ 0 & 0 & dx & dy \\ P & Q & R & S \\ P' & Q' & R' & S' \end{pmatrix} \begin{pmatrix} \frac{\partial u}{\partial x} \\ \frac{\partial u}{\partial y} \\ \frac{\partial v}{\partial x} \\ \frac{\partial v}{\partial y} \end{pmatrix} = \begin{pmatrix} du \\ dv \\ T \\ T' \end{pmatrix} \tag{3.96}$$

which is of the form

$$\overline{A}x = c \tag{3.97}$$

This system of equations can be solved for a unique solution, giving an identical directional derivative above and below the curve Γ, unless the determinant of the matrix $\overline{A}$ of coefficients of the partial derivatives is zero, for which there will be no unique solution. Setting the determinant of the matrix to zero, it can be written in the form:

$$[Q'S - QS']dx^2 + [QR' - Q'R + PS' - P'S]dxdy + [P'R - PR']dy^2 = 0 \tag{3.98}$$

which is a quadratic equation that can be solved for $\frac{dy}{dx}$:

$$A\left(\frac{dy}{dx}\right)^2 + B\frac{dy}{dx} + C = 0 \tag{3.99}$$

where $A = [P'R - PR']$, $B = [QR' - Q'R + PS' - P'S]$ and $C = [Q'S - QS']$.

If $B^2 > 4AC$, the discriminant is positive and the equations are said to be hyperbolic. The solutions will be real and distinct giving the slopes for two real curves from which the curves themselves can be drawn for each point and across which the partial derivatives are not determined. These curves, ξ and η, say, are characteristic lines, or characteristics, for u and v. If the discriminant is negative there are no real solutions so no real characteristic directions and equations (3.92) and (3.93) are said to be elliptic. If it is zero then there are two identical solutions and the equations are classified as parabolic.

The variation of u and v along the characteristics can also be determined. In (3.96), column vector c can be substituted into any column of the determinant matrix as stated by the elementary theorem implemented in the method by Ames (1965) thus giving an equation along each characteristic ξ and η relating the functions u and v:

$$E_{\eta,\xi}du + F_{\eta,\xi}dv + G_{\eta,\xi}dy = 0 \tag{3.100}$$

Equation (3.100) and the solutions of (3.99) can be solved using a numerical method for integrating ordinary differential equations, such as the Runge-Kutta or Adams methods as suggested by Ames (1965). In the special case where T and T' are zero, $G_{\eta,\xi} = 0$ in equation (3.100).

Application to the present smooth case

The two simultaneous equations (3.60) and (3.61) obtained in this problem can be written in the form of equations (3.92) and (3.93) as follows:

$$\frac{\partial h_1}{\partial t} + u_1 \frac{\partial h_1}{\partial x} + 0\frac{\partial u_1}{\partial t} + h_1 \frac{\partial u_1}{\partial x} = 0 \tag{3.101}$$

$$0\frac{\partial h_1}{\partial t} + g'(1-b)\frac{\partial h_1}{\partial x} + R'\frac{\partial u_1}{\partial t} + u_1(1-2a)\frac{\partial u_1}{\partial x} = 0 \tag{3.102}$$

i.e.

$$\begin{aligned} P &= 1 & P' &= 0 \\ Q &= u_1 & Q' &= g'(1-b) \\ R &= 0 & R' &= 1 \\ S &= h_1 & S' &= (1-2a)u_1 \\ T &= 0 & T' &= 0 \end{aligned} \tag{3.103}$$

and x and y are analogous to t and x, respectively.

Along the curve Γ:

$$\delta h_1 = \frac{\partial h_1}{\partial t}\delta t + \frac{\partial h_1}{\partial x}\delta x \tag{3.104}$$

$$\delta u_1 = \frac{\partial u_1}{\partial t}\delta t + \frac{\partial u_1}{\partial x}\delta x \tag{3.105}$$

Thus, for this problem, the system of equations is given, in matrix form $\overline{A}x = c$, as:

$$\begin{pmatrix} dt & dx & 0 & 0 \\ 0 & 0 & dt & dx \\ 1 & u_1 & 0 & h_1 \\ 0 & g'(1-b) & 1 & u_1(1-2a) \end{pmatrix} \begin{pmatrix} \frac{\partial h_1}{\partial t} \\ \frac{\partial h_1}{\partial x} \\ \frac{\partial u_1}{\partial t} \\ \frac{\partial u_1}{\partial x} \end{pmatrix} = \begin{pmatrix} dh_1 \\ du_1 \\ 0 \\ 0 \end{pmatrix} \tag{3.106}$$

If the determinant of the matrix of coefficients is zero, i.e.

$$\begin{vmatrix} dt & dx & 0 & 0 \\ 0 & 0 & dt & dx \\ 1 & u_1 & 0 & h_1 \\ 0 & g'(1-b) & 1 & u_1(1-2a) \end{vmatrix} = 0 \tag{3.107}$$

the quadratic equation (3.99) is obtained for dx/dt:

$$A\left(\frac{dx}{dt}\right)^2 + B\frac{dx}{dt} + C = 0 \tag{3.108}$$

where, on substituting in the coefficients (3.103), $A = -1$, $B = 2(1-a)u_1$ and $C = g'h_1(1-b) - (1-2a)u_1^2$. The discriminant of this equation dictates the type of equation and the type of roots it has:

$$\begin{aligned} B^2 - 4AC &= 4(1-a)^2u_1^2 - 4(-1)[g'h_1(1-b) - (1-2a)u_1^2] \\ &= 4u_1^2 - 8au_1^2 + 4a^2u_1^2 - 4u_1^2 + 8au_1^2 + 4g'h_1(1-b) \\ &= 4[a^2u_1^2 + g'h_1(1-b)] \end{aligned} \tag{3.109}$$

where

$$b = \frac{h_1}{H} + \frac{u_1^2}{g'H}\left(1 - \frac{h_1}{H}\right)^{-2}, \qquad 0 < \frac{h_1}{H} < 1 \tag{3.110}$$

We note the following:

$$\text{as } \frac{h_1}{H} \to 0,\ b \to \frac{u_1^2}{g'H},\ \text{thus } B^2 - 4AC \to 4(a^2u_1^2 + g'h_1) > 0 \tag{3.111}$$

$$\text{as } \frac{h_1}{H} \to 1,\ b \to 1,\ \text{thus } B^2 - 4AC \to 4a^2u_1^2 > 0 \tag{3.112}$$

Therefore, expression (3.108) has two distinct roots and the equations (3.92) and (3.93) are hyperbolic. The solutions of (3.108) are given by:

$$\frac{dx}{dt} = (1-a)u_1 \mp [a^2u_1^2 + g'h_1(1-b)]^{\frac{1}{2}}$$

Thus the directions of the η and ξ characteristics are given by:

$$\left.\frac{\partial x}{\partial t}\right|_\eta = \lambda_+, \qquad \left.\frac{\partial x}{\partial t}\right|_\xi = \lambda_- \tag{3.113}$$

where

$$\lambda_\mp = (1-a)u_1 \mp [a^2u_1^2 + g'h_1(1-b)]^{\frac{1}{2}} \tag{3.114}$$

Substituting the column vector c into the determinant of the coefficient matrix $\overline{A}$, and equating to zero, gives:

$$\begin{vmatrix} dt & dh_1 & 0 & 0 \\ 0 & du_1 & dt & dx \\ 1 & 0 & 0 & h_1 \\ 0 & 0 & 1 & u_1(1-2a) \end{vmatrix} = 0 \tag{3.115}$$

i.e.

$$(-h_1)du_1 + \left[(1-2a)u_1 - \left.\frac{dx}{dt}\right|_{\eta,\xi}\right] dh_1 = 0 \tag{3.116}$$

Notice that since $T = T' = 0$, this is analogous to the special case of equation (3.100). Rearranging equation (3.116) and using equation (3.113) yields the first-order ordinary differential equation for the variation of u_1 and h_1 along each of the characteristics:

$$(-h_1)\frac{du_1}{dh_1} + (1-2a)u_1 - \lambda_{\mp} = 0 \tag{3.117}$$

Thus the problem has been simplified to solving the ordinary differential equation (3.117) for u_1 and h_1 using the expression (3.114) and the initial and boundary conditions (3.51)-(3.53).

3.5.1 Generation of initial flow regions in the domain

At time $t = 0$ a singularity occurs because the speed of the gravity current is defined by the initial conditions with $u_1 = 0$ and height $h_1 = h_0$, but the front condition must also be initialised at $t = 0$ and cannot agree with the condition $u_1 = 0$ at that time. Therefore, although it is possible to generate the characteristics for the region where the variables are known, nothing is given for calculating the characteristics in the rest of this part of the domain except for the front condition. The front speed itself is given simply by the rate at which the distance travelled by the current in the x-direction changes with time, $u_f = \frac{dx}{dt}$. However, the value of u_f is unknown without prior knowledge of the height, h_f, of the front.

The value of u_1 is known to be zero on $x = 0$ and the derivative boundary condition (3.52) implies that h_1 be a constant there, take $h_1 = h_0$. Thus, the gradient of the characteristic curve at this location can be determined from equation (3.114) and a characteristic line can be drawn. For clarity, the values of x and t are normalised, x, by using length scale x_0, the initial length of the denser fluid behind the lock, and t using the time scale $t_0 = x_0/\sqrt{g'h_0}$. Solving the equations for the negative value of λ_- generates a straight

line which, for the case when $h_0/H \rightarrow 0$, has the normalised endpoints (1,0) and (0,1). In general, this line will always have endpoints (1,0) and $(0,t_{int})$, where time t_{int} indicates the time, normalised by t_0, where this line intersects the t-axis or, physically, when the first backward propagating wave hits the end wall. Beneath this line will be a region of constant state with characteristics parallel to this bounding one. This occurs because the values of u_1 and h_1 are known initially and on the boundary, and are the same at every point on the boundary within the region of constant state. Thus the gradients are known and identical for each point along the boundary in this region. The positive, η, lines will also have identical gradient but in the opposite direction. Thus, when the positive and negative characteristics intercept each another, the value of u_1 and h_1 will not change and hence the gradient will not change. In this way the boundary values are propagated throughout the region and so the characteristic curves are a mesh of straight lines, of constant, identical values of u_1 and h_1, parallel and perpendicular to that initial line.

The region of constant state does not continue beyond the boundary characteristic since the front condition takes effect and this disagrees with the condition $u_1 = 0$ as applied thus far. Hence, this line is the last known characteristic and its values of u_1 and h_1 can be used as the starting point for the integration to obtain the characteristics for the other regions between the end wall and the front.

The ordinary differential equation (3.117) is solved for the positive characteristic since it is the values of u_1 and h_1 along the η curves that are required. In the region of constant state, the positive characteristics are a set of parallel lines along which u_1 and h_1 are constant and identical to each other. When these lines leave this region, the values of u_1 and h_1 change and are therefore unknown. Integrating equation (3.117) along η between the last known values and those given by the front condition, the value of u_1 at the front and hence the range of integration are determined. The required values of u_1 and h_1 in the region between the front and the characteristics of constant state can thus be found using these results. Moreover, these curves will remain parallel since the range of integration along one of them is identical to the next.

When the η and ξ characteristics intercept, they must both have the same values for u_1 and h_1. However, since the η curves are parallel, every point of interception along one ξ characteristic will have the same values for u_1 and h_1. Thus, the ξ characteristics will be a set of straight lines, each with different gradients. Hence, solving the ODE (3.117) for the positive characteristic curves (λ_+) enables the negative gradients for the

ξ characteristics to be calculated and this set of lines can then be drawn. The final value for u_1 is also the velocity at the front, u_f, thus its value can be used with $u_f = \frac{dx}{dt}$ to find the location of the front.

The Fortran NAG routine D02AGF is used to integrate the ordinary differential equation (3.117) using the known values and an initial guess for the front height.

Implementation of the Fortran NAG routine D02AGF

The ODE requiring solution by D02AGF is given in section 3.5 by equation (3.117), namely

$$h_1 \frac{du_1}{dh_1} + (1-2a)u_1 - \lambda_{\mp} = 0 \tag{3.118}$$

From the conditions established in sections 3.3.2 and 3.3.3, it is known that

$$u_f = 0 \text{ at } h_1 = h_0 \tag{3.119}$$

and the front condition, for a given h_f, is given by

$$u_f = \left[\frac{\beta^2}{2}\frac{2-h_f/H}{1+h_f/H}(1-h_f/H)g'h_f\right]^{\frac{1}{2}} \tag{3.120}$$

The factor that is unknown is for which range of h_f, the front condition giving u_f holds. Hence for this problem, $n = 1$, $n_1 = 1$ and there is just one parameter q_1, the upper value of the range of integration. The parameter is thus included in the range and boundary condition subroutines as the upper endpoint and matching point in the former and within the calculation of the upper endpoint of the range evaluating y_i (the front condition) in the latter. Thus, in the terminology of the NAG routine, with h_f analogous to x and u_f to y, the ODE is given by:

$$\frac{dx}{dy} = \frac{1}{x}[\lambda_{\mp} - (1-2a)y] \tag{3.121}$$

where

$$a = \frac{x}{(H-x)}, \qquad \lambda_{\mp} = (1-a)y \mp [a^2y^2 + g'x(1-b)]^{\frac{1}{2}} \tag{3.122}$$

and

$$b = \frac{x}{H} + \frac{y^2}{g'H}\left(1-\frac{x}{H}\right)^{-2} \tag{3.123}$$

The conditions are in terms of the parameter q_1:

$$x = x_0, \qquad y = 0 \tag{3.124}$$

$$x = q_1, \qquad y = \left[\frac{\beta^2}{2}\frac{2 - q_1/H}{1 + q_1/H}(1 - q_1/H)g'q_1\right]^{\frac{1}{2}} \tag{3.125}$$

An estimate for q_1 is entered into the program, along with two error values. These control the bound on the local error in the components of the solution during the integration, the convergence testing of the components of the solution at the matching point in the Newton iteration and the convergence testing on the parameter in the Newton iteration. They also control the perturbation of the parameter when approximating the derivatives of the components of the solution with respect to that parameter to be used in the Newton iteration. If the guess is good then results will be generated for the front speed and the residuals, as printed by the program, can be considered for accuracy. Thus the initial estimate and the error values can be altered until an acceptably small residual is determined. In this work, the results with residuals of magnitude smaller than 10^{-6} were used.

The program can be modified to print results for h_f and u_f for as many values as required in the range from x_0 to q_1 so that these values can be used to calculate the slope of the gradients for the characteristic lines of the flow and thus enable the plotting of the characteristics. These can then be compared with those obtained by Rottman and Simpson (1983) and the accuracy of the theoretical results established.

The flow profile as generated by NAG results

The characteristics drawn from results generated by the Fortran NAG routine D02AGF show a simple wave region, generated from the negative gradient, adjacent to the initial region of constant state. Physically, this implies that this constant state, region R_1 in figure 3.3, is a region where the fluid has not yet been affected by the disturbance created by the removal of the lock partition. Subsequently this disturbance initiates the propagation of the current forwards and an expansion wave back towards the end wall of the tank, hence the occurrence of the simple wave region, region R_2 in figure 3.3. The existence of this region is in accordance with the theorem that states: "In a solution containing constant state regions the regions adjacent to constant states are always simple waves." As proven, for example, by Jeffrey and Tanuiti (1964). Another

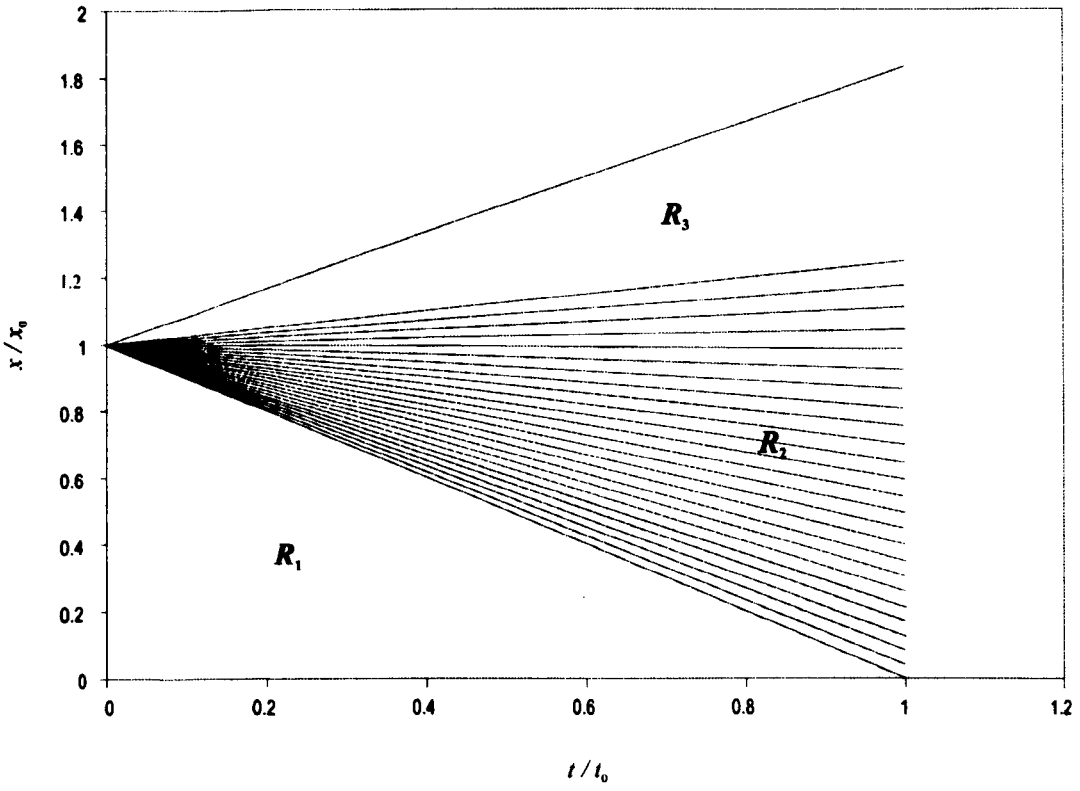

Figure 3.3: Characteristic diagram for the case when $h_0/H = 0$ and $\beta = 1$ showing the simple wave region. Beyond $t/t_0 = 1$, the results are invalid. Regions R_1, R_2, and R_3 correspond to an initial region of constant state, a simple wave region and a further region of constant state, respectively. t_0 is a time scale given by $x_0/\sqrt{g'h_0}$.

region of constant state, established in a similar way to the other, occurs immediately behind the current front. The ξ characteristics are parallel to the final characteristic, determined using the front condition, and the η curves become a set of parallel lines perpendicular to the ξ lines. This region, R_3 in figure 3.3, encompasses the region of constant flow immediately behind the front, between the front and the nearest wave.

The flow profile after $t/t_0 = t_{int}$ (where $t_{int} = 1$ in the case shown in figure 3.3) is not determined using Fortran NAG routine D02AGF. This is due to the more complicated procedure that is necessary for evaluating complex regions that have been shown to occur (Rottman and Simpson, 1983) outside the regions already outlined.

3.5.2 Solution of the characteristic equations for $t > t_{int}$

The Fortran NAG routine D02AGF is sufficient for determining the characteristics within the initial region but it cannot be used beyond this phase where it is necessary to include further boundary conditions for the interaction of the backward propagating simple wave

with the end wall of the tank. Thus, it is necessary to implement a numerical scheme to solve the characteristic equations, as undertaken in this section.

Outline of numerical scheme

The method of characteristics produces four equations for the solution of the problem given by (3.113) and (3.117). These can be written in the general form

$$\left.\frac{dx}{dt}\right|_{\xi} = A'(h_1(x,t), u_1(x,t)) \qquad \left.\frac{dx}{dt}\right|_{\eta} = B'(h_1(x,t), u_1(x,t)) \tag{3.126}$$

$$\left.\frac{du_1}{dh_1}\right|_{\xi} = C'(h_1(x,t), u_1(x,t)) \qquad \left.\frac{du_1}{dh_1}\right|_{\eta} = D'(h_1(x,t), u_1(x,t)) \tag{3.127}$$

and are to be solved numerically. Generally, consider any two adjacent points I and J, say, on the curve Γ on which the values are known. Then, the η characteristic curve from point I must at some point, K, intersect with the ξ characteristic curve from point J, see figure 3.4.

Since equations (3.126) and (3.127) depend on the solutions u_1 and h_1 and the location of K in the (x,y) plane at that point, all these values must be determined. Once the values of u_1 and h_1 are known, the location of the point follows. There are several methods of numerically integrating ordinary differential equations. Ames (1965) suggests some of the most common methods: The Runga-Kutta method, Adams method and the corrected Euler method. The four differential equations can be approximated by relations of the form

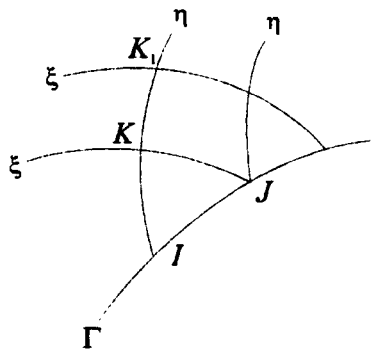

Figure 3.4: The method of characteristics, diagram for the solution process. Values at I and J are known.

$$\frac{x_K - x_J}{t_K - t_J} = \frac{1}{2}[A'(K) + A'(J)] \qquad \frac{x_K - x_I}{t_K - t_I} = \frac{1}{2}[B'(K) + B'(I)] \tag{3.128}$$

$$\frac{u_{1K} - u_{1J}}{h_{1K} - h_{1J}} = \frac{1}{2}[C'(K) + C'(J)] \qquad \frac{u_{1K} - u_{1I}}{h_{1K} - h_{1I}} = \frac{1}{2}[D'(K) + D'(I)] \tag{3.129}$$

where $A'(K)$ implies the value of $A'(h_1(x,t), u_1(x,t))$ at the point K. The set of equations (3.128) and (3.129) are solved by an iterative process.

The Fortran NAG routine can generate as many values as required at time $t/t_0 = t_{int}$, where the first of the backward propagating waves meets the end wall, i.e. where the

inclusion of the additional boundary condition is necessary. Thus we essentially have as many initial values along this line as we choose for the continuation of solution throughout the rest of the domain. Since the position of the front at this time is also known and we know that the ξ characteristics in the region of constant state between the front and the first forward propagating wave are parallel to the ξ characteristic of the wave, we can find as many points as necessary to give initial values throughout the domain at time t_{int}.

The equations (3.128) and (3.129) for this problem are rearranged for simpler implementation in the numerical scheme as follows:

$$t_K = \frac{x_J - x_I - \frac{1}{2}[A'(K) + A'(J)]t_J + \frac{1}{2}[B'(K) + B'(I)]t_I}{\frac{1}{2}[B'(K) + B'(I)] - \frac{1}{2}[A'(K) + A'(J)]} \tag{3.130}$$

$$x_K = x_J + \frac{1}{2}[A'(K) + A'(J)](t_K - t_J) \tag{3.131}$$

$$h_{1K} = \frac{u_{1J} - u_{1I} - \frac{1}{2}[C'(K) + C'(J)]h_{1J} + \frac{1}{2}[D'(K) + D'(I)]h_{1I}}{\frac{1}{2}[D'(K) + D'(J)] + \frac{1}{2}[C'(K) + C'(J)]} \tag{3.132}$$

$$u_{1K} = u_{1J} + \frac{1}{2}[C'(K) + C'(J)](h_{1K} - h_{1J}) \tag{3.133}$$

where

$$\begin{aligned}
A'(h_1(x,t), u_1(x,t)) &= \lambda_- = (1-a)u_1 - [a^2u_1^2 + g'h_1(1-b)]^{\frac{1}{2}} \\
B'(h_1(x,t), u_1(x,t)) &= \lambda_+ = (1-a)u_1 + [a^2u_1^2 + g'h_1(1-b)]^{\frac{1}{2}} \\
C'(h_1(x,t), u_1(x,t)) &= \left(\frac{1}{h_1}\right)[(1-2a)u_1 - \lambda_-] \\
D'(h_1(x,t), u_1(x,t)) &= \left(\frac{1}{h_1}\right)[(1-2a)u_1 - \lambda_+]
\end{aligned}$$

i.e. four equations in four unknowns.

Once the values of all the boundary adjacent points have been determined, their solutions can be used to find the values at the subsequent points, such as K_1, and so on, generating a net over the entire domain, for which values are known at every point. This net can be refined to evaluate more points within the domain if required.

The numerical solution process

The numerical method works by taking the average of the known values at two adjacent points at $t = t_{int}$ to estimate the value of u_1, h_1, x and t at a point forward in time. These initial guesses and the values at the known points are then input into the equations (3.130)-(3.133) to find values of u_1, h_1, x and t at the new point. The new values replace the initial guesses and the difference between these and the values from the previous iterative step is found. The iteration proceeds until this difference is reduced to the desired accuracy, here 10^{-12}.

The procedure continues using the values at the next known point to generate an initial guess for another new point, until it has worked through the known data set. It then advances so that the next 'column' of data can be found using these new values and so on. Thus the information is carried along the characteristics to subsequent time steps throughout the domain. Note that steps in time and space are not specified in this method, they are determined using the same process as for the other variables.

As the solution progresses across the domain, the conditions at the boundaries must be accounted for. Hence, at every other step forward, these conditions are brought into the calculations. On the $x = 0$ boundary, the end wall of the domain, these conditions are included through altering the equations used to solve on the boundary. The derivative boundary condition (3.53) basically implies a symmetry condition at the end wall. Thus, with the values of u_1 and x known, we need only use the two equations that describe the negative characteristic curves intersecting the $x = 0$ boundary to find the unknowns h_1 and t. In this case, equations

$$t_K = \frac{\frac{1}{2}[A'(K) + A'(J)]t_J - x_J}{\frac{1}{2}[A'(K) + A'(J)]} \tag{3.134}$$

$$h_{1K} = \frac{\frac{1}{2}[C'(K) + C'(J)]h_{1J} - u_{1J}}{\frac{1}{2}[C'(K) + C'(J)]} \tag{3.135}$$

where

$$A'(h_1(x,t), u_1(x,t)) = \lambda_- = (1-a)u_1 - [a^2u_1^2 + g'h_1(1-b)]^{\frac{1}{2}}$$

$$C'(h_1(x,t), u_1(x,t)) = \left(\frac{1}{h_1}\right)[(1-2a)u_1 - \lambda_-]$$

Alternatively, the equations can be solved in a larger domain, symmetrical about the t-axis, but u_1 and x must still be imposed on this line since $u = 0$ on $x = 0$ must still hold here.

The upper boundary that describes the front of the current, is slightly more complicated: Initially, the speed of the front, u_f is known as a result of the the NAG method. The front is described by the line $x = u_f t + x_0$ while it is in the initial phase of the flow. However, once the first of the characteristic curves of the reflected waves intercepts with the front. this speed is no longer constant. The waves are travelling at a speed faster than the front and so they overtake it. Hence, the wave becomes the 'new' front and it can no longer be described by a straight line since every time one of these waves intercepts it, the values on it will change.

The positive characteristic equations for the point at the front found on the previous step can be used to give two equations, but two more are necessary since all four variables are unknown for the new front point. The front is not a characteristic curve so the characteristic equations do not hold along it. However, the front condition must still hold and the speed of the front can still be described by $dx/dt = u_f$. Thus, using these two expressions with the characteristics we have obtained sufficient equations to be able to solve for the new front value:

$$\left.\frac{dx}{dt}\right|_{\eta} = B'(h_1(x,t), u_1(x,t)) \tag{3.136}$$

$$\left.\frac{du_1}{dh_1}\right|_{\eta} = D'(h_1(x,t), u_1(x,t)) \tag{3.137}$$

$$u_f = E'(h_f(x,t)) \tag{3.138}$$

$$\left.\frac{dx}{dt}\right|_{front} = E'(h_f(x,t)) \tag{3.139}$$

where

$$B'(h_1(x,t), u_1(x,t)) = \lambda_+ = (1-a)u_1 + [a^2u_1^2 + g'h_1(1-b)]^{\frac{1}{2}}$$

$$D'(h_1(x,t), u_1(x,t)) = \left(\frac{1}{h_1}\right)[(1-2a)u_1 - \lambda_+]$$

and

$$E'(h_1(x,t)) = \left[\frac{\beta^2}{2}\frac{2 - h_1/H}{1 + h_1/H}(1 - h_1/H)g'h_1\right]^{\frac{1}{2}} \tag{3.140}$$

i.e. the front condition that must be satisfied at the new point.

These equations can then be included in the iterative scheme, re-written as follows:

$$t_K = \frac{\frac{1}{2}[B'(K)+B'(I)]t_I - \frac{1}{2}[E'(K)+E'(J)]t_J + x_J - x_I}{\frac{1}{2}[B'(K)+B'(I)] - \frac{1}{2}[E'(K)+E'(J)]} \tag{3.141}$$

$$x_K = x_J + \frac{1}{2}[E'(K)+E'(J)](t_K - t_J) \tag{3.142}$$

$$h_{1K} = \frac{u_{1K} - u_{1I} + \frac{1}{2}[D'(K)+D'(I)]h_{1I}}{\frac{1}{2}[D'(K)+D'(I)]} \tag{3.143}$$

$$u_{1K} = E'(K) \tag{3.144}$$

Once the variables have been found at this point, the scheme can continue as usual using the negative characteristic equations from this new point to contribute to finding the top of the next step and then carrying out this top boundary method again.

3.6 Method of characteristics: rough case

The method of characteristics cannot be used in exactly the same way for the solution of the problem with a rough bed. The additional terms included to describe the roughness mean that the general form of the characteristic ODE, equation (3.100), cannot be reduced to the special case.

Application to the present rough bed case

The two simultaneous equations (3.88) and (3.89) obtained in this case can be written in the form of equations (3.92) and (3.93) as follows:

$$\frac{\partial h_1}{\partial t} + u_1\frac{\partial h_1}{\partial x} + 0\frac{\partial u_1}{\partial t} + h_1\frac{\partial u_1}{\partial x} = 0 \tag{3.145}$$

$$0\frac{\partial h_1}{\partial t} + g'(1-b)\frac{\partial h_1}{\partial x} + R'\frac{\partial u_1}{\partial t} + u_1(1-2a)\frac{\partial u_1}{\partial x} = -\frac{u_1^2}{8Ha}\left[C_3 f_3 a^3 + C_1 f_1 + C_2 f_2 (1+a)^3\right] \tag{3.146}$$

i.e.

$$\begin{aligned} P &= 1 & P' &= 0 \\ Q &= u_1 & Q' &= g'(1-b) \\ R &= 0 & R' &= 1 \\ S &= h_1 & S' &= (1-2a)u_1 \\ T &= 0 & T' &= \overline{f} \end{aligned} \tag{3.147}$$

where

$$\overline{f} = -\frac{u_1^2}{8Ha}\left[C_3 f_3 a^3 + C_1 f_1 + C_2 f_2 (1+a)^3\right] \tag{3.148}$$

and x and y are analogous to t and x, respectively.

Along the curve Γ:

$$\delta h_1 = \frac{\partial h_1}{\partial t}\delta t + \frac{\partial h_1}{\partial x}\delta x \tag{3.149}$$

$$\delta u_1 = \frac{\partial u_1}{\partial t}\delta t + \frac{\partial u_1}{\partial x}\delta x \tag{3.150}$$

Thus, for this problem, the system of equations is given, in matrix form $\overline{A}x = c$, as:

$$\begin{pmatrix} dt & dx & 0 & 0 \\ 0 & 0 & dt & dx \\ 1 & u_1 & 0 & h_1 \\ 0 & g'(1-b) & 1 & u_1(1-2a) \end{pmatrix} \begin{pmatrix} \frac{\partial h_1}{\partial t} \\ \frac{\partial h_1}{\partial x} \\ \frac{\partial u_1}{\partial t} \\ \frac{\partial u_1}{\partial x} \end{pmatrix} = \begin{pmatrix} dh_1 \\ du_1 \\ 0 \\ \overline{f} \end{pmatrix} \tag{3.151}$$

As for the smooth case, we require that the determinant of the matrix of coefficients vanish. Since this matrix is identical to the smooth equivalent, this determinant will be the same, implying that the characteristic directions for both cases are identical. Thus the directions of the η and ξ characteristics are given by:

$$\left.\frac{\partial x}{\partial t}\right|_{\eta} = \lambda_+, \qquad \left.\frac{\partial x}{\partial t}\right|_{\xi} = \lambda_- \tag{3.152}$$

where

$$\lambda_{\mp} = (1-a)u_1 \mp \left[a^2 u_1^2 + g' h_1 (1-b)\right]^{\frac{1}{2}} \tag{3.153}$$

The process differs on substituting the column vector c into the determinant of the coefficient matrix $\overline{A}$ since the term $\overline{f}$ is now present. Equating this new coefficient matrix to zero, gives:

$$\begin{vmatrix} dt & dh_1 & 0 & 0 \\ 0 & du_1 & dt & dx \\ 1 & 0 & 0 & h_1 \\ 0 & \overline{f} & 1 & u_1(1-2a) \end{vmatrix} = 0 \tag{3.154}$$

i.e.

$$(-h_1)du_1 + \left[(1-2a)u_1 - \left.\frac{dx}{dt}\right|_{\eta,\xi}\right] dh_1 = \overline{f} h_1 dt \tag{3.155}$$

This expression is no longer in the form of the special case equation (3.100) generated for the smooth case. However, rearranging equation (3.155) and using equation (3.152) does yield an expression for the variation of u_1 and h_1 along each of the characteristics:

$$h_1 \frac{du_1}{dh_1} - (1-2a)u_1 + \lambda_{\mp} = \overline{f} h_1 \frac{dt}{h_1} \tag{3.156}$$

Thus the problem has been simplified to solving equation (3.156) for u_1 and h_1, including terms for the effects of a rough boundary, using the expression (3.153) and the initial and boundary conditions (3.51)-(3.53).

3.6.1 Solution of the characteristic equations for $t/t_0 > 0.05$

The form of the ordinary differential equation required for solution by the method of characteristics involves the unknown independent variable t which means that the equation cannot simply be integrated using the NAG routine D02AGF, as performed to find the front value in the smooth case. Solution of the characteristic equations cannot be carried out directly from $t = 0$ due to the singularity that occurs at the initial release. As a result of this, the data generated using the NAG routine D02AGF for the smooth case is used to construct a set of initial conditions at a small time, $t/t_0 = 0.05$ say. This is a reasonable assumption since it is not expected that the roughness will have significant affects immediately after the fluid is released, indeed the experimental front speed data supports this. The solution process advances with the numerical scheme to solve the characteristic equations with the rough terms included and the NAG generated data to initialise the variables u_1, h_1, x and t. The smooth case can also be solved using this method whereby the numerical scheme is implemented at an earlier time than $t = t_{int}$. This gives a means to check that the numerical scheme is resolving the initial regions which it did not need to find before. A similar scheme to that outlined in section 3.5.2 is used with modifications to account for the additional terms.

Outline of numerical scheme

As in the smooth case, the method of characteristics produces four equations for the solution of the problem given by (3.152) and (3.156). These can be written in the general form as follows:

$$\left.\frac{dx}{dt}\right|_{\xi} = A'(h_1(x,t), u_1(x,t)) \tag{3.157}$$

$$\left.\frac{dx}{dt}\right|_{\eta} = B'(h_1(x,t), u_1(x,t)) \tag{3.158}$$

$$\left.\frac{du_1}{dh_1}\right|_{\xi} = C'(h_1(x,t), u_1(x,t)) + F'(h_1(x,t), u_1(x,t)) \tag{3.159}$$

$$\left.\frac{du_1}{dh_1}\right|_{\eta} = D'(h_1(x,t), u_1(x,t)) + F'(h_1(x,t), u_1(x,t)) \tag{3.160}$$

The rough terms are contained in the function F'. These four differential equations can be approximated by relations of the form

$$\frac{x_K - x_J}{t_K - t_J} = \frac{1}{2}[A'(K) + A'(J)] \tag{3.161}$$

$$\frac{x_K - x_I}{t_K - t_I} = \frac{1}{2}[B'(K) + B'(I)] \tag{3.162}$$

$$\frac{u_{1K} - u_{1J}}{h_{1K} - h_{1J}} = \frac{1}{2}[C'(K) + C'(J)] + \frac{1}{2}[F'(K) + F'(J)]\frac{t_K - t_J}{h_{1K} - h_{1J}} \tag{3.163}$$

$$\frac{u_{1K} - u_{1I}}{h_{1K} - h_{1I}} = \frac{1}{2}[D'(K) + D'(I)] + \frac{1}{2}[F'(K) + F'(I)]\frac{t_K - t_I}{h_{1K} - h_{1I}} \tag{3.164}$$

where $A'(K)$ implies the value of $A'(h_1(x,t), u_1(x,t))$ at the point K. The set of equations (3.161)-(3.164) are solved numerically using the iterative process.

The Fortran NAG routine can generate as many values as required at time $t/t_0 = 0.05$. Thus we essentially have as many initial values along this line as we choose for the continuation of solution throughout the rest of the domain.

The equations (3.161)-(3.164) for this problem are rearranged for simpler implementation in the numerical scheme as follows:

$$t_K = \frac{x_J - x_I - \frac{1}{2}[A'(K) + A'(J)]t_J + \frac{1}{2}[B'(K) + B'(I)]t_I}{\frac{1}{2}[B'(K) + B'(I)] - \frac{1}{2}[A'(K) + A'(J)]} \tag{3.165}$$

$$x_K = x_J + \frac{1}{2}[A'(K) + A'(J)](t_K - t_J) \tag{3.166}$$

$$h_{1K} = \frac{u_{1J} - u_{1I} - \frac{1}{2}[C'(K) + C'(J)]h_{1J} + \frac{1}{2}[D'(K) + D'(I)]h_{1I} + \frac{1}{2}[F'(J) - F'(I)]t_K}{\frac{1}{2}[D'(K) + D'(J)] + \frac{1}{2}[C'(K) + C'(J)]} \tag{3.167}$$

$$u_{1K} = u_{1J} + \frac{1}{2}[C'(K) + C'(J)](h_{1K} - h_{1J}) + \frac{1}{2}[F'(K) + F'(J)](t_K - t_J) \tag{3.168}$$

where

$$\begin{aligned}
A'(h_1(x,t), u_1(x,t)) &= \lambda_- = (1-a)u_1 - [a^2u_1^2 + g'h_1(1-b)]^{\frac{1}{2}} \\
B'(h_1(x,t), u_1(x,t)) &= \lambda_+ = (1-a)u_1 + [a^2u_1^2 + g'h_1(1-b)]^{\frac{1}{2}} \\
C'(h_1(x,t), u_1(x,t)) &= \left(\frac{1}{h_1}\right)[(1-2a)u_1 - \lambda_-] \\
D'(h_1(x,t), u_1(x,t)) &= \left(\frac{1}{h_1}\right)[(1-2a)u_1 - \lambda_+] \\
F'(h_1(x,t), u_1(x,t)) &= -\frac{u_1^2}{8Ha}\left[C_3 f_3 a^3 + C_1 f_1 + C_2 f_2 (1+a)^3\right]
\end{aligned}$$

The numerical solution process is carried out using the same method as in the smooth case, covered in section 3.5.2, but with slightly different equations for the boundaries so that the roughness terms are included. On the $x = 0$ boundary, $u = 0$ but t and h_1 are unknown. The process requires the negative characteristic equations to iterate on in order to find these values. These are given by:

$$t_K = \frac{\frac{1}{2}[A'(K) + A'(J)]t_J - x_J}{\frac{1}{2}[A'(K) + A'(J)]} \tag{3.169}$$

$$h_{1K} = \frac{\frac{1}{2}[C'(K) + C'(J)]h_{1J} + \frac{1}{2}[F'(K) + F'(J)](t_J - tK) - u_{1J}}{\frac{1}{2}[C'(K) + C'(J)]} \tag{3.170}$$

The values on the front must also be found as before using the known front definition $dx/dt = u_f$ and the front condition u_f along with the positive characteristics from the last determined point nearest the front. These conditions are rearranged and included

in the scheme in the form:

$$t_K = \frac{\frac{1}{2}[B'(K)+B'(I)]t_I - \frac{1}{2}[E'(K)+E'(J)]t_J + x_J - x_I}{\frac{1}{2}[B'(K)+B'(I)] - \frac{1}{2}[E'(K)+E'(J)]} \quad (3.171)$$

$$x_K = x_J + \frac{1}{2}[E'(K)+E'(J)](t_K - t_J) \quad (3.172)$$

$$h_{1K} = \frac{u_{1K} - u_{1I} + \frac{1}{2}[D'(K)+D'(I)]h_{1I} + \frac{1}{2}[F'(K)+F'(I)](t_K - t_J)}{\frac{1}{2}[D'(K)+D'(I)]} \quad (3.173)$$

$$u_{1K} = E'(K) \quad (3.174)$$

Once the values of the variables have been found at this front point, the scheme can continue as usual using the negative characteristic equations from this new point to contribute to finding the top of the next step and then this method is performed again.

3.7 Results

3.7.1 Validation

The theoretical results must be compared to experimental data if their validity is to be obtained. Figure 3.5 shows a comparison of the present theory with that of Rottman and Simpson (1983) and their experimental data for partial to full height lock releases. It is clear that a value of $\beta^2 = 2$ in the front condition does not give close agreement with the experiments. If this value is arbitrarily changed to 1 then much better agreement is obtained. However, as Shin *et al.* (2004) points out, there is no theoretical justification for this choice, it is simply altered for better agreement. For $\beta^2 = 1$ the results from this work and that of Rottman and Simpson (1983) are directly comparable.

The front condition derived theoretically by Shin *et al.* (2004) was also implemented, with the method of characteristics, for comparison with the theoretical results. This condition has no free parameters so it will not require new empirical expressions when a front condition is sought for the rough bed case. The excellent agreement between the present work implementing this front condition can be seen with the experimental data of Rottman and Simpson (1983) and Shin *et al.* (2004) in figure 3.6.

In order to produce a more visual confirmation of the validity of the present theory, the model was simulated using the experimental configuration of Gladstone *et al.* (2004). The dataset therein contains photographs of lock release experiments at different times

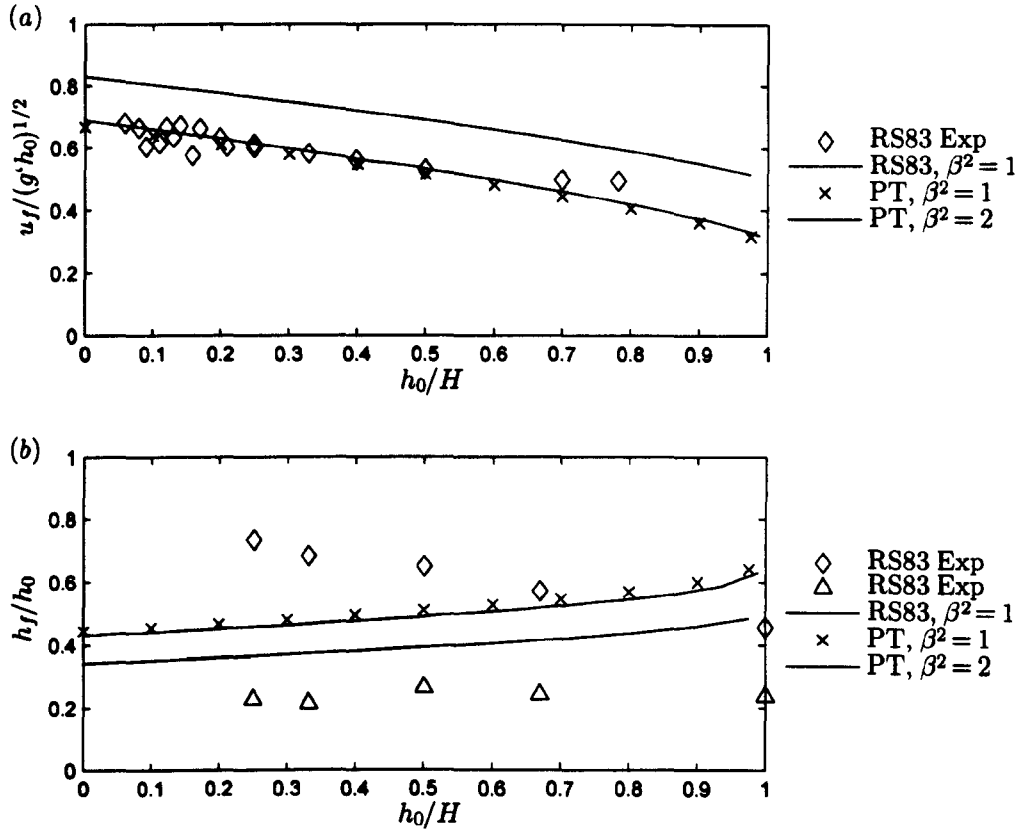

Figure 3.5: Theoretical results from the present theory (PT) with $\beta^2 = 1$ and 2 and Rottman and Simpson (1983) (RS83) with $\beta^2 = 1$. Experimental results of Rottman and Simpson (1983). (a) The front speed and (b) the front height during the initial phase of collapse plotted as a function of h_0/H. Diamonds are the total measured depth of current behind the front and triangles are depth of the unmixed current layer, neither are true front height.

and enables a rare qualitative comparison of the theoretical depth profiles and their 'real' equivalents. This comparison is presented in figure 3.7. This figure also highlights the 1D limitations of the theory, in particular with respect to the mixing and entrainment present at the density interface between the current (blue) and the ambient (clear) fluids. However, despite the limitations, the agreement is remarkably good.

The relationship for the front speed found by Huppert and Simpson (1980) can also be imposed as the front condition for use in the method of characteristics. Their version incorporated analytical and empirical methods, essentially depending on a Fr number, calculated empirically, of 1.19. This value has been used for the generation of the data shown in figure 3.8. However, other studies have found different Fr numbers, for example, Fr=1 (Shin *et al.*, 2004) or Fr= $\sqrt{2}$ (Benjamin, 1968). This front condition could

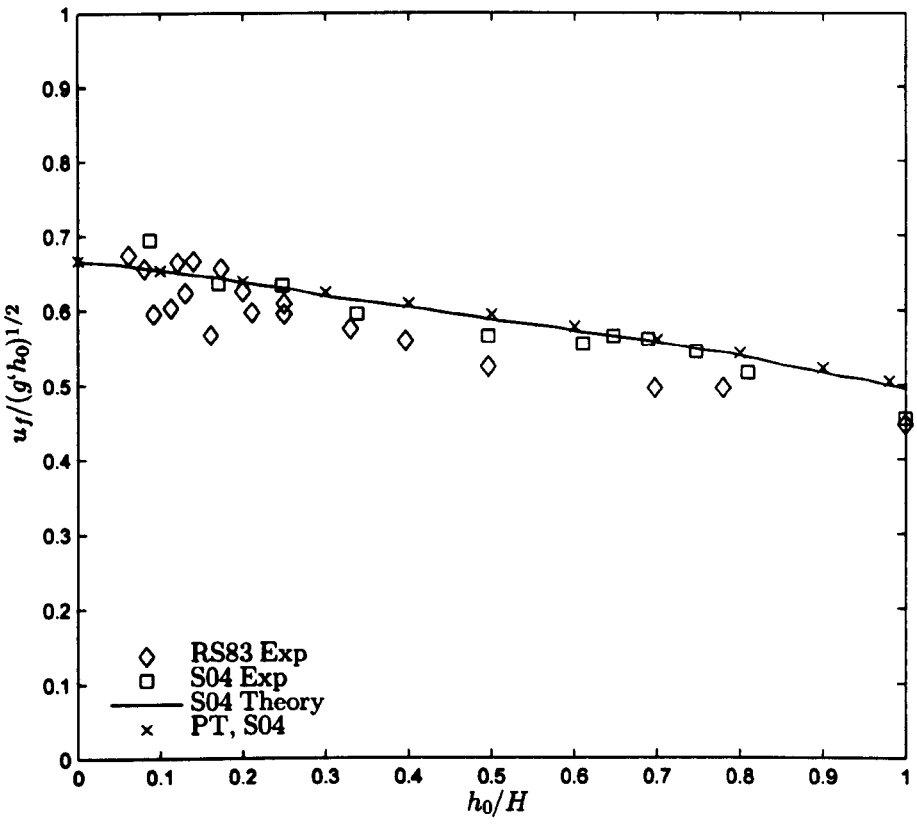

Figure 3.6: The front speed during the initial phase of collapse plotted as a function of h_0/H. Theoretical results from the present theory (PT) with the front condition of Shin *et al.* (2004) (S04) and the experimental and theoretical results of Shin *et al.* (2004).

also be useful for application to the rough case if Froude numbers were calculated from experimental data for flow over a rough bed. However, difficulties in accurate measurement of height can make this method subject to greater errors, as shown by the different existing Fr values for the smooth case.

The normalised front speeds and front heights for different release height ratios generated using the three different front conditions are displayed in figure 3.8. The variation in the experimental results in figure 3.8 (*b*) is due to the differences in location when measuring the height of the current. It can be seen that the results generated using the Shin *et al.* (2004) front condition are in much better agreement for all release heights than they are for those using the Rottman and Simpson (1983) or Huppert and Simpson (1980) conditions for both the front speeds and the front heights. Moreover, the conservative analytical half height solution, $h_f = h_0/2$ is proven to be a good approximation to the height of the front.

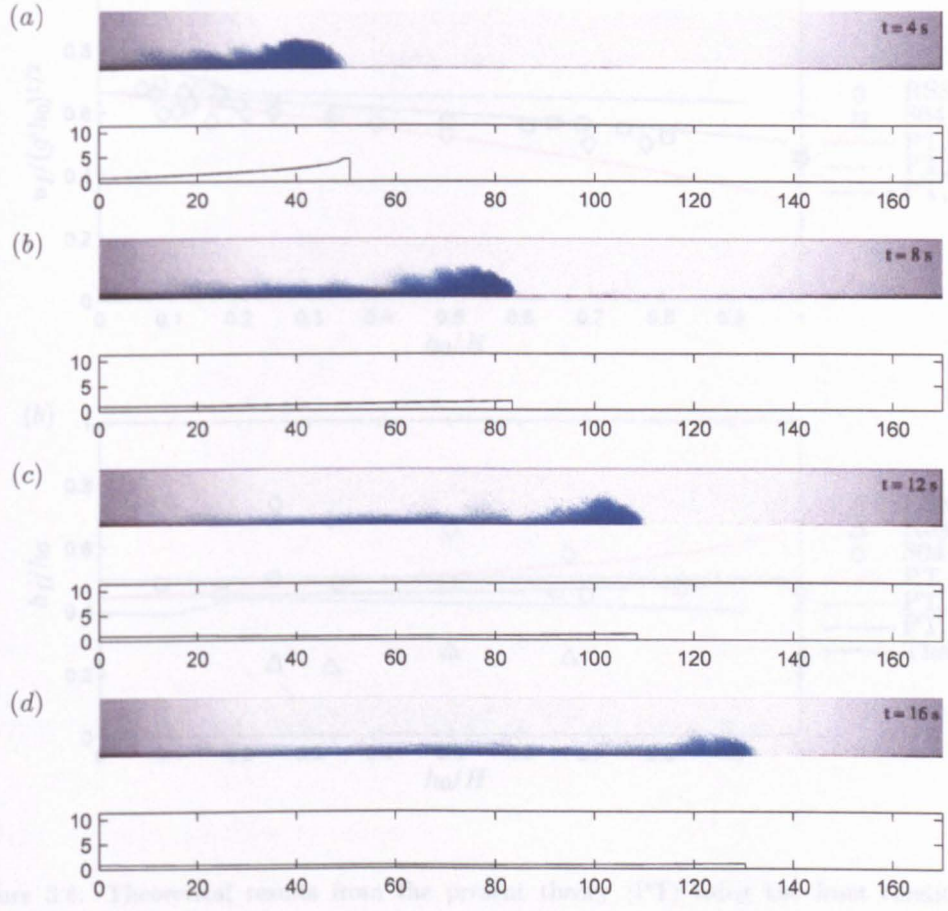

Figure 3.7: Photographs of the experiment from Gladstone *et al.* (2004) and corresponding theoretical depth profiles from the present theory using the front condition of Shin *et al.* (2004).

Huppert and Simpson (1980) published results for a range of 18 'two-dimensional' experiments for full and partial depth currents. They used these experiments for comparison with their box model theory and showed reasonable agreement. The results for the two front conditions used thus far with the box model and experiments 7 and 9 from Huppert and Simpson (1980) can be seen in figure 3.9. Table 3.1 displays the parameters for these two experiments.

It can be seen that the solution using the shallow water equations solved with the method of characteristics gives results in better agreement with the experimental data than the box model equivalent. However, the present theory using the front condition of Shin *et al.* (2004) is close to this result. It is difficult to see differences in accuracy between

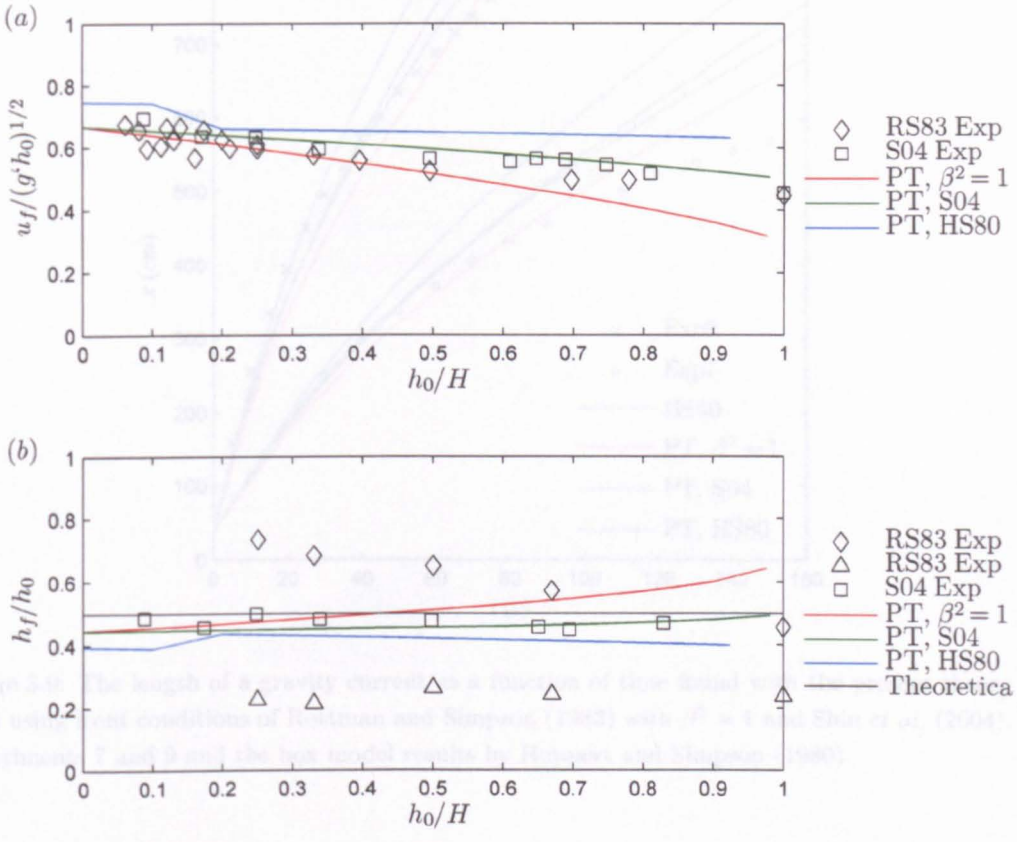

Figure 3.8: Theoretical results from the present theory (PT) using the front conditions of Rottman and Simpson (1983) with $\beta^2 = 1$, Shin *et al.* (2004) (SO4), Huppert and Simpson (1980) (HS80) with the analytical value $h_f = h_0/2$. Experimental results of Rottman and Simpson (1983) and Shin *et al.* (2004). (a) The front speed and (b) The front height during the initial phase of collapse plotted as a function of h_0/H.

Exp. No.	h_0	H	h_0/H	x_0	g'
7	15.0	44.0	0.34	39.1	9.4
9	15.0	44.9	0.33	39.2	64.8

Table 3.1: Parameters of two-dimensional experiments No. 7 and 9 carried out by Huppert and Simpson (1980).

the two present methods although that of Rottman and Simpson (1983) is consistently slower than the Shin *et al.* (2004) version and is not in such good agreement for earlier times.

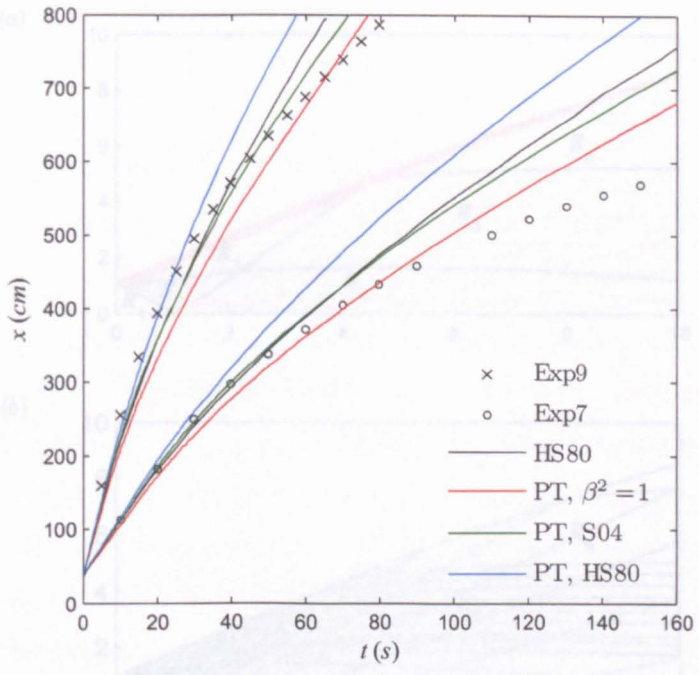

Figure 3.9: The length of a gravity current as a function of time found with the present theory (PT) using front conditions of Rottman and Simpson (1983) with $\beta^2 = 1$ and Shin *et al.* (2004). Experiments 7 and 9 and the box model results by Huppert and Simpson (1980).

3.7.2 Complete flow profiles

Smooth bed

The solutions generated by the NAG method and the numerical scheme can be combined to create a complete profile of the flow domain. The characteristic lines of the flow can be drawn to depict a visual model of the lock release process and the gravity current initiation and propagation. Characteristic diagrams generated by the combined results from the NAG method and the numerical scheme can be seen in figure 3.10[‡]. The diagrams have been created by interpolating the results onto a uniform mesh and tracing the characteristics by projecting the gradients from one point, forward by a small time step, in search of the next nearest point.

The front position calculated by the present theory is plotted on the characteristic diagram reproduced from Rottman and Simpson (1983) figure 3.10 (*a*) showing that the two results are in good agreement and verifying that the method has been implemented correctly. The characteristic lines displayed in figure 3.10 (*b*), and drawn using the present

[‡]Note that the figures in this section have all been generated using a value $\beta^2 = 2$ in the front condition. Changing this parameter has little effect on the essential profile of the flow, its specification is more relevant, however, when more accurate values of the variables throughout the domain are required for comparison with the results from experimental and numerical simulations.

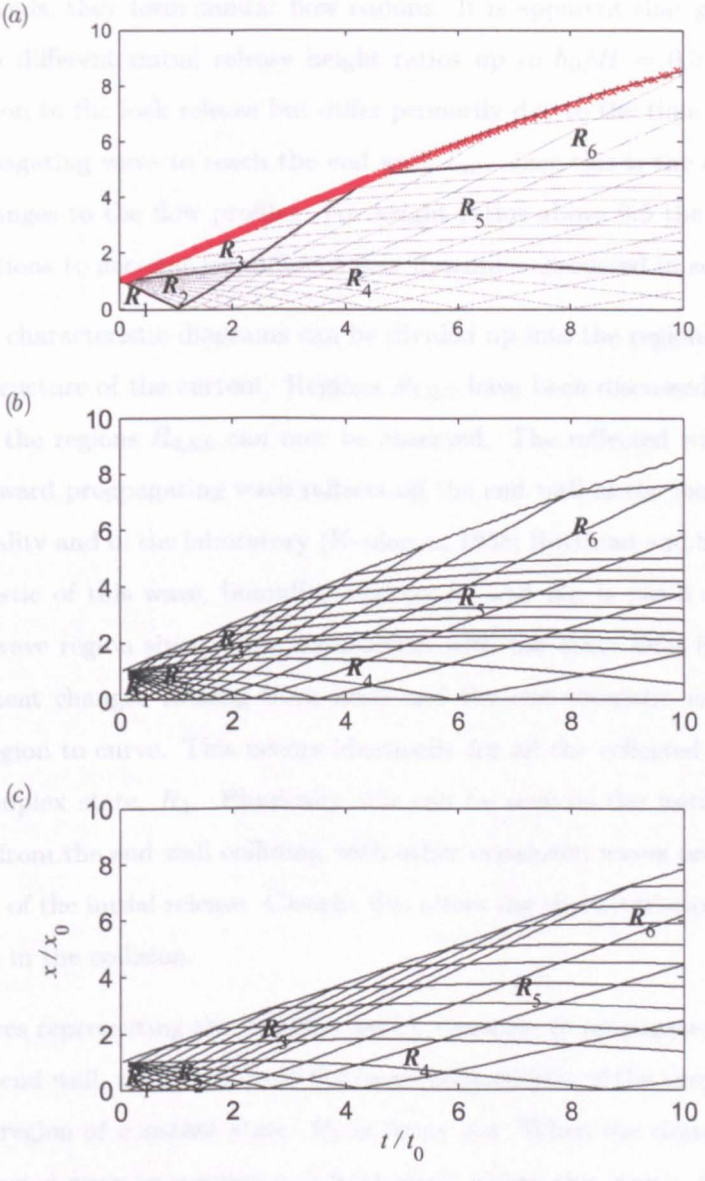

Figure 3.10: Characteristic diagrams for $h_0/H \approx 0$ and $h_0/H = 0.5$ using the front condition of Rottman and Simpson (1983) with $\beta^2 = 2$. (*a*) $h_0/H \approx 0$ reproduced from Rottman and Simpson (1983) with front position of present theory (×) and (*b*) $h_0/H \approx 0$ and (*c*) $h_0/H = 0.5$ both using present theory.

theory, do not coincide exactly with those in (*a*), although they represent the same case. This is because the method for presenting the data selects which lines it displays at fixed intervals for presentational clarity. From the diagrams shown in figure 3.10, it is clear that the regions of the flow are comparable even if specific diagrammatical lines are not present. Rottman and Simpson (1983) do not display diagrams for other cases on the basis that they are expected to be similar and therefore figure 3.10 (*c*) cannot strictly be verified. However, similarities between the cases can be seen in figures 3.10 (*b*) and (*c*) and show that, although the different cases develop uniquely and have dif-

ferent front speeds, they form similar flow regions. It is apparent that gravity currents generated with different initial release height ratios up to $h_0/H = 0.5$ begin with an identical reaction to the lock release but differ primarily due to the time it takes for the backward propagating wave to reach the end wall, t_{int}, since this is the catalyst for the subsequent changes to the flow profiles. For height ratios above 0.5 the present theory requires alterations to account for different flow dynamics discussed in section 3.7.3.

In general, the characteristic diagrams can be divided up into the regions that typically describe the structure of the current. Regions $R_{1,2,3}$ have been discussed in section 3.5. In figure 3.10, the regions $R_{4,5,6}$ can now be observed. The reflected wave that occurs when the backward progpagating wave reflects off the end wall of the lock box has been identified in reality and in the laboratory (Keulegan, 1958; Rottman and Simpson, 1983). The characteristic of this wave, bounding regions R_2 and R_3, is not a straight line as in the simple wave region since, upon intersection with the other lines from the simple wave, its gradient changes causing both itself and the characteristic lines leaving the simple wave region to curve. This occurs identically for all the reflected waves creating a region of complex state, R_4. Physically this can be seen as the initial simple wave reflected back from the end wall colliding with other expansion waves propagating back from the shock of the initial release. Clearly, this alters the characteristics of both of the waves involved in the collision.

The set of curves representing the reflected waves, continue to propagate in this manner away from the end wall, until they cross the final characteristic of the simple wave region into the other region of constant state, R_3 in figure 3.3. When the characteristic curve of the first reflected wave encounters a characteristic within this region, the values of u_1 and h_1 and thus the gradients of both characteristics, change again. This occurs at every subsequent intersection between the wave and the curves in the constant state region. Moreover, since in R_3 the lines are parallel to each other, although the influence of the reflected wave causes them to curve, they remain parallel. This has the effect that the gradients of the reflected characteristics that intersect with them do not change along one curve and thus they become a set of straight lines each of different gradient, i.e. another simple wave region, R_5. This occurs physically when the calm region immediately behind the head gets disturbed by the waves approaching the front. Finally, when the reflected wave catches up with the front, the front begins to slow down from its previous constant speed. Thus, since the values at the front are constantly changing, another region of complex state, R_6, is formed.

Rough bed

Diagrams of the characteristic curves in the rough case, compared to the smooth bed are shown in figure 3.11. A roughness of $f_1 = f_2 = f_3 = 0.1$ was prescribed on the bed only, the bed and the interface and on the bed, interface and top wall, results for which are shown in figures 3.11 (*b*), (*c*) and (*d*), respectively. It can be observed that when any roughness is present the front travels more slowly. Figure 3.11 (*c*) shows that when the effects of roughness at the interface are also included, the current is further retarded. This is confirmed in subsequent sections. When $C_3 = 1$ there are little noticeable affects. This is as desired since these effects will be felt in the overlying fluid and are transferred to the gravity current through the interfacial condition which has already been activated.

With respect to the flow regions identified in the smooth cases, it appears that these are still present. However, subtle differences can be observed. The simple waves that occur on release of the lock are either reduced in quantity or propagate significantly quicker back to the end wall. The last of these waves is seen to reflect at $t/t_0 \approx 6$ in figure 3.11 (*b*) (and sooner in figure 3.11 (*c*)), while in figure 3.11 (*a*) this occurs at $t/t_0 \approx 9$. In the rough case when only $C_1 = 1$, the front appears to remain at a fairly constant speed until the first of these reflected waves intersects with it, as in the smooth case. When $C_2 = 1$, the front appears to slow more rapidly, perhaps due to the roughness effects themselves. It must be noted that the initial conditions, at a very small time, were calculated using the smooth equations, even for the the rough cases as discussed in section 3.6.1. Therefore, in the rough cases, the solution may undergo an adjustment period within which the modifications to the equations due to roughness take affect. This could also be the reason for the apparent lack of constant speed period shown in figure 3.11 (*c*).

In addition to altering the location of the roughness, in order to test the sensitivity of the model to the roughness size, the values of f_1, f_2 and f_3 were also modified. The two other values selected were half (0.05) and double (0.2) the value used in figures 3.11 (*b*) – (*d*). These were applied to the bed only, i.e. $C_1 = 1$, $C_2 = C_3 = 0$, figure 3.11 (*b*). The diagrams of the characteristic curves for these cases are shown in figure 3.12. As observed when the influence of roughness on the interface was included, when the magnitude increases the simple wave region diminishes or, rather, the time at which the backward propagating waves reflect off the end wall of the lock gets earlier. Also, the front appears to diverge from a constant speed earlier as the roughness effects increase.

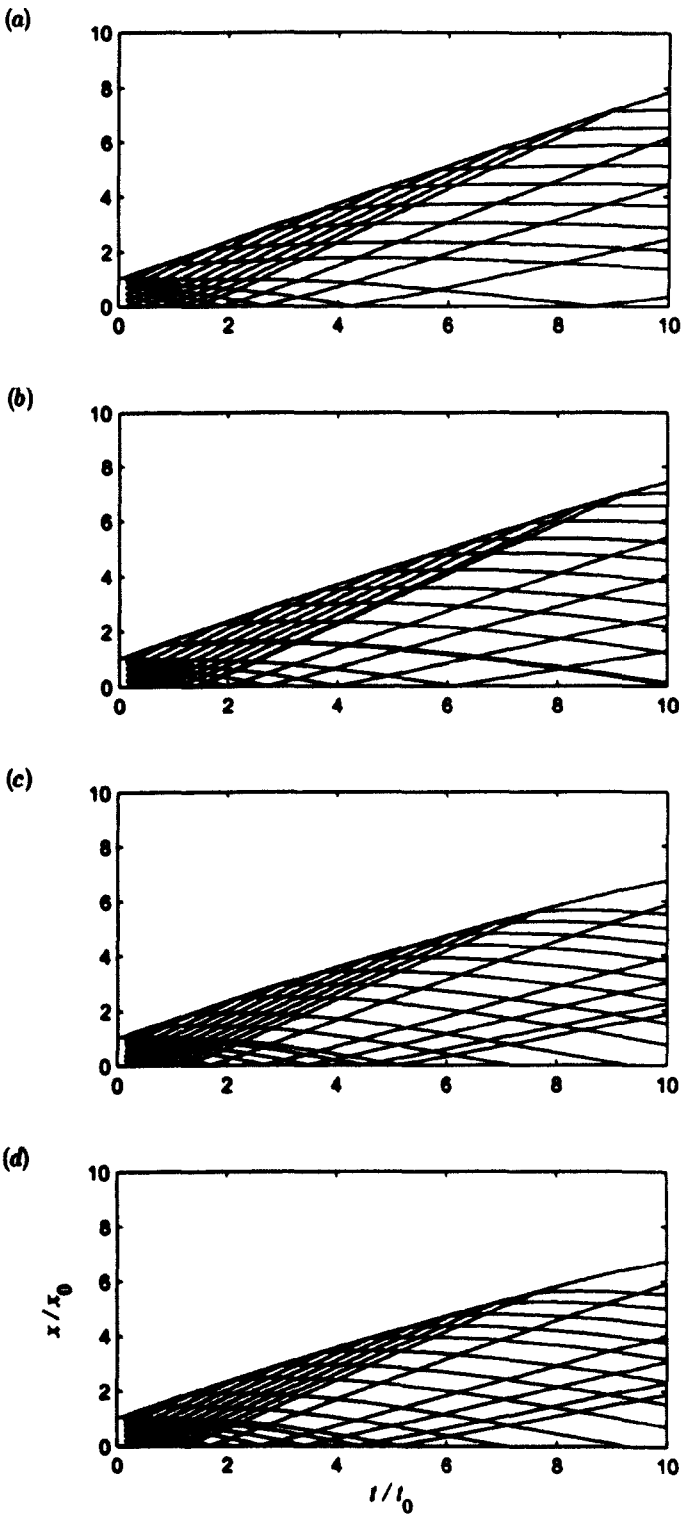

Figure 3.11: Characteristic diagrams for $h_0/H = 0.5$ using the front condition of Rottman and Simpson (1983) with $\beta^2 = 2$ and (*a*) a smooth bed. Rough cases with $f_1 = f_2 = f_3 = 0.1$ (*b*) $C_1 = 1$, $C_2 = C_3 = 0$, (*c*) $C_1 = C_2 = 1$, $C_3 = 0$ and (*d*) $C_1 = C_2 = C_3 = 1$. Where C_1, C_2 and C_3 indicate rough (1) or smooth (0) influence on the bed, interface and top wall, respectively.

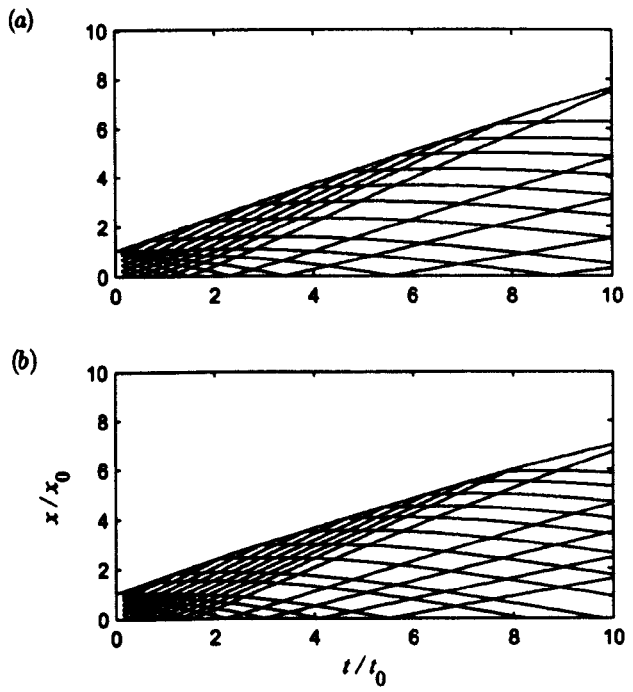

Figure 3.12: Characteristic diagrams for $h_0/H = 0.5$ using the front condition of Rottman and Simpson (1983) with $\beta^2 = 2$ with roughness on the bed, i.e. $C_1 = 1, C_2 = C_3 = 0$. (*a*) $f_1 = 0.05$, (*b*) $f_1 = 0.2$. Where C_1, C_2 and C_3 indicate rough (1) or smooth (0) influence on the bed, interface and top wall, respectively.

3.7.3 Depth and velocity profiles

Smooth bed

Depth profiles of the currents display a one dimensional outline of the denser fluid as it develops through time and are presented in figure 3.13. The backward propagation of the waves from the release at $t = 0$ can be seen along with the 'shock' of the collision with the end wall, the size of which depends on the initial release height of the fluid. After this time, as the current propagates along the tank it retains a constant front height with an identical depth region behind it which implies the presence of a deeper head region. This remains until $t/t_0 \approx 5$ (or $t/t_0 \approx 9$ for $h_0/H = 0.5$) after which the height behind the front deteriorates, consequently suggesting deterioration of the head shape at this later time. It can also be observed in figure 3.13 that as the current propagates its tail remains attached to the end wall with a depth significantly smaller than the head region. Corresponding velocity profiles are shown in figure 3.14. These indicate a steady increase in the velocity from the rear of the current to a maximum near the front. This maximum is initially constant and then begins to decrease at later times. Moreover, the maximum is initially distributed through the head region of the current, as defined

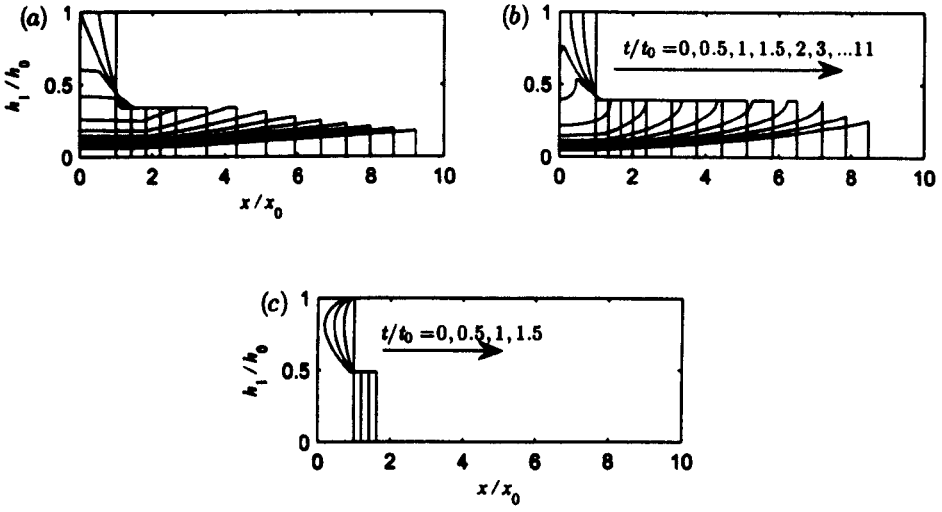

Figure 3.13: Theoretical depth profiles using the front condition of Rottman and Simpson (1983) with $\beta^2 = 2$. (a) $h_0/H \approx 0$, (b) $h_0/H = 0.5$, (c) $h_0/H \approx 1$.

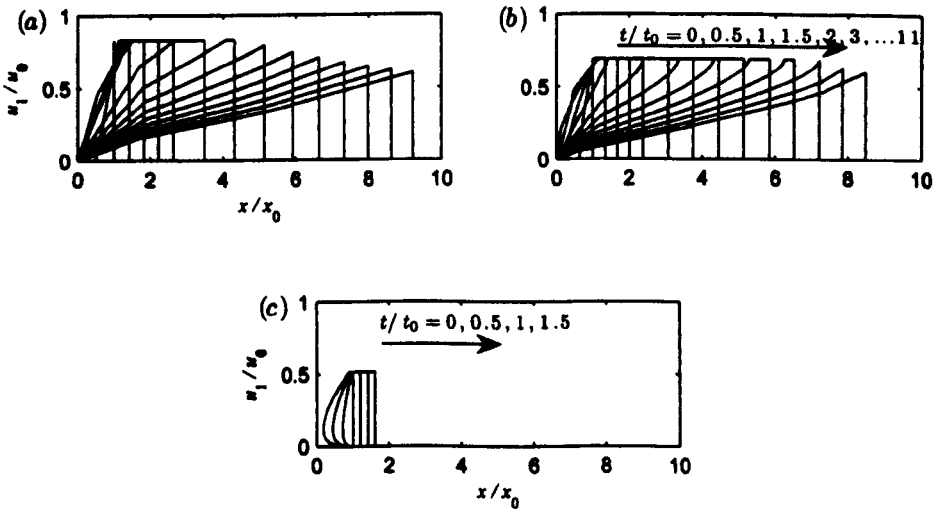

Figure 3.14: Theoretical velocity profiles using the front condition of Rottman and Simpson (1983) with $\beta^2 = 2$. (a) $h_0/H \approx 0$, (b) $h_0/H = 0.5$, (c) $h_0/H \approx 1$.

above, not solely at the current front. It then decreases at the same time as the head begins to lose depth and potentially deteriorate.

A slight discrepancy occurs when comparing the depth profiles for the $h_0/H = 0.5$ case. However, this can be attributed to differences in mesh size and iterative procedure. The methodology used in this work can be shown to produce a similar result if less points are used in the numerical scheme and the order of accuracy of the iterative process is reduced considerably. Note that when the number of points on the initial line generated by the NAG routine is greater than 100, there is very little change in the results, indicating a good degree of mesh independence in the present work.

Figures 3.13 and 3.14 (*c*) show that using the method of characteristics, multivalued solutions are generated in the $h_0/H \approx 1$ case in the depth and velocity profiles. In fact, this occurs for any initial to ambient height ratio greater than 0.5. Essentially, this means that the backward propagating waves generated upon removal of the lock partition are travelling faster than the backward propagating motion on the undisturbed interface at h_0. With reference to the characteristic diagrams, figure 3.10, this implies that the simple wave region R_2 is expanding into the lower constant state region R_1. Physically, this is seen in the formation of a shock or bore for greater partial depth releases instead of the rarefaction wave seen with lower values of h_0/H. The specific criteria for the occurrence of this shock have been explored by e.g. D'Alessio *et al.* (1996). In particular, they found that the fractional depth occupied by the denser fluid does play a crucial role in the development of the bore. The method of characteristics breaks down for these increased depths and requires further conditions or constraints to solve the problem.

Rottman and Simpson (1983) attempted to incorporate a hydraulic jump model into their theory but chose not to present their work. Several authors (Bonnecaze *et al.*, 1993; D'Alessio *et al.*, 1997) have successfully modelled the $h_0/H \approx 1$ case using finite difference methods which can account for the 'hydraulic jump'. Klemp *et al.*, 1994 and Shin *et al.*, 2004 have extended the application of the method of characteristics to full height releases by including additional conditions in the method. Essentially this involves the application of a front condition on the backward propagating wave that bounds the undisturbed region so that it is always faster than the backward propagating waves on the interface travelling towards it from the release point. This effectively reduces the problem of the bore back to one of an expansion wave that the method can resolve as for the smaller depth releases. However, this extension was not performed in the present study and remains as further work. Therefore, the theory and results discussed herein

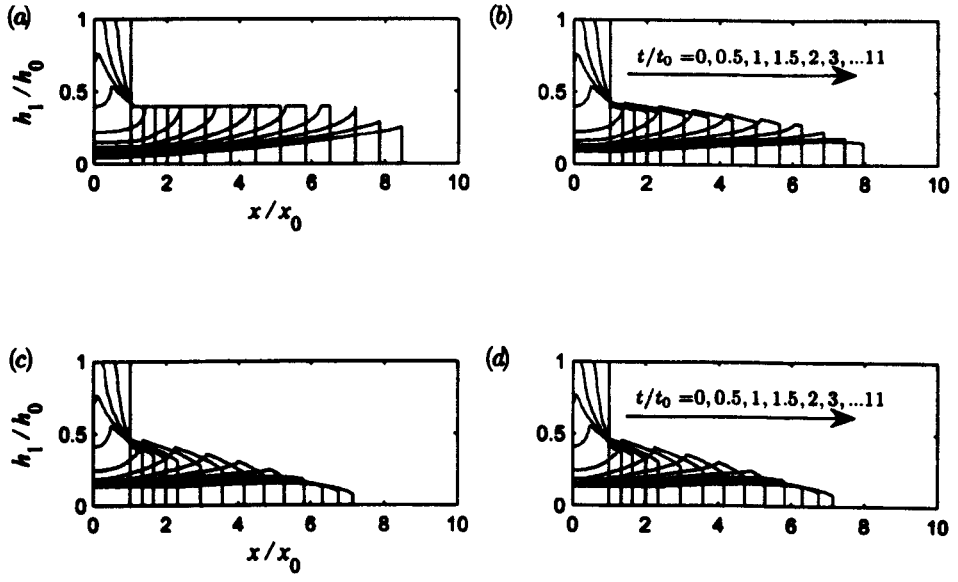

Figure 3.15: Theoretical depth profiles for $h_0/H = 0.5$ using the front condition of Rottman and Simpson (1983) with $\beta^2 = 2$ and (*a*) a smooth bed. Rough cases with $f_1 = f_2 = f_3 = 0.1$ (*b*) $C_1 = 1$, $C_2 = C_3 = 0$, (*c*) $C_1 = C_2 = 1$, $C_3 = 0$ and (*d*) $C_1 = C_2 = C_3 = 1$. Where C_1, C_2 and C_3 indicate rough (1) or smooth (0) influence on the bed, interface and top wall, respectively.

are valid for ratios $0 < h_0/H \leq 0.5$.

Rough bed

Theoretical 1D depth and velocity profiles are shown with roughness present in figures 3.15 and 3.16, respectively. Both of these figures confirm that the roughness influenced current does not propagate as far in the same time period as the smooth case. As for the smooth case, the depth of the current front at later times is significantly reduced, however, when any roughness is present, the current body does not thin as substantially as the smooth equivalent and at later times, is almost the same depth as the head. In fact, when the roughness is included on the interface also (figure 3.15 (*c*)), this is exaggerated to the extent that the current is deeper behind the front and is almost of uniform depth throughout back to the tail. In all rough bed cases, the head region that was previously defined behind the current front in the smooth case is deeper than the front itself. In laboratory gravity currents this is physically observed, the current has a deep head and a reduced height nose. These characteristics are not picked up by the smooth case, probably due to lack of drag in the equations. Therefore, this difference in the smooth and rough cases observed in the theoretical depth outlines in figure 3.15 suggests that in the presence of roughness the head height behind the current further

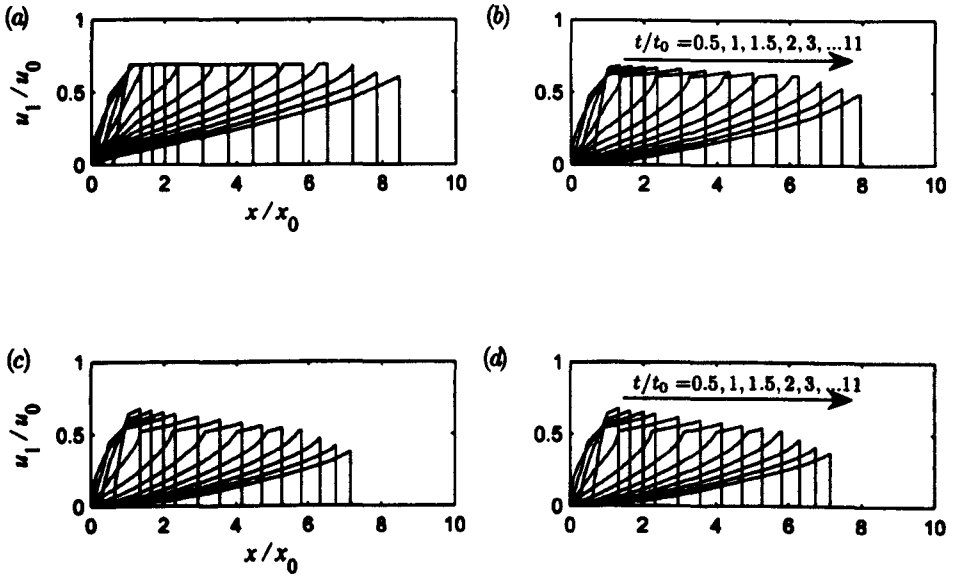

Figure 3.16: Theoretical velocity profiles for $h_0/H = 0.5$ using the front condition of Rottman and Simpson (1983) with $\beta^2 = 2$ and (a) a smooth bed. Rough cases with $f_1 = f_2 = f_3 = 0.1$ (b) $C_1 = 1$, $C_2 = C_3 = 0$, (c) $C_1 = C_2 = 1$, $C_3 = 0$ and (d) $C_1 = C_2 = C_3 = 1$. Where C_1, C_2 and C_3 indicate rough (1) or smooth (0) influence on the bed, interface and top wall, respectively.

increases and the rounding of the head towards the front becomes more exaggerated.

The velocity profiles presented in figure 3.16 show that the deeper region behind the head observed in the corresponding depth profiles in figure 3.15, is slower fluid than the front itself. This head region is still clearly defined as faster than the rest of the current behind it but it does not maintain the same speed as the front as in the smooth case. The front velocity clearly decreases sooner with a rough bed than a smooth bed. When there is only roughness on the bed (3.16 (b)), this decrease occurs at $t/t_0 \approx 3$, while in the smooth case, this value is approximately 8. This is exaggerated further when the interfacial roughness effects are included and the current begins to lose speed almost immediately. Again, in the above, little difference is observed with or without the roughness included on the top wall.

The theoretical depth and velocity profiles presenting the effects of changing the magnitude of the roughness are shown in figures 3.17 and 3.18, respectively. It can be seen that reducing the roughness value to $f_1 = 0.05$ produces significantly less effect on the flow (figures 3.17 and 3.18 (a)), although even at this value, the depth of the current behind the head is slightly increased and the corresponding velocity is decreased. The increased roughness magnitude, $f_1 = 0.2$, shows a further decrease in current speed and height that occurs sooner than the cases with smaller roughness values (figures 3.17 and

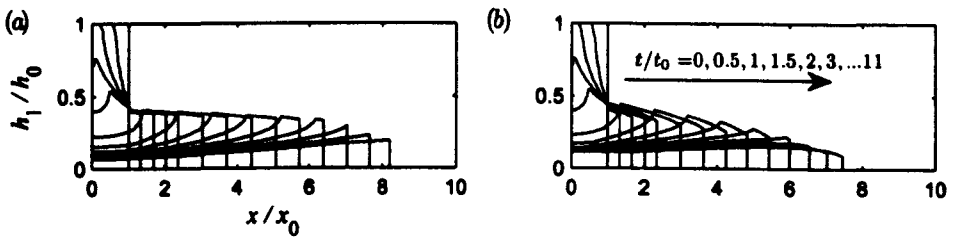

Figure 3.17: Theoretical depth profiles for $h_0/H = 0.5$ using the front condition of Rottman and Simpson (1983) with $\beta^2 = 2$ with roughness on the bed, i.e. $C_1 = 1$, $C_2 = C_3 = 0$. (*a*) $f_1 = 0.05$, (*b*) $f_1 = 0.2$. Where C_1, C_2 and C_3 indicate rough (1) or smooth (0) influence on the bed, interface and top wall, respectively.

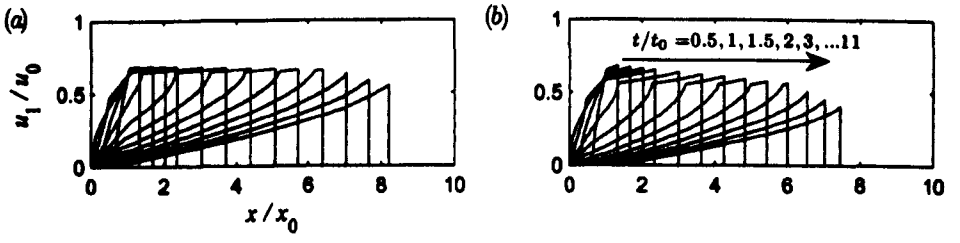

Figure 3.18: Theoretical velocity profiles for $h_0/H = 0.5$ using the front condition of Rottman and Simpson (1983) with $\beta^2 = 2$ with roughness on the bed, i.e. $C_1 = 1$, $C_2 = C_3 = 0$. (*a*) $f_1 = 0.05$, (*b*) $f_1 = 0.2$. Where C_1, C_2 and C_3 indicate rough (1) or smooth (0) influence on the bed, interface and top wall, respectively.

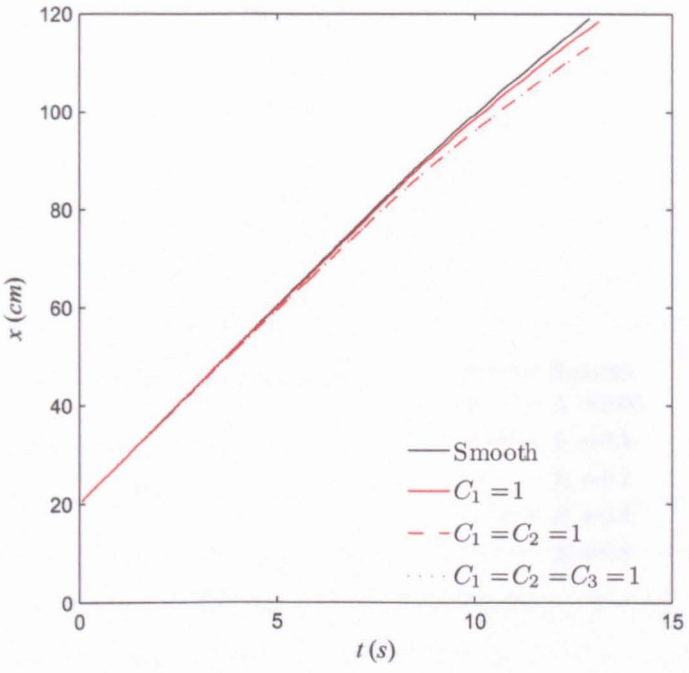

Figure 3.19: Position of the gravity current front as a function of time for $h_0/H = 0.5$ using the front condition of Rottman and Simpson (1983) with $\beta^2 = 2$. Results shown are for a smooth bed and rough cases with $f_1 = f_2 = f_3 = 0.1$ and $C_1 = 1$ with $C_2 = C_3 = 0$, $C_1 = C_2 = 1$ and $C_3 = 0$ and $C_1 = C_2 = C_3 = 1$. Where C_1, C_2 and C_3 indicate rough (1) or smooth (0) influence on the bed, interface and top wall, respectively.

3.18 (*b*)). Moreover, when the roughness effect is increased, the current front height decreases to the extent that it is lower than the rest of the head and indeed the current body and tail. The current depth observed in figure 3.17 (*b*) is almost uniform for later times. It appears that the slowing effects of the bed roughness cause the current fluid to be redistributed more evenly along the current length, rather than accumulating in the head as in the smooth case.

3.7.4 Front position

The effects of bed roughness on the front position of a gravity current are shown in figure 3.19. As observed in the characteristic diagrams and the depth and velocity profiles, the current front does not propagate as far in the same time period under the influence of roughness on the bed (C_1). However, with roughness of this magnitude ($f_1 = 0.1$), the current does appear to propagate with the same constant speed as the smooth case until $t \approx 7.5$ when the rough case slows. When the effects of roughness are also felt at the interface, this retardation is exaggerated and deviates from the constant speed sooner at $t \approx 5$.

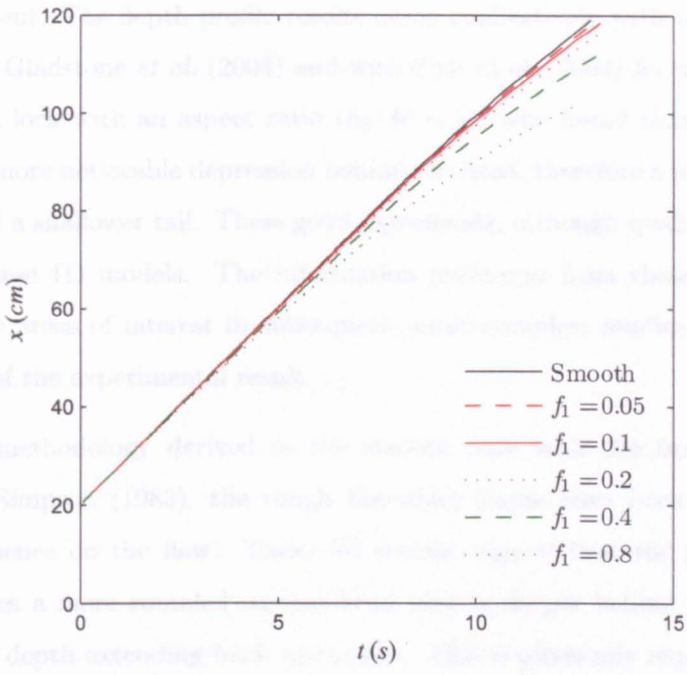

Figure 3.20: Position of the gravity current front as a function of time for $h_0/H = 0.5$ using the front condition of Rottman and Simpson (1983) with $\beta^2 = 2$. Results shown are for the smooth case and with roughness on the bed i.e. $C_1 = 1$, $C_2 = C_3 = 0$ with $f_1 = 0.05$, $f_1 = 0.1$, $f_1 = 0.2$, $f_1 = 0.4$ and $f_1 = 0.8$. Where C_1, C_2 and C_3 indicate rough (1) or smooth (0) influence on the bed, interface and top wall, respectively.

Figure 3.20 shows the effect of changing the magnitude of the roughness value f_1 on the position of the front over time, compared to the smooth case. It can be observed that the reduced value enables the front to maintain its speed while the increased value decreases the distance that the current can propagate in the same time period. Due to the ease of processing this dataset, additional values of $f_1 = 0.4$ and 0.8 have also been included to highlight the influence of the bed roughness. Therefore, it is also apparent from figure 3.20 that the time period over which the current maintains an approximately constant speed is reducing as the magnitude of the bed roughness increases, i.e. the current is slowing earlier.

3.8 Discussion

The results presented above indicate that the method of characteristics with the inclusion of a front condition gives good agreement with experimental front speeds and heights and provides a good approximation to the position of the front of a gravity current. The characteristics of the flow can easily be displayed along with the depth and velocity profiles along the current and have been confirmed to show a good interpretation of a

laboratory current. The depth profile results agree qualitatively with the experimental observations of Gladstone *et al.* (2004) and with Shin *et al.* (2004) for a gravity current released from a lock with an aspect ratio ($h_0/H < 1$), who found that smaller release heights have a more noticeable depression behind the head, therefore a more pronounced raised head and a shallower tail. These good agreements, although qualitative, highlight the value of these 1D models. The information generated from these results can be used to identify areas of interest in subsequent, more complex, studies and indeed aid interpretation of the experimental result.

Adopting the methodology derived in the smooth case with the front condition of Rottman and Simpson (1983), the rough boundary terms have been shown to have significant influence on the flow. These 1D results suggest that the presence of bed roughness causes a more rounded current head that is deeper behind the front and a greater current depth extending back to the tail. This is physically explicable since, as the current is being retarded, the slumping fluid is slower, as shown, and therefore appears to spread more evenly over the length of the current rather than rushing towards the head leaving a shallow tail and creating a 'head-heavy' current as in the smooth case. Moreover, modifications to the current head were observed in the experiments in chapter 2, the most relevant here being the shortening of the head length. It is difficult to confirm this with a 1D illustration of the depth but the present theory does suggest a more rounded and perhaps shorter head region behind the front for earlier times.

Under the influence of bed roughness, the 1D gravity currents eventually propagate at a slower speed than the smooth equivalent but they still propagate at a constant speed for the initial period of time before slowing. The extent of this period has been shown to depend on the magnitude of the roughness on the bed, decreasing with increasing magnitude as might be expected. It also depends on whether the interfacial influence is included. When this factor is activated, the current slows much earlier. The retention of this constant speed phase in the rough cases is in qualitative agreement with the experimental results reported herein, which also observed that the current moved at a similar speed to the smooth case for a period, before slowing. The size of the decrease in speed in the physical experiments was shown to be dependent on the type of roughness, which could correlate to increasing magnitude of roughness value in the present theory. Also in qualitative agreement with the experimental observations for the rough cases, is the reduced downstream velocity behind the front. This was observed for all rough cases and is supported in the theory presented here.

The solutions implementing the front condition derived by Shin *et al.* (2004) appear in closer agreement with experimental data than the same method using the front condition of Rottman and Simpson (1983) or box models of Huppert and Simpson (1980) for the smooth case. This maybe because it is a more theoretical derivation with no free parameters or ambiguous values. It is possible that this theory could be extended to incorporate the effects of bed roughness at the front. This would be an interesting extension to the present study since it would highlight the affects of using the smooth front condition on the current results, as done at present.

These results provide evidence that the inclusion of additional terms into the 2-layer shallow water equations to describe the 'frictional' effects of bed roughness directly at the bed and the influence at the interface between the dense and ambient fluids produce significant results on the current propagation, even in a simplified 1D model that does account for the buoyancy induced changes due to the over-ridden ambient fluid. These predictions further confirm that roughness effects on gravity currents should not be ignored in theoretical models. The immediate implications of these results for real life sediment-laden gravity currents are thicker, slower currents than predicted by smooth models, potentially resulting in more deposition further upstream and more evenly dispersed sedimentation along the current length. Further examination of the flow dynamics with CFD are reported in chapters 5 and 6 enabling further assessment of this interpretation.

Chapter 4

Depth-resolved numerical simulations: Methodology

4.1 Introduction

The previous chapter presented results from depth-averaged, simplified theoretical models. This chapter describes the governing equations and numerical schemes used with the commercial software FLUENT to generate fully depth-resolved models for gravity current flows over smooth and rough surfaces in two and three dimensions. The general model is second order accurate in time and space and a turbulence model is used for closure of the governing equations. Two different methods for the inclusion of bed roughness are proposed along with procedures for verification and validation of the numerical calculations. Full verification, validation with experimental data (see chapter 2) and the results of the 2D and 3D simulations can be found in chapter 5.

4.2 Literature review

The application of depth-resolved 2D and 3D numerical models to the study of gravity currents has become increasingly common during the last few decades and continues to advance with the advance of computing capabilities and the consequent development of more sophisticated models. Models for turbulence closure of the Reynolds-Averaged Navier-Stokes (RANS) equations are continually being improved upon, while the increase in computational power available also means that the ability to resolve gravity current simulations at increasingly high Reynolds numbers with less assumptions has become a more obtainable reality, for example, Large Eddy Simulations (LES) or Direct Numerical Simulations (DNS). Despite technological advances and model development, there is no

one definitive model for non - linear flows such as gravity currents (Straka *et al.*, 1993). Models have to be appropriately selected for the required analyses, for example, prioritising quantitative accuracy or speed of solution or qualitative visualisation might influence model selection. The increasing use of 2D and 3D numerical modelling as an analytical and predictive tool has encouraged the development of commercial CFD software to facilitate modelling and reduce the need for advanced programming specialisation, for example, FLUENT. These packages also undergo continual development and testing of their capabilities, as highlighted by the present study.

This review aims to cover some of the fundamental developments in the numerical modelling of gravity currents and to discuss some of the choices made when selecting solution methods for a study and the merits and drawbacks of these methods. To the author's knowledge there is no one document summarising the existing research on the application of numerical models to gravity currents. Rigorous tests of the accuracy of direct numerical simulations with various solution methods and grids are summarised in Straka *et al.* (1993). However it should be noted that this work is over a decade old and substantial advances in computer power mean that modelling capabilities have increased and an up to date review would be beneficial. The inclusion of bed roughness in the numerical models is discussed herein. A summary of CFD of single-phase flow over rough surfaces can be found in Patel (1998), which also highlights the difficulties involved in modelling bed roughness computationally. To date there is little existing work to warrant an equivalent compilation for gravity currents.

4.2.1 Governing equations: RANS vs. LES and DNS

Turbulent flows are characterised by fluctuating velocity fields which cause the fluctuation and mixing of other flow quantities such as momentum, energy and species. It is the scale of these fluctuations that is the main cause of computational expense. The general governing equations that describe turbulent fluid flow are the Navier - Stokes equations. DNS is when all scales of motion are fully resolved in space and time. The smallest turbulent scales with high frequencies can be too computationally expensive to simulate using DNS in practical engineering calculations without access to substantial computing processes. Reynolds averaging the Navier - Stokes equations involves decomposing the flow quantities into mean and fluctuating components, substituting these expressions into the full set of equations and then takes a time average to obtain the Reynolds-averaged Navier-Stokes equations. The small scales are removed and therefore this system of

equations is more computationally economical. However, the averaging process creates additional unknown variables that require the modelling of turbulence transport for closure, thus limitations are incurred and a 'turbulence model' must be carefully chosen to represent the flow dynamics. There is no single turbulence model that is universally accepted as being superior for all classes of problems (FLUENT, 2006). A general overview of the derivation and uses of several existing turbulence models can be found in Hartel (2000).

In order to include the different flow phases of the current and ambient fluids, supplementary equations for context-specific model scalars or species transport have also been added (e.g. Straka *et al.*, 1993 and Imran *et al.*, 2004, respectively), in addition to the mass and momentum conservation equations, and solved either directly or in Reynolds - averaged form. Equations for the transport of concentration and temperature variables are particularly important in the study of gravity currents and are the common method for modelling the dense underlying fluid (e.g. Baum *et al.*, 1995 and Straka *et al.*, 1993, respectively).

Gravity currents have been modelled relatively successfully with the RANS equations and a turbulence model for lock-release (Chen and Lee, 1999; Zhang *et al.*, 2001; Cantero *et al.*, 2003; Bombardelli *et al.*, 2004; Corney, 2005), lock-exchange (Klemp *et al.*, 1994; Kanarska and Maderich, 2003) and flux induced (Bournet *et al.*, 1999; Kassem and Imran, 2001; Imran *et al.*, 2004; Kassem and Imran, 2004) conditions over smooth beds. Of these, the two equation $k-\varepsilon$ turbulence model modified for buoyancy has been most widely used with near wall treatment using standard wall functions (Bournet *et al.*, 1999; Chen and Lee, 1999; Kassem and Imran, 2001; Imran *et al.*, 2004; Kassem and Imran, 2004). However, the study of Zhang *et al.* (2001) used an enhanced wall function method with two equations for wall adjacent motion. Other turbulence closure models that have been implemented with similar success are the two equation $k-l$ model (Kanarska and Maderich, 2003), a Newtonian model for the viscous stresses (Cantero *et al.*, 2003; Bombardelli *et al.*, 2004) and a first order closure scheme that depends on the relative strengths of stratification and shear (Klemp *et al.*, 1994). All of these models have been shown to display typical gravity current characteristics and to compare reasonably well to experimental data for front velocities (within known dimensional limitations if the model is 2D, see section 4.2.3) and mean velocity profiles. In fact, Kanarska and Maderich (2003) show that their model compares well qualitatively to the DNS of Hartel *et al.* (2000b). However, fully accurate solution of small scale turbulence structures and correspondingly precise turbulence profiles are beyond the capabilities of

these models. This is exemplified in Fukushima and Watanabe (1990) where the $k-\varepsilon$ model underpredicts the turbulence kinetic energy and dissipation distribution within the flow.

An alternative approach that bridges the gap between DNS and RANS simulations is large eddy simulation (LES), whereby the large eddies are explicitly resolved using 'filtered' Navier-Stokes equations (see Hartel (2000)). The full Navier-Stokes equations are manipulated mathematically to remove eddies that are smaller than the size of a filter, which is often the size of the grid (Patterson *et al.*, 2005). Although additional unknown terms still result in the need for modelling to achieve closure, similar to Reynolds-averaging, the smaller scales that require modelling tend to be more isotropic and less affected by features that govern the main body of the flow, like boundary conditions, than the larger eddies that are now fully resolved. The consequences of this filtering process are large eddy simulations that directly solve less turbulence but at higher resolution thus reducing the error introduced by modelling. However, to accurately resolve the energy containing turbulent eddies in time and space for high Reynolds number flows requires significantly greater computer resources than the RANS approach with a turbulence model. But, in comparison to DNS, gravity current simulations using LES are generally computationally quicker and can reach a higher range of Reynolds numbers while retaining good qualitative experimental comparison, as shown by Patterson *et al.* (2005). A 2D study by Ooi *et al.* () showed good agreement with the experimental results of Hacker *et al.* (1996) but with resolution of billows right up to the front which is questionable. Baum *et al.* (1995), Rehm *et al.* (1995) and Fleischmann and McGrattan (1999) also successfully modelled gravity current transport in building fires with LES with good comparison to experimental data. The most extensive work using LES to model gravity currents is in the oceanic modelling of saline underflows (Özgökmen and Chassignet, 2002; Özgöokmen *et al.*, 2003, 2004a, 2004b, 2006, 2007; Özgökmen and Fischer, 2008). They use a 3D non-hydrostatic, spectral element model that combines the high order accuracy of spectral element methods with finite element methods, which enables two methods of achieving convergence: refinement of the grid elements or increase of the polynomial degree used in the intra-element interpolation. A minimum number of elements can be used so that the shape of the domain geometry is adequately captured, then the spectral truncation degree is increased for convergence (Özgökmen *et al.*, 2004b). A known benefit of spectral methods is their lack of numerical dissipation and dispersion errors which is important in problems with propagation of high flow variable gradients and mixing as found in gravity currents. Although slightly dated

now, the review undertaken by Straka *et al.* (1993) finds that high order spectral type schemes perform better than many other methods if the mesh refinement is adequate or even marginal, however these methods were virtually unusable at low mesh resolution due to the amount of computational noise produced. Other monotonic schemes suffered from damping characteristics resulting in less accurate flow features and slower velocities, however, they were able to solve at all levels of mesh refinement.

DNS typically requires fine resolution in order to achieve a converged solution of turbulent fluid motion (Straka *et al.*, 1993). Therefore, as the Reynolds number of the flow and hence the turbulence, increase, further refinement is necessary to retain accuracy. As this continues, the computational cost eventually becomes prohibitive and even modern day parallel processing systems are incapable of solution. Consequently, careful consideration of the scheme used for treatment of the governing equations is necessary to optimise computational expenditure. The first high resolution direct numerical simulation of gravity currents in 2D was carried out for a lock-exchange flow by Hartel *et al.* (1997). This was improved upon and extended to 3D by Hartel *et al.* (2000b) and Hartel *et al.* (2000a) for an in depth study of velocities, front speeds and the lobe and cleft instability. It was further modified for a lock-release study with the inclusion of particles by Necker *et al.* (2002) and Necker *et al.* (2005). They use a mixed spectral/spectral element approach similar to that described previously. The spectral based methodology has been applied to non-Boussinesq lock-release currents (Birman *et al.*, 2005) with successful experimental validation. Recently Cantero *et al.* (2008a;2008b) also performed DNS of depositional particulate density currents in order to study the effects of particle inertia using a psuedo-spectral method. To the author's knowledge, all of the DNS studies of gravity currents have been carried out using spectral/spectral element methods, only LES and RANS models requiring turbulence closure have been undertaken using other approaches such as finite volume methods.

One final consideration that should be taken into account when selecting the turbulence model, and is of particular relevance to the present study, is the physical boundaries of the domain. For example, the presence of non-smooth bounding wall geometries will incur further turbulence modelling complexities. Some relevant cases are discussed in section 4.2.5.

4.2.2 Initial and boundary conditions

Numerical simulations are usually used in conjunction with experimental data for validation and therefore the initial and boundary conditions should reflect the tank setup that has been used. However, some aspects of the experimental configuration present further difficulties in numerical modelling, for example, a free surface is nearly always present at the upper boundary of the domain. The most commonly used method of modelling the free surface is to use a fixed rigid lid and apply no flux, symmetry flow conditions along this boundary. Some studies use no-slip boundaries (Hartel *et al.*, 2000b; Hartel *et al.*, 2000a; Necker *et al.*, 2002; Necker *et al.*, 2005) based on the fact that impurities in the fluids in laboratory flows make a free surface act as a no-slip surface (Britter and Simpson, 1978) and several have included equations to model the surface elevation (Harlow and Welch, 1965; Daly and Pracht, 1968; Fukushima and Watanabe, 1990; Kanarska and Maderich, 2003). However, validation with experimental data shows that the error incurred in using a simple fixed lid, symmetry boundary appears to have little effect on the accuracy of results. In nearly all CFD studies the bottom wall and, if 3D, often the side walls are set with no-slip boundary conditions since this is perceived as more physical unless the difference in slip and no-slip conditions is of specific interest (Hartel *et al.*, 2000b). For the modelling of a more complex bed with, for example, a form or grain roughness (or both) present, the boundary conditions can play an important part in accounting for these features in a model. Section 4.2.5 covers this aspect in more detail.

The flow inducing mechanism is an important initial condition that needs careful calibration in numerical modelling. For lock-release and lock-exchange cases, the flow is typically initialised at rest throughout the domain and when the simulation starts, gravitational effects on the density difference between the cells initialised with higher density and those with lower values, instigate immediate reaction within the domain, analogous to instantaneous release of fluid from the lock. Thus flow commences instantaneously. However, some turbulence initialisation is often required, although values are not often stated explicitly in model descriptions and choice of magnitude appears to vary: Chen and Lee (1999) and Zhang *et al.* (2001) initialise turbulence kinetic energy and dissipation with negligibly small values of $O(10^{-7}m^2s^{-2})$ while Corney (2005) uses a larger value of $O(10^{-4}m^2s^{-2})$. To the author's knowledge there is no experimental data available with lock release initial conditions from which to obtain empirical values of initial turbulence parameters. Fukushima and Watanabe (1990) quote a value of about $1 \times 10^{-7}m^2s^{-2}$

for turbulence kinetic energy within the tank measured prior to a flux induced release. Necker *et al.* (2002) and Necker *et al.* (2005) impose weak turbulence disturbances in the velocity field in the vicinity of the interface in order to enhance the breakdown of the flow into 3D after release. Necker *et al.* (2005) carried out a study of the influence of this initial turbulence in their work on particle driven currents. They increased the initial turbulence kinetic energy in the domain with all other conditions identical and found that the main effect is strongly enhanced mixing within the current fluid and stronger initial turbulence fields which lead to earlier breakdown of the coherent vortices that form behind the head of the current. However, these only result in minor differences in overall flow development reflected in slightly higher front velocities maintained at later times with higher initial kinetic energy. They postulate that the lack of substantial flow altering effects is due to the turbulent motion that exists prior to release being quickly damped by dissipation from the flow acceleration during the formation of the current front.

In addition to turbulence perturbations, Hartel *et al.* (1997), Hartel *et al.* (2000b), Hartel *et al.* (2000a), and Birman *et al.* (2005) use an initial density field with an error function profile whilst Straka *et al.* (1993), Hartel *et al.* (1997) and Bongolan-Walsh *et al.* (2006) apply an initial temperature profile to the domain. Özgökmen *et al.* (2004b), Özgökmen *et al.* (2004a) and Özgökmen and Fischer (2008) also use a lateral sinusoidal salinity perturbation in their initial flux induced conditions to facilitate transition into 3D flow, see figure 4.1 (*a*) p. 165. In flux induced currents, a velocity profile is imposed at the inflow, for example Imran *et al.* (2004) and Kassem and Imran (2004) impose plug flow velocity conditions. Özgökmen *et al.* (2004a), Özgökmen *et al.* (2004b), Özgökmen and Fischer (2008) and Bongolan-Walsh *et al.* (2006) use a time-dependent velocity profile dependent on the propagation speed of the gravity current with reversed flow in the overlying fluid to prevent recirculating flow at the inlet or thinning of the density current downstream which can occur due to inadequate rate of supply (Özgökmen *et al.*, 2004b), see figure 4.1 (*f*) p. 165. Fukushima and Watanabe (1990) also impose a velocity profile inflow from empirical data, however, their results do not model the return flow accurately which could be due to an insufficient return flow condition.

4.2.3 2D vs. 3D models

One of the first studies dedicated specifically to the numerical modelling of gravity currents was undertaken by Daly and Pracht (1968), with the intention that their 2D nu-

merical study could be used as a useful aid to analytical models. While a 2D model fulfills this purpose, 3D models extend this to provide a solution where analytical methods are far more complicated without limiting assumptions. Birman *et al.* (2005) use a 2D model to confirm which of the physical scenarios generated in parallel experimental work (Lowe *et al.*, 2005) is observed in reality. Thus, if their 2D model gives clear confirmation of the physics, an extension to 3D is unnecessary unless further detail beyond the capability of 2D is of interest. Several models in 2D have been developed since that of Harlow and Welch (1965) and Daly and Pracht (1968) and are able to resolve the basic flow characteristics for early times (up to approximately 10 nondimensional time units (Necker *et al.*, 2002)). Hartel *et al.* (2000b) demonstrate that a 2D DNS model can reliably predict integral values such as the Froude number and also more subtle aspects of the flow such as the elevation of the nose and details of the flow structure within the gravity current head (note that this is a DNS simulation). However, the accuracy of the flow characteristics and the resulting data have been shown to diverge from the 3D and experimental datasets for later times (Necker *et al.*, 2002). Although several other variables affect the magnitude of this deviation from the 'true' data (e.g. grid resolution, RANS/DNS, solution schemes etc.) it is generally acknowledged (e.g. Hartel *et al.*, 1997; Necker *et al.*, 2002; Cantero *et al.*, 2003; Patterson *et al.*, 2005) that this is primarily due to the unphysical retention of the large vortices or billows that are not broken down into smaller scales as a consequence of the two-dimensionality of the simulation and hence absence of necessary 3D mechanisms. The resultant effect is increased entrainment of fresh water into the underflow so that the salt water is excessively diluted and the current cannot retain its speed leading to underestimation of the front velocity. The presence of this lateral component of velocity, particularly within the large billows at the interface, is clearly visualised in the results of a 3D simulation carried out by Cantero *et al.* (2003). Quantitative differences in concentration resulting from this limitation have been illustrated by Necker *et al.* (2002) in a comparison of the concentration of a 2D simulation with the centreline of a 3D equivalent.

The main limitation to 3D simulations is the computational cost. As mentioned previously, even with the modern day supercomputers, the increased mesh size and hence number of calculations necessary during computation can result in prohibitively high processing requirements. For example, Hartel *et al.* (2000b) use a 2D mesh of resolution 768×91 (69888 cells) but their 3D mesh has about 4.25 million grid points for simulations at comparative low Reynolds numbers (710 and 750 respectively). Consequently, the Reynolds number dependent, fine meshed, 3D direct numerical gravity current sim-

ulations are extremely limited in the range of Re values that can be studied, while in 2D they can achieve a range of Re values which enables the study of effects of changes in Re and more interesting high Re cases. The difference in real time cost is also substantial, as illustrated by the work of Özgökmen *et al.* (2004b) who carried out 2D LES that took about two hours on 16 processors, while their 3D equivalent runs took 9 days on 32 processors. Moreover, if the effects of particles are included in the flow, as in the recent work of Cantero *et al.* (2008a; 2008b), the computational cost increases further since the mesh must be finer. Thus, even with modern computing power, a 2D model is adopted so that DNS can be performed. Hence, despite known limitations, 2D approximations are still used as a less computationally expensive approach to investigate the general behaviour of gravity currents.

4.2.4 Independent codes vs. commercial codes

Several studies document the development of independent codes for the solution of the equations governing gravity current motion. As modern computing capabilities advance, the ability to generate complex fluid flow models to simulate physical flow processes, before further actions are undertaken in reality, has increased demand for codes that are more flexible and commercially accessible, hence the development of commercial CFD software.

The earliest gravity current models date back several decades (Harlow and Welch, 1965; Daly and Pracht, 1968) but independent numerical models for similar phenomena, for example, jets or plumes, were developed previous to this. Straka *et al.* (1993) summarises the results of several researchers who have modelled a gravity current phenomenon with independent DNS codes implementing different schemes. These codes can take considerable time to write and modify and can be very variable in accuracy and dependent on mesh and method chosen (Straka *et al.*, 1993). They are often complex and difficult to understand by anyone other than the code developers. The immediate advantages of commercial software are that several modelling algorithms are usually available for time and space discretisation, scalar transport equations for variables such as concentration can easily be added and there are a variety of models available for turbulence closure of the RANS. Added to these, is the flexibility to change the 'physical effects' in the model with the click of a button to allow the incorporation of almost any physical behaviour (De Cesare *et al.*, 2001). There are drawbacks however and in a comparative study, Bombardelli *et al.* (2004) state that independent codes give a more true solution to the

Navier-Stokes equations despite the fact that they might not look as physically representative of the experiments as the commercial code generated result. In their simulations, the commercial codes exhibit damped characteristics due to increased numerical diffusion applied in these codes in order to increase chances of convergence and hence appear more physical. They used 20500 nodes for their independent code and 58500 for their commercial code and found that mesh refinement resulted in no change for their own code but large changes with the commercial code, thus commercial code requires many more cells to achieve the same qualitative results as the independent code. Bombardelli *et al.* (2004) postulate that these limitations are due to numerical limiters and 'stability tricks' present in commercial codes to increase robustness resulting in numerical over-damping which is particularly inadequate for instability driven flows such as gravity currents. It should be noted that this study does only compare one independent and one (unnamed) commercial code when, as mentioned previously, there is no generally accepted definitive model for simulating gravity currents and there are various modelling options and solution methods available that may alter this comparison. For example, most commercial code enables the inclusion of user-defined functions which are particularly useful for flexibility in defining source terms, variable flow scalars and other modifications required. The results of Bombardelli *et al.* (2004) imply that commercial codes require the same careful validation and verification as is necessary for all numerical codes.

Some other work has been carried out on gravity currents using commercial codes. Bournet *et al.* (1999) studied a plunging gravity current using the commercial software PHOENICS with the RANS and a $k-\varepsilon$, buoyancy modified turbulence model. They found that their model seemed capable of reproducing entrainment values within the range of the existing experimental values and reasonable agreement with the known characteristics of plunging currents. However, lack of laboratory and field studies at the time meant that they had to validate their model primarily using another semi-empirical model without access to data describing mean flow properties or local flow structures which are essential for model formulation and input values. De Cesare *et al.* (2001) used CFDS-CFX-4 (now ANSYS-CFX) to model sedimentation from turbidity currents entering reservoirs. The study used the RANS with a $k-\varepsilon$ turbulence model and an additional equation for the concentration that incorporated a particle settling velocity. They also applied user defined modules for sedimentation and erosion. Their results showed good agreement with the lateral spreading of a clay-laden laboratory current. Corney (2005) conducted an in depth study in 2D and 3D using the commercial software FLUENT and discusses several solution schemes and options available for that user in-

terface. The results are vigorously verified and validated and limitations are observed and acknowledged. Chen and Lee (1999), Zhang *et al.* (2001), Imran *et al.* (2004) and Kassem and Imran (2004) have also modelled gravity current flow using FLUENT with different conditions and domain configurations. Chen and Lee (1999) and Zhang *et al.* (2001) found good agreement with their results and the general features observed in the laboratory, however their work is only first order accurate in time which has subsequently been shown to limit validity (Corney, 2005). Imran *et al.* (2004) and Kassem and Imran (2004) simulated the flow of a flux initialised current in straight and sinuous, open and confined channels. There was no reference to grid accuracy tests for verification of the models but they do acknowledge that their results should be treated with caution until validated with laboratory data. The analytical and experimental model of Corney *et al.* (2006) contradicts Kassem and Imran (2004) thus highlighting the importance of verification and validation. It is interesting to note that in a discussion of Corney *et al.* (2006), Imran *et al.* (2008) retrospectively present a qualitative examination of the influence of changing the grids on the predictions of Kassem and Imran (2004).

4.2.5 Modelling of bed roughness

To the authors knowledge, there is very little gravity current literature that explicitly examines the effects of bed roughness on the dynamics of gravity currents using numerical simulations. There have been several studies that model the spread of gravity currents over topography in planform but without detail of the internal flow structure (e.g. De Cesare *et al.*, 2001, Özsoy *et al.*, 2001). Özgökmen *et al.* (2003) have numerically modelled the salinity and temperature distributions and velocity field of the gravity current that occurs over a natural bed at the Red Sea outflow but this is a case-specific study and they did not aim to quantitatively study the effects of different roughness parameters on the flow. In subsequent studies (Özgökmen *et al.*, 2004b; Özgökmen *et al.*, 2004a) a more analytical approach has been adopted to study the effects of a small scale, O(1 km) (domain size is 10 km long by 2 km wide), 'bumpy' bed on entrainment in gravity currents. Their 'Nek5000' code has been used to solve non-hydrostatic governing equations using a spectral element method (see section 4.2.1 for discussion of this approach). The bumpy bed is generated by creating a mesh fitted to the geometry. The bumps are included by specifying a wavenumber factor and an amplitude factor which describe the frequency and the elevation and depression of the bumps about the horizontal plane origin, see figure 4.1 (*b*) – (*e*). More recently, this study has been extended (Özgökmen and Fischer, 2008) to encompass a rougher bed generated using a similar sinusoidal per-

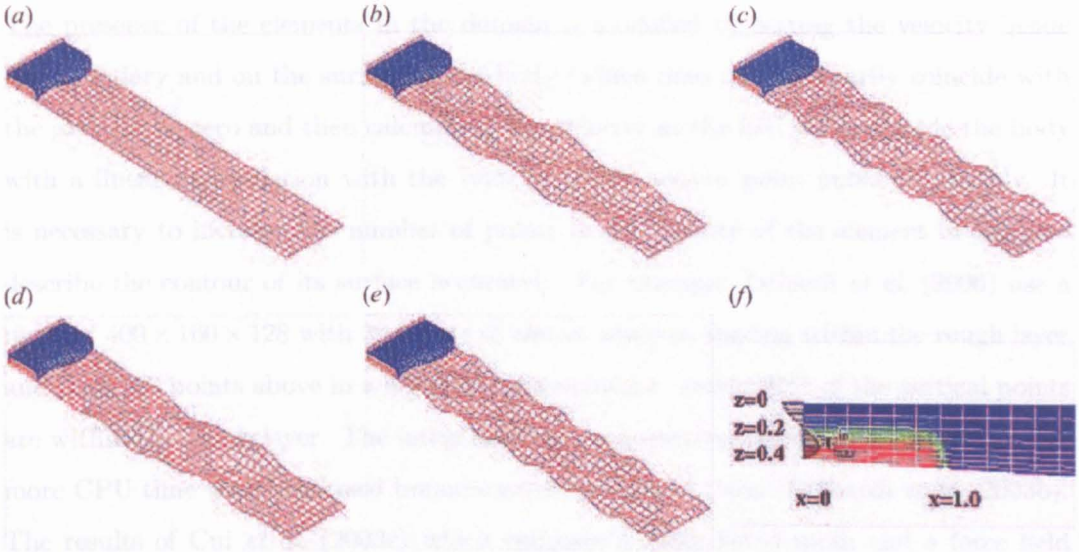

Figure 4.1: (a) The smooth bed model, $(b) - (e)$ the 'bumpy' bed roughness models and (f) the initial conditions of Özgökmen *et al.* (2004a). The domain size is 10 km×2 km such that the bumps are of order O(1 km).

turbation to the bottom boundary of the domain and the same numerical approach, boundary conditions and the majority of the parameters as the previous studies.

Advanced quantitative modelling of bed roughness effects on flow dynamics has been carried out down to very small scales using DNS in 2D and 3D for flow in square ducts with Reynolds numbers up to ≈ 10000. Although this work is not specific to the simulation of gravity current propagation, it is a highly resolved, rigorously verified example of the inclusion of bed roughness in turbulent channel flow and several studies are particularly relevant to the beam-type roughness used in the present study and for illustrating the progression to modelling more complex forms like dunes. Cui *et al.* (2003b), Ashrafian *et al.* (2004), Krogstad *et al.* (2005), Ashrafian and Andersson (2006) and Ikeda and Durbin (2007), among others, successfully use a body-fitted grid around the beam surface which doesn't require additional forcing function techniques. Cui *et al.* (2003a) uses this method for modelling flow over a wavy wall and Yue *et al.* (2005) and Yue *et al.* (2006) apply it to a fixed dune shaped geometry. Several other studies do implement additional forcing techniques, most notably using the 'immersed boundary method' (Fadlun *et al.*, 2000) for the inclusion of 2D square beam-type roughness in 2D and 3D domains (e.g. Leonardi *et al.*, 2003a, Orlandi *et al.*, 2006) or an analogous 'force field' method for 3D flow over a 2D wavy bed (Cui *et al.*, 2003c). This method allows the solution of flows over complex geometries without the need of computationally intensive body-fitted grids. They are particularly useful for irregularly shaped roughness where body fitted grids would result in grid deformation and introduce additional instability.

The presence of the elements in the domain is modelled by setting the velocity inside the boundary and on the surface of the body (which does not necessarily coincide with the grid) to be zero and then calculating the velocity at the first point outside the body with a linear interpolation with the velocity at the second point outside the body. It is necessary to increase the number of points in the vicinity of the element in order to describe the contour of its surface accurately. For example, Orlandi *et al.* (2006) use a mesh of $400 \times 160 \times 128$ with 30 points of almost uniform spacing within the rough layer and then 130 points above in a nonuniform spacing i.e. nearly 20% of the vertical points are within the rough layer. The integration of the governing equations requires only 5% more CPU time with immersed boundaries than without them (Leonardi *et al.*, 2003b). The results of Cui *et al.* (2003c) which compare a body fitted mesh and a force field method show little difference for flow over a wavy wall. However, their example and the above studies are for simple 2D geometries that do not result in high cell deformation with a body fitted method and hence its limitations are not tested.

The numerical modelling of flow in roughened ducts also highlights aspects that require additional consideration for the modelling of bed roughened gravity currents. As discussed previously (section 4.2.3) it is well known that 2D numerical simulations with smooth bed conditions result in inadequate resolution of the large vortices and therefore 3D models that include lateral vortex degeneration mechanisms are required for greater accuracy. Leonardi *et al.* (2004) showed that, for flow in beam-roughened ducts, turbulent vortical structures appear larger in the lateral direction due to the presence of the elements, suggesting a further requirement in 3D modelling of an equivalent gravity current flow. Ikeda and Durbin (2007) agree that because the flow is blocked by the roughness elements, the lateral velocity fluctuation is intensified and this cannot be shown by a 2D model. Studies of the performance of RANS with a turbulence model against LES and DNS have also been carried out in the context of single phase flow in beam - roughened ducts and in channels with fixed dunes. In one LES study, Yoon and Patel (1996) state that the RANS methods are inadequate for modelling the production of coherent structures in flow over fixed dunes. However, they also find a limitation to the LES, it does not adequately account for the upstream flow history. In a comparison with LES, Cui *et al.* (2003b) state that mean velocity profiles calculated with RANS and a turbulence model represent the flow with reasonable accuracy but that there are significant differences between turbulence kinetic energy (TKE) distribution from experimental results and those calculated with the RANS method. Contradictory TKE distributions around the elements have also been observed when compared to DNS

(Ikeda and Durbin, 2007).

The study of Ikeda and Durbin (2007) compares the RANS closed with an eddy viscosity model to DNS, although it should be noted that the RANS model is essentially only a 2D domain while the DNS is 3D. Their results found that the RANS model gives the wrong slope for the log layer velocity profile. They suggest that a reason for this could be that RANS models are calibrated with and dependent on smooth wall data that may not have the correct empirical value to capture the averaged flow over the beam roughness when the geometry is fully resolved. The DNS shows smoothed vortex streaks parallel to the wall for a smooth surface and highly irregular vortex streaks in the rough case. The RANS model does not have the capability to predict the log law displacement caused by these vortices, it is reliant on empirical input which is based on smooth walls and cannot capture the effect of altered turbulence structure. The RANS solution also exhibits an elongated reattachment region between widely spaced elements leading to discrepancies in the modelling of the flow dynamics within the space between the elements with erroneous consequences for the near bed modelling of the flow field. Related to this, Cui *et al.* (2003b) suggest that the RANS approach modified for roughness is suitable for elements with large distances between them but not for closely spaced roughness because it does not account for the effects of spacing. Note that it has, however, been shown that to a first approximation, the closure scheme need not depend on the type of roughness (Leonardi *et al.*, 2003a).

Several CFD studies on flow in open channels and ducts have also investigated ways of implementing a more irregular, non-homogeneous roughness. While all of the above studies apply a no-slip boundary condition on their rough surfaces, some also incorporate the effect of grain type roughnesses as well as the principle form type discussed above. A model that can account for any form roughness with any additional grain roughness is the ultimate aim of many of these studies, including the present work. The main question for the inclusion of grain type roughness is one of how turbulence is to be modelled. Proper treatment of the essential features of the flow demands a numerical method that is robust enough to resolve separating and reattaching flow over a surface of complex geometry, and a turbulence model that is sufficiently accurate to describe such flows and take into account sand grain roughness (Yoon and Patel, 1996). A strict DNS would be almost impossible since the mesh size required to resolve down to the scale of coarse sand, for example, would be prohibitively expensive. The RANS equations with a turbulence model for closure offer a comparatively simple means of including grain roughness through the wall functions or in boundary conditions while retaining a

reasonable size mesh. Yoon and Patel (1996) use the RANS with a $k-\omega$ model for flow over a fixed dune with roughness prescribed through a boundary condition on ω. It should be noted, however, that this model has been shown to be inadequate for the modelling for gravity currents (Corney, 2005). In a similar study, Durbin *et al.* (2001) use a modified $k-\varepsilon$ model with a two-layer approach near the wall and a boundary condition on k. The former find that their model predicts velocity and turbulence fields and pressure and friction distributions and flow separation details in general agreement with experimental data. The latter generates slightly better agreement for these parameters. Durbin *et al.* (2001) also highlight a limitation of the $k-\varepsilon$ model in its inability to describe the near-wall zone, essential to this type of study. Hence they use a two-layer approach rather than wall functions or a 'low Reynolds number' modification.

The primary concern with the use of wall functions is the range of application of the 'log-law' used to model the turbulence near the wall and more disconcertingly, the lack of agreement amongst researchers as to the specification of the two law constants κ, the Von Karman constant, and B whose values in the past have ranged from 0.4 - 0.438 and 5.5 - 6.17, respectively. A summary of different arguments and approaches can be found in (Patel, 1998). Despite these limitations, the $k-\varepsilon$ model is widely used in many areas of fluid dynamics and thus methods for modifying and optimising it for different applications are widely sought after. For example, for atmospheric flow over hilly terrain Kim and Patel (2000) and Kim *et al.* (2000) found that, in particular, the RNG $k-\varepsilon$ model with a body-fitted grid and roughness specified in the wall functions gave good agreement with experimental data for the location of separation and reattachment points and thus the reattachment length (Kim and Patel, 2000). There was also reasonable agreement with field data for models of four different hill topographies (Kim *et al.*, 2000). They conclude that their RNG model is suitable for prediction of local scale wind flow over hilly terrain with or without flow separation.

Although the above methods find good 'general' agreement, the RANS methods have been shown to be inferior for the resolution of coherent structures about dunes, as mentioned in section 4.2.1. With this limitation and the prohibitive expense of DNS, LES models have been developed that show better agreement with the important features of the flow. Cui *et al.* (2003c) carried out a LES study implementing a method that decomposes the roughness into resolved (form) and subgrid (grain) scale roughness, similar to flow decomposition performed in LES. Their idea is that larger, resolved roughness effects the flow momentum and energy dependent on a specific roughness configuration that might be unique to that case study, whereas subgrid scale roughness has less impact

and is expected to have more common features in a variety of problems and can therefore be described more generally. Cui *et al.* (2003c) use a body-fitted grid and a force field method, as discussed previously in this section. The non-resolved subgrid roughness is modelled by a random force distribution which involves the specification of a drag coefficient. Their results show good agreement with experimental data.

Obviously, with the frontal phenomena and instabilities due to stratification involved in modelling gravity currents, the results and treatments used in flow in ducts may not hold equivalently. Gravity currents are highly transient due to the continual entrainment of ambient fluid and they are known to undergo transitions into different regimes at various stages of propagation. In the presence of roughness, it is highly probable that these transitions will be modified in some way incurring further modelling requirements. It should also be taken into account that the aforementioned numerical models of flow in ducts are relatively recent research and still restricted by a limited amount of laboratory work on the topic available for validation (Cui *et al.*, 2003b) despite the fact that research into flow in roughened pipes has been carried out for several decades and, in general, has less flow complexities than gravity currents, as highlighted above. To the author's knowledge, this is the first study to address the lack of both laboratory and numerical data in the research of gravity current flow over bed roughness and hence does not seek to achieve such a high resolution within the timescale of the present study.

4.2.6 Summary

Numerical modelling of complex non-linear flows such as gravity currents is a continually advancing discipline, highly dependent on the computational power available. Clearly, for the greatest accuracy independently coded, 3D DNS should be carried out, however, this is not always feasible without coding specialists and access to several processes running in parallel. 2D RANS with a turbulence model for closure is within the processing capabilities of even a single processor PC and has been shown to model gravity current dynamics with reasonable accuracy when treated with careful analysis and awareness of the model limitations. Similarly, when a commercial code is used, the validity of results is reliant on careful model verification and knowledge of the limitations of the code.

There is a continually expanding amount of literature which documents increasingly high resolution research on the dynamics of gravity current propagation over smooth surfaces. However, only a handful of numerical studies have been carried out on the effect of a more natural bottom boundary or bed roughness. To the author's knowledge, only the

studies of Özgökmen *et al.* (2004a) and Özgökmen and Fischer (2008) have attempted to carry out any quantitative analysis on the effects that different roughness configuration might have on gravity currents but sufficient experimental or field data has yet to be provided for full validation of these studies. Detailed analyses of roughness effects on equivalent single-phase flow in ducts indicate that care should be taken when using 2D RANS models particularly with regards to turbulence kinetic energy distributions near the elements.

4.3 Model setup

4.3.1 General model setup and the lock-box geometry

Continuity and momentum equations

The governing equations are the Navier-Stokes equations for fluid flow, as mentioned previously. Including the continuity equation, for three-dimensional, unsteady flow, they can be written as the following set of equations:

$$\frac{\partial \rho}{\partial t} + \nabla \cdot (\rho \underline{u}) = 0 \tag{4.1}$$

$$\frac{\partial \rho \underline{u}}{\partial t} + \nabla \cdot (\rho \underline{u}\underline{u}) = -\nabla p + \nabla \cdot (\overline{\overline{\tau}}) + \rho \underline{g} + \underline{F} \tag{4.2}$$

where p is the pressure, $\underline{g}$ is the gravitational acceleration, $\underline{F}$ is the external body force (set as zero in the present study) and $\overline{\overline{\tau}}$ is the stress tensor given by

$$\overline{\overline{\tau}} = \mu \left[(\nabla \underline{u} + \nabla \underline{u}^{\mathrm{T}}) - \frac{2}{3} \nabla \cdot \underline{u} I \right] \tag{4.3}$$

where μ is the molecular viscosity and I is the unit tensor.

This is the general system of equations to be used to model flow mass and momentum. Additional equations to model the two phases of the flow and their interaction and the required turbulence parameters are presented in sections 4.3.2 and 4.3.3, respectively.

Numerical geometry, initial and boundary conditions

The numerical domain geometry is generated in the mesh generation package GAMBIT (see FLUENT, 2006 for details). It is maintained as similar to the experimental setup as possible and encompasses a sub-domain that represents the lock-box within which cells

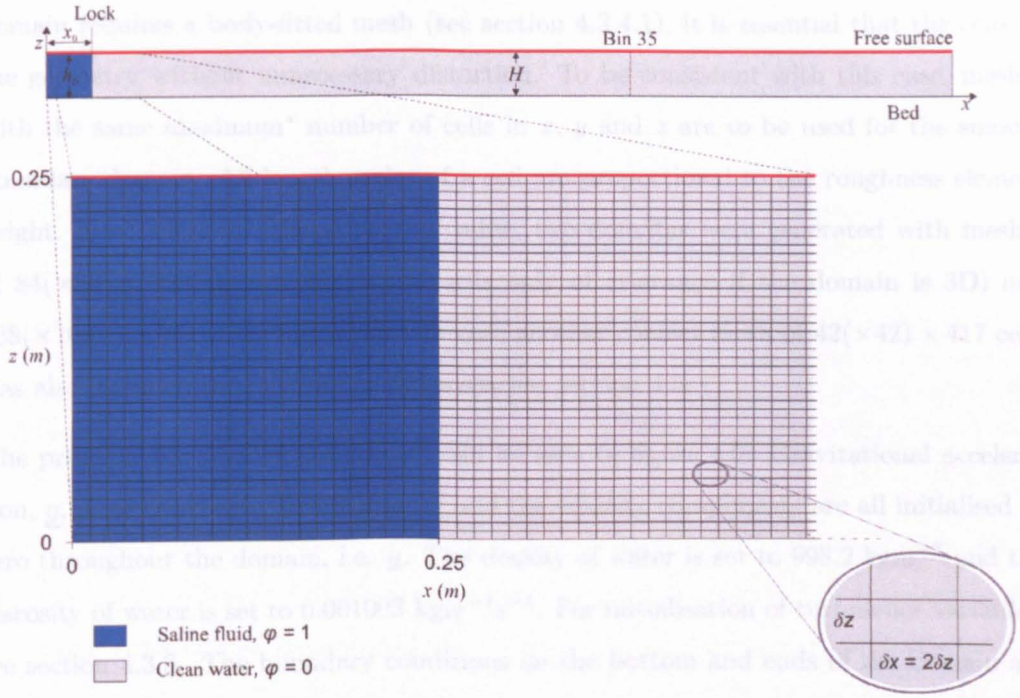

Figure 4.2: Numerical tank geometry with dimensions for the smooth case. Dense fluid (blue) initialised to the left of the lock with volume fraction 1 and ambient fluid (grey) to the right with volume fraction 0. The free surface, treated with a symmetry condition is shown in red and the measurement location is the line Bin 35. Expanded section shows initial part of the 45×417 mesh with emphasis that the cell length is twice the height. For 3D geometries the domain extends 0.2 m laterally (y) and $\delta y = \delta z$.

are partitioned (see section 4.3.2) from the rest of the domain to represent the denser current fluid; a free surface analogy; and a measurement 'line' representing Bin 35 (see later in this section). The mesh used is a hexahedron mesh that divides the domain into rectangular or cuboid cells, depending on whether the mesh is 2D or 3D respectively. The cells have height δz, length $\delta x = 2\delta z$ and width $\delta y = \delta z$. The factor two stretch in the streamwise direction enables reduction of computational cost and since the direction of flow is primarily horizontal, except at the front, the accuracy of the simulation in the main body of the flow should not be compromised. Note that Corney (2005) uses a factor four stretch in the streamwise direction which further decreases computational expense. However, it has been shown that mesh stretching in the streamwise direction may significantly disturb turbulent eddies and therefore adversely affect resultant statistical quantities (Ikeda and Durbin, 2007). The stretch factor also has implications when a rough geometry is included in the bottom wall (see section 4.3.4.1) since an increasing stretch factor decreases the number of cells present in potentially complex flow regions between and above the roughness elements, thus decreasing the resolution and therefore the accuracy in these areas. Since one of the methods of including bed roughness in the

domain requires a body-fitted mesh (see section 4.3.4.1), it is essential that the cells fit the geometry without unnecessary distortion. To be consistent with this case, meshes with the same maximum* number of cells in x, y and z are to be used for the smooth boundary domain. All length scales of a cell are proportional to the roughness element height, $k_r = 0.006$ m. Based on this value, two domains were generated with meshes of 84(×84) × 834 ($x \times y \times z$, where y is only of relevance if the domain is 3D) and 168(×168) × 1668 cells. In the smooth case another coarser mesh of 42(×42) × 417 cells was also included for verification purposes, see section 4.5.

The principle features of the domain can be seen in figure 4.2. Gravitational acceleration, $\underline{g}$, is specified as (0.0,-9.81) ms^{-2} and the velocity components are all initialised as zero throughout the domain, i.e. $\underline{u}$. The density of water is set to 998.2 kgm^{-3} and the viscosity of water is set to 0.001003 $kgm^{-1}s^{-1}$. For initialisation of turbulence variables, see section 4.3.3. The boundary conditions on the bottom and ends of the domain are set to be no-slip, given by

$$\underline{u} = 0 \tag{4.4}$$

A no flux condition holds on the top boundary in order to create an analogy with a free surface (see section 4.2.2) and thus the following condition, equivalent to a free-slip, symmetry boundary, is imposed:

$$w = 0, \qquad \frac{\partial u}{\partial z} = 0 \qquad \frac{\partial v}{\partial z} = 0 \tag{4.5}$$

It is possible to model a free surface, for example using another multiphase flow model for the interaction of water and air, however, this would cause further computational expense and the disturbance to the free surface during experiments was seen to be negligible. It should also be noted that in a deep submarine context, the free surface would be far above the current and again its effects would be negligible.

A further condition on the model is the time step. This prevents information passing all the way through one computational cell in a single time step and thus prevents loss of information and inaccurate solution. The condition is specified using the Courant-Friedrichs-Lewy (CFL) limit given by the following expression:

$$\frac{U\delta t}{\delta x} < 1 \tag{4.6}$$

where U is a characteristic velocity scale of the simulation given by $\sqrt{g'h_0/2}$, δt is the size of the time-step and δx is the streamwise length of a cell. The streamwise length

*Some rows or columns of the domain will have voids where there are no cells due to the presence of the roughness geometry, thus the number of cells along them will fall below the maximum.

Mesh	No. cells	$\delta z (= \delta y = 1/2\delta x)$ (m)	δt (s)
Coarse	42 × 417	0.006	0.02
Medium	84 × 834	0.003	0.01
Fine	168 × 1668	0.0015	0.005

Table 4.1: The number of cells used in the mesh of the domain and the vertical length of a cell corresponding to that mesh tabulated with the respective time-steps. The meshes are defined as coarse, medium and fine for qualitative description. The number of cells is given only for two dimensions since the number of lateral cells is identical to the vertical. The values of δx are proportional to the height of the roughness elements when a body-fitted domain is used and δt is calculated using δx and a characteristic velocity defined by $\sqrt{g'h_0/2}$ in the present study. Note that the coarsest mesh is only used in the smooth case for the purpose of verification.

scale is used in preference to the vertical or lateral equivalents since this is perceived as the primary direction of flow. Using equation (4.7) and a value of δx dependent on the particular mesh in use, the value of the time-step δt can be calculated. In the present study, the time-step is multiplied by a 'safety' factor of 1/2 for all simulations as used by Daly and Pracht (1968) and Corney (2005). i.e. half the CFL limit. This results in an actual time-step given by

$$\delta t = \frac{\delta x}{2U} \tag{4.7}$$

Note that if U is replaced by u_f, found empirically, the limit given by equation (4.6) still holds since the characteristic velocity scale, U, is always greater than the experimental value of u_f due to its use of the conservative approximation $h_f = h_0/2$. For example, for a 5% excess density current with the tank dimensions of the present study and $\delta x = 0.012$ (i.e. the 42 × 417 coarse mesh), $U = 0.248$ ms^{-1}, while $u_f = 0.153$ ms^{-1} (see section 2.5) resulting in time-steps calculated using equation (4.7) of $\delta t = 0.02$ s and $\delta t = 0.04$ s, respectively. A summary of the number of cells, their dimensions and the corresponding time-steps used for each mesh can be found in table 4.1.

4.3.2 Multiphase flow model

FLUENT has three integral multiphase flow options, the Euler, mixture and volume of fluid (VOF) models which use an Euler-Euler approach whereby the phases are considered interpenetrating continua, and a discrete phase model that uses an Euler-Lagrange alternative in which the governing equations are solved for the fluid phases and then a dispersed phase is solved by tracking particles through the calculated flow field. This latter method is not suitable for liquid-liquid flows, such as gravity currents, or scenarios where the secondary phases have high volume fractions since the number of particles re-

quired, and hence the computational cost, becomes prohibitively large. Under rigorous analyses, it has been shown that none of these models can truly account for the mixing that occurs within a gravity current flow and generally tend to over-(mixture model) or under-(VOF model) estimate this process (Corney, 2005). The nature of the multiphase flow models available also limits the accuracy of the entire simulation to first order in time, which has substantial effects on the validity of the results (Corney, 2005).

Scalar transport equation

To overcome these limitations in the model, Corney (2005) developed a method for the inclusion of a second phase of flow by adding a time dependent transport equation for the concentration, C, given by the following:

$$\frac{\partial \rho C}{\partial t} + \nabla \cdot (\rho \underline{v} C) = \nabla \cdot (\rho \kappa_s \nabla C) \tag{4.8}$$

where $\kappa_s = 5.22 \times 10^{-9}$ m^{2}s^{-}1 is the coefficient of the diffusivity of the salt solution in water (Gebhart *et al.*, 1988). Note that the FLUENT solver requires a "mass diffusivity" that is specified as 5.2106×10^{-6} kgm^{2}s^{-}1. If the density of the ambient and current fluids and the diffusivity of the saline solution in water are assumed to be constant, it is possible to generate a gravity current by modelling the transport of concentration with the above equation (4.8) and a user-defined source term, i.e. by specifying a function for $\rho \underline{g} + \underline{F}$ in equation (4.2) that is dependent on C. However, Corney (2005) proved that the current model is more accurate since it enables the density to vary in space and time and the diffusivity, κ_s, to be a function of turbulence which is a more intuitive, physical condition since the turbulence should enhance the mixing of the saline gravity current with the surrounding water. Hence, the present method sets $\underline{F} = 0$ and models the transport of concentration throughout the domain with equation (4.8) and maps this to the density field using a user-defined function (UDFs), written in the C programming language, given by

$$\rho = \rho_w(1 - C) + \rho_g C \tag{4.9}$$

For the fluid in the domain, equation (4.9) means that when $C = 0$, the density reduces to the density of clear water, ρ_w, and increases linearly to ρ_g, the initial and maximum density of the gravity current, when $C = 1$. In order to enable the effects of turbulence on the diffusivity of the saline fluid in the water a turbulent diffusivity, κ_t, was added to the laminar diffusivity, κ_s. The fluid viscosity, ν, in the momentum equations is modified when turbulence is present so that the viscosity distribution is variable throughout the

flow field. Thus, the expression $\nu + \nu_t$, where ν_t is the eddy viscosity, is used so that ν_t can be defined separately, dependent on the model. The turbulent diffusivity of salt into the ambient water can be expressed in the same way and therefore in equation (4.8) κ_s is modified to read $(\kappa_s + \kappa_t)$. κ_t can be calculated using the Schmidt number, Sc, which is the ratio of the turbulent eddy viscosity to the turbulent diffusivity of mass, given by

$$\mathrm{Sc} = \frac{\nu_t}{\kappa_t} \tag{4.10}$$

To determine an exact value for Sc would require experimental information beyond the capabilities and time of the present study. However, it has been shown that the exact value of Sc does not effect the results (Rehm *et al.*, 1995). It still remains to specify a value for the calculation of κ_t. Hartel *et al.* (2000b) state that the Schmidt number should be of order one and adopt the value Sc = 0.71 in their simulations. Hence, the present study uses a value of Sc = 0.7.

Initialising the 'second phase'

The second phase, which represents the dense current fluid, is created by 'patching' a region into one end of the domain within which the volume fraction or concentration of fluid, C, in the cells is initialised as 1, while in the rest of the domain it is initialised as 0. Thus, by equation (4.9), dense fluid is initialised in this region creating the lock-box, see figure 4.2.

4.3.3 Turbulence model

Reynolds-Averaged continuity and momentum equations

Since this study requires the use of a turbulence model and does not intend to use LES or DNS, Reynolds-Averaging is performed. The solution variables are decomposed into the mean (time-averaged) and fluctuating components, for example for the horizontal velocity:

$$u = \overline{u} + u' \tag{4.11}$$

where $\overline{u}$ and u' are the mean and fluctuating parts, respectively. Equation (4.11) and similar expressions for the other two components of velocity, the pressure and concentration are substituted into the exact Navier-Stokes equations, (4.8) and (4.3), and a time average is taken resulting in the Reynolds-Averaged Navier-Stokes equations, as

discussed in section 4.2.1. Further details of the averaging process can be found in Hartel (2000) or FLUENT (2006). Equations (4.3) and (4.2) become (in cartesian tensor form):

$$\frac{\partial \rho}{\partial t} + \frac{\partial \rho u_i}{\partial x_j} = 0 \tag{4.12}$$

$$\frac{\partial \rho u_i}{\partial t} + \frac{\partial \rho u_i u_j}{\partial x_j} = -\frac{\partial p}{\partial x_i} + \frac{\partial}{\partial x_j}\left[\mu\left(\frac{\partial \rho u_i}{\partial x_j} + \frac{\partial \rho u_j}{\partial x_i} - \frac{2}{3}\delta_{ij}\frac{\partial \rho u_l}{\partial x_l} + \frac{\partial}{\partial x_j}(-\rho\overline{u_i' u_j'})\right)\right] \tag{4.13}$$

where the overbar has been dropped for simplicity. They have a very similar form to the exact equations but the solution variables now represent time-averaged values. The obvious difference is the additional terms that represent the effects of turbulence, i.e. the Reynolds stresses, $-\rho\overline{u_i' u_j'}$ in equation (4.13). These must be modelled in order to achieve closure of equation (4.13). For most of the RANS based turbulence models, not including the Reynolds stress model (RSM), FLUENT uses a Boussinesq approach to model the Reynolds stresses and lower computational cost. This involves the following expression that relates the stress terms to mean velocity gradients:

$$-\rho\overline{u_i' u_j'} = \mu_t\left(\frac{\partial u_i}{\partial x_j} + \frac{\partial u_j}{\partial x_i}\right) - \frac{2}{3}\left(k + \mu_t\frac{\partial u_i}{\partial x_i}\right)\delta_{ij} \tag{4.14}$$

where k is the turbulent kinetic energy which is calculated using a transport model, dependent on the turbulence model selected and μ_t is the turbulent viscosity, and function which depends on the turbulent variables solved by the turbulence model. The main limitation of the Boussinesq approach lies in the assumption that this value is an isotropic scalar quantity which does not always hold. The RSM model avoids the necessity for this by solving seven equations (five in 2D) including the transport of the Reynolds stresses and the dissipation rate. However this is computationally more expensive on average and using FLUENT has been found to take longer to converge in some cases and require 50-60% more CPU time and 15-20% more memory compared to $k-\omega$ and $k-\varepsilon$ models (FLUENT, 2006).

Turbulence transport equations

The turbulence model used in the present study is the RNG $k-\varepsilon$ model given by the following equations for the transport of the turbulence quantities turbulence kinetic energy, k, and turbulence dissipation ε:

$$\frac{\partial \rho k}{\partial t} + \frac{\partial \rho k u_i}{\partial x_i} = \frac{\partial}{\partial x_j}\left(\alpha_k \mu_{eff}\frac{\partial k}{\partial x_j}\right) + G_k + G_b - \rho\varepsilon - Y_m + S_k \tag{4.15}$$

$$\frac{\partial \rho \epsilon}{\partial t} + \frac{\partial \rho \epsilon u_i}{\partial x_i} = \frac{\partial}{\partial x_j}\left(\alpha_\epsilon \mu_{eff} \frac{\partial \epsilon}{\partial x_j}\right) + C_{1\epsilon}\frac{1}{k}(G_k + C_{3\epsilon}G_b) - C_{2\epsilon}\rho\frac{\epsilon^2}{k} - R_\epsilon + S_\epsilon \quad (4.16)$$

The unfamiliar terms present in these equations are defined as follows:

G_k represents generation of mean TKE due to mean velocity gradients and is defined as $-\rho\overline{u_i' u_j'}\frac{\partial u_j}{\partial x_i}$ which can be expressed in a manner consistent with the Boussinesq approach in the form

$$G_k = 2\mu_t S_{ij} S_{ij} \quad (4.17)$$

where S is the mean rate-of-strain tensor (s^{-1}).

G_b represents the production of turbulence due to buoyancy and is given by the equation:

$$G_b = -g_i \frac{\mu_t}{\rho Pr_t}\frac{\partial \rho}{\partial x_i} \quad (4.18)$$

where Pr_t is the turbulent Prandtl number. TKE tends to be augmented in an unstable stratification, $G_b > 0$, but the buoyancy effects suppress turbulence in a stable stratification, $G_b < 0$. Note that equations (4.18) and (4.17) hold for all $k - \epsilon$ models.

The term Y_m in equation (4.15) represents the 'dilation dissipation' and describes the way that compressibility effects turbulence. It is given by the equation:

$$Y_m = 2\rho\epsilon M_t^2 \quad (4.19)$$

where M_t is the turbulent Mach number, described as $M_t = \sqrt{\frac{k}{a_s^2}}$ and a_s is the speed of sound. This function is not relevant in the present study since the flow is incompressible, however, it is included here for completion.

The scale elimination procedure in RNG theory results in the following differential equation for turbulence viscosity:

$$d\left(\frac{\rho^2 k}{\sqrt{\epsilon\mu}}\right) = 1.72\frac{\hat{\nu}}{\sqrt{\hat{\nu}^3 - 1 + C_\nu}}d\hat{\nu} \quad (4.20)$$

where $\hat{\nu} = \mu_{eff}/\mu$ and $C_\nu \approx 100$. Integrating this equation enables the model to accurately describe how the effective turbulent transport varies with effective Reynolds number so that it can handle low Reynolds number and near-wall flows more efficiently. At the high Reynolds number limit, equation (4.20) results in the following expression

$$\mu_t = \rho C_\mu \frac{k^2}{\epsilon} \quad (4.21)$$

where $C_\mu = 0.0845$ has been derived using the RNG theory and is notably close to the standard $k-\varepsilon$ model value of 0.09. By default, FLUENT adopts equation (4.21) to calculate the effective viscosity, however, it is an option to use equation (4.20) where low Reynolds number dynamics are involved.

The term R_ε in equation (4.16) makes the RNG model more responsive to the effects of rapid strain and streamline curvature than the standard model and is given by the following:

$$R_\varepsilon = \frac{C_\mu \rho \eta_s^3 (1 - \eta_s/\eta_0)}{1 + \beta_0 \eta_s^3} \frac{\varepsilon^2}{k} \tag{4.22}$$

where η_s is equivalent to Sk/ε, $\eta_0 = 4.38$ and $\beta_0 = 0.012$. Thus, depending on the magnitude of the strain, S, either $\eta_s < \eta_0$ or $\eta_s > \eta_0$ resulting in a positive or negative contribution to equation (4.16), respectively.

The inverse effective Prandtl numbers, α_k and α_ε, are derived analytically by the RNG theory and calculated using the following formula:

$$\left|\frac{\alpha - 1.3929}{1 - 1.3929}\right|^{0.6321} \left|\frac{\alpha + 2.3929}{1 + 2.3929}\right|^{0.6321} = \frac{\mu}{\mu_{eff}} \tag{4.23}$$

and in the high Reynolds number limit, where $\mu/\mu_{eff} \ll 1$, $\alpha_k = \alpha_\varepsilon \approx 1.393$.

The model constants $C_{1\varepsilon}$ and $C_{2\varepsilon}$ are also derived analytically by the RNG theory and have default FLUENT values of 1.42 and 1.68, respectively. S_k and S_ε are user-defined source terms.

The RNG $k-\varepsilon$ model has been used with success in previous research on gravity currents (see section 4.2.1) and is suggested by Corney (2005) to be the most appropriate of the RANS turbulence models available in FLUENT, with respect to accuracy and computational cost[†]. The RNG $k-\varepsilon$ model differs from the standard $k-\varepsilon$ model through the additional terms and functions in the transport equations for k and ε ((4.15) and (4.16), respectively) and in the model constants. It is derived using a rigorous statistical technique called renormalisation group theory (Choudhury, 1993). The influential additional term, R_ε (equation (4.22)), appears in the ε equation and significantly improves the accuracy for simulations of rapidly strained flows. While the standard model uses user-specified constants for the turbulent Prandtl numbers, the RNG theory adopts an analytical formula, equation (4.23). It also provides an analytically derived formula for the effective viscosity that accounts for low-Reynolds-number effects, equation (4.20).

[†]Corney (2005) carried out a rigorous test on the accuracy of all of the turbulence models available in FLUENT and different multiphase options for modelling lock-release gravity currents.

The changes also result in the inclusion of the effects of swirl on turbulence, enhancing the accuracy for swirling flows. Due to these extra terms and functions and a greater degree of non-linearity, simulations undertaken using FLUENT have been found to take 10-15% more CPU time that with the standard $k-\varepsilon$ model (FLUENT, 2006). However, where the standard model is known to be slightly over-diffusive the RNG model is designed so that under high rates of strain the turbulent viscosity is reduced. Although this means that the model is more susceptible to instability, since the stabilising effects of diffusion are reduced, the result is a model that is more responsive to important physical instabilities such as time-dependent vortex shedding.

Initialisation of k and ε

For unsteady calculations using a $k-\varepsilon$ model, as in the present study, the solution after a sufficient amount of time has elapsed should be independent of the initial values of k and ε. However, for better convergence and thus a more cost efficient simulation it is beneficial to prescribe reasonable initial estimates for k and ε. In the majority of experiments fluid is initially 'quiescent' and therefore there is little attention given to the values of these variables prior to flow commencement and with reasonable cause: k would predictably be so small that very high specification equipment would be required to carry out this analysis and thus it is often taken as negligible. In general, FLUENT (2006) suggests initialising with a fully developed turbulence state, which for complex flows (defined in this context as flows with multiple in/outlets and boundary conditions) it recommends specifying the initial values in terms of turbulence intensity, I_t, where an intensity between 5-10% should be considered in the fully turbulent regime. With this parameter, an initial guess for k can then be calculated using the following formula:

$$k = 1.5(I_t U)^2 \tag{4.24}$$

where U is the characteristic mean velocity magnitude of the problem, i.e. $U = \sqrt{g'h_0/2}$. In order to calculate an initial guess for ε, the condition that the eddy viscosity, $\nu_t = C_\mu \frac{k^2}{\varepsilon}$, is large in comparison to the molecular viscosity, μ, is implemented. This is based on the assumption that in fully developed turbulent flow, μ_t, given by equation (4.21), is approximately two orders of magnitude larger than μ[‡]. Hence, an initial approximation for ε can be calculated from the following equation:

[‡]Note that Chen and Lee (1999) state that $\mu_t < 0.001\mu$ which would imply the opposite of the condition suggested by FLUENT (2006). They do not specify the exact input values that they use as a result of this, only that they are 'negligibly small' therefore it is not possible to qualify if this is a superficial error or not.

$$\varepsilon \approx \frac{\rho C_\mu k^2}{\mu_t} \tag{4.25}$$

The estimated initial conditions for 1% and 5% density excess gravity currents, calculated with the tank geometry of the present study can be seen in table 4.2.

ρ excess	k (m^2s^{-2})	ε (m^2s^{-3})
1%	$4.6 \times 10^{-5} - 1.84 \times 10^{-4}$	$1.78 \times 10^{-6} - 2.85 \times 10^{-5}$
5%	$2.3 \times 10^{-4} - 9.2 \times 10^{-4}$	$4.46 \times 10^{-5} - 7.13 \times 10^{-4}$

Table 4.2: The range of initial estimates for k and ε for the present study, calculated using equations (4.24) and (4.25) as suggested by FLUENT (2006), for gravity currents with initial density excesses of 1% and 5%. The equations assume turbulence intensity in the range of 5-10% thus implying fully developed turbulence. The values shown represent the limits of this range.

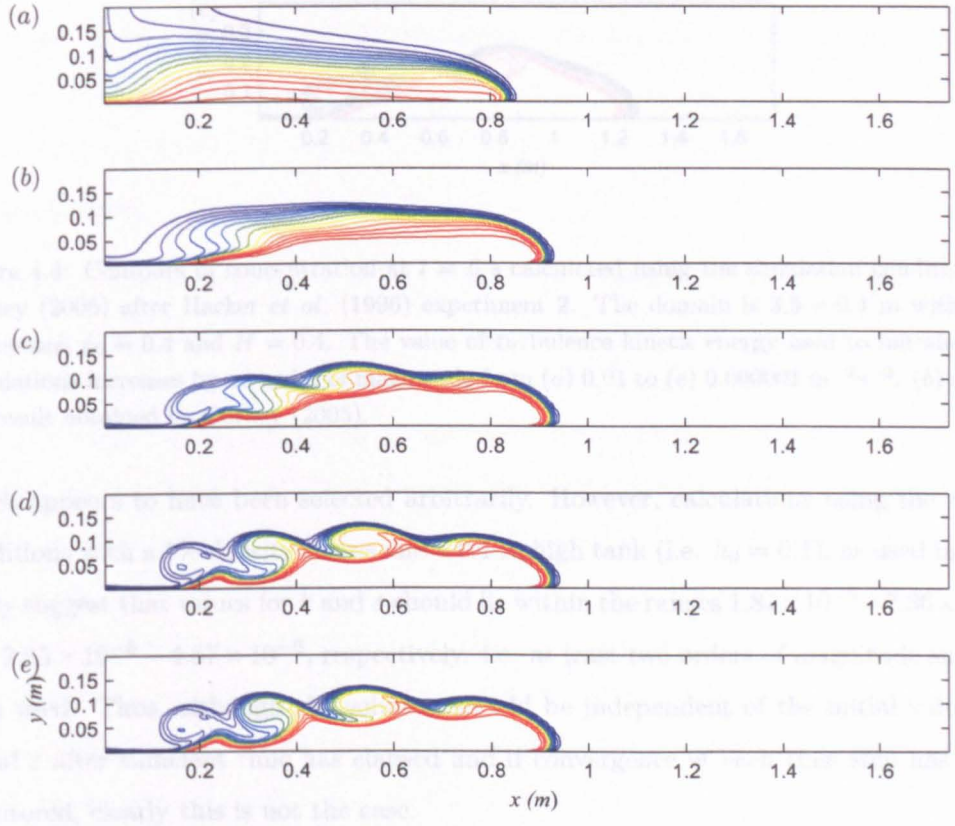

Figure 4.3: Contours of concentration at $t = 9.5$ s calculated using the simulation conditions of Corney (2005) after Hacker *et al.* (1996) experiment 1. The tank was 3.5×0.2 m with lock dimensions $x_0 = 0.3$ and $H = 0.2$. The value of turbulence kinetic energy used to initialise the calculations increases by an order of magnitude from (*a*) 0.01 to (*e*) 0.000001 $m^{-2}s^{-2}$. (*b*) shows the result obtained by Corney (2005).

As discussed in section 4.2.2, Corney (2005) uses a value of 0.001 to initialise k and ε

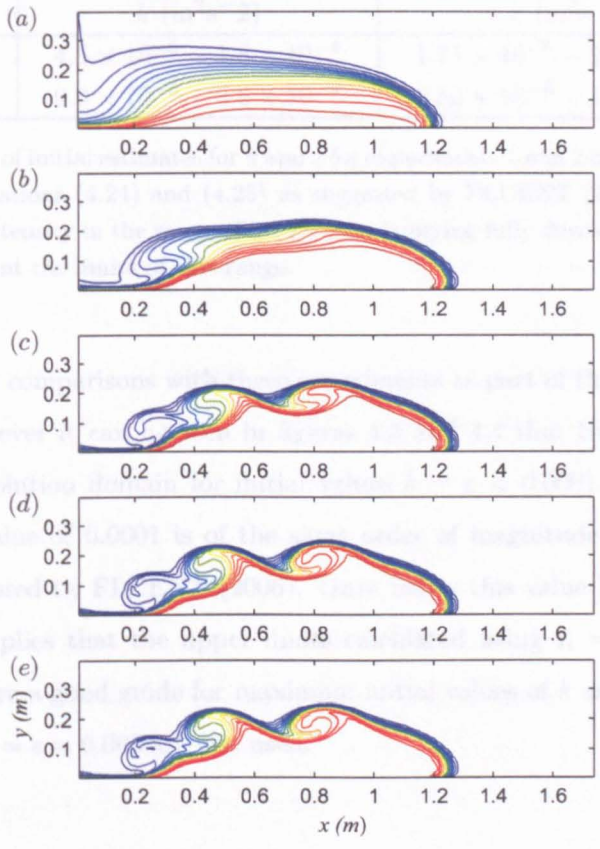

Figure 4.4: Contours of concentration at $t = 6$ s calculated using the simulation conditions of Corney (2005) after Hacker *et al.* (1996) experiment 2. The domain is 3.5×0.4 m with lock dimensions $x_0 = 0.4$ and $H = 0.4$. The value of turbulence kinetic energy used to initialise the calculations increases by an order of magnitude from (*a*) 0.01 to (*e*) 0.000001 $\mathrm{m^{-2}s^{-2}}$. (*b*) shows the result obtained by Corney (2005).

which appears to have been selected arbitrarily. However, calculations using the above conditions with a 1% density excess and a 0.1 m high tank (i.e. $h_0 = 0.1$), as used in that study suggest that values for k and ε should lie within the ranges $1.84 \times 10^{-5} - 7.36 \times 10^{-5}$ and $2.85 \times 10^{-6} - 4.57 \times 10^{-6}$, respectively. i.e. at least two orders of magnitude smaller than used. Thus, although the solution should be independent of the initial values of k and ε after sufficient time has elapsed and if convergence at each time step has been monitored, clearly this is not the case.

In order to study the effects that these values are having on the solution, two of the experiments of Hacker *et al.* (1996) (experiments 1 and 2 therein) were computed with the same model as used by Corney (2005) (model $UDS_{2,2}$ therein) but with k and ε both initialised with values of 0.01, 0.001, 0.0001, 0.00001 and 0.000001. According to equations (4.24) and (4.25) with the density excess and tank height from the experiments of Hacker *et al.* (1996), k and ε should be initialised within the ranges shown in table 4.3.

Exp. no.	k (m^2s^-2)	ε (m^2s^-3)
1	$4.5 \times 10^{-5} - 1.8 \times 10^{-4}$	$1.71 \times 10^{-6} - 2.73 \times 10^{-5}$
2	$9.0 \times 10^{-5} - 3.6 \times 10^{-4}$	$6.83 \times 10^{-6} - 1.09 \times 10^{-4}$

Table 4.3: The range of initial estimates for k and ε for experiments 1 and 2 of Hacker *et al.* (1996), calculated using equations (4.24) and (4.25) as suggested by FLUENT (2006). The equations assume turbulence intensity in the range of 5-10% thus implying fully developed turbulence. The values shown represent the limits of this range.

Corney (2005) uses comparisons with these experiments as part of the validation process for his model, however it can be seen in figures 4.3 and 4.4 that there is a substantial difference in the solution domain for initial values $k = \varepsilon < 0.0001$. It can be seen in table 4.3 that a value of 0.0001 is of the same order of magnitude as the upper limit of the range suggested by FLUENT (2006). Once below this value little change can be observed which implies that the upper limits calculated using $I_t = 10\%$ in equations (4.24) and (4.25) are a good guide for maximum initial values of k and ε. In the present study, a value of $k = \varepsilon = 0.000001$ was used.

Wall functions

Simulations of wall-bounded turbulent flows require careful treatment in the near-wall region. In this part of the domain, very near the wall, where the no-slip, no-flux boundary conditions must hold, turbulence is damped. However, as distance from the wall increases, large increases in the gradients of the flow variables occur and vigorous momentum and scalar transport result in increased production of turbulence kinetic energy. Typically, these near-wall characteristics are identified by a boundary layer divided into three layers: a viscous sublayer, an outer layer and a buffer layer in which the forces governing the former two layers are of equal importance and the transition from one to the other must occur. As a result of these characteristics, the walls are a primary source of mean vorticity and turbulence and therefore inaccurate modelling of this near-wall region has significant implications for the validity of the numerical solutions. Gravity current propagation is governed by the 'nose' region which is highly dependent on the bottom boundary (Simpson, 1972; Hartel *et al.*, 2000b). Thus, accurate treatment of the near-wall region which is subject to substantial spatial and temporal variations, is of tantamount importance in the present study.

For exact computation of the flow under examination, the governing equations have to be solved throughout the entire domain right up to the boundaries. If a low Reynolds

number model is used (e.g. the Spalart-Allarmas model) the flow field is solved up to the walls but these methods introduce further modelling uncertainties and require very fine meshing in the near-wall region to resolve the high spatial gradients with potentially massive increase to the computational cost. They have also been shown inadequate for modelling gravity currents (Corney, 2005). Alternatively, there are several turbulence models ($k-\epsilon$, RSM, LES) specifically derived to capture high Reynolds number flow that cannot represent the viscous layer since they neglect important viscous effects near the wall and treat the boundaries with wall functions that effectively bridge the gap to overcome this problem. This method depends on placing the first grid point near the wall within the fully turbulent logarithmic layer, i.e. $y^+ > 11.225$ where y^+ is a dimensionless wall unit given by

$$y^+ = \frac{\rho u_\tau}{\mu} y \tag{4.26}$$

where u_τ is the shear velocity defined using the wall shear stress, τ_w, by $\sqrt{\tau_w/\rho}$[§]. Numerous experiments have proven that the law-of-the-wall is valid in this layer, and hence the following equation can be used to find the wall shear stress,

$$\frac{\overline{u}}{u_\tau} = \frac{1}{\kappa} ln \frac{\rho u_\tau}{\mu} y + C_\tau \tag{4.27}$$

where $C_\tau = 5.5$. If $y^+ < 11.225$, i.e. within the viscous sublayer, the wall shear stress is calculated by treating the flow as laminar.

Due to the complex spatial and temporal variations at the wall involved in gravity current propagation, ideally a dynamic mesh would be used that can ensure that the first grid point is located within the logarithmic layer. However, strict boundary layer mesh would be dependent on the physical flow and therefore not subject to mesh refinement required by most verification procedures which would involve the inevitable relocation of this vital grid point and possibly subsequent solution misrepresentation. The present study uses wall functions and does not implement a dynamic meshing hence care must be taken when conducting refinement studies to check that the first grid point near the wall falls within the logarithmic layer.

[§]The boundary layers can be subdivided with $y^+ \lesssim 5$ lying within the viscous layer, $5 < y^+ \lesssim 30$ in the buffer layer and $30 < y^+ < 300$ in the logarithmic layer however it is quite common to dispose of the buffer layer by linking the linear velocity profile in the viscous sublayer to the logarithmic velocity profile in the inertial (logarithmic) sublayer adopting an abrupt change from purely viscous stress to purely turbulent stress at $y^+ \approx 11.225$ (Tennekes and Lumley, 1972).

4.3.4 Bed roughness

Different methods for the inclusion of bed roughness within the domain have been discussed in section 4.2.5. In order to compare to the experimental data and to obtain a range of roughnesses, including more natural roughness like dunes, methods that allow the inclusion of a form or a grain type roughness or a combination are used. A body-fitted mesh is used for the larger scale form roughness and a law-of-the-wall model for the grain roughness.

4.3.4.1 Body-fitted approach

The body-fitted mesh approach has been adopted successfully in previous studies for single-phase flows, see section 4.2.5. Since the cells used in the present study are rectangular (or cuboid in 3D) and proportional to the size of the bodies (roughness elements), rigorous body fitting equivalent to that performed in these previous studies is not necessary and no cell distortion occurs. However, the principle involved in the approach, i.e. changing the mesh to incorporate voids representing the bed geometry (in comparison to using a 'force field' method) still holds, and hence the term 'body-fitted' is maintained in the present context. The majority of the mesh geometries used in the present study represent the beam type roughness. As in the experimental work in section 2, the beams have dimensions 0.006 × 0.006 m and have been designed so that they have no lateral variation enabling direct comparison of 2D and 3D results. One interest of the present study is in the quantitative analysis of the effects of element spacing on gravity currents. As mentioned in chapter 2 the following terminology is used as shorthand to describe the element in use: $beams_{height,spacing}$, where *beams* is a qualitative description of the element, *height* is the maximum element height k_r (mm) and *spacing* is the ratio of the distance between adjacent elements and the height w/k_r. For example, $\text{beams}_{6,1}$ refers to the beam type roughness with equal height and spacing of 6 mm. The coarsest mesh used with this method is the equivalent of the 84 × 834 'medium' mesh used in the smooth case. It is not possible to use the 42 × 417 mesh since the height of the cells in that case is identical to that of the elements and for the $\text{beams}_{6,2}$ case, also identical to the spacing between them.

A diagram of the domain mesh and cell configuration with roughness elements included via the body-fitted approach can be seen in figure 4.5. The length scales that are used in the quantitative analysis of the roughness effects of the beam-type roughness are also depicted. It can be seen that the cell dimensions have not been altered in the vicinity

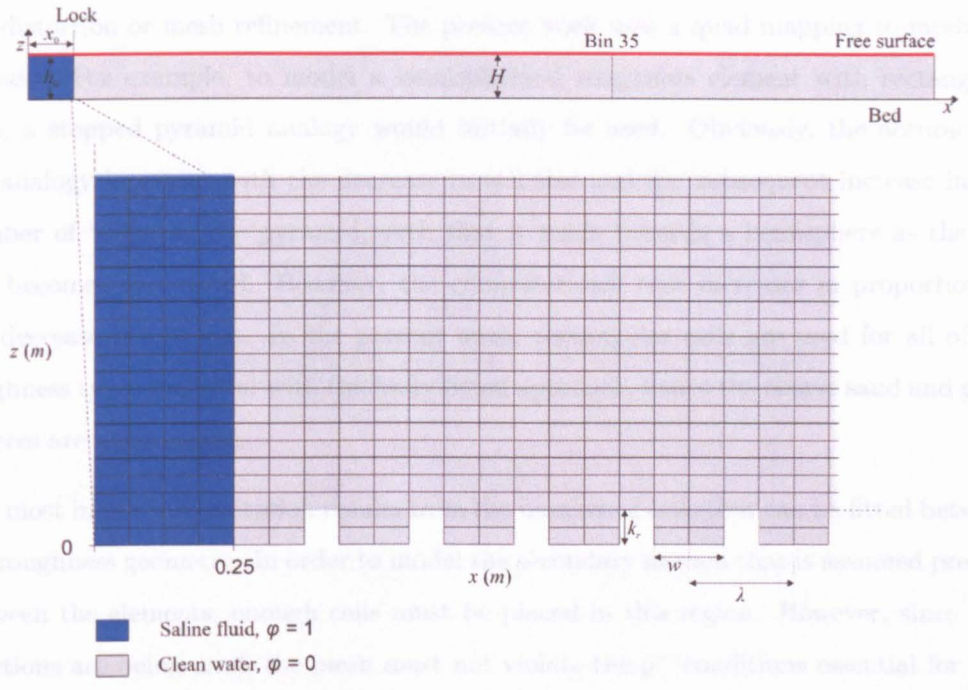

Figure 4.5: Numerical tank geometry with dimensions for the rough cases. Dense fluid (blue) initialised to the left of the lock with volume fraction 1 and ambient fluid (grey) to the right with volume fraction 0. The free surface, treated with a symmetry condition is shown in red and the measurement location is the line Bin 35. Expanded section shows mesh in the lower half of the domain in the vicinity of the lock partition. The wall geometry to the left of this divide is smooth while to the right the computational mesh has been fitted to the roughness geometry. The geometry shown is the $beam_{6,2}$ beam roughness along with the length scales used in the quantitative analysis of roughness effects in chapter 5. The mesh equivalent for a smooth bed is the 84 × 834 'medium' mesh, this is the coarsest mesh used in the body-fitted approach to modelling the bed roughness. For 3D geometries the domain and the roughness elements extend 0.2 m laterally (y) with no variations in this direction.

of the elements. This is because any clustering or grading of the cells in these regions would involve further cell stretching and the associated negative effects of increased diffusion, or require mesh adaption incurring additional computational expense beyond the processing capabilities of the present study. In fact, a graded mesh where cells near the top boundary of the domain were chosen too large could result in substantial inaccuracies in the modelling of the ambient return flow and consequently the inaccurate computation of the gravity current itself in other regions. Hence, without a vigorous analysis of different mesh grading ratios it would be difficult to select an appropriate mesh to avoid these complications.

Limitations

The method is limited by the shape of the bodies or elements that can be fitted without

cell distortion or mesh refinement. The present work uses a quad mapping to mesh the domain. For example, to model a hemispherical roughness element with rectangular cells, a stepped pyramid analogy would initially be used. Obviously, the accuracy of the analogy increases with the decrease in cell size and the subsequent increase in the number of 'steps' in the pyramid, such that it tends towards a hemisphere as the cell size becomes very small. However, the computational cost increases in proportion to the decrease in cell size. In the present work, rectangular cells are used for all of the roughness types modelled with the body-fitted approach, hence the coarse sand and glass spheres are not covered.

The most inhibiting limitation results from the number of cells that can be fitted between the roughness geometry. In order to model the secondary motion that is assumed present between the elements, enough cells must be placed in this region. However, since wall functions are being used, the mesh must not violate the y^+ conditions essential for wall functions to hold (see section 4.3.3). Note that this limitation might suggest better use of a different turbulence model, however, (Corney, 2005) showed that a high Reynolds number turbulence model is required to capture the turbulent core of the flow and therefore wall functions are required.

4.3.4.2 Law-of-the-wall approach

This method also essentially enables the inclusion of a grain type roughness that can be used alone or in conjunction with the body-fitted approach to generate a composite (grain + form) roughness on the bed (e.g. Durbin *et al.*, 2001). As has been used in models for single-phase flow the FLUENT software provides the option to include roughness at the boundaries by specifying an equivalent roughness height (or physical roughness height if a grain roughness is used), k_s, and a roughness constant, c_s, in the conditions panel for the boundary required. This activates extra terms in the wall functions which are used by the governing equations during solution hence altering the flow dynamics. The law-of-the-wall, given for the smooth case by equation (4.27), for the rough boundary is now given by the following

$$\frac{\overline{u}}{u_\tau} = \frac{1}{\kappa} ln \frac{\rho u_\tau}{\mu} y + C_\tau - \Delta B \tag{4.28}$$

where ΔB represents the velocity shift away from the mean velocity distribution for a smooth bed. As discussed previously, there is no generally accepted universal roughness function valid for any type of roughness but for sand grain roughness and similar scale,

homogeneous roughness elements, ΔB can be correlated to the dimensionless roughness height $k_s^+ = \frac{\rho k_s u_\tau}{\mu}$. k_s is a sand grain roughness height (or equivalent roughness height) calculated empirically as in section 2.3. Turbulent flow is classified into three regimes identified by the value of k_s^+. Thus, ΔB is defined differently depending on the perception of the flow at the boundary:

Hydrodynamically smooth: $k_s^+ \leq 2.25$

$$\Delta B = 0 \tag{4.29}$$

Transitional: $2.25 < k_s^+ \leq 90$

$$\Delta B = \frac{1}{\kappa} ln \left[\frac{k_s^+ - 2.25}{87.75} + c_s k_s^+ \right] sin 0.4258 (ln k_s^+ - 0.811) \tag{4.30}$$

Fully rough: $k_s^+ > 90$

$$\Delta B = \frac{1}{\kappa} ln(1 + c_s k_s^+) \tag{4.31}$$

The method of calculation for c_s is undefined (FLUENT, 2006) except that a value of 0.5 is proposed to agree with the results of Nikuradse (1933) for sand roughened pipes. They suggest higher values, $0.5 < c_s < 1$ might be more appropriate for other roughnesses, for example ribs and wire mesh. Without and accurate guideline, in the present study c_s is assumed to lie between 0 and 1 and is thus taken as 1 to imply maximum effect. Given the roughness parameters, the solver calculates $\Delta B(k_s^+)$ using one of the formulae given by equations (4.29), (4.30) and (4.31) to modify equation (4.28) and hence calculate the shear stress at the wall and other wall functions. Although it does not physically alter the geometry of the domain, when used in 2D this method enables the incorporation of more 3D effects since the k_s values are generated directly from experimental data and hence are subject to 3D flow dynamics.

Limitations

One limitation of this method is that the chosen roughness height, k_s, cannot be higher than the distance to the centroid of the wall adjacent cell in order to be properly incorporated into the wall functions. This means that the mesh either has to be adapted so that the wall adjacent cell is larger than the general mesh size if a small mesh is required, or that the roughness height for the simulation has a maximum dependent on the mesh in use. The former of these solutions would mean a decrease in resolution near the bed which is not acceptable in the simulation of gravity currents in which accurate solution

of the flow dynamics near the bed are particularly important to the main body of flow. Further problems with resolution would arise with inter-element cells when using this method in conjunction with the body-fitted approach. Thus, in the present study, the range of k_s values and hence grain roughness modelled with this approach is restricted to those that are smaller in height than the distance to the centroid of the wall adjacent cell, e.g. 0.0015 for an 84×834 mesh.

Another drawback of this method is the dependency on empirical values and the law-of-the-wall assumption. It has been contested that the equivalent roughness, k_s, is a bad parameterisation of roughness resulting in very different roughness geometries having very different effects on the turbulent stresses but with nominally identical roughness functions (ΔB)(Krogstad and Antonia, 1999). Hence risking misrepresentation of the required roughness with potentially serious inaccuracies in the flow field. The use of the law-of-the-wall is also still under dispute in single-phase flow applications. However, since there is no consensus on an alternative approach and DNS is not an option, the law-of-the-wall method, with an equivalent roughness k_s value is adopted as one method in the present study.

4.4 Solution procedure

4.4.1 Numerical schemes

FLUENT uses a control-volume based technique that divides the domain into discrete control volumes using a computational grid. The governing equations are integrated over each control volume to generate algebraic equations for each dependent variable. These discretised equations are linearised and the resulting system of equations is solved to obtain updated values of the dependent variables in each computational cell. A description of all the available numerical schemes including the linearisation and discretisation schemes used in the present study can be found in most comprehensive CFD texts, for example Hartel (2000), and more specifically, at FLUENT (2006) and are therefore not covered in detail herein.

The QUICK scheme was used for the solution of the momentum equations and transport equations for scalar and turbulence quantities. A second order accurate, implicit time-stepping scheme was used for the temporal integration of the governing equations. The PRESTO! scheme was used for the pressure interpolation and the SIMPLE scheme was used to treat the continuity equation for pressure-velocity coupling. The under-relaxation

factors were defined as the following: pressure 0.3, density 1, body forces 1, momentum 0.7 and concentration 0.2.

4.4.2 Solver

In the present study a segregated solver is used in FLUENT to solve the governing integral equations for the conservation of mass and momentum, concentration and turbulence quantities. As the name suggests, the equations are solved sequentially, i.e. segregated from each other. This is an implicit solver with the following steps performed at each iteration:

1. **Fluid properties updated:** Including the user-defined fluid density and diffusivity. If this is the first calculation the values are based on the initialised solution.
2. **Velocity field updated:** u,v and w momentum equations solved in turn with current values of pressure and face mass fluxes.
3. **Pressure and velocity field corrected:** Velocities in step 2 may not satisfy the continuity equation, thus a 'Poisson-type' equation is derived from the continuity and linearised momentum equations to determine the pressure correction. The solution of this equation gives the necessary corrections for the pressure and velocity fields and face mass fluxes such that continuity is satisfied.
4. **Concentration and turbulence fields updated:** Using the previously updated values of the other variables.
5. **Check for iterative convergence.**
6. **Stop:** If convergence has been achieved, solution stops and proceeds to the next time-step. If not, steps 1-5 are repeated.

Several iterations of this solution loop are usually required before a converged solution is obtained because the governing equations are non-linear and coupled.

4.4.3 Data capture

A virtual 'line surface' is located within the computational domain in the same position as the bin in the laboratory experiments and exports text data files of the required flow variables every quarter of a second (except in the 42 × 417 case where the time step size prevents multiples of 0.25 and is set to record every fifth of a second). This line

is purely for post-processing purposes, it is not a boundary entity and the rest of the computational domain is unaware of its presence. The data is reported at the points where the line intersects a cell face and hence at regular intervals since the mesh is not graded. Note that these points do not necessarily correspond to the exact locations of the probes in the experiments and hence the data is either presented for the depth of the entire flow domain at every cell height or in post-processed form, interpolated to compare more exactly with the experimental data. Which presentation format is used depends on the analysis required. The solver is set to export text data files of flow variables throughout the entire domain after every three minutes of flow time. A UDF finds the front position of the current every quarter of a second (again except in the 42×417 cell case) and exports its location to a text file. Post-processing of the text data files is performed using Matlab scripts.

4.5 Model verification and validation procedures

4.5.1 Verification

A CFD simulation may have the physical characteristics of the required flow but this does not automatically mean that it is verified to truly represent the original governing equations (Bombardelli *et al.*, 2004). In fact, when the governing partial differential equations of a problem are transformed into finite difference equations, they cannot be considered truly equivalent due to truncation errors introduced in the transformation. These errors can result in some numerical schemes solving a set of equations that are not consistent with the actual governing equations. In the present study, three methods of model verification are employed: Monitoring of the flow variable residuals during iteration which is used as a convergence parameter during solution and an analytical method by which a grid convergence index (GCI) for the meshes is calculated using a mesh refinement/coarsening technique (Roache, 1994) in order to verify spatial and temporal convergence. The actual process of verification of the models is carried out for 2D and 3D models in chapters 5 and 6, respectively.

Iterative convergence

The segregated solver is implicit and therefore the calculations are dependent on initial guesses which are iterated upon until convergence is achieved. Iterative convergence can be monitored within the FLUENT solver by calculating the sum of the residuals of each

of the conserved variables after each solver iteration. With infinite computer precision, the residuals will vanish as the solution converges. With realistic levels of precision, the residuals decay to a small value and then level out. When the residual decreases by a specified order of magnitude the solution is said to have iteratively converged. In the present study, the level of convergence is set to three orders of magnitude. In this way the results do however depend on the residuals of the early iterations and therefore on the suitability of the initial guess. If the initial guess is not good for some reason, the initial residuals will be very large and whatever reduction in order of magnitude has been selected to quantify convergence, convergence is not guaranteed. Conversely, a very accurate initial guess would result in little decrease in residuals and hence several orders of magnitude decrease could not be expected.

The procedure for monitoring the residuals is the same for all conserved variables and is demonstrated for u:

After discretisation, the conservation equation for u at a cell p can be written as

$$a_p u_p = \sum_{nb} a_{nb} u_{nb} + b \tag{4.32}$$

where a_p is the centre coefficient for the cell, a_{nb} are the influence coefficients for the neighbouring cells and b represents the source term including boundary conditions. Note that the above notation is standard notation in control volume methods (Versteeg and Malalasekera, 1995). The residual R^u that is calculated by the segregated solver is the summation of the imbalance in equation (4.32) over all the computational cells p. This can be expressed as follows:

$$R^u = \sum_{cells\ p} \left| \sum_{nb} a_{nb} u_{nb} + b - a_p u_p \right| \tag{4.33}$$

where R^u is called the 'unscaled' residual. Convergence is difficult to judge without scaling, take for example the computational lock-box domain of the present study, there is no inlet flow condition for u (or any of the other variables) with which to compare the residual. To overcome this, FLUENT uses a scaling factor to represent the variables throughout the domain in order to scale the residual equation (4.33). With this scaling employed, the 'scaled' residual can be defined as

$$R^u = \frac{\sum_{cells\ p} \left| \sum_{nb} a_{nb} u_{nb} + b - a_p u_p \right|}{\sum_{cells\ p} |a_p u_p|} \tag{4.34}$$

This is the residual formula used as an indicator of iterative convergence for all variables.

For the continuity equation, the scaled residual for the segregated solver is defined by

the following expression

$$\frac{R_n^{con}}{R_{1-5}^{con}} \tag{4.35}$$

which represents the continuity residual calculated for the n^{th} time step scaled with the largest value of the continuity residual in the first five iterations. Note that the superscript *con* should not be confused with meaning *concentration*, for which the residual is written R^C.

Spatial convergence

Dependence of the numerical solution on the computational grid must be determined in order to establish errors that may result from simulations using a particular mesh size. Strictly, spatial convergence implies complete mesh independence, however, depending on the problem in question, this is not always possible without a comprehensive, computationally demanding study. Therefore, the means to quantitatively describe the level of spatial convergence are desired, for example the 'grid convergence index' (GCI) approach proposed by Roache (1994) used by (Corney, 2005) and in the present study. However, even with this approach, computational expense is high if the procedure is performed for all numerical parameters and escalates as the number of mesh refinements increases. For expense to be minimised while retaining an efficient verification methodology in the present study, three variables u, w and C were chosen to quantify spatial convergence of the flow field with three second order mesh refinements 42×417, 84×834 and 168×1668. The principle of the method proposed by Roache (1994) is that if a numerical scheme is truly second order accurate then the errors should reduce with the square of the mesh size. Hence, the error in the spatial resolution can be quantitatively verified (Roache, 1997). What is required is to verify the fidelity of a numerical solution at a certain mesh resolution to the true solution. However, the exact solution is rarely obtainable and hence the error using a chosen mesh cannot be calculated by comparison. Consequently, the fidelity of the solution with the current mesh is quantified relative to numerical solutions of the same equations computed on different meshes. This idea translates analytically to a modified version of the Richardson extrapolation technique which the grid convergence index is based upon. Methods based on Richardson extrapolation of the results from systematic mesh refinement analysis are considered as acceptable methods of truncation error evaluation (ASME, 1993), hence their use for verification in the present study. The method is as follows:

Richardson extrapolation assumes that the numerical solution (i.e. the solution of any variable throughout the domain), ϕ, computed with a first order method with a grid spacing δx, can be represented in series form by

$$\phi = \phi_* + g_1 \delta x + g_2 \delta x^2 + g_3 \delta x^3 + ... \tag{4.36}$$

where $g_1, g_2...$ are defined throughout the domain and independent of any discretisation and ϕ_* represents the exact solution to the original equations. For a second order method, $g_1 = 0$. Hence, if a solution ϕ_1 is obtained from a fine mesh (δx_1) and ϕ_2 is obtained from a coarser mesh (δx_2), the leading order term in equation (4.36) can be eliminated and a value for g_2 can be calculated. Then a more accurate solution for ϕ_* can be determined by substituting this updated g_2 into equation (4.36). Roache (1994) shows that this exact solution can be approximated in terms of a correction to the fine grid solution, ϕ_1, by the following expression

$$\phi_* \approx \phi_1 + \frac{\phi_1 - \phi_2}{\varrho^2 - 1} \tag{4.37}$$

where $\varrho = \delta x_2 / \delta x_1$ is the grid refinement ratio and higher order terms have been dropped. For example, if a coarse mesh is doubled (or a fine mesh is halved) then $\varrho = 2$ and equation (4.37) gives

$$\phi_* \approx \frac{4\phi_1}{3} - \frac{\phi_2}{3} \tag{4.38}$$

This approximation is third order accurate. For the general case, where ϱ is not necessarily 2 and a ϖ^{th} order numerical method is used, (4.37) can be written as

$$\phi_* \approx \phi_1 + \frac{\phi_1 - \phi_2}{\varrho^{\varpi} - 1} \tag{4.39}$$

which is $(\varpi + 1)^{th}$ order accurate. This level of accuracy can be shown to hold in two and three dimensional simulations as long as ϱ and ϖ are fixed in all space and time directions (Roache, 1994). Based on the foregoing approximations, the GCI for a fine mesh can be defined in the following way:

Using equation (4.39), the fractional fine mesh error estimate E_1, is given by

$$E_1 = \frac{e}{\varrho^{\varpi} - 1} \tag{4.40}$$

where $e = (\phi_2 - \phi_1)/\phi_1$. The actual fractional fine mesh error is given by

$$A_1 = \frac{\phi_1 - \phi_*}{\phi_*} \tag{4.41}$$

Roache (1994) shows that A_1 can be written in terms of E_1 using the following expression

$$A_1 = E_1 + O(\delta x^{\varpi+\varpi_0}, E_1^2) \tag{4.42}$$

where $\varpi_0 = 1$ if forward or backward differences have been used in the discretisation and $\varpi_0 = 2$ if central differences have been used. Therefore, we can say that E_1 is an 'ordered error estimator' and represents a good approximation to the actual error A_1 if $E_1 \ll 1$. It follows from equation (4.40) that the GCI for a fine mesh can be given by

$$GCI[fine\ grid] = \frac{3|e|}{\varrho^{\varpi} - 1} \tag{4.43}$$

where the coefficient 3 is recommended by Roache (1994) and has been used in previous verification calculations (e.g. Hardy *et al.*, 2003; Corney, 2005). The GCI of the coarse grid can then be given by

$$GCI[coarse\ grid] = \varrho^{\varpi} GCI[fine\ grid] \tag{4.44}$$

The problem of division by zero can be encountered in these analyses. This is eliminated by calculating the GCIs only at cells containing $\phi_1 > 0.01\phi_{1,max}$, where $\phi_{1,max}$ is the maximum absolute value of ϕ_1 in the whole domain at the current time step. As mentioned previously, due to computational restrictions, the GCIs for the velocity components and concentration are calculated in the present study and performed at time $t = 6$ s. This time was chosen so that the gravity current has had time to develop but is short enough to minimise computational expense. All GCIs herein are presented as percentages.

Temporal convergence

The above procedure for the spatial convergence holds for assessing the dependence of the numerical solution on the time-step size since all the simulations are second order accurate in space and time and a refinement ratio of order two is applied (Roache, 1994). The equivalent time-steps for the above meshes are 0.02, 0.01 and 0.005 s.

4.5.2 Validation

Essentially, the full potential of a code as a general tool cannot be validated. It is only the calculations carried out with that code that are subject to validation. In the present study, validation of all numerical solutions is undertaken rigorously, with comparison to the experimental datasets from the present laboratory work (see chapter 2) for the fundamental velocity and turbulence profiles within the flow in the smooth and rough cases. It should be noted that validation is limited by the inevitable error incurred during the experiments with which the numerical calculation is being compared. The immediate limitation of laboratory studies is the scale. Ideally, data for use in validation would be obtained at a field scale but the length scales required for this study cannot typically be setup in the laboratory. Data from the field is subject to the specific conditions of the locality and due to the highly spontaneous and transient nature of gravity currents and their relative inaccessibility (for example, consider data collection from active submarine currents), is often impossible to obtain.

One of the advantages of using CFD is that the data obtainable from the simulations can often cover a much wider range of flow variables and statistics than an equivalent experimental study, particularly with respect to 3D data sets. Where sufficient experimental data is available for a flow variable, numerical results are validated. However, where appropriate, results that cannot be fully validated due to limited experimental data for that flow variable are still presented as a predictive foundation for future study. For example, without PIV or high resolution data, the secondary motion of the flow in the region of the roughness elements cannot be captured in the laboratory, so there is limited data for accurate validation of the numerical flow fields in that vicinity. However, it is important that this data is presented since it is expected to have substantial influence on the main current flow field.

Some simulations have no experimental equivalents either in the present study or others to date where laboratory time and equipment availability do not permit an experimental study. However, despite the lack of experimental data, the numerical simulations have been undertaken to seek relationships between variations in the distribution, shape and relative size of the roughness elements and the resulting gravity current dynamics. Although results from these models cannot be validated within the scope of this investigation, they can be analysed with reference to the differences between other experimental runs and their numerical counterparts and implications for further effects of bed roughness on gravity currents can be deduced and are left open for future study.

Chapter 5

Depth-resolved numerical simulations: 2D model results

5.1 Introduction

The previous chapter presented the computational methodology used in the 2D and 3D numerical simulations, including the verification and validation procedures. This chapter presents the results of the depth-resolved 2D numerical simulations calculated using the commercial CFD software FLUENT. The 3D model results are presented in the next chapter. Several important observations resulting from the 2D simulations that do not have a 3D equivalent are discussed here. The full discussion of the combined 2D and 3D numerical results can be found in section 6.8. However, for ease of reading and to highlight features that may be explained by the subsequent 3D model, the salient predictions of the simulations so far are also summarised. The CFD study herein allows further detailed insight into the processes induced by the presence of bed roughness and enables the generation of turbulence kinetic energy and concentration fields which are not available from the present experiments. Detailed emphasis is given to the effects of the ambient fluid between the elements. Verification and validation with experimental data have been rigorously completed and are presented in detail.

5.2 Outline of models

The exact setup of the models has been explained in detail in chapter 4. The tank dimensions are directly comparable to the experimental setup and the initial conditions for all simulations represent a gravity current with the equivalent of a 5% initial density excess. For all of the geometries considered, the walls have the 'no-slip' condition except the

No.	Mesh	Bed type	Exp. equivalent
1	42 × 417	Smooth	Y
2	84 × 834	Smooth	Y
3	168 × 1668	Smooth	Y
4	168 × 1668	$\text{Beams}_{6,1}$	N
5	84 × 834	$\text{Beams}_{6,2}$	Y
6	168 × 1668	$\text{Beams}_{6,2}$	Y
7	84 × 834	$\text{Beams}_{6,4}$	Y
8	168 × 1668	$\text{Beams}_{6,4}$	Y
9	168 × 1668	$\text{Beams}_{6,8}$	Y
10	168 × 1668	$\text{Beams}_{6,16}$	N
11	168 × 1668	$\text{Beams}_{6,2}$ (D)	Y
12	168 × 1668	$\text{Beams}_{6,8}$ (D)	Y
13	42 × 417	$k_{s,0.00075}$	N
14	42 × 417	$k_{s,0.0015}$	Y
15	42 × 417	$k_{s,0.003}$	N

Table 5.1: 2D numerical simulations undertaken in the present study. Tank dimensions are directly comparable to experimental data. The initial conditions for all simulations represent a gravity current with the equivalent of a 5% initial density excess in the laboratory. All walls have the 'no-slip' condition except the top wall which has a 'symmetry' condition. 'D' means that dense fluid is also initialised between the roughness elements. Mesh relates to the maximum number of cells in the vertical and horizontal directions. Also included is whether there exists an experimental equivalent for validation (Y) or not (N).

top boundary which has a 'symmetry' condition. All of the 2D numerical simulations carried out in the present study are listed in table 5.1, including the mesh resolution (*maximum cells vertically* × *maximum cells horizontally*), the bed type and whether a corresponding experimental dataset is available for validation. The simulation of two additional beam roughness spacings, $\text{beams}_{6,1}$* and $\text{beams}_{6,16}$ (No. 4 & 10), were undertaken to complement the other three beam-roughened cases and enable further analysis of the effects of spacing and the relevance of d-type and k-type configurations to gravity current dynamics. The three mesh resolutions for the smooth case (No. 1 - 3) and two for the $\text{beams}_{6,2}$ (No. 5 & 6) and $\text{beams}_{6,4}$ (No. 7 & 8) are used for verification. These two beams cases were chosen to represent a d-type and k-type bed respectively. Note that there is no coarse mesh in the body-fitted rough cases because the longitudinal dimension of the cells in this case is greater than the roughness element width and so

*This terminology was defined in chapter 2 and is used as shorthand to describe the element in use. It was defined as follows: $\textit{beams}_{\textit{height,spacing}}$ where *beams* is a qualitative description of the element, *height* is the maximum element height k_r (mm) and *spacing* is the ratio of the distance between adjacent elements and the height w/k_r. For example, $\text{beams}_{6,1}$ refers to the beam type roughness with equal height and spacing of 6 mm.

cannot be fitted to the elements. The choice of mesh is discussed in the next section.

5.3 Verification

Iterative convergence

Iterative convergence is monitored by calculating scaled residuals for each of the variables by solving equation (4.34) ((4.35) for continuity) every iteration, as explained in full in section 4.5 in the previous chapter. When the residuals all decrease below the critical level, chosen herein to be 10^{-3}, convergence is assumed to have been achieved for that time step and the solution procedure continues. Evidence of this process is shown in figure 5.1 for time steps between 6 s and 7 s for the smooth domain with the coarsest (42 × 417) mesh. It can be observed clearly that although the initial guess each time step is somewhat inaccurate, after subsequent iterations the solution is consistently satisfying the convergence criteria for all variables each time step. Equivalent convergence characteristics are observed for the 84 × 834 and 168 × 1668 resolutions and in the rough case. However, since they are similar it is of no additional benefit to present them all.

Spatial and temporal convergence

The spatial and temporal convergence of a simulation are parameterised jointly herein by the grid convergence index (GCI) as detailed in section 4.5. The results for the three mesh resolutions used for the smooth case in the present study, generated by a factor 2 refinement, can be seen in table 5.2 for the horizontal and vertical velocity variables and the user-defined scalar (concentration), i.e. u, v and C respectively. The GCIs are calculated using linear interpolation[†] of the results of a finer mesh onto the next coarsest mesh, except for the 42 × 417 model where no finer mesh is available and therefore the GCI of the 84 × 834 mesh must be used. For the rough case, as mentioned in section 5.2 it was not possible to use the coarsest mesh, therefore the GCIs were calculated using the two finer meshes. In this case, the GCI for the finer of these two meshes, 84 × 834, cannot be calculated by comparison to the next coarse mesh and is therefore generated using the 168 × 1668 GCIs. Using this characterisation of the error in the different grids it appears that there is substantially more error incurred with the coarsest mesh, particularly with respect to the concentration field. In order to examine the GCIs more thoroughly in the context of the actual gravity current model, the concentration field for

[†]Corney (2006, p. 61) discusses the implications of the use of different interpolation techniques and concludes that linear interpolation is suitable in these studies.

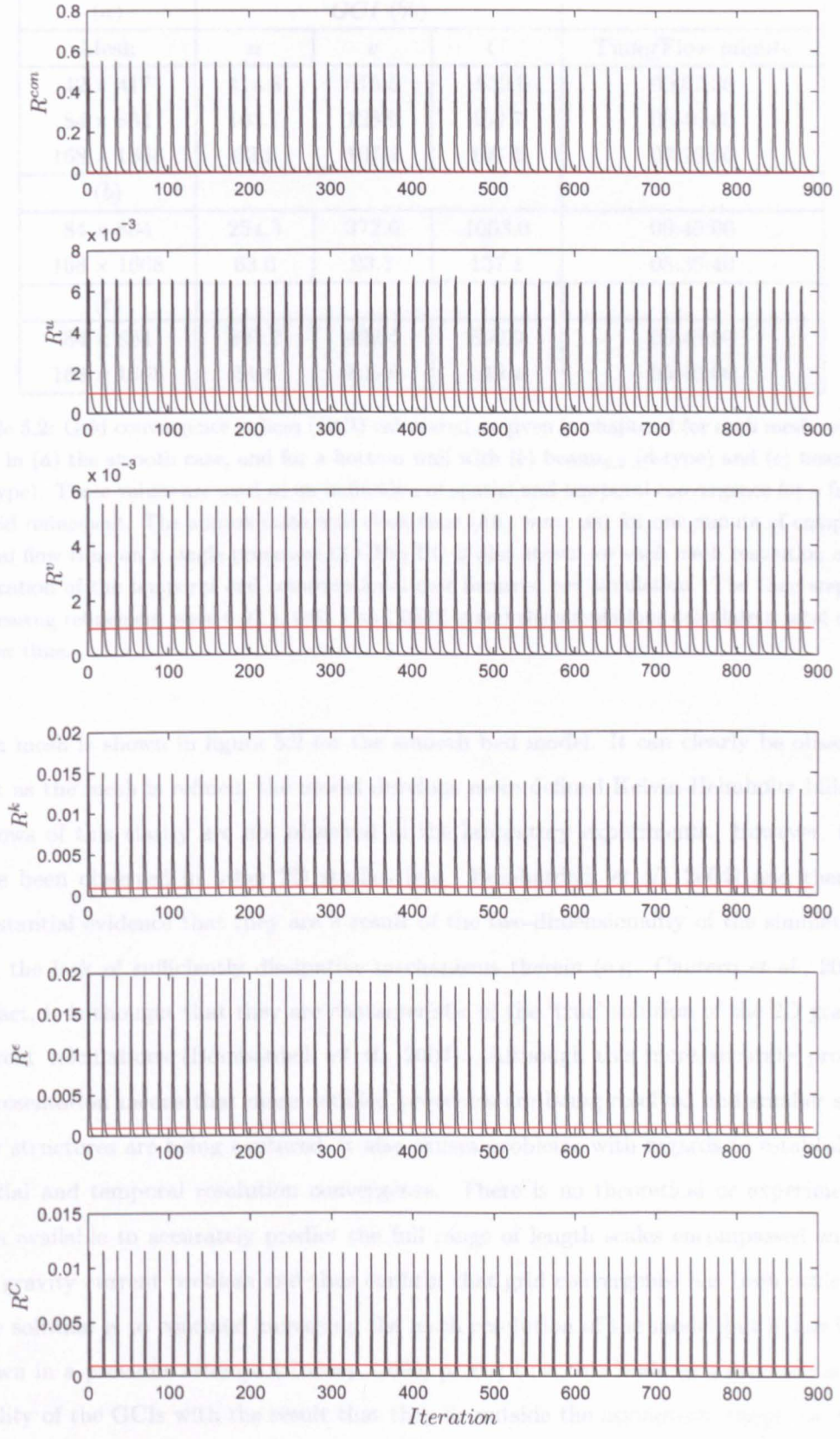

Figure 5.1: Iterative convergence shown in the form of residuals, calculated as given in chapter 4 for the 42×417 resolution mesh for the smooth case. The convergence criteria, 10^{-3}, below which the residuals are assumed to indicate convergence is shown in red.

(*a*)	*GCI* (%)			
Mesh	u	v	C	**Time/Flow minute**
42 × 417	414.8	515.5	1839.0	00:07:30
84 × 834	103.7	128.9	459.7	00:45:00
168 × 1668	62.9	107.4	197.5	07:20:00
(*b*)				
84 × 834	254.3	372.6	1063.0	00:45:00
168 × 1668	63.6	93.1	137.1	05:36:40
(*c*)				
84 × 834	207.2	422.4	890.9	00:45:00
168 × 1668	51.8	105.6	142.4	05:40:00

Table 5.2: Grid convergence indices (GCI) calculated as given in chapter 4 for each mesh resolution in (*a*) the smooth case, and for a bottom wall with (*b*) $\text{beams}_{6,2}$ (d-type) and (*c*) $\text{beams}_{6,4}$ (k-type). These values are used as an indication of spatial and temporal convergence for a factor 2 grid refinement. The approximate wall clock time ($hh : mm : ss$) for one minute of computational flow time on a single processor (3 GHz) PC is also shown for each mesh resolution as an indication of the temporal and computational cost incurred per simulation. The time steps in increasing refinement were 0.02 s, 0.01 s and 0.005 s and the simulations calculate a total of 30 s flow time.

each mesh is shown in figure 5.2 for the smooth bed model. It can clearly be observed that as the mesh is refined, the model develops more defined Kelvin-Helmholtz billows. Billows of this clarity are not observed in the laboratory experiments. However, they have been observed in other 2D studies (e.g. Bombardelli *et al.*, 2004) and there is substantial evidence that they are a result of the two-dimensionality of the simulations and the lack of sufficiently dissipative mechanisms therein (e.g. Cantero *et al.*, 2003). In fact, it is thought that they are characteristic of the 'true' solution of the 2D gravity current calculations (Bombardelli *et al.*, 2004). Although this more accurate process representation means that more detailed processes are being resolved and smaller scale flow structures are being captured, it also causes problems with regards to establishing spatial and temporal resolution convergence. There is no theoretical or experimental data available to accurately predict the full range of length scales encompassed within the gravity current problem and thus confirm that grid convergence has been achieved. One solution is to continue increasing the mesh resolution of the model but it has been shown in a previous attempt (Corney, 2005, p. 60) that this leads to a decrease in the quality of the GCIs with the result that they lie outside the asymptotic range, i.e. they do not decrease by a factor of $1/\varrho^{\varpi}$ (Roache, 1994). Based on the approximate wall clock time taken to calculate one minute of computational flow time, see table 5.2, simulations on finer meshes would also incur prohibitive computational cost, beyond the scope of the

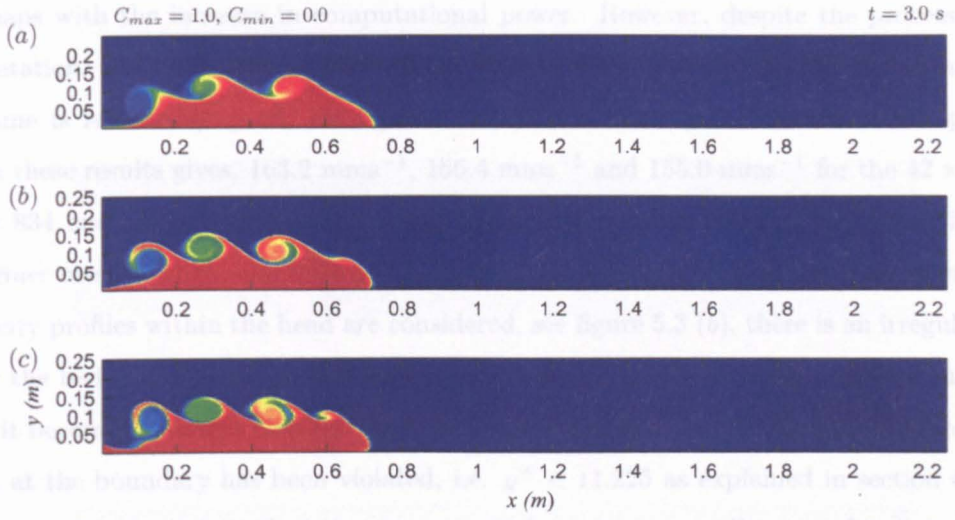

Figure 5.2: UDS (concentration), C, fields at $t = 3\ s$ resulting from the 2D simulations for the smooth bed with three mesh refinements: (a) 42×417, (b) 84×834 and (c) 168×1668. Red and blue are high and low concentration, respectively. Maximum and minimum values are displayed at the top of the figure.

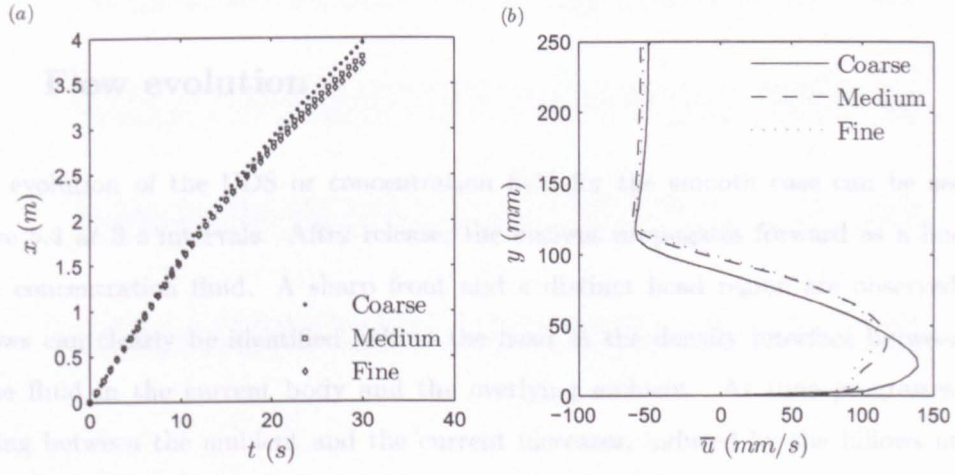

Figure 5.3: (a) Position of the current front as a function of time generated from the 2D numerical simulations. Three mesh refinements (42×417, 84×834 and 168×1668) are shown for the smooth case. (b) Comparison of the downstream horizontal velocity, u, profiles for the smooth bed case for the total domain depth at one location ('bin 35') generated from the 2D numerical simulations for three mesh refinements: 42×417, 84×834 and 168×1668.

computational resources available.

The GCIs in table 5.2 have highlighted the problems involved with accurately modelling a physically complex flow, such as a gravity current, numerically. Clearly the unphysical coherence of the Kelvin-Helmholtz billows is a numerical phenomena that must be acknowledged and treated cautiously until the means to assess them becomes available,

perhaps with the increase in computational power. However, despite the process representation, the agreement between the meshes in terms of front position as a function of time is reasonably good, see figure 5.3 (*a*). Calculating the smooth front speeds from these results gives, 163.2 mms^{-1}, 156.4 mms^{-1} and 155.0 mms^{-1} for the 42 × 417, 84 × 834 and 168 × 1668 meshes, respectively. There is an issue with the validity of the finer meshes when used with the wall functions in the RANS model since when the velocity profiles within the head are considered, see figure 5.3 (*b*), there is an irregularity near the bed. This is not present in a typical velocity profile through a gravity current and it becomes apparent that for the finer meshes the condition for the wall functions to hold at the boundary has been violated, i.e. $y^+ < 11.225$ as explained in section 4.3.3. An example calculation of y^+ (equation (4.26)) in the near-wall region for each mesh resulted in values of 26.8, 10.9 and 5.37 for the 42×417, 84×834 and 168×1668 meshes, respectively proving that the violation has certainly occurred with the fine mesh. After careful consideration of these results, the 42 × 417 mesh was chosen in favour of the 84 × 834 and 168 × 1668 meshes.

5.4 Flow evolution

The evolution of the UDS or concentration field for the smooth case can be seen in figure 5.4 at 3 s intervals. After release, the current propagates forward as a body of high concentration fluid. A sharp front and a distinct head region are observed and billows can clearly be identified behind the head at the density interface between the dense fluid in the current body and the overlying ambient. As time progresses, the mixing between the ambient and the current increases, induced by the billows at this interface. The high concentration current becomes more elongated and shallower and the billows become more dilute due to this mixing and diffusion but they maintain their coherence (12 - 18 s). After 21 s, the billows appear much more diffuse and the body of the current is significantly shallower. The head remains distinct from the rest of the current but much dilution has occurred such that the highest concentration fluid is a thin layer at the bottom of the head. An irregularity in the form of a wave-like disturbance in the high concentration fluid within the current body can be seen in these 2D concentration fields and apparently remains stationary from 18 - 24 s. This 'blip' appears to be the result of a large, probably unphysical, billow retained at the density interface directly above it. After 27 s, both the billow and the blip have more or less dissipated. This phenomenon could be percieved as a bore or an interfacial wave as Ooi

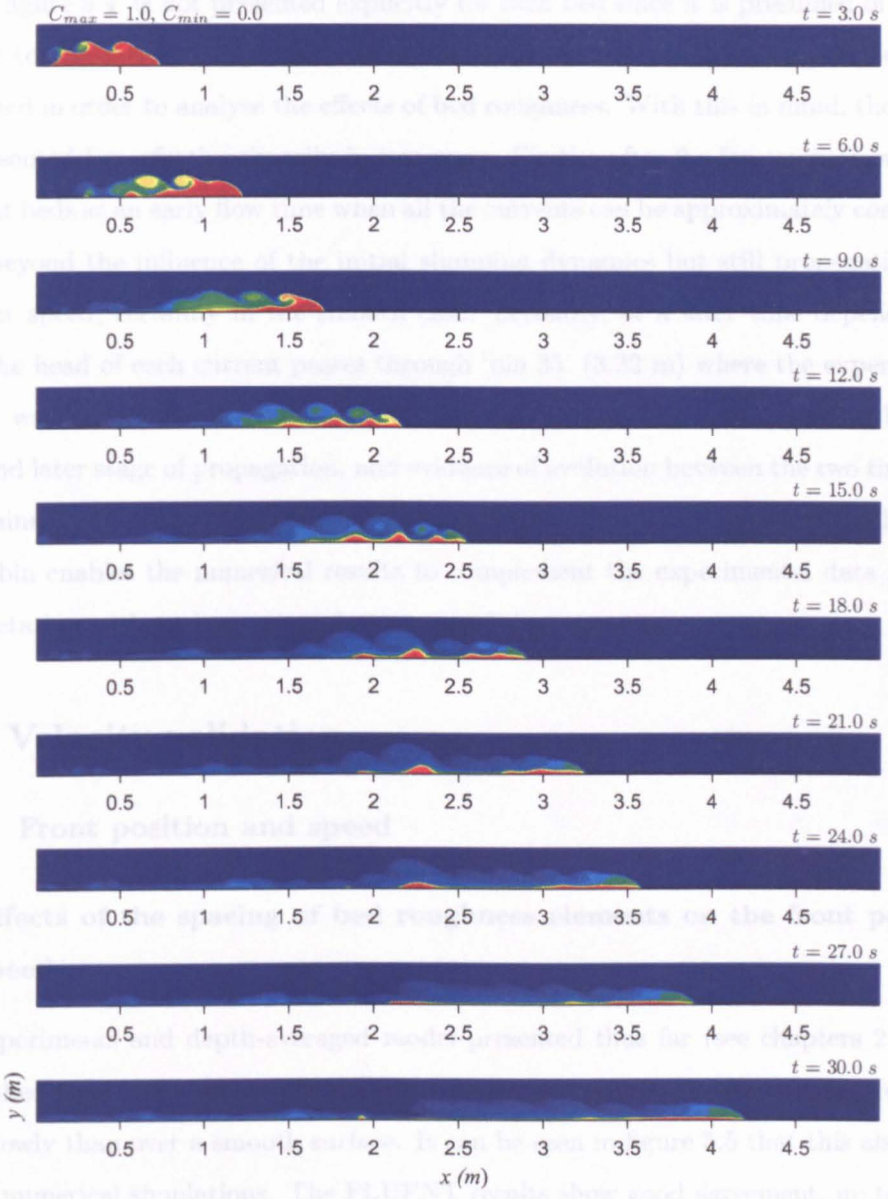

Figure 5.4: The evolution of the concentration field every 3 s up to 30 s for 2D numerical simulation of the smooth case. Red and blue are high and low concentration, respectively, maximum and minimum values are displayed at the top of the figure.

et al. (2005) interpret from their 2D LES. However, it is likely that this is an attribute of the two-dimensionality of their model and that of the present study. Notice that it is at about this distance that the slowing of the front occurred (figure 5.3 (*a*)) indicating a correlation between the unphysical size and lack of motion of the irregularity and the retardation of the current. When compared to the experimental data in section 5.5.1 it is observed that the reduction in speed of the current in the CFD at this point is premature.

In the following results, the flow evolution of a simulation, as shown for the smooth

case in figure 5.4, is not presented explicitly for each bed since it is presumed of greater interest to consider more specific internal dynamics of the currents that can be better quantified in order to analyse the effects of bed roughness. With this in mind, the results are presented henceforth primarily in two ways. Firstly, after 9 s for comparison of the different beds at an early flow time when all the currents can be approximately considered to be beyond the influence of the initial slumping dynamics but still propagating at a constant speed, certainly in the smooth case. Secondly, at a later time dependent on when the head of each current passes through 'bin 35' (3.22 m) where the experimental dataset was sampled in the laboratory. Thus, the currents can be analysed at both an early and later stage of propagation, and evidence of evolution between the two times can be obtained. Also, coordination of the numerical results with the experimental results at the bin enables the numerical results to complement the experimental data and aid interpretation without large spatial or temporal discrepancies.

5.5 Velocity validation

5.5.1 Front position and speed

The effects of the spacing of bed roughness elements on the front position and speed

The experiments and depth-averaged model presented thus far (see chapters 2 and 3) established that the presence of roughness on the bed causes the current to propagate more slowly than over a smooth surface. It can be seen in figure 5.5 that this also holds for the numerical simulations. The FLUENT results show good agreement, up to about 10 s, for the smooth and body-fitted boundaries. However, beyond this time, compared to the experimental data, the numerical predictions all show a premature slowing of the current. In the smooth case, the current has been observed to move at a constant velocity in the first ten lock-box lengths of the tank ($x \approx 10x_0$, e.g. Rottman and Simpson (1983) and the present study, see section 2.4) after which it undergoes a transition to a slower speed. Figure 5.5 suggests that the simulations are able to model this phase of constant speed but that they begin to decrease in speed too early. This inaccurate transition occurs earlier as the spacing of the roughness elements increases. However, as found in the experimental results (chapter 2), an earlier transition is a characteristic of increased element spacing although it appears to occur at about the same time for all spacings. This implies that the difference in the numerical predictions is not necessarily dependent on

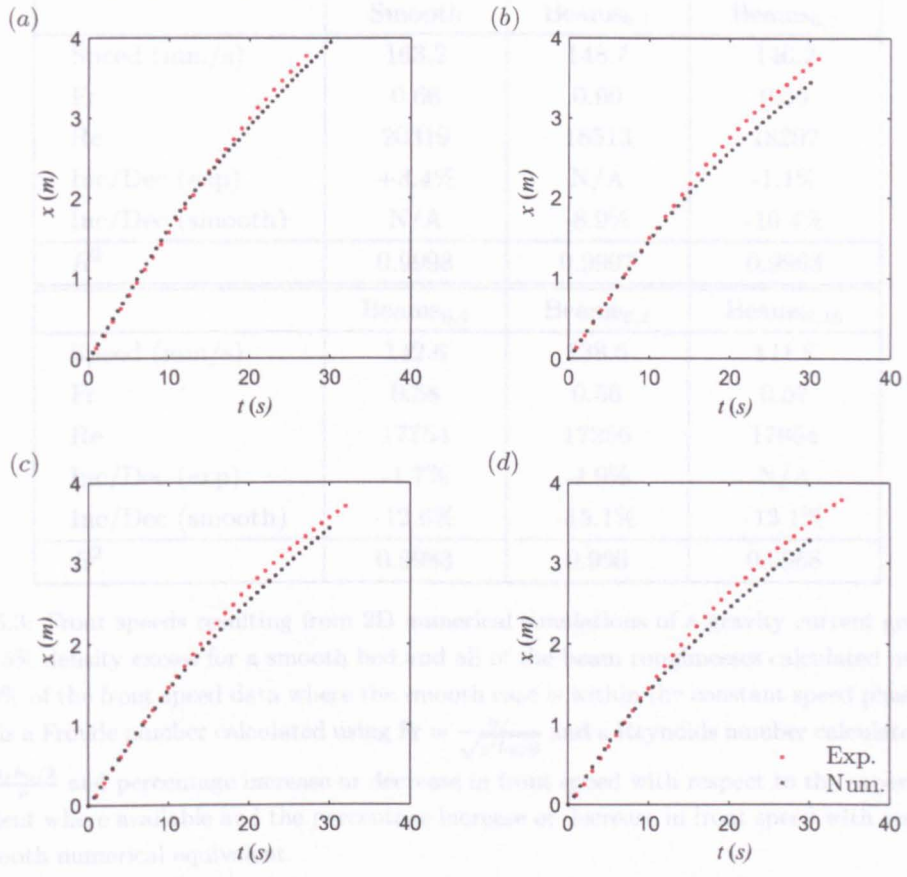

Figure 5.5: Position of the front as a function of time resulting from 2D numerical simulations compared to the equivalent experimental results for (*a*) a smooth bottom wall and bottom walls with (*b*) beams$_{6,2}$, (*c*) beams$_{6,4}$, and (*d*) beams$_{6,8}$.

the bed change but mainly a result of the two-dimensionality of the simulations as found by other investigators (e.g. Cantero *et al.*, 2003). Therefore with acknowledgement that the 2D computations have limitations, the results can be considered valid representations of their experimental equivalents.

The corresponding front speeds for the data are displayed in table 5.3. 39% of the smooth dataset was well correlated to represent the constant speed phase. Therefore the same percentage of data was also used to calculate comparative speeds for the rough cases. The percentage difference between these speeds with respect to their experimental equivalent and the smooth simulation are also included. It can be seen that in this constant speed region, despite the premature decrease at later times, the smooth case actually produces a faster current than the corresponding experimental case but only by 3.4%. The front positions of the current with the beams$_{6,2}$ and beams$_{6,4}$ boundaries show very good agreement, however, the beams$_{6,8}$ case shows an increased error. This is probably due to the fact that, for the calculation as for the experimental data, 39% of the data is taken

	Smooth	$\text{Beams}_{6,1}$	$\text{Beams}_{6,2}$
Speed (mm/s)	163.2	148.7	146.2
Fr	0.66	0.60	0.59
Re	20319	18513	18202
Inc/Dec (exp)	+3.4%	N/A	-1.1%
Inc/Dec (smooth)	N/A	-8.9%	-10.4%
R^2	0.9998	0.9997	0.9993
	$\text{Beams}_{6,4}$	$\text{Beams}_{6,8}$	$\text{Beams}_{6,16}$
Speed (mm/s)	142.6	138.6	141.8
Fr	0.58	0.56	0.57
Re	17754	17256	17654
Inc/Dec (exp)	-1.7%	-4.9%	N/A
Inc/Dec (smooth)	-12.6%	-15.1%	-13.1%
R^2	0.9983	0.996	0.9968

Table 5.3: Front speeds resulting from 2D numerical simulations of a gravity current generated with a 5% density excess for a smooth bed and all of the beam roughnesses calculated using the first 39% of the front speed data where the smooth case is within the constant speed phase. Also shown is a Froude number calculated using $\text{Fr} = \frac{u_f}{\sqrt{g' h_0/2}}$ and a Reynolds number calculated using $\text{Re} = \frac{u_f h_0/2}{\nu}$ and percentage increase or decrease in front speed with respect to the experimental equivalent where available and the percentage increase or decrease in front speed with respect to the smooth numerical equivalent.

based on good correlation for the period of constant speed for the smooth case, rather than the constant speed relative to this specific case.

It is clear from figure 5.6 and table 5.3 that in general the front speed decreases in the presence of any bed roughness and the magnitude of the decrease is dependent on the element spacing with an increase in the distance between the beams leading to a greater decrease in the speed. This was also found in the experiments. It it can be observed that the predictions for $\text{beams}_{6,16}$ and $\text{beams}_{6,8}$ are almost identical. This suggests that the critical element spacing $w/k_r \approx 7$ (where w = distance between elements and k_r = element height, which is always 0.006 m herein) above which few changes to the flow dynamics are observed in open channel and pipe flows (Cui *et al.*, 2003b; Leonardi *et al.*, 2003b; Ashrafian *et al.*, 2004; Ikeda and Durbin, 2007) might also hold in the gravity current context. Measurement of the reattachment length at the bed between two elements further confirms this, see section 5.5.2. With reference to d-type ($\text{beams}_{6,1}$ and $\text{beams}_{6,2}$) and k-type ($\text{beams}_{6,4}$, $\text{beams}_{6,8}$ and $\text{beams}_{6,16}$) spacings, there does not appear to be a noticeable impact on the front speed that enables definitive differentiation between these two classifications. However, it is interesting to note that there is some similarity between the predictions for the $\text{beams}_{6,2}$ and $\text{beams}_{6,4}$ surfaces. This perhaps

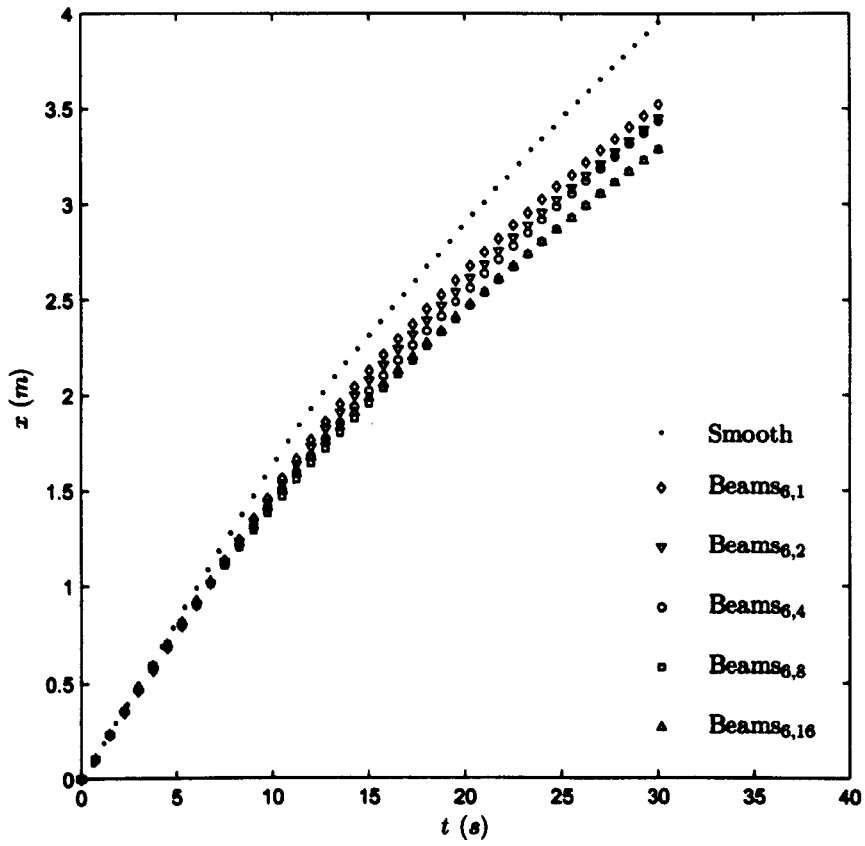

Figure 5.6: Position of the front as a function of time resulting from 2D numerical simulations with a smooth bottom wall, and bottom walls with $\text{beams}_{6,1}$, $\text{beams}_{6,2}$, $\text{beams}_{6,4}$, $\text{beams}_{6,8}$ and $\text{beams}_{6,16}$.

indicates that the classification of a middle 'intermediate' bed roughness configuration ($w/k_r \approx 4$), as some investigators have postulated (Chow, 1959; Cui *et al.*, 2003b), could be justified. When the velocity fields throughout the entire domain are considered in the next section, the differences between the bed types are more obvious and the data predicts that the flow fields for the $\text{beams}_{6,4}$ boundary are more like the k-type cases. This does not repudiate these observations made for the front positions but rather suggests that the $\text{beams}_{6,4}$ case has some d-type and some k-type attributes as an intermediate classification would imply.

The effects of the presence of less dense fluid between the roughness elements on the front position and speed

In the laboratory, two experiments were undertaken with fluid of the same initial density as the current (i.e. 5% excess) injected between the roughness elements for the $\text{beams}_{6,2}$ and $\text{beams}_{6,8}$ beds in order to try and identify the contribution of the fluid in these

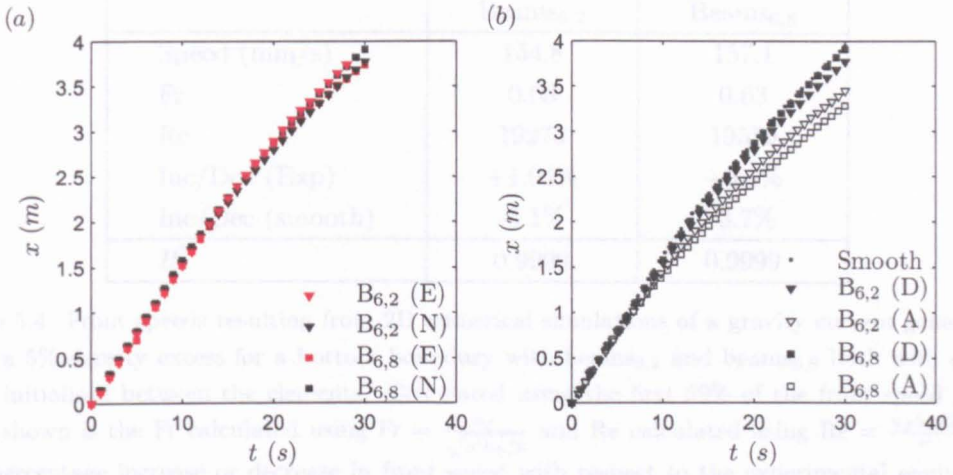

Figure 5.7: Position of the front as a function of time resulting from 2D numerical simulations (N) of a gravity current generated with a 5% density excess for a bottom boundary with beams$_{6,2}$ ($B_{6,2}$) and beams$_{6,8}$ ($B_{6,8}$) both with dense fluid initialised between the elements (D). (*a*) with experimental equivalents (E) and (*b*) with the models without dense fluid between the beams (A) and the smooth case for reference.

gaps to the flow dynamics of the overflowing current. Simulations equivalent to these configurations were also performed numerically. The resulting front positions of the currents as a function of time and the experimental equivalents, can be seen in figure 5.7 (*a*). Again, the agreement is very good for early times. At later times, the d-type case is observed to be slightly inaccurate due to the aforementioned premature decrease in speed. Conversely, the k-type bed is not only faster than the regular case with ambient fluid in the gaps but faster than the d-type numerical simulations and both of the experimental cases, almost equal to the smooth case. In this case, it is possible that the energy losses due to lateral motion, which is not possible in 2D, is necessary for accurate retardation of the flow.

The good agreement with corresponding experimental data for the constant phase is reflected in the front speeds calculated from the data shown in table 5.4. The FLUENT prediction is only $\approx 1\%$ faster than the experimental result in the d-type case and $\approx 3\%$ faster in the k-type. Comparing the model with dense fluid between the elements to the equivalent with ambient fluid and the smooth result, see figure 5.7 (*b*), it is clear that the presence of the less dense fluid between the elements contributes to a reduction in the speed but is not the only cause of the decrease in speed, i.e. the entrainment of the ambient fluid between the elements as the current flows over is significant but so are the elements themselves. This agrees with the experimental observations presented in chapter 2. If the reduction in speed with respect to the smooth case is considered

	$Beams_{6,2}$	$Beams_{6,8}$
Speed (mm/s)	154.8	157.1
Fr	0.63	0.63
Re	19273	19559
Inc/Dec (Exp)	+1.04%	+3.4%
Inc/Dec (smooth)	-5.1%	-3.7%
R^2	0.9999	0.9999

Table 5.4: Front speeds resulting from 2D numerical simulations of a gravity current generated with a 5% density excess for a bottom boundary with $beams_{6,2}$ and $beams_{6,8}$ both with dense fluid initialised between the elements. Calculated using the first 39% of the front speed data. Also shown is the Fr calculated using $\mathrm{Fr} = \frac{u_f}{\sqrt{g' h_0/2}}$ and Re calculated using $\mathrm{Re} = \frac{u_f h_0/2}{\nu}$ and the percentage increase or decrease in front speed with respect to the experimental equivalent and the percentage increase or decrease in front speed with respect to the smooth numerical equivalent.

in the d-type case, it can be observed that there is a $\approx 5\%$ reduction with dense fluid between the elements which increases to a $\approx 10\%$ reduction with ambient fluid between the elements. Although these magnitudes are slightly exaggerated in comparison to the experimental equivalent ($\approx 3.5\%$ and $\approx 7\%$, respectively), they essentially produce the same conclusion, namely that during the period of constant speed, there is an approximately 50:50 split governing the reduction in speed due to the presence of beam roughness, $\approx 50\%$ can be attributed to buoyancy effects of the ambient fluid trapped between the elements and the other $\approx 50\%$ to other effects resulting from presence of the elements. This statistic also holds approximately for the k-type case in the experimental result. However, the 2D numerical results do not agree and find that, while removal of the ambient fluid between the elements reduces the speed by $\approx 4\%$, the total effect of the beams with this ambient fluid increases this reduction to $\approx 15\%$. It is possible that, as mentioned above, this is a result of the different spacings being subject to different magnitudes of lateral motion, therefore the 3D model data should provide a conclusive result. This does not hold at later times where inspection of figure 5.7 (*b*) suggests that, the ambient fluid between the elements results in increasingly reduced front positions, most notably in the k-type case.

The effects of the the law-of-the-wall method for specifying the bed roughness on the front position and speed

The results presented thus far have been generated from the data using the body-fitted mesh method for the inclusion of bed roughness. To examine the performance of the

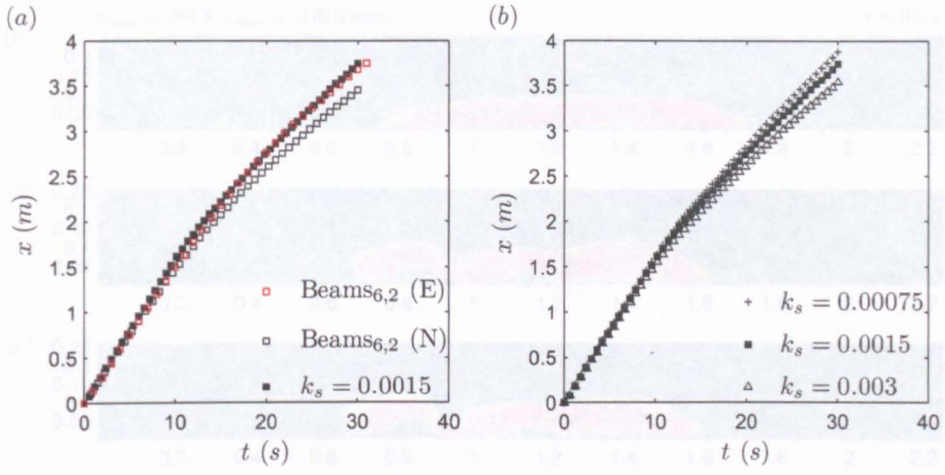

Figure 5.8: Position of the front as a function of time resulting from (a) the 2D numerical simulation with a bed roughened using the law-of-the-wall method with $k_s = 0.0015$ and the experimental (E) and numerical (N) equivalent beams$_{6,2}$ (i.e. $k_s \approx 0.0017$) and (b) the 2D simulations with $k_s = 0.0075$, 0.0015 and 0.003.

law-of-the-wall method, the 42×417 mesh was used with a k_s value of 0.0015. This is almost equivalent to the experimental beams$_{6,2}$ case for which it was established in chapter 2 that $k_s \approx 0.0017$, and is therefore compared to that experimental data and the body-fitted method numerical equivalent. The results of the simulation for the front position as a function of time can be seen in figure 5.8 (a). The law-of-the-wall method appears to show very good overall agreement, although it is interesting to note that the body-fitted method agrees better for early times while the law-of-the-wall method shows better agreement at later times. This is possibly because the body-fitted method resolves the rotating fluid between the elements and, similar to the billows at the interface, these are not broken down efficiently since a 3D mechanism is necessary for this to occur and consequently the current slows down unphysically. However, by specifying a k_s value which has been generated from experiments and thus by nature is subject to 3D mechanisms, the decrease in front speed that results from higher resolution with the finer mesh used in the body-fitted model, does not occur.

The results of an investigation to examine the sensitivity of the method of specifying a k_s value on position of the front as a function of time are shown in figure 5.8 (b). The $k_s = 0.0015$ value was halved and doubled with the result that the smaller value causes less of a slowing effect on the current and the larger value increases the retardation, as expected. Thus, it can be confirmed that the simulations are sensitive to the value prescribed through implementing the law-of-the-wall method.

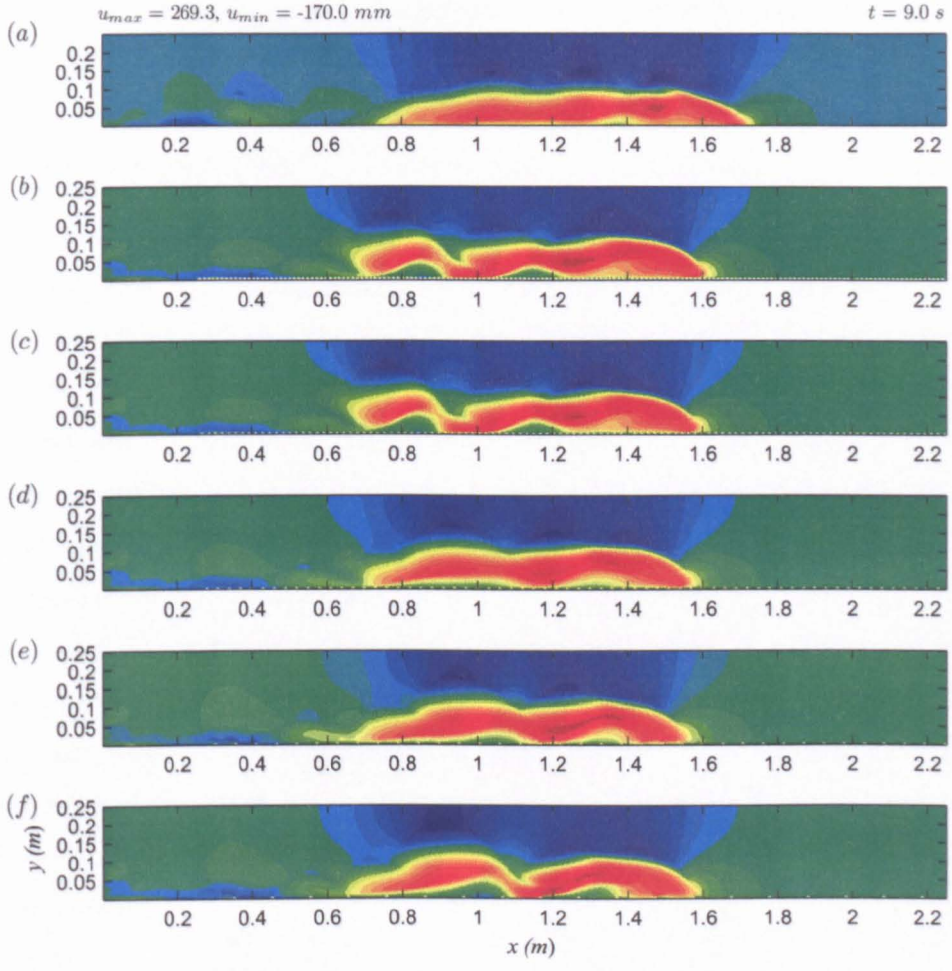

Figure 5.9: Horizontal velocity component, u, fields at $t = 9$ s resulting from the 2D simulation with (a) smooth bottom wall and (b) beams$_{6,1}$, (c) beams$_{6,2}$, (d) beams$_{6,4}$, (e) beams$_{6,8}$ and (f) beams$_{6,16}$. Downstream motion is from left to right. Red and blue are high and low velocities, respectively. Maximum and minimum values are displayed at the top of the figure.

5.5.2 Velocity structure

The effects of the spacing of bed roughness elements on the velocity structure

Figures 5.9 and 5.10 show the velocity fields for horizontal and vertical motion throughout the domain, respectively. In both rough and smooth cases the horizontal and vertical motion at the front of the current is almost identical. However, within the head, for the bed-roughened cases (figures 5.9 $(b) - (f)$), the horizontal velocity maximum appears to be located higher in the current than in the smooth case. Further disruption has occurred to the horizontal motion near the bed and within the return flow (negative) of ambient fluid above the primarily downstream horizontal flow (positive) of the main current body. Figures 5.9 and 5.10 also confirm that, as mentioned previously, the effects of the d-type and k-type spacings can be observed in the velocity fields. The two d-type

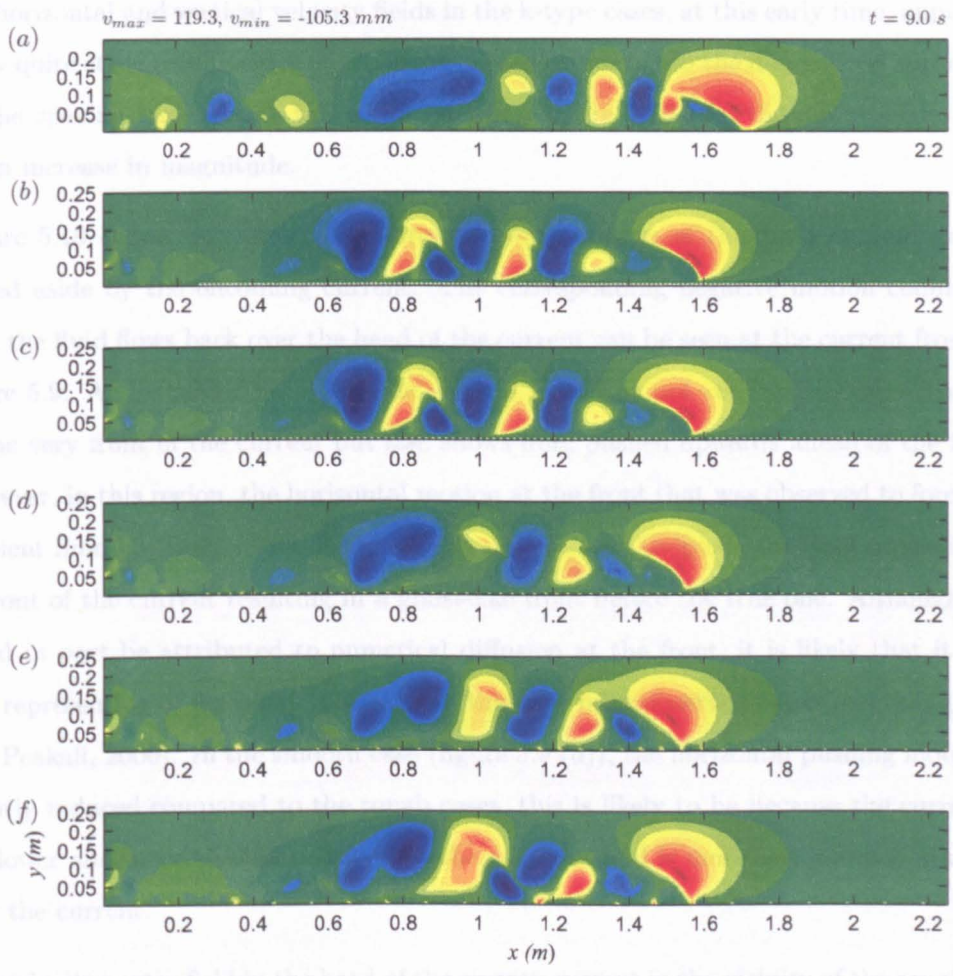

Figure 5.10: Vertical velocity component, v, fields at $t = 9$ s resulting from the 2D simulation with (a) smooth bottom wall and (b) beams$_{6,1}$, (c) beams$_{6,2}$, (d) beams$_{6,4}$, (e) beams$_{6,8}$ and (f) beams$_{6,16}$. Downstream motion is from left to right. Red and blue are high and low velocities, respectively. Maximum and minimum values are displayed at the top of the figure.

cases, figures 5.9 and 5.10 (b) and (c), depict very similar flow fields for this classification of bed. The k-type cases, figures 5.9 and 5.10 $(d) - (f)$, also show close similarity within the velocity domain and, as mentioned previously, are noticeably different to the d-type case. The d-type cases show significant disturbance to the tail of the current, unlike the smooth or the k-type cases. Increased disruption to the return flow above can also be observed, again this is apparently more substantial than in the smooth or k-type cases. These features correspond to increased magnitude in the regions of high positive and negative flow visible in the vertical velocity fields (figures 5.10 (b) and (c)) which collectively indicate the presence of strong billows in the vicinity of these fluctuations at the density interface. In the smooth and k-type simulations (figures 5.10 (a) and $(d) - (f)$, respectively), the regions of high negative or positive vertical velocities appear more diffuse than for the d-type models. It can also be observed that the distribution of

the horizontal and vertical velocity fields in the k-type cases, at this early time, appear to show quite strong similarities to the smooth case compared to the d-type case, although, as the spacing increases to the widest spacing, figure 5.10 (f), the disturbances once again increase in magnitude.

Figure 5.10 shows very clearly the strong upward motion of the ambient fluid as it is forced aside by the oncoming current. The corresponding negative motion confirming that the fluid flows back over the head of the current can be seen at the current fronts in figure 5.9. Additionally, note that the vertical motion is not confined to the extremity of the very front of the current but also shows fluid pushed upwards ahead of the front. However, in this region, the horizontal motion at the front that was observed to force the ambient fluid backwards over the head, can now be seen to 'push' the fluid immediately in front of the current resulting in a ghost-like front before the true one. Although this could in part be attributed to numerical diffusion at the front, it is likely that it is in fact representing of a realistic phenomena that has been observed experimentally (Felix and Peakall, 2006). In the smooth case (figure 5.9 (a)), the horizontal pushing motion is slightly reduced compared to the rough cases, this is likely to be because the current is shallower and more streamlined so that the ambient fluid is more easily forced upwards over the current.

The velocity vector field in the head of the gravity current in the vicinity of the roughness elements can be seen in figure 5.11. Note that the elements themselves are represented by NaN[‡] in the datasets. Therefore the linear interpolation used to produce the contours causes loss of definition of their true shape but does not influence the rest of the data. Rotating vortices trapped between the elements can be observed in the d-type cases, figures 5.11 (a) and (b). In the closest spaced case, $\text{beams}_{6,1}$ (figure 5.11 (a)), these vortices are weaker and no disturbance to the flow above the elements occurs. When this spacing is doubled (figure 5.11 (b)), the vortices are considerably stronger but still there is no clear disturbance to the overflowing current. As the spacing increases to $\text{beams}_{6,4}$ (figure 5.11 (c)) vortices can still be observed at the downstream faces of the elements but they do not fill the whole gap. This suggests that flow separation is occurring at the top of each element and the separating flow is attempting to reattach in the space between the elements and generating a vortex beneath it at the downstream face. Disturbance to the overlying flow is now evident although it does not extend far above the top of the

[‡]NaN, or 'not a number' is usually used to indicate an attempted operation on invalid values, for example, the square root of a negative number. It is used here rather than zero so that mean values are not affected and so that there are no true holes in the dataset for ease of processing.

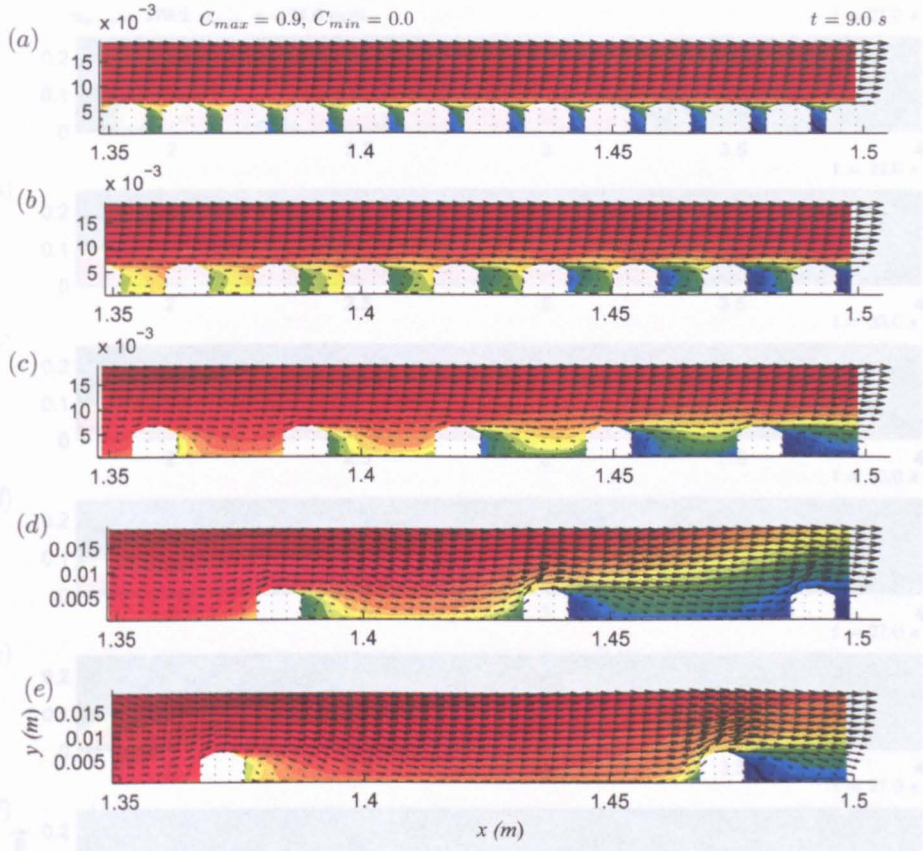

Figure 5.11: Vectors of velocity magnitude and contours of UDS (concentration) distribution in the current head in the vicinity of the roughness elements at $t = 9\ s$ resulting from the 2D simulation with (*a*) $\text{beams}_{6,1}$, (*b*) $\text{beams}_{6,2}$, (*c*) $\text{beams}_{6,4}$, (*d*) $\text{beams}_{6,8}$ and (*e*) $\text{beams}_{6,16}$. Note that the elements are represented by NaN ('not a number') in the datasets, therefore the linear interpolation used to produce the contours causes loss of definition of their true square shape. Downstream motion is from left to right. Red and blue are high and low concentration, respectively. Maximum and minimum values are displayed at the top of the figure.

elements. Further increasing the spacing to the $\text{beams}_{6,8}$ and $\text{beams}_{6,16}$ cases (figures 5.11 (*d*) and (*e*), respectively) gives rise to distinct flow separation at the top of an element with reattachment further downstream between that element and the adjacent one. This creates a larger rotating vortex at the downstream face of the element and potentially a smaller vortex at the upstream face of the subsequent element. However, at the current resolution, the postulated secondary smaller vortex is not clear and can only be inferred by the small region of stationary flow at the upstream face of the element which appears to deflect the primary downstream flow in the gap upwards and over the element apex. Increased distortion to the flow field above the elements can clearly be observed in both cases.

The concentration contours in figure 5.11 are mainly for reference. However, they also

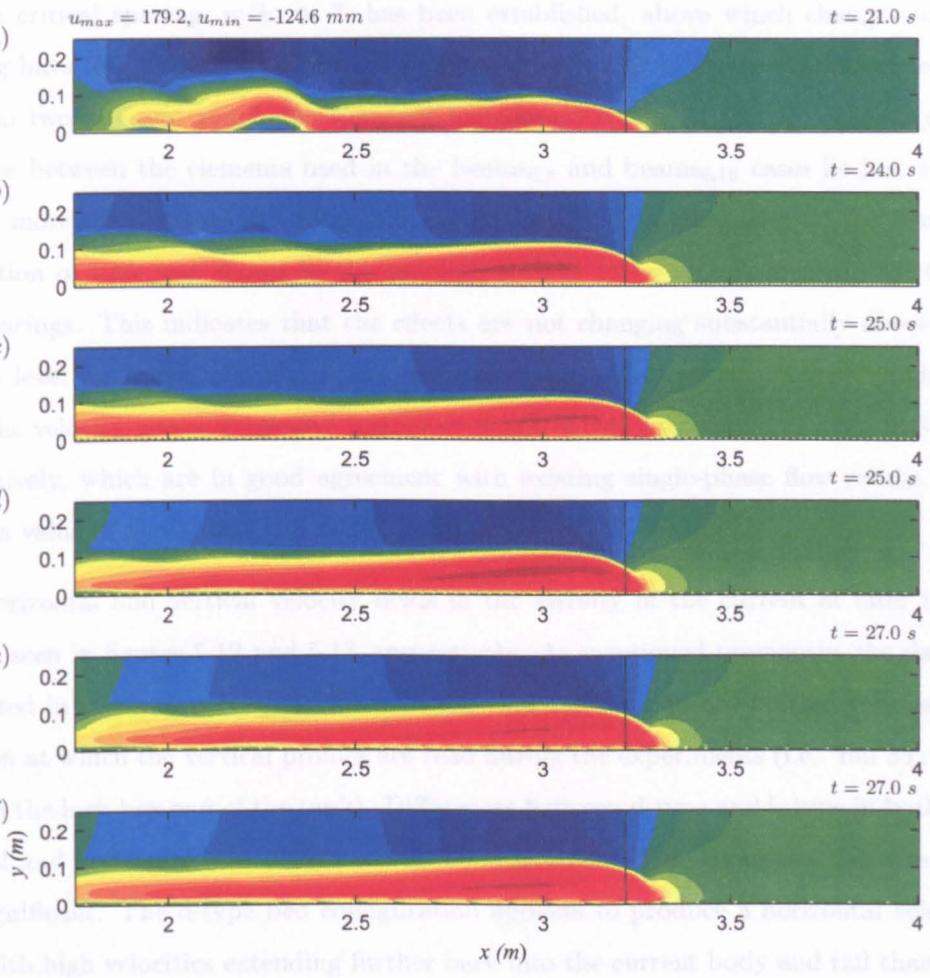

Figure 5.12: Horizontal velocity component, u, fields at the approximate time the head passes through 'bin 35' where the vertical profile data is read (shown as a line) resulting from the 2D simulation with (*a*) smooth bottom wall and (*b*) beams$_{6,1}$, (*c*) beams$_{6,2}$, (*d*) beams$_{6,4}$, (*e*) beams$_{6,8}$ and (*f*) beams$_{6,16}$. Downstream motion is from left to right. Red and blue are high and low velocities, respectively. Maximum and minimum values are displayed at the top of the figure.

confirm that the dense spacing of the elements in the d-type cases enable the vortices to maintain the less dense fluid trapped between the elements while high concentration fluid passes above, despite the lack of strength apparent in these gaps. In the k-type cases, the lighter fluid does not appear to be maintained between the elements. Instead, there is a greater amount of light fluid potentially entrained due to the strong flow separation that occurs which can 'engulf' the less dense fluid downstream of the element. Thus different flow dynamics for the entrainment of the lighter ambient fluid beneath the head can be expected for the d-type and k-type cases. Further effects on concentration resulting from the presence of the bed roughness are presented in section 5.7.

As discussed in section 1.3.3, in open channel and pipe flow studies with beam-roughened

walls a critical spacing, $w/k_r \approx 7$, has been established, above which changes to the spacing have less effects on the flow. In particular, the size of the reattachment length between two adjacent roughness elements remains constant. In the present study the distance between the elements used in the $\text{beams}_{6,8}$ and $\text{beams}_{6,16}$ cases lie just above and at more than double this threshold, respectively. The propagation of the front as a function of time was shown in the previous section to be almost identical for these two spacings. This indicates that the effects are not changing substantially above this critical level for gravity currents. Aalculations of the reattachment lengths, predicted from the velocity vector fields give further evidence of this with values of $3.8k_r$ and $4k_r$, respectively, which are in good agreement with existing single-phase flow results that found a value of about $4k_r$ (Cui *et al.*, 2003b)[§].

The horizontal and vertical velocity fields in the vicinity of the current at later times can be seen in figures 5.12 and 5.13, respectively. As mentioned previously, the data is presented in order to correspond to the time that the head of the current reaches the location at which the vertical profiles are read during the experiments (i.e. 'bin 35', 3.22 m from the lock-box end of the tank). Differences between d-type and k-type in both the vertical and horizontal flow fields can still be observed at these times but they are now less significant. The d-type bed configuration appears to produce a horizontal velocity field with high velocities extending further back into the current body and tail than any of the other beds. In the k-type case the velocity field extends upstream far behind the head but is more diffuse, lower velocities can be observed in the tail region. Both classifications show reduced negative velocities in the return flow above the current.

The difference between the rough cases and the smooth case is clearer at this later time. The current body has elongated with time as for the rough cases but not as extensively. As for the early time, the smooth simulation retains the disruptions within the current body and high return flow above the current in the horizontal field and distinct fluctuations in the vertical field (figure 5.12 (a) and figure 5.13 (a), respectively) indicating maintained coherence in the billows at the density interface. The only strong vertical motion remaining in the rough cases (figures 5.13 (b) – (f)) is the positive motion of the ambient fluid being forced upwards at the front, most other vertical motion appears to have been damped. The pushing motion in the fluid ahead of the front observed at the earlier time can still be seen at these later times.

Notice that at both early and later times, the velocity field of the $\text{beams}_{6,4}$ case appears

[§]note that there is some variation in this result, Cui *et al.* (2003b) suggests a value of about $4k_r$, while Ikeda and Durbin (2007) find a value of $4.5k_r$ and Leonardi *et al.* (2003b) report a value of $4.8k_r$.

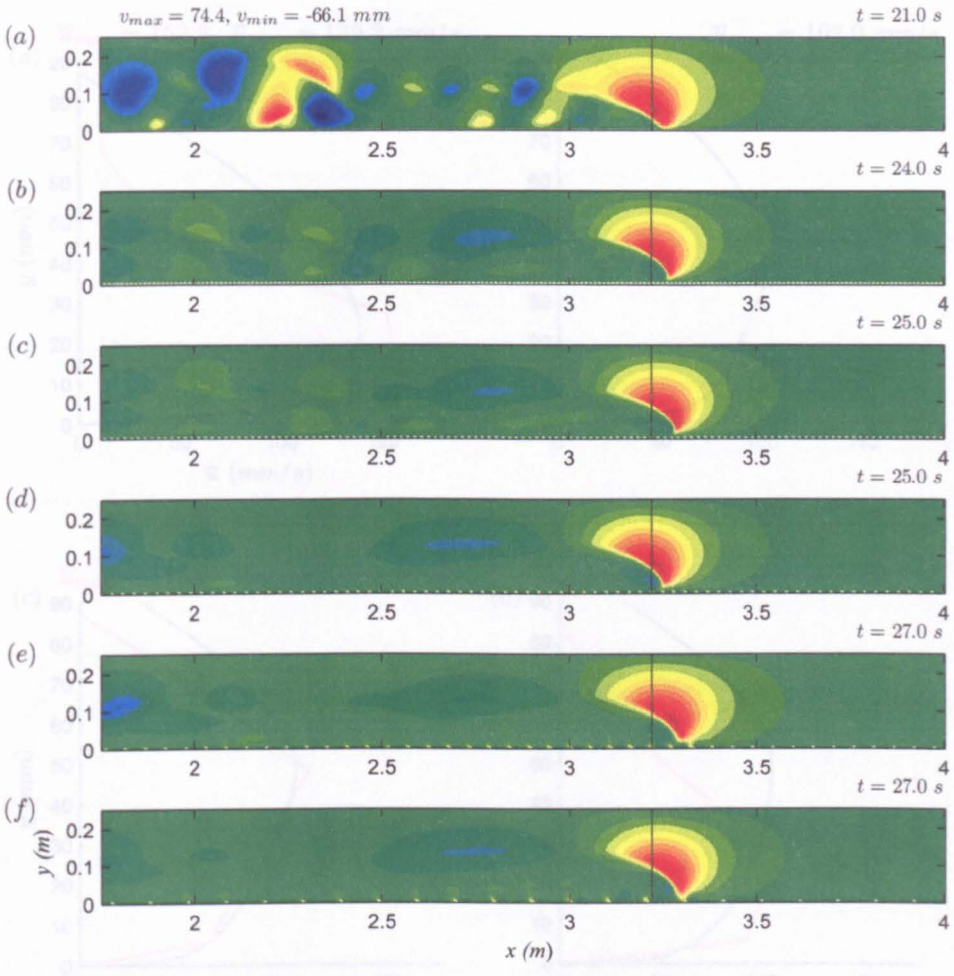

Figure 5.13: Vertical velocity component, v, fields at the approximate time the head passes through 'bin 35' where the vertical profile data is read (shown as a line) resulting from the 2D simulation with (a) smooth bottom wall and (b) beams$_{6,1}$, (c) beams$_{6,2}$, (d) beams$_{6,4}$, (e) beams$_{6,8}$ and (f) beams$_{6,16}$. Downstream motion is from left to right. Red and blue are high and low velocities, respectively, maximum and minimum values are displayed at the top of the figure.

to conform to the k-type characteristics, and not the d-type (figures 5.9-5.13 (d)). Thus the velocity field prediction shows no indication of this bed representing an intermediate spacing configuration.

The downstream horizontal velocity profiles within the current head at 'bin 35', which corresponds to the vertical lines shown on the velocity field data at later times, can be seen in figure 5.14. Where available, the experimental equivalents are also displayed. Note that in the experiments the probes are rigged above the elements, with the element top taken to be zero for data analysis. Therefore, the numerical results shown are from the first cell above the top of the elements. From figures 5.14 (a), (c) and (e) it can be seen that the data from the numerical simulations shows very good agreement with the

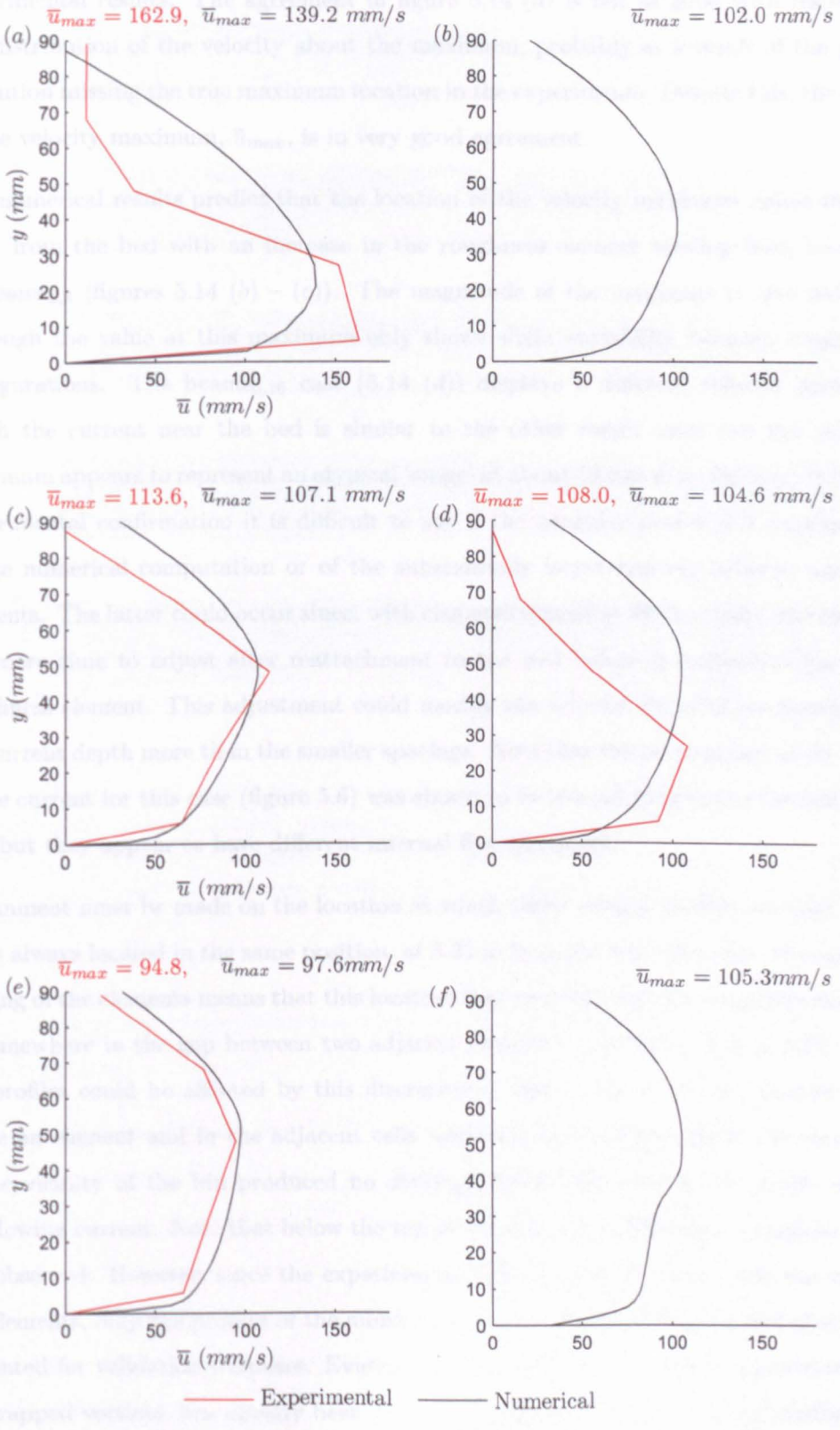

Figure 5.14: Downstream horizontal velocity, u, profiles within the current head resulting from 2D numerical simulations with the equivalent experimental results where available. Results for (a) a smooth bottom wall, and bottom walls with (b) beams$_{6,1}$, (c) beams$_{6,2}$, (d) beams$_{6,4}$, (e) beams$_{6,8}$, and (f) beams$_{6,16}$.

experimental results. The agreement in figure 5.14 (*d*) is not as good with respect to the distribution of the velocity about the maximum, probably as a result of the probe resolution missing the true maximum location in the experiments. Despite this, the value of the velocity maximum, $\overline{u}_{max}$, is in very good agreement.

The numerical results predict that the location of the velocity maximum moves further away from the bed with an increase in the roughness element spacing from $\text{beams}_{6,1}$ to $\text{beams}_{6,8}$ (figures 5.14 (*b*) – (*e*)). The magnitude of the maximum is also reduced, although the value at this maximum only shows slight variability between rough bed configurations. The $\text{beams}_{6,16}$ case (5.14 (*d*)) displays a different velocity profile in which the current near the bed is similar to the other rough cases but the velocity maximum appears to represent an atypical 'surge' at about 40 mm from the bed. Without experimental confirmation it is difficult to say if the irregular profile is a consequence of the numerical computation or of the substantially larger spacing between adjacent elements. The latter could occur since, with elements spaced at 96 mm apart, the current has more time to adjust after reattachment to the bed before it encounters the next roughness element. This adjustment could modify the velocity distribution throughout the current depth more than the smaller spacings. Note that the propagation of the front of the current for this case (figure 5.6) was shown to be almost identical to the $\text{beams}_{6,8}$ case but they appear to have different internal flow dynamics.

A comment must be made on the location at which these vertical profiles are read. The bin is always located in the same position, at 3.22 m from the lock. However, the varying spacing of the elements means that this location may lie at the top of a roughness element or somewhere in the gap between two adjacent elements. Therefore, it is possible that the profiles could be affected by this discrepancy. Inspection of velocity profiles read above an element and in the adjacent cells upstream and downstream of the elements in the vicinity of the bin produced no distinguishable difference in the profile of the overflowing current. Note that below the top of the elements in the gaps, a negative flow was observed. However, since the experimental data is read from level with the top of the elements, only the profiles of the numerical prediction from this point and above are presented for validation purposes. Evidence of the negative flow, which is generated by the trapped vortices, has already been presented in figure 5.11. This lack of distinction between motion above the element or in the gaps means that comparison of the profiles regardless of location is valid. This does not hold for the turbulence kinetic energy profiles as shown in section 5.6.

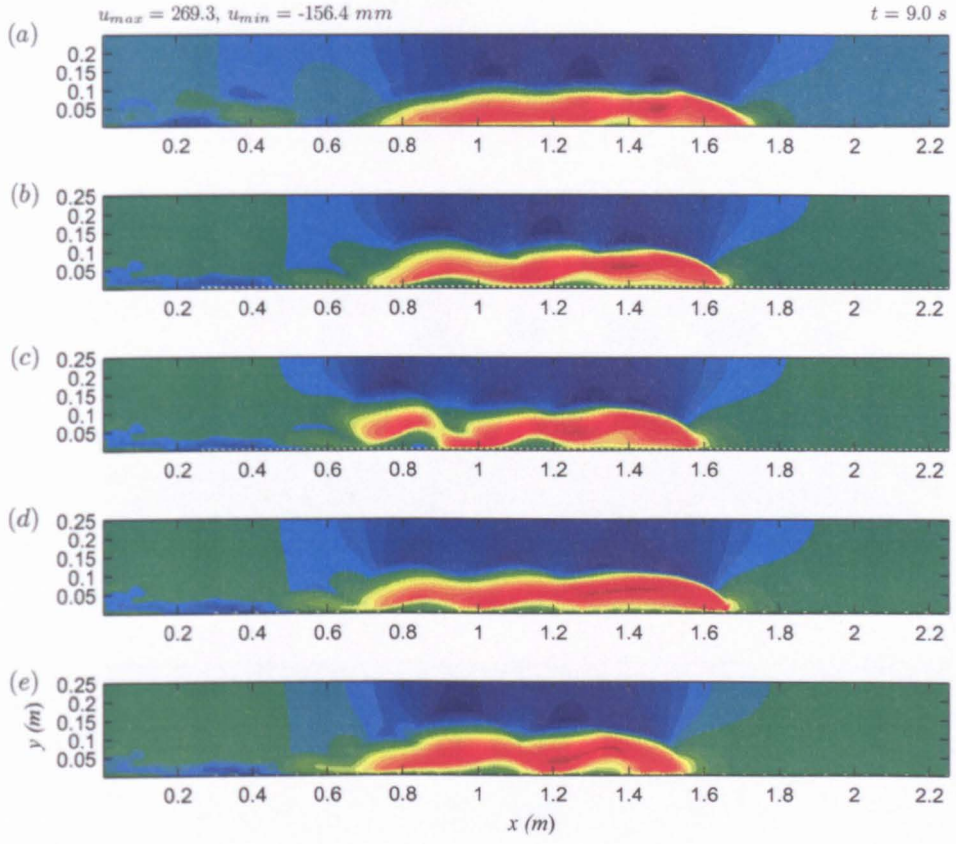

Figure 5.15: Horizontal velocity component, u, fields at $t = 9$ s resulting from the 2D simulation with (a) smooth bottom wall, and (b) beams$_{6,2}$ with dense fluid initialised between the elements, (c) beams$_{6,2}$, (d) beams$_{6,8}$ with dense fluid initialised between the elements and (e) beams$_{6,8}$. Red and blue are high and low velocities, respectively. Maximum and minimum values are displayed at the top of the figure.

The effects of the presence of less dense fluid between the roughness elements on the velocity structure

The velocity fields after 9 s for the rough cases with dense fluid replacing the ambient fluid between the elements show strong similarities with the smooth case, compare (b) and (d) with (a) in figures 5.15 and 5.16. The horizontal velocities show that there are still fluctuations at the bed but the disruption to the overlying fluid has been reduced. The regions of high positive and negative vertical motion are more diffuse than in the regular case with ambient fluid filling the space between the elements (figures 5.15 and 5.16 (c) and (e)), again they are more like the smooth case. However, the position of the horizontal velocity maximum appears to extend further back into the body of the current similar to the regular rough cases.

Figures 5.17 (a) and (b) show the simulated velocity and concentration fields in the vicinity of the roughness elements for a d-type bed roughness (beams$_{6,2}$) with and without

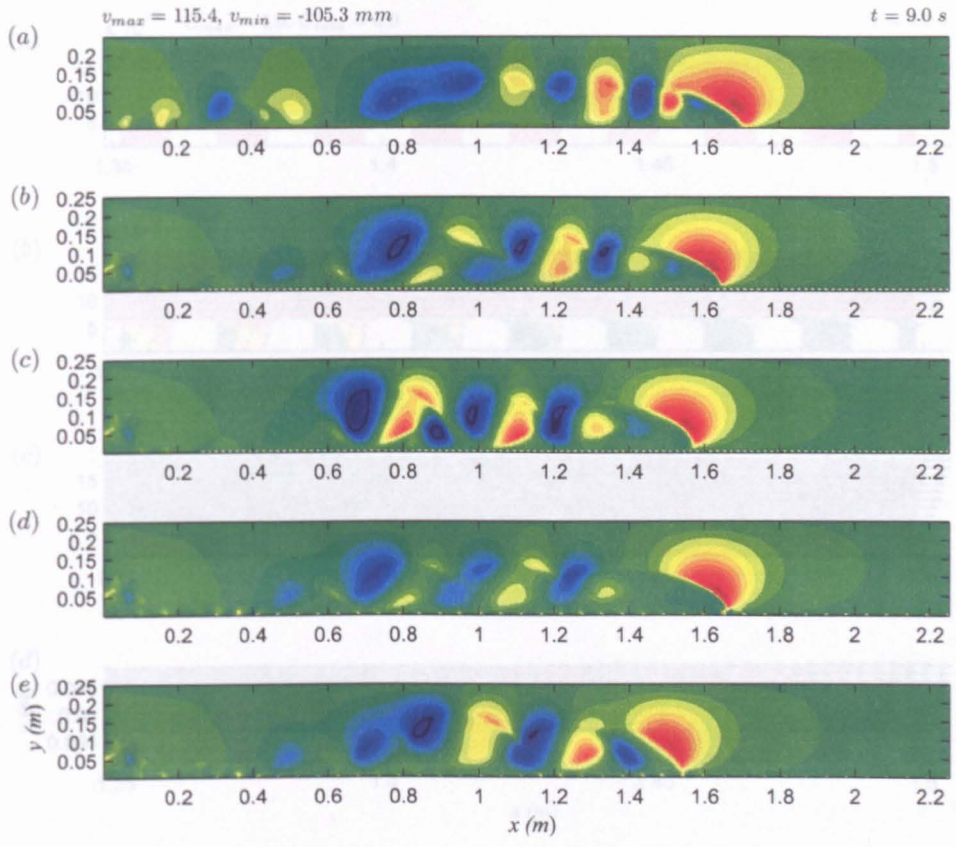

Figure 5.16: Vertical velocity component, v, fields at $t = 9$ s resulting from the 2D simulation with (a) smooth bottom wall, and (b) beams$_{6,2}$ with dense fluid initialised between the elements, (c) beams$_{6,2}$, (d) beams$_{6,8}$ with dense fluid initialised between the elements and (e) beams$_{6,8}$. Red and blue are high and low velocities, respectively. Maximum and minimum values are displayed at the top of the figure.

dense fluid initialised between the elements. Despite the obvious difference in the concentration of the fluid trapped between the elements, there is little apparent difference in the velocity. It can be observed in figure 5.17 (a) that the trapped fluid is marginally less dense than the highest concentrations observed in the overflowing fluid. This suggests that there is minimal entrainment of the ambient fluid occurring at the front. However, in the k-type case (figure 5.17 (c)), this entrainment appears to occur to a lesser extent, with less contrast in the fluid concentration between the elements compared to the overlying dense current. Inspection of figures 5.17 (c) and (d) shows that flow separation at the upstream corner of the top of the elements appears to occur in the k-type case, with or without ambient fluid initially between the roughness elements. However, the motion between the elements is weaker in the case with dense fluid in the cavities and the disruption to the overflowing fluid that results from the motion around the elements is significantly reduced compared to the regular case with ambient fluid between the

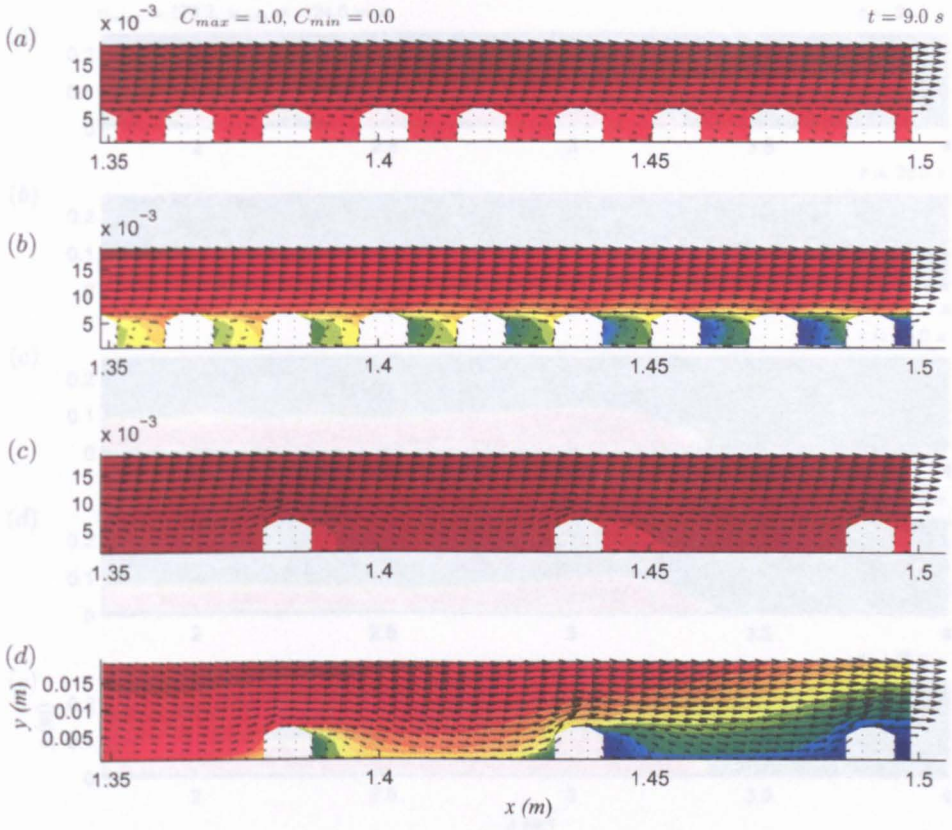

Figure 5.17: Vectors of velocity magnitude and contours of UDS (concentration) distribution in the current head in the vicinity of the roughness elements at $t = 9$ s resulting from the 2D simulation with (a) beams$_{6,2}$ with dense fluid initialised between the elements and (b) the regular beams$_{6,2}$ case with ambient fluid between the elements, (c) beams$_{6,8}$ with dense fluid initialised between the elements and (d) beams$_{6,8}$. Red and blue are high and low concentration, respectively. Maximum and minimum values are displayed at the top of the figure.

elements. These observations suggest that although comparable flow separation is occurring, the strength of the reattachment at the bed between the elements is weaker. Instead, the downward motion in the reattachment region appears to be diminished, perhaps 'cushioned' by the higher concentration fluid in this location compared to the more disruptive buoyant characteristics of the less dense fluid in the regular case.

If the horizontal and vertical velocity fields at later times are considered, see figures 5.18 and 5.19 respectively, it becomes apparent that although the cases with dense fluid between the roughness elements appeared similar to the smooth case at earlier times, at later times they are more like the predictions with ambient fluid in the cavities. Vertical motion (figures 5.19 (b) and (d)) has been substantially damped except at the head and the horizontal velocity fields (figures 5.18 (b) and (d)) within the current indicate that downstream propagating motion extends further back into the tail of the current than in the smooth case. Reduced return flow in the ambient fluid above the current can also

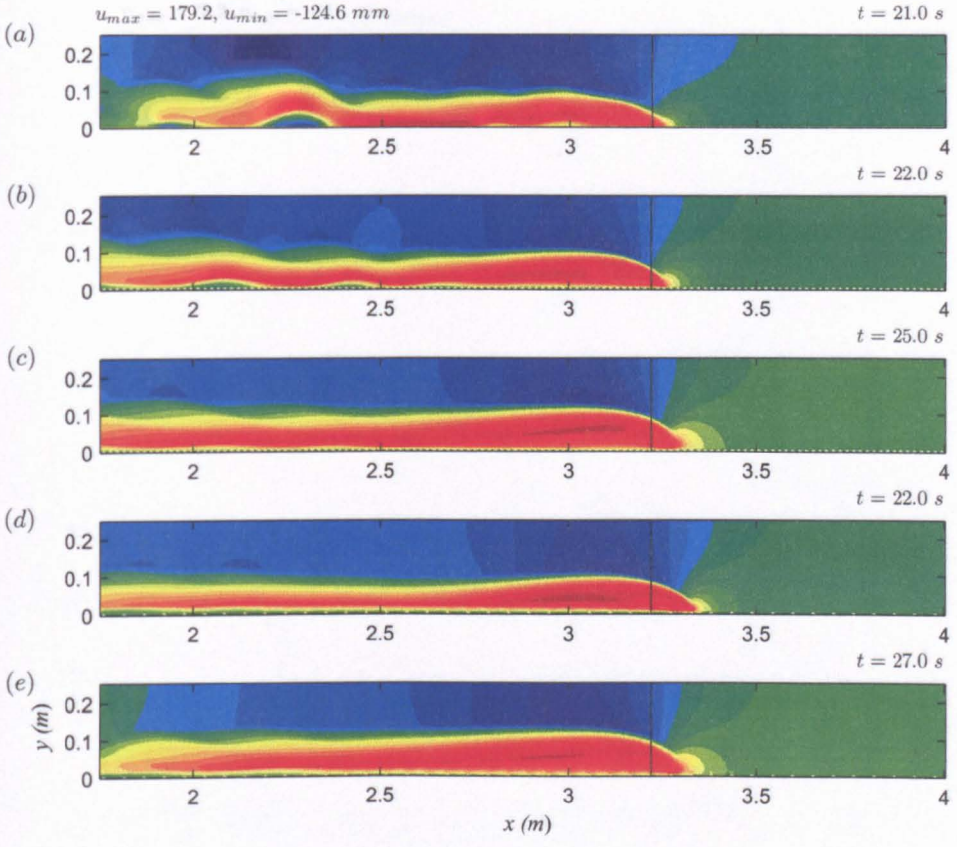

Figure 5.18: Horizontal velocity component, u, fields at the approximate time the head passes through 'bin 35' where the vertical profile data is read (shown as a line) resulting from the 2D simulation with (a) smooth bottom wall, and (b) beams$_{6,2}$ with dense fluid initialised between the elements, (c) beams$_{6,2}$, (d) beams$_{6,8}$ with dense fluid initialised between the elements and (e) beams$_{6,8}$. Red and blue are high and low velocities, respectively. Maximum and minimum values are displayed at the top of the figure.

be observed and again bears closer resemblance to the rough cases with ambient fluid between the elements than the smooth case, although the d-type case does retain smooth characteristics in this respect.

Corresponding velocity profiles for the numerical simulations for the cases with dense fluid initialised between roughness elements are shown in figure 5.20. Figures 5.20 (a) and (b) confirm that the numerical results agree well with distribution of the velocities for the experimental data and the value of the velocity maximum. Particularly good agreement is observed in the overall profile shape predicted in the beams$_{6,2}$ case and there is little difference in the value of $\bar{u}_{max}$ achieved in the beams$_{6,8}$ case compared to the experimental equivalent. Figures 5.20 (c) and (d) demonstrate that the presence of the dense fluid between the elements causes the current profile to tend towards that of the smooth case, with the velocity maximum occurring lower in the flow such that

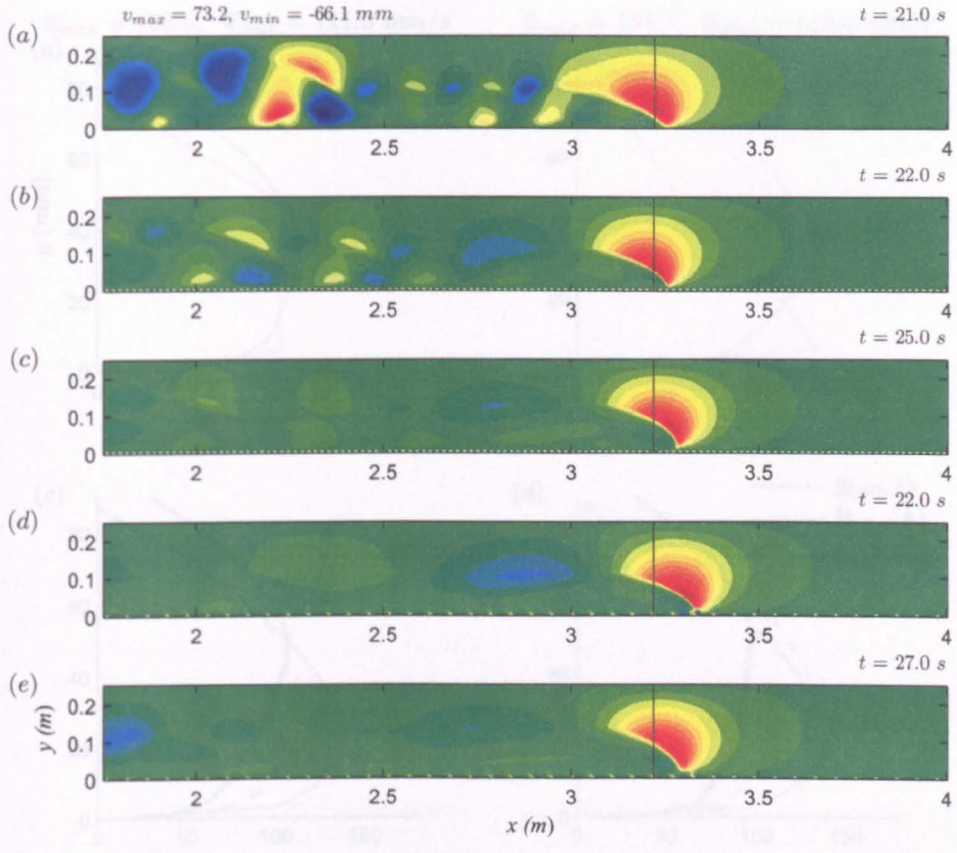

Figure 5.19: Vertical velocity component, v, fields at the approximate time the head passes through 'bin 35' where the vertical profile data is read (shown as a line) resulting from the 2D simulation with (a) smooth bottom wall, and (b) beams$_{6,2}$ with dense fluid initialised between the elements, (c) beams$_{6,2}$, (d) beams$_{6,8}$ with dense fluid initialised between the elements and (e) beams$_{6,8}$. Red and blue are high and low velocities, respectively. Maximum and minimum values are displayed at the top of the figure.

the profiles almost represent an average of the smooth and the regular rough cases. The profile does not entirely revert to that of the smooth case. This implies that the fluid between the elements contributes strongly to the current dynamics but there are also other mechanisms present as was postulated previously from the front speed results (section 5.5.1). Note that here was no distinguishable difference observed between the flow profiles in the results taken above an element or above the gap between two elements.

The effects of the law-of-the-wall method for specifying the bed roughness on the velocity structure

The velocity fields using the law-of-the-wall method for bed roughness with $k_s = 0.0015$, equivalent to the beams$_{6,2}$ case, can be seen in figures 5.21 and 5.22. Strong similarities with the smooth case can be observed by comparing (a) and (b) in figures 5.21 and 5.22.

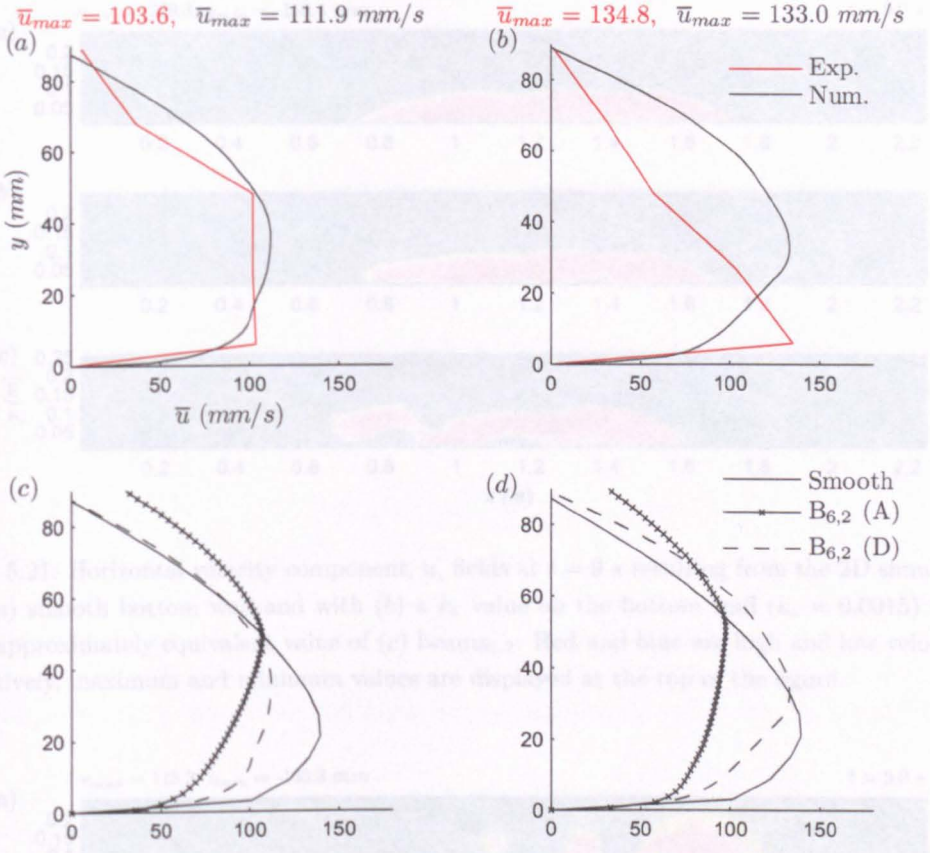

Figure 5.20: Downstream horizontal velocity, u, profiles within the head of the current resulting from (a) the 2D simulation and experimental equivalent with a bottom wall of beams$_{6,2}$ ($B_{6,2}$) with dense fluid initialised between the elements; (b) the 2D simulation and experimental equivalent with a bottom wall of beams$_{6,8}$ ($B_{6,8}$) with dense fluid between the elements; (c) the 2D simulation with a smooth bottom wall and a bottom wall of beams$_{6,2}$ with (D) and without (A) dense fluid initialised between the elements; and (d) the 2D simulation with a smooth bottom wall and a bottom wall of beams$_{6,8}$ with (D) and without (A) dense fluid initialised between the elements.

There is little disturbance to the ambient return flow and the location and streamwise distribution of the velocity maximum. This could in part be attributed to the fact that the law-of-the-wall method essentially uses an identical domain configuration to the smooth case, except for the change of k_s value at the wall. Despite this, some disruption to the horizontal flow at the bottom boundary can be seen in figure 5.21 (b), and in figure 5.22 (b) an increase in the vertical velocities are also present, perhaps causing the disruptions in the vicinity of the bottom boundary.

The velocity fields at a later time for the law-of-the-wall bed can be seen in figures 5.23 and 5.24. As for the early time, little difference can be observed between the k_s method and the smooth case. The vertical field shows clear fluctuations within the current body albeit slightly weaker but not as reduced as the body-fitted method and the horizontal

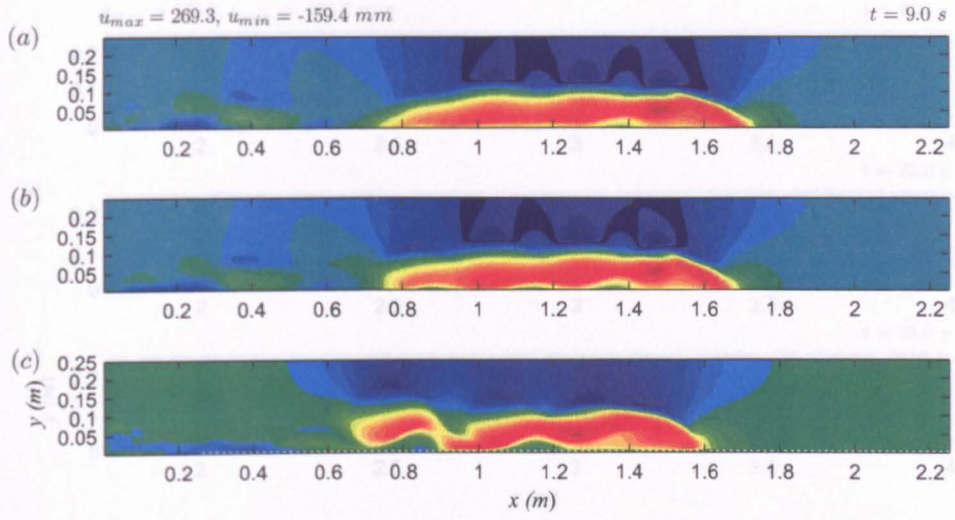

Figure 5.21: Horizontal velocity component, u, fields at $t = 9$ s resulting from the 2D simulation with (a) smooth bottom wall and with (b) a k_s value on the bottom wall ($k_s = 0.0015$) which is the approximately equivalent value of (c) beams$_{6,2}$. Red and blue are high and low velocities, respectively, maximum and minimum values are displayed at the top of the figure.

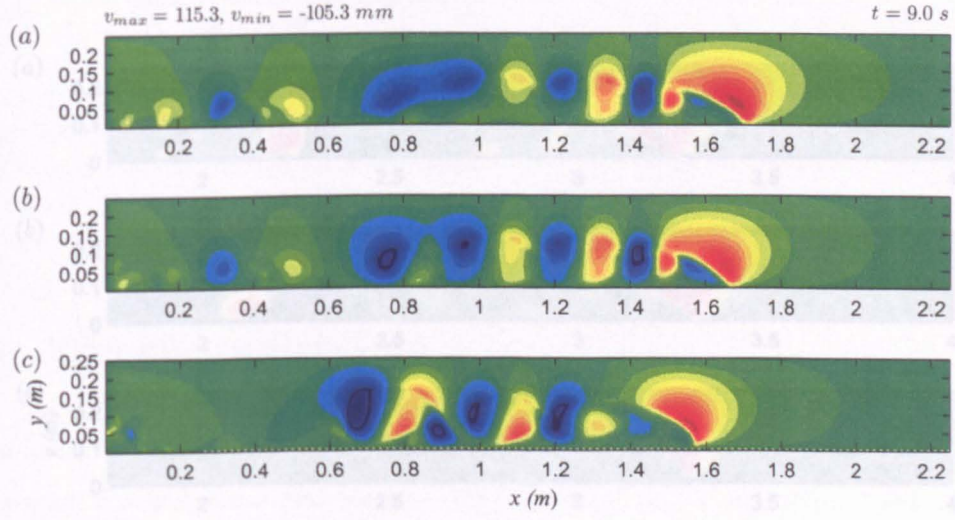

Figure 5.22: Vertical velocity component, v, fields at $t = 9$ s resulting from the 2D simulation with (a) smooth bottom wall and with (b) a k_s value on the bottom wall ($k_s = 0.0015$) which is the approximately equivalent value of (c) beams$_{6,2}$. Red and blue are high and low velocities, respectively. Maximum and minimum values are displayed at the top of the figure.

field is distributed very similarly to the smooth bed case.

The downstream horizontal velocity profile data at the bin for the simulation using the law-of-the-wall method can be seen in figure 5.25. The law-of-the-wall method produces a slightly different velocity profile to the experimental and body-fitted equivalent cases. The value of the velocity maximum is greater and located lower within the head region

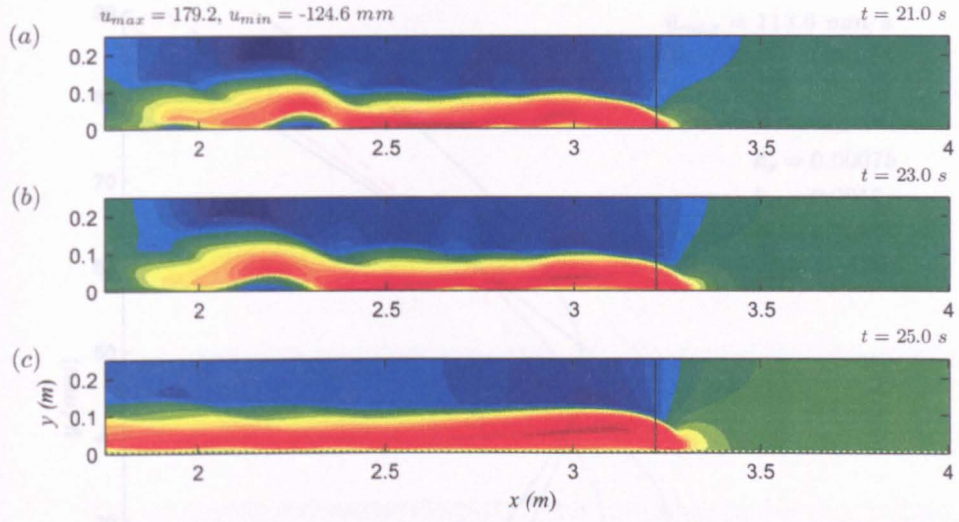

Figure 5.23: Horizontal velocity component, u, fields at the approximate time the head passes through 'bin 35' where the vertical profile data is read (shown as a line) resulting from the 2D simulation with (a) smooth bottom wall and with (b) a k_s value on the bottom wall ($k_s = 0.0015$) which is the approximately equivalent value of (c) beams$_{6,2}$. Red and blue are high and low velocities, respectively. Maximum and minimum values are displayed at the top of the figure.

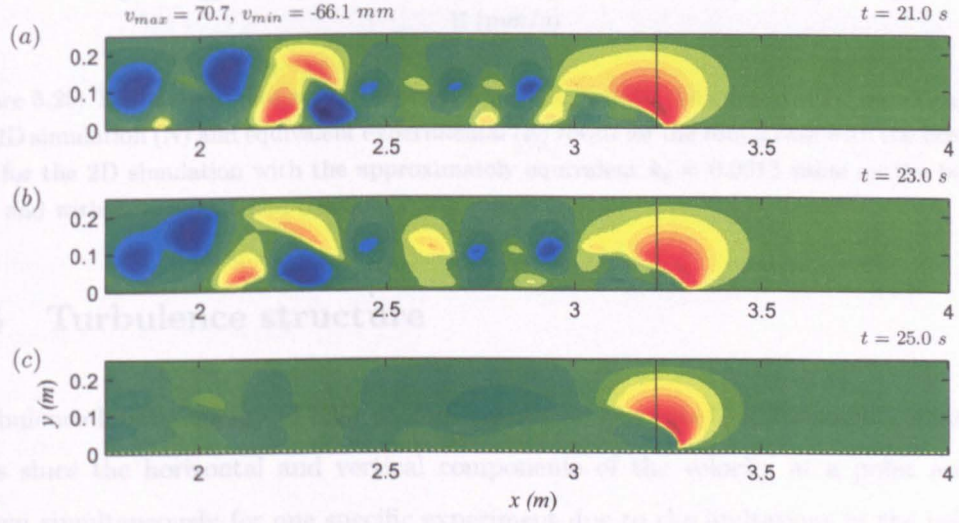

Figure 5.24: Vertical velocity component, v, fields at the approximate time the head passes through 'bin 35' where the vertical profile data is read (shown as a line) resulting from the 2D simulation with (a) smooth bottom wall and with (b) a k_s value on the bottom wall ($k_s = 0.0015$) which is the approximately equivalent value of (c) beams$_{6,2}$. Red and blue are high and low velocities, respectively. Maximum and minimum values are displayed at the top of the figure.

and the distribution of the velocities about this maximum is smaller and tends towards the smooth profile.

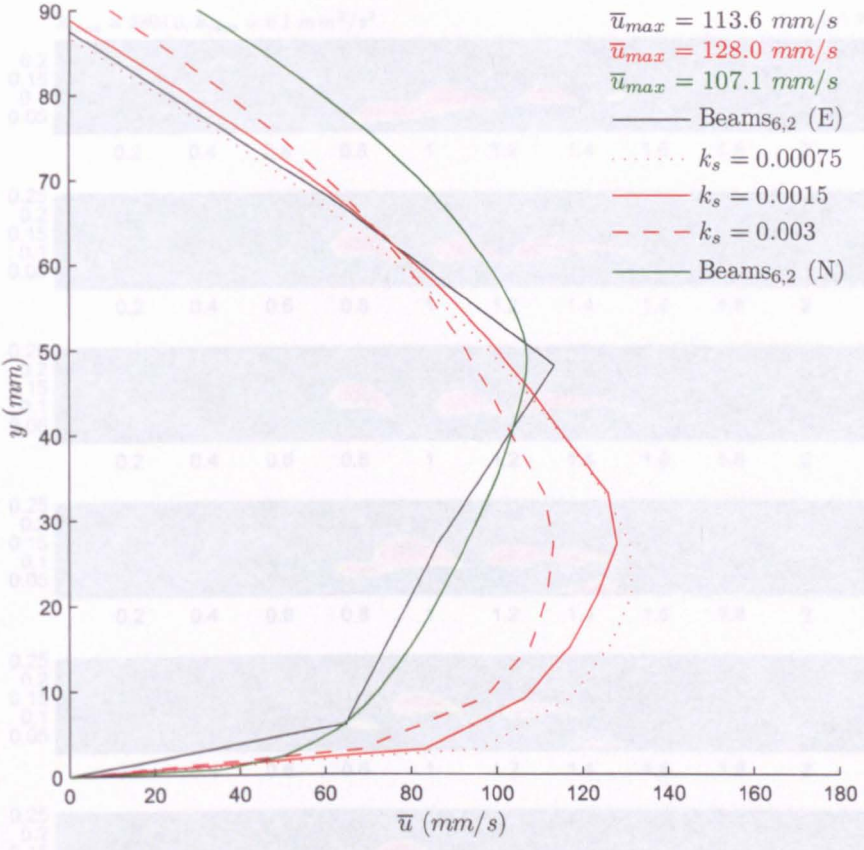

Figure 5.25: Downstream horizontal velocity, u, profiles within the current head resulting from the 2D simulation (N) and equivalent experimental (E) result for the rough case with the beams$_{6,2}$ and for the 2D simulation with the approximately equivalent $k_s = 0.0015$ value on the bottom wall and with $k_s = 0.0075$ and 0.003.

5.6 Turbulence structure

Turbulence kinetic energy (TKE) profiles cannot be generated for the experimental results since the horizontal and vertical components of the velocity at a point are not known simultaneously for one specific experiment due to the limitations in the velocity range of the UDVP required for accuracy. One of the benefits of the numerical simulations is that this data is available. The velocity data has been shown to be a good prediction of the experimental equivalents and thus it can be postulated that the TKE data is of equal ability. However, the results for TKE remain unvalidated and as such should be treated with some caution until confirmed with an experimental dataset.

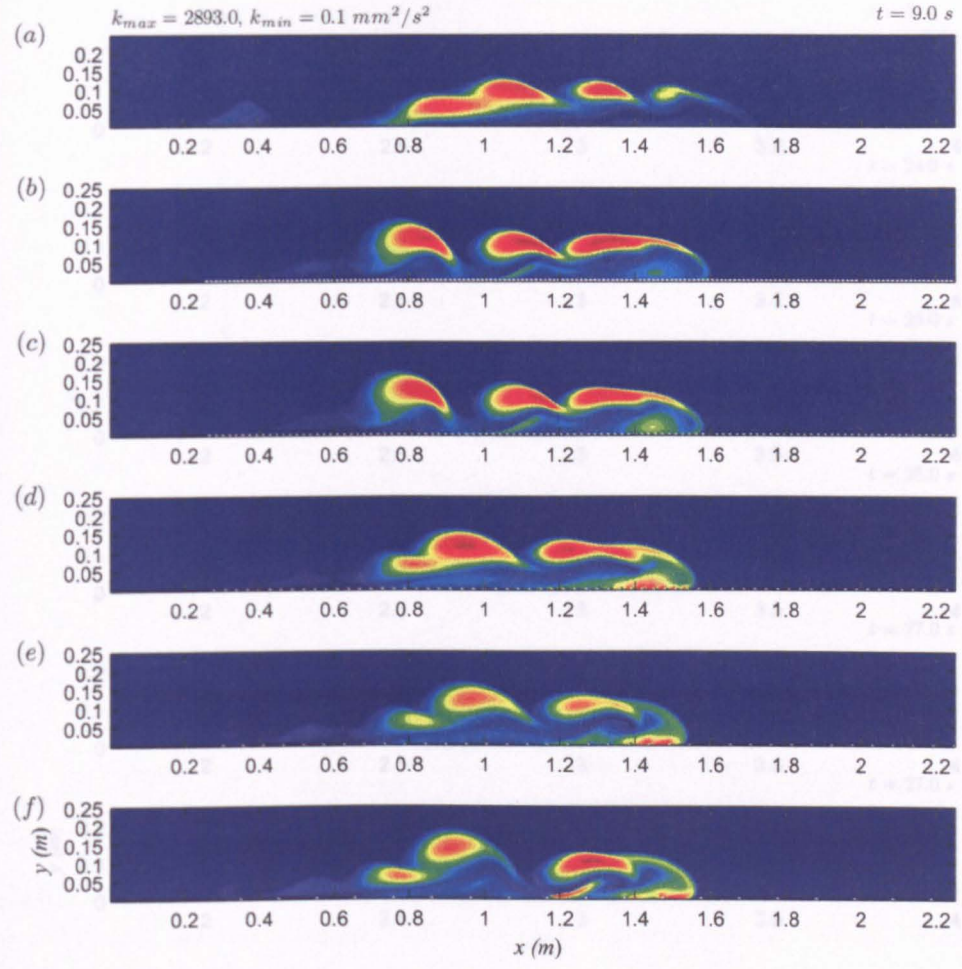

Figure 5.26: Turbulence kinetic energy, k, fields at $t = 9\ s$ resulting from the 2D simulation with (a) smooth bottom wall, and (b) beams$_{6,1}$, (c) beams$_{6,2}$, (d) beams$_{6,4}$, (e) beams$_{6,8}$ and (f) beams$_{6,16}$. Red and blue are high and low TKE, respectively. Maximum and minimum values are displayed at the top of the figure.

The effects of the spacing of bed roughness elements on the turbulence structure

The turbulence kinetic energy (TKE) fields predicted for the early stage of gravity current propagation over each bed are presented in figure 5.26. There is a distinct region of high magnitude TKE just above the bottom boundary in the head that increases with increasing spacing between the elements (figures 5.26 $(b) - (f)$). Possibly as a result of this, increased levels of TKE can also be seen further from the bed within the body of the gravity current and in particular penetrating into the head and towards the front of the current, also increasing as the roughness element spacing increases. Note that at this time (9 s), the d-type rough bed cases have higher values of TKE at the density interface above the current body than at this location in the smooth case.

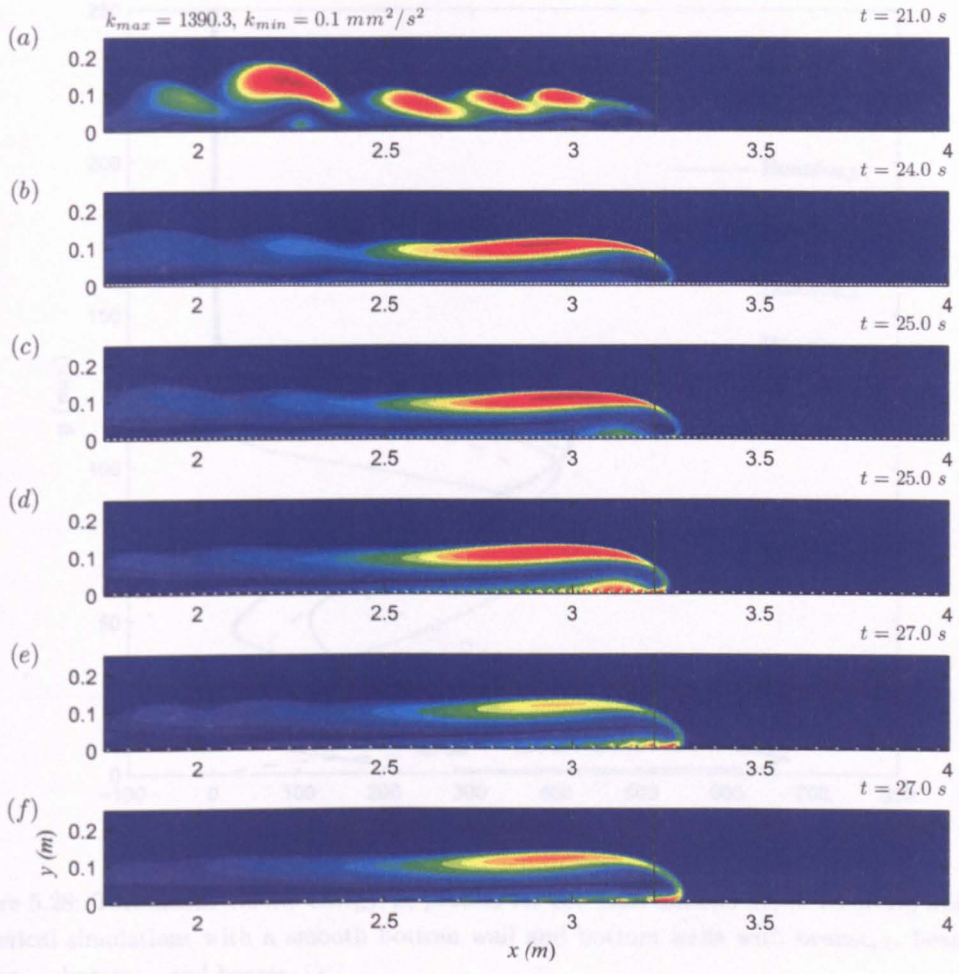

Figure 5.27: Turbulence kinetic energy, k, fields at the approximate time the head passes through 'bin 35' where the vertical profile data is read (shown as a line) resulting from the 2D simulation with (a) smooth bottom wall, and (b) beams$_{6,1}$, (c) beams$_{6,2}$, (d) beams$_{6,4}$, (e) beams$_{6,8}$ and (f) beams$_{6,16}$. Red and blue are high and low TKE, respectively. Maximum and minimum values are displayed at the top of the figure.

The differences between d-type and k-type can clearly be observed in figure 5.26 (b) & (c) and (d) – (f), respectively. The d-type case shows strong TKE at the density interface where the billows are formed and lower TKE at the bed while the k-type case shows high values at the bed within the head and at the interface although the magnitude of these values varies for different spacings. In the k-type case, distinct areas of high TKE can be observed localised about the individual elements beneath the head. This is not so evident for the d-type case.

In the TKE fields at later times, shown in figure 5.27, it can be observed that in the smooth case (figure 5.27 (a)) there is still high TKE at the density interface above the current body maintaining the presence of coherent billows in this locality. The strong

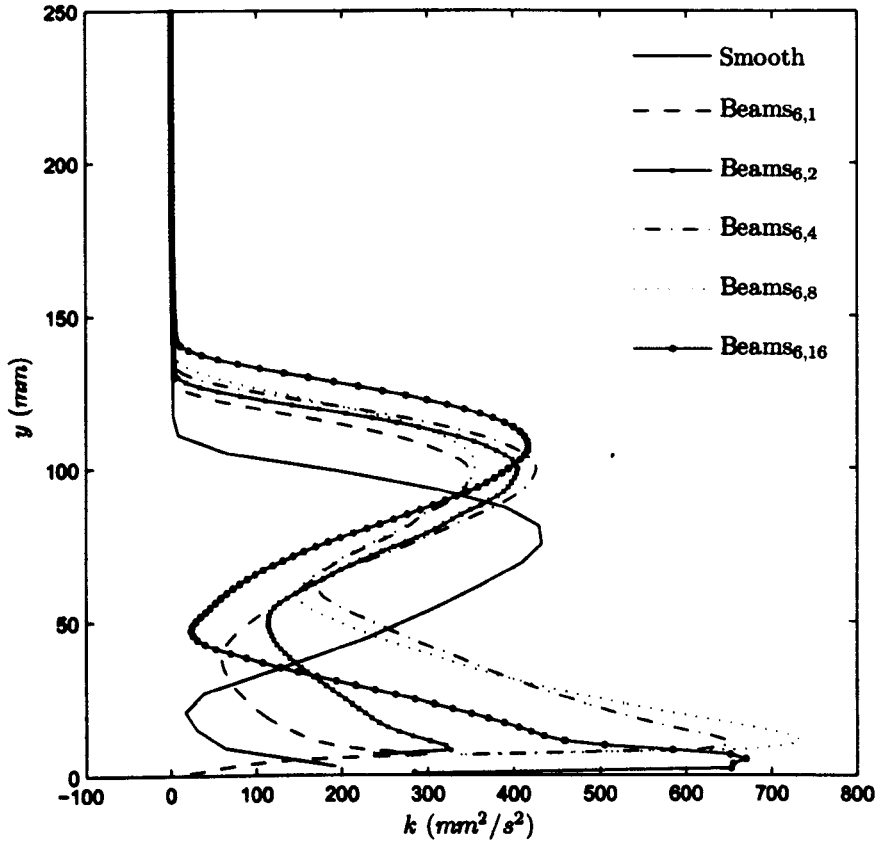

Figure 5.28: Turbulence kinetic energy, k, profiles for the total domain depth resulting from 2D numerical simulations with a smooth bottom wall and bottom walls with $\text{beams}_{6,1}$, $\text{beams}_{6,2}$, $\text{beams}_{6,4}$, $\text{beams}_{6,8}$ and $\text{beams}_{6,16}$.

TKE maintaining the large unphysical billow can clearly be observed to the rear of the current. In the rough cases, the localised TKE in the billows which confirms their coherence has dissipated and a damped region of high TKE has formed behind the head that does not extend as far into the current body as in the smooth case. The TKE is substantially reduced in this region for the two widest k-type roughness spacings (figures 5.27 (*e*) and (*f*)), but not for the $\text{beams}_{6,4}$ case. Mixing in the head is seen to have decreased significantly in the d-type cases and in the $\text{beams}_{6,16}$ case (figures 5.27 (*b*), (*c*) and (*f*), respectively) but is still high and localised about the elements in the other two k-type cases (figures 5.27 (*d*) and (*e*)), although the magnitude is somewhat reduced.

Figure 5.28 enables comparison of the TKE profiles through the tank depth (shown as a vertical line in figure 5.27) for the smooth bed and each of the regular body-fitted beam-roughened cases. In order for these profiles to be consistent with the vertical velocity profiles, and therefore used as a predictive tool to compliment the experimental data, they were generated from numerical data read at bin 35 (3.22 m from the lock-box end

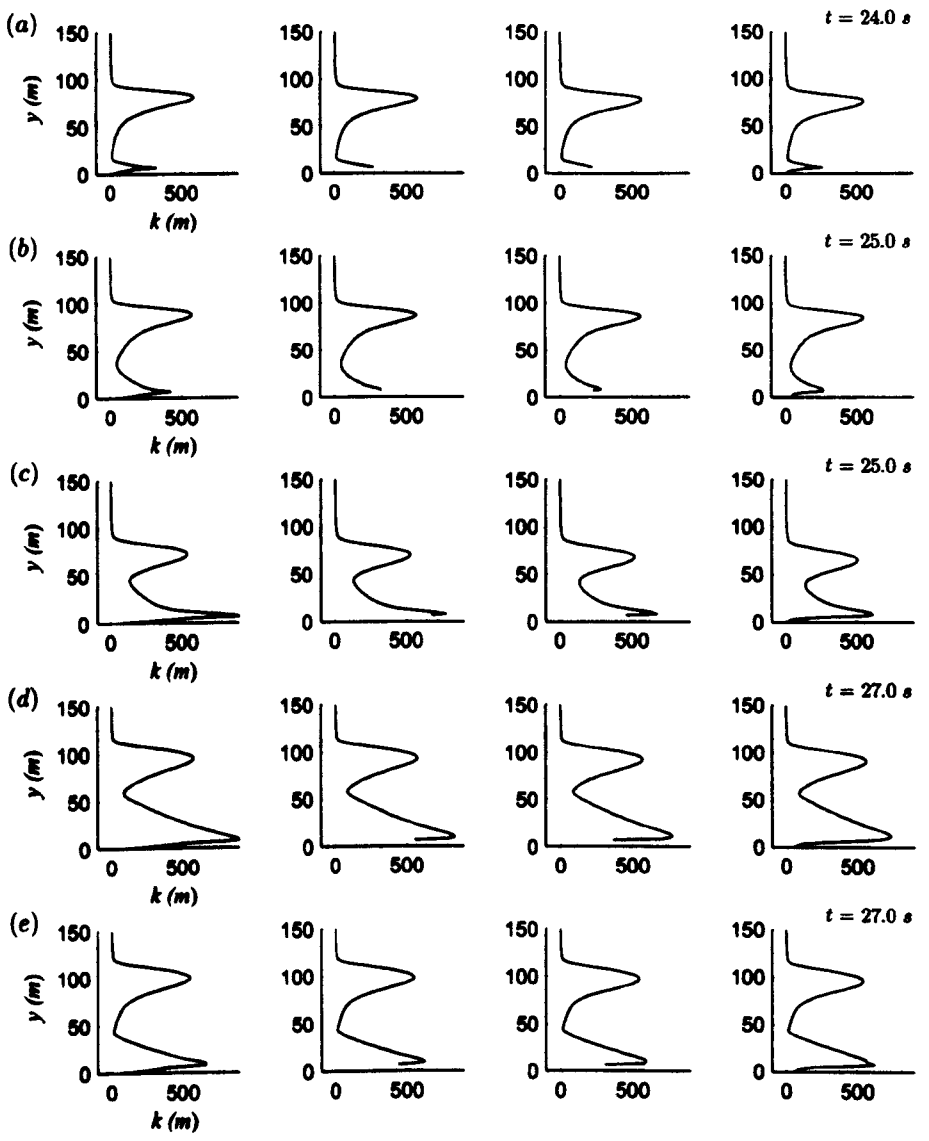

Figure 5.29: Turbulence kinetic energy, k, profiles in the vicinity of 'bin 35' resulting from 2D numerical simulations with bottom walls with (a) beams$_{6,1}$, (b) beams$_{6,2}$, (c) beams$_{6,4}$, (d) beams$_{6,8}$ and (e) beams$_{6,16}$. From left to right the vertical profiles represent data in four locations, namely, one in the cavity just upstream of an element, two at the top of an element and one in the adjacent cavity just downstream of an element.

of the tank). For models generated with the beams$_{6,2}$, beams$_{6,4}$ and beams$_{6,8}$ bed types, the bottom cell lies on top of a roughness element. Hence the first data point is within the cell adjacent to the top of the element, not at the bed in the gap. However, in the two other cases, the TKE profile is shown right down to the bed. Due to this discrepancy, profiles in the cells above, upstream and downstream of an element in the vicinity of the bin are shown in figure 5.29 and should be considered in conjunction with the predictions in figure 5.28.

In all cases investigated, a TKE minima occurs in the vicinity of the velocity maximum with an increase towards the interface and towards the bed, as has typically been observed in experimental gravity currents (e.g. Kneller *et al.*, 1999). Figure 5.29 confirms that there is no distinguishable effect on the vertical distribution of the TKE in the main body of flow away from the top of the elements, if the data is taken above the elements or from within the gap between them. However, there are differences in the flow dynamics immediately above the elements as will be discussed subsequently. This again shows that the effects of the elements does not penetrate high into the current. Considering levels of TKE at the velocity maximum for the rough cases, an increase with increasing spacing occurs, except for the $\text{beams}_{6,16}$ case where it is almost identical to the smooth case. The distance from the bed for this minimum turning point in the TKE profile also increases with increasing spacing except again for the $\text{beams}_{6,16}$ case which agrees in height with the $\text{beams}_{6,2}$ case. At the density interface above the current body, there is no consistent increase or decrease in magnitude dependent on element spacing that is obvious from the profiles in figure 5.28. The smooth case has the highest TKE in this region and $\text{beams}_{6,1}$, the lowest. This turning point occurs lowest in the flow profile for the smooth case. For the bed-roughened cases, it is located at almost identical distances from the bed regardless of element spacing, except for the $\text{beams}_{6,16}$ case which occurs higher in the current.

The main effects of bed roughness on the vertical TKE profiles can be observed to occur near the bed, as indicated by the TKE fields in figure 5.27. The results shown in figure 5.28 suggest that the TKE can increase dramatically in this region with increasing element spacing and then decrease abruptly down to the bed. The smooth boundary condition results in a TKE value that is greater than that of the velocity maximum but lower than the value at the interface and continues increasing down to the bed. Figure 5.28 shows that in the presence of the roughness elements another turning point occurs in the profile near the bed. For the d-type cases ($\text{beams}_{6,1}$ and $\text{beams}_{6,2}$), the value at this point is again greater than the velocity maximum but smaller than the TKE at the density interface. However, in figure 5.29 (a) for the $\text{beams}_{6,1}$ case, it can be observed that this turning point is representative of the flow dynamics between the elements and this does not occur above the elements (middle two profiles of figure 5.29 (a)). In fact, above an element, the $\text{beams}_{6,1}$ case is similar to the smooth bed in both the upstream and downstream cells and in the upstream cell of the $\text{beams}_{6,2}$ case i.e. a maxima does not occur and the TKE continues increasing down to the boundary but remains smaller than the maximum at the density interface. The k-type beds ($\text{beams}_{6,4}$, $\text{beams}_{6,8}$ and

beams$_{6,16}$) have near-wall turning points both above the elements and upstream and downstream of the elements with greater magnitude than the value at the interface in the beams$_{6.16}$ case and significantly greater magnitudes in the beams$_{6,4}$ and beams$_{6,8}$ cases, i.e. the maximum of the entire vertical TKE profile in the k-type cases occurs just above the bed and not at the interface. For all roughnesses, in the gap between the elements (figure 5.29, lefthand and righthand profiles), the TKE decreases substantially from the maxima just above the bed down to the bed itself. Figure 5.29 highlights that the increase in spacing increases the likelihood of a maxima in TKE occurring above the elements. Further, as the spacing increases, the magnitude of this maxima appears to increase, except for the beams$_{6,16}$ case.

The case that appears to be an exception to the general trends observed above is the beams$_{6,16}$ case, and this was also found in the vertical velocity profiles. In this case, the magnitudes of the maxima at the bed and the interface are very similar regardless of whether the profile is read above the element or in an adjacent gap (figure 5.29 (*e*)). The lower location of the TKE minima suggests that perhaps this case is regaining some attributes of the smooth case but the high maxima near the bed shows that it is also still under the influence of the individual roughness elements.

The effects of the presence of less dense fluid between the roughness elements on the turbulence structure

Figure 5.30 shows the TKE field for the cases with and without dense fluid initialised between the roughness elements after 9 s. Once the buoyant fluid between the elements is eliminated, there is a substantial change to the TKE field throughout the domain and it becomes similar to that for the smooth bed (compare figures 5.30 (*b*) with (*a*)). However, the increased level of TKE immediately behind the head that occurs for the other rough cases at this time and a slight increase at the bed can still be observed. Notice that with the ambient fluid removed there is also a closer similarity between the TKE fields over the d-type and k-type beds, although the k-type case still shows increased TKE in the head. The localised TKE about the elements in the k-type case is significantly smaller, as might be predicted since the dense fluid between the elements is about the same concentration as the highly concentrated overlying current and therefore 'cushions' the current from some of the effects of the roughness elements allowing it to float more smoothly over the top, i.e. the removal of the surface friction at the bed by the gaps between the elements is more effective when there is dense fluid in these gaps.

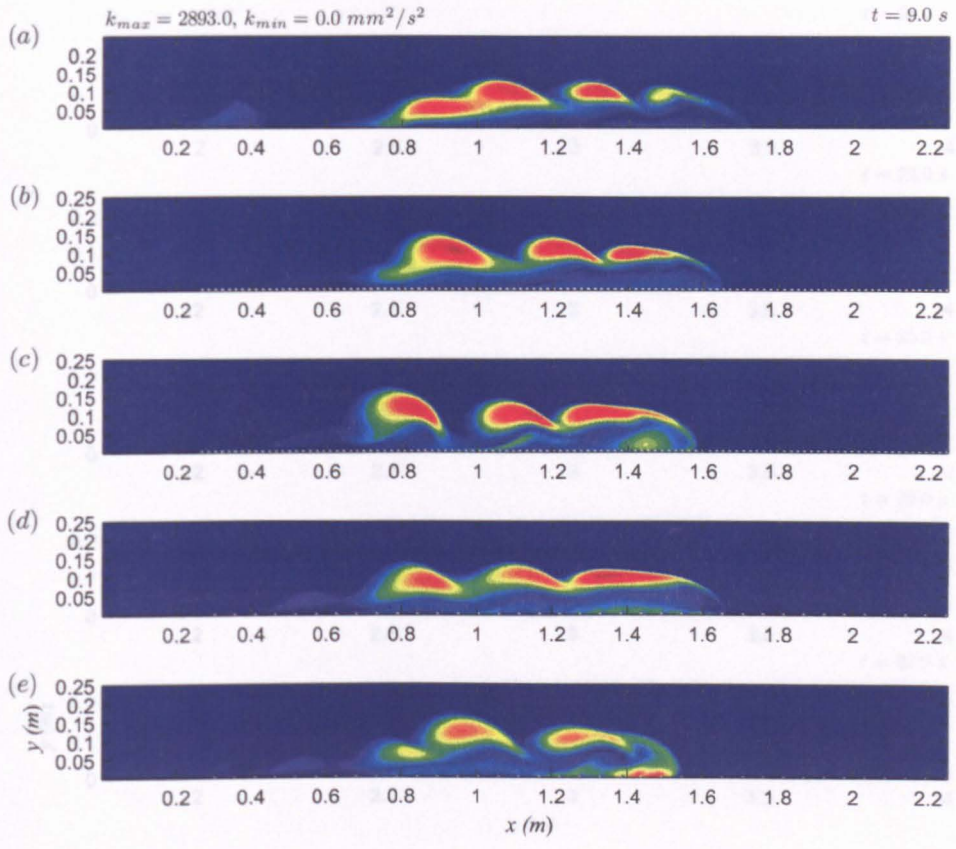

Figure 5.30: Turbulence kinetic energy, k, fields at $t = 9\ s$ resulting from the 2D simulation with (a) smooth bottom wall, and (b) beams$_{6,2}$ with dense fluid initialised between the elements, (c) beams$_{6,2}$, (d) beams$_{6,8}$ with dense fluid initialised between the elements and (e) beams$_{6,8}$. Red and blue are high and low TKE, respectively. Maximum and minimum values are displayed at the top of the figure.

At later times when the current is approximately passing through the bin location, as seen after 9 s, the cushioning effect felt at the head is such that the TKE is more substantially reduced at the bed in both the d-type and k-type cases compared to the equivalent predictions with ambient fluid between the elements, see figure 5.31. The d-type case has retained stronger TKE distributed along the density interface, indicating coherence in the structures in this region similar to the smooth case, while the k-type case has not and displays similar streamwise distribution of TKE within the current body as the regular k-type cases at the density interface, although with greater magnitudes. The profiles in figure 5.32 confirm that the turbulence kinetic energy distribution within the current is substantially affected by the introduction of the dense fluid between the elements. The results for this case closely resemble the smooth data, particularly the value at the velocity maximum. At the density interface, the magnitude of the TKE agrees more closely with the lower value of the beams$_{6,2}$ case than the smooth case but

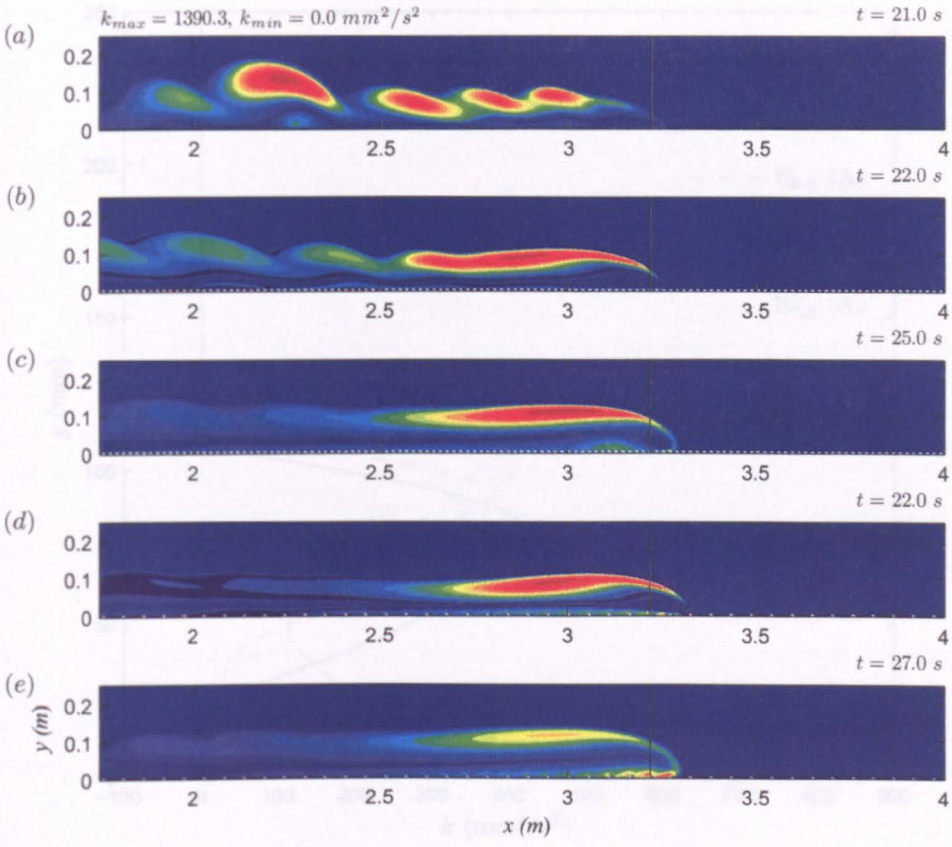

Figure 5.31: Turbulence kinetic energy, k, fields at the approximate time the head passes through 'bin 35' where the vertical profile data is read (shown as a line) resulting from the 2D simulation with (a) smooth bottom wall, and (b) beams$_{6,2}$ with dense fluid initialised between the elements, (c) beams$_{6,2}$, (d) beams$_{6,8}$ with dense fluid initialised between the elements and (e) beams$_{6,8}$. Red and blue are high and low TKE, respectively. Maximum and minimum values are displayed at the top of the figure.

it still occurs at a similar, smaller distance from the bed as in the latter case. Unlike the smooth profile, the third turning point does occur at the bed, although the value of TKE at this point is not as high as in the case with buoyant fluid between the elements. It can also be observed that the profile for the k-type case is more qualitatively similar to both of the d-type cases with the maximum TKE now at the interface and reduced at the bed, while the profile for the regular k-type cases shows the maximum at the bed. Again, the effects of the location about an element at which the profiles are read can be considered. However, they show that the same general trends as recorded in the cases with ambient fluid between the elements also hold here and no further significant effects than those shown in figure 5.32 can be observed.

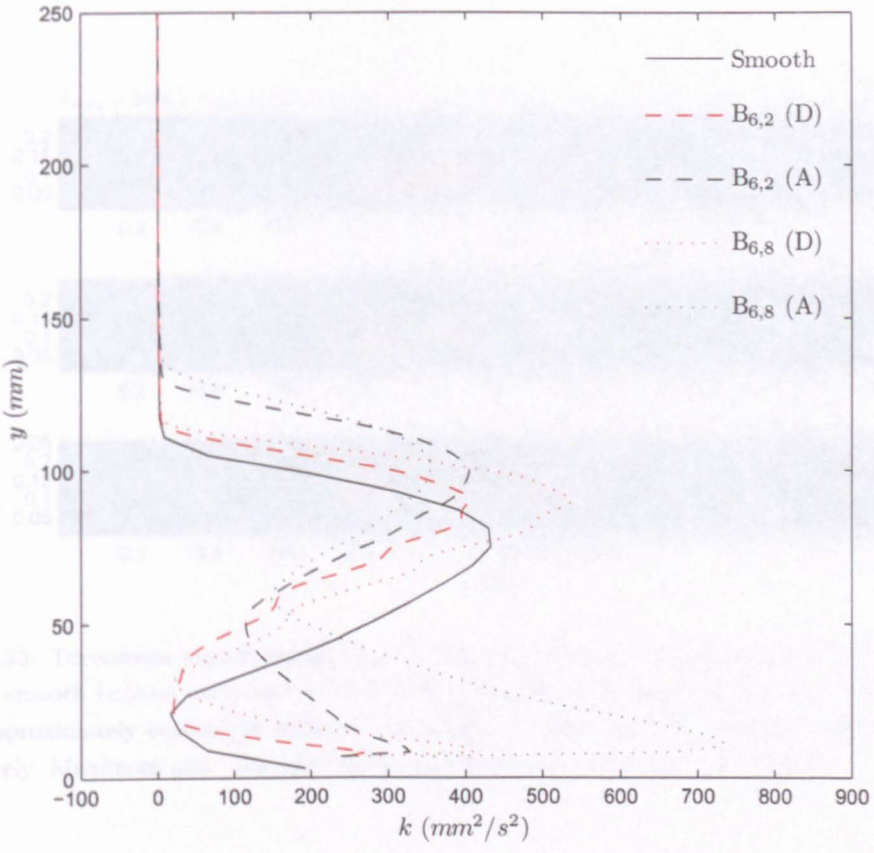

Figure 5.32: Turbulence kinetic energy, k, profiles for the total domain depth resulting from the 2D simulation with a smooth bottom wall and a bottom wall with the beams$_{6,2}$ ($B_{6,2}$) and beams$_{6,8}$ ($B_{6,8}$) with (D) and without (A) dense fluid initialised between the roughness elements.

The effects of the law-of-the-wall method for specifying the bed roughness on the turbulence structure

The TKE field throughout the domain after 9 s shows that the law-of-the-wall method is again visibly more similar to the smooth case, compare figure 5.33 (b) to (a). However, it appears that in this case, the maximum TKE at the interface has shifted to the back of the current whereas in the smooth case it is more central and in the body-fitted case it is just behind the head. In figure 5.34, at the later times, greater differences can be observed between the law-of-the-wall prediction and the smooth case in the form of slightly increased TKE apparent near the bed and decreased TKE in the region of the billows at the density interface, although the distribution of TKE here is still analogous to the smooth case. The large unphysical billow that was observed in the evolution of the smooth case, section 5.4, is also present in the k_s model.

The vertical profiles using the law-of-the-wall method for the bed roughness can be seen in figure 5.35 and confirm the similarity with the smooth case in the vicinity of the

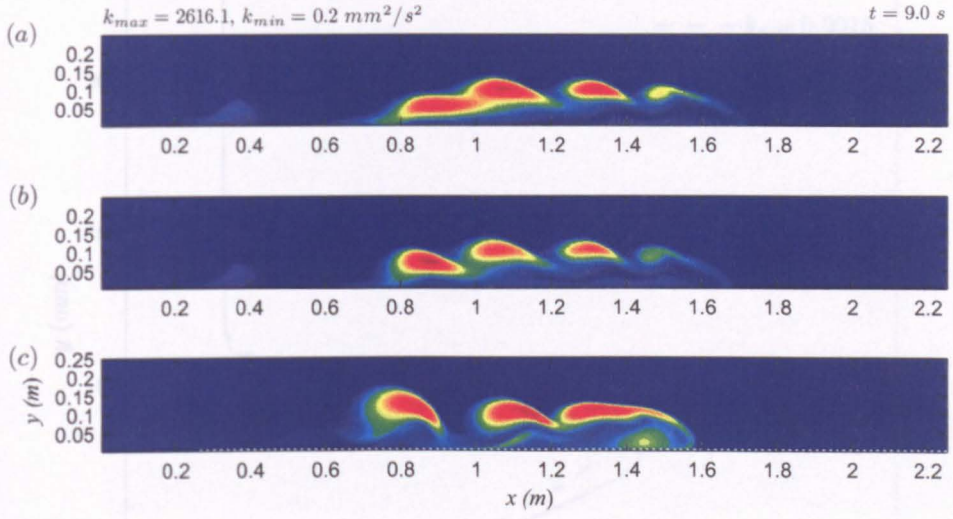

Figure 5.33: Turbulence kinetic energy, k, contours at $t = 9\ s$ resulting from the 2D simulation with (a) smooth bottom wall, and with (b) a k_s value on the bottom wall ($k_s = 0.0015$) which is the approximately equivalent value of (c) beams$_{6,2}$. Red and blue are high and low TKE, respectively. Maximum and minimum values are displayed at the top of the figure.

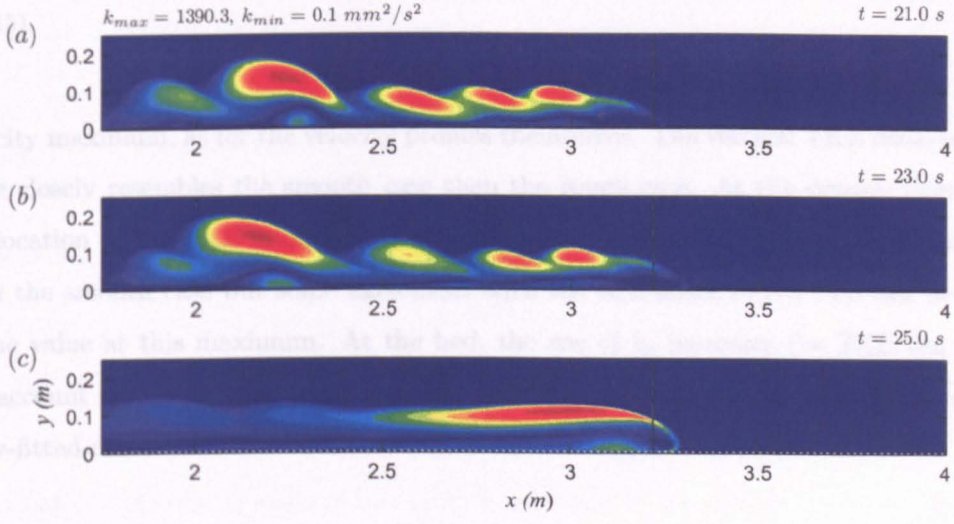

Figure 5.34: Turbulence kinetic energy, k, contours at the approximate time the head passes through 'bin 35' where the vertical profile data is read (shown as a line) resulting from the 2D simulation with (a) smooth bottom wall, and with (b) a k_s value on the bottom wall ($k_s = 0.0015$) which is the approximately equivalent value of (c) beams$_{6,2}$. Red and blue are high and low TKE, respectively. Maximum and minimum values are displayed at the top of the figure.

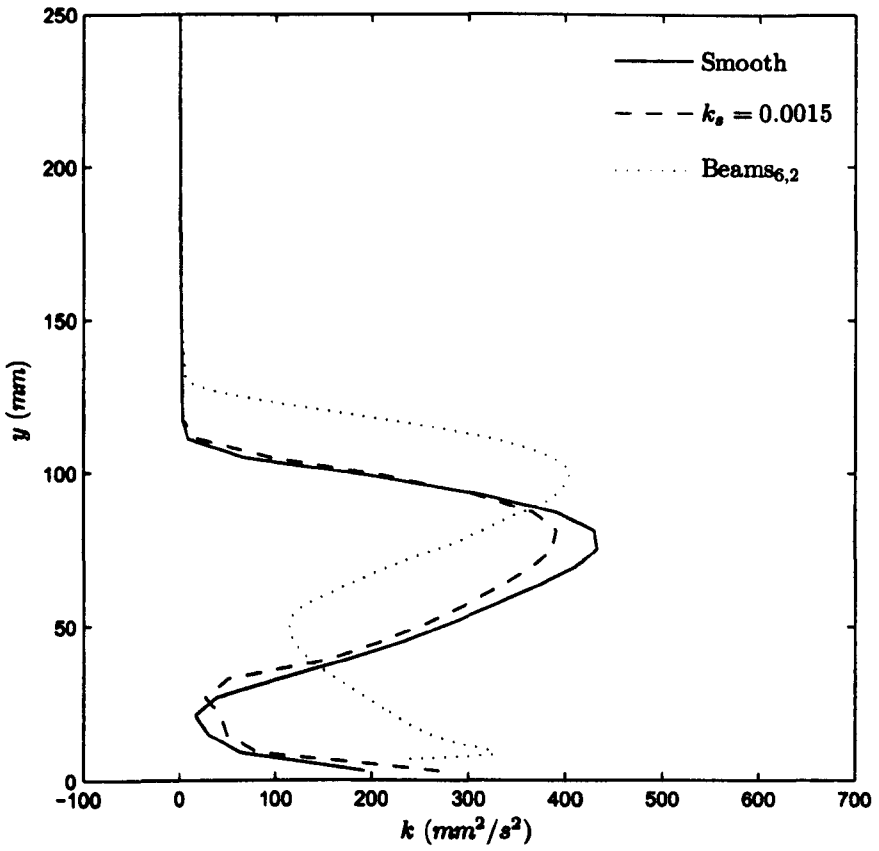

Figure 5.35: Turbulence kinetic energy, k, profiles within the current head resulting from the 2D simulation with a smooth bed and for the equivalent body-fitted rough case with the beams$_{6,2}$ and for the 2D simulation with the approximately equivalent k_s value on the bottom wall (k_s = 0.0015).

velocity maximum, as for the velocity profiles themselves. The vertical TKE distribution more closely resembles the smooth case than the rough case. At the density interface, the location of the TKE maximum is at approximately the same distance from the bed as in the smooth case but some agreement with the equivalent rough case can be seen in the value at this maximum. At the bed, the use of k_s increases the TKE but does not account for the turning point that had been observed to occur in this region in the body-fitted case.

5.7 Concentration

One of the significant benefits of the CFD simulations is that concentration data is readily available for all of the bed roughnesses. Concentration data from the present experiments is not available for validation of the simulations. Therefore the numerical concentration results are considered as an indicative tool and are used as such to aid

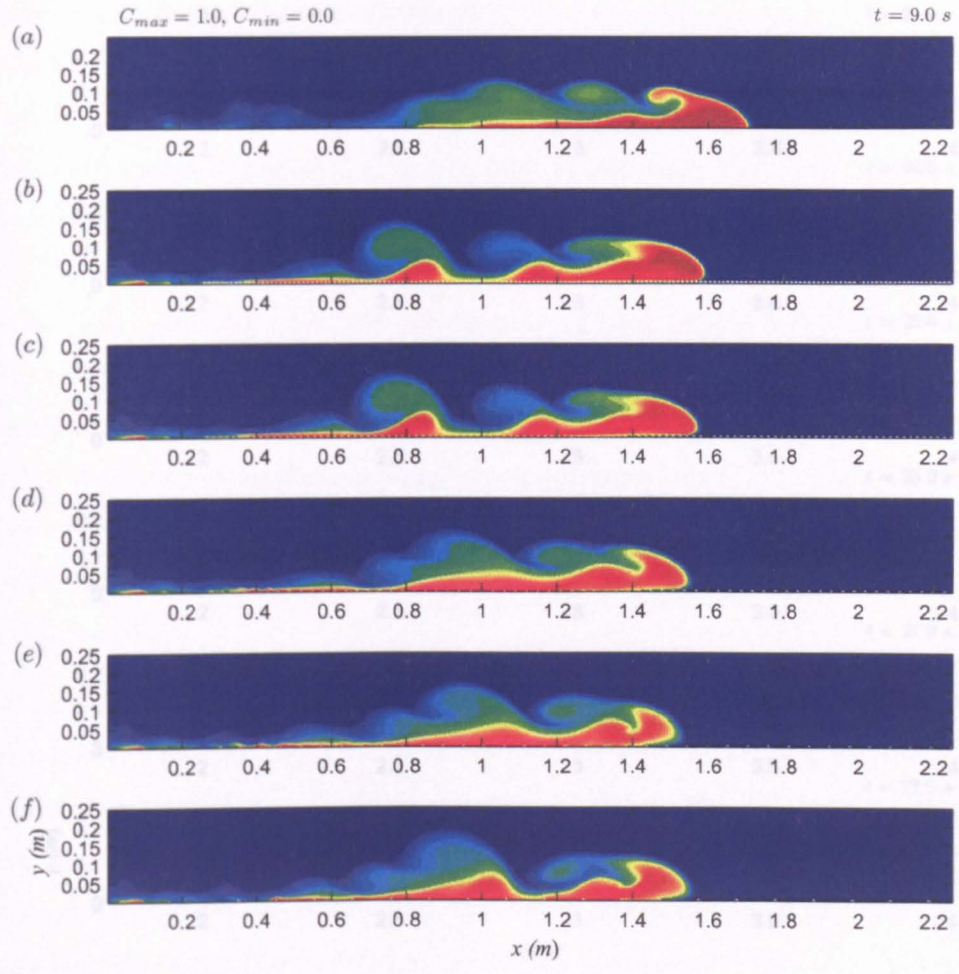

Figure 5.36: UDS (Concentration), C, fields at $t = 9\ s$ resulting from the 2D simulation with (a) smooth bottom wall and (b) beams$_{6,1}$, (c) beams$_{6,2}$, (d) beams$_{6,4}$, (e) beams$_{6,8}$ and (f) beams$_{6,16}$. Red and blue are high and low concentration, respectively. Maximum and minimum values are displayed at the top of the figure.

understanding in conjunction with validated data.

The effects of the spacing of bed roughness elements on the concentration

The user defined scalar or concentration fields after 9 s can be seen in figure 5.36. It is immediately apparent that there is a lack of definition in the billows at the interface in the smooth case. This could be attributed to the lower resolution used in this simulation or this could also indicate greater dilution occurring at the density interface. The large unphysical billows present within the density interface above the body of the current occur in all cases because the 2D nature of the simulations means that the 3D mechanism necessary for their degeneration is not present. In all of the rough models generated with the body-fitted mesh, figures 5.36 $(b) - (f)$, the head of the current is more diluted than

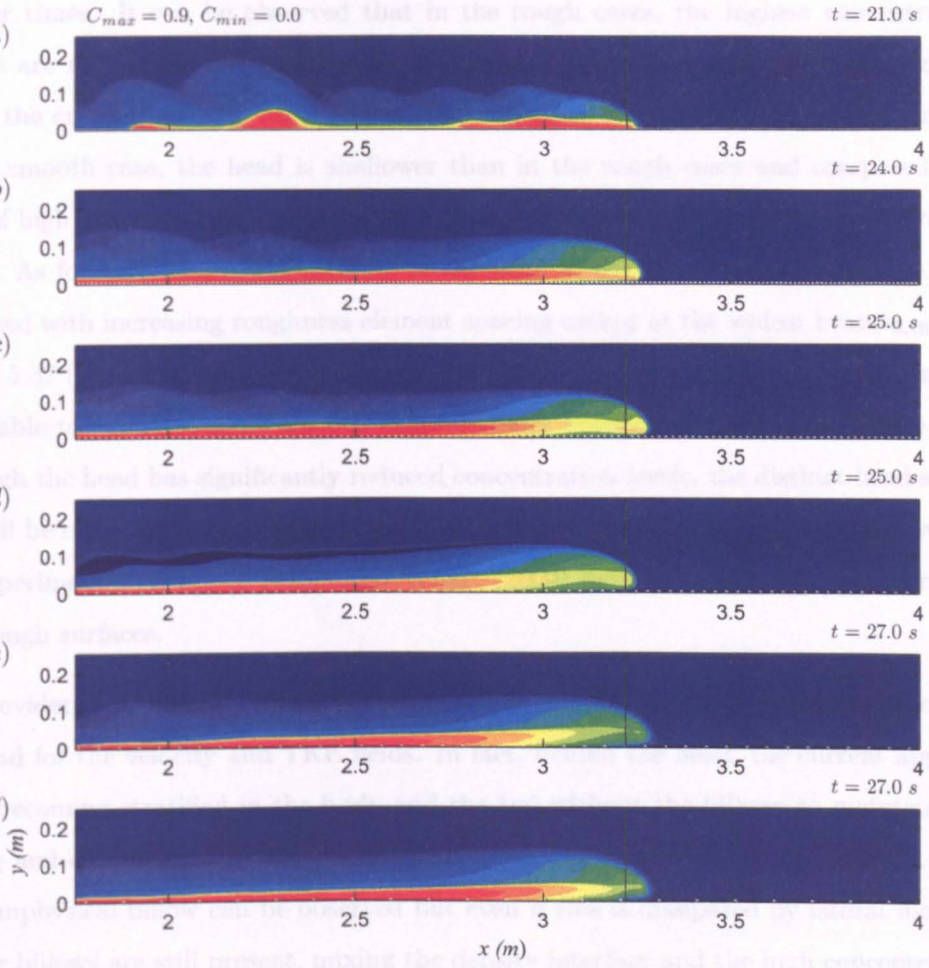

Figure 5.37: UDS (Concentration), C, fields at the approximate time the head passes through 'bin 35' where the vertical profile data is read (shown as a line) resulting from the 2D simulation with (a) smooth bottom wall and (b) beams$_{6,1}$, (c) beams$_{6,2}$, (d) beams$_{6,4}$, (e) beams$_{6,8}$ and (f) beams$_{6,16}$. Red and blue are high and low concentration, respectively. Maximum and minimum values are displayed at the top of the figure.

for the smooth case (a). However, higher concentration fluid is distributed streamwise within the current body which cannot be seen in the smooth case. This occurs to a greater extent for the k-type roughness element spacings, figures 5.36 (d) – (f), while the d-type beds, figures 5.36 (b) and (c), maintain a higher concentration of dense fluid within the head. In the d-type case, the billows can be observed as well-defined surges of concentration at the interface that are of a similar scale to the current depth and correlate with the disturbance to the high concentration at the bed. In the k-type case, the billows are more dilute and therefore less powerful and as a result the region of high concentration near the bed within the body is less distorted.

Figure 5.37 shows the distribution of the concentration fields in the vicinity of the current

at later times. It can be observed that in the rough cases, the highest concentration regions are not within the head region but extend upstream along the body and the tail of the current actually increasing in concentration towards the rear of the current. In the smooth case, the head is shallower than in the rough cases and composed of a layer of high concentration fluid near the bed and a thinner layer of dilute concentration above. As for early times, the dilution of the head in the rough cases appears to have increased with increasing roughness element spacing except at the widest beams$_{6,16}$ case (figure 5.37 (f)) where the head is slightly less dilute. This is possibly due to the current being able to revert to some smooth characteristics between the elements. Notice that although the head has significantly reduced concentration levels, the distinct head shape can still be observed to be supplied by dense fluid to the rear. This was also observed in the experimental results of Peters and Venart (2000) for constant flux gravity currents over rough surfaces.

Little evidence of billows can be observed at the density interface in the rough cases, as found for the velocity and TKE fields. In fact, behind the head, the current appears to be becoming stratified in the body and the tail without the billows to maintain the mixing and entrainment in this region. This is not the case with the smooth bed. The large unphysical billow can be observed but even if this is dissipated by lateral motion, smaller billows are still present, mixing the density interface and the high concentration fluid would still appear to be retained nearer the head of the current and not to extend upstream as in the rough cases. However, it should be noted that in section 5.4, figure 5.4 showed that at still later times the current in the smooth case does extend upstream but the high concentration is retained near the head and the billows continue to mix the ambient and current fluid at the density interface. This continued mixing is probably what prevents stratification in this case and enables the higher concentration fluid to be maintained near the head where mixing is negligible in this case. Conversely, with the rough beds, the continued mixing at the head and negligible mixing at the interface results in a dilute head and an extended body.

Vertical profiles of concentration throughout the domain depth at the bin are shown in figure 5.38. In the smooth case, an almost linear increase in concentration can be observed from the density interface at the top of the current down to the bed, confirming that the high concentration fluid is at the bed as observed in the concentration fields. In the rough cases, higher concentrations can be observed at the density interface at the top of the current head, increasing slightly with increasing spacing. Using this approximate distance of the interface from the bed as an estimate of the height of the

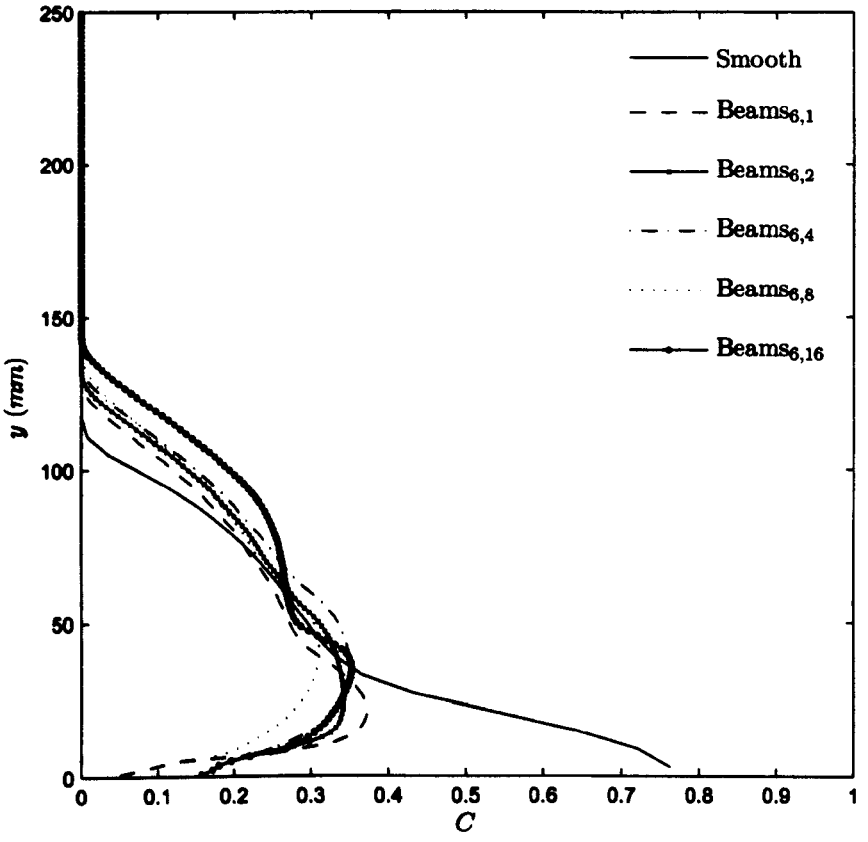

Figure 5.38: Concentration profiles for the total domain depth resulting from 2D numerical simulations with a smooth bottom wall and bottom walls with beams$_{6,1}$, beams$_{6,2}$, beams$_{6,4}$, beams$_{6,8}$ and beams$_{6,16}$.

head, figure 5.38 also suggests that the height increases slightly with increasing spacing. As for the smooth case, in the rough cases there is an increase in concentration below the interface but it is non-linear and a maxima occurs in the lower part of the head below which the concentration decreases substantially down to the bed. This concentration maxima appears to decrease with increasing element spacing, except for the beams$_{6,16}$ case where an irregular increase is apparent. The nonlinear profile observed for the rough cases confirms that dilution due to the roughness elements occurs at the bed and causes higher concentration fluid to be forced higher into the head. The location of the highest concentration fluid appears to correlate with the location of the velocity maximum, being just below it. This indicates that mixing of the dense fluid is hindered in this region, perhaps implying a slow diffusion zone similar to the observations of Buckee *et al.* (2001). However, since the higher concentration fluid is heavier, buoyancy requires that it sink below the lower concentrations. In the smooth case this is observed as a layer of high concentration at the bed seen in figures 5.38 and 5.37 (*a*), but in the rough cases, this means that the high concentration fluid is subject to mixing from the roughness elements.

Thus the high concentrations are diluted and the vertical profile is as shown in figure 5.38.

To obtain another quantitative means to analyse the temporal evolution of the concentration, the cumulative percentage of the domain that is above specified levels in concentration was calculated as a function of time and is shown in figure 5.39. At the start of the simulation, $t = 0$ s, the percentage of the domain with concentration levels within the gravity current ($C > 0.01$) is the percentage of the domain that is in the lock box, i.e. 5%[¶]. For all the bed configurations, this percentage increases with time. This increase must be a result of entrainment and mixing of high concentration current with the ambient fluid. Except for the constant increase in the percentage of the domain at the lowest concentration level, after about twelve seconds the percentage of the domain within which lies concentration levels up to 0.6, for the body-fitted mesh roughened cases (figures 5.39 $(b) - (f)$), becomes almost constant (this is included within the data for percentage of cells containing concentrations of 0.5 and above in figure 5.39). Cells containing concentration above these levels (i.e. $C > 0.6$) continue decreasing. In all rough cases investigated with ambient fluid between the elements, the occurrence of concentration levels above 0.9 decreases to zero within the first ten seconds. In the smooth case (figure 5.39 (a)), concentrations of this level and above are maintained for longer. However, after approximately 12 s the percentage of cells with concentration levels above 0.3 decreases to a constant level, which is below that of all the rough cases. This implies that after this time a higher percentage of the gravity current with a smooth boundary is actually more dilute than the currents with rough boundary conditions. This can be explained in conjunction with the velocity fields. In the smooth case, the high concentration fluid is maintained in the current head and there are strong coherent billows that form behind it and cause entrainment and dilution at the density interface. These billows are not maintained in the k-type case and therefore the flow is able to stratify in the body behind the head without the disruptions at the interface. The head continues to be diluted but it has a tail of higher concentration fluid as a buoyancy source. Thus, the dilution dynamics of the smooth case and the k-type case are different with the smooth case retaining higher concentrations for longer but apparently undergoing continual dilution at all concentration levels and the rough cases losing high concentration fluid quickly but then stabilising.

After the total 30 s of flow time, it appears that about 30% of the domain is above

[¶]The tank is 0.25 m high and 5 m long and the lock box is 0.25 m long. Therefore the lock box amounts to 5% by volume of the tank.

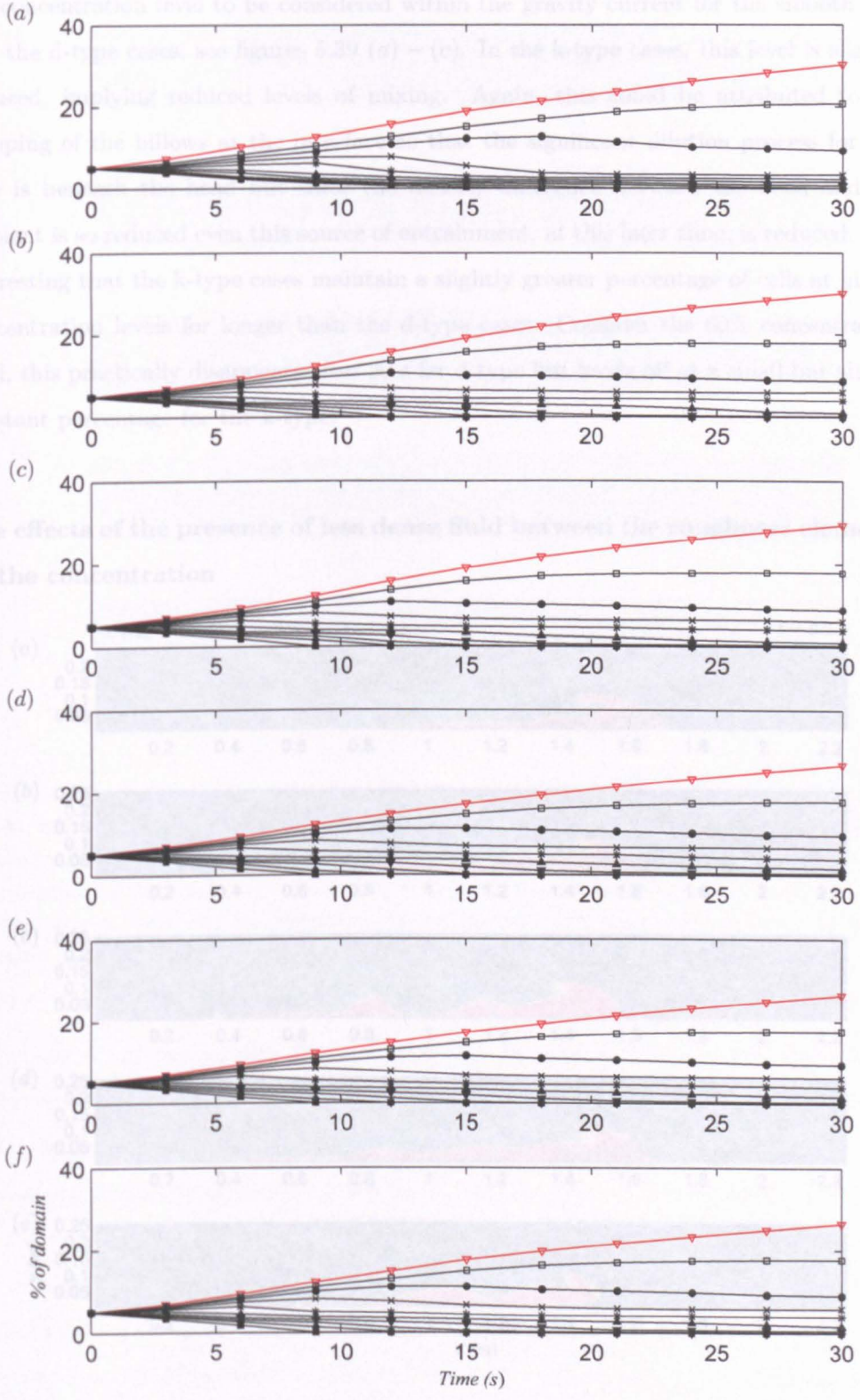

Figure 5.39: UDS (Concentration), C, as a function of time given as a cumulative percentage of the total domain with (a) smooth bottom wall and (b) beams$_{6,1}$, (c) beams$_{6,2}$, (d) beams$_{6,4}$, (e) beams$_{6,8}$ and (f) beams$_{6,16}$. The data coloured red represents the percentage of cells in the domain that contain concentration levels that meet the minimum criteria to be considered within the gravity current entity. The data below this line represents cumulative concentration levels from 0.1 and above (open squares) to 0.9 and above (filled squares).

the concentration level to be considered within the gravity current for the smooth case and the d-type cases, see figures 5.39 $(a) - (c)$. In the k-type cases, this level is slightly reduced, implying reduced levels of mixing. Again, this could be attributed to the damping of the billows at the interface so that the significant dilution process for this case is beneath the head but since the density difference between the head and the ambient is so reduced even this source of entrainment, at this later time, is reduced. It is interesting that the k-type cases maintain a slightly greater percentage of cells at higher concentration levels for longer than the d-type cases. Consider the 60% concentration level, this practically disappears after 20 s for d-type but levels off at a small but almost constant percentage for the k-type.

The effects of the presence of less dense fluid between the roughness elements on the concentration

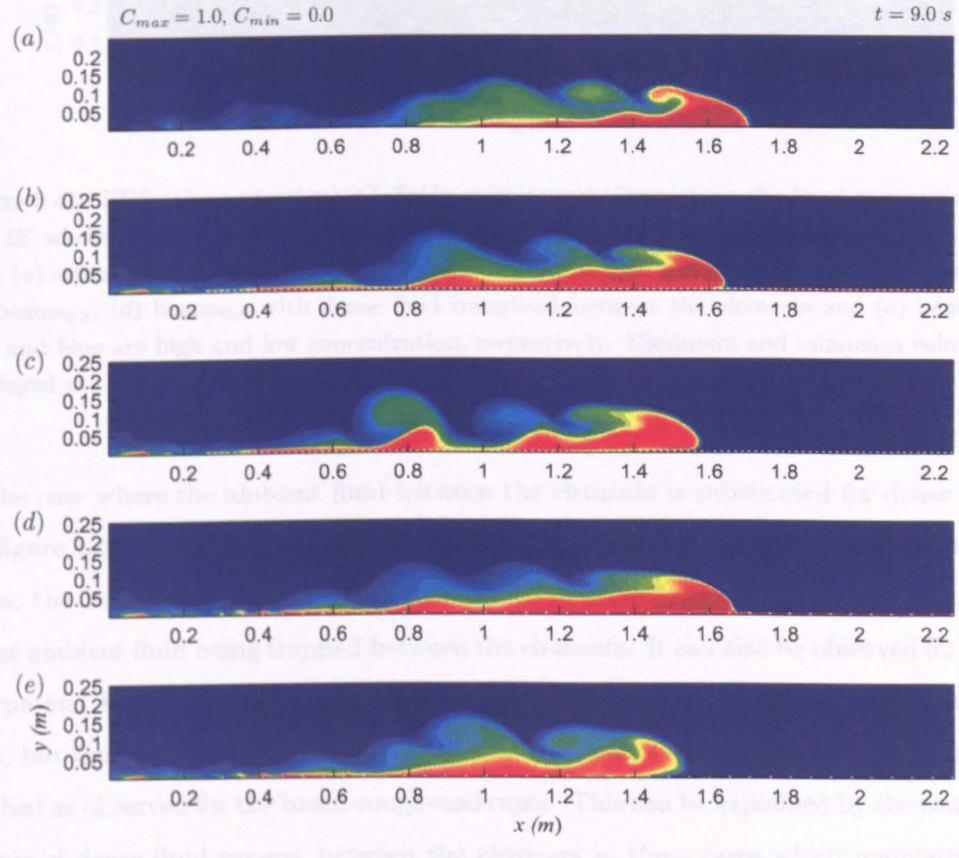

Figure 5.40: UDS (Concentration), C, fields at $t = 9\ s$ resulting from the 2D simulation with (a) smooth bottom wall and (b) beams$_{6,2}$ with dense fluid initialised between the elements, (c) beams$_{6,2}$, (d) beams$_{6,8}$ with dense fluid initialised between the elements and (e) beams$_{6,8}$. Red and blue are high and low concentration, respectively. Maximum and minimum values are displayed at the top of the figure.

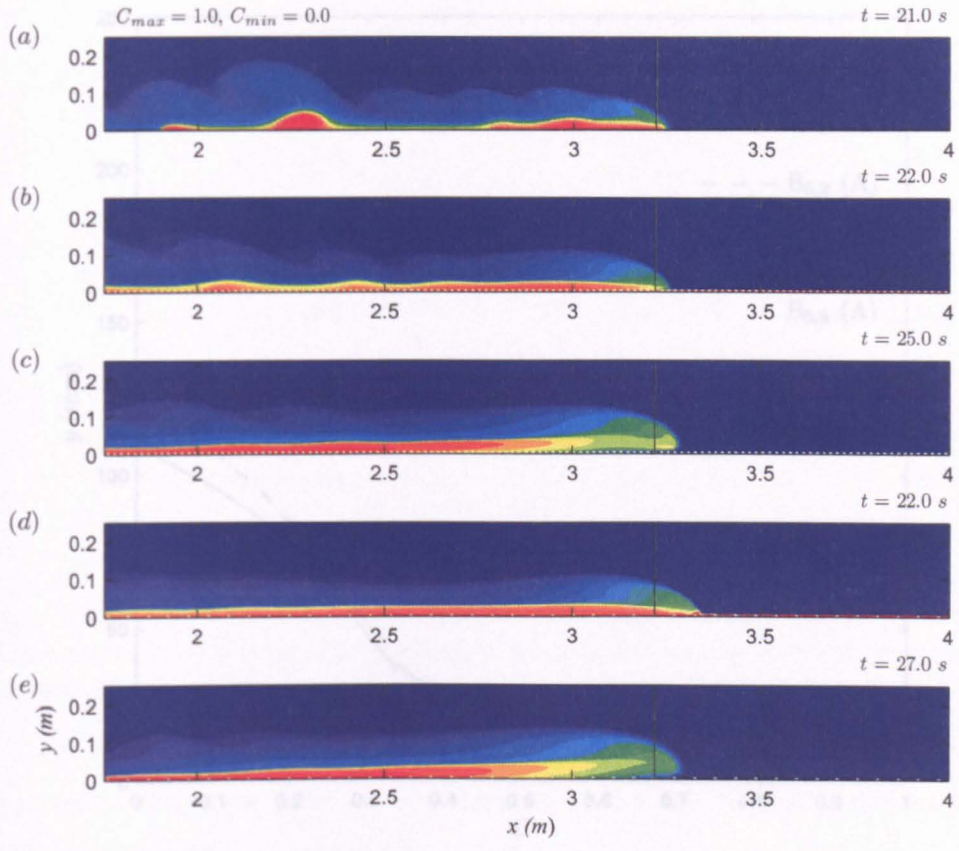

Figure 5.41: UDS (Concentration), C, fields at the approximate time the head passes through 'bin 35' where the vertical profile data is read (shown as a line) resulting from the 2D simulation with (a) smooth bottom wall and (b) beams$_{6,2}$ with dense fluid initialised between the elements, (c) beams$_{6,2}$, (d) beams$_{6,8}$ with dense fluid initialised between the elements and (e) beams$_{6,8}$. Red and blue are high and low concentration, respectively. Maximum and minimum values are displayed at the top of the figure.

In the case where the ambient fluid between the elements is substituted for dense fluid, see figure 5.40 (b), the billows are more diffuse. This suggests that, certainly in the d-type cases, the beam-roughened bed has stronger billows partially due to the buoyant, less dense ambient fluid being trapped between the elements. It can also be observed for both d-type and k-type cases that the head remains highly concentrated, as in the smooth case, but the main body of the current behind the head also has high concentrations at the bed as observed for the beam-roughened cases. This can be explained by the constant source of dense fluid present between the elements in these cases which maintains the head at a high concentration and is not available in the runs over the regular beams roughness where less dense fluid below the head causes significantly increased levels of dilution in the current head and body.

Figure 5.41 shows the distribution of the concentration fields in the vicinity of the current

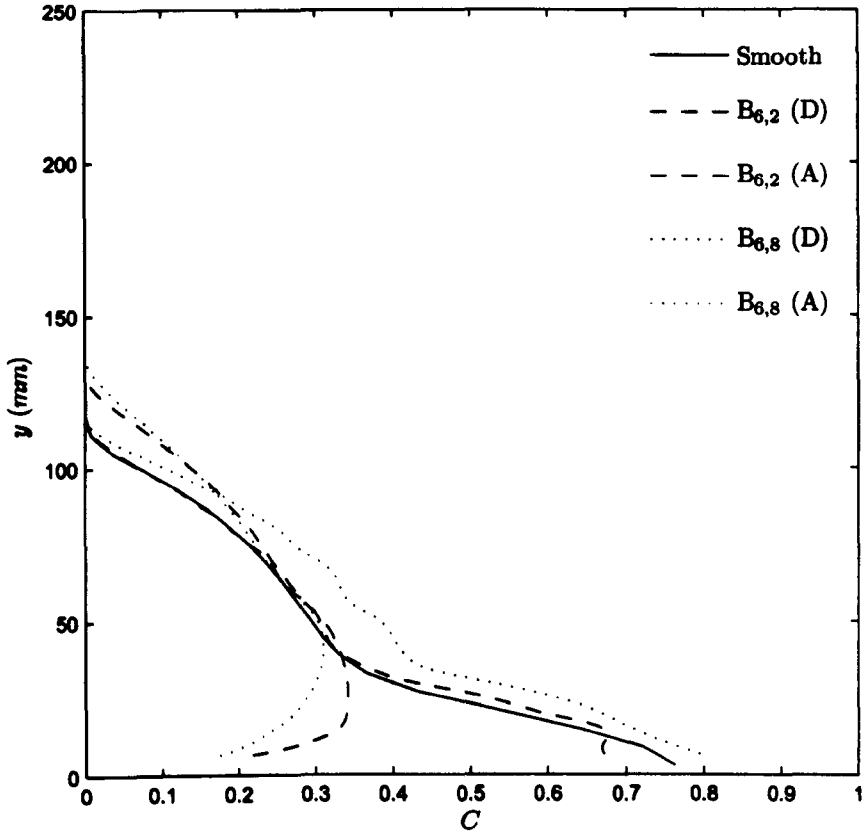

Figure 5.42: Concentration profiles for the total domain depth resulting from 2D numerical simulations for a smooth bottom boundary and bottom walls with beams$_{6,2}$ ($B_{6.2}$) and beams$_{6,8}$ ($B_{6.8}$) with (D) and without (A) dense fluid initialised between the elements.

at the later times for the simulations with and without dense fluid between the elements. Figures 5.41 (*b*) and (*d*) show that despite the constant source of dense fluid between the elements, the current head has still been diluted in these cases similar to the smooth case, although not as much as the regular rough beds. This is probably because although there is a constant source of dense fluid between the elements, at later times it has a substantially higher density than the overflowing current and therefore the current floats over the top of it and cannot entrain it by buoyancy; thus the current cannot readily increase its concentration. The simulations with dense fluid between the elements agree more closely with their regular rough bed equivalents in the upstream extent of the current behind the head than with the smooth case. Like those cases, the billows are clearly damped or very dilute which has allowed the current fluid to stratify behind the head. However, the head of the current itself is shallower than the regularly rough cases and composed of reduced quantities of dilute fluid, more like the smooth case. This implies that the roughness elements themselves, and not the buoyant ambient fluid, cause the elongation and stratification upstream of the head of the current. However,

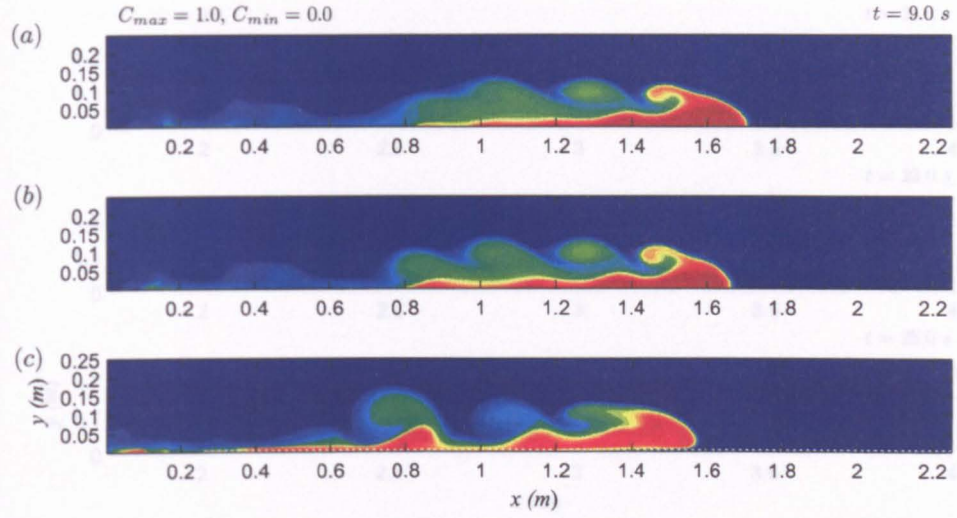

Figure 5.43: UDS (Concentration), C, fields at $t = 9\ s$ resulting from the 2D simulation with (a) smooth bottom wall and with (b) a k_s value on the bottom wall ($k_s = 0.0015$) which is the approximately equivalent value of (c) beams$_{6,2}$. Red and blue are high and low concentration, respectively. Maximum and minimum values are displayed at the top of the figure.

as observed at early times, the ambient fluid does cause the dilution of the head and therefore its subsequent increase in size at later times.

The vertical concentration profiles at the bin for the cases with dense fluid initialised between the elements are shown in figure 5.42. It is immediately apparent that the removal of the buoyant ambient fluid from between the roughness elements removes the mixing at the bed and causes the profiles to agree more closely with the smooth case with a layer of high concentration fluid at the bed. In fact, in the d-type case, very good agreement can be seen with the concentration distribution above a smooth bed.

The effects of the law-of-the-wall method for specifying the bed roughness on the concentration

The concentration fields for the law-of-the-wall bed roughness condition after 9 s can be seen in figure 5.43 (b). Clearly, the result resembles the smooth case, (a), more closely than the body-fitted case, (c). However, an increase in the size of the billows at the interface that occurs in the body-fitted equivalent can be observed as can a slight decrease in concentration within the head and an increased streamwise distribution of higher concentration fluid at the bed. At later times, figure 5.44 shows that the k_s method still maintains closest similarity with the smooth case.

Figure 5.45 shows the vertical concentration through the current head for the law-of-the-

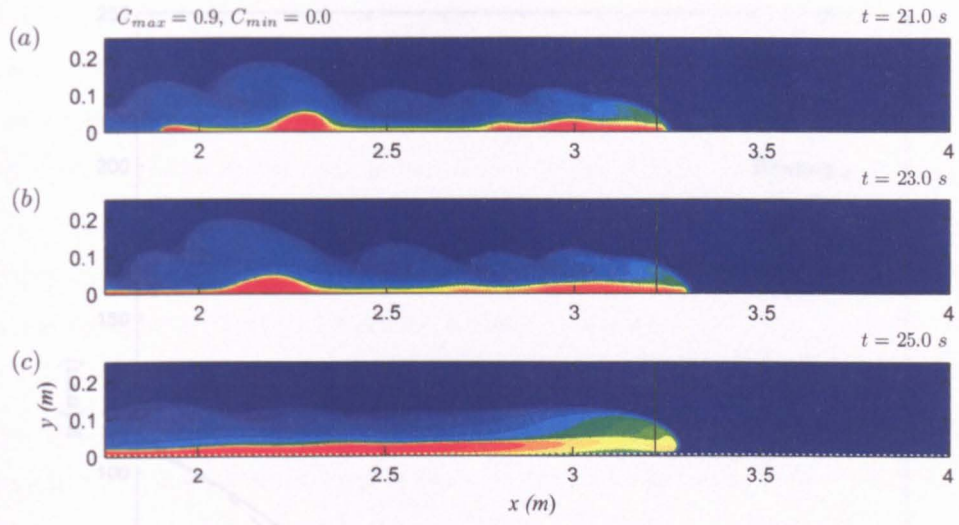

Figure 5.44: UDS (Concentration), C, fields at at the approximate time the head passes through 'bin 35' where the vertical profile data is read (shown as a line) resulting from the 2D simulation with (a) smooth bottom wall and with (b) a k_s value on the bottom wall ($k_s = 0.0015$) which is the approximately equivalent value of (c) beams$_{6,2}$. Red and blue are high and low concentration, respectively. Maximum and minimum values are displayed at the top of the figure.

wall method compared with the smooth bed and rough body-fitted method equivalent. Again, as seen for other variables, specifying a k_s value for the bed roughness results in a current with very similar internal dynamics to the smooth case. A slight reduction in concentration can be observed at the bed but a maxima further in the flow with a dilute, mixed region beneath it is not present.

5.8 Discussion

The lower computational cost incurred in 2D simulations allowed further models to be generated with closer roughness element d-type spacing (beams$_{6,1}$) and a much wider k-type spacing (beams$_{6,16}$). This enables further insight into the effects of element spacing that is not available from the experimental study and is not performed in 3D due to the increased temporal and computational cost. The present 2D results agree with some open channel studies in finding a spacing of $w/k_r \approx 4$ (beams$_{6,4}$) that could be classified as 'intermediate'. This spacing shows some flow characteristics in common with the d-type cases and others in common with the k-type cases. The 2D simulations herein show that the close proximity of the elements in the beams$_{6,1}$ and beams$_{6,2}$ spacings cause rotating fluid to become trapped beneath the current. In these cases, the ambient fluid is trapped for longer and there is little disruption observed in the flow field of

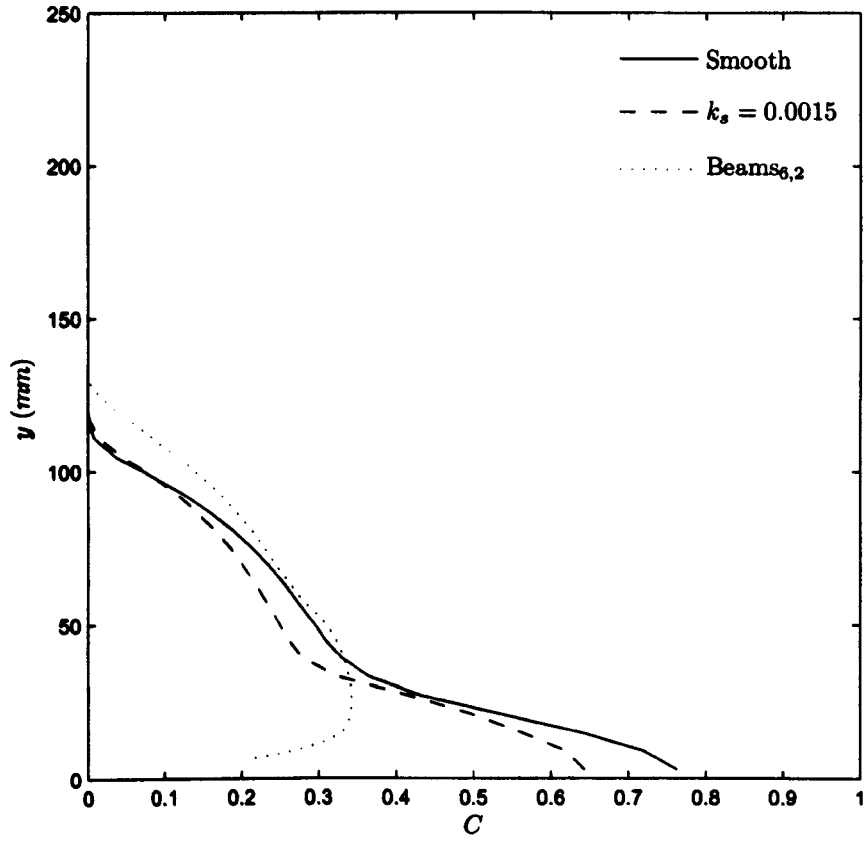

Figure 5.45: Concentration profiles for the total domain depth resulting from 2D numerical simulations with a smooth bottom boundary and with $k_s = 0.0015$ specified on the bottom wall and the body-fitted method equivalent (beams$_{6,2}$).

the overflowing fluid. The head of the current is diluted but not as quickly as in the k-type cases. However, energy must be lost to maintaining the vortices in motion. In the k-type cases (beams$_{6,8}$ and beams$_{6,16}$) separation occurs at the top of the elements and reattaches downstream, before the next element is encountered. The disruption to the flow field penetrates higher into the current, the TKE is increased and the head is diluted. In the intermediate case, the fluid is not trapped in vortical motion as in the d-type case but neither does it reattach between the elements without significant effects from the downstream element. The overall effects are a combination of the two cases.

The results predict that in the presence of bed roughness the front speed decreases and the magnitude of the decrease depends on the spacing with wider spacings leading to a greater decrease in speed. These predictions agree well with the experimental findings of the present study. The two widest spacings (beams$_{6,8}$ and beams$_{6,16}$) show very similar development of the front position with time, which indicates a critical spacing of $w/k_r \approx 7$, as observed for open channel flows. Further evidence of the existence of a

critical spacing and the similarity with open channel flows over bed roughness is observed in the reattachment lengths upstream of the elements. These have a value of $\approx 4k_r$ for the two widest spacings, in approximate agreement with several open channel studies. In open channel flow these critical values define the criteria beyond which increasing the spacing has little changing effect on the flow dynamics. This critical spacing is probably due to the elements being far enough apart such that the downstream element does not interfere with the reattachment that occurs after separation from top of the upstream element, such that the over-flowing fluid becomes similarly affected regardless of the spacing. Interestingly, despite the similarities in the front position, the widest $\text{beams}_{6,16}$ case shows several irregularities in the internal flow profiles. This is could result from the presence of the buoyant ambient in gravity currents that does not exist in open channel cases. The predictions for the widest $\text{beams}_{6,16}$ may also indicate an upper spacing limit beyond which the flow dynamics undergo further transitions, perhaps because the elements are so far apart that the flow is able to partially revert back to smooth characteristics in the cavities.

The following observations will be confirmed or modified in the subsequent chapter once the 3D numerical data is available for clarity. They are presented here simply to summarise the foregoing work and highlight the salient points brought to light by the 2D simulations.

- The 2D simulations agree well with the experimental data for the distance that the front travels over a period of time in the constant speed phase but the slowing transition occurs prematurely and is exaggerated in the rough cases. Unphysical billows and a stationary wave-like structure are observed in the smooth case and it is likely that the 3D model is needed to disperse these features. Conversely, the removal of the buoyant ambient fluid from between the elements in the $\text{beams}_{6,8}$ case caused the current to propagate further in the simulation than in the laboratory equivalent. Since the flow slows prematurely in the simulations with ambient fluid in the cavities this fluid must cause significantly increased lateral motion that the 2D model cannot resolve.

- The 50:50 split governing the reduction in speed that was observed in the experimental data is confirmed for the d-type case. The split was postulated to result from $\approx 50\%$ due to the presence of ambient fluid between the elements and $\approx 50\%$ due to other roughness effects. In the experimental data this was also observed in the k-type case. It is probable that the 3D resolution is required to model the in-

creased lateral flow dynamics in the k-type case that the 2D model cannot account for.

- The agreement between the 2D numerical and experimental velocity profiles is very good and confirms a decreased velocity maximum located further from the bed. This result implies that a 2D model may be adequate if an approximate internal velocity profile is required.

- The positive downstream and vertical motion ahead the gravity current front indicates that fluid is being forced ahead of the front as a 'ghost front'. The effective range of this motion increases in the presence of bed roughness.

- Increased TKE is predicted in the head of the current in the rough cases. In the k-type cases the TKE is particularly high at the bottom of the head and localised around the roughness elements. In the smooth and d-type cases, there is high TKE at the interface where billows are more coherent. This increase in TKE in the head is primarily caused by the overridden ambient fluid, although some of the effect is due to the elements themselves. This is particularly true for the k-type cases.

- The head is more dilute in all of the rough cases and the level of dilution increases with spacing. This coincides with the increased TKE and is primarily due to the trapped ambient fluid. The higher concentration fluid is distributed streamwise behind the head and appears to be becoming stratified, particularly in the k-type cases. This likely results from the diffuse density interface in these cases, where large billows are not present to disrupt the current body.

- Despite increased dilution, the current maintains a distinct head region, which is shorter, deeper and more rounded in profile. This is probably caused by entrainment at the bed causing continual dilution. Since the velocity maximum is further from the bed, the higher concentration fluid that is fed to the head from the body is forced higher. Since this fluid is heavier than the dilute fluid at the bottom of the head, buoyancy forces cause it to sink and become diluted by entrainment and mixing due to the elements at the bed.

- The simulation implementing the law-of-the-wall method for generating numerical bed roughness showed good agreement with the experimental results for the front position and the simulations were shown to be sensitive to the choice of value, which indicates the potential of this method as a simple means of proscribing bed roughness in simulations. However, the internal distributions of velocity, TKE and

concentration showed very little difference from the smooth case. This may be because describing the multiple effects of bed roughness with one value is subject to significant errors, which may be exaggerated for gravity currents due to the ambient fluid trapped between the elements.

Chapter 6

Depth-resolved numerical simulations: 3D model results

6.1 Introduction

The previous chapter presented the results of the depth-resolved 2D numerical simulations calculated using the commercial CFD software FLUENT and included a brief discussion and comments on the performance of this 2D model. This chapter presents the results for the 3D model and discussion and analysis of the performance of the 2D model compared with the 3D model. A combined discussion of both CFD models herein can also be found at the end of the chapter. The 3D results focus primarily on two bed roughnesses, representing one d-type and one k-type configuration. More detailed emphasis is given to the effects of the ambient fluid between the elements. Verification and validation with experimental data have again been rigorously completed and are presented in detail.

6.2 Outline of models

The 3D numerical simulations carried out in the present study are listed in table 6.1 including the mesh resolution (*maximum cells vertically* × *maximum cells horizontally*) and the bed type. The 3D simulations were chosen to compare directly to equivalent 2D numerical and experimental results for validation. Since they are more computationally and temporally expensive, simulations of the extra cases included in the 2D versions have not been performed except for the model implementing the law-of-the-wall method with $k_s = 0.0015$ to again enable comparison of the two methods of incorporating bed roughness. The three mesh resolutions for the smooth case (No.'s 1 - 3) are used for

No.	Mesh	Bed type
1	$42 \times 16 \times 417$	Smooth
2	$42 \times 17 \times 417$	Smooth
3	$84 \times 33 \times 834$	Smooth
4	$84 \times 33 \times 834$	$\text{Beams}_{6,2}$
5	$84 \times 33 \times 834$	$\text{Beams}_{6,8}$
6	$84 \times 33 \times 834$	$\text{Beams}_{6,2}$ (D)
7	$84 \times 33 \times 834$	$\text{Beams}_{6,8}$ (D)
8	$42 \times 17 \times 417$	$k_{s,0.0015}$

Table 6.1: 3D numerical simulations undertaken in the present study. Tank dimensions are directly comparable to experiments. The initial conditions for all simulations represent a gravity current with the equivalent of a 5% initial density excess in the laboratory. All walls have the 'no-slip' condition except the top wall which has a 'symmetry' condition. 'D' means that dense fluid is also initialised between the roughness elements. Mesh relates to the maximum number of cells in the vertical, lateral and horizontal directions. All simulations have experimental and 2D equivalents for validation.

verification. Choice of mesh is discussed in section, 6.3.

The number of cells increases dramatically from 2D to 3D. Therefore the 3D simulations were performed using FLUENT in parallel on eight processors on the 'White Rose Grid'. Since the domain configurations used in the present study were relatively simple in design, the grid and processing tasks were divided between the processors using FLUENT's auto-partitioning facility.

6.3 Verification

Iterative convergence

Iterative convergence is monitored for the 3D case in a similar manner to the 2D equivalent case but the calculation of the scaled residuals now includes the third, lateral component. Again, when the residuals all decrease below a critical level, chosen herein to be 10^{-3}, convergence is assumed to have been achieved for that time step and solution proceeds. Evidence of this process is shown in figure 6.1 for time steps between 6 s and 7 s for the smooth domain with a coarse ($42 \times 17 \times 417$) mesh. As for the 2D model, it can be observed clearly that although the initial predictions of the variable values each time step are somewhat inaccurate, after subsequent iterations the solution is consistently satisfying the convergence criteria for all variables at each time step. Equivalent convergence characteristics are seen for the $84 \times 33 \times 834$ resolution and for the rough cases. However, as in the 2D model, they are similar and it is therefore assumed unnecessary

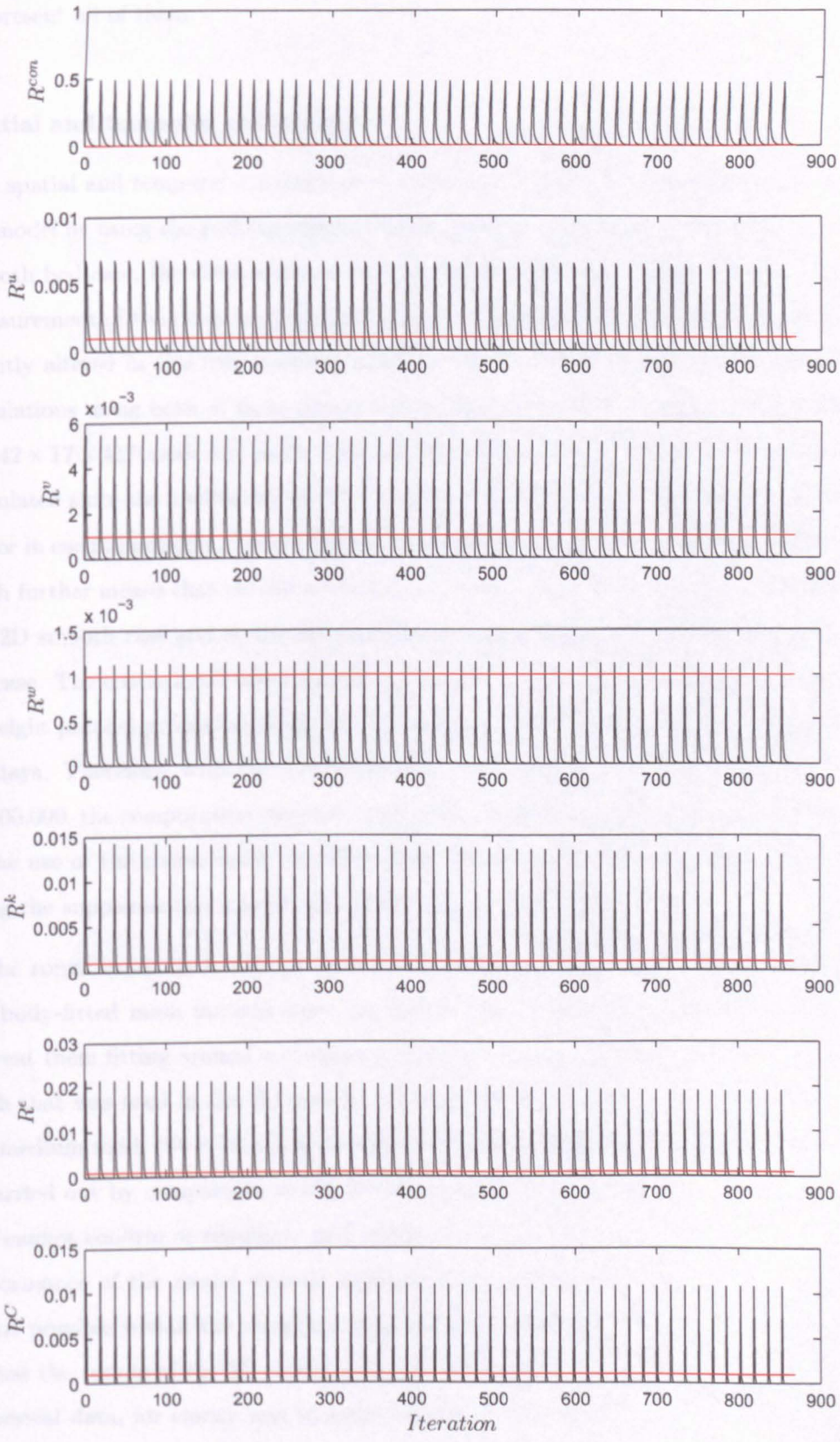

Figure 6.1: Iterative convergence shown in the form of residuals, calculated as given in chapter 4 for the $42 \times 17 \times 417$ resolution mesh for the smooth case. The convergence criteria, 10^{-3}, below which the residuals are assumed to indicate convergence is shown in red.

to present all of them.

Spatial and temporal convergence

The spatial and temporal convergence of a simulation were parameterised jointly in the 2D model by using the grid convergence index (GCI), see section 5.3. However, in the 3D smooth bed case, the dimensions of the cells means that they cannot divide the lateral measurement of the domain in the coarse case. Therefore the cell dimensions have been slightly altered in this case resulting in either 16 or 17 cells laterally. The smooth bed simulations using both of these lateral resolutions were indistinguishable, and therefore the $42 \times 17 \times 417$ mesh was used. As a result of this indivisibility, the GCI has not been calculated since the medium mesh ($84 \times 33 \times 834$) cannot be said to be refined by the same factor in each dimension. The prohibitive computational expense involved in refining the mesh further means that the 3D extension to the fine case that is used for verification in the 2D smooth case and in the 2D body-fitted mesh rough cases cannot be used in the 3D case. The coarse mesh takes approximately 24 hours to complete the computation on the eight parallel processors while for the medium mesh this increases to approximately six days. Therefore, with the fine mesh, where the number of cells escalates to almost 20,000,000, the computation incurs an unfeasible temporal cost. Despite this, verification of the use of the coarse mesh for the smooth bed is performed with the medium mesh using the supplementary checks also performed in the 2D case.

In the rough cases, as in the 2D model, it is not possible to use the coarsest mesh for the body-fitted mesh method since the lateral and streamwise dimensions of the cells prevent them fitting around a roughness element (beam). As mentioned above, the fine mesh that was used in the 2D case is now prohibitively expensive in 3D and therefore the medium mesh ($84 \times 33 \times 834$) is used in all subsequent simulations and verification is carried out by comparison to the 2D equivalent case. Although this is not infallible and cannot confirm or repudiate grid independence, it does give some indication of the performance of the model without entering into an in depth verification study which is not possible within the temporal scope of this investigation. Since it is relevant to discuss the results of the 3D model with reference to the experimental data and the 2D numerical data, for clarity and to avoid repetition, the verification of the 3D results is presented alongside the validation in the following sections.

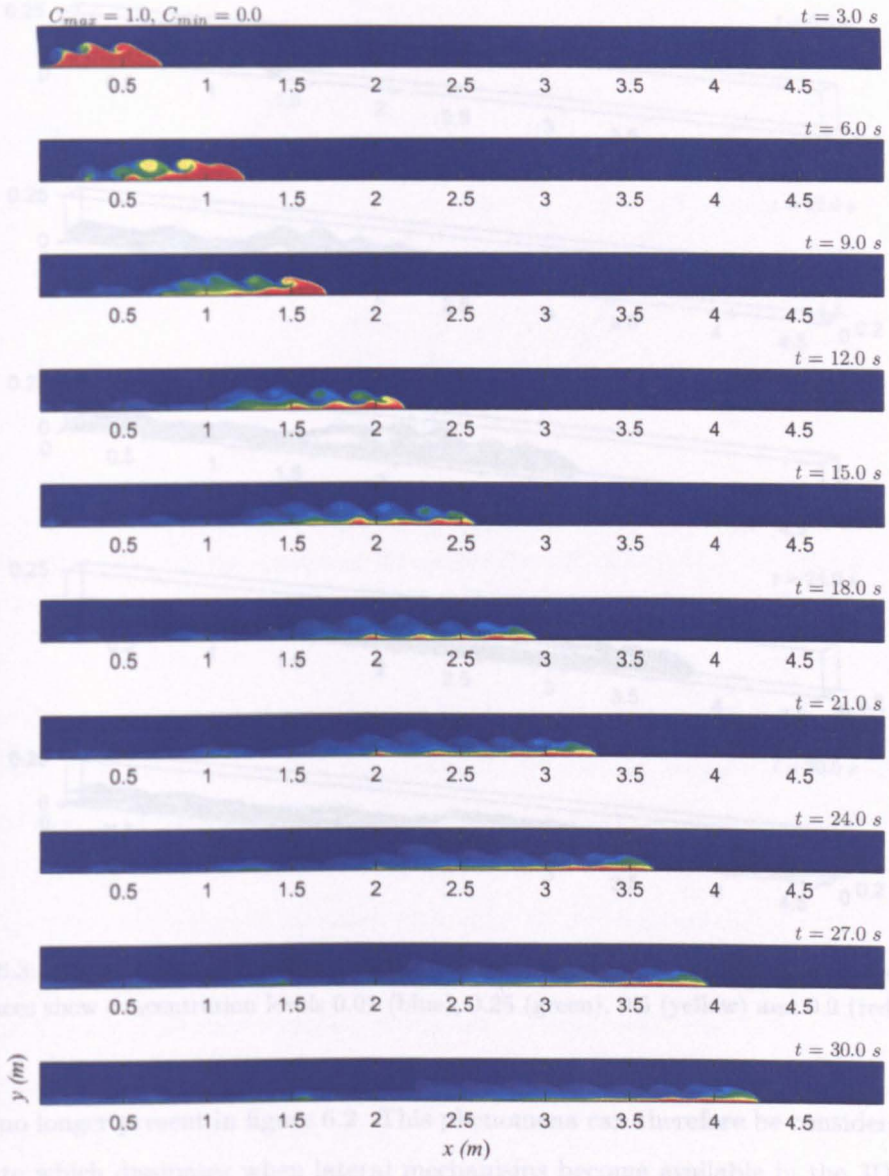

Figure 6.2: The evolution of the laterally-averaged concentration field every 3 s up to 30 s for the 3D numerical simulation of the smooth case. Red and blue are high and low concentration, respectively. Maximum and minimum values are displayed at the top of the figure.

6.4 Flow evolution

The laterally averaged evolution of the UDS or concentration field for the smooth case can be seen in figure 6.2 at 3 s intervals. Good agreement with the 2D smooth case (figure 5.4) is observed implying that certainly for the smooth case, the 2D model is able to capture similar characteristics to the 3D model. Notice that the irregular wave-like disruption to the bed and the corresponding large unphysical billow at the density interface that was observed to remain stationary from 18 - 24 s in the 2D case (figure

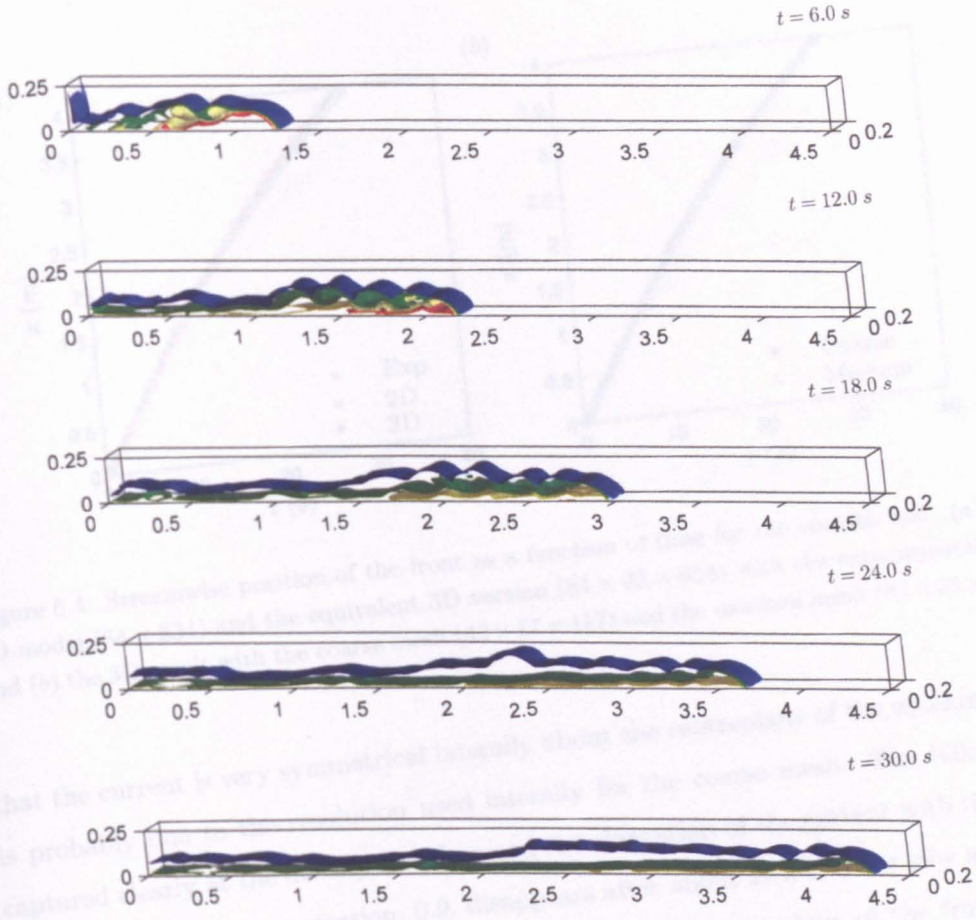

Figure 6.3: The evolution of the 3D concentration field every 6 s up to 30 s for the smooth case. Isosurfaces show concentration levels 0.01 (blue), 0.25 (green), 0.5 (yellow) and 0.9 (red).

5.4) is no longer present in figure 6.2. This phenomena can therefore be considered a 2D attribute which dissipates when lateral mechanisms become available in the 3D model, enabling the current to retain a higher speed beyond this time period.

Perhaps as a result of the removal of the unphysical blip feature, the billows at the density interface are more regularly spaced and smaller in the 3D model resulting in less disruption apparent in the high concentration in the current body than was observed in 2D. At later times (figure 6.2 from 21 s onwards), the billows are dilute but coherent at the density interface and the current head appears to decrease in size, more so than the 2D model.

The full 3D prediction for flow evolution every 6 s up to 30 s in the smooth case without lateral averaging can be seen in figure 6.3. Isosurfaces of concentration levels 0.01, 0.25, 0.5 and 0.9 are displayed. The lowest level represents a dilute concentration below which smaller concentrations are assumed to be within the ambient fluid. It can be observed

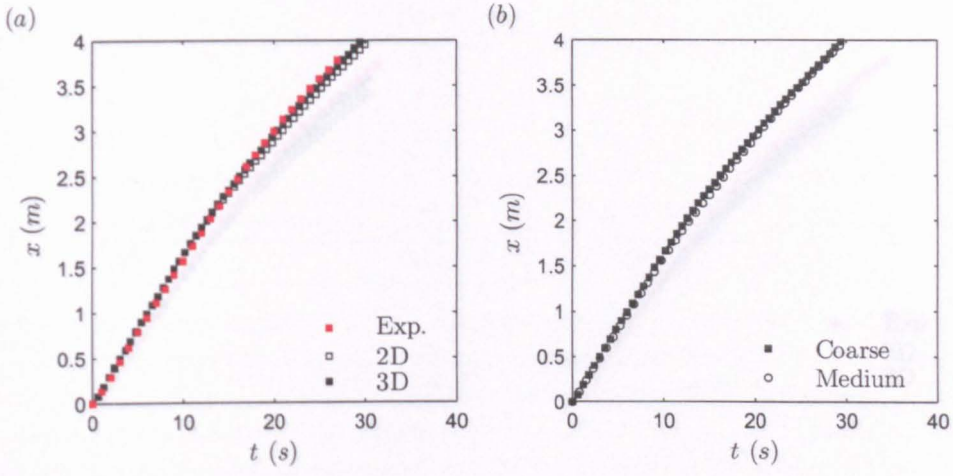

Figure 6.4: Streamwise position of the front as a function of time for the smooth bed. (*a*) The 2D model (84×834) and the equivalent 3D version ($84 \times 33 \times 834$) with the experimental data and (*b*) the 3D result with the coarse mesh ($42 \times 17 \times 417$) and the medium mesh ($84 \times 33 \times 834$).

that the current is very symmetrical laterally about the centreplane of the domain. This is probably due to the resolution used laterally for the coarse mesh. The billows are captured clearly at the density interface and the elongation of the current with time can be seen. The high concentration, 0.9, disappears after about 18 s and the lobe and cleft formation becomes apparent at about this time at the centreplane of the front. The occurrence of only one cleft in this simulation is probably the result of using a relatively coarse grid with a turbulence model, rather than a finer mesh (e.g. Corney, 2005) or the fine scale resolution of DNS. The lobes and clefts do not occur before this time for the same reason.

6.5 Velocity validation

6.5.1 Front position and speed

The effects on the front position and speed of the d-type and k-type bed roughness configurations with and without ambient fluid between the elements*

It can be seen in figure 6.4 (*a*) that at early times there is very little difference in the results of the 2D and 3D models for the smooth case. However, for later times, the

*Only one example of each bed classification, d-type or k-type, is considered in the 3D model with their experimental and 2D equivalents. Hence, to avoid repetitive figures the results of the regular simulations and of those with dense fluid replacing the ambient fluid between the elements are presented simultaneously for the 3D model rather than separating them as was done in the 2D.

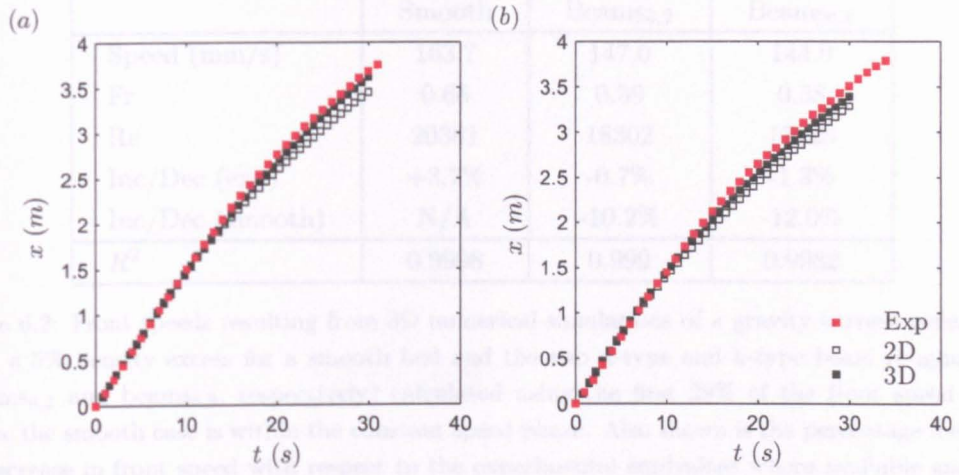

Figure 6.5: Position of the front as a function of time resulting from 2D and 3D numerical simulations compared to the equivalent experimental results for bottom walls with (*a*) $\text{beams}_{6,2}$ and (*b*) $\text{beams}_{6,8}$.

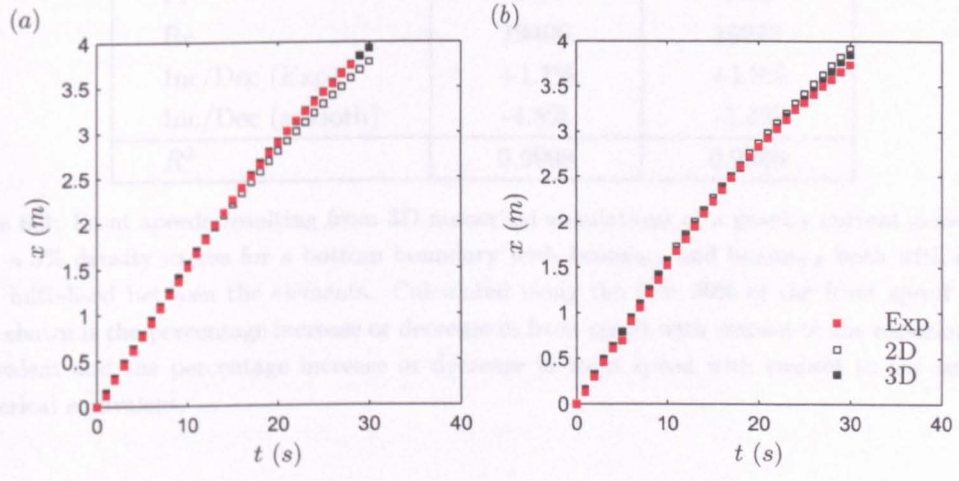

Figure 6.6: Position of the front as a function of time resulting from 2D and 3D numerical simulations compared to the equivalent experimental results for bottom walls with (*a*) $\text{beams}_{6,2}$ and (*b*) $\text{beams}_{6,8}$ with dense fluid between the roughness elements.

3D model is not as susceptible to the premature slowing of the current that occurs in 2D and therefore has very good agreement with the experimental data. Figure 6.4 (*b*) is evidence of the good agreement between the coarse mesh and the medium mesh, showing an excellent level of mesh independence for the front speed.

When bed roughness is present, figure 6.5 shows that the 3D model is still susceptible to the premature slowing at later times that occurred in the 2D model for both the d-type and k-type cases. However, it is now able to maintain a faster speed. The simulated gravity current is still not quite able to retain the same front position as observed in the

	Smooth	$Beams_{6,2}$	$Beams_{6,8}$
Speed (mm/s)	163.7	147.0	144.0
Fr	0.66	0.59	0.58
Re	20381	18302	17928
Inc/Dec (exp)	+3.7%	-0.7%	-1.3%
Inc/Dec (smooth)	N/A	-10.2%	-12.0%
R^2	0.9998	0.999	0.9982

Table 6.2: Front speeds resulting from 3D numerical simulations of a gravity current generated with a 5% density excess for a smooth bed and the two d-type and k-type beam roughnesses ($beams_{6,2}$ and $beams_{6,8}$, respectively) calculated using the first 39% of the front speed data where the smooth case is within the constant speed phase. Also shown is the percentage increase or decrease in front speed with respect to the experimental equivalent where available and the percentage increase or decrease in front speed with respect to the smooth numerical equivalent.

	$Beams_{6,2}$	$Beams_{6,8}$
Speed (mm/s)	155.9	154.8
Fr	0.63	0.63
Re	19400	19273
Inc/Dec (Exp)	+1.7%	+1.9%
Inc/Dec (smooth)	-4.8%	-5.4%
R^2	0.9998	0.9996

Table 6.3: Front speeds resulting from 3D numerical simulations of a gravity current generated with a 5% density excess for a bottom boundary with $beams_{6,2}$ and $beams_{6,8}$ both with dense fluid initialised between the elements. Calculated using the first 39% of the front speed data. Also shown is the percentage increase or decrease in front speed with respect to the experimental equivalent and the percentage increase or decrease in front speed with respect to the smooth numerical equivalent.

experimental data at later times but in the initial period of constant speed, the prediction has improved, see table 6.2. It can be observed that the d-type bed configuration (figure 6.5 (*a*)) shows closer agreement with the experimental data than the k-type model (figure 6.5 (*b*)). It is possible that in the k-type model there is increased lateral motion and although the 3D has captured some of this, the lateral resolution may not be high enough to resolve the necessary mechanisms to dissipate the effects of the retarding dynamics on the current. Since it was predicted in the 2D model that the k-type cases have more diffuse billows, which do not require high lateral dissipation, it can be postulated that it is increased lateral motion between the roughness elements in this case that causes this effect. Evidence of this is presented in section 6.5.2.

The front position for the cases with dense fluid initially replacing the ambient fluid between the elements is shown in figure 6.6. The d-type case (figure 6.6 (*a*)) which was

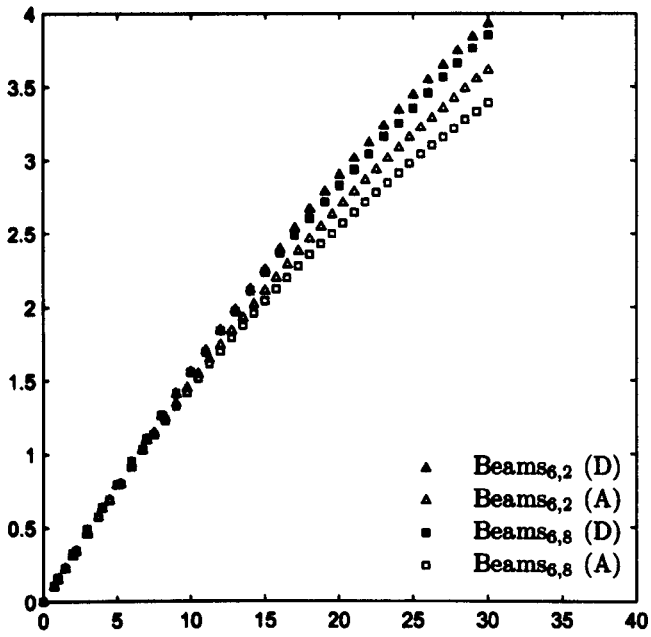

Figure 6.7: Position of the front as a function of time resulting from 3D numerical simulations for bottom walls with $\text{beams}_{6,2}$ and $\text{beams}_{6,8}$ with (D) and without (A) dense fluid between the roughness elements.

also susceptible to the premature slowing in 2D can now be seen to efficiently maintain its position. In fact, the agreement between the 3D model and the experimental data is exceptionally good. Comparison of figure 6.6 (*a*) with the rough bed with ambient fluid between the elements and its experimental equivalent, shown in figure 6.5 (*a*), indicates that it is the presence of the ambient fluid between the elements that is causing the premature retardation compared to the experiment in the d-type case. In the k-type case (figure 6.6 (*b*)) the agreement between the 3D and the experimental data is not quite as good but it does show an improvement on the 2D, which for this case was shown to over-estimate the front speed. The better agreement compared with the experimental data can also be seen in table 6.3 for the initial period of constant speed. This supports the suggestion made in section 5.5.1 that this case requires the lateral motion to remove energy from the front and thus slow the current more accurately.

Figure 6.7 highlights the significant effect that removing the ambient fluid from between the elements has on the front position. The cases with dense fluid between the elements clearly undergo a much later transition than the regular rough cases. Note that in the d-type case, with dense fluid between the elements, the gravity current is now predicted to propagate faster than the k-type equivalent, unlike the prediction shown by the 2D model (figure 5.7). It is also apparent from the 3D model that there is less difference

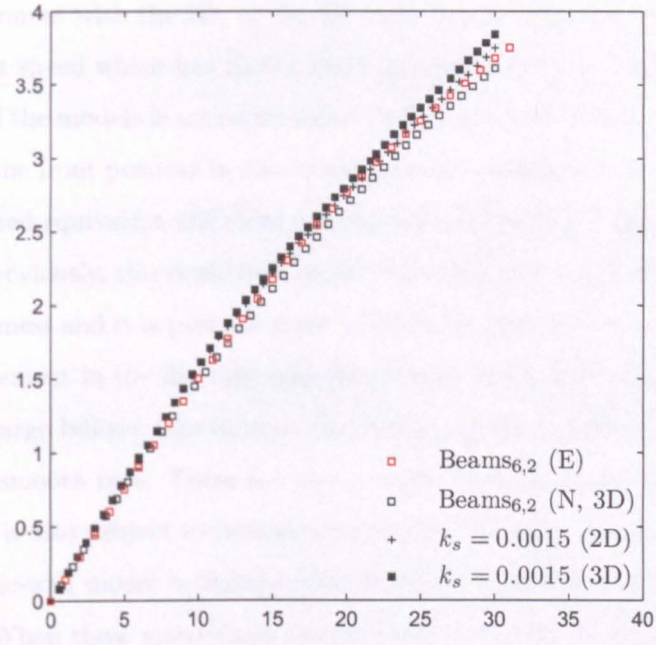

Figure 6.8: Position of the front as a function of time resulting from the 3D numerical simulation with a bed roughened using the law-of-the-wall method with $k_s = 0.0015$ and the experimental (E) and 3D numerical (N) equivalent beams$_{6,2}$ (i.e. $k_s \approx 0.0017$).

in the position of the front for these cases compared to the beds with ambient fluid between the elements. This implies that the presence of the ambient fluid increases the differentiation between the two classifications of element spacing.

The results in tables 6.2 and 6.3 show that in the initial period of constant speed the 3D model agrees with the experimental data in suggesting that the presence of the ambient fluid between the elements contributes to $\approx 50\%$ of the reduction in current front speed due to the presence of roughness and this implies the elements themselves cause the rest of the retardation. Agreement for the d-type case was also found in the 2D model but the k-type case predicted increased effects due to the trapped ambient (see section 5.5.1). However, as shown above, the 2D model for the k-type case with dense fluid between the elements can not estimate the front position as accurately as the 3D model and with the lateral motion present this statistic appears to hold. Note that as found in the 2D model, this does not necessarily hold at later times.

The effects of the law-of-the-wall method for specifying the bed roughness on the front position and speed

Figure 6.8 shows the predictions from the 3D model implementing the law-of-the-wall method for specifying bed roughness along the bottom boundary. The model does not

show good agreement with the 2D, or the 3D body-fitted equivalent models. The period of constant front speed which has shown good agreement with the experimental equivalents for most of the models is misrepresented in this case and results in a faster current. At later times, the front position is also exaggerated in comparison to the 2D model and the 3D body-fitted equivalent and does not appear to represent a good choice of model. As mentioned previously, this could be a result of the inability of the method to cope with form-type roughness and it is perhaps more suitable for describing grain-type roughness. The better agreement in the 2D case may result from the lack of lateral mechanisms in that case. The large billows that form at the density interface cause the 2D model to be retarded in the smooth case. These are also present in the k_s model which would imply that this model is also subject to premature slowing. Therefore the good fit apparent in the 2D law-of-the-wall model is slightly false since it is an attribute of the restrictions of 2D modelling. When these restrictions are removed in the 3D model and lateral motion is resolved, the k_s value is shown be less effective at slowing the current accurately.

6.5.2 Laterally averaged horizontal and vertical velocity structure

The effects on the laterally averaged horizontal and vertical velocity structure of the d-type and k-type bed roughness configurations with and without ambient fluid between the elements

As demonstrated above, the 2D and 3D front speed data can easily be compared. However, for the vertical profiles through the current depth and for the flow field data, it is necessary to transform the laterally variable 3D datasets into 2D for comparison. To achieve this, it is possible to either select one plane laterally or to width average the data over the lateral extent of the domain. The most obvious solution in the present study is to choose one plane at the lateral centreplane since this corresponds to the location of the probes from which the experimental datasets were generated. Figure 6.9 shows, in the smooth case, that there is little difference between the choice of 3D representation after 9 s, except perhaps in the billows where the centreline option (figure 6.9 (*b*)) appears to be in slightly better agreement with the 2D. However, in the rough boundary cases, if, for example, the d-type rough case is considered, figure 6.10 shows that there is a significant difference between the two options. The reason for this discrepancy is the formation of a cleft at the front lying approximately at the lateral centreplane (presented in detail in section 6.7). The low lateral resolution and use of a turbulence model prevents the formation of many lobes and clefts at the front as occurs naturally. Hence,

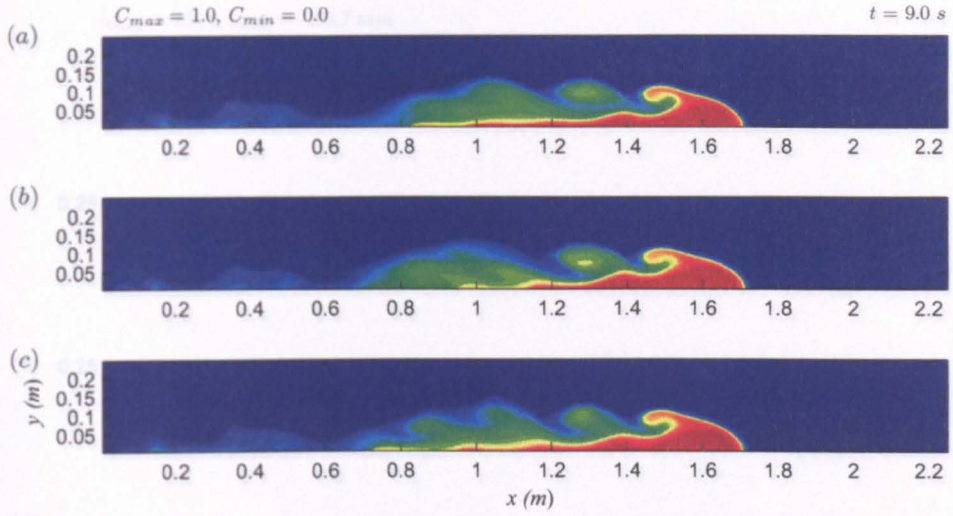

Figure 6.9: UDS (concentration), C, fields at $t = 9\ s$ for the smooth bed resulting from (a) the 2D simulation, (b) the 3D simulation along the centreplane and (c) the laterally averaged 3D simulation. Red and blue are high and low concentration, respectively. Maximum and minimum values are displayed at the top of the figure.

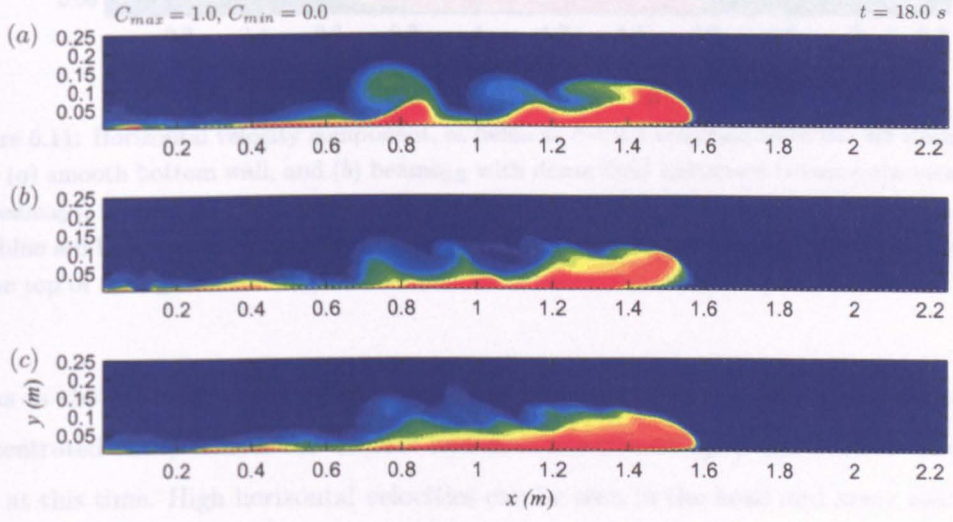

Figure 6.10: UDS (concentration), C, fields at $t = 9\ s$ for the bed with beams$_{6,2}$ resulting from (a) the 2D simulation, (b) the 3D simulation along the centreplane and (c) the laterally averaged 3D simulation. Red and blue are high and low concentration, respectively. Maximum and minimum values are displayed at the top of the figure.

although reading the numerical data at the centreplane corresponds more equivalently with the location of the data reading in the experiments, the laterally averaged result is a more representative characterisation of the domain taking into account lateral variation. Therefore those results are presented in the following section. Figures 6.11 and 6.12 show the vertical and horizontal velocity fields in the vicinity of the current after 9

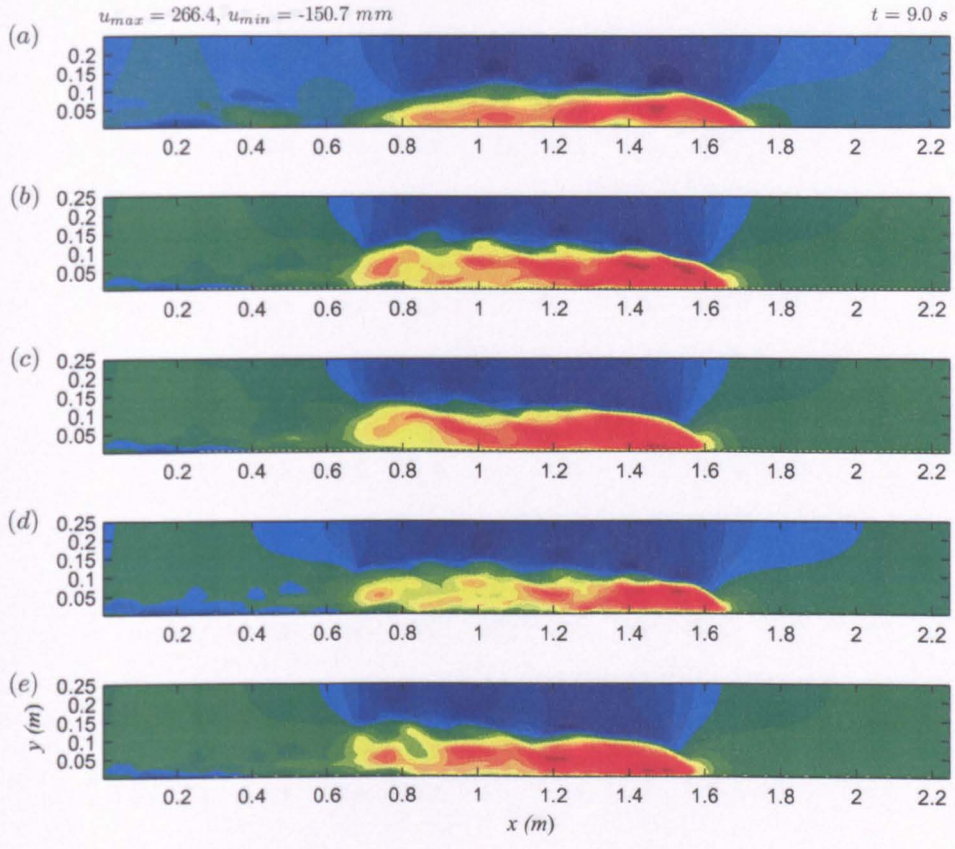

Figure 6.11: Horizontal velocity component, u, fields at $t = 9$ s resulting from the 3D simulation with (a) smooth bottom wall, and (b) beams$_{6,2}$ with dense fluid initialised between the elements, (c) beams$_{6,2}$, (d) beams$_{6,8}$ with dense fluid initialised between the elements and (e) beams$_{6,8}$. Red and blue are high and low velocities, respectively. Maximum and minimum values are displayed at the top of the figure.

s. As in the 2D case, it can be observed that the current appears to move as a highly concentrated entity within the domain and does not extend upstream towards the end-wall at this time. High horizontal velocities can be seen in the head and lower velocities in the body and tail of the current for all configurations (figure 6.11). However, unlike the 2D case, significant reduction in the horizontal velocity can already be observed at the tail end of the currents. In the rough cases, this is increased and is exaggerated in the cases without ambient fluid between the elements (figures 6.11 (b) and (d)). If the corresponding vertical motion observed in figures 6.12 (b) and (d) is considered, a different pattern in the vertical fluctuations at the density interface in these cases can be seen, compared to the regularly rough cases (figures 6.12 (c) and (e)). These potentially indicate smaller but stronger billows at the density interface and reduced motion within the current body beneath it, when the ambient fluid has been initially removed from between the elements. Conversely, for the regular cases, the billows are weaker but larger

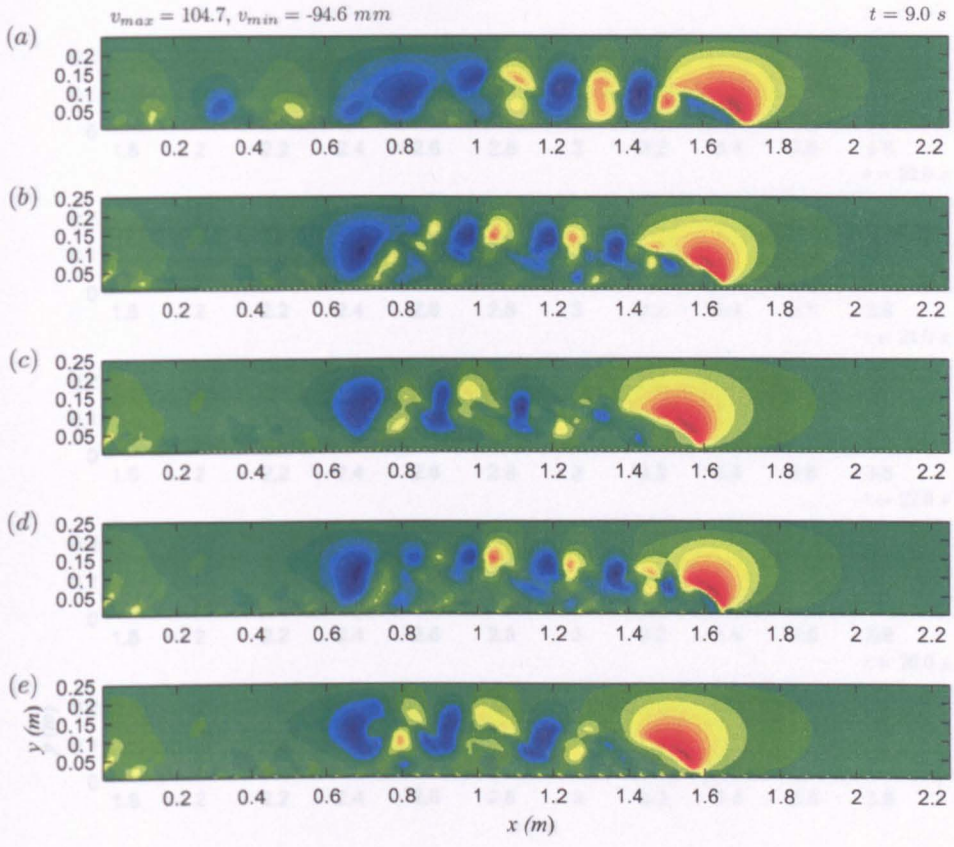

Figure 6.12: Vertical velocity component, v, fields at $t = 9$ s resulting from the 3D simulation with (a) smooth bottom wall, and (b) beams$_{6,2}$ with dense fluid initialised between the elements, (c) beams$_{6,2}$, (d) beams$_{6,8}$ with dense fluid initialised between the elements and (e) beams$_{6,8}$. Red and blue are high and low velocities, respectively. Maximum and minimum values are displayed at the top of the figure.

and penetrate into the current body, and hence a higher horizontal motion is apparent in these cases. This highlights the lack of lateral dissipation in the 2D model. The billows could not be dissipated laterally and therefore all cases demonstrated larger billows of varying strength which penetrated the current body.

Notice that figures 6.11 and 6.12 confirm the presence of fluid being pushed ahead of the current front for all cases, as was observed in the 2D model (figures 5.15 and 5.16). However, the effective range of this motion appears to have diminished with the inclusion of 3D dynamics. This indicates that the increase previously observed in this region was likely a result of the 2D nature of the model.

The velocity fields at later times are presented in figures 6.13 and 6.14. As in the 2D results, this data is presented in order to correspond to the time that the head of the current in each specific case reaches the location at which the vertical profiles are read in the experimental setup (i.e. 'bin 35' 3.22 m from the lock-box end of the tank). It can be

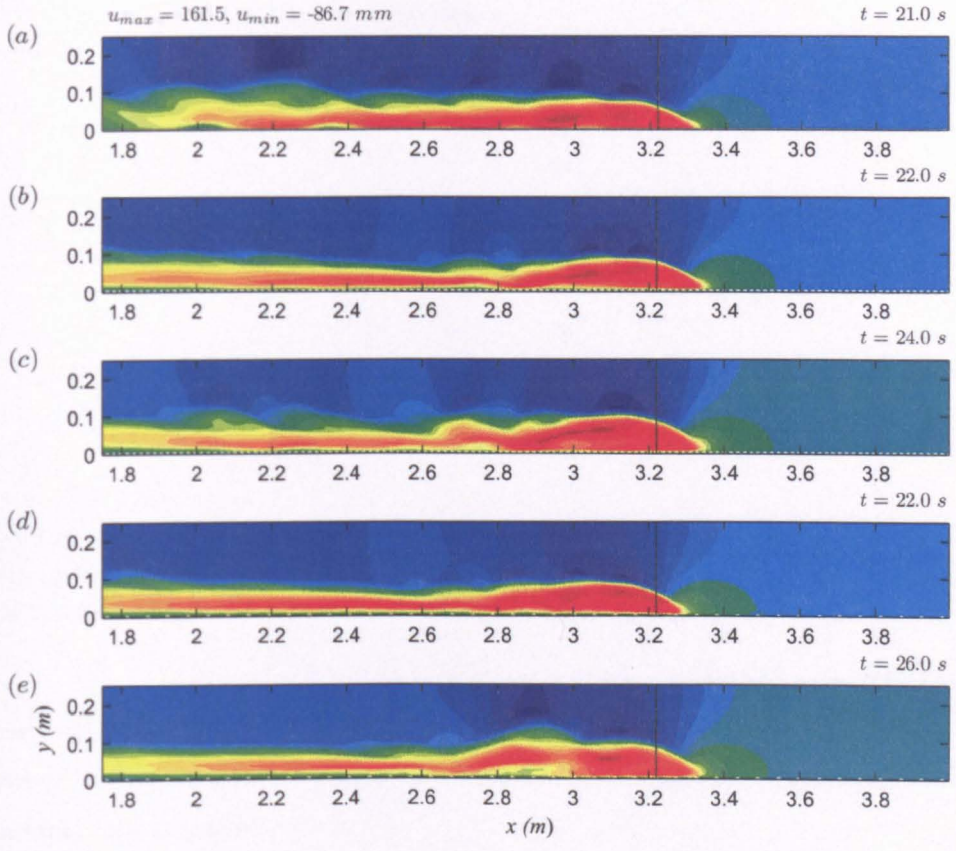

Figure 6.13: Horizontal velocity component, u, fields at the approximate time the head passes through 'bin 35' where the vertical profile data is read (shown as a line) resulting from the 3D simulation with (a) smooth bottom wall, and (b) beams$_{6,2}$ with dense fluid initialised between the elements, (c) beams$_{6,2}$, (d) beams$_{6,8}$ with dense fluid initialised between the elements and (e) beams$_{6,8}$. Red and blue are high and low velocities, respectively. Maximum and minimum values are displayed at the top of the figure.

observed that the smooth case still has high horizontal velocities distributed well into the body and tail of the current at this later time. It can be qualitatively observed that the velocity field in the body of the current is of approximately the same depth as the current head. However, in the rough cases, the region of high positive horizontal velocity appears to be deeper in the current head and significantly shallower in the current upstream of it, diffusing upwards to the interface with the ambient return flow. In this shallower tail region, the velocity is also slower, most of the high velocity being in the head itself and it extends back further upstream than in the smooth case, as observed in the 2D model.

In comparison to the 2D model, the lateral extension in the 3D simulations appear to enable more detail to be captured and thus greater clarity at these later times when much diffusion has occurred. In contrast to previous observations (figure 5.19), the vertical velocity fields for the rough bed cases display fluctuations behind the current

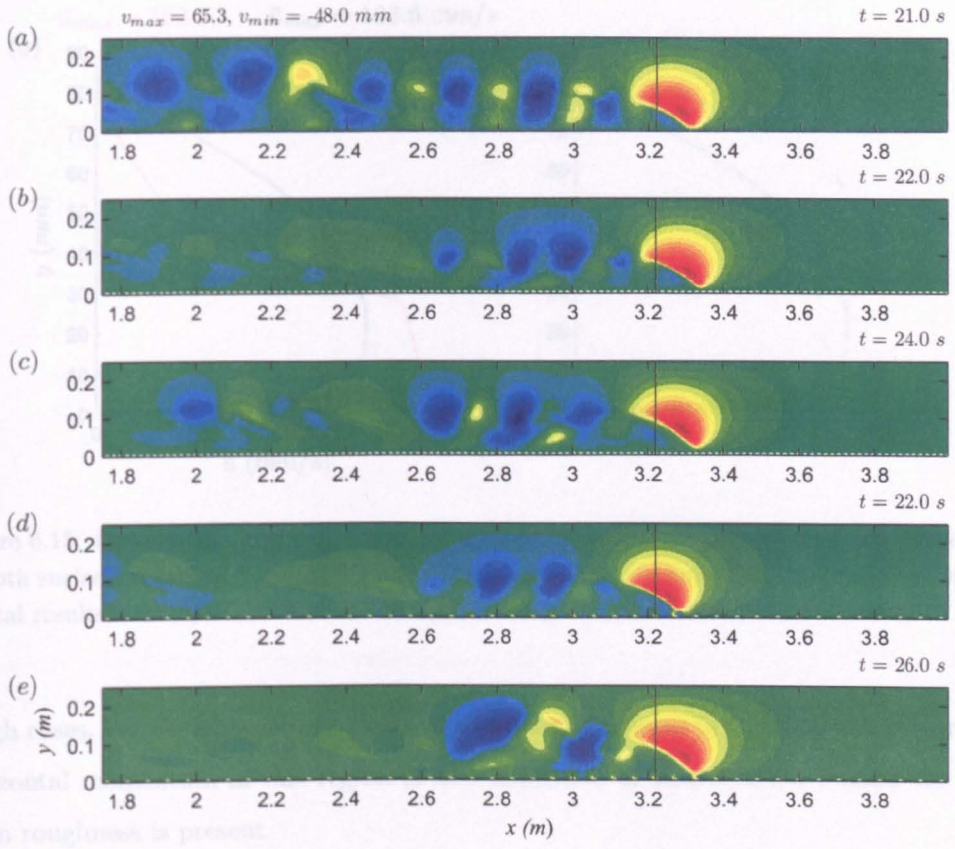

Figure 6.14: Vertical velocity component, v, fields at the approximate time the head passes through 'bin 35' where the vertical profile data is read (shown as a line) resulting from the 3D simulation with (a) smooth bottom wall, and (b) beams$_{6,2}$ with dense fluid initialised between the elements, (c) beams$_{6,2}$, (d) beams$_{6,8}$ with dense fluid initialised between the elements and (e) beams$_{6,8}$. Red and blue are high and low velocities, respectively. Maximum and minimum values are displayed at the top of the figure.

head that are characteristic of the presence of billows (figures 6.14 (b) – (e)). Thus implying that the 3D model has enabled the rough cases to retain more coherence in the billows, rather than increasing their dissipation. However, it is also possible that the lateral motion has activated other flow dynamics in the rough bed cases, for example, the lobe and cleft instability, that has increased the presence of the billows. These billows do not extend along the current length as they are observed to do in the smooth case (figure 6.14 (a)), and they are restricted to the region immediately behind the head of the current. This suggests that they are damped before they can propagate further upstream along the current body. Notice that this damping effect is also characteristic of the cases with dense fluid initialised between the roughness elements (figures 6.14 (b) and (d)) implying that this is a result of the presence of the roughness elements and not an effect of the ambient fluid trapped between them. The lack of vertical motion in the

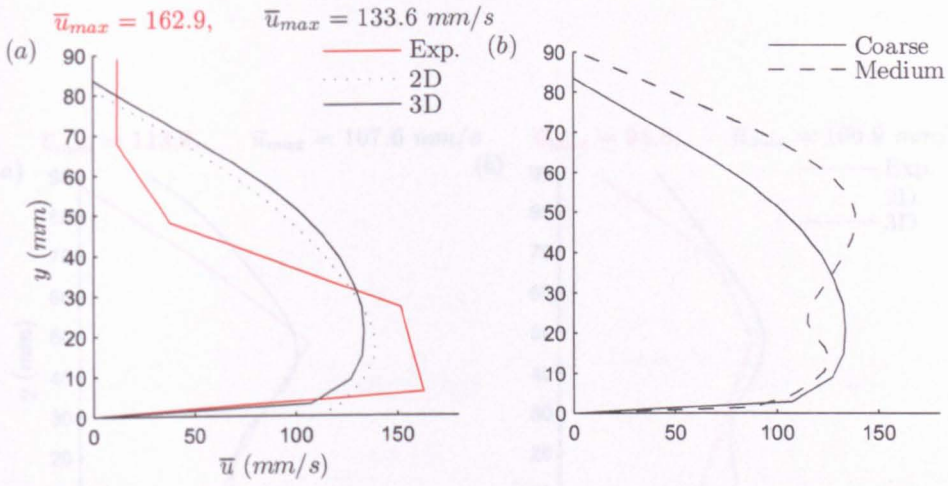

Figure 6.15: Downstream horizontal velocity, u, profiles within the current head for flow over a smooth surface, resulting from (a) 2D and 3D numerical simulations with the equivalent experimental results, and (b) 3D numerical simulations using the coarse and medium meshes.

rough cases, i.e. the absence of billows, upstream of the head in the tail, and the greater horizontal momentum in this region is also indicative of stratification behind the head when roughness is present.

Figure 6.15 (a) shows the vertical velocity profiles through the current depth at the location of bin 35 (3.22 m from the lock-box end of the tank) for the smooth bed. They show good agreement between the 2D and the 3D predictions but no better agreement with the experimental data. Figure 6.15 (b) shows the difference between the coarse and medium mesh. Once again it appears that violation of the wall functions has occurred and on calculation of an approximate y^+ value within the head at the bed for the coarse and medium meshes result in values of $y^+ \approx 22.6$ and $y^+ \approx 11.28$, respectively. Although these results do not indicate strict violation of y^+ in the medium mesh, the profile is irregular. Since the predicted front locations of both the coarse and the medium mesh show good agreement with the experimental data and in order to be consistent with the 2D case, the coarse mesh was again adopted.

The downstream horizontal velocity profiles through the flow depth at the bin are compared to the 2D models in figures 6.16 and 6.18 (a) and (b) for the rough beds with and without ambient fluid between the elements, respectively. For both the d-type and k-type beds bin 35 lies at the element top. However, as for the 2D model, inspection of the vertical profiles above, upstream and downstream of an element showed no distinguishable difference in the effects on the overflowing current which is used for validation with the experimental data.

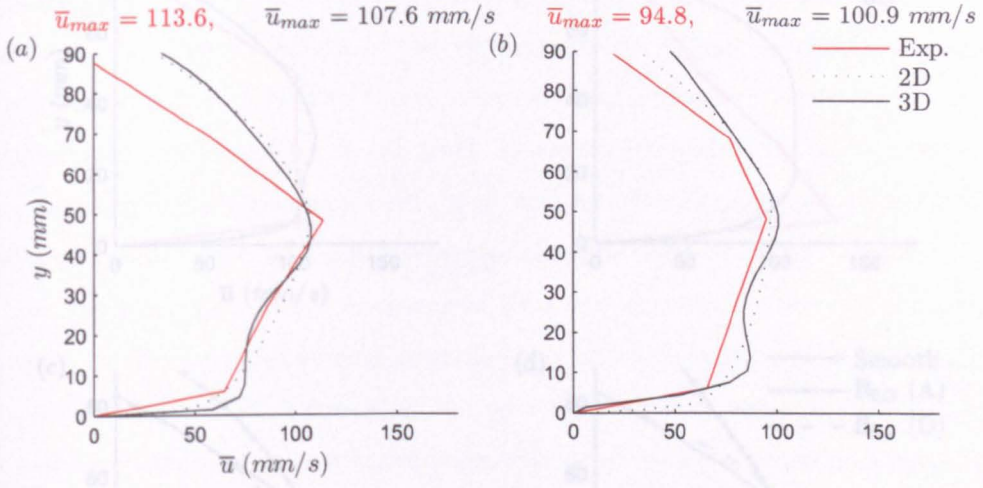

Figure 6.16: Downstream horizontal velocity, u, profiles within the current head resulting from 3D numerical simulations with the equivalent experimental results. Results for bottom boundaries with (a) beams$_{6,2}$, and (b) beams$_{6,8}$.

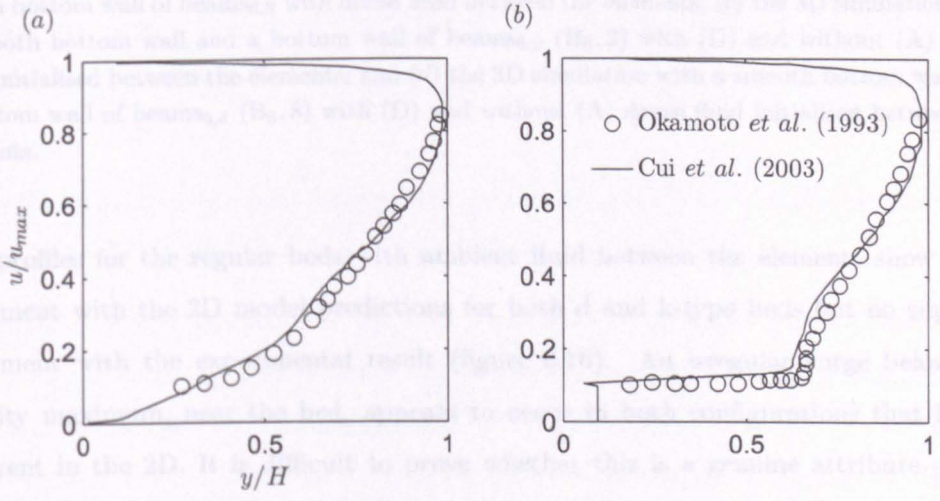

Figure 6.17: Velocity profiles for single phase pipe flow over a beam-roughened k-type bed, replotted from Cui *et al.* (2003b). (a) Above a cavity and (b) above a beam. The top boundary is subject to the no-slip condition.

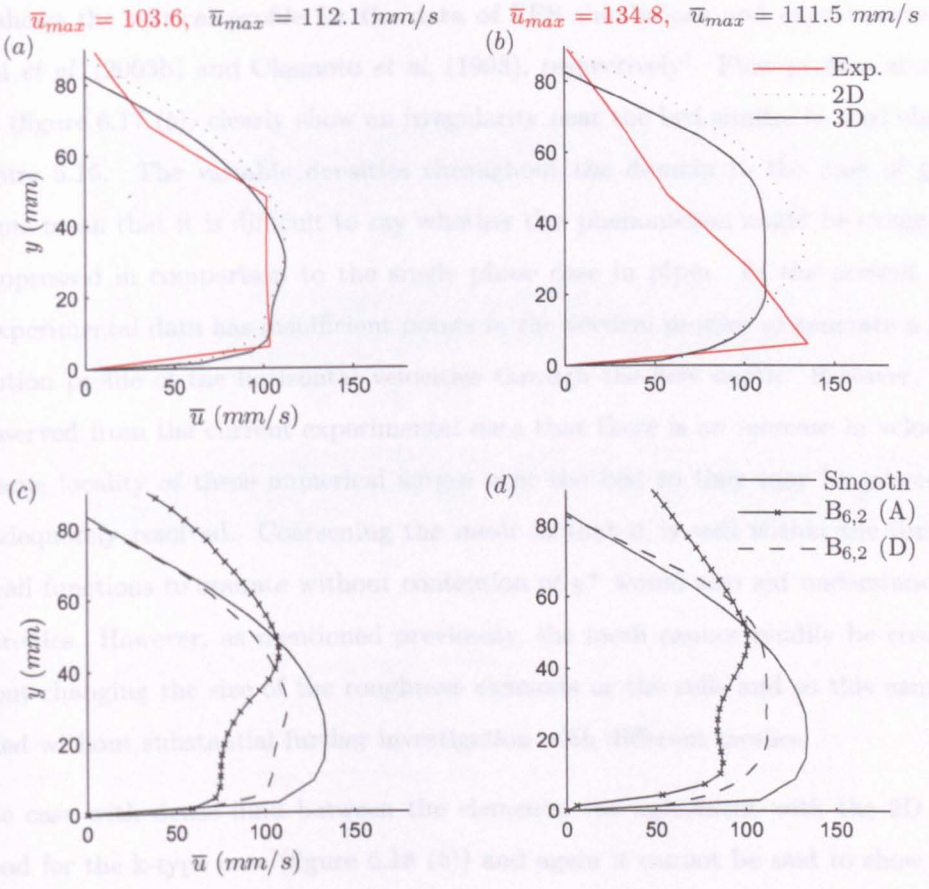

Figure 6.18: Downstream horizontal velocity, u, profiles within the head of the current resulting from (a) the 3D simulation and experimental equivalent with a bottom wall of beams$_{6,2}$ with dense fluid initialised between the elements; (b) the 3D simulation and experimental equivalent with a bottom wall of beams$_{6,8}$ with dense fluid between the elements; (c) the 3D simulation with a smooth bottom wall and a bottom wall of beams$_{6,2}$ ($B_6, 2$) with (D) and without (A) dense fluid initialised between the elements; and (d) the 3D simulation with a smooth bottom wall and a bottom wall of beams$_{6,8}$ ($B_6, 8$) with (D) and without (A) dense fluid initialised between the elements.

The profiles for the regular beds with ambient fluid between the elements show good agreement with the 2D model predictions for both d and k-type beds but no superior agreement with the experimental result (figure 6.16). An irregular surge below the velocity maximum, near the bed, appears to occur in both configurations that is not apparent in the 2D. It is difficult to prove whether this is a genuine attribute of the velocity distribution over rough beds or a violation of y^+, as occurred in the smooth model. If example y^+ values are calculated for these beds, results of 10.5 and 12.5 are obtained for d-type and k-type configurations, respectively. Although these values indicate potential violation of the wall functions, it has been observed in pipe flow studies that irregular features in the vertical flow profiles, such as this, can be physical. Figure

6.17 shows the vertical profile for the data of LES simulations and experimental data of Cui *et al.* (2003b) and Okamoto *et al.* (1993), respectively†. Flow profiles above the beam (figure 6.17 (*b*)) clearly show an irregularity near the bed similar to that observed in figure 6.16. The variable densities throughout the domain in the case of gravity currents mean that it is difficult to say whether this phenomenon might be exaggerated or suppressed in comparison to the single phase case in pipes. In the present study, the experimental data has insufficient points in the vertical profiles to generate a higher resolution profile of the horizontal velocities through the flow depth. However, it can be observed from the current experimental data that there is an increase in velocity in the same locality of these numerical surges near the bed so they may be present but not adequately resolved. Coarsening the mesh so that it is well within the limits for the wall functions to operate without contention of y^+ would also aid understanding of the profiles. However, as mentioned previously, the mesh cannot readily be coarsened without changing the size of the roughness elements or the cells and so this cannot be checked without substantial further investigation with different meshes.

In the case with dense fluid between the elements, the agreement with the 2D is not as good for the k-type case (figure 6.18 (*b*)) and again it cannot be said to show better agreement with the experimental equivalents. Figures 6.18 (*c*) and (*d*) confirm that, as for the 2D model (figures 5.20 (*c*) and (*d*)), the cases where dense fluid has been initialised between the elements have profiles that appear to represent a compromise between the smooth and the regularly rough cases. Notice that the surge at the bed is not as distinct in these cases.

The effects on the laterally averaged horizontal and vertical velocity structure of the law-of-the-wall method for specifying the bed roughness

The horizontal and vertical velocity fields after 9 s for the law-of-the-wall method of specifying bed roughness are shown in figures 6.19 (*b*) and 6.20 (*b*). Comparison with the smooth case and the body-fitted equivalents ((*a*) and (*c*) respectively in figures 6.19 and 6.20) confirms the 2D observations that the internal dynamics remain almost identical to the smooth case. At the later time when the current head passes through the bin (figures 6.21 (*b*) and 6.22 (*b*)), slight differences can be observed, the horizontal velocities are distributed differently in the tail region and penetrate higher into the domain depth. There are also regions of lower velocity near the bed, not observed in the smooth case.

† The data of Cui *et al.* (2003b) and Okamoto *et al.* (1993) have been replotted with the axes exchanged in the present study so that it is directly comparable to the vertical profiles displayed herein.

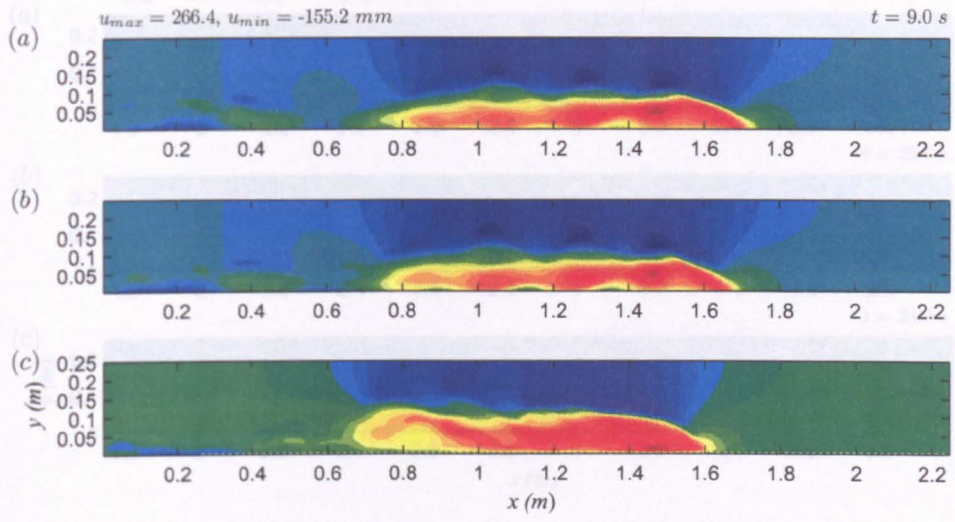

Figure 6.19: Horizontal velocity component, u, fields at $t = 9$ s resulting from the 3D simulation with (a) smooth bottom wall, and with (b) a k_s value on the bottom wall ($k_s = 0.0015$) which is the approximately equivalent value of (c) beams$_{6,2}$. Red and blue are high and low velocities, respectively. Maximum and minimum values are displayed at the top of the figure.

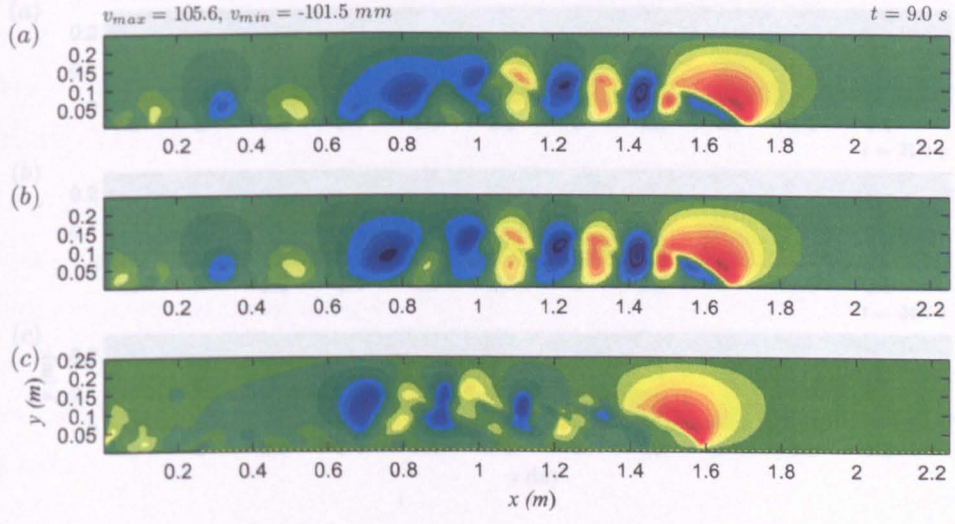

Figure 6.20: Vertical velocity component, v, fields at $t = 9$ s resulting from the 3D simulation with (a) smooth bottom wall, and with (b) a k_s value on the bottom wall ($k_s = 0.0015$) which is the approximately equivalent value of (c) beams$_{6,2}$. Red and blue are high and low velocities, respectively. Maximum and minimum values are displayed at the top of the figure.

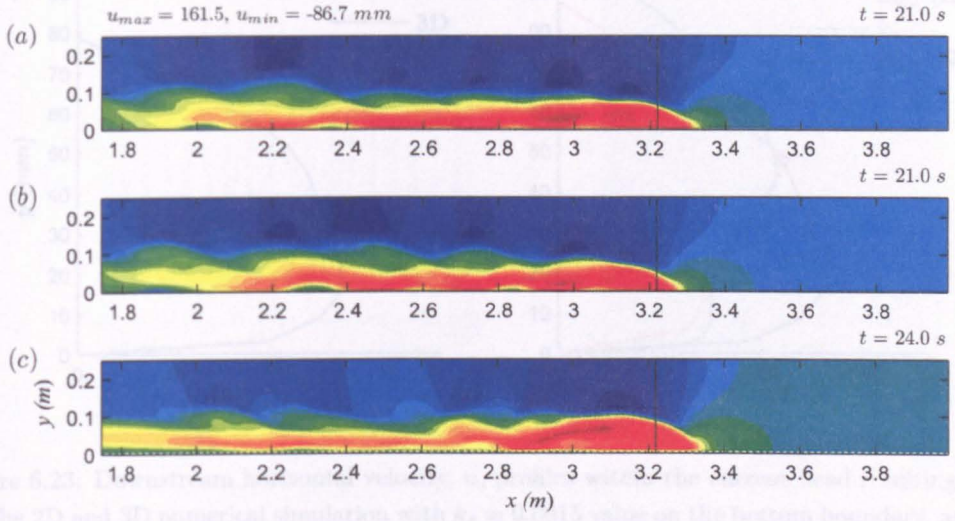

Figure 6.21: Horizontal velocity component, u, fields at the approximate time the head passes through 'bin 35' where the vertical profile data is read (shown as a line) resulting from the 3D simulation with (a) smooth bottom wall, and with (b) a k_s value on the bottom wall ($k_s = 0.0015$) which is the approximately equivalent value of (c) beams$_{6,2}$. Red and blue are high and low velocities, respectively. Maximum and minimum values are displayed at the top of the figure.

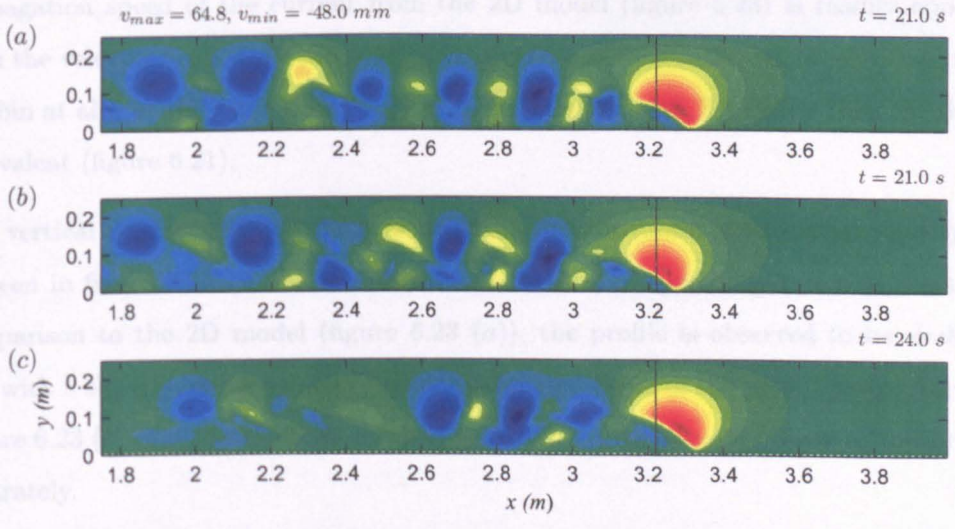

Figure 6.22: Vertical velocity component, v, fields at the approximate time the head passes through 'bin 35' where the vertical profile data is read (shown as a line) resulting from the 3D simulation with (a) smooth bottom wall, and with (b) a k_s value on the bottom wall ($k_s = 0.0015$) which is the approximately equivalent value of (c) beams$_{6,2}$. Red and blue are high and low velocities, respectively. Maximum and minimum values are displayed at the top of the figure.

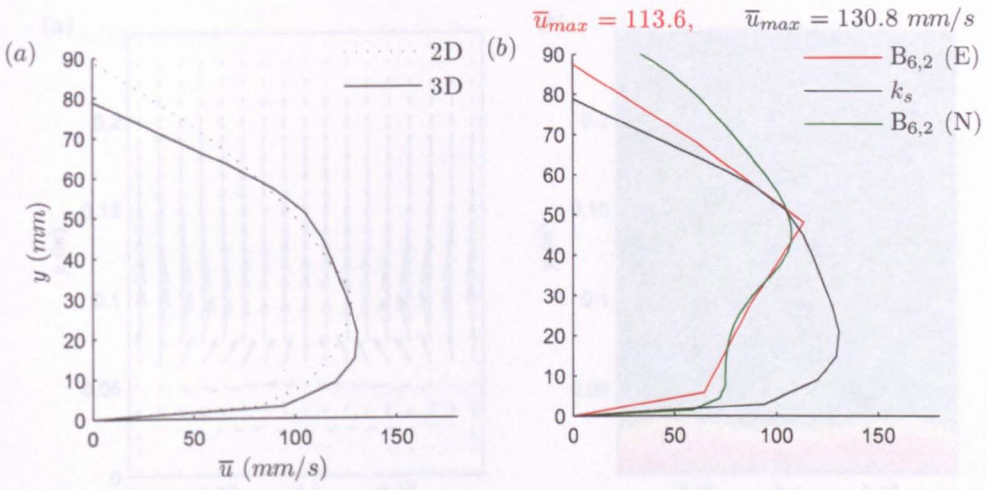

Figure 6.23: Downstream horizontal velocity, u, profiles within the current head resulting from (a) the 2D and 3D numerical simulation with $k_s = 0.0015$ value on the bottom boundary, and (b) the numerical simulation (N) and equivalent experimental (E) result for the rough case with the beams$_{6,2}$ and for the 3D simulation with the approximately equivalent $k_s = 0.0015$ value on the bottom wall. Red and blue are high and low velocities, respectively. Maximum and minimum values are displayed at the top of the figure.

The vertical velocities also show some difference in distribution of the fluctuations at the interface at this later time compared to the smooth case. However, they do not display similar characteristics to the numerical beams$_{6,2}$ equivalent. The difference in propagation speed of the current from the 2D model (figure 5.23) is readily apparent from the velocity fields since the head of the current in the k_s case is now shown to reach the bin at almost the same time ($\approx$ 21 s) as the smooth case, 3 s earlier than the d-type equivalent (figure 6.21).

The vertical profiles through the flow depth of the horizontal downstream velocity can be seen in figure 6.23 for the law-of-the-wall method of specifying bed roughness. On comparison to the 2D model (figure 6.23 (a)), the profile is observed to be shallower and with a slightly higher velocity maximum located lower in the profile, nearer the bed. Figure 6.23 (b) confirms that this method is unable to reproduce the vertical flow profiles accurately.

6.5.3 Lateral velocity structure

Slices through the domain of cross-stream vectors of lateral and vertical velocity can be seen for the smooth case in figure 6.24. Figures 6.25 and 6.26 display equivalent figures for the d-type case with and without ambient fluid between the roughness elements and

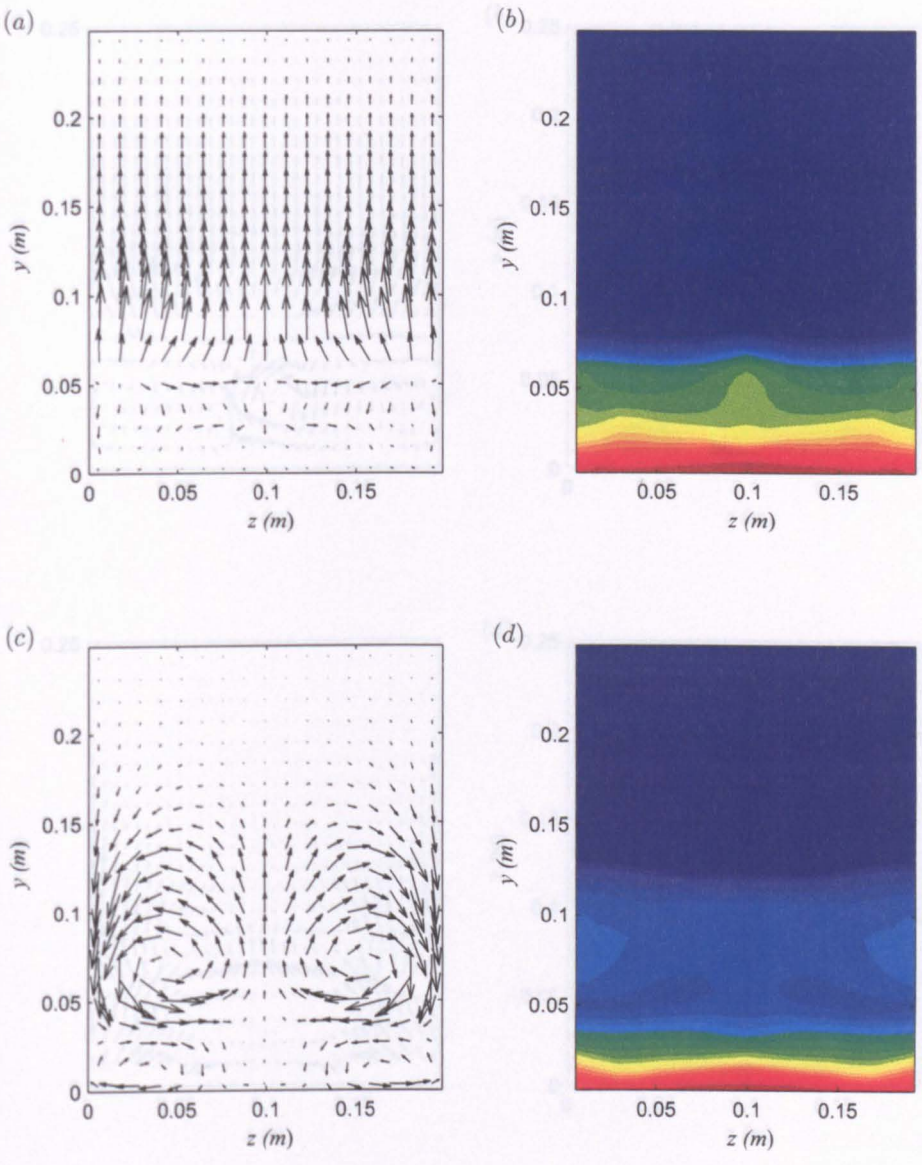

Figure 6.24: Lateral slices of the tank depth for the smooth bottom boundary. (*a*) Velocity magnitude vectors of vertical and lateral velocity components at 'bin 35', and (*b*) lateral concentration field at this location for reference. (*c*) Equivalent vectors upstream at 2.52 m, and (*d*) concentration field at this location. Red and blue are high and low concentration, respectively. Downstream motion is towards the reader.

figures 6.27 and 6.28 are an analogous set for the k-type bed. In all five of these figures, (*a*) and (*b*) are slices corresponding to the velocity and concentration data, respectively, at the bin location at the approximate time the current head passes through (vertical lines shown on the laterally averaged flow field data) and (*c*) and (*d*) correspond to a location upstream at 2.52 m in the current body at the same time. Thus, motion in the head and body of the current can be compared.

In the current head over a smooth bed, figure 6.24 (*a*) shows that vertical motion is

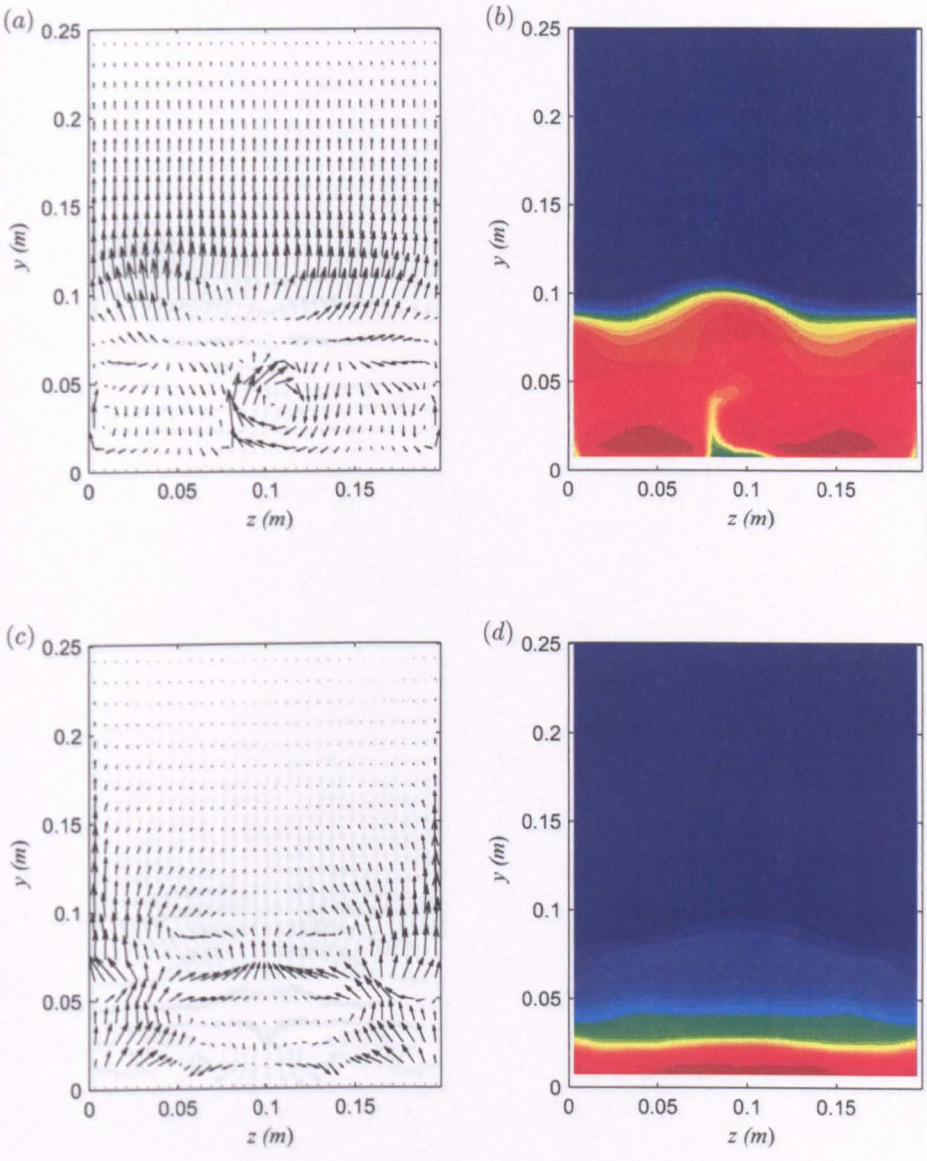

Figure 6.25: Lateral slices of the tank depth for the bottom boundary with beams$_{6,2}$. (*a*) Velocity magnitude vectors of vertical and lateral velocity components at 'bin 35', and (*b*) lateral concentration field at this location for reference. (*c*) Equivalent vectors upstream at 2.52 m, and (*d*) concentration field at this location. Red and blue are high and low concentration, respectively. Downstream motion is towards the reader.

significantly stronger than lateral motion. This is primarily observed in the positive vertical flow of the ambient fluid as it is forced above the forward propagating current. There is very little lateral motion in this overlying region. However, at the interface between the ambient and the current and within the current head, some lateral motion is apparent. This motion appears symmetrical about the centreplane, indicating the possible presence of a cleft and hence lobes at the front. Further back in the tail, the lateral motion is much stronger (figure 6.24 (*c*)) at the density interface where the diffuse

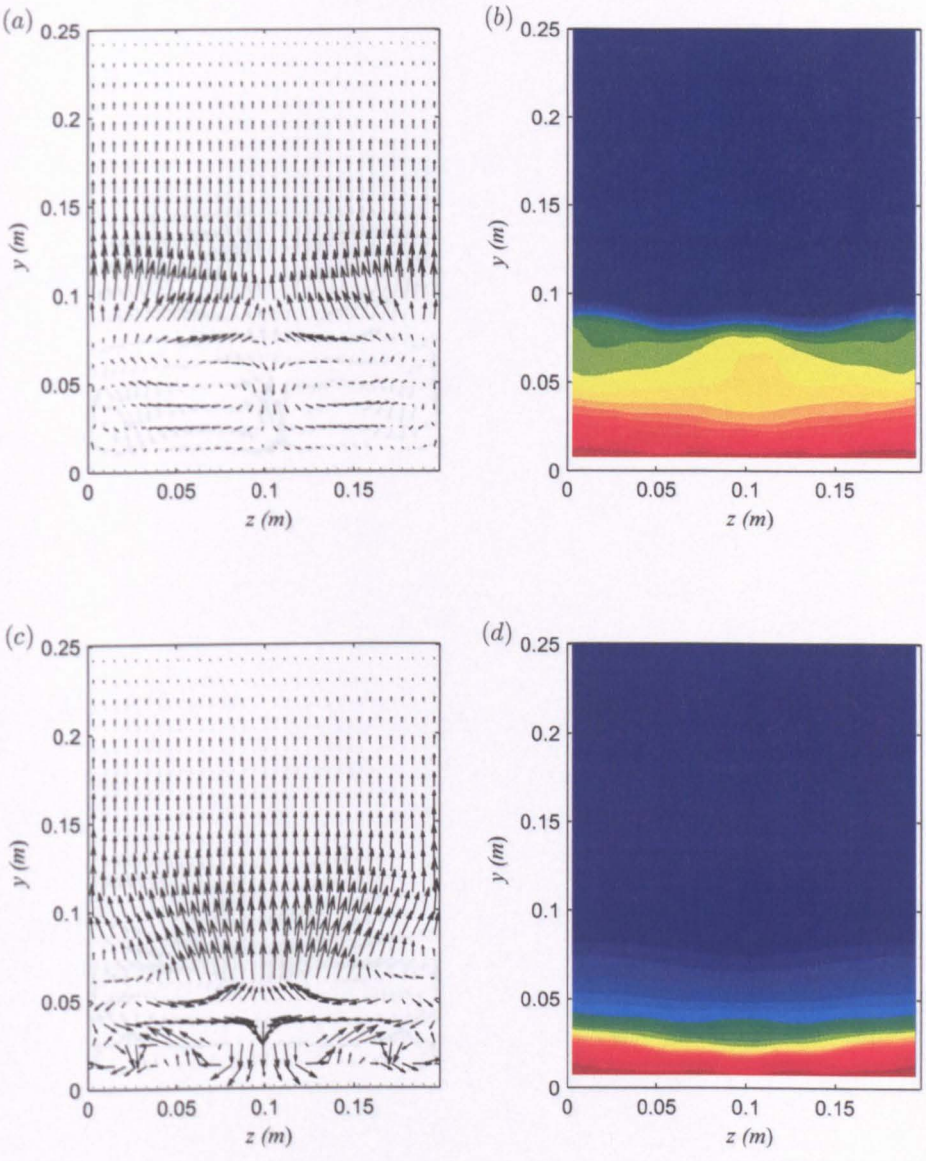

Figure 6.26: Lateral slices of the tank depth for the bottom boundary with beams$_{6,2}$ and dense fluid initialised between the elements. (*a*) Velocity magnitude vectors of vertical and lateral velocity components at 'bin 35', and (*b*) lateral concentration field at this location for reference. (*c*) Equivalent vectors upstream at 2.52 m, and (*d*) concentration field at this location. Red and blue are high and low concentration, respectively. Downstream motion is towards the reader.

billows are present. Thus the present study agrees with other investigators that there is significant enough lateral motion in the billows to require a 3D model to accurately simulate their dynamics. The lower two rotating cells that can be observed below the large rotors of the billows agree qualitatively with the simulations of Imran *et al.* (2004)[‡]

[‡]It is interesting to note that, to the author's knowledge, there is very little existing experimental or numerical data on the lateral motion within a gravity current in a channel. In the numerical studies, of which there are an increasing amount, only Cantero *et al.* (2003, 2007b), Imran *et al.* (2004) and Corney *et al.* (2006) present images and discussion of this component.

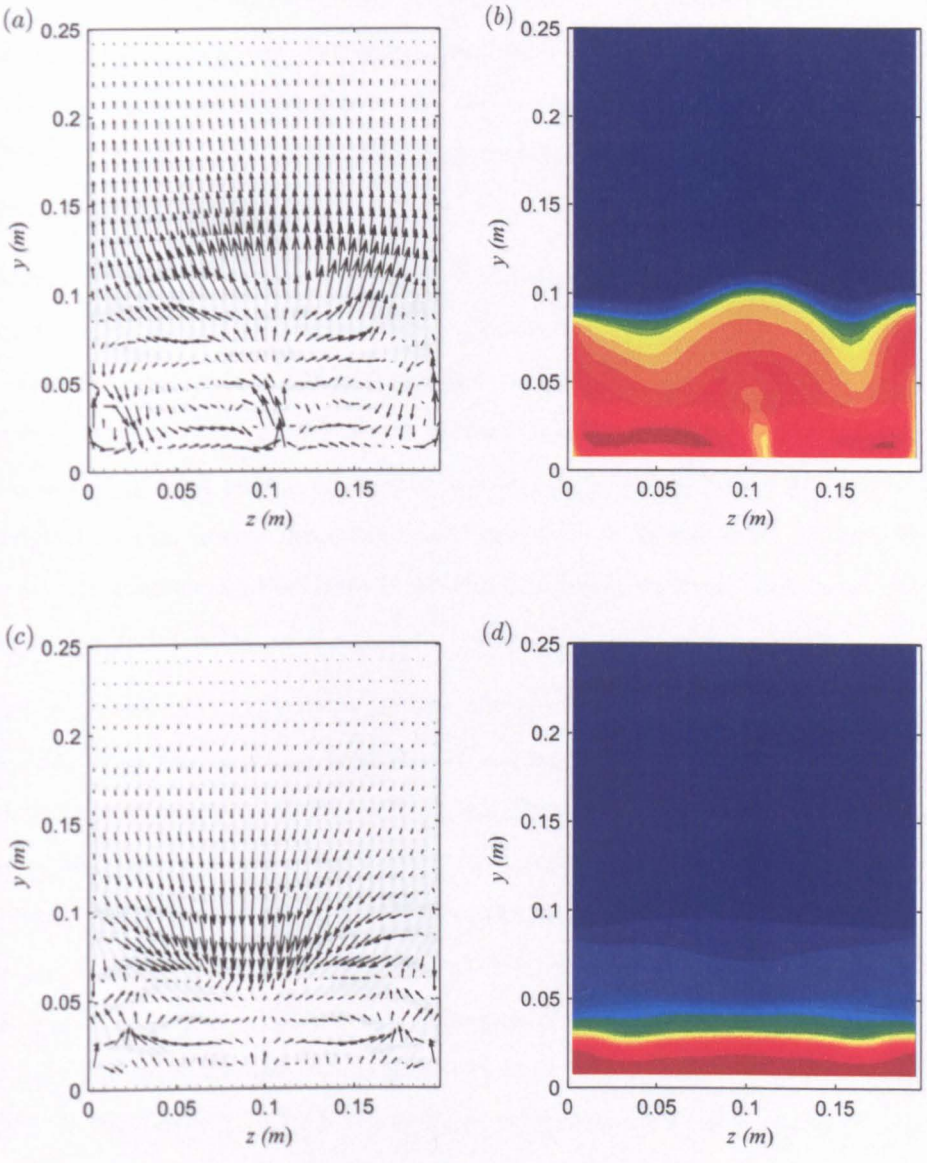

Figure 6.27: Lateral slices of the tank depth for the bottom boundary with $\text{beams}_{6,8}$. (*a*) Velocity magnitude vectors of vertical and lateral velocity components at 'bin 35', and (*b*) lateral concentration field at this location for reference. (*c*) Equivalent vectors upstream at 2.52 m, and (*d*) concentration field at this location. Red and blue are high and low concentration, respectively. Downstream motion is towards the reader.

for flow in a confined channel. Although it should be noted that in that study the current is pumped to steady state and there is no other motion apparent at the interface.

At the head in all of the rough cases strong upward motion in the ambient fluid can still be observed (figures 6.25-6.28 (*a*) and (*b*)). Above the body of the current the strong lateral motion observed in the smooth case is not apparent in the rough cases (compare figures 6.24 (*c*) and (*d*) with figures 6.25-6.28 (*c*) and (*d*)) indicating that the large interfacial billows are not present. Instead, there is strong positive or negative vertical

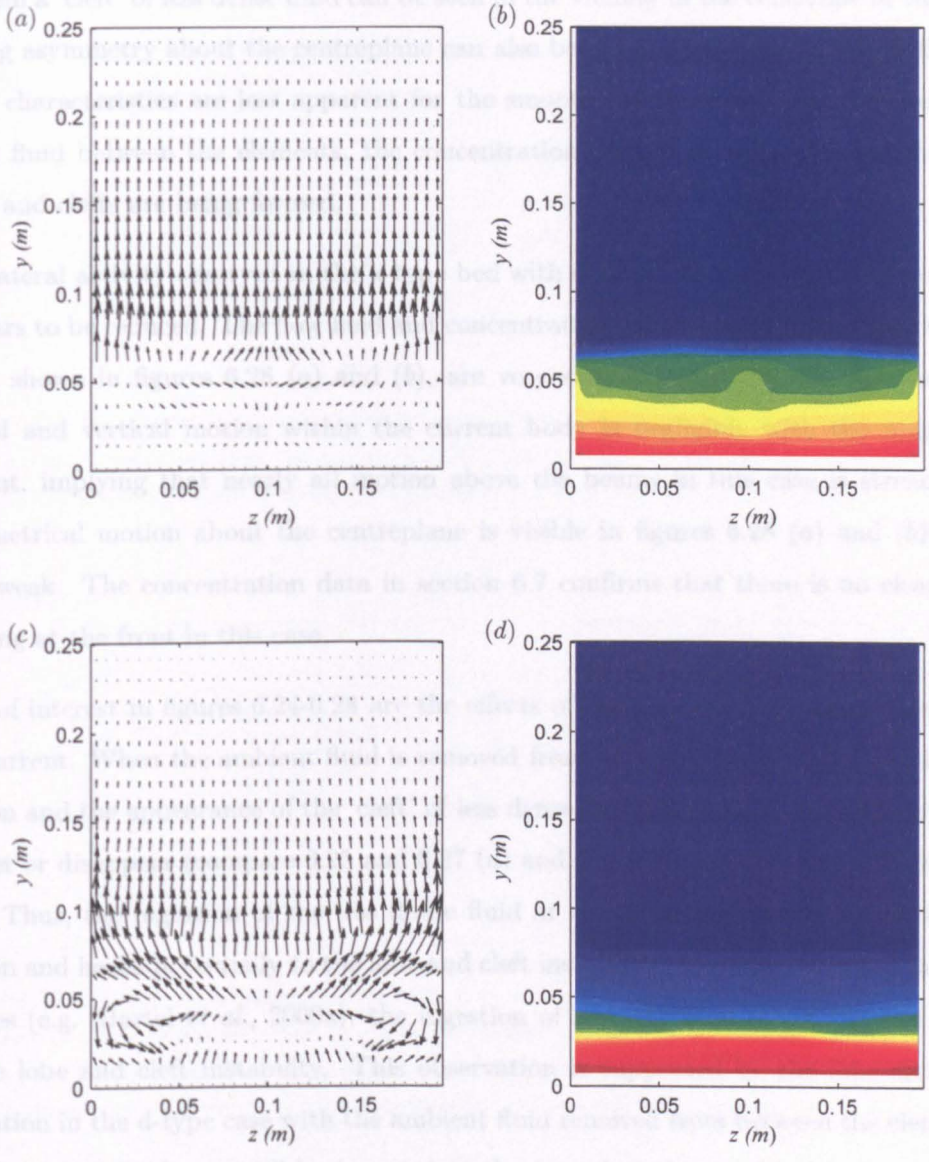

Figure 6.28: Lateral slices of the tank depth for the bottom boundary with beams$_{6,8}$ and dense fluid initialised between the elements. (a) Velocity magnitude vectors of vertical and lateral velocity components at 'bin 35', and (b) lateral concentration field at this location for reference. (c) Equivalent vectors upstream at 2.52 m, and (d) concentration field at this location. Red and blue are high and low concentration, respectively. Downstream motion is towards the reader.

motion above the density interface suggesting the presence of undulations affecting the ambient return flow in this region. Although, the regular d-type case with ambient fluid between the elements shows a different distribution of this motion.

Within the head of the current, figures 6.24-6.27 (a) show distinct lateral motion near the centreline. As mentioned above, this suggests the presence of a cleft and thus lobe and cleft formation at the front. In the d-type and k-type cases with ambient fluid between the elements, this observation is supported by figures 6.25 (b) and 6.27 (b), respectively,

wherein a 'cleft' of less dense fluid can be seen in the vicinity of the centreline at the bed. Strong asymmetry about the centreplane can also be observed in these cases. Although these characteristics are less apparent for the smooth case and the beams$_{6,2}$ bed with dense fluid between the elements, the concentration data in section 6.7 confirms that lobes and clefts are being formed.

The lateral activity observed in the k-type bed with dense fluid in the gaps (figure 6.28) appears to be reduced. The flow field and concentration distributions within the current head, shown in figures 6.28 (*a*) and (*b*), are very similar to the smooth case but the lateral and vertical motion within the current body is negligible with the roughness present, implying that nearly all motion above the beams in this case is streamwise. Symmetrical motion about the centreplane is visible in figures 6.28 (*a*) and (*b*)but is very weak. The concentration data in section 6.7 confirms that there is no clear cleft forming at the front in this case.

Also of interest in figures 6.24-6.28 are the effects of the ambient fluid interaction with the current. When the ambient fluid is removed from between the elements, the lateral motion and the appearance of the 'cleft' of less dense concentration at the bed are much weaker or disappear (compare 6.25 and 6.27 (*a*) and (*b*) to figures 6.26 and 6.28 (*a*) and (*b*)). Thus, the ingestion of the less dense fluid at the front contributes to the lateral motion and hence potentially to the lobe and cleft instability. However, as noted in other studies (e.g. Hartel *et al.*, 2000a), the ingestion of ambient fluid is not the sole cause of the lobe and cleft instability. This observation is supported by the lobe and cleft formation in the d-type case with the ambient fluid removed from between the elements. Some ambient fluid may still be ingested at the front but this would also occur in the k-type case which at the times shown has not formed a cleft. It is more likely that the lobes and clefts are augmented by the surface friction that is still present in the d-type case due to the density of the roughness elements. In the k-type equivalent case, this surface friction is decreased due to the sparsity of the elements and at the cavities the current is 'cushioned' by the dense fluid providing a frictionless surface.

Plan view slices laterally through the tank can be seen for the smooth bed and the body-fitted rough beds in figures 6.29-6.33. In the rough cases, the slices move from the bed (*a*) to immediately beneath the crest of the roughness elements (*b*). In the smooth case, figure 6.29 (*a*) is also wall-adjacent. However, due to the lower vertical resolution in this case, the data in the next slice, figure 6.29 (*b*), corresponds to a location above the height of the elements. The gravity current front can be identified approximately in

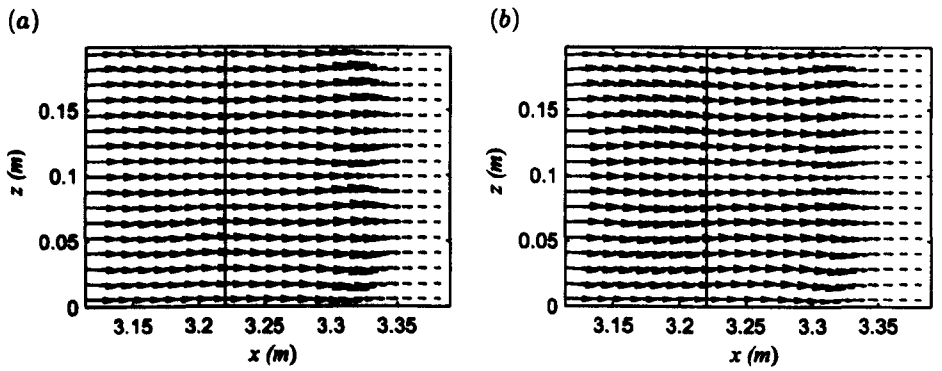

Figure 6.29: Plan view of velocity magnitude vectors of downstream horizontal and lateral velocity components in the first two layers of cells above the bed in the vicinity of 'bin 35' (solid line) for the smooth bottom boundary. (*a*) Nearest the bed and (*b*) the layer above.

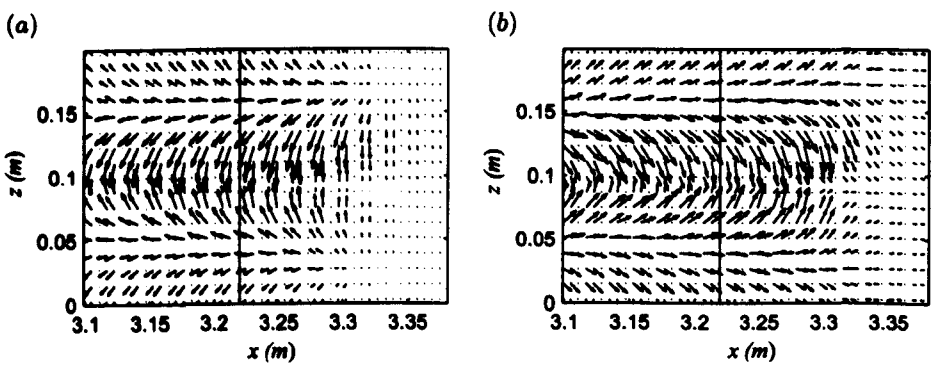

Figure 6.30: Plan view of velocity magnitude vectors of downstream horizontal and lateral velocity components in the first four layers of cells above the bed in the vicinity of 'bin 35' (solid line) for the bottom boundary with beams$_{6,2}$. (*a*) Nearest the bed and (*b*) beneath the crest of the roughness elements which can be identified by parallel regions of still motion.

the figures by the region beyond which motion is significantly reduced.

In the rough cases with ambient fluid initialised in the cavities between the elements (figures 6.30 and 6.32) significant lateral motion can be observed between the elements and in the overflowing current where the 'cleft' was shown to be forming (figures 6.25 and 6.27 (*a*)). The flow field in both cases is asymmetrical. For the d-type bed, negative, upstream motion near the bed (figure 6.30 (*a*)) and the positive downstream motion in the plane above (figure 6.30 (*b*)) indicate the presence of vortices filling the gaps between the elements. For the k-type bed, figure 6.32 (*a*) shows a recirculating region at the downstream face of the elements and a stagnation region (for these lateral and downstream velocity components) where the fluid that separated at the top of the upstream element reattaches at the bed. These dynamics are also present in the cases with dense fluid between the elements but with comparatively minimal effects on the overflowing

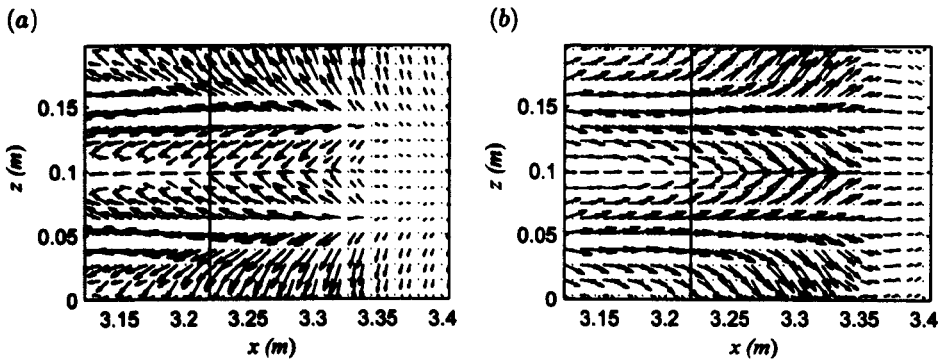

Figure 6.31: Plan view of velocity magnitude vectors of downstream horizontal and lateral velocity components in the first four layers of cells above the bed in the vicinity of 'bin 35' (solid line) for the bottom boundary with beams$_{6,2}$ and dense fluid initialised between the elements. (*a*) Nearest the bed and (*b*) beneath the crest of the roughness elements which can be identified by parallel regions of still motion.

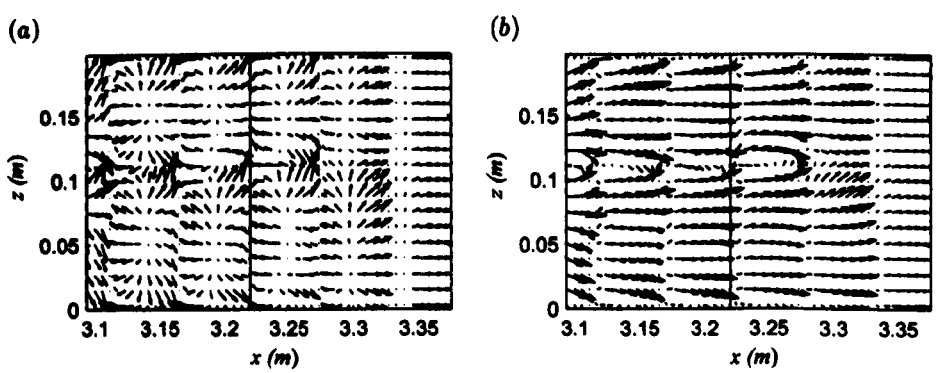

Figure 6.32: Plan view of velocity magnitude vectors of downstream horizontal and lateral velocity components in the first four layers of cells above the bed in the vicinity of 'bin 35' (solid line) for the bottom boundary with beams$_{6,8}$. (*a*) Nearest the bed and (*b*) beneath the crest of the roughness elements which can be identified by parallel regions of still motion.

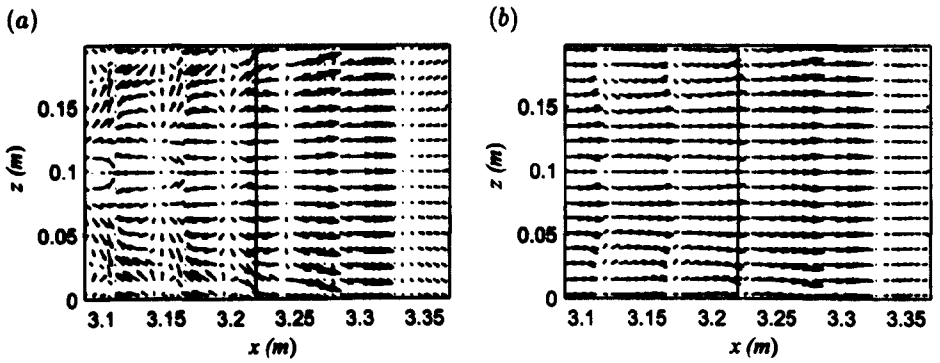

Figure 6.33: Plan view of velocity magnitude vectors of downstream horizontal and lateral velocity components in the first four layers of cells above the bed in the vicinity of 'bin 35' (solid line) for the bottom boundary with $beams_{6,8}$ and dense fluid initialised between the elements. (*a*) Nearest the bed and (*b*) beneath the crest of the roughness elements which can be identified by parallel regions of still motion.

current. Again, increased lateral motion in the cases with ambient fluid between the elements is confirmed.

In the smooth case, the downstream velocity is substantially higher than the cross-stream motion. Combined with figure 6.24 this implies that within the head of a current flowing over a smooth bed lateral motion is weak relative to vertical and downstream components and therefore a 2D model could achieve a good degree of accuracy. It is the billows behind the head in this case that require 3D mechanisms. This also holds true for the k-type bed with dense fluid between the elements. Even the trapped rotating vortices between the elements are primarily 2D in this case (figure 6.33 (*a*) and (*b*)). Moreover, the lack of lateral motion higher in the flow above the current body (figure 6.28) implies that the majority of the flow dynamics within the current with this bed configuration are 2D. Although, the front speeds have been shown to be susceptible to 2D limitations, requiring the loss of energy provided in the 3D model.

6.6 Turbulence structure

The effects on the turbulence structure of the d-type and k-type bed roughness configurations with and without ambient fluid between the elements

The turbulence kinetic energy fields after 9 s for all of the beds investigated, except the law-of-the-wall method, are shown in figure 6.34. No significant difference can be observed between the laterally averaged 3D prediction and the 2D model for the smooth bed case (figure 5.30). In all of the rough cases there is increased TKE in the current

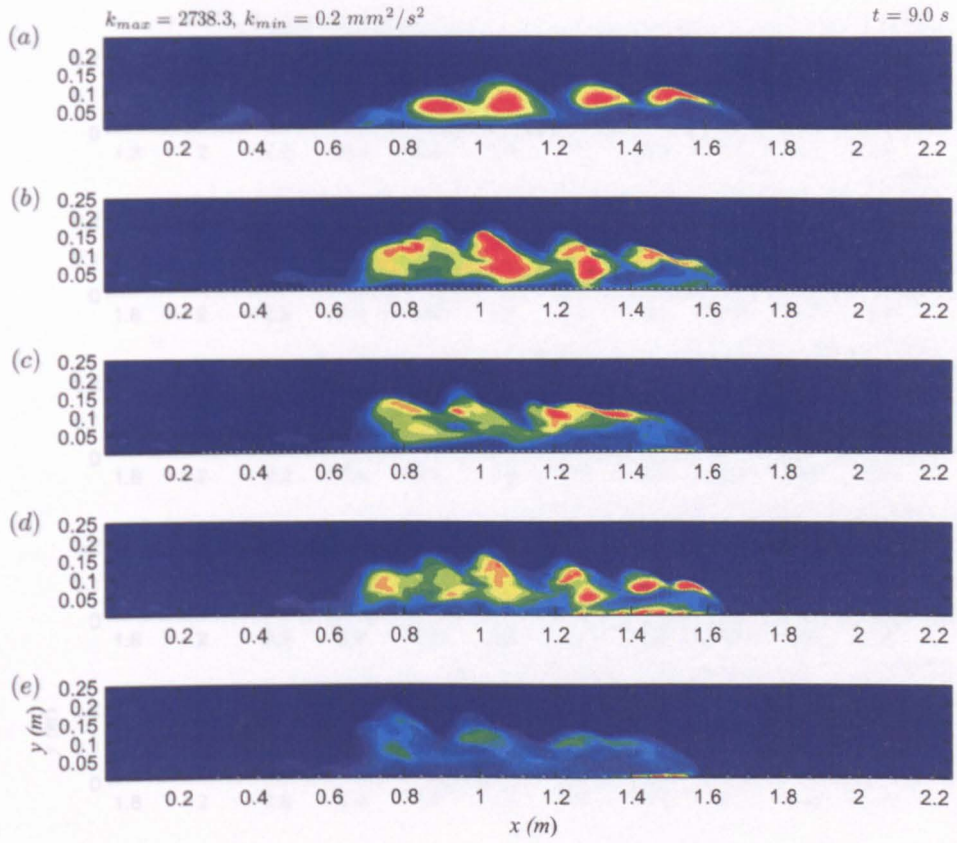

Figure 6.34: Turbulence kinetic energy, k, fields at $t = 9\ s$ resulting from the 3D simulation with (a) smooth bottom wall, and bottom walls with (a) smooth bottom wall and (b) $beams_{6,2}$ with dense fluid initialised between the elements, (c) $beams_{6,2}$, (d) $beams_{6,8}$ with dense fluid initialised between the elements and (e) $beams_{6,8}$. Red and blue are high and low TKE, respectively. Maximum and minimum values are displayed at the top of the figure.

body except the k-type case with dense fluid between the elements (figure 6.34 (e)). In the head of the current, compared to the 2D model, converse magnitudes can be observed. The cases with ambient fluid in the cavities (figures 6.34 (c) and (e)) have reduced levels of TKE in the head while the cases with dense fluid therein show increased TKE (figures 6.34 (b) and (d)).

The striking prediction shown in figure 6.34 (e) is that, even after 9 s, the TKE within the current flowing over the regular k-type bed is substantially less than observed in the 2D version (figure 5.30 (e)). Although high pockets of TKE can still be seen in the locality of the roughness elements beneath the head. Again this highlights the necessity of resolving 3D mechanisms in this case. In the 2D d-type case, high TKE was observed in the current head. The 3D equivalent (figure 6.34 (c)) predicts reduced TKE in the head above the elements but regions of high TKE localised around the elements as in the k-type case. This is likely to be a result of the improved resolution of skin friction

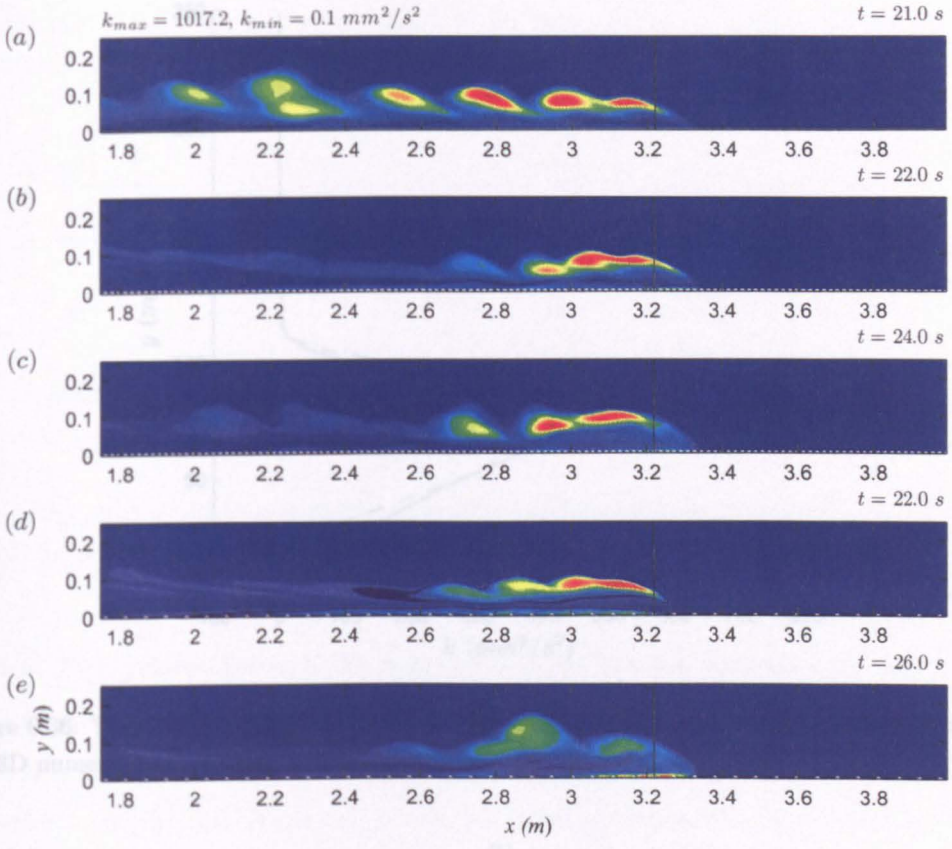

Figure 6.35: Turbulence kinetic energy, k, fields at the approximate time the head passes through 'bin 35' where the vertical profile data is read (shown as a line) resulting from the 3D simulation with (a) smooth bottom wall, and (b) beams$_{6,2}$ with dense fluid initialised between the elements, (c) beams$_{6,2}$, (d) beams$_{6,8}$ with dense fluid initialised between the elements and (e) beams$_{6,8}$. Red and blue are high and low TKE, respectively. Maximum and minimum values are displayed at the top of the figure.

effects in 3D.

At later times, the 2D and 3D models for the smooth case (figures 5.31 and 6.35 (a), respectively) show additional differences but the distribution of TKE is still maintained within the billows at the density interface. For the rough cases, the elongated region of TKE at the density interface, behind the head, observed in the 2D case is much less extensive in 3D (figures 6.35 (b) – (e)) and differentiation between d-type and k-type, using the magnitude of this upstream elongation that was suggested from the 2D model predictions, is no longer relevant. However, the general qualitative agreement between the 2D and 3D models at the later times is reasonably good.

The smaller region of high TKE behind the head observed in the 3D models corresponds to the location of the billows at this later time, as predicted by the downstream horizontal and vertical velocity fields in section 6.5.2. The 2D and 3D models agree that the high

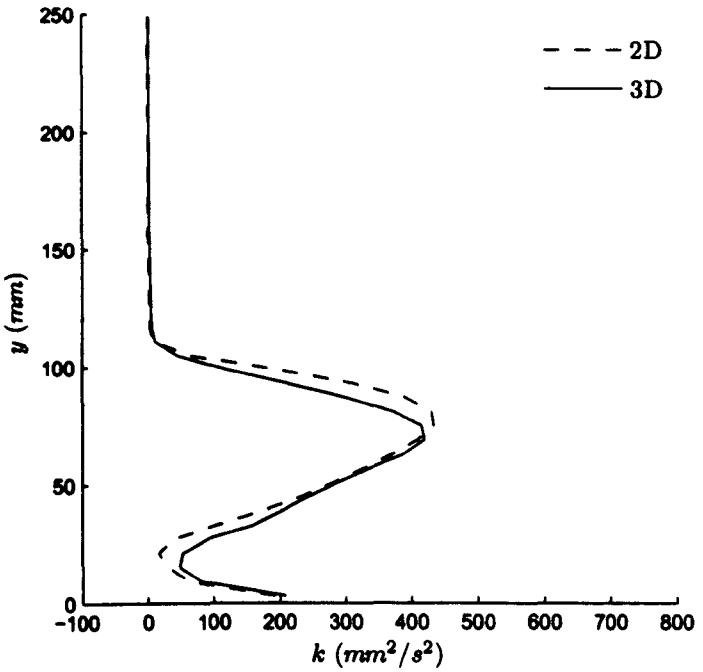

Figure 6.36: Turbulence kinetic energy, k, profiles for the total domain depth resulting from 2D and 3D numerical simulations with a smooth bottom wall.

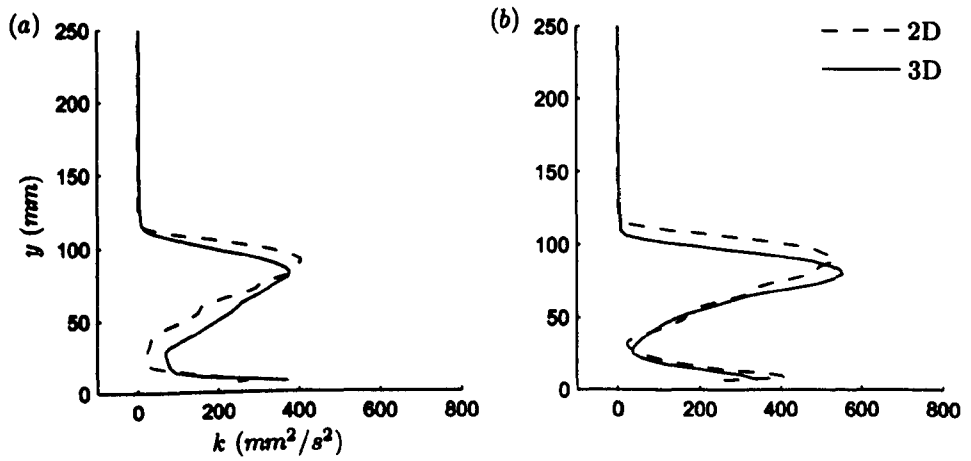

Figure 6.37: Turbulence kinetic energy, k, profiles for the total domain depth resulting from 2D and 3D numerical simulations for bottom walls with (a) $\text{beams}_{6,2}$, and (b) $\text{beams}_{6.8}$ with dense fluid initialised between the elements.

TKE observed in the head near the bed at early times has reduced significantly in both d-type cases and the k-type case with dense fluid between the elements but is maintained in the regular k-type case (figure 6.35 (e)). Unlike the early time, the d-type case and both cases with dense fluid between the elements show TKE distributions similar to the head region of the smooth case as they pass through the bin.

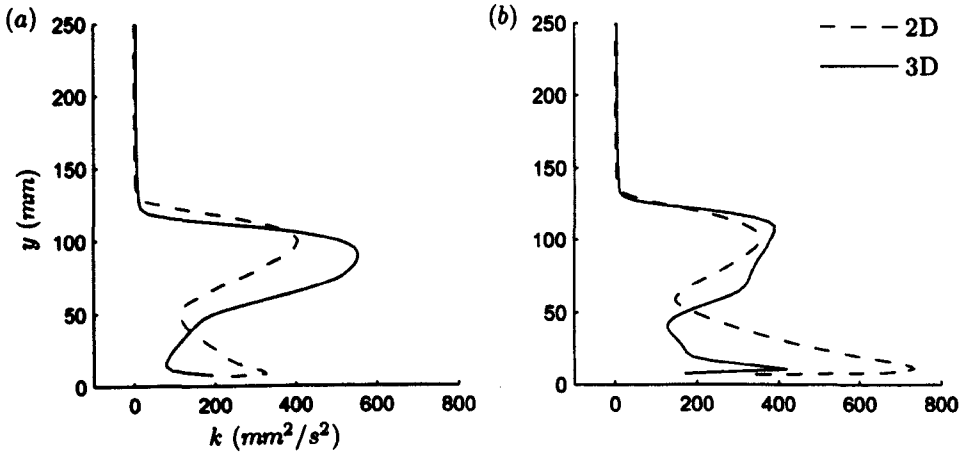

Figure 6.38: Turbulence kinetic energy, k, profiles for the total domain depth resulting from 2D and 3D numerical simulations for bottom walls with (a) beams$_{6,2}$, and (b) beams$_{6,8}$.

Vertical TKE profiles through the flow depth at the bin are shown for the 2D and 3D models of the smooth bed in figure 6.36. As the corresponding TKE field suggested, there is little distinguishable difference between the models. Figure 6.37 presents the equivalent data for the d-type and k-type bed configurations with dense fluid initialised in the gaps. The 3D model predicts the removal of the turning point at the bed that occurs in the k-type case but otherwise little difference is observed between the 2D and 3D models. Compared to the cases with ambient fluid in the gaps, lateral motion is suppressed and therefore a 2D model can achieve reasonable accuracy.

Figure 6.38 presents the data for the d-type and k-type bed configurations with ambient fluid initialised in the gaps. In these cases, more distinct differences between the 2D and 3D models can be observed. The most distinguishable difference is that the high TKE is not localised just at the top and bottom of the current head but now appears to be more greatly distributed below the top maxima and this indicates mixing penetrating into the top of the current head. This can also be observed in the TKE fields (figures 6.35 (c) and (e)). The 3D model predicts for both configurations that the TKE has not increased as substantially at the bed as was implied by the 2D model, which indicates that lateral dissipation has probably occurred due to the 3D dynamics. Conversely, at the density interface, the TKE appears to have increased, particularly in the d-type case. The maximum TKE value is still inverted from the density interface to just above the bed in the k-type case but the magnitude has decreased compared to the 2D model.

Note that the differences apparent at the bed may not be due to the limitations of the 2D model. As noted in section 5.6, certainly in the d-type case, the vertical TKE distribution

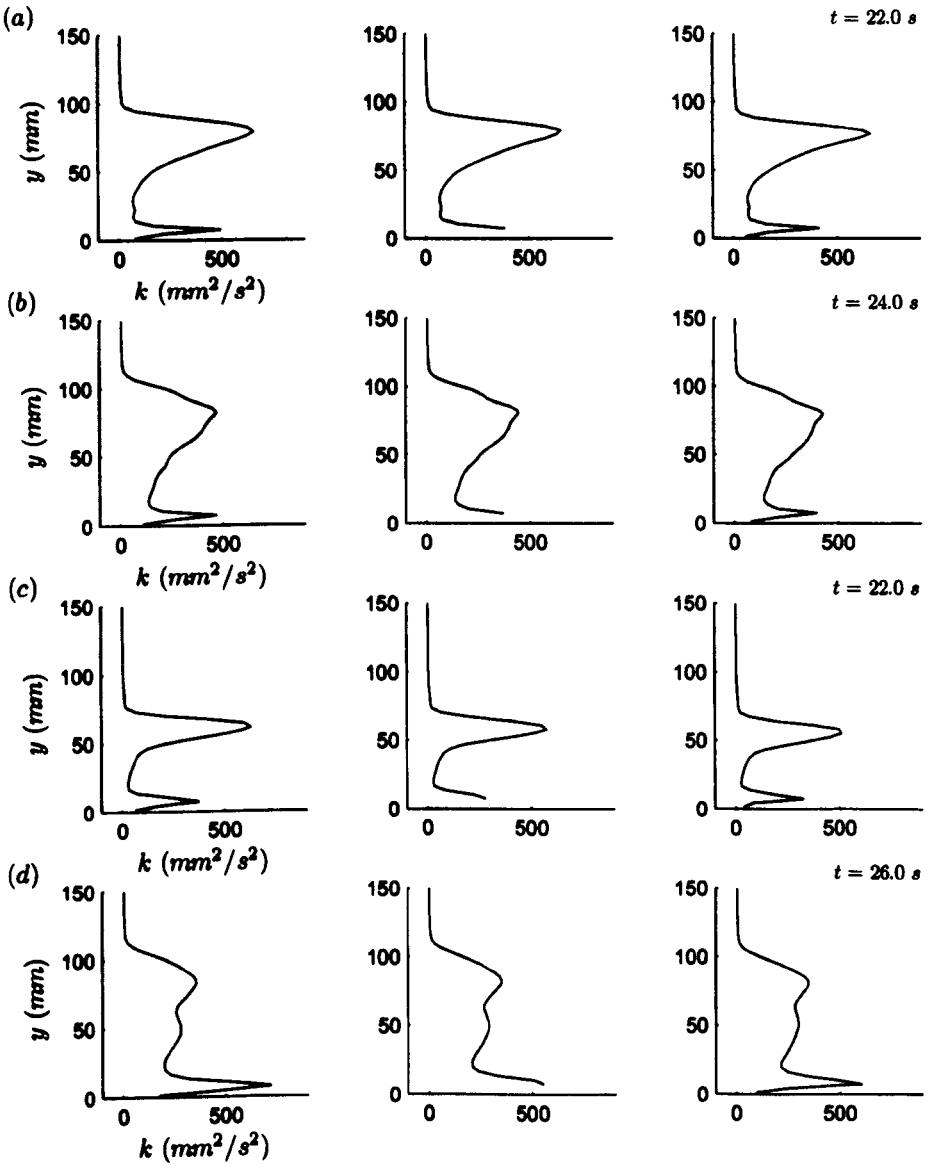

Figure 6.39: Turbulence kinetic energy, k, profiles in the vicinity of 'bin 35' resulting from 3D numerical simulations with bottom walls with (a) beams$_{6,2}$ with dense fluid between the elements, (b) beams$_{6,2}$, (c) beams$_{6.8}$ with dense fluid between the elements and (d) beams$_{6.8}$. From left to right the vertical profiles represent data in three locations, namely, one in the cavity just upstream of an element, one at the top of an element and one in the adjacent cavity just downstream of an element.

just above the bed depends on whether the profile is taken above the element or not and also, if above the element, whether it is through the cells at the upstream or downstream corner. In the 3D model the resolution is coarser and there is only one cell above an element. Therefore variation in the location of the profiles occurring above the element are not observed. Despite this observation, vertical profiles of TKE through the flow depth taken above, upstream and downstream of an element in the vicinity of the bin

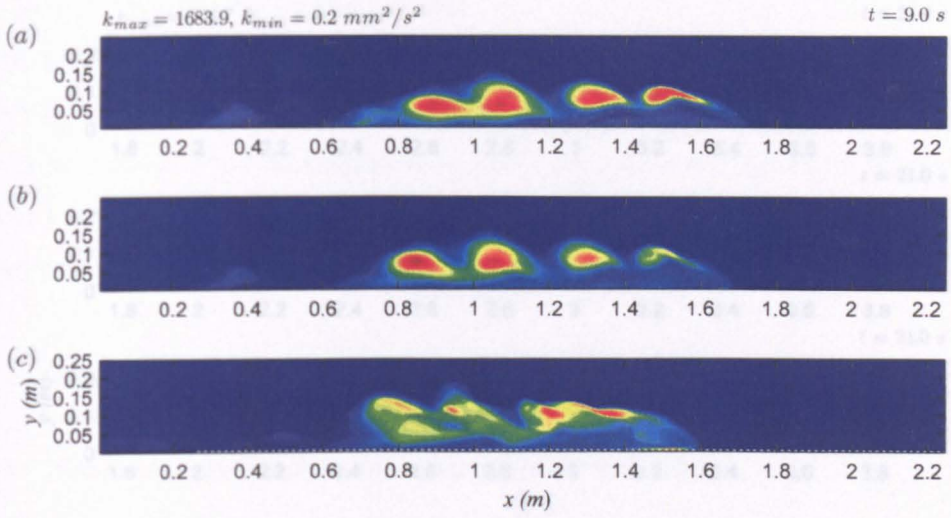

Figure 6.40: Turbulence kinetic energy, k, fields at $t = 9\ s$ resulting from the 3D simulation with (a) smooth bottom wall and with (b) a k_s value on the bottom wall ($k_s = 0.0015$) which is the approximately equivalent value of (c) beams$_{6,2}$. Red and blue are high and low TKE, respectively. Maximum and minimum values are displayed at the top of the figure.

do suggest that the turning point that occurred above the beam in the 2D models does not in fact occur in this location and occurs only in the gaps, see figure 6.39. However, this figure does maintain the observation made from the 2D model and the TKE fields that both d-type cases and the k-type case with dense fluid between the elements have higher TKE at the top of the head while the regular k-type configuration has maximum values at the bed. Again, the similarity between the two cases with dense fluid in the gaps can be observed. Without a high resolution experimental dataset through the flow depth, it is difficult to establish whether the turning point at the bed that occurs in the 2D model is a genuine physical attribute of the flow over the element top or a result of a lack of lateral flow dynamics.

The effects on the turbulence structure of the law-of-the-wall method for specifying the bed roughness

The TKE field for the law-of-the-wall model after 9 s is shown in figure 6.40 (b). A slight increase in TKE at the bed appears to be present in the 3D model that was not resolved in 2D (figure 5.33 (b)) but in most other respects the models are in good agreement and show that the law-of-the-wall method predicts a TKE distribution very similar to the smooth case, as has also been shown for other flow variables. At later times, the models diverge slightly and in the 3D model (figure 6.41 (b)) the TKE fields in the locality of the

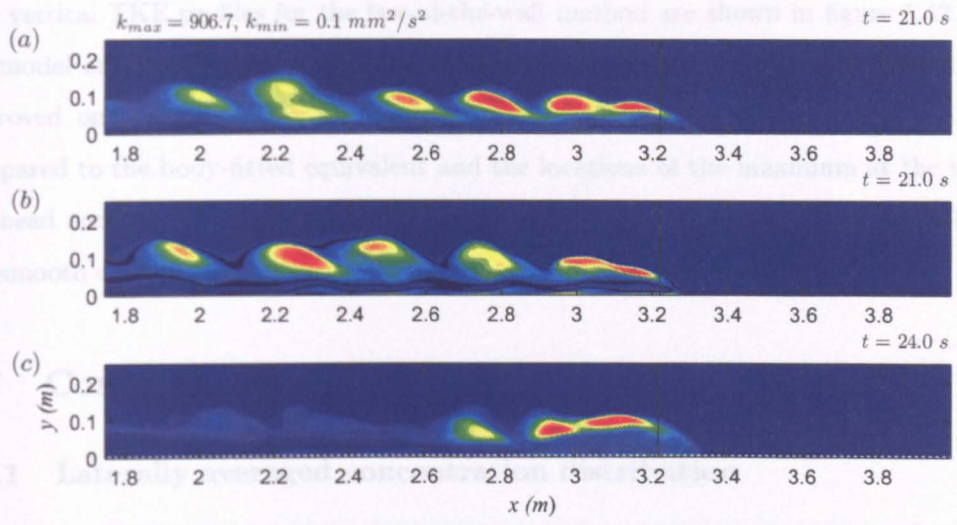

Figure 6.41: Turbulence kinetic energy, k, fields at the approximate time the head passes through 'bin 35' where the vertical profile data is read (shown as a line) resulting from the 3D simulation with (a) smooth bottom wall and with (b) a k_s value on the bottom wall ($k_s = 0.0015$) which is the approximately equivalent value of (c) beams$_{6,2}$. Red and blue are high and low TKE, respectively. Maximum and minimum values are displayed at the top of the figure.

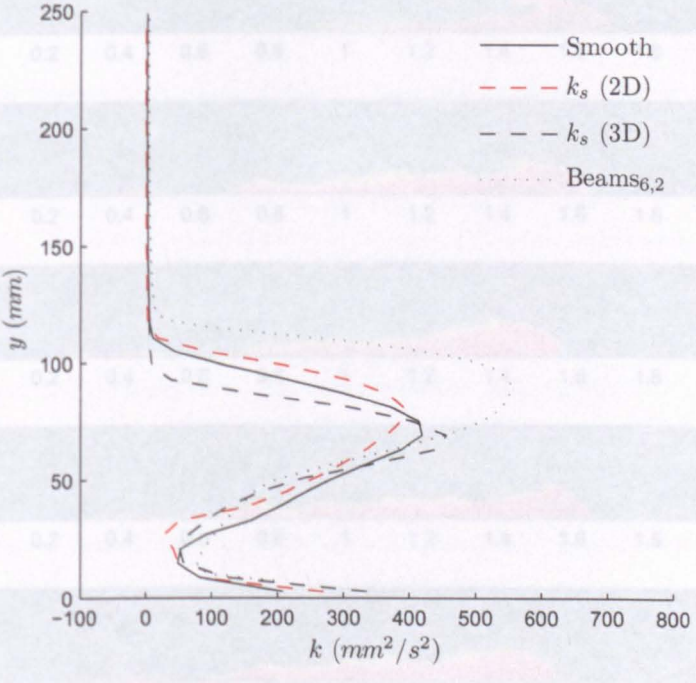

Figure 6.42: Turbulence kinetic energy, k, profiles for the total domain depth resulting from 2D and 3D numerical simulations with $k_s = 0.0015$ specified on the bottom wall, and the 3D numerical simulation of the body-fitted equivalent (beams$_{6,2}$, and a smooth bottom boundary).

billows at the interface are different to the smooth case but still show strong coherence in the billows, unlike the equivalent body-fitted beams$_{6,2}$ case (figure 6.41 (c)).

The vertical TKE profiles for the law-of-the-wall method are shown in figure 6.42. The 3D model still underestimates the magnitude of the TKE at the interface but it has improved on the 2D model. However, the increase in TKE at the bed is too high compared to the body-fitted equivalent and the locations of the maximum at the top of the head and the minimum in the vicinity of the velocity maximum are very similar to the smooth case.

6.7 Concentration

6.7.1 Laterally averaged concentration distribution

The effects on the laterally averaged concentration distribution of the d-type and k-type bed roughness configurations with and without ambient fluid between the elements

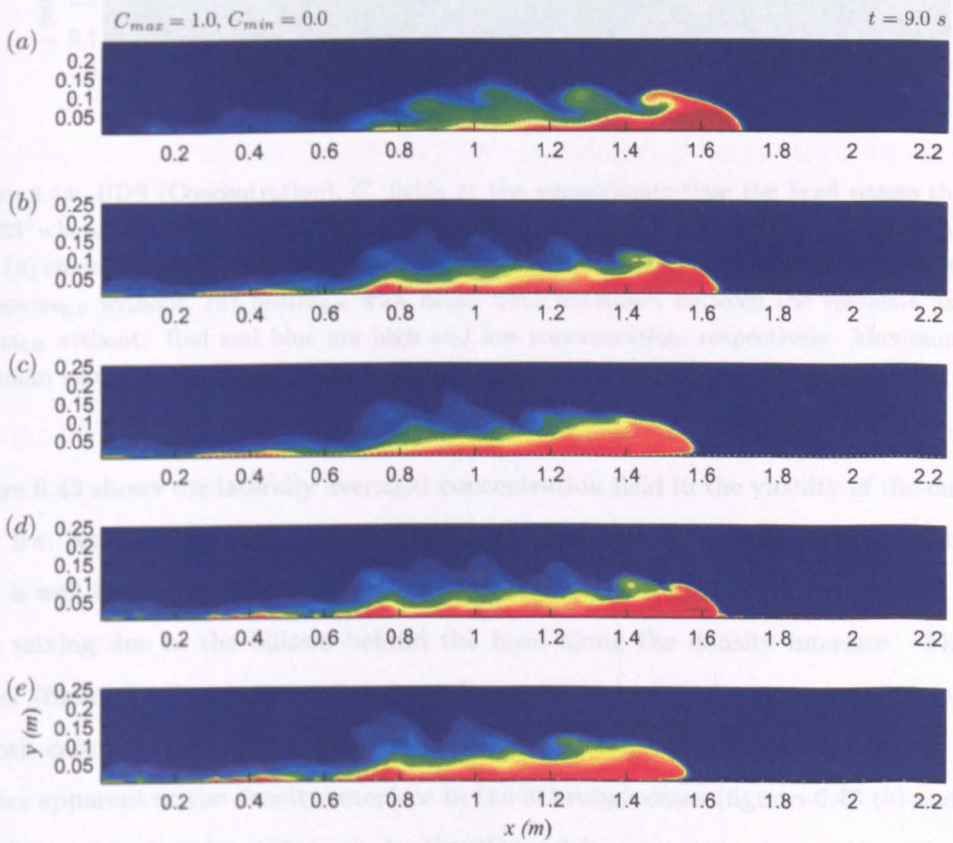

Figure 6.43: UDS (Concentration), C, fields at $t = 9\ s$ resulting from the 3D simulation with (a) smooth bottom wall, and bottom walls with (b) beams$_{6,2}$ with dense fluid initialised between the elements, (c) beams$_{6,2}$, (d) beams$_{6,8}$ with dense fluid initialised between the elements and (e) beams$_{6,8}$. Red and blue are high and low concentration, respectively. Maximum and minimum values are displayed at the top of the figure.

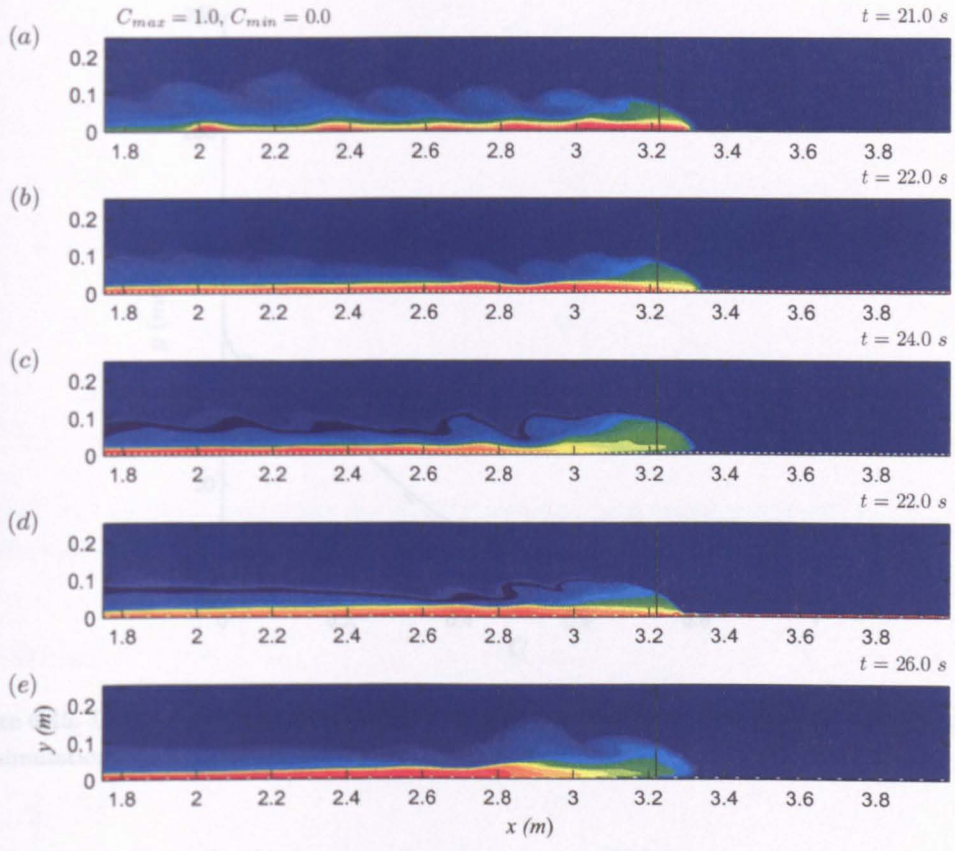

Figure 6.44: UDS (Concentration), C, fields at the approximate time the head passes through 'bin 35' where the vertical profile data is read (shown as a line) resulting from the 3D simulation with (a) smooth bottom wall, and (b) beams$_{6,2}$ with dense fluid initialised between the elements, (c) beams$_{6,2}$ without, (d) beams$_{6,8}$ with dense fluid initialised between the elements and (e) beams$_{6,8}$ without. Red and blue are high and low concentration, respectively. Maximum and minimum values are displayed at the top of the figure.

Figure 6.43 shows the laterally averaged concentration field in the vicinity of the current after 9 s. As was observed in the 2D model, all of the simulations show gravity currents with a well defined, high concentration head region and a shallower, more dilute body with mixing due to the billows behind the head along the density interface. The 2D model (figure 5.40) appears to be a good representation of the concentration for the smooth case and the two beds with dense fluid between the elements. There are more billows apparent at the density interface in the 3D rough cases (figures 6.43 (b) and (d)) but they are captured qualitatively by the 2D model.

For the two regularly rough cases the agreement is not quite as good, compare figures 5.40 and 6.43 (c) and (e). For the d-type case, the 2D model predicts the overall distribution of the concentration reasonably well but retains higher concentration fluid within the current head while the 3D model shows that it is more dilute in this locality and

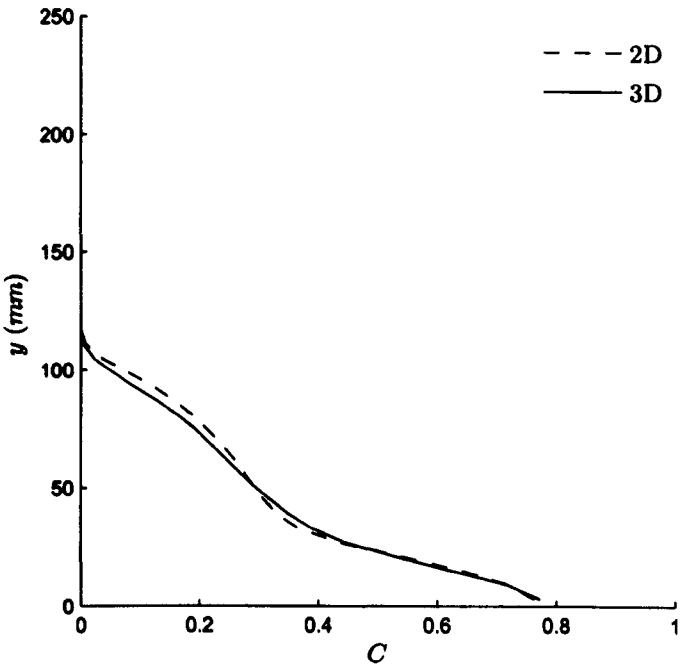

Figure 6.45: Concentration profiles for the total domain depth resulting from 2D and 3D numerical simulations with a smooth bottom wall.

higher further back. In the k-type case, the regions of high concentration appears reasonably accurate in 2D but the dilution in the top and back of the current head has been exaggerated. Again these results imply that the lateral motion is necessary to accurately capture the characteristics of the fully rough beds.

Figures 6.44 (c) and (e) show dramatic dilution within the head of the gravity currents flowing over rough boundaries compared to the smooth case (figure 6.44 (a)), and thus confirm this observation in the 2D case (figures 5.18 (c) and (e)). As observed in section 6.4, at later times in the smooth case (figure 6.44 (a)), the 3D model removes the unphysical retention of a large billow and corresponding disruption to the current body that was present in the 2D model (figure 5.41 (a)). With this removed, the 3D model of the smooth bed predicts regular billows at the interface and a thin layer of high concentration fluid within the current body below them. The head of the current remains partially stratified with a thin layer of high concentration fluid at the bottom and dilute fluid above but the concentration is maintained at higher levels. The good agreement in the current head between the 2D and 3D models in the smooth case can be observed in the vertical profile data obtained at the bin location (the vertical lines in figure 6.44) that is presented in figure 6.45.

For the cases with dense fluid between the elements, figures 6.44 (b) and (d), the vertical

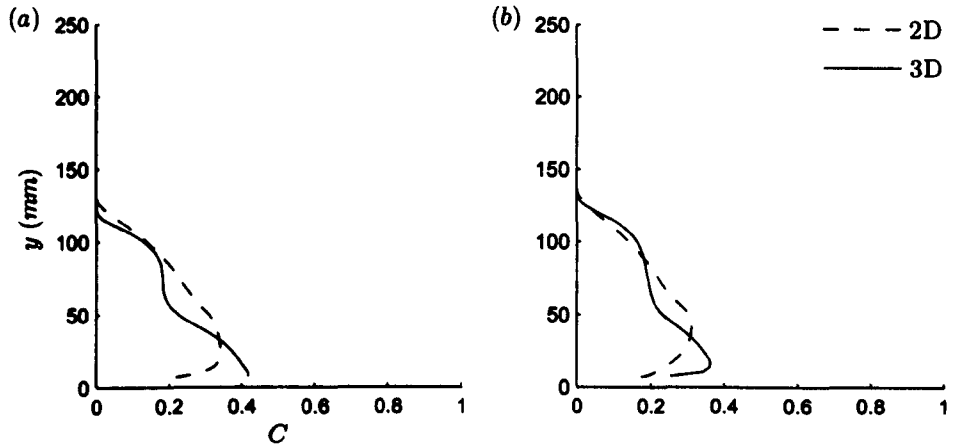

Figure 6.46: Concentration profiles for the total domain depth resulting from 2D and 3D numerical simulations for bottom walls with (*a*) $\text{beams}_{6,2}$ and (*b*) $\text{beams}_{6,8}$.

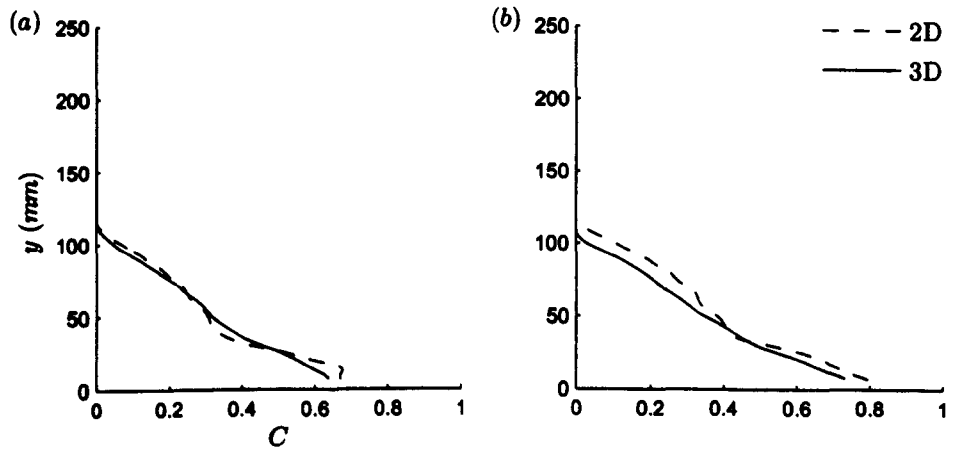

Figure 6.47: Concentration profiles for the total domain depth resulting from 2D and 3D numerical simulations for bottom walls with (*a*) $\text{beams}_{6,2}$ and (*b*) $\text{beams}_{6,8}$ with dense fluid initialised between the elements.

profiles at the bin (figure 6.47) show that the 2D model is capable of remarkably good representation of the concentration field at the time the current head passes through the bin (see figure 5.42). In fact, this is also, in general, true for the rough cases with ambient fluid in the cavities, shown in figures 6.44 (*c*) and (*e*), and in figure 6.46. The main discrepancy in the concentration fields is that the 2D model does not capture a similarly shaped current head. This is probably because, as observed previously, it cannot resolve the billows that have been shown to occur in this locality and therefore it does not account for the redistribution of concentration that results from them, as in the 3D model. The vertical profiles show that in the d-type case with ambient fluid between the elements, the reduction in concentration at the bed which occurs for the 2D model,

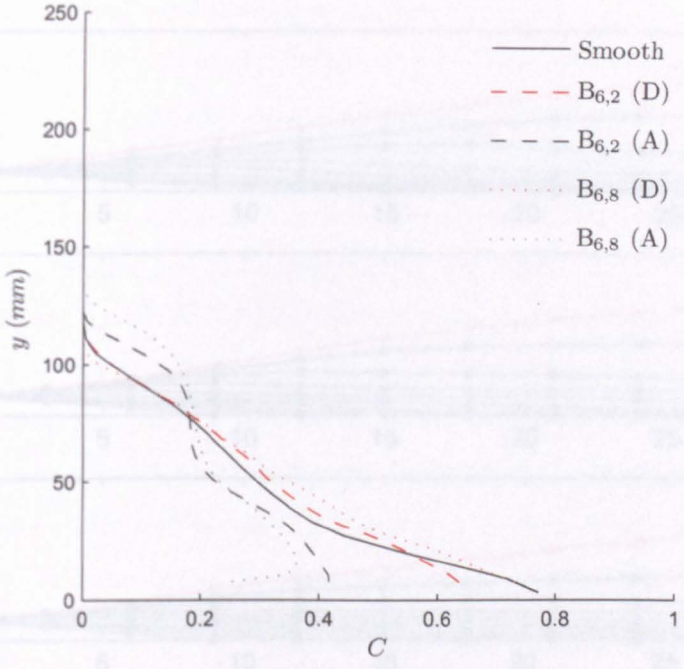

Figure 6.48: Concentration profiles for the total domain depth resulting from 3D numerical simulations for a smooth bottom boundary and bottom walls with beams$_{6,2}$ ($B_{6,2}$) and beams$_{6,8}$ ($B_{6,8}$) with (D) and without (A) dense fluid initialised between the elements.

is not observed for both roughness types in the 3D case. This implies that dilution near the bed in this case is not as acute as the 2D model suggests. However, this does not negate the fact that there is a significant reduction compared to the smooth case and, overall, the dilution within the head in the rough cases with ambient fluid between the elements is dramatically accelerated. Figure 6.48 confirms this and furtehr highlights the similarity between the smooth case and the rough beds with dense fluid between the elements. This implies that although the overridden ambient fluid only contributes $\approx 50\%$ to the retardation of the current, it is the primary cause of the dilution within the current head.

As was generated in the 2D model, cumulative percentages of the concentration throughout the domain as a function of time are presented in figure 6.49. Comparison of the predictions for the rough cases with the 2D and 3D models (figures 6.49 (*b*) and (*d*) versus (*c*) and (*e*), respectively) indicate that most of the observations made for the 2D version also hold true for the 3D. There were no distinguishable differences in the smooth case and hence the 2D version is not replotted here. The most significant variation in the rough cases is in the amount of dense fluid remaining after 30 s for both d and k-type configurations. In both models it is apparent that as soon as the flow is released, the percentage of the domain that contains high concentration fluid decreases and the

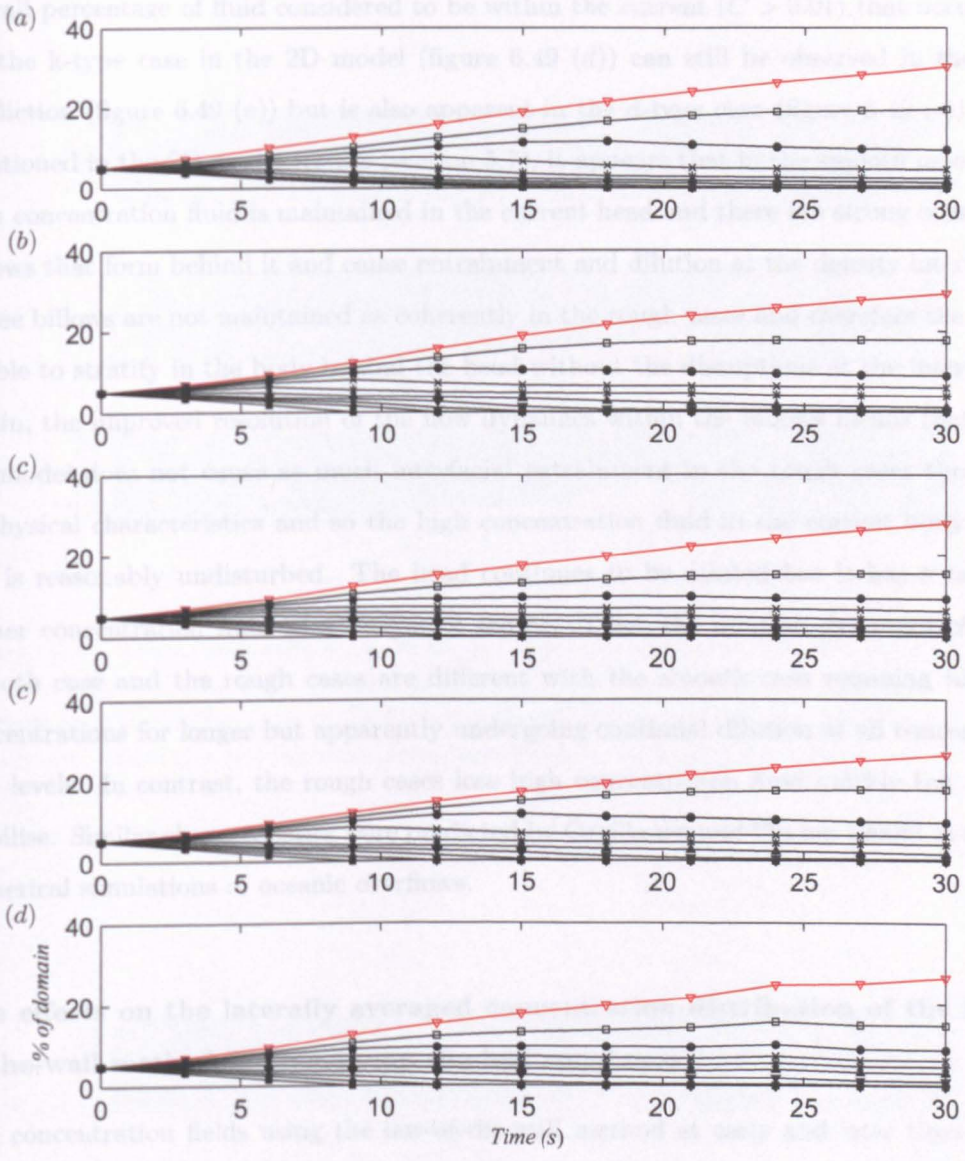

Figure 6.49: UDS (Concentration), C, as a function of time given as a cumulative percentage of the total domain with (a) smooth bottom wall and (b) beams$_{6,2}$ (2D), (c) beams$_{6,2}$ (3D), (d) beams$_{6,8}$ (2D) and (e) beams$_{6,8}$ (3D). The data coloured red represents the percentage of cells in the domain that contain concentration levels that meet the minimum criteria to be considered within the gravity current entity. The data below this line represents cumulative concentration levels from 0.1 and above (open squares) to 0.9 and above (filled squares).

percentage of low concentration fluid increases as would be anticipated from mixing and entrainment of ambient fluid. However, the decrease in high concentration fluid in the 3D model occurs more slowly and while in the 2D versions after 20 s the percentage of the domain above the 0.5 concentration level is much reduced, in the 3D models, the level has increased to 0.6, i.e. there is more dense fluid remaining in the domain. Despite the increase in dense fluid remaining within the current, the slight decrease in

overall percentage of fluid considered to be within the current ($C > 0.01$) that occurred for the k-type case in the 2D model (figure 6.49 (*d*)) can still be observed in the 3D prediction (figure 6.49 (*e*)) but is also apparent in the d-type case (figure 6.49 (*c*)). As mentioned in the 2D model results (section 5.7), it appears that in the smooth case, the high concentration fluid is maintained in the current head and there are strong coherent billows that form behind it and cause entrainment and dilution at the density interface. These billows are not maintained as coherently in the rough cases and therefore the flow is able to stratify in the body behind the head without the disruptions at the interface. Again, the improved resolution of the flow dynamics within the billows means that the 3D model does not cause as much interfacial entrainment in the rough cases through unphysical characteristics and so the high concentration fluid in the current body and tail is reasonably undisturbed. The head continues to be diluted but it has a tail of higher concentration fluid as a buoyancy source. Thus, the dilution dynamics of the smooth case and the rough cases are different with the smooth case retaining higher concentrations for longer but apparently undergoing continual dilution at all concentration levels. In contrast, the rough cases lose high concentration fluid quickly but then stabilise. Similar characteristics were predicted by Özgökmen and Fischer (2008) in their numerical simulations of oceanic overflows.

The effects on the laterally averaged concentration distribution of the law-of-the-wall method for specifying the bed roughness

The concentration fields using the law-of-the-wall method at early and later times are shown in figures 6.50 and 6.51, respectively. The vertical concentration through the bin as the head passes through that location, corresponding to the vertical line in figure 6.51, is shown in figure 6.52. All three of these images provide evidence that there is very little difference between the 2D and 3D models (compare figures 5.43-5.45 and figures 6.50-6.52) using this method and little difference using either model between this case and the smooth bed. It is clear that the k_s method cannot model the internal dilution and fundamental changes to the concentration distribution and other flow dynamics that occur in the presence of the form roughness, failing to model the dilution in the head.

6.7.2 Lateral concentration distribution

Figure 6.53 shows 3D isosurface representations, for the smooth bed case, of two concentration levels within the current head after 9 s and at the time the current passes

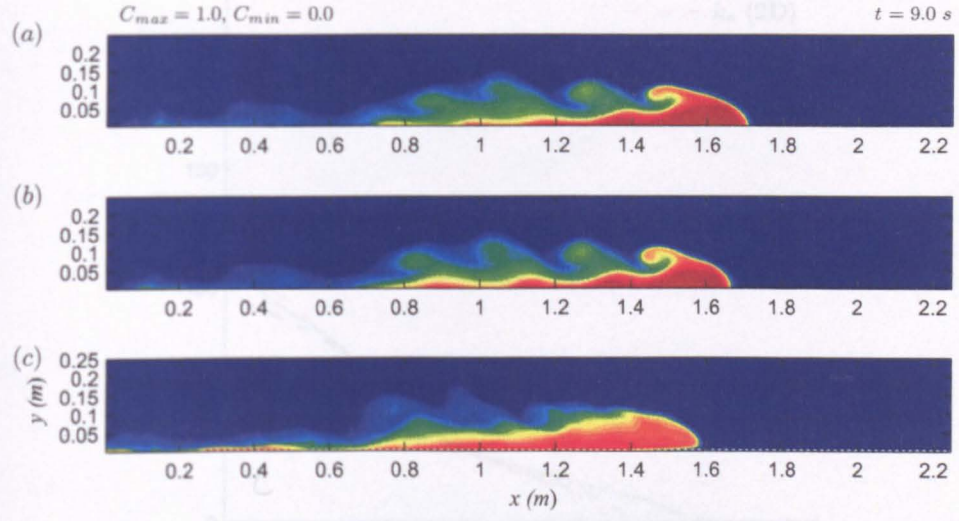

Figure 6.50: UDS (Concentration), C, fields at $t = 9$ s resulting from the 3D simulation with (a) smooth bottom wall, and with (b) a k_s value on the bottom wall ($k_s = 0.0015$) which is the approximately equivalent value of (c) beams$_{6,2}$. Red and blue are high and low concentration, respectively. Maximum and minimum values are displayed at the top of the figure.

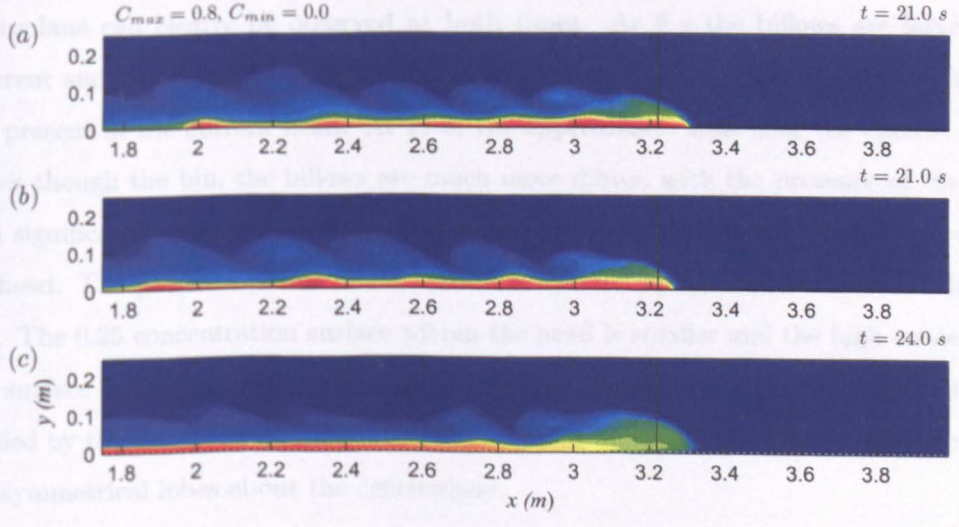

Figure 6.51: UDS (Concentration), C, fields at the approximate time the head passes through 'bin 35' where the vertical profile data is read (shown as a line) resulting from the 3D simulation with (a) smooth bottom wall, and with (b) a k_s value on the bottom wall ($k_s = 0.0015$) which is the approximately equivalent value of (c) beams$_{6,2}$. Red and blue are high and low concentration, respectively. Maximum and minimum values are displayed at the top of the figure.

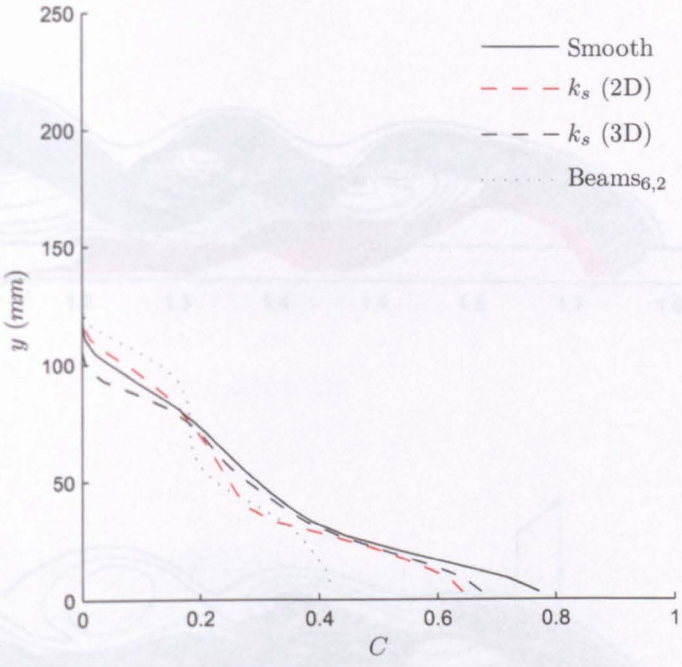

Figure 6.52: Concentration profiles for the total domain depth resulting from 2D and 3D numerical simulations with $k_s = 0.0015$ specified on the bottom wall, the 3D numerical simulation with the body-fitted method equivalent (beams$_{6,2}$) and a smooth bottom boundary.

through the bin. The 0.25 surface captures features of the current outline while the 0.9 surface shows the location of high concentration fluid. The symmetry along the lateral centreplane can clearly be observed at both times. At 9 s the billows are large and coherent and well-defined by the 0.25 concentration surface. High concentration fluid is still present in the current head. At 21 s, the approximate time that the current head passes though the bin, the billows are much more dilute, with the presence of the 0.25 level significantly reduced and restricted to the stronger structures immediately behind the head. The presence of less dilute billows is inferred by the contour lines on the far wall. The 0.25 concentration surface within the head is smaller and the high concentration surface has disappeared as a result of dilution. Formation of a cleft at the front, as implied by the vectors of lateral motion (figures 6.24 and 6.29) can be observed creating two symmetrical lobes about the centreplane.

Equivalent 3D images within the current heads of the d-type and k-type cases with and without ambient fluid between the elements can be seen in figures 6.54 and 6.55 at 9 s and later times, respectively. Even after 9 s the high concentration surface in the rough cases with ambient fluid between the elements (figures 6.54 (*b*) and (*d*)) has already been reduced to small pockets trapped between the roughness elements. The head profile at this early time, represented by the 0.25 surface can be seen to extend upstream further

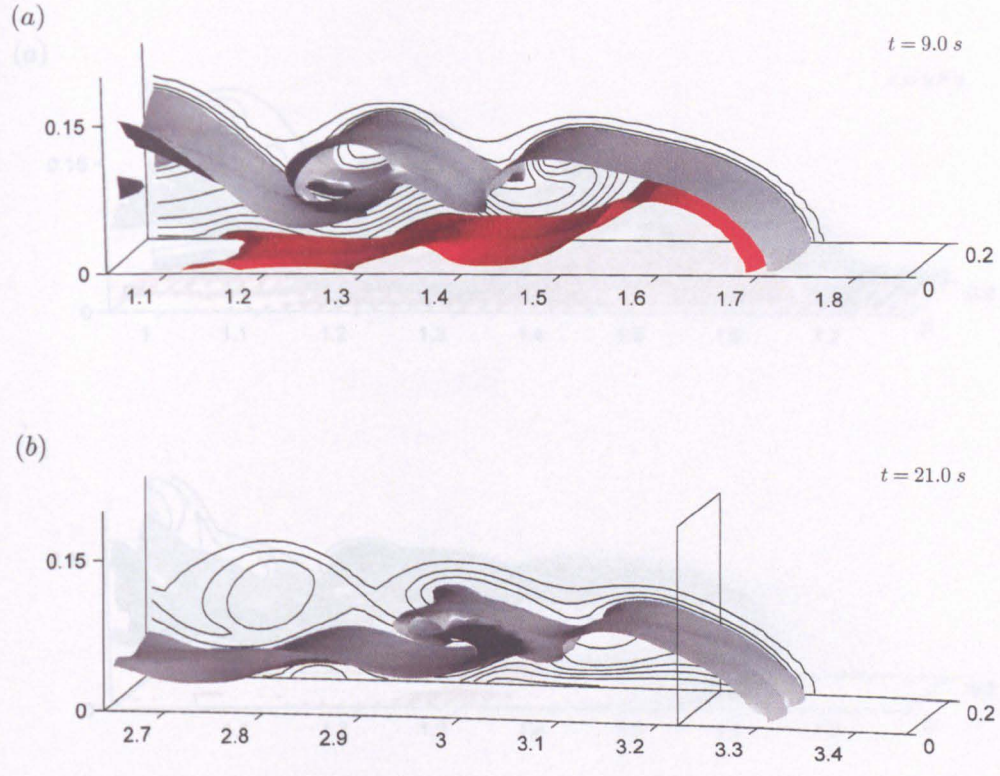

Figure 6.53: UDS (Concentration), C, field in the head of the current for the smooth case. (a) after 9 s, (b) at 21 s, the approximate time the head passes through 'bin 35' where the vertical profile data is read (shown as a plane). Isosurfaces show concentration levels 0.25 (grey) and 0.9 (red). Lines of contour levels 0.01 at the density interface then at intervals of 0.1 from 0.1 to 0.9 are included at the far wall.

than in the smooth case and those with the dense fluid between the roughness elements (figure 6.54 (a) and (c)). The 0.25 concentration surface also highlights the increased amount of lower concentration fluid beneath the head in the cases with ambient fluid between the elements as a result of ingestion at the nose. This process is maintained and perhaps enhanced at the later time. Conversely, the head profiles are not maintained at later times. Figures 6.55 (b) and (d) demonstrate the dramatic difference in the evolution of the gravity current heads for the d and k-type roughnesses with ambient fluid between the elements. Certainly at the 0.25 concentration level, the head of the current in the k-type case has become significantly shorter in length and more rounded, with a prominent head and nose. The d-type beds and the equivalent k-type bed with dense fluid between the elements (figures 6.55 (a), (b) and 6.55 (c), respectively) retain a more elongated head shape similar to the smooth case (figures 6.53 (b)).

As could be expected, there is more dense fluid trapped between the elements at 9 s in the cases with this high concentration fluid initialised in that location. It is interesting

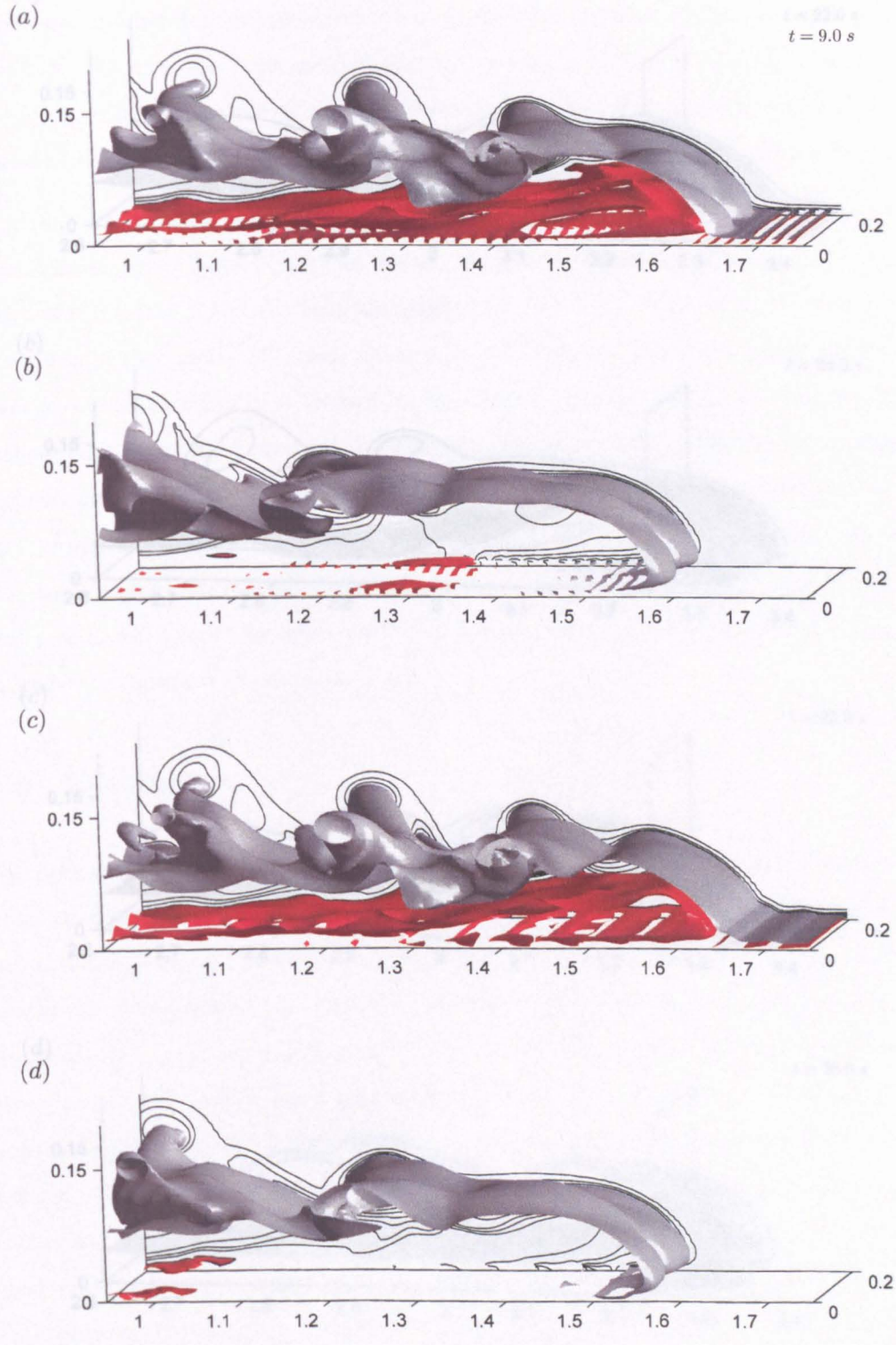

Figure 6.54: UDS (Concentration), C, field in the head of the current after $t = 9\ s$ for beams$_{6,2}$ with (a) dense fluid initially between the elements, (b) with ambient, and for beams$_{6,8}$ (c) with dense fluid initially between the elements, and (d) with ambient. Isosurfaces show concentration levels 0.25 (grey) and 0.9 (red). Lines of contour levels 0.01 at the density interface then at intervals of 0.1 from 0.1 to 0.9 are included at the far wall.

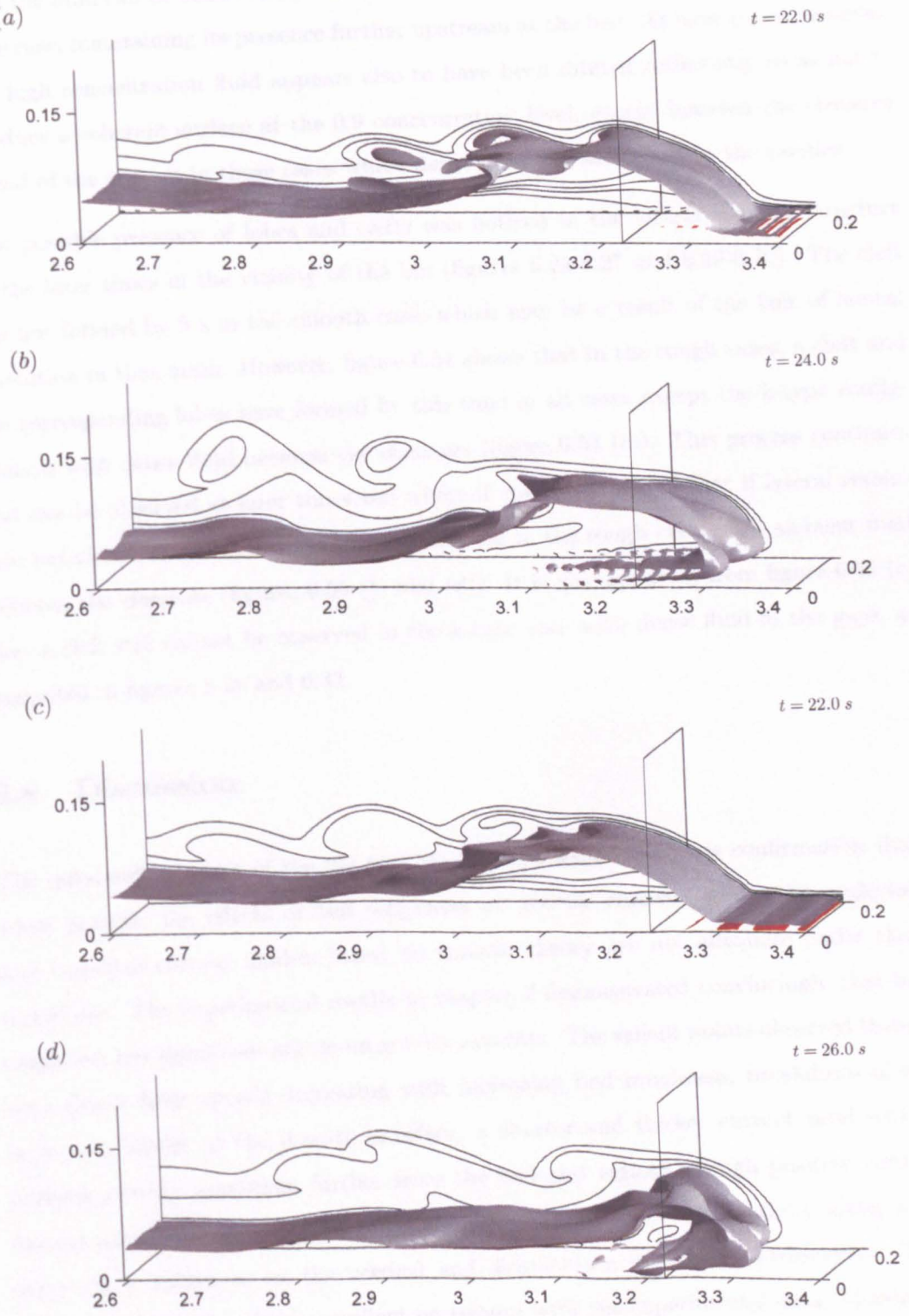

Figure 6.55: UDS (Concentration), C, field in the head of the current at the approximate time the head passes through 'bin 35' where the vertical profile data is read (shown as a box) for beams$_{6,2}$ with (a) dense fluid initially between the elements, (b) with ambient, and for beams$_{6,8}$ (c) with dense fluid initially between the elements, and (d) with ambient. Isosurfaces show concentration levels 0.25 (grey) and 0.9 (red). Lines of contour levels 0.01 at the density interface then at intervals of 0.1 from 0.1 to 0.9 are included at the far wall.

that the fluid can be observed to remain trapped beneath the current for longer in the d-type case, maintaining its presence further upstream at the bed. At later times, however, the high concentration fluid appears also to have been diluted sufficiently so as not to produce a coherent surface at the 0.9 concentration level, except between the elements ahead of the current in those cases where dense fluid was initialised in the cavities.

The possible presence of lobes and clefts was noticed in the lateral velocity structure at the later times in the vicinity of the bin (figures 6.24-6.27 and 6.29-6.32). The cleft has not formed by 9 s in the smooth case, which may be a result of the lack of lateral resolution in that mesh. However, figure 6.54 shows that in the rough cases, a cleft and the corresponding lobes have formed by this time in all cases except the k-type configuration with dense fluid between the elements (figure 6.54 (*c*)). This process continues and can be observed at later times too where it could be implied that if lateral resolution permitted, more lobes and clefts would form in the rough cases with ambient fluid between the elements (figures 6.55 (*b*) and (*d*)). It is also apparent from figure 6.55 (*c*) that a cleft still cannot be observed in the k-type case with dense fluid in the gaps, as suggested in figures 6.28 and 6.33.

6.8 Discussion

The outstanding result of the 2D and 3D CFD presented herein is confirmation that, when present, the effects of bed roughness on gravity currents cannot be neglected, and therefore current models based on smooth theory are not adequate under these conditions. The experimental results in chapter 2 demonstrated convincingly that bed roughness has significant affects on gravity currents. The salient points observed therein were slower front speeds decreasing with increasing bed roughness, breakdown of the large instabilities at the density interface, a shorter and thicker current head with a reduced velocity maximum further from the bed and regions of high positive vertical motion associated with regions of reduced downstream horizontal activity along with many other influences on the vertical and downstream flow field distributions. The CFD, in general, has shown excellent agreement with the experimental data. Moreover, the CFD confirms the approximately equal contribution of the ambient fluid and the presence of surface friction to the retardation of the current in the constant speed phase.

The novelty of the CFD is its ability to provide additional insights into the roughness effects. Significant dilution of the head both at early and late stages of the flow has been predicted with increased preservation and stratification of higher concentrations of

fluid within the current body due to the breakdown of the large interfacial instabilities, and a larger region of faster water pushed ahead of the current compared to the smooth surfaced case. The turbulence kinetic energy is shown to generally increase within the head. Earlier commencement of lobe and cleft generation is predicted and potential trends resulting from the spacing of the elements have been identified. The mechanisms for many of these affects are postulated and discussed in detail below in which the CFD corroborates the suggestion that many of the present gravity current models, based on smooth surface approximations, are inappropriate for many natural and industrial contexts.

The effects of the presence of the ambient fluid between the elements

The results show that once the ambient fluid between the elements is replaced with dense fluid, the level of dilution within the current head and body decreases. This is to be expected since when the head of a gravity current propagates along a smooth surface then the surface friction from the bottom boundary is continuous. Therefore the current has a slightly raised nose that causes a small amount of the ambient fluid to be overridden and entrained due to the buoyancy difference between this fluid and the current (Simpson and Britter, 1979). Peters *et al.* (1997) showed for continuous flux currents that this process is dependent on the surface roughness, the presence of which contributes significantly to the mixing within the current. The cavities between the elements essentially create holes in the bottom boundary and therefore reduce the continuous surface friction present in the smooth bed case. These cavities are not bottomless and fluid is trapped within them and induced into vortical motion which removes energy from the current and thus still provides a slowing effect. When this fluid is less dense, as in the regular case where ambient fluid is initialised between the elements, there are also buoyancy effects generated due to the lower density of the trapped fluid and the higher density of the overflowing current. Therefore, despite the removal of surface friction at a cavity, when the gravity current flows over it, the fluid within the current is subject to intrusions in these localities from the buoyant fluid, particularly in the head where ambient fluid is overridden at the front and the density difference is large, certainly for early times. As a result, the quantity of ingested less dense fluid is increased and it can be demonstrated that the velocity maximum is forced further from the bed and retarding mechanisms are increased. The lobe and cleft instability and the asymmetry of the front propagation are potentially augmented. Conversely, when dense fluid replaces the initial ambient fluid between the elements, the buoyancy effects are removed and thus a cushioning effect can

occur in the gaps which, for the overflowing current, amounts to more efficient removal of the surface friction at the bed. The current can therefore maintain higher concentrations for longer and is primarily subject to mixing due to instabilities at the density interface. However, the currents do not propagate at speeds similar to, or greater than, the smooth case probably due to energy losses to the vortices that still occur in the trapped fluid or other non-ambient induced effects of the roughness elements.

The fluid into which the ambient fluid is mixed in the head and the near-wall region of the body of the current will be the highest density fluid. Therefore the subsequent entrainment causes a reduction in the highest concentration fluid and an almost immediate decrease in the high concentration fluid in the current, as shown in the cumulative percentage results for the rough cases. Thus, a decrease in the buoyant driving force of the current occurs, as reflected by the front speeds. However, as time progresses and the concentration of the fluid in the current body decreases, the density difference between the ambient fluid and the overflowing current and therefore the buoyancy effects will also decrease and hence the mixing and dilution at the bed will reduce. This explains why the percentage of the domain at higher concentrations becomes more or less constant after a certain time in the rough cases. With the reduced billows at the density interface in the rough cases, the flow is also able to stratify within the body and the tail of the current, creating a more or less undisturbed source of dense fluid that can feed the current head. Thus despite the low dilution in the head, its definition is maintained and the current continues to propagate.

Despite the entrainment of ambient fluid into the bottom of the current, the percentage of fluid within the gravity current (i.e. concentration levels in the domain of $C > 0.01$) has been predicted to be slightly less in the rough cases than in the smooth case. Since the billows at the interface in the rough cases are significantly reduced, this confirms that more entrainment and mixing occurs due to interfacial instabilities than at the bed. It also shows that this entrainment mechanism is greater in the smooth case since the percentage of fluid in the gravity current increases and the amount of high concentration fluid decreases but with little contribution from the processes near the bed (Simpson and Britter, 1979). If the interfacial processes were as efficient in the rough cases then, coupled with the entrainment at the bed, it could be expected that the percentage of fluid within the current would be higher than in the smooth case but this is not the case. In fact, the billows at the interface are more diffuse. It is particularly interesting that the overall result here is that the total amount of fluid in smooth and rough currents is actually very similar but with very different entrainment characteristics. This prediction

is supported by similar observations by Özgökmen and Fischer (2008). These predictions also imply that interfacial entrainment and mixing, although greater than the processes at the bed within the current head, do not have such a significant effect at reducing the current speed as those processes caused by the presence of roughness, which dilute the velocity core.

The effects of roughness element spacing

The smooth case is subject to unbroken surface friction for the entire length of its propagation down the tank and lobes and clefts form. In the d-type case, the elements are relatively densely spaced so that there is still sufficient surface friction for the lobes and clefts to generate and the current also slows due to the removal of some of its energy to maintain the fluid trapped between the elements in rotation. In the k-type case, surface friction is so reduced that the lobes and clefts only form convincingly due to the presence of the ambient fluid between the elements. The current still slows down, again due to the loss of energy to power vortices in the cavities, regardless of the fluid density therein. Despite the increased removal of surface friction by placing dense fluid in the cavities in the k-type case, this case is slower than the equivalent d-type configuration. In this case, the energy removal must come from lateral motion since in the corresponding 2D case the k-type current retains faster propagating speeds.

In single-phase pipe flow investigations over this type of square beam roughness, the vortices that occur between the elements have been observed to eject into the overflow. The strength of the 'ejections' increases until the critical spacing $w/k_r \approx 7$ is attained, after which it remains more or less constant (Cui *et al.*, 2003b; Leonardi *et al.*, 2003b; Ashrafian *et al.*, 2004; Ikeda and Durbin, 2007). Evidence that this critical spacing also applies to gravity currents has been presented. Therefore, it is highly likely that this observation also holds for gravity currents. In fact, it can be postulated that it will be enhanced due to the added buoyancy difference of these multi-phase flows. The fluid is ejected from between the elements within the current head and increases the mixing and therefore the turbulence kinetic energy in the head, as the results have shown and is particularly evident in the k-type cases where this critical value can be applied. In the present numerical and experimental results, the resolution means that it cannot be determined if distinct ejections occur or if the ambient fluid between the elements is simply gradually mixed into the current. However, in the CFD, trapped regions of lower concentration fluid are not observed further back beneath the current body

implying that these pockets of fluid may eject into the overlying flow. As the current head dilutes, the difference between the density of the current and the overridden ambient fluid also reduces. Therefore, the buoyancy force reduces and so it can be inferred that any ejections due to this force will only occur early on in propagation or progressively further back in the flow, behind the current head. However, ejection of fluid does not only occur due to buoyancy, as demonstrated by their presence in single phase problems. Therefore, mixing induced by the ejecting vortices may continue regardless of the head dilution. A DNS study or a significantly higher resolution version of the current approach with further investigation into enhancing the wall functions is required to confirm this.

The widest element spacing ($\text{beams}_{6,16}$) shows a slightly different phenomena to the other k-type results. Although the front speed indicates that it conforms to the flow over elements at the critical spacing suggested above, the profiles and flow fields show evidence of different internal dynamics that have shown agreement with aspects of the smooth case as well as rough bed characteristics. It is possible that for larger values of w/k_r, as has been found for single-phase flows, the normal wall motion induced by the roughness is confined to smaller regions and the overlying fluid dynamics are once again similar to those encountered above a smooth wall (Leonardi *et al.*, 2004). The $\text{beams}_{6,16}$ result herein is a 2D prediction (no 3D simulations were performed). Thus, it is also possible, with the lateral motion available in 3D, that other flow dynamics may be resolved, which can further explain this case.

The law-of-the-wall method

The numerical models using a body-fitted mesh have been discussed thus far. The law-of-the-wall model appears able to predict front speeds over bed roughness more accurately than the body-fitted equivalent in 2D but for most other variables cannot account for the changes to the internal dynamics due to the presence of form roughness elements. However, this good front speed result is largely a false agreement and it has been shown to be more likely that the result is benefitting from the premature slowing of the current due to 2D limitations. Once the model was extended to 3D, the lateral dynamics were resolved and reduction in the effectiveness of the method could be observed.

Some of the discrepancies could be because the internal dynamics presented are characteristic of a beam-type bed roughness and cannot therefore be generated when the roughness is categorised by a k_s value. Different bed roughness configurations might result in the same front speeds with the result that more accurate agreement for this

parameter is possible while masking very different internal dynamics. This concern has been raised previously, see section 4.3.4.1 or Krogstad and Antonia (1999). It is possible that this method could be more accurate for grain type roughnesses since the original k_s model was correlated to sand grains (Nikuradse, 1933) and the roughness elements in these cases are perhaps less likely to affect the flow individually as the beam-type roughness appears to do. Therefore, the combination of the two methods of modelling bed roughness, using a body-fitted mesh to describe the form roughness and a k_s value to describe the grain roughness is still plausible but has not been tested in the present study.

This work has identified that there are substantial limitations to modelling larger roughness heights with the k_s method due to the coarseness of mesh required at the walls. However, if the roughness is small and the k_s value is known then, with careful verification procedures in place, the cell size of the mesh could be scaled to accommodate the roughness criteria at the bed and optimise computational and temporal costs. This could be beneficial compared with the refinement required to implement a body-fitted mesh on a small bed roughness.

Model performance

Validation of the 2D and 3D models with the experimental data has resulted in the conclusion that the 3D model is demonstrably better. In fact, it is vital for accuracy that a 3D model is adopted to simulate gravity current propagation over beam type bed roughness, since the lateral fluid mechanics are substantially increased. This should be expected, since the presence of transverse beams is likely to force the lateral motion of some of the fluid that interacts with them. Figure 6.56 highlights the salient differences between the 2D and 3D models. The 2D model is able to accurately predict vertical velocity and concentration profiles and the fundamental qualitative observation of a diluted head and a concentrated body in the rough cases. However, the 3D model excels with improved front propagation, realistic physical features at the upper density interface and no unphysical fixed waves within the body. Moreover, the lobe and cleft instability, which is 3D by nature, is generated (although increased lateral resolution would improve this) and is augmented by the lateral activity increased under the influence of bed roughness.

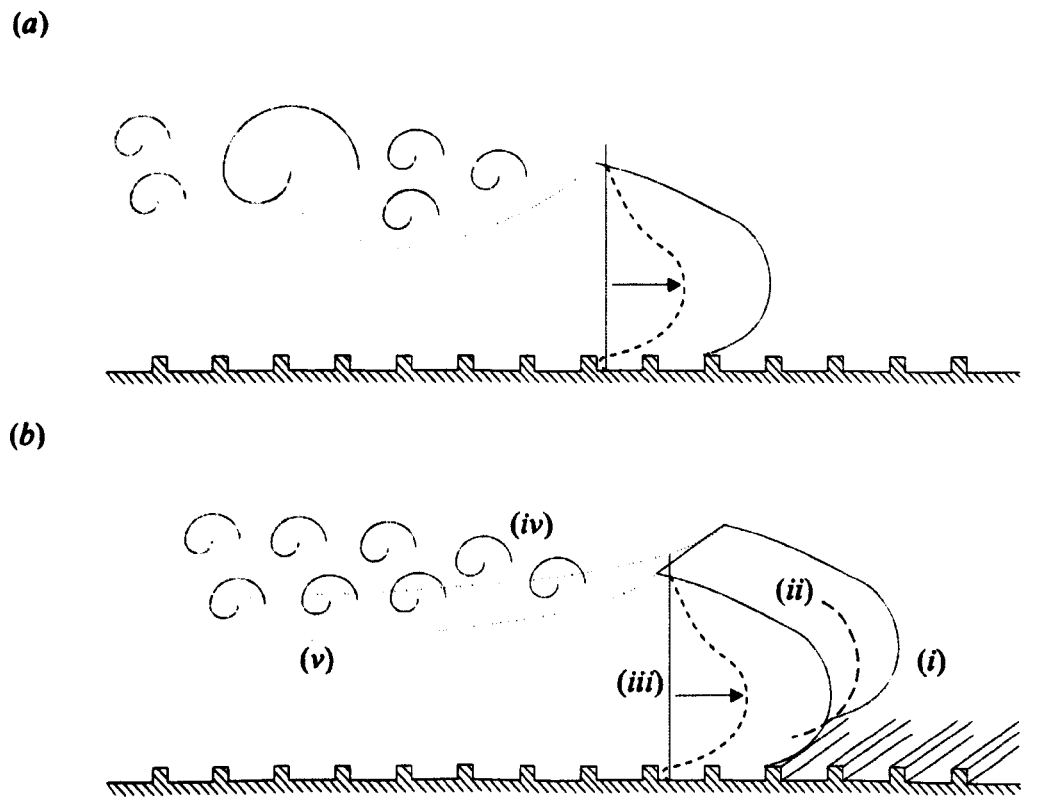

Figure 6.56: Schematic of flow processes within a gravity current head for flow over rough surfaces simulated using (*a*) a 2D model and, (*b*) a 3D model. Highlighted aspects draw attention to (*i*) improved speed with 3D model, (*ii*) presence of lobes and clefts (perhaps dependent on mesh resolution), (*iii*) accurate profiles in both 3D and 2D predictions, (*iv*) removal of unphysical billows at the density interface, and (*v*) removal of unphysical stationary waves with the 3D model.

Summary

The CFD concludes the results of the present investigation, within which the influence of form and grain roughness on gravity currents has been demonstrated for the first time. A wide range of flow variables have been shown to be influenced by the presence of roughness. These include propagation rates, location of the velocity maximum, head height, entrainment and concentration within the head and body of the current, magnitude of water pushed ahead of the current, turbulence kinetic energy distribution in the current head and the lobe and cleft instability. Figure 6.57 presents the first schematic description of the principal effects of bed roughness on gravity currents. Namely, decreased speed and a raised velocity maximum, increased depth, breakdown or lack of generation of larger billows at the density interface resulting in decreased entrainment, increased ambient fluid pushed ahead of the front, increased amount of ambient fluid ingested beneath the head, significant dilution in the head with higher concentration levels retained in the current body and loss of energy to vortices between the elements.

Also clarified are the principal differences in the effects of the d-type and k-type spacing of the roughness elements. Namely, a shorter head length and augmentation of the aforementioned characteristics.

This investigation has also illustrated that whilst 2D models are relatively accurate for smooth boundaries, the 3D model is demonstrably better, particularly for the rough bed cases, and shows an excellent match with the experimental datasets. The 3D model is required to capture the more complex flow dynamics and has provided further new information to supplement the experimental data and resolve the more detailed flow structure and mechanics in the gravity current flow over bed roughness.

Figure 6.57: (*Next page*) Schematic of flow processes within a gravity current head, adapted from Simpson (1972). (*a*) Flow over a smooth bed, (*b*) over a d-type rough bed and (*c*) over a k-type rough bed. Highlighted aspects draw attention to (*i*) decrease in speed and raised velocity maximum, (*ii*) increased depth, (*iii*) breakdown or lack of generation of larger billows at the density interface with decreased entrainment, (*iv*) increase in ambient fluid pushed ahead of the front, (*v*) increased amount of ambient fluid ingested beneath the head augmenting lobe and cleft formation, (*vi*) significant dilution within the head fluid but higher levels retained in the body, (*vii*) loss of energy to vortices between elements, and (*viii*) shorter head length (k-type roughness only).

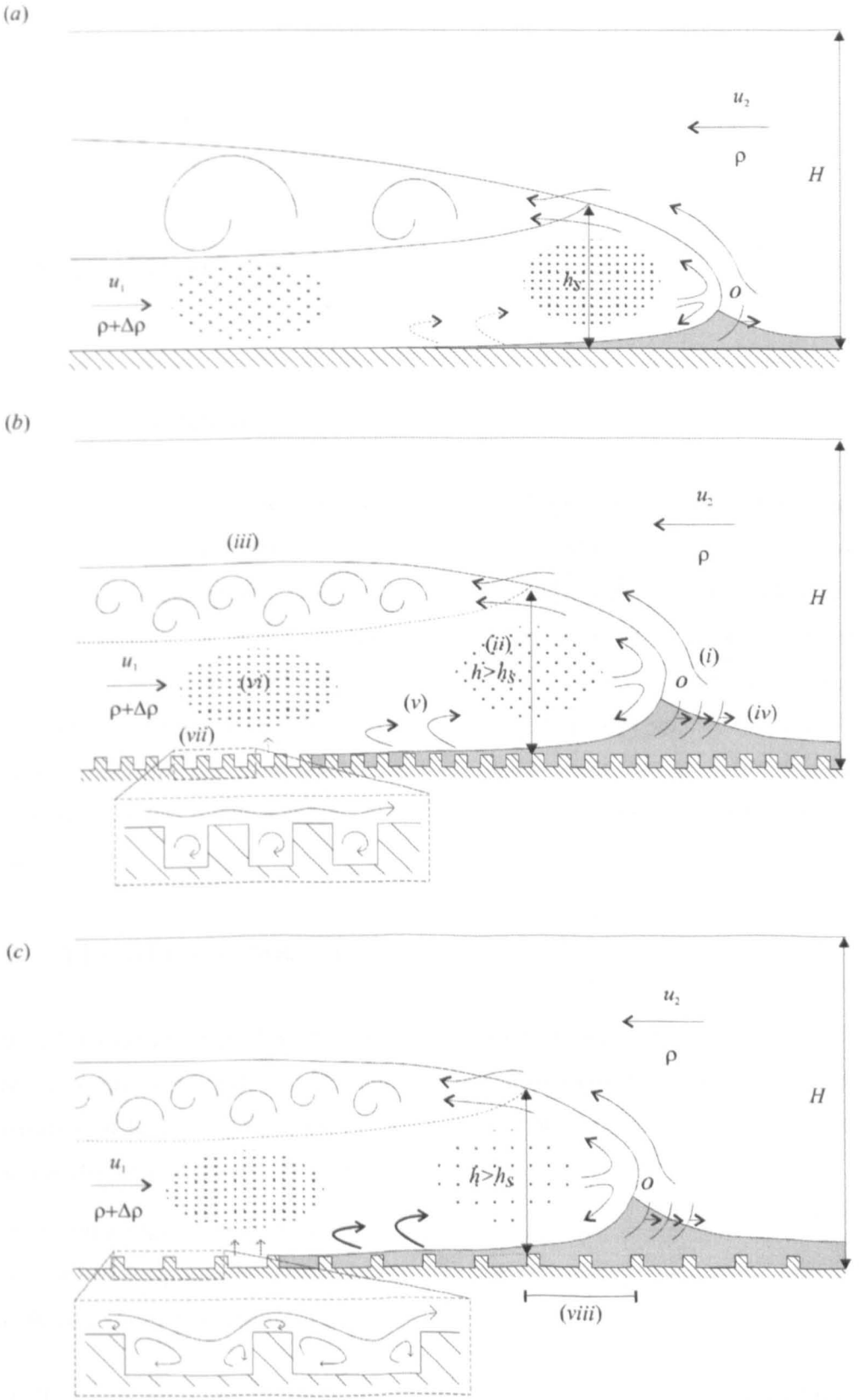
(a)
u_2
ρ
H
u_1
ρ+Δρ
h_s
o
(b)
u_2
ρ
(iii)
H
u_1
ρ+Δρ
(vi)
(ii)
$h_1 > h_s$
(i)
o
(v)
(iv)
(vii)
(c)
u_2
ρ
H
u_1
ρ+Δρ
$h_1 > h_s$
o
(viii)

Chapter 7

Conclusions

7.1 Introduction

The results of the present study on the influence of bed roughness on lock-release gravity currents have been presented and discussed in the foregoing chapters. This chapter concludes the present study. Firstly, the reader is reminded of the original aims of the thesis and testimony of fulfillment of these aims. The overall conclusions of this study and the implications of the effects of bed roughness on gravity currents are stated and conclusions have been drawn on the performance of the experimental and numerical techniques used for this investigation. Finally, further work for the development and extension of the investigation of bed roughness is suggested, based on the findings of the present study.

7.2 The aims of the thesis

The global aim of this thesis was to use experimental and numerical methods to create a knowledge database of the fundamental dynamics and flow structure of lock-release gravity currents flowing over rough surfaces and to discuss the implications for this case.

To the author's knowledge, there was little existing work dedicated to understanding the effects of bed roughness on lock release gravity currents. With this in mind, this thesis had three primary investigatory aims:

1. To carry out a reproducible and easily modified set of experiments in order to compile a new, accurate data set to extend and compliment the existing smooth bed studies. This data will be analysed in an experimental context and used for

rigorous theoretical comparison.

2. To study existing depth-averaged gravity current models and mathematical forms of including bed roughness in order to create a model for the rough surface and to fully validate this model using available data.

3. To use the CFD commercial software FLUENT to study the fully depth-resolved forms of the governing equations, including modifications for bed roughness, in order to create 2D and 3D numerical models and to fully validate this model using experimental data.

To address these aims, a new fundamental experimental dataset has been presented. This essentially comprises front positions, vertical and horizontal downstream velocity data and photographic footage of lock-release gravity currents propagating over five rough surfaces representing grain, d-type and k-type bed roughnesses. This has been extended to quantify the effects of bed roughness with changes in current density, height and the effect of dense fluid between the elements in controlling the dynamics of the d-type and k-type cases. This data has enabled the calculation of depth-averaged heights and velocities, Froude numbers, Reynolds numbers and equivalent roughness values, k_s, for each set of conditions.

A 1D depth-averaged model has been developed which extends current smooth models using 2-layer shallow water theory and the method of characteristics with new terms to account for the bed roughness effects at the bed and, if required, on the interface and top boundary. The model has been validated using available data and the extension for bed roughness shows convincing qualitative agreement with experimental roughness effects. The symbiotic relationship between experimental work and CFD has been highlighted in the present study. The experiments provide effective validation for the numerical models and in return the CFD is able to extend the velocity data and predict concentration fields and turbulence mechanics that are fundamental to the interpretation of gravity current flow over rough surfaces. Thus, the primary investigatory aims of this project have been accomplished and confirm that the proposed global aim has been achieved.

7.3 The effects of bed roughness on gravity currents

Figure 6.57 presented the first schematic description of the principal effects of bed roughness on gravity currents. The following remarks are the principal conclusions for the

present study and directly address the question of what influence bed roughness has on the dynamics of gravity currents. The reader is referred to figure 6.57 for illustration of the majority of these points.

Slows and deepens the current. The presence of any bed roughness reduces the distance travelled by the current before phase change occurs. Caused by increased turbulence mixing in the head due to increased ingestion of ambient fluid beneath the nose. The velocity core of the current is broken down and redistributed which creates a rounded, deeper flow profile with a velocity maximum further from the bed.

Removal of large instabilities at the density interface decreases entrainment. The Kelvin-Helmholtz billows at the density interface are either broken down or unable to form, particularly in the k-type case. Dilution in the head causes the front to slow which decreases the shear at the interface and thus removes the large instabilities. The significant result of this process is the substantial decrease in entrainment.

Overridden ambient fluid has significant effects on the internal flow structure. Increased regions of vertical motion are present within the currents and can be associated with reductions in horizontal motion which may represent ejections of buoyant fluid at the bed into the current. The disruption due to the presence of this fluid increases with the wider beam type element spacings since there is a greater volume of ambient fluid ejected into the flow which is less likely to be entrained near the bed and more likely to penetrate higher into the current depth.

Increased lateral motion and augmentation of lobe and cleft instability. The beam type roughness elements significantly increase lateral motion, particularly at the base of the current. This and the presence of the ambient fluid between the roughness elements augments the production of the lobe and cleft instabilities. In the k-type case, these are the predominant mechanisms causing this instability. In the d-type case, the increased surface friction due to the greater number of roughness elements is also a contributory factor.

$\approx$50% of loss of front speed is due to overridden ambient fluid. However, the increased entrainment of ambient fluid at the bed is not the sole contributory factor effecting the flow in the presence of roughness. The remaining effects are likely due to loss of energy to the vortices trapped between the elements which occur independent of the density of this trapped fluid.

The general rule $w/k_r \approx 7$ holds for gravity currents. This has been established

for pipe and duct flows and appears also to hold for gravity currents. Beyond this value the time the current takes to propagate a distance is almost independent of the spacing and similar reattachment lengths of approximately $4k_r$ have been observed. This means that if the value of w/k_r can be identified for a rough bed then theoretically there are a set of typical flow characteristics that can be assumed to hold within the gravity current.

Small-scale grain roughness shows little effect. The coarse sand shows little influence on the internal flow dynamics but does increase the basal friction. The larger scale grain type roughness showed similarities in effects with the closest spaced d-type beams case.

Dependency on the ratio of roughness element height to current depth. Increasing the relative height of the elements has significantly greater impact on the current.

3D modelling is required. Validation of the 2D and 3D models with the experimental data has resulted in the conclusion that the 3D model is vital for accurate simulation of internal dynamics of gravity current propagation over beam type bed roughness, since the lateral fluid mechanics are substantially increased.

These wide-ranging influences on the flow speed, flow structure, turbulence distribution and flow evolution of gravity currents illustrate the fundamental importance of including bed roughness when determining the properties of these complex flows. The results presented herein clearly demonstrate that the application of existing models that rely on experimental validation with smooth beds to situations where a rough boundary is present may lead to significant errors. In reality, where the majority of these currents are particulate, such as turbidity currents, there is also the potential for feedback processes.

7.4 Implications

This study has proven that the effects of bed roughness on gravity currents is significant. The results can be applied in many industrial and natural settings. In a geomorphological context, river dunes have wavelength to height ratios characterised by $h_d = 0.0677\lambda^{0.8098}$ (Ashley, 1990). In shallow canyon, sub-marine settings, dunes have also been identified. The dimensions of these features have been described similarly to those in rivers by $h_d = 0.0677\lambda^{0.8089}$ (Flemming, 2000). They can therefore be categorised as a k-type bed roughness. However, the resulting values of w/k_r are typically greater than 16, which is beyond the maximum used in the present study but would suggest limited influence on the flow dynamics. Even if they lay within the scope of this work, dunes have attributes

that have not been assessed herein. In particular, their asymmetry and the combination of grain and form roughness. These characteristics could form the basis for a future extension to this study.

The most detailed dataset of gravity current flow over dunes is that for the Monterey Canyon, where flows on the order 30 m thick (Xu *et al.* 2004, 2008) have been observed in conjunction with dunes of wavelength to height ratios of approximately $18 - 50$ (Xu *et al.*, 2008). The dunes are approximately 1-2 m high, which results in a relative roughness height of 3-7%. This is small compared to the present study where flow depths of approximately 40-60 mm encountered obstacles of height 6 mm producing relative roughness heights of 10-15% (5-10% concentrations). This, and the wide k-type spacing suggests that the dune roughness might not be that important in the Monterey example and similar settings. However, in a different context, the results of Gurioli *et al.* (2002) showed that even small steps 0.1-0.5 m high affected the turbulence and particle deposition of the pyroclastic overflow, although unfortunately the flow depth is unknown. In open channel flows, effects were observed for roughnesses as small as 1.7% of the channel height (Ashrafian *et al.* (2004); Krogstad *et al.* (2005)), and are postulated to be effective for channel half heights up to $40k_r$, suggesting that roughness effects should not be neglected even at such small scales, but need investigating further. Moreover, particulate currents with sand grade material will have high basal concentrations, relative to the saline current in the present study. Therefore, basal roughness will likely have a more pronounced effect, as demonstrated in Gurioli *et al.* (2002) where a step of 0.5 m, not high enough to affect the entire flow, was found to induce the settling of heavier particles and partial removal of fine material. This highlights a key extension to the present work into roughness effects on particulate flows.

In the deep sea, there is very little information on bed roughness. This is primarily due to the limited amount of high resolution multi-beam data and, moreover, the vertical resolution of even high resolution multi-beam. To fully comprehend gravity currents in such settings, the results of this study recommend that the magnitude and type of roughness be examined from detailed multi-beam datasets.

In industrial environments, the presence of bed roughness will have implications for smoke propagation or the release of heavy gases. For example, in transport tunnels where a fire accident may take place, a smoke (heat) generated gravity current propagates along the top of the tunnel and can cause a major hazard to tunnel users. Roughness on the walls of the tunnel would cause the propagation speed of the smoke to reduce.

The implications in this case might be detrimental or beneficial to the tunnel occupants and would be an interesting extension in that context. Another major hazard where roughness effects should be studied is that of avalanches. Powder-snow avalanches are a form of gravity current and are commonly managed using 'avalanche fences', which are known to slow their advance. The present study could have implications, with further investigation, for factors such as the spacing of these fences and thus their overall performance.

Implications derived from the effects of bed roughness that have been observed and predicted in the present study, and with further investigation may represent effects in the foregoing examples, are suggested below.

- Bed roughness leads to increased ejections into the flow at the bottom boundary. This augments dilution at the bed in saline currents but, conversely, may increase entrainment of bed material in natural flows. Buoyant ejections will enhance the mixing and vertical transport of particles to higher regions within the flow. This will impact significantly on the vertical distribution of the particles.

- Higher $\bar{u}_{max}$ positions will result in a reduction in basal shear stresses and may therefore reduce erosion. However, this may be offset by the increased turbulent ejections mentioned above. Higher $\bar{u}_{max}$ positions may also influence the nature of the secondary flow within sinuous channelised currents (Corney *et al.*, 2006, 2008; Keevil *et al.*, 2006).

- For saline currents, the smooth cases are driven by high concentrations in the head. Since there is little disruption the high concentration fluid is maintained in this region while the current behind is gradually diluted by the large interfacial billows. Eventually the dense fluid behind will become very dilute and without the continual supply of concentrated fluid, the head will also become dilute and the current will disperse. In the rough cases because the interfacial billows are reduced, the high concentration fluid to the rear is not diluted as quickly and so the body stratifies early on and the head has a continual feed of concentrated fluid to keep it maintained. However, the head becomes dilute very quickly due to basal entrainment of ambient fluid and loses energy to vortices trapped beneath it, which slow the current. In saline cases, this may imply that although slower, the rough cases may actually achieve greater run-out distances than the smooth cases since they appear more stable. However, this would strongly depend on the speed of dilution of the head or body in the smooth case or rough cases,

respectively, i.e. which loses its driving force sooner. These mechanisms imply very different entrainment characteristics compared to previous models and suggests that previous work has for the most part over-estimated entrainment rates and has implications for the stratification in particulate currents, with the upper part of the body potentially less dilute than previously predicted.

- The substantial reduction of concentration and velocities in the head and the shift of higher concentrations to the body of the current in rough cases have implications for the grading of sediment in particulate current deposits, although it is difficult to assess the relative strengths of the mechanisms.

- In the particulate cases, the billows over a smooth bed have been postulated to penetrate the body sufficiently to suspend sediment from the bed (Kneller *et al.*, 1999), which means that they provide a concentration supply to the current, as well as the means for its reduction by entrainment of ambient, achieving a balance. This would imply that the smooth currents would transport sediment loads composed of a combination of the sediment that was initially in suspension, plus that picked up by the billows during propagation. However, in the rough cases, the reduction in the billows and shear below the head would imply that it is relatively unlikely that significant amounts of sediment would be lifted from the bed, either in the head or the body. Therefore, in the rough case, the balance is achieved due to lack of these mechanisms. Consequently this implies that the currents would be more likely to transport material that they were composed of at flow initiation and not pick up and transport significant amounts of other sediment during propagation.

- There are implications following the above for particulate current run-out distances, although it is again difficult to assess the relative strengths of the mechanisms. Slower currents may lead to earlier and potentially greater sediment deposition, but reduced entrainment will result in the ability to achieve longer run-out distances. Moreover, the above does not account for flow transitions which will also impact on deposition and run-out distances.

7.5 Techniques

The experimental method using UDVP and video capture has been proven ideal for the efficient generation of quantitative datasets. The experimental setup is readily repeatable and could be easily reproduced and adjusted for extensions to the present study.

The 1D depth-averaged model predictions showed good agreement with available smooth bed data and encouraging qualitative comparison with features observed experimentally. The techniques used were well validated for the smooth case. The front condition is currently derived from smooth theory and the method also requires more complex extensions to account for full depth releases. However, as it stands this model has demonstrated that there is potential to adapt 1D models relatively simply to account for the 1D effects of bed roughness on gravity currents using existing expressions in pipe and open channel literature.

The 2D and 3D model setup using FLUENT successfully calculate the propagation and flow dynamics of a lock-release gravity current over smooth and rough surfaces. There are limitations in the turbulence model with regards to the wall functions being violated that must be considered and result in difficulties in checking the spatial and temporal convergence. Process representation increases with each mesh refinement which is essentially a positive result but means that accurate quantitative verification of one mesh using a coarser or finer mesh is less convincing. Without the ability to compute direct numerical simulations on successively finer meshes these limitations remain a hazard of modelling gravity currents numerically. However, by performing careful verification and validation the results from the less computationally intensive models used in the present study have been optimised in their capacity as predictive tools.

Modelling the bed roughness using a body-fitted mesh produces velocity profiles with particularly good accuracy and provides evidence of more realistic velocity profiles and concentration and turbulence distributions than the law-of-the-wall method. The limitation of this method is the shape of the roughness restricting the mesh or vice versa. Using a k_s value avoids limitations of cell shape but still has problems with reproducing internal dynamics accurately and has limits on the size of its value due to mesh resolution near the wall.

For accuracy, a 3D model should be used that can better resolve the lobe and cleft instability and Kelvin-Helmholtz billows and their accurate turbulent dissipation. This is particularly true in the bed-roughened cases since there are increased turbulence structures and lateral motion at the bed.

7.6 Future work

- It would be highly informative to compile a detailed database of known natural occurrences of gravity currents with details such as the speed, spread, depth and concentration of the current and finer details of the bed such as the presence of, for example, bed forms, and the height and distribution of these 'roughness elements'.
- Field data of bed roughness should be collected to assess the performance of all of the models.
- A laboratory project to obtain higher resolution data, for example from PIV or LDA would enable analyses of the detailed flow characteristics at the bed, particularly turbulence structures and concentration fields. This would confirm the accuracy of the k_s values and further validate the CFD models.
- Natural currents are more commonly particulate. Therefore investigations including particles, similar to that of Kubo (2003), should be developed further in both experiments and CFD simulations in order to establish the exact effects of bed roughness on sedimentation and sedimentary flow processes.
- Further investigation of the mechanisms controlling the roughness effects is necessary. For example, for the grain type beds could also be tested with a thin layer of dense fluid initialised between the elements. Tracer or particle tracking experiments could also be performed.
- The 1D depth-averaged model predictions showed good agreement with available smooth bed data and encouraging qualitative comparison with features observed experimentally. A study developing the rough front condition theory, coupled with high resolution experimental data would make an excellent future project.
- As computational power increases, large eddy and direct numerical simulations will be increasingly possible and will enable further detail of flow processes in the influential near wall region down to substantially smaller scales.
- The use of different roughness types would also be of interest. For example, non-homogeneous roughness; different shaped beams; a combination of grain and form roughness. Again, similar theoretical and experimental techniques, as adopted herein, could be modified to accommodate different roughnesses relatively simply.

References

Abbott, M.B. (1975). Method of characteristics. In K. Mahmood and V. Yevjevich (Eds.), *Unsteady Flow in Open Channels*, Volume 1, Chapter 3, pp. 63–88. Colorado: Water Resources Publications.

Acheson, D. J. (1990). *Elementary Fluid Dynamics*. Oxford: Oxford University Press.

Alahyari, A.A. and Longmire, E.K. (1996). Development and structure of a gravity current head. *Experiments in Fluids* **20**, 410–416.

Ames, W.F. (1965). *Nonlinear Partial Differential Equations in Engineering*. London: Academic Press.

Amy, L.A., Hogg, A.J., Peakall, J. and Talling, P.J. (2005). Abrupt transitions in gravity currents. *Journal of Geophysical Research* **110**, doi:10.1029/2004JF000197, 1–19.

Antar, N. and Moodie, T.B. (2003). Weakly nonhydrostatic effects in compositionally-driven gravity flows. *Studies in Applied Mathematics* **111**, 236–267.

Antar, N. and Moodie, T.B. (2005). Self-similarity and the evaluation of long-time nonhydrostatic effects in compositionally driven gravity flows in deep surroundings. *Studies in Applied Mathematics* **114**, 211–239.

Ashley, G.M. (1990). Classification of large-scale subaqueous bedforms; a new look at an old problem. *Journal of Sedimentary Research* **60**, 161–172.

Ashrafian, A. and Andersson, H. I. (2006). The structure of turbulence in a rod-roughened channel. *International Journal of Heat and Fluid Flow* **27**, 65–79.

Ashrafian, A., Andersson, H. I. and Manhart, M. (2004). DNS of turbulent flow in a rod-roughened channel. *International Journal of Heat and Fluid Flow* **25**, 373–383.

ASME (1993). Editorial policy statement on the control of numerical accuracy. *Journal of Fluids Engineering* **27**, 113–122.

Baines, P.G. (1984). A unified description of two-layer flow over topography. *Journal of Fluid Mechanics* **146**, 127–167.

Baines, P.B. and Guest, F. (1988). The nature of upstream blocking in uniformly stratified flow over long obstacles. *Journal of Fluid Mechanics* **188**, 23–45.

Bandyopadhyay, P. (1987). Rough-wall turbulent boundary layers in the transition regime. *Journal of Fluid Mechanics* **180**, 231–266.

Baum, H.R., Cassel, K.W., McGratten, K.B. and Rehm, R.G. (1995). Gravity-current transport in building fires. Technical Report 20899, National Institute of Standards and Technology, Society of Fire Protection Engineers, Boston.

Benjamin, B.T. (1968). Gravity currents and related phenomena. *Journal of Fluid Mechanics* **31**, 209–248.

Best, J. L., Kirkbride, A. D. and Peakall, J. (2001). Mean flow and turbulence structure of sediment-laden gravity currents: new insights using ultrasonic doppler velocity profiling. In W. McCaffrey, J. Peakall and B. Kneller (Eds.), *Special Publication of the International Association of Sedimentologists: Particulate Gravity Currents*, Volume 31, pp. 159–172. International Association of Sedimentologists.

Birman, V.F., Martin, J.E. and Meiburg, E. (2005). The non-Boussinesq lock-exchange problem. Part 2. high resolution simulations. *Journal of Fluid Mechanics* **537**, 125–144.

Bombardelli, F.A., Cantero, M.I., Buscaglia, G.C. and García, M.H. (2004). Comparative study of convergence of CFD commercial codes when simulating dense underflows. *Mecanica Computacional* **23**, 1187–1199.

Bongolan-Walsh, V. P., Duan, J., Fischer, P., özgökmen, T. and Iliescu, T. (2006). Impact of boundary conditions on entrainment and transport in gravity currents. *Applied Mathematical Modelling* **31**, 1338–1350.

Bonnecaze, R.T., Huppert, H.E. and Lister, J.R. (1993). Particle-driven gravity currents. *Journal of Fluid Mechanics* **250**, 339–369.

Bonnecaze, R.T., Huppert, H.E. and Lister, J.R. (1996). Patterns of sedimentation from polydispersed gravity currents. *Proceedings of the Royal Society of London* **452**, 2247–2261.

Bonnecaze, R.T. and Lister, J.R. (1999). Particle driven gravity currents down planar slopes. *Journal of Fluid Mechanics* **390**, 75–91.

Bournet, P. E., Dartus, D., Tassin, B. and Vincon-Leite, B. (1999). Numerical investigation of plunging density current. *Journal of Hydraulic Engineering* **125**, 584–594.

Britter, J.E. and Linden, P.F (1980). The motion of the front of a gravity current travelling down an incline. *Journal of Fluid Mechanics* **99**, 531–543.

Britter, R.E. and Simpson, J.E. (1978). Experiments on the dynamics of a gravity current head. *Journal of Fluid Mechanics* **88**, 223–240.

Buckee, C., Kneller, B. and Peakall, J. (2001). Turbulence structure in steady, solute-driven gravity currents. In W. McCaffrey, J. Peakall and B. Kneller (Eds.), *Special Publication of the International Association of Sedimentologists: Particulate Gravity Currents*, Volume 31, pp. 173–187. International Association of Sedimentologists.

Cantero, M.I., Balanchandar, S. and García, M.H. (2007a). High resolution simulations of cylindrical density currents. *Journal of Fluid Mechanics* **590**, 437–469.

Cantero, M.I., Balanchandar, S. and García, M.H. (2008a). An Eulerian-Eulerian model for gravity currents driven by inertial particles. *International Journal of Multiphase Flow* **34**, 484–501.

Cantero, M.I., García, M.H. and Balanchandar, S. (2008b). Effect of particle inertia on the dynamics of depositional particulate density currents. *Computers and Geosciences* **34**, 1307–1318.

Cantero, M.I., García, M.H., Buscaglia, G.C., Bombardelli, F.A. and Dari, E.A. (2003). Multidimensional CFD simulation of a discontinuous density current. In *Proceedings of the XXX International Association of Hydraulic Research Congress. Theme C (Density currents and stratified flow)*, Volume 1, pp. 405–411. August (2003), Thessaloniki, Greece.

Cantero, M.I., Lee, J.R., Balanchandar, S. and García, M.H. (2007b). On the front velocity for gravity currents. *Journal of Fluid Mechanics* **586**, 1–39.

Cebeci, T. and Bradshaw, P. (1977). *Momentum Transfer in Boundary Layers.* Washington: Hemisphere Publishing Corporation.

Chen, G.Q. and Lee, J.H.W. (1999). Turbulent gravity current of lock release type: A numerical study. *Communications in Nonlinear Science and Numerical Simulation* **4**, 20–24.

Choudhury, D. (1993). Introduction to renormalisation group method and turbulence modeling. Technical Report TM-107, Fluent Inc. Technical Memorandum.

Chow, V.T. (1959). *Open channel hydraulics.* London: McGraw-Hill.

Corney, R.K.T. (2005). *Numerical, analytical and experimental modelling of channelised gravity currents.* Phd thesis, University of Leeds.

Corney, R.K.T., Peakall, J., Parsons, D.R., Elliott, L., Amos, K.J., Best, J.L., Keevil, G.M. and Ingham, D.B. (2006). The orientation of helical flow in curved channels. *Sedimentology* **53**, 249–257.

Corney, R.K.T., Peakall, J., Parsons, D.R., Elliott, L., Amos, K.J., Best, J.L., Keevil, G.M. and Ingham, D.B. (2008). Reply to discussion of Imran *et al.* on "The orientation of helical flow in curved channels" by Corney *et al.*, Sedimentology, 53, 249-257. *Sedimentology* **55**, 241–247.

Cui, J., Lin, C-L. and Patel, V.C. (2003a). Use of large-eddy simulation to characterise roughness effect of turbulent flow over a wavy wall. *Journal of Fluids Engineering* **125**, 1075–1077.

Cui, J., Patel, V.C. and Lin, C-L. (2003b). Large-eddy simulation of turbulent flow in a channel with rib roughness. *International Journal of Heat and Fluid Flow* **24**, 372–388.

Cui, J., Patel, V.C. and Lin, C-L. (2003c). Prediction of turbulent flow over rough surfaces using a force field in large eddy simulation. *Journal of Fluids Engineering* **125**, 2–9.

D'Alessio, S.J.D., Moodie, T.B., Pascal, J.P. and Swaters, G.E. (1996). Gravity currents produced by a sudden release of a fixed volume of heavy fluid. *Studies in Applied Mathematics* **96**, 359–385.

D'Alessio, S.J.D., Moodie, T.B., Pascal, J.P. and Swaters, G.E. (1997). Intrusive gravity currents. *Studies in Applied Mathematics* **98**, 19–46.

Daly, B. J and Pracht, W. E. (1968). Numerical studies of density current surges. *Physics of Fluids* **11**, 15–30.

De Cesare, G., Schleiss, A. and Hermann, F. (2001). Impact of turbidity currents on reservoir sedimentation. *Journal of Hydraulic Engineering* **127**, 6–16.

Didden, N. and Maxworthy, T. (1982). The viscous spreading of plane and axisymmetric gravity currents. *Journal of Fluid Mechanics* **121**, 27–42.

Durbin, P.A., Medic, G., Seo, J-M., Eaton, J.K. and Song, S. (2001). Rough wall modification of two-layer k-e. *Journal of Fluids Engineering* **123**, 16–21.

Ellison, T.H. and Turner, J.S. (1959). Turbulent entrainment in stratified flows. *Journal of Fluid Mechanics* **6**, 423–448.

Engblom, W.A., Lake, L.W. and Bonnecaze, R.T. (2001). A front-capture scheme for the simulation of homogeneous and particle-laden gravity currents. *International Journal for Numerical Methods in Fluids* **35**, 961–982.

Fadlun, E.A., Verzicco, R., Orlandi, P. and Mohd-Yusof, J. (2000). Combined immersed boundary finite-difference methods for three-dimensional complex flow simulations. *Journal of Computational Physics* **161**, 35–60.

Fannelop, T.K. and Waldman, G.D. (1972). Dynamics of oil slicks. *AIAA* **10**, 506–510.

Felix, M. and Peakall, J. (2006). Transformation of debris flows into turbidity currents: mechanisms inferred from laboratory experiments. *Sedimentology* **53**, 107–123.

Fleischmann, C.M. and McGrattan, K.B. (1999). Numerical and experimental gravity currents related to backdrafts. *Fire Safety Journal* **33**, 21–34.

Flemming, B.W. (2000). The role of grain size, water depth and flow velocity as scaling factors controlling the size of subaqueous dunes. In *Marine Sandwave Dynamics*, pp. 55–60. March (2000), Lille, France.

FLUENT (2006). *FLUENT 6.2 User's Guide*. Sheffield Business Park, 6 Europa View, Sheffield, S9 1XH, UK: FLUENT Europe. www.fluent.co.uk.

French, R.H. (1994). *Open-Channel Hydraulics*. New York: McGraw-Hill.

Fukushima, Y. and Watanabe, M. (1990). Numerical simulation of density current underflow by the k-e turbulence model. *Journal of Hydroscience and Hydraulic Engineering* **8**, 31–40.

Gebhart, B., Jaluria, Y., Mahajan, R.L. and Sammikia, B. (1988). *Buoyancy-Induced Flows and Transport*. pp 1001. USA: Hemisphere.

Gladstone, C., Ritchie, L.J., Sparks, R.S.J and Woods, A.W. (2004). An experimental investigation of density-stratified inertial gravity currents. *Sedimentology* **51**, 767–789.

Gratton, J. and Vigo, C. (1994). Self-similar gravity currents with variable inflow revisited: Plane currents. *Journal of Fluid Mechanics* **258**, 77–104.

Grobelbauer, H.P., Fannelop, T.K. and Britter, R.E. (1993). The propagation of intrusion fronts of high density ratios. *Journal of Fluid Mechanics* **250**, 669–687.

Grundy, R.E. and Rottman, J.W. (1985). The approach to self-similarity of the solutions of the shallow water equations representing gravity-current releases. *Journal of Fluid Mechanics* **156**, 39–53.

Gurioli, L., Cioni, R., Sbrana, A. and Zanella, E. (2002). Transport and deposition of pyroclastic density currents over an inhabited area: the deposits of the AD 79 eruption of Vesuvius at Herculaneum, Italy. *Sedimentology* **49**, 929–953.

Hacker, J., Linden, P.F. and Dalziel, S.B. (1996). Mixing in lock-release gravity currents. *Dynamics of Atmospheres and Oceans* **24**, 183–195.

Hallworth, M.A., Hogg, A.J. and Huppert, H.E. (1998). Effects of external flow on compositional and particle gravity currents. *Journal of Fluid Mechanics* **359**, 109–142.

Hallworth, M.A., Huppert, H.E., Phillips, J.C. and Sparks, S.J. (1996). Entrainment into two-dimensional and axisymmetric gravity currents. *Journal of Fluid Mechanics* **308**, 289–311.

Hardy, R.J., Lane, S.N, Ferguson, R.I. and Parsons, D.R. (2003). Assessing the credibility of a series of computational fluid dynamic simulations of open channel flow. *Hydrological Processes* **17**, 1539–1560.

Harlow, F.H. and Welch, J.E. (1965). Numerical calculation of time-dependent viscous incompressible flow of fluid with free surface. *Physics of Fluids* **8**, 2182–2189.

Hartel, C. (2000). *Handbook of Computational Fluid Mechanics.* London: Academic Press.

Hartel, C., Carlsson, F. and Thunblom, M. (2000a). Analysis and direct numerical simulation of the flow at a gravity current head. Part 2: The lobe and cleft instability. *Journal of Fluid Mechanics* **418**, 213–229.

Hartel, C., Kleiser, L., Michaud, M. and Stein, C.F (1997). A direct numerical simulation approach to the study of intrusion fronts. *Journal of Engineering Mathematics* **32**, 103–120.

Hartel, C., Meiburg, E. and Necker, F. (2000b). Analysis and direct numerical simulation of flow at a gravity current head. Part 1: Flow topology and front speed for slip and no-slip boundaries. *Journal of Fluid Mechanics* **418**, 189–212.

Hatcher, L., Hogg, A.J. and Woods, A.W. (2000). The effect of drag on turbulent gravity currents. *Journal of Fluid Mechanics* **416**, 297–314.

Hogg, A.J., Ungarish, M. and Huppert, H.E. (2000). Particle-driven gravity currents: asymptotic and box model solutions. *European Journal of Mechanics B - Fluids* **19**, 139–165.

Hogg, A.J. and Woods, A.W. (2001). The transition from inertia- to bottom-drag dominated motion of turbulent gravity currents. *Journal of Fluid Mechanics* **449**, 201–224.

Hoult, D.P. (1972). Oil spreading on the sea. *Annual Review of Fluid Mechanics* **4**, 341–368.

Huppert, H. (1982). The propagation of two-dimensional and axisymmetric viscous gravity currents over a rigid horizontal surface. *Journal of Fluid Mechanics* **121**, 43–58.

Huppert, H. (2006). Gravity currents: A personal perspective. *Journal of Fluid Mechanics* **554**, 299–322.

Huppert, H. and Simpson, J.E. (1980). The slumping of gravity currents. *Journal of Fluid Mechanics* **99**, 785–799.

Ikeda, T. and Durbin, A. (2007). Direct simulations of a rough-wall channel flow. *Journal of Fluid Mechanics* **571**, 235–263.

Imran, J., Islam, M.A. and Kassem, A. (2008). "The orientation of helical flow in curved channels" by Corney *et al.*, Sedimentology, 53, pp. 249-257 - discussion. *Sedimentology* **55**, 235–239.

Imran, J., Kassem, A. and Khan, S. M. (2004). Three-dimensional modelling of density current, I. Flow in straight confined and unconfined channels. *Journal of Hydraulics Research* **42**, 578–590.

Jeffrey, A. and Tanuiti, T. (1964). *Nonlinear Wave Propagation with Application to Physics and Magnetohydrodynamics.* Academic Press.

Jimenez, J. (2004). Turbulent flows over rough walls. *Annual Review of Fluid Mechanics* **105**, 173–196.

Jin, S. and Xin, Z. (1995). The relaxation schemes for systems of conservation laws in arbitrary space dimensions. *Communications on Pure and Applied Mathematics* **48**, 235–276.

Kanarska, Y. and Maderich, V. (2003). A non-hydrostatic numerical model for calculating free-surface stratified flows. *Ocean Dynamics* **53**, 176–185.

Kassem, A. and Imran, J. (2001). Simulation of turbid underflows generated by the plunging of a river. *Geology* **29**, 655–658.

Kassem, A. and Imran, J. (2004). Three-dimensional modelling of density current, II. Flow in sinuous confined and unconfined channels. *Journal of Hydraulics Research* **42**, 591–602.

Keevil, G.M., Peakall, J., Best, J.L. and Amos, K.J. (2006). Flow structure in sinuous submarine channels: velocity and turbulence structure of an experimental submarine channel. *Marine Geology* **229**, 241–257.

Keulegan, G.H (1957). An experimental study of the motion of saline water from locks into fresh water channels. Technical Report 5168, U.S. National Bureau of Standards, U.S.

Keulegan, G.H (1958). The motion of saline fronts in still water. Technical Report 5831, U.S. National Bureau of Standards, U.S.

Kim, H.G. and Patel, V.C. (2000). Test of turbulence models for wind flow over terrain with separation and recirculation. *Boundary Layer Meteorology* **94**, 5–21.

Kim, H.G., Patel, V.C. and Lee, C.M. (2000). Numerical simulation of wind flow over hilly terrain. *Journal of Wind Engineering and Industrial Aerodynamics* **87**, 45–60.

Klemp, J.B., Rotunno, R. and Skamarock, W.C. (1994). On the dynamics of gravity currents in a channel. *Journal of Fluid Mechanics* **269**, 169–198.

Kneller, B.C., Bennett, S.J. and McCaffrey, W.D. (1997). Velocity and turbulence structure of density currents and internal solitary waves: potential sediment transport and the formation of wave ripples in deep water. *Sedimentary Geology* **112**, 235–250.

Kneller, B.C., Bennett, S.J. and McCaffrey, W.D. (1999). Velocity structure, turbulence and fluid stresses in experimental gravity currents. *Journal of Geophysical Research* **104**, 5381–5391.

Kneller, B. and Buckee, C. (2000). The structure of fluid mechanics of turbidity currents: a review of some recent studies and their geological implications. *Sedimentology* **47**, 62–94.

Krogstad, P.-A., Andersson, H.I., Bakken, O.M. and Ashrafian, A. (2005). An experimental and numerical study of channel flow with rough walls. *Journal of Fluid Mechanics* **530**, 327–352.

Krogstad, P.-A. and Antonia, R.A. (1999). Surface roughness effects in turbulent boundary layers. *Experiments in Fluids* **27**, 450–460.

Kubo, Y. (2003). Experimental and numerical study of topographic effects on deposition from two-dimensional, particle-driven density currents. *Sedimentary Geology* **164**, 311–326.

Lane-Serff, G.F., Beal, L.M and Hadfield, T.D. (1995). Gravity current flow over obstacles. *Journal of Fluid Mechanics* **292**, 39–53.

Lawrence, G.A. (1993). The hydraulics of steady two-layer flow over a fixed obstacle. *Journal of Fluid Mechanics* **254**, 605–633.

Leonardi, S., Orlandi, P and Antonia, R.A. (2003a). Turbulent channel flow with rod and square bar roughness. *QNET-CFD Network Newsletter* **2**, 22–25.

Leonardi, S., Orlandi, P., Djenidi, L. and Antonia, R. A. (2004). Structure of turbulent channel flow with square bars on one wall. *International Journal of Heat and Fluid Flow* **25**, 384–392.

Leonardi, S., Orlandi, P., Smalley, R. J., Djenidi, L. and Antonia, R. A. (2003b). Direct numerical simulation of turbulent channel flow with transverse square bars on one wall. *Journal of Fluid Mechanics* **491**, 229–238.

LeVeque, R.J. (1997). *Numerical Methods for Conservation Laws* (2nd ed.). Lectures in mathematics - ETH Zurich series. Basel: Birkhauser Verlag.

Liggett, J.A. (1975). Basic equations of unsteady flow. In K. Mahmood and V. Yevjevich (Eds.), *Unsteady Flow in Open Channels*, Volume 1, Chapter 2, pp. 29–62. Colorado: Water Resources Publications.

Lowe, R.J., Rottman, J.W. and Linden, P.F (2005). The non-Boussinesq lock-exchange problem. part 1. theory and experiments. *Journal of Fluid Mechanics* **537**, 101–124.

Maddux, T. B., McLean, S. R. and Nelson, J.M (2003a). Turbulent flow over three dimensional dunes: 2. fluid and bed stresses. *Journal of Geophysical Research* **108**, doi:10.1029/2003JF000018, 1–17.

Maddux, T. B., Nelson, J.M and McLean, S. R. (2003b). Turbulent flow over three dimensional dunes: 1. free surface and flow response. *Journal of Geophysical Research* **108**, doi:10.1029/2003JF000017, 1–19.

Marino, B.M. and Thomas, L.P. (2002). Spreading of a gravity current over a permeable surface. *Journal of Hydraulic Engineering*, 527–533.

Marino, B.M., Thomas, L.P. and Linden, P.F. (2005). The front condition for gravity currents. *Journal of Fluid Mechanics* **536**, 49–78.

Middleton, G.V (1966a). Experiments on density and turbidity currents. I. Motion of the head. *Canadian Journal of Earth Sciences* **3**, 523–546.

Middleton, G.V (1966b). Experiments on density and turbidity currents. II. Uniform flow of density currents. *Canadian Journal of Earth Sciences* **3**, 627–637.

Mills, A.F. and Huang, X. (1983). On the skin friction coefficient for a fully rough flat plate. *Journal of Fluids Engineering* **105**, 364–365.

Montgomery, P.J. (1999). *Shallow-water models for gravity currents.* Phd thesis, University of Alberta, Edmonton.

Montgomery, P.J. and Moodie, T.B. (1998). Analytical and numerical results for flow and shock formation in two-layer gravity currents. *Journal of the Australian Mathematics Society* **40(B)**, 35–58.

Montgomery, P.J. and Moodie, T.B. (1999). Two-layer gravity currents with topography. *Studies in Applied Mathematics* **102**, 221–266.

Montgomery, P.J and Moodie, T.B. (2001). Jump conditions for hyperbolic systems of conservation laws with an application to gravity currents. *Studies in Applied Mathematics* **106**, 367–392.

Montgomery, P.J. and Moodie, T.B. (2003). Generalisation of a relaxation scheme for systems of conservation laws with spatially dependent flux functions. *Studies in Applied Mathematics* **110**, 1–19.

Moodie, T.B. (2000). Hydraulic theory and particle-driven gravity currents. *Studies in Applied Mathematics* **105**, 115–120.

Moodie, T.B. (2002). Gravity currents. *Journal of Computational and Applied Mathematics* **144**, 49–83.

Moodie, T.B. and Pascal, J.P. (2001). Nonhydraulic effects in particle driven gravity currents in deep surroundings. *Studies in Applied Mathematics* **107**, 217–251.

Moodie, T.B., Pascal, J.P. and Swaters, G.E. (1998). Sediment transport and deposition from a 2-layer fluid model of gravity currents on sloping bottoms. *Studies in Applied Mathematics* **100**, 215–244.

Moody, L. F. (1944). Friction factors for pipe flow. *Transactions of the American Society of Mechanical Engineers* **66**, 671–684.

Necker, F., Hartel, C., Kleiser, L. and Meiburg, E. (2002). High-resolution simulations of particle-driven gravity currents. *International Journal of Multiphase Flow* **28**, 279–300.

Necker, F., Hartel, C., Kleiser, L. and Meiburg, E. (2005). Mixing and dissipation in particle-driven gravity currents. *Journal of Fluid Mechanics* **545**, 339–372.

Nikuradse, J. (1933). Stromungsgesetze in rauhen rohren. Technical Report 361, VDI Forschungsheft. English translation. 1950. Laws of flows in rough pipes. NACA TM 1292.

O'Brien, M.P and Cherno, J. (1934). Model law for the motion of salt water through fresh. *Transactions of the American Society of Civil Engineers* **99**, 576–594.

Okamoto, S., Seo, S., Nakaso, K. and Kawai, I. (1993). Turbulent shear flow and heat transfer over the repeated two-dimensional square ribs on a ground plane. *Journal of Fluids Engineering* **115**, 631–637.

Ooi, S-K., Constantinescu, G. and Weber, L. Large eddy simulation of lock-exhange gravity current flows at high Grashof numbers. *Journal of Hydraulic Engineering*.

Ooi, S-K., Constantinescu, G. and Weber, L. (2005). 2-d large eddy simulation of lock-exhange gravity current flows. In *XXXIst International Association of Hydraulic Research Congress*. September (2005), Seoul, South Korea.

Orlandi, P. and Leonardi, S. (2008). Direct numerical simualtion of three-dimensional turbulent rough channels: parameterisation and flow physics. *Journal of Fluid Mechanics* **606**, 399–415.

Orlandi, P., Leonardi, S. and Antonia, R.A. (2006). Turbulent channel flow with either transverse or longitudinal roughness elements on one wall. *Journal of Fluid Mechanics* **561**, 279–305.

Özgökmen, T.M. and Chassignet, E. (2002). Dynamics of two-dimensional turbulent bottom gravity currents. *Journal of Physical Oceanography* **32**, 1460–1478.

Özgökmen, T.M and Fischer, P.F. (2008). On the role of bottom roughness on overflows. *Ocean Modelling* **20**, 336–361.

Özgökmen, T.M., Fischer, P.F., Duan, J. and Iliescu, T. (2004a). Entrainment in bottom gravity currents over complex topography from three-dimensional non-hydrostatic simulations. *Geophysical Research Letters* **31**, 1–4.

Özgökmen, T.M., Fischer, P.F., Duan, J. and Iliescu, T. (2004b). Three-dimensional turbulent bottom density currents from a high-order non-hydrostatic spectral element model. *Journal of Physical Oceanography* **34**, 2006–2026.

Özgökmen, T.M., Fischer, P.F. and Johns, W. (2006). Product water mass formation by turbulent density currents from a high-order non-hydrostatic spectral element model. *Ocean Modelling* **12**, 237–267.

Özgökmen, T.M., Iliescu, T., Fischer, P.F., Srinivasan, A. and Duan, J. (2007). Large eddy simulation of stratified mixing in two-dimensional dam-break problem in a rectangular enclosed domain. *Ocean Modelling* **16**, 106–140.

Özgöokmen, T.M., Johns, W.E., Peters, H. and Matt, S. (2003). Turbulent mixing in the Red Sea outflow plume from a high-resolution nonhydrostatic model. *Journal of Physical Oceanography* **33**, 1846–1869.

Özsoy, E., Di Iorio, D., Gregg, M.C. and Backhaus, J.O (2001). Mixing in the Bosphorus Strait and the Black Sea continental shelf: observations and a model of the dense water underflow. *Journal of Marine Systems* **31**, 99–135.

Parsons, J. and García, M. (1998). Similarity of gravity current fronts. *Physics of Fluids* **10**, 3209–3213.

Patel, V.C. (1998). Perspective: Flow at high Reynolds number and over rough surfaces - Achilles heel of CFD. *Journal of Fluids Engineering* **120**, 434–444.

Patterson, M.D., Simpson, J.E., Dalziel, S.B. and Nikiforakis, N. (2005). Numerical modelling of two-dimensional and axisymmetric gravity currents. *International Journal for Numerical Methods in Fluids* **47**, 1221–1227.

Perry, A.E., Scholfield, W.H. and Joubert, P.N. (1969). Rough wall turbulent boundary layers. *Journal of Fluid Mechanics* **37**, 383–413.

Peters, W.D. (1999). *Rough-surface gravity current flows.* Phd thesis, University of New Brunswick.

Peters, W.D., Cogswell, S.R and Venart, J.E.S (1997). *Developments in Laser Techniques and Fluid Mechanics*, Chapter 3, pp. 325–339. Berlin: Springer.

Peters, W.D and Venart, J.E.S (2000). Rough-surface gravity current flows. In *Tenth Int. Symp. on Appl. of Laser Techniques to Fluid Mechanics*, Lisbon.

Petersen, R.L. (1987). Effect of roughness effects on heavier-than-air gas diffusion. *American Petroleum Institute, Health and Environment Sciences Department*, p. 44.

Petersen, R.L. and Ratcliffe, M.A. (1989). Effect of homogeneous and heterogeneous surface roughness on heavier-than-air gas dispersion. *American Petroleum Institute, Health and Environment Sciences Department, Session IIB: Modelling of Aerosol Clouds*, p. 16.

Prandtl, L. (1952). *Essentials of Fluid Dynamics.* Blackie and Son.

Rehm, R.G., McGrattan, K. ., Bau, H.R. and Cassel, K.W. (1995). Transport by gravity currents in building fires. In *Fire Safety Science - Proceedings of the Fifth International Symposium*, pp. 391–402.

Roache, P.J. (1994). Perspective: A method for uniform reporting of grid refinement studies. *Journal of Fluids Engineering* **116**, 405–413.

Roache, P.J. (1997). Quantification of uncertainty in Computational Fluid Dynamics. *Annual Review of Fluid Mechanics* **29**, 123–160.

Rottman, J.W. and Simpson, J.E. (1983). Gravity currents produced by instantaneous release of a heavy fluid in a rectangular channel. *Journal of Fluid Mechanics* **135**, 95–110.

Rottman, J.W., Simpson, J.E., Hunt, J.C.R. and Britter, R.E. (1985). Unsteady gravity current flows over obstacles: Some observations and analysis related to the phase ii trials. *Journal of Hazardous Mechanics* **11**, 325–340.

Rouse, H. (1965). Critical analysis of open-channel flow resistance. *Journal of the Hydraulics Division, Proceedings of the American Society of Civil Engineers* **91**, 1–25.

Schlichting, H. (1936). Experimentelle untersuchungen zum rauhigkeitsproblem. Technical Report 7, Ing. Arch. English translation. 19370. Experimental investigation of the problem of surface roughness. NACA TM 823.

Schlichting, H. (1960). *Boundary Layer Theory.* Series in Mechanical Engineering. McGraw Hill.

Schmidt, W. (1911). Zer mechanik der boen. *Z. Meterol.* **28**, 355–362.

Shin, J.O., Dalziel, S.B. and Linden, P.F. (2004). Gravity currents produced by lock exchange. *Journal of Fluid Mechanics* **521**, 1–34.

Sigurdsson, H., Cashdollar, S. and Sparks, S.R.J (1982). The eruption of Vesuvius in AD 59 - Reconstruction from historical and volcanological evidence. *American Journal of Archaeology* **86**, 39–51.

Simpson, J.E. (1972). Effects of the lower boundary on the head of a gravity current. *Journal of Fluid Mechanics* **53**, 759–768.

Simpson, J.E and Britter, R.E. (1979). The dynamics of the head of a gravity current advancing over a horizontal surface. *Journal of Fluid Mechanics* **94**, 477–495.

Simpson, J. E. (1997). *Gravity Currents in the Environment and the Laboratory* (2nd ed.). Cambridge University Press.

Southard, J. B. (2006). *An introduction to fluid motions, sediment transport, and current-generated sedimentary structures.* Department of Earth, Atmosphere and Planetary Sciences, MIT, Cambridge, Massechusetts 02139, USA: SC1 Course notes, ISC 2006, Fukuoka, Japan.

Straka, J.M., Wilhelmson, R.B., Wicker, L.J., Anderson, J.R and Droegemeier, K.K. (1993). Numerical solutions of a non-linear density current: A benchmark solution and comparisons. *International Journal for Numerical Methods in Fluids* **17**, 1–22.

Streeter, V.L. and Wylie, E.B. (1983). *Fluid Mechanics, First SI Metric Edition.* Tokyo: McGraw-Hill.

Tani, J. (1987). Turbulent boundary layer development over rough surfaces. In *Perspectives in Turbulence Studies.* Springer.

Tanino, Y., Nepf, H. and Kulis, P.S. (2005). Gravity currents in aquatic canopies. *Water Resources Research* **41**, 1–9.

Tennekes, H. and Lumley, J.L. (1972). *A First Course in Turbulence.* The MIT Press, USA.

Thomas, L.P., Dalziel, S.B. and Marino, B.M. (2003). The structure of the head of an inertial gravity current determined by particle tracking velocimetry. *Experiments in Fluids* **34**, 708–716.

Thompson, W.T., Holt, T. and Pullen, J. (2007). Investigation of a sea breeze in an urban environment. *Quarterly Journal of the Royal Meteorological Society* **133**, 579–594.

Tian, Z.Z., Kyte, M.D and Messer, C.J. (2002). Parallax error in video-image systems. *Journal of Transport Engineering* **128**, 218–223.

Van Rijn, L.C. (1984). Sediment transport, part iii: Bedforms and alluvial roughness. *Journal of Hydraulic Engineering* **110**, 1733–1753.

Versteeg, H. K and Malalasekera, W. (1995). *An Introduction to Computational Fluid Dynamics: The Finite Volume Method.* Essex, UK: Longman Scientific & Technical.

Von Karman, T. (1940). The engineer grapples with nonlinear problems. *Bulletin of the American Mathematics Society* **46**, 615.

Weng, W.G., Fan, W.C., Qin, J. and Yang, L.Z. (2002). Study on salt water modelling of gravity currents prior to backdrafts using flow visulaisation and digital particle image velocimetry. *Experiments in Fluids* **33**, 398–404.

Xu, J.P., , Wong, F.L., Kvitek, R., Smith, D.P. and Paull, C.K. (2008). Sand-wave migration in Monterey Submarine Canyon, Central California. *Marine Geology* **248**, 193–212.

Xu, J.P., Noble, M.A. and Rosenfeld, L.K. (2004). In-situ measurements of velocity structure within turbidity currents. *Geophysical Research Letters* **31 L09311**, 1–4.

Yen, B.C. (2002). Open channel flow resistance. *Journal of Hydraulic Engineering* **128**, 20–39.

Yoon, J. Y. and Patel, V. C. (1996). Numerical model of turbulent flow over sand dune. *Journal of Hydraulic Engineering* **122**, 10–18.

Yue, W., Lin, C-L. and Patel, V.C. (2005). Coherent structures in open-channel flows over a fixed dune. *Journal of Fluids Engineering* **127**, 858–864.

Yue, W., Lin, C-L. and Patel, V.C. (2006). Large-eddy simulation of turbulent flow over a fixed two-dimensional dune. *Journal of Hydraulic Engineering* **132**, 643–651.

Zhang, L., An, Y., Zhi, L., Chen, G.Q. and Lee, J.H.W. (2001). Numerical anatomy of lock release gravity current. *Communications in Nonlinear Science and Numerical Simulation* **6**, 183–192.

Zhu, D.Z. and Lawrence, G.A. (1998). Non-hydrostatic effects in layered shallow water flows. *Journal of Fluid Mechanics* **355**, 1–16.

Zhu, J.B., Lee, C.B., Chen, G.Q and Lee, L.H.W. (2006). PIV observation of instantaneous velocity structure of lock release gravity currents in the slumping phase. *Communications in Nonlinear Science and Numerical Simulation* **11**, 262–270.